Studies On Therapeutic Potential Of Various Nanomaterials And Ethnobotanical Ingredients In Preclinical Disease Model

THESIS

SUBMITTED FOR THE DEGREE OF

DOCTOR OF PHILOSOPHY (SCIENCE)

IN BIOCHEMISTRY

BY

ANIRUDDHA ADHIKARI

DEPARTMENT OF BIOCHEMISTRY

UNIVERSITY OF CALCUTTA

2021

Acknowledgements

Completing my Ph.D. and writing this dissertation was an amazing journey that would not have been possible without the support and encouragement of many outstanding people. I would like to take this opportunity to acknowledge them all for their kind support, motivation and various contributions towards the successful completion of my study.

First and foremost, I owe my deepest gratitude to my ever enthusiastic supervisor, Prof. Samir Kumar Pal for accepting me into his lab to work under his supervision and providing me with a fantastic intellectual environment. I am grateful for his constant motivation, belief in my abilities, and persistent availability to clarify my doubts despite his extremely busy schedule. It was his ability to cross the space between the knowledge levels and to bring closer some insights into the biological mysteries that actually initiated my commitment to fulfil this thesis. His continuous support and guidance, his unlimited enthusiasm, profound knowledge in the cross-disciplinary field of science and technology, commitment to the highest scientific standards, and unconditional backing during crisis that, taken together, make him an exemplary mentor. I have never seen him getting tired of work, which motivated me never to be exhausted. He like an affectionate father made me what I am today. He, sometimes being the toughest, has constantly forced me to remain focused on achieving my goal. I was fortunate enough to learn from his instrumental expertise and insights in nitty-gritties of experimental problems. His thoughtful guidance, warm encouragements, constructive criticisms, positive vibes, disciplined nature, and great leadership quality are the cornerstones of this thesis work. Thank you very much sir for being with me in all the ups and downs of my tiny research career and inspiring me to believe in my dreams.

I would like to express my sincere gratitude to Prof. Maitryee Bhattacharya for referring me to Prof. Pal. Without her recommendation I could never been selected in this project. I get amazed when I think about how much I disturbed her before I get into the Ph.D. She is also the person because of whom I fall in love with biophysical studies. Without her support I could not even cross the level of master's degree. Thank you ma'am for always being in my side and unconditionally supporting me in every corners of my life whenever I needed it.

I am also thankful to Dr. Siddhartha Bhattacharya and Dr. Debasish Pal for encouraging me to take the path of research from the bachelor's days. Without their unconditional support, and enthusiasm of making a world class animal house and molecular biology lab, this thesis could have taken a different shape. Thank you sir for keeping faith on me and providing such an exceptional research facility.

I am grateful to get the opportunity to actively work with many talented researchers from various national and international institutes. I would like to thank Dr. Asim Kumar Mallick, NRSMH, India, Dr. Anjan Das, NMCH, India, Prof. Vinod K. Bhutani, Stanford University, USA, Dr. Prantar Chakraborty, NRSMH, India, Dr. Debasish Bhattacharya, NRSMH, India, Dr. Supata Neogy, PHFI,

India, Prof. Samit K. Ray, SNBNCBS, India, Prof. Tanusri Saha-Dasgupta, SNBNCBS, India, Prof. Ranjan Das, WBSU, India, Dr. Subhananda Chakraborty, IIT-B, India, Dr. Sukhen Das, JU, India, Dr. Bhaskar Roy-Chowdhury, India, Dr. Sudeshna S. Chowdhury, St. Xavier's College, India, Dr. Omprakash Singh, India and Dr. Tapan Adhikari, IISS, India for fruitful collaborations.

I am especially grateful to you Nabarun da (Dr. Nabarun Polley, my mentor). You introduced me thoroughly and patiently to experimental working and always helped at potential scientific pitfalls. You supported me in both the practical and analytic part of the experiment, and gave me useful comments on my scientific writing, pushing me to improve myself. You always had an open ear, an open mind and great motivation.

I am also thankful to you, Soumendra Da (Dr. Soumendra Darbar). You are the person who though me the minute details of the animal studies and supported me in every phases of this Ph.D. tenure. I would also like to thank Srimoyee di (Dr. Srimoyee Saha) for introducing me to animal studies.

I'd like to express my sincere gratitude to all my seniors and colleagues for providing an enriching work environment. I want to thank all former and current members of the AOSL lab for helpful discussions and creating an atmosphere, which made the whole work fun! Thank you: Samim Da, Damayanti Di, Uttam Da, Shreasi Di, Priya Di, Anupam Da, Subrata Da, Susobhan Da, Prosenjit Da, Siddhi Di, Sayan Da, Ranajay Da, Tanushri Di, Tatini Di, Srabanti Di, Gulmi Di, Prasanna Da, Goutam Da, Nirmal Da, Animesh Da, Soumendra Da, Susmita, Monojit, Pritam, Ria, Tanima, Probir, Jayita, Tuhin, Santanu, Arnab, Somtirtha, Ramesh, Manali, Ankur, Sounak, Aman, Neha, Mahasweta, Arka, Arpan, Dipanjan, Nur, Deep Shikha, Amrita, Lopa, Nilanjana, Sanchari, Rajarshi, Nivedita, Oidrila, Anindita, Debanjana, Annie, Poulami, Avik, Shayantani, Sayan, Abhinava.

Damayanti Di, what to say about you! I always feel jealous thinking about your patience, dedication to work and basic understanding of science. Your politeness, ability to manage a "politically" difficult situation and calmness is something to be learned not only in the field of science but also in the way of life. How can I forget the moments while in Santa Barbara or Coorg or in other conferences. Thank you a lot.

A special thank goes to my beloved juniors, Susmita, Monojit, Pritam and Ria. I always feel fortunate to have enthusiastic and caring juniors like you. You supported your senior in every bit of his life. The funny moments you shared at or outside lab will always remain as twinkling stars in the sky of my mind. Alongside them Soumendra Da, and Uttam da are the part of my team with whom I shared many wonderful and glorious moments. Especial thanks to Susmita for being with me at difficult times of my Ph.D. career and working on behalf of me. I would specially like to thank Tanima for his continuous mental (the gossips) and experimental support.

Special thanks to Susmita, Pritam, Monojit and Ria for carefully proofreading my thesis. Special thanks to Animesh Da and Soumendra Da with whom I shared many joyful moments. Thanks to Nabarun Da, Samim Da, Susobhan Da, Susmita, Ria, Probir, Arka, Arpan for making the hostel stay a fun. Thanks to Priya Di and Damayanti Di for the precious moments I shared with you.

Writing this dissertation was not the lonely experience what it could have been because of cherished friends who provided enthusiasm and empathy in just the right doses. The wonderful companionship of Reshmita, Tanima, Cia, AD, Surupa, Debjyoti, Sreeparna, Sabina di, Rohini, Debashis, Madhushree, Indranil, Somesh, Alka, Somnath, Chumki, and many others ensures that I can only think back upon the last few years with feelings of fondness and reminisce.

I owe my thanks to all my teachers at Dept. of Biochemistry, University of Calcutta for teaching me the basics in the field of biological research. Special thanks go to Prof. Maitryee DasGupta and Dr. Sanjay Ghosh. Thank you ma'am, my 1st protocol in research became successful only because of you. You are the one who always asked to design experiments during classes. Whatever I may say about sir is very little. He tolerated my stupid questions outside the class and encouraged positively for research. He is the first person who taught me how to cite references in research articles. Thank you ADG sir (Prof. Anjan dasgupta) for always encouraging me. Thanks also to Prof. Prasanta Kr. Bag and Dr. Anirban Siddhanta for their precious teaching.

I also like to thank all my previous teachers at college and schools for giving me the light of education and directing me towards my passion. Thanks to all those technicians and support stuffs I met during the student life.

I am also thankful for the financial support and stipend, which I received as a Research Fellow by SNBNCBS who also provided me accommodation during the research tenure. A sincere appreciation to all the non-academic staffs, cleaners and gardeners of SNBNCBS who have maintained the magnificent ambience of the centre.

Finally, a great deal of gratitude is due to my family and friends, and especially my parents and Dada (Late Hemchandra Sarkhel) to whom this thesis is dedicated, for uncommon, unwavering and unsurpassed support throughout my studies. Without them, I could neither have completed my graduate or undergraduate studies nor have travelled such a long path. Thank you immensely.

Aniruddha Adhikari

Sector-III, Salt Lake City
Kolkata-106
April, 2021

To my friend, philosopher, and guide
(Dada, Late Hemchandra Sarkhel)
and my family

CONTENTS

Chapter 02: Overview of Experimental Techniques and Animal Models

CHAPTER 01

Introduction

1.1. BACKGROUND

Since prehistoric times, medicinal problems had been a major quest for all civilizations. Even in the present era of advanced bio-medical technologies, the worldwide burden of an aged population, threats of climate change, frequent incidence of new epidemic infections, the greater occurrence of chronic diseases, irregular and sedentary lifestyle along with shortcomings of conventional drugs, which include poor bioavailability, non-targeted delivery, nonspecific bio-distribution, unwanted metabolism in gastro-intestinal (GI) tract, low retention in the target organ, and undesired adverse effects have forced the researchers to look for alternative resources of medicines like nanomaterials (i.e., nanomedicines) and ethnobotanical substances (i.e., natural products).

The enthusiasm surrounding nanomedicines emerges from the unique possibility of precisely engineering their physicochemical properties such as size, shape, elasticity, surface charge, and surface functionalization to achieve desired *in vivo* behaviors [1,2]. Moreover, nanomaterials can integrate numerous targeting, sensing, diagnostic, and therapeutic functions and localize to almost any physiological compartment [3]. Moreover, the ability to use innovative materials or create composite particles, e.g., made from inorganic and polymeric materials, enables theranostic modalities that provide simultaneous diagnostic and therapeutic functionality [1].

Despite having innovative functionality and versatility, the therapeutic use of nanomaterials is still in its infancy. In most cases, it is used only as a functional component of a medical product, or as cargo for drug delivery [4]. Poor aqueous solubility, problem in large scale manufacturing, limited understanding about *in vivo* behavior and concern over the biocompatibility and safety has limited their use as medicine [5].

On the other hand, natural products from plants and other biological sources have historically provided an endless source of medicine, and remain an undiminished source of new pharmaceuticals [6-8]. Compounds derived from natural extracts are appealing for several reasons. They are often stereochemically complex, multi- or macrocyclic molecules (i.e., secondary metabolites) with limited likelihood of prior chemical synthesis, and they tend to have fascinating biological properties. But perhaps most notably, parent extracts have been 'clinically' tested in their traditional *milieu*, in some cases over millennia [6,9]. Despite having huge popularity and such long use, ethnobotanical substances are not embraced by the western physicians due to insufficient scientific understanding about their safety, efficacy and molecular mechanism of action [9].

Therefore, both nanomedicines and ethnobotanical substances hold great promise to become alternatives to molecular pharmaceuticals, but comprehensive research is required at first along a pathway of discovery, isolation, and mechanistic studies before eventual deployment in the clinic.

1.2. NANOMEDICINE

Engineered nanomaterials embrace the outstanding potential to improve disease diagnosis and treatment specificity [10-14]. They could help surmount the constraints of conventional therapeutics – from large-scale issues such as biodistribution, adverse side effects, and nonspecific delivery to small-scale obstacles like intracellular trafficking – through cell-specific targeting, molecular transport to specific organelles and other eccentric inherent properties [15]. By virtue of their size, nanomaterials hold enormous design freedom along with the ability to access

biological features at the subcellular level [3]. The versatile prospect of engineered nanomaterials in healthcare applications can be envisaged from four paradigm shifting properties which are absent in their bulk counterpart: 'scaffolds' to build upon, high surface area per unit volume (i.e., high proportion of atoms on and beneath the surface area), shape (e.g., sphere, cylinder, disk, hollow sphere, flower, tube etc.), and unique optical (e.g., multiple photoluminescence etc.) and magnetic properties (room temperature ferromagnetism etc.) [16]. Most importantly, nanomaterials often embrace all of these properties simultaneously.

1.2.1. Definition

Although, defining a term like 'nanomedicine' may sound easy, but, the difference in opinion among leading scientific apex bodies from around the world has ruled out the existence of a unified international definition of 'nanomedicine'. The two best possible definitions that come from the European Science Foundation (ESF) and the United States' National Institutes of Health (NIH) are:

> *"Nanomedicine uses nano-sized tools for the diagnosis, prevention and treatment of disease and to gain increased understanding of the complex underlying patho-physiology of disease. The ultimate goal is to improve quality of life."* [17]

and,

> *"An offshoot of nanotechnology, [which] refers to highly specific medical interventions at the molecular scale for curing disease or repairing damaged tissues, such as bone, muscle, or nerve."* [18]

Fundamentally, two schools of thought are eminent in the various definitions of 'Nanomedicine'. One thought is very general claiming nanomedicine as a technology that uses molecular tools and knowledge of the human body to treat, prevent or diagnose diseases [4]. The other thought focuses on the medicinal use of the original concept of nanotechnology; the unique physicochemical effects that take place at the interface between the molecular and macroscopic world in which quantum mechanics still reign [19]. It is worth mentioning here that this thesis broadly deals

with both the concepts and particularly focuses on understanding the therapeutic effects of nanoparticles at the molecular level. Likewise, the nanoparticles can be defined as, "*a natural, incidental or manufactured material containing particles, in an unbound state or as an aggregate or as an agglomerate and where, for 50% or more of the particles in the number size distribution, one or more external dimensions is in the size range 1 nm–100 nm*" [20].

1.2.2. Healthcare Applications of Nanomedicine

The term 'Nanomedicine' can be traced back to the late 1990s, and first appeared in scientific literature in the year 2000 (Institute for Scientific Information, Thompson, Philadelphia, PA, USA) [21]. Since then, various nanoscale materials have turned out to be useful for application in health and diseases. Some of the materials have already been approved by the US Food and Drug Administration (US FDA) for human use [22-24]. Following is a summary of few notable usages of nanomaterials in healthcare applications.

1.2.2.1. Drug delivery

Nanoscale materials serve as excellent carriers of other active molecular or macromolecular agents, and have several advantages [25]. They enable stable aqueous dispersions of active, but poorly water soluble molecular agents. Their exquisitely tailored physicochemical and surface properties can protect the encapsulated agents from degradation by various endogenous defense mechanisms including enzymatic or immune degradation, mucociliary clearance in the lungs and acid hydrolysis in the stomach [26]. Control of their size, shape, and surface properties allows them to target not only specific organs/tissues in the body, but also the subcellular organelles [27]. Another major benefit is that a nanocarrier matrix can be designed for controlled release of drugs at target areas for optimal and sustained drug action [28-30]. Drug delivery using polymeric nanoparticles is perhaps the most widely used application of nanomaterials in the field of healthcare and therapeutics.

1.2.2.2. Medicine and therapy

Direct use of nanoparticles as a pharmaceutical agent is sparse in literature, except for cancer therapeutics. Recently, some studies have explored the possibility of using inorganic nanoparticles for the treatment of neurodegenerative diseases [31-33], diabetes [34-36], cardiovascular diseases [37-39] and wound healing [40-42]. However, with the unique physico-chemical properties which are different from conventionally used small-molecule drugs, nanoparticles hold an enormous promise of being effective therapeutics against many more unmet diseases. Particularly, the redox properties of the transition metal oxide nanoparticles can help in cellular health modulation, which is the principal aim of this thesis.

1.2.2.3. Diagnostics

The previously mentioned optical and magnetic properties have led to significant advancement of nanoparticle mediated disease diagnostics. Nanoparticle are used as contrast agents, particularly for MRI and ultrasound that provide improved contrast and favorable biodistribution [4]. For example, superparamagnetic iron oxide nanoparticles (SPION) for use as MRI contrast agents, which have also been approved by the FDA [43-45]. Novel sensor concepts based on nanotubes, nanowires, cantilevers or atomic force microscopy have been applied to diagnostic devices/sensors [46,47]. These sensors aim to improve the sensitivity, reduce production costs or measure novel analytes (e.g., Alzheimer plaques) that until recently could not be detected.

1.2.2.4. Implants

Self-assembling particles or other types of nanomaterial that improve the mechanical properties and the biocompatibility of biomaterials have been used for medical implants [48,49]. Examples include nanocomposite materials used as dental fillers [50] and nano hydroxyapatite used for implant coatings and bone substitutes [51,52]. Also decoration of implant materials with biologically active signal molecules that stimulate, for example, cell growth or differentiation [4,53].

1.2.3. Challenges for Clinical Translation of Nanomedicine

The transformation of nanomedicines from bench to bedside clinical usage is a costly, laborious and lengthy procedure. The complexity of nano-based drugs in comparison to conventional formulations containing free drug dispersed in a base (e.g., tablets, capsules and injections) makes the whole translation process more challenging [5,54-56]. Fundamental challenges related to the clinical translation of nanomedicines are briefed in Table 1.1, which includes biological challenges, large-scale manufacturing issue, biocompatibility and safety, intellectual property (IP), government regulations, and overall cost-effectiveness in comparison to the current therapies [57-60]. In the following section some of the key concerns relevant to this thesis have been discussed in the details.

1.2.3.1. Biological challenges

The biodistribution of nanoparticles, and of any other agent, is primarily governed by their ability to negotiate biological barriers [61]. Several extremely effective physiological obstacles, called biological barriers, largely prevent injected chemicals, biomolecules, nanoparticles and any other foreign agents from reaching their intended destinations and manifesting their effects. These barriers include: the reticulo-endothelial system, endothelial or epithelial membranes, complex networks of blood vessels, abnormal flow of blood, and interstitial pressure gradients [62]. Understanding the mutual association between biology and nanotechnology, including the influence of disease pathophysiology on nanomedicine accumulation, distribution, retention and efficacy, as well as the biopharmaceutical correlation between their inherent properties and *in vivo* behavior in animals (eventually in humans) are essential determinants for the successful translation of nanomedicines [5]. Therefore, implementation of a disease-driven approach by rationally designing and developing nanomedicines that can take advantage of pathophysiological changes in disease conditions is believed to be fruitful in widespread use of nanomedicines in current healthcare scenario [5,63].

Table 1.1. Challenges for the translational development of nanomedicine [5].

Nanopharmaceutical Design	
Key Considerations	Route of administration
	Reduction of complexity in formulation design
	Final dosage form for human usage
	Biocompatibility and biodegradability
	Pharmaceutical stability (both physical and chemical)
Current Obstacles	Large scale production according to GMP standard *e.g., reproducibility, infrastructure, techniques, expertise and cost*
	Quality control assays for characterizations *e.g., size and polydispersity, morphology, charge, encapsulation, surface modification, purity and stability*
Preclinical Evaluation	
Key Considerations	Need for validated and standardized assay for early detection of toxicity
	Evaluation in appropriate animal models of the disease
	Adequate understanding of *in vivo* behavior including cellular and molecular interactions *Pharmacokinetics (absorption, distribution, metabolism, excretion)* *Pharmacodynamics (intracellular trafficking, functionality, toxicity, degradation)*
Current Obstacles	Development of more specific toxicology study protocol for nanomedicines
	Adequate understanding of the interaction of nanomedicines with cells and tissues
	Adequate structural stability of nanomaterials after *in vivo* administration
Clinical Evaluation for Commercialization	
Key Considerations	Simplification of development pathways from invention to commercialization to minimize time and expense
	Evaluation of safety/toxicity in humans
	Evaluation of safety and efficacy in patients
	Optimal clinical trial design
Current Obstacles	Lack of clear regulatory guideline specific for nanomedicines
	Limited understanding of the biological interaction of nanomaterials with the biological environment (i.e., target site) in the body of the patient

1.2.3.2. Biocompatibility and safety

With the growing number of nanomaterials for applications in various sectors of day-to-day human life, concerns about their potential adverse health effects are rising [64-66]. Knowledge about the interactions of nanostructures with biological systems with an emphasis on elucidating the relationship between the physical and

chemical properties (e.g. size, shape, surface chemistry, composition, and aggregation) of nanostructures with induction of toxic biological responses is becoming an important factor for the rational design of nanomedicines [67-69]. In the last decade, mainstream nanotoxicity research has been concentrated on cell culture systems; however, the results from these studies could be deceptive and necessitates the need for authentication from animal experiments [67]. It is worth mentioning here that *in vivo* systems are extremely complicated and the interactions of the nanostructures with biological components, such as proteins and cells, could lead to unique biodistribution, clearance, immune response, and metabolism [70,71]. An understanding of the relationship between the physical and chemical properties of the nanostructure and their *in vivo* behavior is extremely needed to provide a basis for assessing toxic response and more importantly could lead to predictive models for assessing toxicity [64,72]. These parameters need to be well-investigated based on dose, dosage form and route of administration to establish safe limits prior to clinical trials [5,73,74].

1.3. ETHNOBOTANICAL SUBSTANCES

Historically, ethnomedicines or traditional medicines have been used by various ethnic groups (i.e., indigenous communities) for generations to cure diseases [75]. Before the 20th century, therapeutic strategies relied almost exclusively on ethnopharmacological knowledge of multicomponent medicines, acquired from natural resources [6]. Natural products particularly plant based ingredients (i.e., ethnobotanical substance) still remain as one of the integral components of traditional medicines [76-79]. Even after discovery of modern medicines, the majority of new drugs have been generated from natural products (i.e., secondary metabolites) and from compounds derived from natural products [80-82]. The therapeutic success of natural product based drugs ranges from cancer and infectious diseases [7,83], to cardiovascular diseases (e.g., statins) and multiple sclerosis (e.g., fingolimod) [84-86].

Natural products have several distinct features when compared with orthodox synthetic molecules, in turn making the drug discovery process both advantageous and challenging [87]. Natural products hold enormous scaffold diversity and structural complexity. They typically have a higher molecular mass, a larger number of sp3

carbon atoms and oxygen atoms but fewer nitrogen and halogen atoms, higher numbers of H-bond acceptors and donors, lower calculated octanol–water partition coefficients (cLogP values, indicating higher hydrophilicity) and greater molecular rigidity compared with synthetic compound libraries [88-90]. While the structural complexity and associated rich functionalities are attributed for their great potency and exquisite selectivity, natural products often interacts with multiple biological targets, challenging the prevailing paradigm of mechanism-based drug discovery [91]. The intricate interplay between natural products and the complex biological networks, thereby provides novel drug designing opportunities. Additionally, natural products are structurally 'optimized' by evolution to serve particular biological functions, including the regulation of endogenous defence mechanisms and the interaction (often competition) with other organisms, which explains their high relevance for treatment of infectious diseases and cancer [87]. Finally, the natural products pool is enriched with 'bioactive' compounds covering a wider area of chemical space compared to typical synthetic small-molecule libraries [92,93].

Despite these advantages and multiple successful drug discovery examples, during the past 15 years, pharmaceutical industry research into natural products has declined. The reasons include unavailability of low cost and budget-friendly 'smart screening' methods for identification of the bioactive compounds or active ingredients, and concerns over getting intellectual property rights (IPR) on parent natural products [94,95]. This de-emphasis in ethnobotany-inspired drug discovery unfortunately correlated with the overall reduction in new leads in the drug development pipeline and the substantial decline in new drug approval [88,91]. Therefore, improved analytical tools, *in silico* prediction methods, fundamental understanding of natural product biosynthesis, genome mining and engineering strategies are urgently needed to uphold the interest of pharmaceutical industries on ethnomedicines and natural product driven drug discovery.

1.3.1. Challenges for Ethnobotanical Medicines

Botanical therapies comprising complex mixture of natural compounds have long fascinated researchers because of the prospective synergistic healing effects of

constituent components within the mixture [6]. Yet, the variability of the natural compounds present in the starting plant material due to factors like environmental disparities in the location at which the plants were grown up and collected is the major challenge for the development of botanical drugs [7]. Concern about their safety and efficacy, limited knowledge about their molecular mechanism of action, and lack of standardized screening methodology hinders the proper rationalization and limits the widespread use of traditional medicines as therapeutics. However, with the advances in characterization techniques, such as metabolomics, along with development of regulatory guidelines for complex mixtures of natural products, it is becoming more feasible to develop such complex mixtures as medicine, rather than to identify and purify a single active ingredient which is time consuming, cumbersome and expensive [96]. The following sections discuss in details some of the challenges about the rationalization and use of ethnobotanical ingredients as alternative therapeutic strategy which falls within the scope of this thesis.

1.3.1.1. Identification of bioactive compounds (i.e., active ingredients)

Identification of the active components of an ethnomedicine is important as traditional knowledge and traditional plant species both are being lost at an alarming rate [9]. Therefore, knowledge of the bioactive compounds can be effective in developing synthetic analogs or biosynthesis using cell culture or transgenesis to enable large-scale productions. However, experimentally identifying active ingredients from a complex mixture of numerous natural molecules having different polarities is tremendously challenging. The incompatibility of naturally extracted compounds even in state-of-the-art high throughput screening (HTS) platforms due to presence of partially purified compounds, in addition to the pure ones, makes the process more daunting [91]. In this regard bioinformatics tools can play a positive role as a screening technique to sieve potential bioactive molecules. The bioactivity of a compound is dictated by its ADMET (Absorption, Distribution, Metabolism, Excretion and Toxicity) properties [97-100]. Due to the presence of effective high performance computing resources, the ADMET properties of a natural compound can easily be calculated [97,99]. And those having favorable ADMET characteristics can further be evaluated using sophisticated experimental facilities.

1.3.1.2. Identification of the molecular mechanism of action

While traditional medicines, particularly herbal formulations, have been used for millennia and showed efficiency in treatment of several chronic diseases, their molecular mechanism of action still remains a 'black box' due to lack of both standardized experimental protocols and interest of the modern scientists [101-103]. Many a promising therapeutic natural product has faltered due to lack of a clear-cut mechanism of action [9]. One of the major reasons may be the synergistic effect of hundreds of bioactive molecules present in a single formulation that targets numerous intracellular protein networks which is difficult and expensive to study [104-106]. This type of complex interaction is completely opposite to the dominant paradigm of drug discovery which is based upon the concept of designing maximally selective ligands to act on individual drug targets [107-109]. Although, identification of a definitive mechanism of action is not required to use a formulation in clinical settings so far as it can treat the disease without adverse effects, but knowledge about its *in vivo* behavior provides chances of rational derivatization to improve affinity, specificity, pharmacokinetics and stability [9]. Therefore, it is of considerable interest to develop a cost-effective easier evidence-based approach for understanding the molecular mechanism of action of enthnobotanical drugs.

1.4. SCOPE OF THE THESIS

Nanomedicines and ethnomedicines represent the fastest growing and most promising areas of alternative medicine. However, several challenges remain in the way of their clinical translation. Both the fields are greatly unexplored and have the potential to dramatically change the current concept of therapeutics.

The innovative use of engineered nanomaterials in medicine, be it in therapy or diagnosis, is emerging sharply. This is motivated by the current extraordinary control over the synthesis of complex nanomaterials with a variety of biological functions. While the use of nanoparticles in diagnosis particularly as imaging agents is in advanced stage, the direct therapeutic application of nanoparticles is significantly

lagging behind. The major limiting factors are concerns and lack of evidence about their therapeutic action, pharmacokinetic properties, biodistribution, toxicity and molecular mechanism of action (described in details in previous section). To circumvent these challenges more detailed studies are required. Rational designing of nanomaterials along with comprehensive and systemic animal trials can help to overcome these matters.

On the other hand ethnobotanical ingredients are attractive because of their wide availability, low cost and biocompatibility due to co-evolution with human race. However, lack of knowledge about their complex molecular mechanism of action is a major limiting factor. Rationalization of ethonomedicines requires high-throughput screening (HTS) which is laborious and time consuming, resulting into a decreasing interest of the pharma companies. Therefore easier and low-cost methods are required for rationalization of these medicines which can eventually be trialed on animal models to get further insights.

However, despite recent advances, more comprehensive studies are required for both the systems. For example, i) proper testing in animal models following standard guideline along with required modifications which are essential for these innovative class of molecules, ii) proper dose determination by studying the *in vivo* pharmacokinetic and pharmacodynamics parameters, ii) understanding about systemic toxicity both acute and chronic, iv) understanding the molecular mechanism of action, v) for ethnobotanical ingredients, an easier approach for rationalization which will take lower time and low resources. These crucial requirements create the scope of this thesis.

Therefore, the key focus of this thesis is A) to explore whether inorganic nanoparticles can be efficacious in treatment of chronic diseases, B) to explore how an engineered nanomaterial interacts with bodily parameters *in vivo* or to explore its systemic toxicity, C) to understand the molecular mechanism of action of the nanomaterials and how they differ from the traditional synthetic drugs, D) to design a combined computational and experimental approach for rationalization of traditional ethnobotanical ingredients for use in therapeutics and to understand the molecular mechanism of action.

The first part of this thesis explores the therapeutic potential of a promising surface functionalized inorganic nanoparticle (citrate functionalized Mn_3O_4 nanoparticles, C-Mn_3O_4 NPs) as a model system. C-Mn_3O_4 NPs have shown unprecedented catalytic activity towards bilirubin. Here, using animal model, we have shown that it can potentially treat severe neonatal hyperbilirubinemia and bilirubin encephalopathy. We further explored the pharmacokinetic and pharmacodynamic properties along with *in vivo* biodistribution which describes its translocation to the liver, kidney and brain. The organ specific biodistribution and translocation profile of C-Mn_3O_4 NPs helped in considering the nanoparticle for treatment of related diseases like hepatic fibrosis, chronic kidney disease and neurodegenerative disorders. While exploring the molecular mechanism of action it was discovered that the nanoparticle mimics glutathione peroxisdase (GPx) enzyme and thus protects mitochondria, the master regulator of intracellular ROS. Consequently, the NPs maintain the cellular redox homeostasis. Detailed study suggests that, in fact, the NPs function as a redox buffer in cellular *milieu*. Furthermore, we have demonstrated that the nanoparticle can chelate heavy metals inside the body and treat heavy metal toxicity. A detailed chronic toxicity study depicts the nanoparticle to be safe at the therapeutic regime. Moreover, the nanoparticle could be administered orally which is a very difficult route of administration. In brief, the first part of the thesis provides a comprehensive framework for the transition of a nanomedicine from bench to clinical trial.

In the second part of the thesis, a protocol is developed to understand the active ingredients in a poly herbal formulation by using HR-LCMS and computational studies. The process is efficient enough to rationalize any polyherbal formulation to a disease. Moreover, the process can predict the molecular mechanism of action using simple bioinformatics tools. A detailed experimental study proved the functionality of the approach.

1.5 SUMMARY OF THE WORK DONE

1.5.1. Nanotherapy of Neonatal Hyperbilirubinemia

1.5.1.1. A novel nanoceutical agent for chemoprevention of bilirubin encephalopathy [110]

Targeted degradation of bilirubin *in vivo* may enable safer and more effective approach to manage incipient bilirubin encephalopathy consequent to severe neonatal hyperbilirubinemia (SNH). This study builds upon the use of a spinel structured mixed-valence transition metal oxide (trimanganese tetroxide) nanoparticle duly functionalized with biocompatible ligand citrate (C-Mn_3O_4 NP) having the ability to degrade bilirubin without photo-activation. The efficiency of C-Mn_3O_4 NP in *in vivo* degradation of serum bilirubin and amelioration of severe bilirubin encephalopathy and associated neurobehavioral changes was evaluated in C57BL/6j animal model of SNH. Oral single dose (0.25 mg kg^{-1} body weight) of the NPs efficiently reduced serum bilirubin levels (both conjugated and unconjugated) in study mice. It prevents bilirubin-induced neurotoxicity with reduction of SNH as observed by neurobehavioral and movement studies of SNH-mice. Pharmacokinetic data suggests intestinal reabsorption of the NPs and explain sustainable action. Biodistribution, pharmacokinetics, and biocompatibility of the NPs were tested during sub-chronic exposure. Therefore, we report preliminary studies that explore a chemoprevention mechanism to acutely prevent or minimize bilirubin neurotoxicity.

1.5.2. Oral Nanotherapy of Chronic Liver Diseases

1.5.2.1. Citrate functionalized Mn_3O_4 nanoparticles in nanotherapy of hepatic fibrosis by oral administration [111,112]

Hepatic fibrosis is a common response to chronic liver injury from a number of causes including alcohol, toxin, and persistent viral and helminthic infections, which may ultimately lead to hepatic carcinoma. Although billions of people are affected throughout the world, there is no drug available for the treatment of this chronic disease. Here, in a preclinical study using CCl_4-intoxicated Swiss-albino mice, we have

shown that oral administration of citrate functionalized Mn_3O_4 nanoparticles (C-Mn_3O_4 NPs) can effectively reduce the extent of liver fibrosis. Further investigations revealed that C-Mn_3O_4 NPs show increased antioxidant activity upon acid treatment (both *in vitro* and *in vivo* i.e., stomach), which is in turn responsible for its hepatoprotective nature. Assessment of various liver function parameters along with histopathology and immunohistochemistry were performed to evaluate pathophysiological condition of the liver. To unravel the mechanisms involved in attenuation of liver injury by NPs, various antioxidant parameters (like superoxide dismutase, catalase, glutathione peroxidase, reduced glutathione etc.) were also examined. An in depth study of the effect of C-Mn_3O_4 NPs on mitochondria, the cellular mediator of oxidative stress further revealed the molecular mechanism behind its therapeutic efficacy. To the best of our knowledge, this is the first study that demonstrates direct oral treatment of an inorganic NP (i.e., C-Mn_3O_4 NPs) without any delivery system can efficiently reduce chronic hepatotoxicity and liver fibrosis through its antioxidant and mitoprotective activity.

1.5.3. Nanomedicine for Chronic Kidney Disease

1.5.3.1. Redox nanomedicine cures chronic kidney disease (CKD) by mitochondrial reconditioning [113]

Targeting reactive oxygen species (ROS) while maintaining cellular redox signaling is crucial in the development of redox medicine for the therapeutic benefit as the origin of several prevailing diseases including chronic kidney disease (CKD) is linked to ROS imbalance and associated mitochondrial dysfunction. Here, we have shown that an indigenously developed nanomedicine comprising of Mn_3O_4 nanoparticles duly functionalized by biocompatible ligand citrate (C-Mn_3O_4 NPs) can maintain cellular redox balance in an animal model. We developed a cisplatin-induced CKD model in C57BL/6j mice where severe mitochondrial dysfunction resulting in oxidative distress leads to the pathogenesis. Four weeks of treatment with C-Mn_3O_4 NPs restored renal function, preserved normal kidney architecture, ameliorated overexpression of pro-inflammatory cytokines, and arrested glomerulosclerosis and interstitial fibrosis in CKD mice. A detailed study involving human embryonic kidney

(HEK 293) cells and isolated mitochondria from experimental animals revealed that the molecular mechanism behind the pharmacological action of the nanomedicine involves protection of structural and functional integrity of mitochondria from oxidative damage, the subsequent reduction in intracellular ROS, and maintenance of cellular redox homeostasis. To the best of our knowledge, such studies that efficiently treated a multifaceted disease like CKD using a biocompatible redox nanomedicine are sparse in the literature.

1.5.4. Nanoformulation for Amelioration of Manganese Neurotoxicity

1.5.4.1. Manganese neurotoxicity: Nano-oxide compensates the ion-damage in mammals [114]

In this study, we have compared the behavioral neurotoxicity of C-Mn_3O_4 NPs with that of the well-known neurotoxicant, ionic Mn, in an animal model. We found that mice administered with C-Mn_3O_4 NPs showed no signs of a neurobehavioral disorder, instead C-Mn_3O_4 NPs ameliorated Mn-induced neurobehavioral toxicity (Parkinson's-like syndrome) through the chelation of excess Mn ions and subsequent reduction of oxidative damage.

1.5.5. Dual Function Nanochelator for the Treatment of Heavy Metal Toxicity

1.5.5.1. A smart nanotherapeutic agent for *in vitro* and *in vivo* reversal of heavy metal induced causality: Key information from optical spectroscopy [115]

Human exposure to heavy metals can cause a variety of life-threatening disorders, affecting almost every organ of the body, including the nervous, circulatory, cardiac, excretory, and hepatic systems. The presence of heavy metal (cause) and induced oxidative stress (effect) are both responsible for the observed toxic effects. The

conventional and effective way to combat heavy metal overload diseases is through the use of metal chelators. However, they possess several side effects and most importantly they fail to manage the entire causality. In this study, we introduce citrate-functionalized Mn_3O_4 nanoparticles (C–Mn_3O_4 NPs) as an efficient chelating agent for the treatment of heavy metal overload diseases. By using UV/Vis absorbance and steady-state fluorescence spectroscopic techniques we investigated the efficacy of the NPs in chelation of a model heavy metal, lead (Pb). We also explored the retention of antioxidant properties of the Pb-chelated C–Mn_3O_4 NPs using a UV/Vis-assisted DPPH assay. Through CD spectroscopic studies we established that the NPs can reverse the Pb-induced structural modifications of biological macromolecules. We also studied the in vivo efficacy of NPs in Pb-intoxicated C57BL/6j mice. The NPs were not only able to mobilize the Pb from various organs through chelation, but also saved the organs from oxidative damage. Thus, the C–Mn_3O_4 NPs could be an effective nanotherapeutic agent for a complete reversal of heavy-metal-induced toxicity through chelation of the heavy metal and healing of the associated oxidative stress.

1.5.6. Biomimetic Nanozyme for the Treatment of Neurodegenerative Disorder

1.5.6.1. Incorporation of a biocompatible nanozyme in cellular antioxidant enzyme cascade reverses Huntington's like disorder in preclinical mouse model [116]

The potentiality of nano-enzymes in therapeutic use has directed contemporary research to develop a substitute for natural enzymes, which are suffering from several disadvantages including low stability, high cost, and difficulty in storage. However, inherent toxicity, inefficiency in the physiological *milieu*, and incompatibility to function in cellular enzyme networks limit the therapeutic use of nanozymes in living systems. Here, it is shown that citrate functionalized manganese-based biocompatible nanoscale material (C-Mn_3O_4 NP) efficiently mimics glutathione peroxidase (GPx) enzyme in the physiological *milieu* and easily incorporates into the cellular multienzyme cascade for H_2O_2 scavenging. A detailed computational study reveals the

mechanism of the nanozyme action. The *in vivo* therapeutic efficacy of C-Mn_3O_4 nanozyme is further established in a preclinical animal model of Huntington's disease (HD), a prevalent progressive neurodegenerative disorder, which has no effective medication to date. Management of HD in preclinical animal trial using a biocompatible (non-toxic) nanozyme as a part of the metabolic network may uncover a new paradigm in nanozyme based therapeutic strategy.

1.5.7. Redox Buffering Capacity of Nanomaterials as an Index of ROS-Based Therapeutics and Toxicity

1.5.7.1. Redox buffering capacity of nanomaterials as an index of ROS-based therapeutics and toxicity: A preclinical animal study [117]

Precise control of intracellular redox status, i.e., maintenance of physiological level of reactive oxygen species (ROS) for mediating normal cellular functions (oxidative eustress) while evading the excess ROS stress (distress) is central to the concept of redox medicine. In this regard, engineered nanoparticles with unique ROS generation, transition, or depletion functions have the potential to be the choice of redox therapeutics. However, it is always challenging to estimate whether ROS-induced intracellular events are beneficial or deleterious to the cell. Here, we propose the concept of redox buffering capacity as a therapeutic index of engineered nanomaterials. As a steady redox state is maintained for normal functioning cells, we hypothesize that the ability of a nanomaterial to preserve this homeostatic condition will dictate its therapeutic efficacy. Additionally, the redox buffering capacity is expected to provide information about the nanoparticle toxicity. Here, using citrate functionalized trimanganese tetroxide nanoparticles (C-Mn_3O_4 NPs) as a model nanosystem we explored its redox buffering capacity in erythrocytes. Furthermore, we went on to study the chronic toxic effect (if any) of this nanomaterial in animal model in order to co-relate with the experimentally estimated redox buffering capacity. This study could function as a framework for assessing the capability of a nanomaterial as redox medicine (whether it maintains eustress or causes damage by creating distress), thus orienting its application and safety for clinical use.

1.5.8. Rationalization of A Polyherbal Liver Medicine

1.5.8.1. Spectroscopic studies on dual role of natural flavonoids in detoxification of lead poisoning: Bench to bedside-preclinical trial [118]

Ubiquitousness in the target organs and associated oxidative stress are the most common manifestations of heavy-metal poisoning in living bodies. While chelation of toxic heavy metals is important as a therapeutic strategy, scavenging of increased reactive oxygen species, reactive nitrogen species and free radicals are equally important. Here, we have studied the lead (Pb) chelating efficacy of a model flavonoid morin using steady-state and picosecond-resolved optical spectroscopy. The efficacy of morin in presence of other flavonoid (naringin) and polyphenol (ellagic acid) leading to synergistic combination has also been confirmed from the spectroscopic studies. Our studies further reveal that antioxidant activity (2,2-diphenyl-1-picrylhydrazyl assay) of the Pb–morin complex is sustainable compared to that of Pb-free morin. The metal–morin chelate is also found to be significantly soluble compared to that of morin in aqueous media. Heavy-metal chelation and sustainable antioxidant activity of the soluble chelate complex are found to accelerate the Pb-detoxification in the chemical bench (*in vitro*). Considering the synergistic effect of flavonoids in Pb-detoxification and their omnipresence in medicinal plants, we have prepared a mixture (SKP17LIV01) of flavonoids and polyphenols of plant origin. The mixture has been characterized using high-resolution liquid chromatography assisted mass spectrometry. The mixture (SKP17LIV01) containing 34 flavonoids and 76 other polyphenols have been used to investigate the Pb detoxification in mouse model. The biochemical and histopathological studies on the mouse model confirm the dual action in preclinical studies.

1.5.8.2. Rationalization of a traditional liver medicine using systems biology approach and its evaluation in preclinical trial [119]

'Bottom-up', i.e., molecule to medicine strategy for the discovery of new drugs takes enormous time and cost. In most of the cases, inherent toxicity and undesired side effects of the developed drug hinder its way beyond the early stages of

development. In this regard, the systems pharmacology can play an excellent role by reducing the cost and time of drug development through rationalization and/or repurposing of traditional drugs with known side effects. In the present study, our aim was to develop an integrated systems biology method for the prediction of active ingredients of a traditional medicine and their potential targets inside the body. Further, we evaluated the predictive capacity of the developed method in a preclinical animal model. Here, we have prepared a formulation (SKP17LIV01) from an extract of eight medicinal plants traditionally used as liver medicine and identified the constituents using UHPLC-MS technique. Using systems biology approach, we have rationalized the components of the formulation for potential use in the treatment of heavy metal-induced hepatotoxicity. The active ingredients and potential therapeutic targets were also predicted. A detailed biochemical, histopathological and molecular study on the mice model of lead toxicity confirms the efficacy of the formulation as per prediction by the systems pharmacology approach. The study may open a new frontier for re-discovery of drugs that are already used in traditional medicine.

1.6. PLAN OF THE THESIS

The plan of the thesis is as follows:

Chapter 1: This chapter provides a brief introduction to the scope and motivation behind the thesis work. A brief summary of the work done is also included in this chapter.

Chapter 2: This chapter gives a brief overview of the different steady state and dynamical tools, animal models and chemical probes used in the experiments.

Chapter 3: This chapter describes the instrumental details, experimental protocols and data analysis procedures.

Chapter 4: In this chapter, the role of citrate functionalized Mn_3O_4 nanoparticles in treatment of neonatal hyperbilirubinemia and associated neurobehavioral disorders has been investigated using phenyl-hydrazine intoxicated animal model.

Chapter 5: In this chapter, the efficacy of citrate functionalized Mn_3O_4 nanoparticles in treatment of hepatic fibrosis has been investigated using CCl_4-intoxicated animal model. The molecular mechanism of action involving protection from oxidative damages and mitochondrial protection has been identified.

Chapter 6: In this chapter, using cellular and animal models the mitoprotective role of citrate functionalized Mn_3O_4 nanoparticles to ameliorate chronic kidney disease has been investigated.

Chapter 7: The neuroprotective role of citrate functionalized Mn_3O_4 nanoparticles against Mn-induced neurotoxicity has been described in this chapter.

Chapter 8: This chapter describes the ability of citrate functionalized Mn_3O_4 nanoparticles to chelate heavy metals both *in vitro* and *in vivo* in order to treat heavy metal induced multi-organ toxicity.

Chapter 9: This chapter describes that citrate functionalized Mn_3O_4 nanoparticles can function as glutathione peroxidase mimic and can be incorporated into cellular enzyme network to treat Huntington's disorder.

Chapter 10: This chapter using citrate functionalized Mn_3O_4 nanoparticles as a model describes how redox buffering capacity could indicate the potential therapeutic activity and biocompatibility of a nanomaterial. This chapter further provides details about the effect of citrate functionalized Mn_3O_4 nanoparticles on different organ systems for evaluation of toxic effects upon chronic 90 days oral exposure.

Chapter 11: This chapter describes a combined computational and experimental approach to rationalize a traditional liver medicine for the treatment of heavy metal toxicity. Further this chapter provides a computational method to predict molecular mechanism of action of traditional medicines.

REFERENCES

[1] C. Kinnear, T. L. Moore, L. Rodriguez-Lorenzo, B. Rothen-Rutishauser, A. Petri-Fink, Chem. Rev. 117 (2017) 11476.

[2] B. Pelaz, C. Alexiou, R. A. Alvarez-Puebla, F. Alves, A. M. Andrews, S. Ashraf, L. P. Balogh, L. Ballerini, A. Bestetti, C. Brendel, S. Bosi, M. Carril, W. C. W. Chan, C. Chen, X. Chen, X. Chen, Z. Cheng, D. Cui, J. Du, C. Dullin, A. Escudero, N. Feliu, M. Gao, M. George, Y. Gogotsi, A. Grünweller, Z. Gu, N. J. Halas, N. Hampp, R. K. Hartmann, M. C. Hersam, P. Hunziker, J. Jian, X. Jiang, P. Jungebluth, P. Kadhiresan, K. Kataoka, A. Khademhosseini, J. Kopeček, N. A. Kotov, H. F. Krug, D. S. Lee, C.-M. Lehr, K. W. Leong, X.-J. Liang, M. Ling Lim, L. M. Liz-Marzán, X. Ma, P. Macchiarini, H. Meng, H. Möhwald, P. Mulvaney, A. E. Nel, S. Nie, P. Nordlander, T. Okano, J. Oliveira, T. H. Park, R. M. Penner, M. Prato, V. Puntes, V. M. Rotello, A. Samarakoon, R. E. Schaak, Y. Shen, S. Sjöqvist, A. G. Skirtach, M. G. Soliman, M. M. Stevens, H.-W. Sung, B. Z. Tang, R. Tietze, B. N. Udugama, J. S. VanEpps, T. Weil, P. S. Weiss, I. Willner, Y. Wu, L. Yang, Z. Yue, Q. Zhang, Q. Zhang, X.-E. Zhang, Y. Zhao, X. Zhou, W. J. Parak, ACS Nano 11 (2017) 2313.

[3] C. D. Walkey, W. C. W. Chan, Chem. Soc. Rev. 41 (2012) 2780.

[4] V. Wagner, A. Dullaart, A.-K. Bock, A. Zweck, Nat. Biotechnol. 24 (2006) 1211.

[5] S. Hua, M. B. C. de Matos, J. M. Metselaar, G. Storm, Front. Pharmacol. 9 (2018) 790.

[6] B. M. Schmidt, D. M. Ribnicky, P. E. Lipsky, I. Raskin, Nat. Chem. Biol. 3 (2007) 360.

[7] A. G. Atanasov, B. Waltenberger, E.-M. Pferschy-Wenzig, T. Linder, C. Wawrosch, P. Uhrin, V. Temml, L. Wang, S. Schwaiger, E. H. Heiss, J. M. Rollinger, D. Schuster, J. M. Breuss, V. Bochkov, M. D. Mihovilovic, B. Kopp, R. Bauer, V. M. Dirsch, H. Stuppner, Biotechnol. Adv. 33 (2015) 1582.

[8] A. D. Kinghorn, L. Pan, J. N. Fletcher, H. Chai, J. Nat. Prod. 74 (2011) 1539.

[9] T. W. Corson, C. M. Crews, Cell 130 (2007) 769.

[10] M. Galetti, S. Rossi, C. Caffarra, A. G. Gerboles, M. Miragoli, in: N. Marmiroli, J.C. White, J. Song (Eds.), Exposure to Engineered Nanomaterials in the Environment, Elsevier, (2019), 235.

[11] J. O. Szablowski, A. Bar-Zion, M. G. Shapiro, Acc. Chem. Res. 52 (2019) 2427.

[12] X. Ma, Y. Zhao, X.-J. Liang, Acc. Chem. Res. 44 (2011) 1114.

[13] P. N. Navya, H. K. Daima, Nano Converg. 3 (2016) 1.

[14] K. Riehemann, S. W. Schneider, T. A. Luger, B. Godin, M. Ferrari, H. Fuchs, Angew. Chem. Int. Ed. Engl. 48 (2009) 872.

[15] M. J. Mitchell, M. M. Billingsley, R. M. Haley, M. E. Wechsler, N. A. Peppas, R. Langer, Nat. Rev. Drug Discov. 20 (2021) 101.

[16] T. L. Doane, C. Burda, Chem. Soc. Rev. 41 (2012) 2885.

[17] ESF, Forward Look Nanomedicine: An Emrc Consensus Opinion. European Science Foundation, 2005.

[18] NIH, National Institute of Health Roadmap for Medical Research: Nanomedicine. National Institute of Health, 2006.

[19] TRS, TRAE, Nanoscience and Nanotechnologies: Opportunities and Uncertainties. The Royal Society and The Royal Academy of Engineering, 2004.

[20] EU, Commission Recommendation of 18 October 2011 on the Definition of Nanomaterial. European Union, 2011.

[21] S. Bayda, M. Adeel, T. Tuccinardi, M. Cordani, F. Rizzolio, Molecules 25 (2020) 112.

[22] C. M. Dawidczyk, C. Kim, J. H. Park, L. M. Russell, K. H. Lee, M. G. Pomper, P. C. Searson, J. Control. Release 187 (2014) 133.

[23] M. L. Etheridge, S. A. Campbell, A. G. Erdman, C. L. Haynes, S. M. Wolf, J. McCullough, Nanomedicine: 9 (2013) 1.

[24] S. R. D'Mello, C. N. Cruz, M.-L. Chen, M. Kapoor, S. L. Lee, K. M. Tyner, Nat. Nanotechnol. 12 (2017) 523.

[25] G. Chen, I. Roy, C. Yang, P. N. Prasad, Chem. Rev. 116 (2016) 2826.

[26] P. N. Prasad, Introduction to Nanomedicine and Nanobioengineering, John Wiley & Sons, Hookben, NJ, (2012).

[27] J. R. McCarthy, R. Weissleder, Adv. Drug. Deliv. Rev. 60 (2008) 1241.

[28] J. Lu, E. Choi, F. Tamanoi, J. I. Zink, Small 4 (2008) 421.

[29] S. S. Agasti, A. Chompoosor, C.-C. You, P. Ghosh, C. K. Kim, V. M. Rotello, J. Am. Chem. Soc. 131 (2009) 5728.

[30] I. I. Slowing, J. L. Vivero-Escoto, C.-W. Wu, V. S. Y. Lin, Adv. Drug. Deliv. Rev. 60 (2008) 1278.

[31] S. Mukherjee, V. S. Madamsetty, D. Bhattacharya, S. Roy Chowdhury, M. K. Paul, A. Mukherjee, Adv. Funct. Mater. 30 (2020) 2003054.

[32] A. Nowacek, L. M. Kosloski, H. E. Gendelman, Nanomedicine 4 (2009) 541.

[33] G. Modi, V. Pillay, Y. E. Choonara, Ann. N. Y. Acad. Sci. 1184 (2010) 154.

[34] O. Veiseh, B. C. Tang, K. A. Whitehead, D. G. Anderson, R. Langer, Nat. Rev. Drug Discov. 14 (2015) 45.

[35] L. R. Lemmerman, D. Das, N. Higuita-Castro, R. G. Mirmira, D. Gallego-Perez, Trends Endocrinol. Metab. 31 (2020) 448.

[36] J. C. Pickup, Z.-L. Zhi, F. Khan, T. Saxl, D. J. S. Birch, Diabetes Metab. Res. Rev. 24 (2008) 604.

[37] B. Godin, J. H. Sakamoto, R. E. Serda, A. Grattoni, A. Bouamrani, M. Ferrari, Trends Pharmacol. Sci. 31 (2010) 199.

[38] V. M. Martín Giménez, D. E. Kassuha, W. Manucha, Ther. Adv. Cardiovasc. Dis. 11 (2017) 133.

[39] M. Iafisco, A. Alogna, M. Miragoli, D. Catalucci, Nanomedicine 14 (2019) 2391.

[40] S. K. Nethi, S. Das, C. R. Patra, S. Mukherjee, Biomat. Sci. 7 (2019) 2652.

[41] S. Sharifi, M. J. Hajipour, L. Gould, M. Mahmoudi, Mol. Pharmaceutics 18 (2021) 550.

[42] M. A. Mofazzal Jahromi, P. Sahandi Zangabad, S. M. Moosavi Basri, K. Sahandi Zangabad, A. Ghamarypour, A. R. Aref, M. Karimi, M. R. Hamblin, Adv. Drug Deliv. Rev. 123 (2018) 33.

[43] L. O. Sillerud, N. O. Solberg, R. Chamberlain, R. A. Orlando, J. E. Heidrich, D. C. Brown, C. I. Brady, T. A. Vander Jagt, M. Garwood, D. L. Vander Jagt, J. Alzheimer's Dis. 34 (2013) 349.

[44] R. Alwi, S. Telenkov, A. Mandelis, T. Leshuk, F. Gu, S. Oladepo, K. Michaelian, Biomed. Opt. Express 3 (2012) 2500.

[45] A. S. Thakor, J. V. Jokerst, P. Ghanouni, J. L. Campbell, E. Mittra, S. S. Gambhir, J. Nucl. Med. 57 (2016) 1833.

[46] P. Nasimi, M. Haidari, Int. J. Green Nanotechnol. 1 (2013) 1.

[47] K. Kim, M.-J. Kim, D. W. Kim, S. Y. Kim, S. Park, C. B. Park, Nat. Commun. 11 (2020) 119.

[48] M. Kendall, I. Lynch, Nat. Nanotechnol. 11 (2016) 206.

[49] S. Y. Bhong, N. More, M. Choppadandi, G. Kapusetti, SN Appl. Sci. 1 (2018) 76.

[50] M. Siang Soh, A. Sellinger, A. Uj. Yap, Curr. Nanosci. 2 (2006) 373.

[51] J. I. González Ocampo, M. M. Machado de Paula, N. J. Bassous, A. O. Lobo, C. P. Ossa Orozco, T. J. Webster, Acta Biomater. 83 (2019) 425.

[52] M. Roy, A. Bandyopadhyay, S. Bose, J. Biomed. Mater. Res. Part B: Applied Biomaterials 99B (2011) 258.

[53] Y. Sun, C. Hu, Y. Yang, B. Dong, Y. Deng, Mater. Sci. Eng. C 103 (2019) 109836.

[54] T. Mahesh Kumar, M. Srinivas, G. K. Rajanikant, Curr. Pharm. Des. 16 (2010) 1882.

[55] S. Tinkle, S. E. McNeil, S. Mühlebach, R. Bawa, G. Borchard, Y. Barenholz, L. Tamarkin, N. Desai, Ann. N.Y. Acad. Sci. 1313 (2014) 35.

[56] V. Sainz, J. Conniot, A. I. Matos, C. Peres, E. Zupanǒiǒ, L. Moura, L. C. Silva, H. F. Florindo, R. S. Gaspar, Biochem. Biophys. Res. Commun. 468 (2015) 504.

[57] T. M. Allen, P. R. Cullis, Science 303 (2004) 1818.

[58] L. Zhang, F. X. Gu, J. M. Chan, A. Z. Wang, R. S. Langer, O. C. Farokhzad, Clin. Pharmacol. Ther. 83 (2008) 761.

[59] A. Narang, R.-K. Chang, M. A. Hussain, J. Pharm. Sci. 102 (2013) 3867.

[60] B. Y. S. Kim, J. T. Rutka, W. C. W. Chan, N. Engl. J. Med. 363 (2010) 2434.

[61] M. Ferrari, Nat. Rev. Cancer 5 (2005) 161.

[62] W. R. Sanhai, J. H. Sakamoto, R. Canady, M. Ferrari, Nat. Nanotechnol. 3 (2008) 242.

[63] J. I. Hare, T. Lammers, M. B. Ashford, S. Puri, G. Storm, S. T. Barry, Adv. Drug. Deliv. Rev. 108 (2017) 25.

[64] J. M. Hillegass, A. Shukla, S. A. Lathrop, M. B. MacPherson, N. K. Fukagawa, B. T. Mossman, WIREs Nanomed. Nanobiotechnol. 2 (2010) 219.

[65] C. Long Thomas, J. Tajuba, P. Sama, N. Saleh, C. Swartz, J. Parker, S. Hester, V. Lowry Gregory, B. Veronesi, Environ. Health Perspect. 115 (2007) 1631.

[66] M. Balbus John, D. Maynard Andrew, L. Colvin Vicki, V. Castranova, P. Daston George, A. Denison Richard, L. Dreher Kevin, L. Goering Peter, M. Goldberg Alan, M. Kulinowski Kristen, A. Monteiro-Riviere Nancy, G. Oberdörster, S. Omenn Gilbert, E. Pinkerton Kent, S. Ramos Kenneth, M.

Rest Kathleen, B. Sass Jennifer, K. Silbergeld Ellen, A. Wong Brian, Environ. Health Perspect. 115 (2007) 1654.

[67] H. C. Fischer, W. C. W. Chan, Curr. Opin. Biotechnol. 18 (2007) 565.

[68] A. D. Maynard, R. J. Aitken, T. Butz, V. Colvin, K. Donaldson, G. Oberdörster, M. A. Philbert, J. Ryan, A. Seaton, V. Stone, S. S. Tinkle, L. Tran, N. J. Walker, D. B. Warheit, Nature 444 (2006) 267.

[69] J. S. Tsuji, A. D. Maynard, P. C. Howard, J. T. James, C.-w. Lam, D. B. Warheit, A. B. Santamaria, Toxicol. Sci. 89 (2006) 42.

[70] J. Wang, W. Sun, S. F. Ali, in: S.C. Sahu, D.A. Casciano (Eds.), Nanotoxicity: From in Vivo and in Vitro Models to Health Risks, John Wiley & Sons, West Susex, UK, (2009), 171.

[71] A. M. Alkilany, C. J. Murphy, J. Nanopart. Res. 12 (2010) 2313.

[72] A. Sukhanova, S. Bozrova, P. Sokolov, M. Berestovoy, A. Karaulov, I. Nabiev, Nanoscale Res. Lett. 13 (2018) 44.

[73] R. Gaspar, R. Duncan, Adv. Drug Deliv. Rev. 61 (2009) 1220.

[74] A. M. Nyström, B. Fadeel, J. Control. Release 161 (2012) 403.

[75] A. Pieroni, L. L. Price, I. Vandebroek, J. Ethnobiol. Ethnomed. 1 (2005) 1.

[76] A. Gurib-Fakim, Mol. Aspects Med. 27 (2006) 1.

[77] G. Brahmachari, Bioactive Natural Products, World Scientific, (2011), 1.

[78] G. M. Cragg, D. J. Newman, Biochim. Biophys. Acta. - General Subjects 1830 (2013) 3670.

[79] H. Yuan, Q. Ma, L. Ye, G. Piao, Molecules 21 (2016) 559.

[80] A. L. Harvey, Drug Discov. Today 13 (2008) 894.

[81] M. Gordaliza, Clin. Transl. Oncol. 9 (2007) 767.

[82] F. E. Koehn, G. T. Carter, Nat. Rev. Drug Discov. 4 (2005) 206.

[83] A. L. Harvey, R. Edrada-Ebel, R. J. Quinn, Nat. Rev. Drug Discov. 14 (2015) 111.

[84] D. J. Newman, G. M. Cragg, J. Nat. Prod. 79 (2016) 629.

[85] B. Waltenberger, A. Mocan, K. Šmejkal, E. H. Heiss, A. G. Atanasov, Molecules 21 (2016) 807.

[86] M. Tintore, A. Vidal-Jordana, J. Sastre-Garriga, Nat. Rev. Neurol. 15 (2019) 53.

[87] A. G. Atanasov, S. B. Zotchev, V. M. Dirsch, I. E. Orhan, M. Banach, J. M. Rollinger, D. Barreca, W. Weckwerth, R. Bauer, E. A. Bayer, M. Majeed, A. Bishayee, V. Bochkov, G. K. Bonn, N. Braidy, F. Bucar, A. Cifuentes, G. D'Onofrio, M. Bodkin, M. Diederich, A. T. Dinkova-Kostova, T. Efferth, K. El Bairi, N. Arkells, T.-P. Fan, B. L. Fiebich, M. Freissmuth, M. I. Georgiev, S. Gibbons, K. M. Godfrey, C. W. Gruber, J. Heer, L. A. Huber, E. Ibanez, A. Kijjoa, A. K. Kiss, A. Lu, F. A. Macias, M. J. S. Miller, A. Mocan, R. Müller, F. Nicoletti, G. Perry, V. Pittalà, L. Rastrelli, M. Ristow, G. L. Russo, A. S. Silva, D. Schuster, H. Sheridan, K. Skalicka-Woźniak, L. Skaltsounis, E. Sobarzo-Sánchez, D. S. Bredt, H. Stuppner, A. Sureda, N. T. Tzvetkov, R. A. Vacca, B. B. Aggarwal, M. Battino, F. Giampieri, M. Wink, J.-L. Wolfender, J. Xiao, A. W. K. Yeung, G. Lizard, M. A. Popp, M. Heinrich, I. Berindan-Neagoe, M. Stadler, M. Daglia, R. Verpoorte, C. T. Supuran, Nat. Rev. Drug Discov. 20 (2021) 200.

[88] J. W. H. Li, J. C. Vederas, Science 325 (2009) 161.

[89] M. Feher, J. M. Schmidt, J. Chem. Inf. Comput. Sci. 43 (2003) 218.

[90] E. C. Barnes, R. Kumar, R. A. Davis, Nat. Prod. Rep. 33 (2016) 372.

[91] B. Shen, Cell 163 (2015) 1297.

[92] H. Lachance, S. Wetzel, K. Kumar, H. Waldmann, J. Med. Chem. 55 (2012) 5989.

[93] C. M. Dobson, Nature 432 (2004) 824.

[94] G. A. Cordell, M. D. Colvard, J. Nat. Prod. 75 (2012) 514.

[95] C. Harrison, Nat. Biotechnol. 32 (2014) 403.

[96] J. J. Kellogg, T. N. Graf, M. F. Paine, J. S. McCune, O. M. Kvalheim, N. H. Oberlies, N. B. Cech, J. Nat. Prod. 80 (2017) 1457.

[97] H. van de Waterbeemd, E. Gifford, Nat. Rev. Drug Discov. 2 (2003) 192.

[98] U. Norinder, C. A. S. Bergström, ChemMedChem 1 (2006) 920.

[99] J. Hodgson, Nat. Biotechnol. 19 (2001) 722.

[100] M. P. Gleeson, A. Hersey, D. Montanari, J. Overington, Nat. Rev. Drug Discov. 10 (2011) 197.

[101] X. Zhou, S. W. Seto, D. Chang, H. Kiat, V. Razmovski-Naumovski, K. Chan, A. Bensoussan, Front. Pharmacol. 7 (2016) 201.

[102] F. A. Tausk, Arch. Dermatol. 134 (1998) 1422.

[103] F.-S. Li, J.-K. Weng, Nat. Plants 3 (2017) 17109.

[104] R. J. Rickles, G. Short, W. F. Tam, T. Giordano, A. Myaskovsky, P. Grossman, A. Necheva, G. Zimmermann, J. Ledell, M. S. Lee, Cancer Res. 70 (2010) 5509.

[105] M. C. Berenbaum, in: G. Klein, S. Weinhouse (Eds.), Adv. Cancer Res., Academic Press, (1981), 269.

[106] W. Zhou, J. Wang, Z. Wu, C. Huang, A. Lu, Y. Wang, Sci. Rep. 6 (2016) 36985.

[107] S. Li, B. Zhang, N. Zhang, BMC Syst. Biol. 5 (2011) S10.

[108] A. L. Hopkins, Nat. Chem. Biol. 4 (2008) 682.

[109] X.-Q. Hu, Y. Sun, E. Lau, M. Zhao, S.-B. Su, Curr. Cancer Drug Targets 16 (2016) 346.

[110] A. Adhikari, V. K. Bhutani, S. Mondal, M. Das, S. Darbar, R. Ghosh, N. Polley, A. K. Das, S. S. Bhattacharya, D. Pal, A. K. Mallick, S. K. Pal, bioRxiv (2021) https://doi.org/10.1101/2020.12.31.425023.

[111] A. Adhikari, N. Polley, S. Darbar, D. Bagchi, S. K. Pal, Future Sci. OA 2 (2016) FSO146.

[112] A. Adhikari, N. Polley, S. Darbar, S. K. Pal, Mat. Focus 6 (2017) 280.

[113] A. Adhikari, S. Mondal, T. Chatterjee, M. Das, P. Biswas, S. Darbar, H. Alessa, J. T. Al-Thakafy, S. A. Ahmed, A. K. Das, M. Bhattacharyya, S. K. Pal, bioRxiv (2021) https://doi.org/10.1101/2021.03.14.435287.

[114] A. Adhikari, M. Das, S. Mondal, S. Darbar, A. K. Das, S. S. Bhattacharya, D. Pal, S. K. Pal, Biomater. Sci. 7 (2019) 4491.

[115] A. Adhikari, P. Biswas, S. Mondal, M. Das, S. Darbar, A. M. Hameed, A. Alharbi, S. A. Ahmed, S. S. Bhattacharya, D. Pal, S. K. Pal, ChemMedChem 15 (2020) 420.

[116] A. Adhikari, S. Mondal, M. Das, P. Biswas, U. Pal, S. Darbar, S. S. Bhattacharya, D. Pal, T. Saha-Dasgupta, A. K. Das, A. K. Mallick, S. K. Pal, Adv. Healthcare Mater. 10 (2021) 2001736.

[117] A. Adhikari, S. Mondal, M. Das, R. Ghosh, P. Biswas, S. Darbar, S. Singh, A. K. Das, S. S. Bhattacharya, D. Pal, A. K. Mallick, S. K. Pal, bioRxiv (2021) https://doi.org/10.1101/2021.03.14.435286.

[118] A. Adhikari, S. Darbar, T. Chatterjee, M. Das, N. Polley, M. Bhattacharyya, S. Bhattacharya, D. Pal, S. K. Pal, ACS Omega 3 (2018) 15975.

[119] A. Adhikari, S. Darbar, M. Das, S. Mondal, S. S. Bhattacharya, D. Pal, S. K. Pal, Comp. Biol. Chem. 84 (2020) 107196.

CHAPTER 02

Overview of Experimental Techniques and Animal Models

In order to investigate the various processes involved in synthesis, characterization and potential biomedical applications of the nanomaterials and ethnobotanical ingredients, different steady state and dynamical tools including molecular quenching, time correlated single photon counting, dynamic light scattering have been used. To understand therapeutic efficacy of the developed nanomaterials, several preclinical animal models were employed to mimic the human disease conditions like hepatic fibrosis, heavy-metal toxicity, and neurodegenerative disorders. In this chapter, a brief overview of the theoretical aspects of the spectroscopic tools and insights about the animal models are provided. Also, particulars about various systems used in different studies have been discussed.

2.1. FLUORESCENCE QUENCHING

Fluorescence quenching is the non-radiative loss of excitation energy from a fluorophore through interaction with another molecule, called quencher, resulting into decrease in fluorescence intensity. The stationary and time-dependent observations of such processes can reveal the deactivation mechanism of the excited molecule and can be used to probe bimolecular interactions. Quenching can occur through numerous

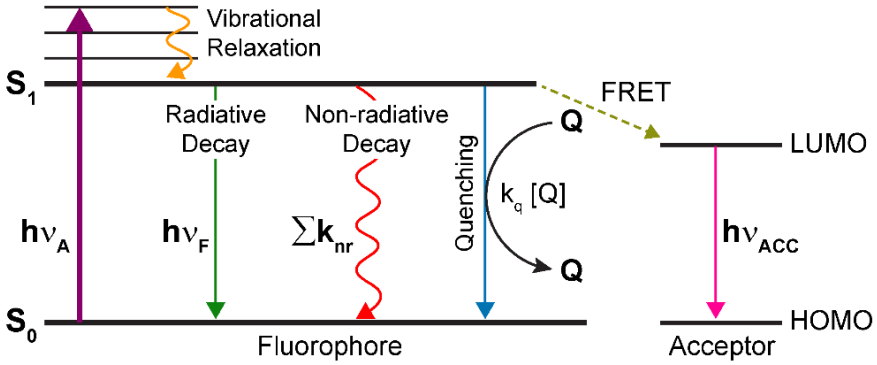

Figure 2.1. *Schematic representation of modified Jablonski diagram.*

mechanisms including excited-state reactions, molecular rearrangements, energy transfer, ground-state complex formation, and collision. However, there are two main classes of mechanisms of fluorescence quenching namely dynamic and static.

2.1.1. Dynamic or Collisional Quenching

Dynamic or collisional quenching is a process where depopulation of excited-state takes place upon collisional encounter between fluorophore and the quencher (illustrated on the modified Jablonski diagram in Figure 2.1). Herein, the excited state fluorophore is returned to the ground state without any chemical alterations through a diffusive encounter with the quencher. The collisional quenching is described by the popular Stern-Volmer equation (Equation – 2.1) [1].

$$\frac{F_0}{F} = 1 + k_q \tau_0 [Q] = 1 + K_D [Q]$$

[Equation – 2.1]

Here, F_0 and F are the fluorescence intensities of the fluorophore in presence and absence of quencher, k_q is the bimolecular quenching constant and τ_0 is the initial lifetime of the fluorophore. K_D is the Stern-Volmer quenching constant and [Q] is the quencher concentration. K_D points toward the sensitivity of the fluorophore to a quencher. Larger K_D values indicate more accessibility of the fluorophore to a

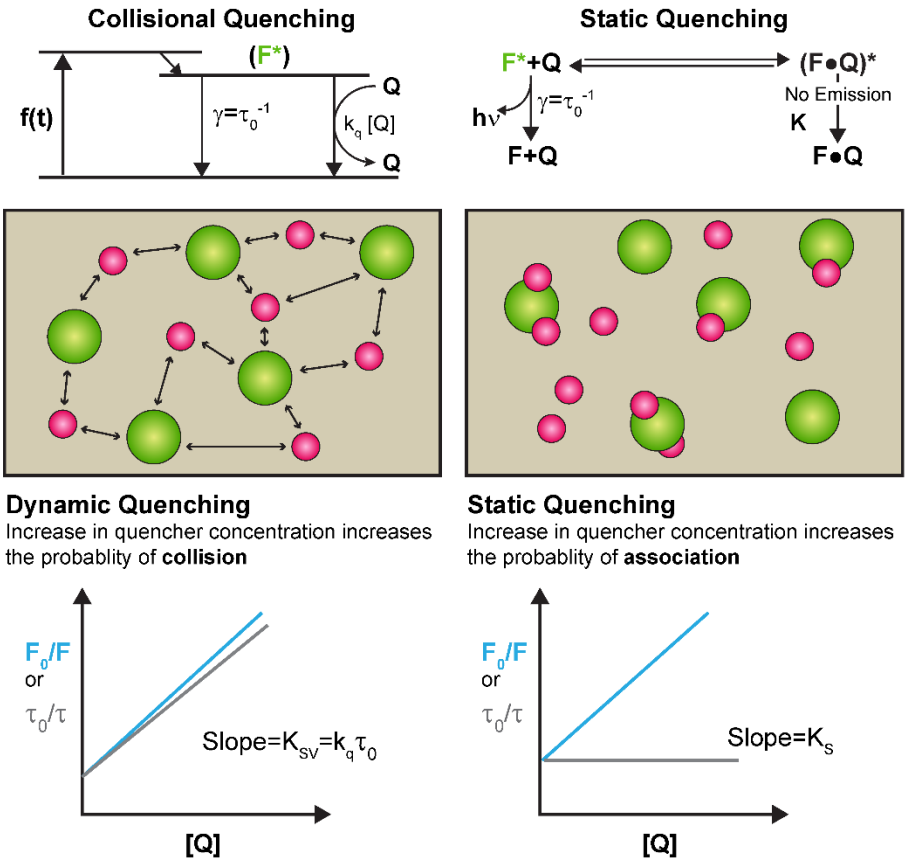

Figure 2.2. *Schematic representation of collisional (i.e., dynamic) and static quenching phenomena.*

quencher. If the quenching is identified to be dynamic, the Stern-Volmer constant is represented by K_D. Otherwise it is replaced with K_{SV}.

2.1.2. Static Quenching

In static quenching, a complex formation happens between the fluorophore and the quencher at the ground state, and this complex is non-fluorescent. When this complex absorbs light it immediately returns to the ground state without emission of a photon. Static quenching can be described by Equation – 2.2.

$$\frac{F_0}{F} = 1 + K_S[Q]$$

[Equation – 2.2]

In this expression, K_S is the association constant. It has to be noted that unlike dynamic quenching, static quenching causes no change to the fluorescence lifetime.

Quenching data are usually presented as plots of F_0/F versus [Q]. This is because F_0/F is expected to be linearly dependent upon the concentration of quencher. A plot of F_0/F versus [Q] yields an intercept of one on the y-axis and a slope equal to K_D or K_S (Figure 2.2). The possible mechanistic diagram of dynamic and static quenching are shown in Figure 2.2.

2.1.3. Combined Dynamic and Static Quenching

Often, collisional quenching and ground state complex formation simultaneously occurs between the fluorophore and the quencher, causing an upward curvature of the Stern-Volmer plot (Figure 2.3). This kind of mixed quenching can be expressed using Equation – 2.3 and 2.4.

$$\frac{F_0}{F} = (1+K_D[Q])(1+K_S[Q])$$

[Equation – 2.3]

$$\frac{F_0}{F} = K_{app}[Q]$$

[Equation – 2.4]

Here, K_{app} is the apparent quenching constant which is calculated at each quencher concentration. A plot of K_{app} versus [Q] yields a straight line with an intercept of K_D+K_S and a slope of K_SK_D (Figure 2.3).

2.1.4. Quenching Sphere of Action

In some instances, the positive deviation of the Stern-Volmer plot could be explained in terms of a "sphere of action" within which the possibility of quenching is unity [Equation – 2.5]. According to this model, quenching occurs when the quencher molecule is adjacent to the fluorophore at the moment of excitation, but fluorophores

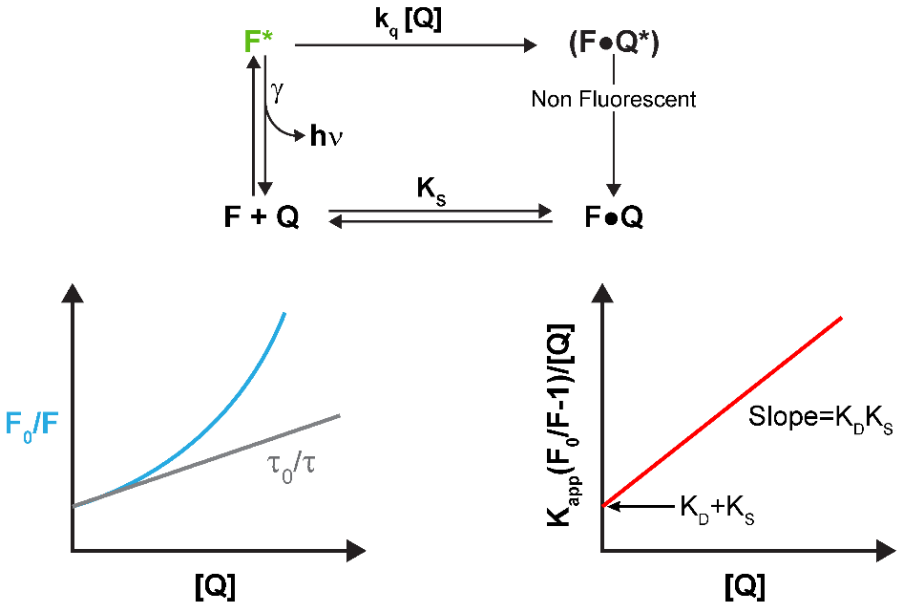

Figure 2.3. *Dynamic and static quenching of the same population of fluorophores.*

and quenchers do not actually form a ground-state complex. These closely spaced fluorophore–quencher pairs are instantaneously quenched, and thus appear to be dark complexes. The quenching phenomena can be explained as:

$$\frac{F_0}{F} = (1 + K_D[Q])e^{\frac{[Q]VN}{1000}}$$

[Equation – 2.5]

In this expression, V is the volume of the sphere, $\frac{[Q]N}{1000}$ is the average concentration in molecules/cm^3, and $\frac{[Q]VN}{1000}$ is the average number of molecules in the sphere.

2.2. FLUORESCENCE LIFETIME

The fluorescence lifetime of a fluorophore is defined by the average time the molecule spends in the excited state before returning to the ground state via loss of energy through fluorescence and other non-radiative processes (Figure 2.4).

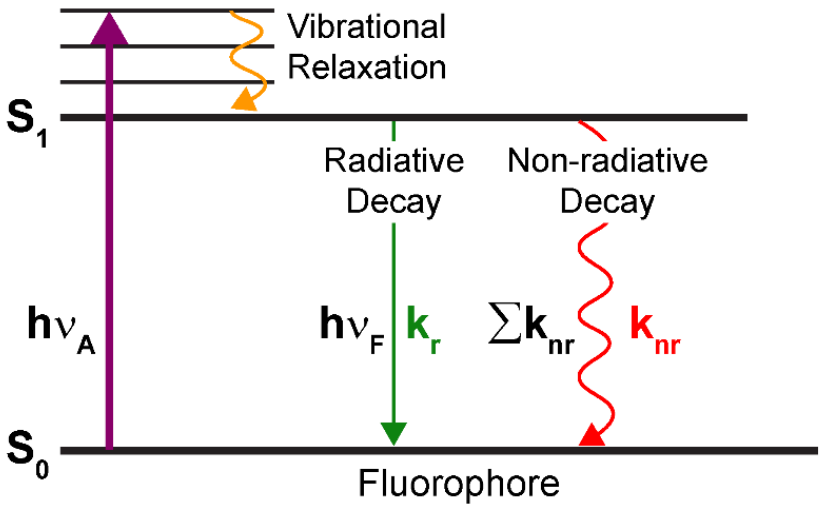

Figure 2.4. *A simplified Jablonski diagram to illustrate the meaning of fluorescence lifetime. k_r and k_{nr} are the radiative and non-radiative rates of decay.*

2.2.1. Theory

The excited state lifetime, τ, is defined by the following equation (Equation – 2.6).

$$\tau = \frac{1}{k_r + k_{nr}}$$

[Equation – 2.6]

Where, k_r and k_{nr} is the radiative and non-radiative rates of decay. The lifetime of the fluorophore in the absence of non-radiative processes is called the intrinsic or natural lifetime, and is given by, $\tau = \frac{1}{k_r}$.

2.2.2. Experimental Methods

The fluorescence transients were measured with commercially available time correlated single photon counting (TCSPC) setup from Edinburgh Instruments Ltd. (Livingston, UK) having an instrument response function, IRF=80 ps.

Curve fitting of the time-resolved fluorescence transients was performed using a nonlinear least square fitting procedure to a function (Equation – 2.7) comprised of convolution of the IRF (E(t)) with a sum of exponentials (Equation – 2.8) with pre-exponential factors (B_i), characteristic lifetimes (τ_i), and a background (A).

$$\left(X(t)=\int_0^t E(t')R(t-t')dt' \right)$$

[Equation – 2.7]

$$\left(R(t)=A+\sum_{i=1}^{N} B_i e^{\frac{-t}{\tau_i}} \right)$$

[Equation – 2.8]

Relative concentration in a multi-exponential decay is expressed as Equation – 2.9.

$$C_n=\frac{B_n}{\sum_{i=1}^{N} B_i}\times 100$$

[Equation – 2.9]

The average lifetime (amplitude-weighted) of a multi-exponential decay is finally expressed as,

$$\tau_{avg}=\sum_{i=1}^{N} C_i\tau_i$$

[Equation – 2.10]

The quality of the curve fitting is evaluated by reduced χ^2 and residual data.

2.3. CIRCULAR DICHROISM (CD)

Circular dichroism (CD) spectroscopy is a widely used technique for probing the structures of biomolecules, in particular determining the relative abundance of secondary structures (α-helix and β-sheets) of proteins [2,3].

2.3.1. Theory

When a plane polarized light passes through an optically active substance, not only do the left (L) and right (R) circularly polarized light rays travel at different speeds, $c_L \neq c_R$, but these two rays are absorbed to a different extent, i.e. $A_L \neq A_R$. The difference in the absorbance of the left and right circularly polarized light, i.e., $\Delta A = A_L - A_R$, is defined as circular dichroism (CD). Circular dichroism spectroscopy follows Beer-Lambert law. If I_0 is the intensity of light incident on the cell, and I, that of emergent light, then the absorbance of the sample is given by,

$$A = \log_{10}\left(\frac{I_0}{I}\right) = \varepsilon c l$$

[Equation – 2.11]

i.e., A is proportional to concentration (c) of the optically active substance and optical path length (l). If 'c' is in mol L^{-1} and 'l' is in cm, then ε is called the molar absorptivity or molar extinction coefficient. If in an optically active medium two absorbances, A_L and A_R are considered then the intensity of left and right circularly polarized light are

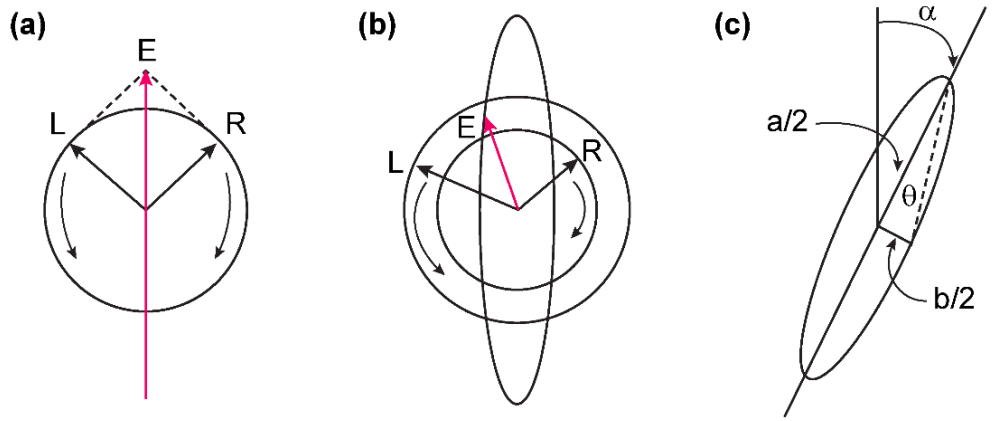

Figure 2.5. *(a) Left (L) and right (R) circularly polarized light components having same intensities and phases lying in one plane and oscillating with same magnitude, (b) R component being less intense (more absorbed) than L component leading to elliptically polarized light and (c) θ, ellipticity is the angle made by semi-major and semi-minor axes of the ellipse. The major axis has rotated through angle α corresponding to optical rotation.*

same, i.e. $I_0=I_L=I_R$ at the time of incidence on the sample. Any dicrograph passes periodically changing light through the medium, oscillating between left and right circular polarization, and the difference in absorbances are recorded directly.

$$\Delta A=A_L-A_R=\log_{10}\left(\frac{I_0}{I_L}\right)-\log_{10}\left(\frac{I_0}{I_R}\right)=\log_{10}\left(\frac{I_R}{I_L}\right)$$

[Equation – 2.12]

$$\Delta A=(\Delta\varepsilon)cl$$

[Equation – 2.12]

As seen from equation 2.12, I_0 does not appear in this final equation, so there is no need for a reference beam. The instruments are, therefore, of single beam type.

After passing through an optically active substance, light is changed in two aspects. The maximal amplitude of intensity is no longer confined to a plane; instead it traces out an ellipse. Ellipticity is defined as the arctangent of the ratio of minor axis to the major axis of the ellipse (Figure 2.5). The orientation of ellipse is another aspect. The major axis of the ellipse no longer remains parallel to the polarization of the incident light. Thus, after passing through an optically active substance, neither do the absorbance nor do the radii of the emergent left and right circularly polarized light remains same. Hence, CD is equivalent to ellipticity.

Most of the CD spectropolarimeters, although they measure differential absorption, produce a CD spectrum in units of ellipticity (θ) expressed in milli-degrees versus λ, rather than ΔA versus λ. The relation between ellipticity and CD is given by,

$$\theta=\frac{2.303\times180\times(A_L-A_R)}{4\pi}\text{ (in degrees)}$$

[Equation – 2.13]

To compare the results from different samples, optical activity is computed on a molar or residue basis. Molar ellipticity, $[\theta]$ is defined as,

$$[\theta]=\frac{\theta}{cl}$$

[Equation – 2.14]

Where (θ) is in degrees, *'c'* is in mol L^{-1} and *'l'* is in cm. The unit of molar ellipticity is deg M^{-1} cm^{-1}. Sometimes, CD is reported as $\Delta\varepsilon=\Delta\varepsilon_L-\Delta\varepsilon_R$. From Beer-Lambert law and molar ellipticity relation it can be shown that,

$$[\theta]=3300\Delta\varepsilon$$

[Equation – 2.15]

2.3.2. Experimental Methods

In biophysical studies, CD is mostly used to determine the secondary structures of proteins and nucleic acids and the changes in secondary structures upon recognition by small molecules and other biomolecules. Through CD spectropolarimeter, we obtain CD spectrograph having a plot of optical rotation in millidegrees versus wavelength in nm. In order to obtain information about the secondary structures of proteins, the graph is fitted with non-linear least square fitting method using freely available software. The percentages of different secondary structures are calculated by matching the experimental data with that of reference standard. In proteins, the secondary structural content includes α–helix, β–sheet, β–turn and random coil. The CD spectrum of α–helix contains two negative peaks, one at 208 nm (π–π* transition) and 222 nm (n–π* transition). β–sheet has a negative band at 216 nm and a positive band of similar magnitude at 195 nm. β–turn has weak negative peak at 225 nm (n–π* transition), a strong positive peak between 200 nm and 205 nm due to π–π* transition and a strong negative band between 180 nm and 190 nm. Random coil or unordered conformation has a strong negative band below 200 nm; a positive band at 218 nm and in some cases has a very weak negative band at 235 nm.

2.4. DYNAMIC LIGHT SCATTERING

According to semi-classical theory of light scattering, when light impinges on matter, the electric field of the light induces an oscillating polarization of electrons in the molecules. Hence, the molecules provide a secondary source of light and subsequently scatter light. The frequency shift, the angular distribution, the

polarization, and the intensity of scattered light are determined by size, shape and molecular interactions in the scattering material. Dynamic light scattering (DLS) also known as photon correlation spectroscopy (PCS) or quasi-elastic light scattering (QELS) is one of the most popular techniques used to determine the size of the particle.

2.4.1. Theory

DLS experiments are based on two assumptions:

A) Particles exhibit Brownian motion (also called 'random walk'). The probability density function is given by the formula,

$$P(r,t|0,0)=(4\pi DT)^{\frac{3}{2}}e^{\frac{-r^2}{4Dt}}$$

[Equation – 2.16]

Where D is the translational diffusion coefficient.

B) The particles are spherical in shape with particles of molecular dimensions. If it is so, then it is possible to apply the Stoke-Einstein relation and hence have a formula that easily gives the diffusion constant,

$$D=\frac{k_B T}{3\pi\eta d_H}$$

[Equation – 2.17]

Where d_H is the hydrodynamic diameter of the particles, k_B is the Boltzmann constant, T is the temperature in Kelvin and η is the viscosity of the solvent.

2.4.2. Experimental Methods

It has been seen that particles in dispersion are in a constant, random Brownian motion and this causes the intensity of scattered light to fluctuate as a function of time. The correlator used in a DLS instrument constructs the intensity autocorrelation function $G(\tau)$ of the scattered intensity,

$$G(\tau)=\langle I(t)I(t+\tau)\rangle$$

[Equation – 2.18]

Where τ is the time difference (the sample time) of the correlator. For a large number of monodisperse particles in Brownian motion, the correlation function (given the symbol G) is an exponential decaying function of the correlator time delay τ,

$$G(\tau)=A\left[1+Be^{-2\Gamma\tau}\right]$$

[Equation – 2.19]

Where A is the baseline of the correlation function, B is the intercept of the correlation function. Γ is the first cumulant and is related to the translational diffusion coefficient as, $\Gamma=Dq^2$, where q is the scattering vector and its magnitude is defined as,

$$q=\left(\frac{4\pi n}{\lambda_0}\right)\sin\left(\frac{\theta}{2}\right)$$

[Equation – 2.20]

Where n is the refractive index of dispersant, λ_0 is the wavelength of the laser and θ, the scattering angle. For polydisperse samples, the equation can be written as,

$$G(\tau)=A\left[1+B\left|g^{(1)}(\tau)\right|^2\right]$$

[Equation – 2.21]

Where the correlation function $g^{(1)}(\tau)$ is no longer a single exponential decay and can be written as the Laplace transform of a continuous distribution $G(\Gamma)$ of decay times,

$$g^{(1)}(\tau)=\int_0^\infty G(\Gamma)e^{(-\Gamma\tau)d\Gamma}$$

[Equation – 2.22]

The size distribution of the particles are obtained by fitting, using non-linear least square fitting or CONTIN program, the autocorrelation function to multi-exponential function. The size distribution obtained is a plot of the relative intensity of light scattered by particles and is therefore known as an intensity size distribution. However, in the intensity distribution graph, the area of the peak for the larger particle appears at least 10^6 times larger than the peak for the smaller particle. This is because large

particles scatter much more light than small particles, as the intensity of light scattering by a particle is proportional to the sixth power of its diameter (Rayleigh's approximation).

2.5. ENZYME KINETICS

2.5.1. Michaelis-Menten Kinetics

A classical enzyme catalyzed reaction contains two elementary reactions in which the substrate forms a complex with the enzyme to produce product and enzyme. The equation can be expressed as followed:

$$E+S \underset{k_{-1}}{\overset{k_1}{\rightleftharpoons}} ES \xrightarrow{k_2} E+P$$

[Equation – 2.23]

Here E, S, ES & P denote the enzyme, substrate, enzyme-substrate complex and product respectively. So the production rate of enzyme-substrate complex i.e. ES complex is the difference between the rate of its formation and the rate of its decomposition to the product.

$$\frac{d[ES]}{dt} = k_1[E][S] - k_{-1}[ES] - k_2[ES]$$

[Equation – 2.24]

Now two assumptions can be made,

A) Assumption of equilibrium: It can be assumed that $k_{-1} >> k_2$, so that the first step of the reaction achieves equilibrium.

$$k_s = \frac{k_{-1}}{k_1} = \frac{[E][S]}{[ES]}$$

[Equation – 2.25]

Here, k_s is the dissociation constant for the first elementary reaction step.

B) Assumption of steady state: In this assumption the concentration of ES complex is thought to be remained at equilibrium, i.e., the rate of synthesis of ES is exactly equal with the rate of decomposition of ES complex. That means [ES] maintains a steady state.

$$\frac{d[ES]}{dt}=0$$

[Equation – 2.26]

To derive the kinetic equation the overall reaction must be converted to measurable quantities. The total amount of enzyme, i.e., [E] can be written as

$$[E]_T=[E]+[ES]$$

[Equation – 2.27]

Now the combination of Equation – 2.24 & Equation – 2.25 yields Equation – 2.28.

$$k_1([E]_T-[ES])[S]=(k_{-1}+k_2)[ES]$$

[Equation – 2.28]

By rearranging and dividing both side by k_1 we get

$$[ES]=\frac{[E]_T[E]}{K_M+[S]}$$

[Equation – 2.29]

Where K_M is known as Michaelis constant.

Now the initial velocity of the reaction, v_0, can be expressed in the terms of measurable quantities $[E]_T$ and [S]:

$$v_0=\left(\frac{d[P]}{dt}\right)=k_2[ES]=\frac{k_2[E]_T[S]}{K_M+[S]}$$

[Equation – 2.30]

The maximal velocity can be denoted as V_{max} and be expressed as:

$$V_{max}=k_2[E]_T$$

[Equation – 2.31]

Therefore combination of Equation – 2.30 & Equation – 2.31 results into Equation – 2.32.

$$v_0 = \frac{V_{max}[S]}{K_M + [S]}$$

[Equation – 2.32]

Equation – 2.32 is known as Michaelis-Menten equation, one of the fundamental equations in the field of enzyme kinetics.

To determine the value of V_{max} and K_M more accurately Hans Lineweaver and Dean Burk formulated a reciprocal equation of equation 8 known as Lineweaver-Burk Plot or Double-reciprocal Plot:

$$\frac{1}{v_0} = \left(\frac{K_M}{V_{max}}\right)\frac{1}{[S]} + \frac{1}{V_{max}}$$

[Equation – 2.33]

If v_0 and [S] are plotted in this equation then the slope of the line will be equal to K_M/V_{max}, the intercept at Y axis will be $1/V_{max}$ and intercept at X axis will be $-1/K_M$.

2.5.2. Catalytic Efficiency

Another important kinetic parameter to measure the catalytic efficiency of an enzyme is k_{cat}/K_M. Here k_{cat} is catalytic constant and can be defined as:

$$k_{cat} = \frac{V_{max}}{[E]_T}$$

[Equation – 2.34]

This constant is also known as turnover number as it is the number of substrate molecules that each active site catalyzes per unit time.

When $[S] << K_M$, the formation of ES is very low and subsequently $[E] \approx [E]_T$, so the Equation – 2.32 becomes a second order rate equation (Equation – 2.35):

$$v_0 \approx \left(\frac{k_2}{K_M}\right)[E]_T[S] \approx \left(\frac{k_{cat}}{K_M}\right)[E][S]$$

[Equation – 2.35]

This k_{cat}/K_M is the apparent second-order rate constant. The rate of this reaction directly proportional with the chances of encounter of enzyme and substrate in the solution. Therefore, the k_{cat}/K_M actually determines the catalytic efficiency of an enzyme.

2.6. PRECLINICAL ANIMAL MODELS

2.6.1. General Handling of Animals

All animal studies and experimental procedures were performed either at the Central Animal Facility, Uluberia College, India (Reg. No.: 2057/GO/ReRcBi/S/19/CPCSEA) or at the Animal House, Dey's Medical Stores (Mfg.) Ltd. (Reg. No.: 50/PO/ReBi/99/CPCSEA) following the protocol approved by respective Institutional Animal Ethics Committee (IAEC) as per the standard guideline of Committee for the Purpose of Control and Supervision of Experiments on Animals (CPCSEA), Govt. of India. Non-diabetic C57BL/6j or Swiss albino mice of both sex were used for the studies. Animals were housed under specific-pathogen-free (SPF) conditions (maximum 5 mice per polypropylene cage; temp: 20±1.5ºC; ~55% relative humidity) under a 12-h light and 12-h dark cycle with access to food (standard chow for mice, Saha Enterprize, India) and water *ad libitum*. Autoclaved nest material and paper houses served as cage enrichment for mice. Animal cages were always randomly assigned to treatment or control groups.

2.6.2. Phenyl Hydrazine-Induced Bilirubin Encephalopathy

The study described in Chapter 04 of this thesis was conducted in two phases. In the first phase, the *in vivo* bilirubin degradation ability of C-Mn_3O_4 NPs was tested in time dependent manner along with plasma pharmacokinetics (PK), and pharmacodynamics (PD). In the second phase, sustainability of the treatment and

potential chemoprevention effect against bilirubin induced neurotoxicity were evaluated. For induction of severe neonatal hyperbilirubinemia (SNH) and associated bilirubin encephalopathy, the well-known phenyl hydrazine (PHz) intoxication model was used [4,5]. PHz drastically breaks down hemoglobin inside the rodent body, in turn, simulates a pathological condition of SNH and hemolytic anemia. One of the major reasons for choosing this particular model is the non-involvement of liver in the whole pathophysiology.

2.6.2.1. Phase 1

Mice were randomly divided into five groups (N=10/group). Animals of Group 1 served as control and received normal saline (150 µL; oral). Animals of Group 2 – 4 received two doses (i.p.) of PHz; 60 mg kg^{-1} BW at day-1 and 30 mg kg^{-1} BW at day-3. Animals of Group 3 were further treated with C-Mn_3O_4 NPs (0.25 mg kg^{-1} BW; oral) at day-3. Group 4 animals received citrate (0.15 mg kg^{-1} BW; oral) at day-3. Animals of Group 5 served as NP control and administered with C-Mn_3O_4 NPs (0.25 mg kg^{-1} BW; oral) at day-3. In phase-1, all measurements were performed on day-3.

2.6.2.2. Phase 2

Animals were randomly divided into five groups. Animals of Group 1 (N=10) served as control and received normal saline (150 µL; oral). Animals of Group 2 – 4 (N=30/group) received three doses (i.p.) of PHz; 45 mg kg^{-1} BW at day-1 and 30 mg kg^{-1} BW at day-3 and day-5 for induction of SNH. At day-1, -3, and -5, animals of Group 3 were further treated with C-Mn_3O_4 NPs (0.25 mg kg^{-1} BW; oral). Group 4 animals received citrate (0.15 mg kg^{-1} BW; oral) at day-1, -3, and -5. Group 5 animals were administered with C-Mn_3O_4 NPs (0.25 mg kg^{-1} BW; oral) at day-1, -3, and -5. In phase-2, all biochemical and neurobehavioral measurements were performed on day-6.

The time gap between two treatments on same day was ~1 h. PHz was always administered first. The optimum doses (both for intoxication and therapy) as well as treatment protocol was designed based on published literature and prior pilot studies performed by us.

2.6.3. CCl_4-Induced Hepatic Fibrosis Model

For induction of hepatic fibrosis in the work described in Chapter 05, we used CCl_4, a well-known hepatotoxic agent widely used to study hepato-protective activity of new drugs in *in vivo* experimental models of liver cirrhosis and fibrosis [4-6]. Chronic CCl_4 administration induces critical liver damage in mice which in turn simulates a condition of acute hepatitis showing similar symptoms as humans [6-8]. The liver fibrosis induced by CCl_4 is the result of reductive dehalogenation. The highly reactive metabolite trichloromethyl radical ($\bullet CCl_3$) is formed from the metabolic conversion of CCl_4 by cytochrome P-450. These radicals readily interacts with O_2 to form a more reactive trichloromethylperoxy radical ($CCl_3OO\bullet$), [9] which is capable of binding to protein or lipid, or of abstracting hydrogen atoms to form chloroform, that leads to lipid peroxidation and liver damage [10-12]. For the study, animals were randomized

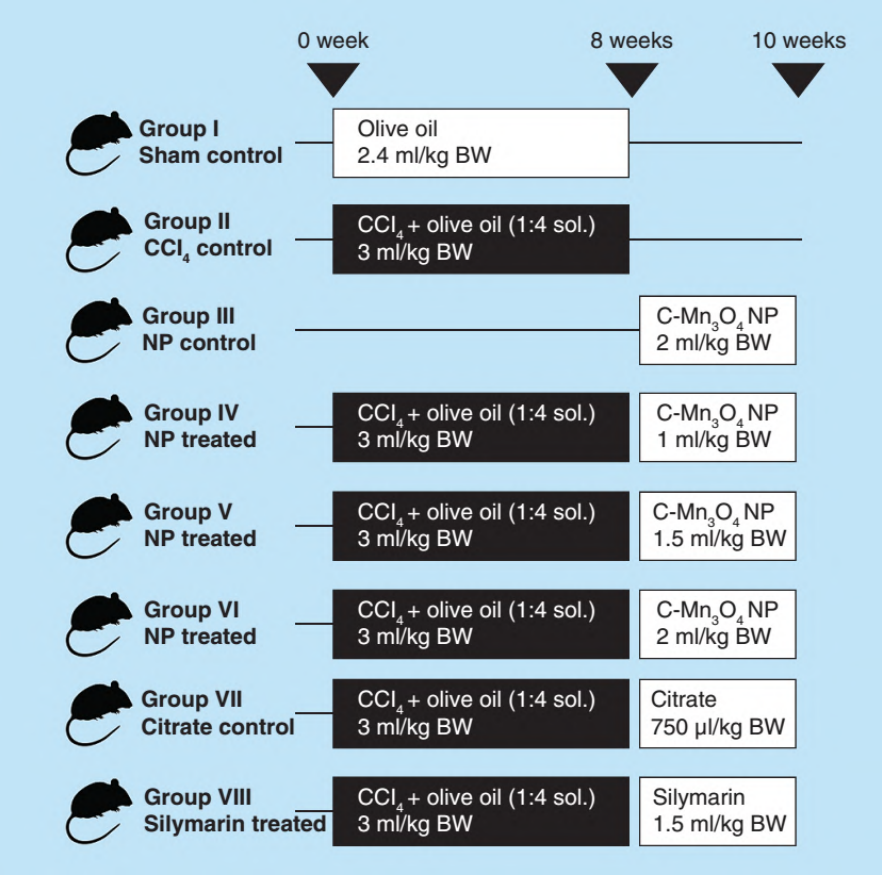

Figure 2.6. *Group division and treatment protocol of in vivo animal studies. Aqueous solution of NP: OD_{430} = 0.5; Silymarin concentration: 70 mg ml^{-1}.*

into eight groups (N=10/group). The division of groups and treatment protocol is described in Figure 2.6. Intraperitoneal injection (i.p.) of CCl_4 solution was used to introduce hepatic fibrosis and chronic hepatotoxicity. NPs were administered as aqueous solutions. Standard hepato-protective drug Silymarin was used as control. All treatments were performed via oral administration.

2.6.4. Cisplatin-Induced Chronic Kidney Disease (CKD)

In Chapter 06 study, we evaluated the potential of C-Mn_3O_4 NPs in the treatment of cisplatin-induced chronic kidney disease (CKD) in C57BL/6j mice, a well-known animal model for testing therapeutic interventions against CKD [13-15]. Cisplatin accumulates in mitochondria and reduces the activity of all four respiratory complexes (I–V) involved in the electron transport chain, thereby a surge in mitochondrial ROS formation takes place along with mitochondrial permeability transition pore (mPTP) opening, membrane depolarization and impairment in ATP production, leading to cell death [16,17]. The mitotoxic mechanism of cisplatin essentially mimics the pathogenesis of CKD. Therefore, an efficient reversal of damage in this rodent model is supposed to reflect the possible effects of a compound in higher animals.

In the study, mice were randomly divided into five groups (N=16/group): (1) control; (2) cisplatin; (3) cisplatin + C-Mn_3O_4 NPs; and (4) C-Mn_3O_4 NPs; (5) cisplatin + citrate. The experimental model of CKD was established according to the previous description. In brief, for induction of CKD, we used 8 mg kg^{-1} BW cisplatin (i.p.) in each alternative day for 28 days. After induction, we treated C-Mn_3O_4 NPs at 0.25 mg kg^{-1} BW (i.p.) for another 28 days. There was an overlap of 7 days between induction and treatment. Citrate was used at a dose of 0.25 mg kg^{-1} BW for 28 days. All doses were finalized based on reported literature and pilot experimentation.

2.6.5. Manganese-Induced Idiopathic Parkinson's Disorder

In the study described in Chapter 07, we evaluated the ameliorative effect of C-Mn_3O_4 NPs on manganese induced idiopathic Parkinson's disorder. Although manganese is an essential trace element for proper functioning of several crucial enzymes, excessive Mn in its ionic form (both 2+ and 3+) accumulates in the brain, particularly in basal ganglia, cerebellum, hippocampus and cause clinical signs and morphological lesions analogous to idiopathic Parkinson's disease (PD) [18-20].

For the study, the treatment protocol was as follows (N=10/group):

Group 1: Control (Normal saline 28 days)

Group 2: $MnCl_2$ treated (10 mg Mn kg^{-1} body weight (BW) for 28 days)

Group 3: $MnCl_2$ (10 mg Mn kg^{-1} body weight (BW) for 28 days) + C-Mn_3O_4 NPs (5 mg kg^{-1} BW for 21 days)

Group 4: C-Mn_3O_4 NPs (5 mg kg^{-1} BW for 28 days)

2.6.6. Heavy Metal-Induced Toxicity

In the studies described in Chapter 08 and Chapter 11 of this thesis, we used lead nitrate ($Pb(NO_3)_2$) as the intoxication material to mimic heavy metal toxicity in animals. Among all the heavy metals, lead (Pb) is a ubiquitous environmental as well as industrial pollutant that affects almost every organ system of the human body starting from nervous to excretory, hepatic to circulatory. Although, lead (Pb) itself is a non-redox metal and does not possess any pro-oxidant catalytic activity, rather coverts to some indirect mechanisms (e.g., auto-oxidation of hemoglobin (Hb), accumulation and subsequent auto-oxidation of δ-aminolevulinic acid (δ-ALA) induced by Pb) for imparting pathogenesis via oxidative disturbances [21-24].

In the Chapter 08 study, animals were randomly divided into 3 groups. First group (Control) of animals (N=10) orally received 200 µl physiological saline (0.9% NaCl) for 49 days (the entire study period). Remaining two groups (N=12/group) received $Pb(NO_3)_2$ solution (45 mg kg^{-1} body weight (BW)) intraperitoneally (i.p.) on

alternative days for a period of 28 days in order to induce Pb(II) mediated damage. The second group (Pb(II)) was left untreated for the rest of the experimental period (negative control) while, the third group (Pb(II)+C-Mn_3O_4 NP) was orally administered with C-Mn_3O_4 NPs (0.25 mg kg^{-1} BW) for the last 21 days. All agents were administered postprandial.

In the Chapter 11 study, animals were randomly divided into four groups (N=10/group) and treated according to the following protocol:

Group 1: Received Pb free water and daily given physiological saline (0.9% NaCl) by oral gavage during the whole course of the experiment.

Group 2: Intra-peritoneally (i.p.) received an aqueous solution of $Pb(NO_3)_2$ (50 mg/kg body weight (BW)) in every alternative day for 4 weeks for induction of oxidative stress and associated liver damage and then left untreated.

Group 3: Received aqueous solution of $Pb(NO_3)_2$ (50 mg/kg body weight (BW)) in every alternative day for the first 3 weeks. In 4th week it received both Pb(II) (i.p., every alternative day) and orally received SKP17LIV01 extract (3.5 ml/kg BW) daily. In the last week of treatment, it only received SKP17LIV01.

Group 4: Same as group 3 but orally received silymarin (100 mg/kg BW) instead of SKP17LIV01.

2.6.7. 3-Nitro Propionic Acid (3-NPA)-Induced Huntington's Disorder

In Chapter 09 study, we evaluated the role of C-Mn_3O_4 NPs in the treatment of neurodegenerative disorders. We selected a well-studied 3-NPA induced C57BL/6j mice model of HD to test the *in vivo* therapeutic efficacy of C-Mn_3O_4 nanozyme [25-28]. 3-NPA is known to inhibit mitochondrial respiratory complex-II (succinate dehydrogenase, SDH) in neuronal cells instigating mitochondrial impairment, ATP depletion, increase in reactive oxygen species (ROS), excitotoxicity and thereby, simulates a neurobehavioral condition exactly similar to mHtt toxicity and HD [29].

In this study, animals were randomly divided into five groups (N=10/group). The treatments were as follows,

Group 1: Control (Normal saline 16 days).

Group 2: 3-NPA treated (10 mg kg^{-1} body weight (BW) for alternative 4 days).

Group 3: 3-NPA (10 mg kg^{-1} body weight (BW) for alternatively first 4 days) + C-Mn_3O_4 NPs (0.5 mg kg^{-1} (BW) for 16 days).

Group 4: 3-Nitropropionic acid (10 mg kg^{-1} body weight (BW) for alternatively first 4 days) + Citrate (0.5 mg kg^{-1} (BW) for 16 days).

Group 5: C-Mn_3O_4 NPs (0.5 mg kg^{-1} (BW) for 16 days).

All treatments were performed by intraperitoneal (i.p.) administration.

2.6.8. Chronic Toxicity and Biodistribution of C-Mn_3O_4 NPs

In Chapter-10, we evaluated the systemic toxicity C-Mn_3O_4 NPs upon oral administration. For biodistribution and toxicity studies, animals were randomly assigned into four groups. Each group contained 20 male and 20 female mice. Three of these groups were treated with high (0.5 mg kg^{-1} BW), medium (0.25 mg kg^{-1} BW) and low (0.1 mg kg^{-1} BW) doses of C-Mn_3O_4 NPs, respectively. The remaining group was administered with normal saline and consider as a control. All treatments were performed through oral gavage for 90 consecutive days. At 91^{th} day all animals were sacrificed after 24 hours of last administration of doses.

2.7. SYSTEMS AND MOLECULAR PROBES

2.7.1. Human Serum Albumin (HSA)

Serum albumins are multi-domain proteins forming the major soluble protein constituent (60% of the blood serum) of the circulatory system [30]. Human Serum Albumin (HSA) (molecular weight 66,479 Da) is a heart-shaped tri-domain protein

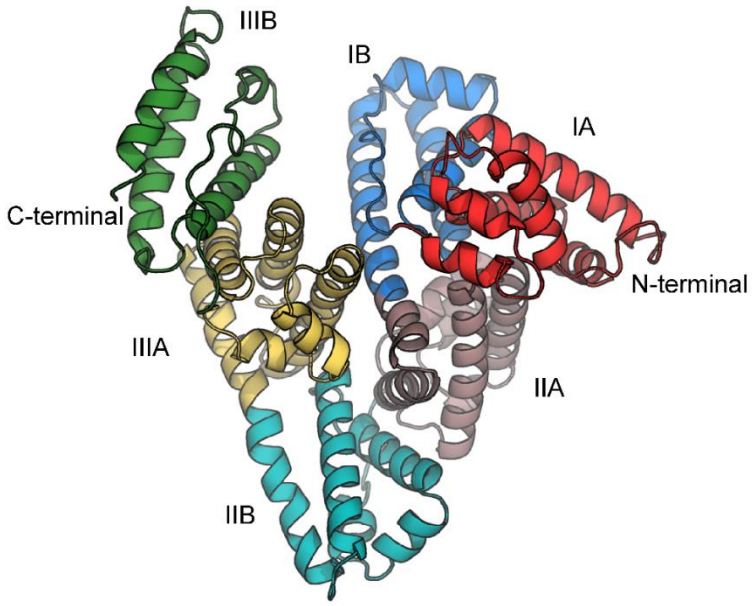

Figure 2.7. *Structure of Human Serum Albumin (HSA). Different domains and subdomains are marked with different colors.*

(Figure 2.7) with each domain comprising of two identical subdomains A and B with each domain depicting specific structural and functional characteristics [31]. HSA having 585 amino acid residues assumes solid equilateral triangular shape with sides ~80 Å and depth ~30 Å [32]. Its amino acid sequence comprises of 17 disulfide bridges distributed over all domains, one free thiol (Cys34) in domain-I and a tryptophan residue (Trp214) in domain-IIA. About 67% of HSA is α-helical while the rest of the structure being turns and extended polypeptides [32]. Each domain contains 10 principle helices (h1-h10). Subdomains A and B share a common motif that includes h1, h2, h3 and h4 for subdomain-A, and h7, h8, h9, h10 for subdomain-B. The non-existence of disulfide linkage connecting h1 and h3 in subdomain-IA is an exception. HSA is engaged with various physiological functions involving maintenance of osmotic blood pressure, transportation of a wide variety of ligands in and out of the physiological system. The protein binds various kinds of ligands [33] including photosensitizing drugs and nanoparticles [34]. The principal binding regions are located in subdomains IIA and IIIA of which IIIA binding cavity is the most active one [32] and binds digitoxin, ibuprofen and tryptophan. Warfarin, however, occupies a single site in domain-IIA. It is known that HSA undergoes reversible conformational transformation with change in pH of the protein solution [30,35], which is very

essential for picking up and releasing the drugs at sites of differing pH inside the physiological system. At normal pH (pH = 7), HSA assumes the normal form (N) which abruptly changes to fast migrating form (F) at pH values less than 4.3, as this form moves "fast" upon gel electrophoresis [36]. Upon further reduction in pH to less than 2.7 the F-form changes to the fully extended form (E). On the basic side of the normal pH (above pH = 8), the N-form changes to basic form (B) and above pH = 10, the structure changes to the aged form (A). Serum albumin undergoes an ageing process when stored at low ionic strength and alkaline pH. The ageing process is catalyzed by the free sulfhydryl group and involves sulfhydryl-disulfide interchange that results in the conservation of the sulfhydryl at its original position.

2.7.2. Glutahione Reductase (GR)

Glutathione reductase (GR) [EC 1.8.1.7] is one of a chain of enzymes which serves to maintain glutathione in the reduced form. GR restores intracellular GSH by reducing GSSG in the presence of NADPH and flavine adenine dinucleotide (FAD). GR represents the product of a single gene, but has been observed in association with cytoplasm, mitochondria, nuclei, and with subnuclear structures. GR homodimer

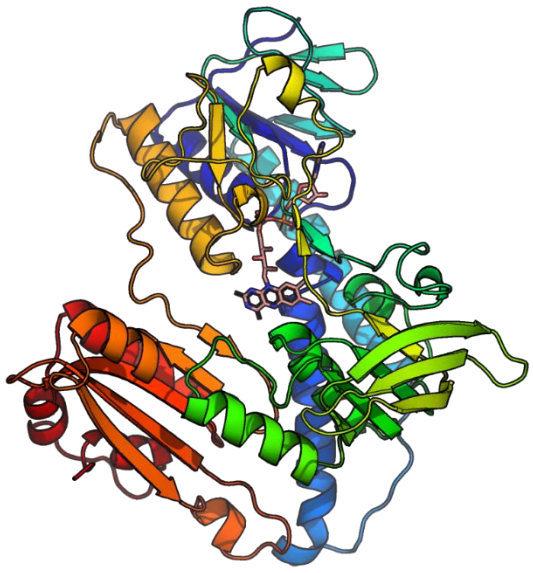

Figure 2.8. *Structure of human glutathione reductase (GR) bound to FAD.*

consists 3 domain (52 KDa); exhibits a Rossmann fold ($\beta_1\alpha_1\beta_2\beta_3$) single sheet, double layered topology. Each of the monomer consists 478 amino acid residues and an FAD molecule (Figure 2.8) [37-39]. GR requires functional SH groups for its activity. The enzyme is therefore completely inhibited by salyrgan, but can be reactivated by excess cysteine. Divalent cations also inhibit its activity. For example, zinc causes more than a 50% inhibition at 10^{-6} M. Insulin with a high zinc content inhibits strongly. Pre-incubation of the enzyme with TPNH and GSSG can protect the enzyme from the action of zinc or insulin. It is not possible to reactivate the enzyme with EDTA after heavy metal inhibition. Heparin inhibits (pH-dependent), especially the DPNH reaction. Under the optimum conditions for the reaction (pH 6.2) the enzyme is completely inhibited by 2×10^{-6} M heparin.

2.7.3. Bilirubin (BR)

Bilirubin (BR), the yellow-orange breakdown product of normal heme catabolism in mammalian systems, introduces great biological and diagnostic values [40]. Both antioxidant and toxic properties have been attributed to BR [41], which is normally conjugated with glucuronic acid and then excreted in the bile. However, when its conjugation with glucuronic acid is inhibited, as in neonatal jaundice and in hereditary forms of congenital jaundice, excess BR bind and deposit to various tissues, giving rise to severe hyperbilirubinemia and neurotoxicity. Phototherapy, the most effective treatment for jaundice to date, decreases the BR levels in the blood by changing the *ZZ*-BR isomer into water-soluble *ZE*-BR [42-44]. Because this reaction is readily reversible, equilibrium is established between native BR and the *ZE* isomer when BR is photoirradiated in a closed system. The second fastest reaction that occurs when BR is exposed to light is the production of lumirubin, a structural isomer of BR.

2.7.4. 2,2-Diphenyl-1-picrylhydrazyl (DPPH)

2,2-Diphenyl-1-picrylhydrazyl (DPPH) is a stable nitrogen centered free radical having a strong purple color and is conventionally used to determined free radical

scavenging activities of natural and synthetic antioxidants [45]. Neutralization of this radical by antioxidants can happen through either direct reduction via electron transfers or radical quenching via hydrogen atom transfer [46]. The strong absorption band centered at 520 nm disappears upon neutralization and the solution becomes colorless. In conventional literature, the change in DPPH absorbance after the addition of a test material is often used as an index of the antioxidant capacity of the material [47].

2.7.5. 2'-7' Dichlorofluorescin diacetate (DCFH-DA)

Dichlorofluorescin diacetate (DCFH-DA) is a cell permeable fluorogenic probe widely used in measurement of various reactive oxygen species (ROS). After internalization into the cell, DCFH-DA is readily deacetylated by cellular esterases to non-fluorescent DCFH carboxylate anion (for *in vitro* assays de-esterification is achieved using NaOH). Subsequently, two-electron oxidation of DCFH by intracellular (or extracellular for *in vitro* assays) ROS results in the formation of a fluorescent product, 2'-7'dichlorofluorescein (DCF), which can be monitored by several fluorescence-based techniques (e.g., spectroscopy, confocal microscopy, flow cytometry). The fluorescence intensity of DCF quantifies the intracellular (or extracellular) ROS and oxidative stress.

2.7.6. 3-(4,5-dimethylthiazol-2-yl)-2,5-diphenyl tetrazolium bromide (MTT)

2'-7'3-(4,5-Dimethylthiazol-2-yl)-2,5-diphenyltetrazolium bromide (MTT) is a water-soluble tetrazolium dye that is converted into an insoluble purple formazan due to the catalytic activity of mitochondrial succinate dehydrogenase in living cells. Hence, the reduction of MTT to formazan crystal is dependent on mitochondrial respiration and reflects to the metabolic activity of a cell [48]. The formazan product is estimated by measuring the absorbance at 550 nm after dissolution in DMSO and widely used to determine cell viability. It has to be noted that, cells with low metabolic

activities i.e., thymocytes and splenocytes reduce very low amount of MTT, whereas, rapidly dividing cells reduce more. Moreover, the assay condition can greatly influence the metabolic activity of a cell, subsequently leading to altered tetrazolium dye reduction without affecting cell viability.

2.7.7. Rhodamine-123 (Rh-123)

Rhodamine 123 (Rh-123) is a cell-permeable, cationic, green-fluorescent dye (λ_{ex}=503 nm; λ_{em}=527 nm) that is readily sequestered by active mitochondria without any cytotoxic effects. This is widely used as a sensitive and specific probe to monitor mitochondrial membrane potential ($\Delta\psi_M$) as mitochondrial energization induces red shift along with quenching of Rh-123 fluorescence. The rate of fluorescence decay is proportional to the mitochondrial membrane potential [49]. The measurements can be performed using flow cytometry, fluorescence microscopy and spectroscopy.

2.7.8. Luminol

Luminol (5-Amino-2,3-dihydro-1,4-phthalazinedione) is one of the best known and most widely used chemiluminescent compounds, which glows with a bright blue light when activated with an oxidizing agent like hydrogen peroxide (H_2O_2) in an alkaline solution in the presence of a catalyst. Reaction of the compound with the oxidant results in replacement of nitrogen and hydrogen with oxygen. As a result, the vibrational energy created by the reaction is transferred to an electron which is pushed up to a higher energy level which is subsequently emitted in the form of a photon (λ_{em}=425 nm) during its return to the stable lower energy ground state. Luminol chemiluminescence is often used as an indicator to detect present of OH• radicals in a solution [50].

2.7.9. Reduced Nicotinamide Adenine Dinucleotide Phosphate (NADPH)

Reduced nicotinamide adenine dinucleotide phosphate (NADPH) preserves cellular redox homeostasis by providing reducing equivalents for GR and thioredoxin reductase, which maintain GSH and thioredoxin in their biologically reduced state. The major source of NADPH in animals and other non-photosynthetic organisms is the pentose phosphate pathway. NADPH is produced from $NADP^+$. In general, $NADP^+$ is synthesized before NADPH is. Such a reaction usually starts with NAD^+ from either the *de novo* or the salvage pathway, with NAD^+ kinase adding the extra phosphate group. $NAD(P)^+$ nucleosidase allows for synthesis from nicotinamide in the salvage pathway, and $NADP^+$ phosphatase can convert NADPH back to NADH to maintain a balance.

2.7.10. MitoSOX™ Red

MitoSOX™ Red (Thermo Fisher Scientific, USA) is a non-toxic cell-permeable fluorogenic dye (λ_{ex}=510 nm; λ_{em}=580 nm) that specifically targets mitochondria in living cells. As it produces red fluorescence explicitly in presence of superoxide (not in presence of other reactive oxygen or nitrogen species), it is widely used to probe mitochondrial superoxide content as a marker of oxidative stress. This reagent may be used to distinguish artifacts of isolated mitochondrial preparations from direct measurements of superoxide generated in the mitochondria of live cells. It may also provide a valuable tool in the discovery of agents that modulate mitochondrial redox state in various pathologies.

2.7.11. JC-1

JC-1 is a lipophilic, fluorescent, cationic carbocyanine dye which accumulates in the mitochondria in a concentration-dependent manner. The dye exists as a monomer at low concentrations and yields green fluorescence (λ_{ex}=510 nm; λ_{em}=527

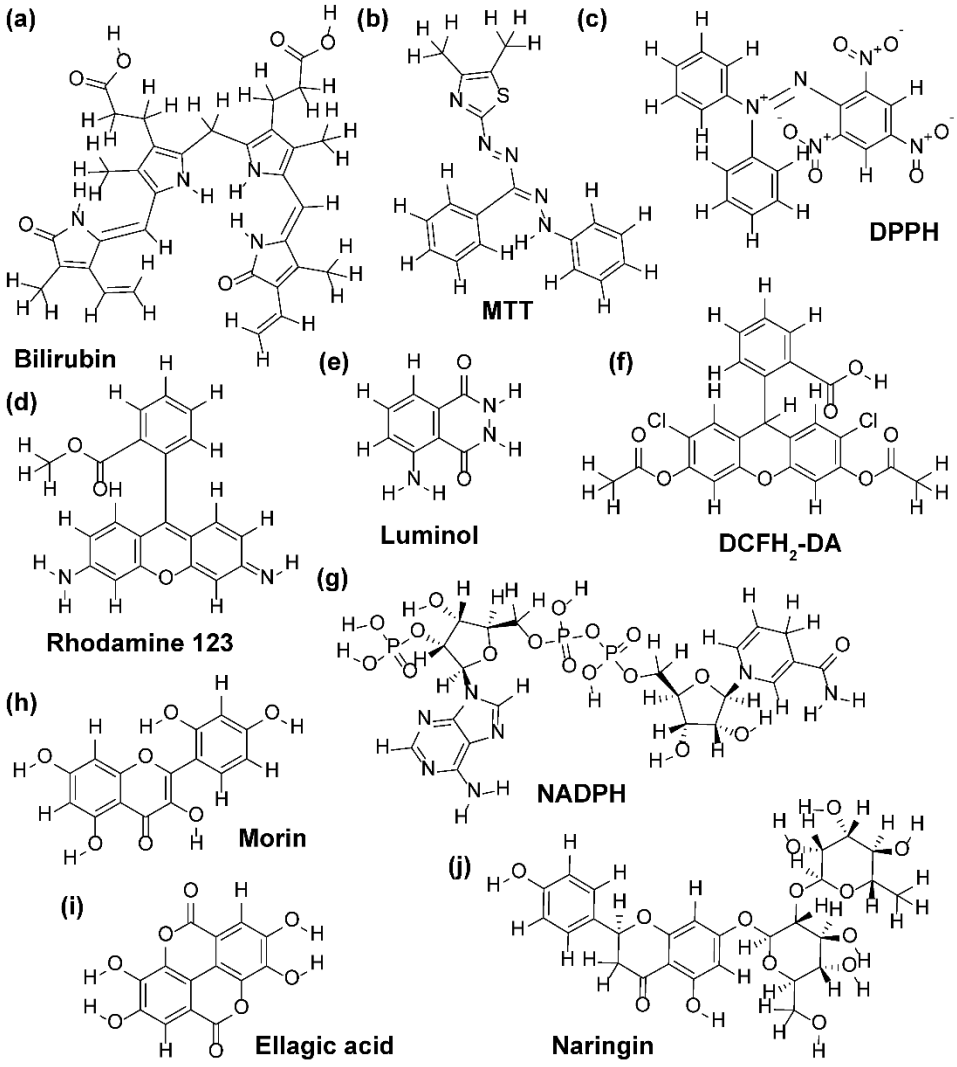

Figure 2.9. *Chemical structures of the different molecular probes used in the studies.*

nm). While, at higher concentrations, the dye forms J-aggregates that exhibit a broad excitation spectrum and a red shift in the emission maxima (λ_{ex}=585 nm; λ_{em}=590 nm). Thus, in healthy cells with a normal $\Delta\psi_M$, the JC-1 dye enters and accumulates in the energized and negatively charged mitochondria and spontaneously forms red fluorescent J-aggregates. By contrast, in unhealthy or apoptotic cells it enters the mitochondria but to a lesser degree since the inside of the mitochondria is less negative because of increased membrane permeability and consequent loss of electrochemical potential. Under this condition, JC-1 does not reach a sufficient concentration to trigger the formation of J aggregates thus retaining its original green fluorescence.

Based on these premises, the red/green fluorescence ratio of the dye in the mitochondria can be considered as a direct assessment of the state of the mitochondria polarization whereas the higher is the $\Delta\psi_M$, the more elevated is the red shift of the dye (more J aggregates are formed). Vice-versa; the lower is the $\Delta\psi_M$ of the mitochondria and the lower is the red to green ratio of the fluorescent marker (few J aggregates are formed). Therefore, mitochondrial depolarization is indicated by a reduction in the red to green fluorescence intensity ratio.

2.7.12. Morin

Morin is a pentahydroxyflavone that is a 7 hydroxyflavonol bearing 3 additional hydroxy substituents at positions 2' 4' and 5. It is a potent antioxidant [51] and generally extracted from *Maclura pomifera* (Osage orange), *Maclura tinctoria* (old fustic) and from leaves of *Psidium guajava* (common guava) [52]. Previously, it exhibited inhibitory action against IgE-mediated allergic response. Morin treatment significantly down-regulated expressions of BLT2, NF-κB, and Th2-cytokine (TNF-α, IL-1β, IL-4, IL-6, and IL-13) in lungs of murine model of allergic asthma [53]. Studies have also indicated the inhibitory action of Morin on the enzyme fatty acid synthase [54] as well as prevents amyloid formation and disaggregates amyloid fibers [55].

2.7.13. Naringin

Naringin (4′,5,7-trihydroxyflavanone-7-rhamnoglucoside) is an abundant flavone glycoside present in citrus fruits with interesting biological and pharmacological actions [56]. Naringin is responsible for the bitter taste of fruits [57]. *In vitro* studies have shown Naringin to significantly affect osteogenic differentiation and cell proliferation by improving signalling pathway activity [58]. In animal models of inflammation Naringin reduces the expression of signalling factors associated with the inflammatory response, e.g., interleukin-6 (IL-6), interleukin-8 (IL-8), inducible nitric oxide synthase (iNOS), nuclear factor erythroid 2-related factor 2 (Nrf2) and TNF-α [59]. Naringin also exhibits active anticancer activity by acting as a suppressing

and blocking agents [60]. Naringin inhibits cell proliferation and promotes cell apoptosis in tumour cells, including triple-negative breast cancer (TNBC) cells, human cervical cancer (SiHa) cells and bladder cancer cells [61].

2.7.13. Ellagic Acid (EA)

Ellagic acid (EA) is a natural polyphenol found in strawberry, raspberry, blackberry grapes, green tea, pomegranates, and the stem and bark of *Eucalyptus globulus* and *Eucalyptus maculate* [62]. EA and its derivatives have a number of health benefits, many of which are attributed to its antioxidant properties [63]. Studies on EA have shown potent antimicrobial activity. EA was effective against several bacterial strains, exhibiting bactericidal activity against group A *Streptococcus*, *Corynebacterium diphtheria,* and inhibitory activity against *Bacillus subtilis*, *Clostridium sporogenes*, *Staphylococcus aureus*, *Neisseria meningitidis* and *Moraxella catarrhalis* [64].

REFERENCES

[1] J. R. Lakowicz, Principles of Fluorescence Spectroscopy, Springer, Boston, MA, (2006).

[2] A. Rodger, B. Norden, Circular Dichroism and Linear Dichroism, Oxford University Press, Oxford, (1997).

[3] N. Berova, K. Nakanishi, R. W. Woody, Circular Dichroism, Wiley-VCH, New York, (2000).

[4] G. Bortolussi, A. F. Muro, Pediatr. Res. 87 (2020) 17.

[5] A. C. Rice, S. M. Shapiro, Pediatr. Res. 64 (2008) 265.

[6] L. W. Weber, M. Boll, A. Stampfl, Crit. Rev. Toxicol. 33 (2003) 105.

[7] S. Basu, Toxicology 189 (2003) 113.

[8] N. Kabir, H. Ali, M. Ateeq, M. F. Bertino, M. R. Shah, L. Franzel, RSC Adv. 4 (2014) 9012.

[9] J. Weerachayaphorn, A. Chuncharunee, S. Jariyawat, B. Lewchalermwong, S. Amonpatumrat, A. Suksamrarn, P. Piyachaturawat, J. Ethnopharmacol. 129 (2010) 254.

[10] W. J. Brattin, E. A. Glende, R. O. Recknagel, J. Free Radic. Biol. Med. 1 (1985) 27.

[11] R. O. Recknagel, E. A. Glende, J. A. Dolak, R. L. Waller, Pharmacol. Ther. 43 (1989) 139.

[12] N. Jia, J. Wen, L. Qian, X. Qian, Y. Wu, G. Fan, Toxicology 237 (2007) 1.

[13] M. Shi, K. L. McMillan, J. Wu, N. Gillings, B. Flores, O. W. Moe, M. C. Hu, Lab. Invest. 98 (2018) 1105.

[14] S. V. Shah, M. M. Rajapurkar, Hemoglobin 33 (2009) 378.

[15] S. I. Landau, X. Guo, H. Velazquez, R. Torres, E. Olson, R. Garcia-Milian, G. W. Moeckel, G. V. Desir, R. Safirstein, Kidney Int. 95 (2019) 797.

[16] G. y. Nowak, J. Biol. Chem. 277 (2002) 43377.

[17] R. Marullo, E. Werner, N. Degtyareva, B. Moore, G. Altavilla, S. S. Ramalingam, P. W. Doetsch, PLoS ONE 8 (2013) e81162.

[18] T. R. Guilarte, N. C. Burton, J. L. McGlothan, T. Verina, Y. Zhou, M. Alexander, L. Pham, M. Griswold, D. F. Wong, T. Syversen, J. Neurochem. 107 (2008) 1236.

[19] R. G. Lucchini, C. J. Martin, B. C. Doney, NeuroMolecular Med. 11 (2009) 311.

[20] M. G. Cersosimo, W. C. Koller, Neurotoxicology 27 (2006) 340.

[21] P. C. Hsu, Y. L. Guo, Toxicology 180 (2002) 33.

[22] K. Chander, K. Vaibhav, M. Ejaz Ahmed, H. Javed, R. Tabassum, A. Khan, M. Kumar, A. Katyal, F. Islam, M. S. Siddiqui, Food Chem. Toxicol. 68 (2014) 297.

[23] H. Gurer, N. Ercal, Free Radic. Biol. Med. 29 (2000) 927.

[24] S. Dewanjee, R. Sahu, S. Karmakar, M. Gangopadhyay, Food Chem. Toxicol. 55 (2013) 78.

[25] P. Kumar, S. S. V. Padi, P. S. Naidu, A. Kumar, Fundam. Clin. Pharmacol. 21 (2007) 297.

[26] A. C. Ludolph, F. He, P. S. Spencer, J. Hammerstad, M. Sabri, Can. J. Neurol. Sci. 18 (2015) 492.

[27] R. G. Mealer, S. Subramaniam, S. H. Snyder, J. Neurosci. 33 (2013) 4206.

[28] C. E. Teunissen, H. W. M. Steinbusch, M. Angevaren, M. Appels, C. de Bruijn, J. Prickaerts, J. de Vente, Neuroscience 105 (2001) 153.

[29] M. N. Herrera-Mundo, D. Silva-Adaya, P. D. Maldonado, S. Galván-Arzate, L. Andrés-Martínez, V. Pérez-De La Cruz, J. Pedraza-Chaverrí, A. Santamaría, Neurosci. Res. 56 (2006) 39.

[30] J. F. Foster, The Plasma Proteins, Academic Press, New York, (1960).

[31] M. Dockal, D. C. Carter, F. Ruker, J. Biol. Chem. 274 (1999) 29303.

[32] X. M. He, D. C. Carter, Nature 358 (1992) 209.

[33] J. Ghuman, P. A. Zunszain, I. Petitpas, A. A. Bhattacharya, M. Otagiri, S. Curry, J. Mol. Biol. 353 (2005) 38.

[34] M. Wardell, Z. Wang, J. X. Ho, J. Robert, F. Ruker, J. Ruble, D. C. Carter, Biochem. Biophys. Res. Commun. 291 (2002) 813.

[35] J. A. Luetscher, J. Am. Chem. Soc. 61 (1939) 2888.

[36] J. F. Foster, Some Aspects of the Structure and Conformational Properties of Serum Albumin, Pergamon, Oxford, (1977).

[37] R. Masella, R. Di Benedetto, R. Varì, C. Filesi, C. Giovannini, J. Nutr. Biochem. 16 (2005) 577.

[38] O. Dym, D. Eisenberg, Protein Sci. 10 (2001) 1712.

[39] R. H. Garrett, C. M. Grisham, Biochemistry. Thomson Brooks/Cole, Belmont, CA, 2005.

[40] J. D. Ostrow, Bile Pigments and Jaundice: Molecular, Metabolic and Medical Aspects, Marcel Dekker, New York, (1986).

[41] R. Stocker, A. N. Glazer, B. N. Ames, Proc. Natl. Acad. Sci. 84 (1987) 5918.

[42] D. A. Lightner, A. F. McDonagh, Acc. Chem. Res. 17 (1984) 417.

[43] A. A. Lamola, W. E. Blumberg, R. McClead, A. Fanaroff, Proc. Natl. Acad. Sci. 78 (1981) 1882.

[44] S. E. Braslavsky, A. R. Holzwarth, K. Schaffner, Angew. Chem. Int. Ed. Engl. 22 (1983) 656.

[45] S. C. Ghagane, S. I. Puranik, V. M. Kumbar, R. B. Nerli, S. S. Jalalpure, M. B. Hiremath, S. Neelagund, R. Aladakatti, Integr. Med. Res. 6 (2017) 79.

[46] L. Cerretani, A. Bendini, in: V.R. Preedy, R.R. Watson (Eds.), Olives and Olive Oil in Health and Disease Prevention, Academic Press, San Diego, USA, (2010), 625.

[47] R. W. Holtz, in: N. Dayan (Ed.), Skin Aging Handbook, William Andrew Publishing, Norwich, NY, (2009), 329.

[48] J. van Meerloo, G. J. L. Kaspers, J. Cloos, in: I.A. Cree (Ed.), Cancer Cell Culture: Methods and Protocols, Humana Press, Totowa, NJ, (2011), 237.

[49] A. Baracca, G. Sgarbi, G. Solaini, G. Lenaz, Biochim. Biophys. Acta. - Bioenergetics 1606 (2003) 137.

[50] Y. Nosaka, S. Komori, K. Yawata, T. Hirakawa, A. Y. Nosaka, Phys. Chem. Chem. Phys. 5 (2003) 4731.

[51] Q. K. Panhwar, S. Memon, J. Coord. Chem. 64 (2011) 2117.

[52] P. Rattanachaikunsopon, P. Phumkhachorn, Fitoterapia 78 (2007) 434.

[53] D. K. Amit, L. Zihao, A. M. Anwesha, L. B. Subhash, Curr. Mol. Pharmacol. 12 (2019) 122.

[54] T. Wei-Xi, Curr. Med. Chem. 13 (2006) 967.

[55] H. Noor, P. Cao, D. P. Raleigh, Protein Sci. 21 (2012) 373.

[56] S. Srinivasan, V. Vinothkumar, R. Murali, in: R.R. Watson, V.R. Preedy (Eds.), Bioactive Food as Dietary Interventions for Diabetes (Second Edition), Academic Press, (2019), 335.

[57] M. H. Ribeiro, Appl. Microbiol. Biotechnol. 90 (2011) 1883.

[58] Z. Peng, K.-r. Dai, S.-g. Yan, W.-q. Yan, Z. Chao, D.-q. Chen, X. Bo, Z.-w. Xu, Eur. J. Pharmacol. 607 (2009) 1.

[59] V. Habauzit, S. M. Sacco, A. Gil-Izquierdo, A. Trzeciakiewicz, C. Morand, D. Barron, S. Pinaud, E. Offord, M.-N. Horcajada, Bone 49 (2011) 1108.

[60] O. Benavente-García, J. Castillo, J. Agric. Food Chem. 56 (2008) 6185.

[61] R. Chen, Q.-L. Qi, M.-T. Wang, Q.-Y. Li, Pharm. Biol. 54 (2016) 3203.

[62] E. H. Kang, T. Y. Kown, G. T. Oh, W. F. Park, S.-I. Park, S. K. Park, Y. I. Lee, Antiviral Res. 72 (2006) 100.

[63] D. V. Ratnam, D. D. Ankola, V. Bhardwaj, D. K. Sahana, M. N. V. R. Kumar, J. Control Release 113 (2006) 189.

[64] M. Krauze-Baranowska, M. Majdan, R. Hałasa, D. Głód, M. Kula, I. Fecka, A. Orzeł, Food Funct. 5 (2014) 2536.

CHAPTER 03

Instrumentation and Sample Preparation

In this chapter, the details of the instrumental setups, sample preparation techniques, and experimental protocols used for the studies described in this thesis have been described. Furthermore, details about the *in silico* (i.e., computational) studies have been included in this chapter.

3.1. INSTRUMENTAL SETUP

3.1.1. Steady-State Absorption and Fluorescence Spectroscopy

Steady-state UV-vis absorption and emission spectra of the molecules of interest were recorded using Shimadzu Model UV-2600 spectrophotometer (Shimadzu Corporation, Kyoto, Japan) and Jobin Yvon Fluoromax-3® spectrofluorimeter (Horiba, Kyoto, Japan), respectively. Schematic ray diagrams of these two instruments are shown in Figures 3.1 and 3.2.

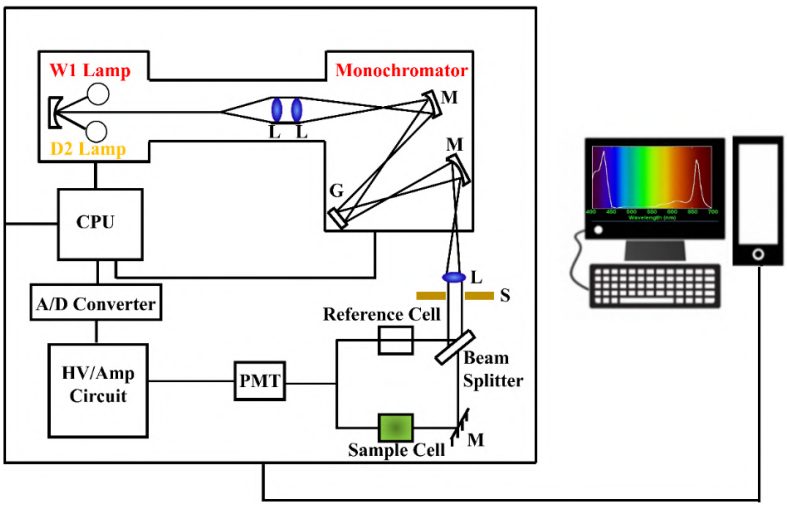

Figure 3.1. *Schematic ray diagram of an absorption spectrophotometer. Tungsten halogen (W1) and deuterium lamps (D2) are used as light sources in the visible and UV regions, respectively. M, G, L, S, PMT designate mirror, grating, lens, shutter and photomultiplier tube, respectively. CPU, A/D converter and HV/amp indicate central processing unit, analog to digital converter and high-voltage/amplifier circuit, respectively.*

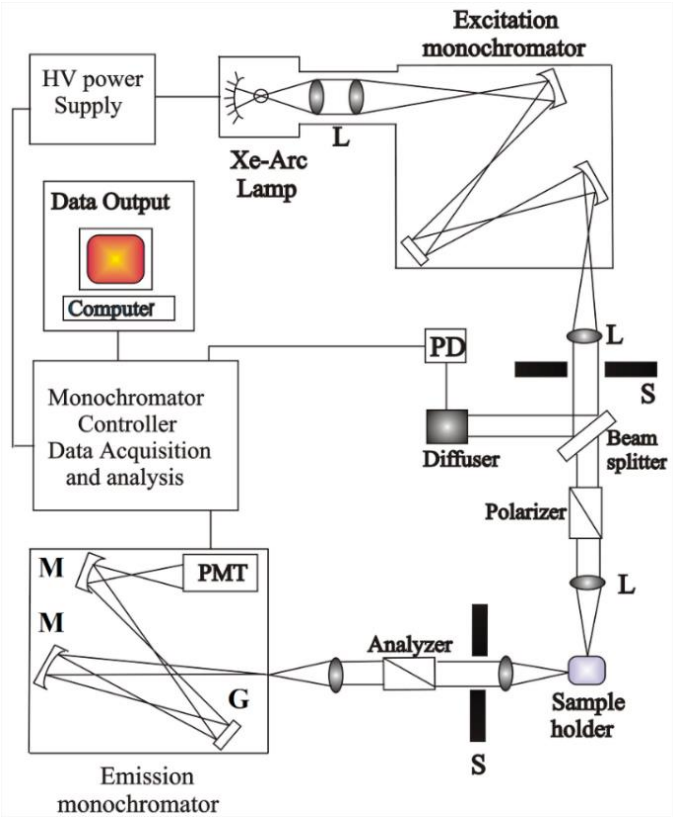

Figure 3.2. *Schematic ray diagram of an emission spectrofluorometer. M, G, L, S, PMT and PD represent mirror, grating, lens, shutter, and photomultiplier tube and reference photodiode, respectively.*

3.1.2. Circular Dichroism (CD) Measurement

CD is a form of spectroscopy which is based on the differential absorption of left and right-handed circularly polarized light. It is generally used to determine the structure of macromolecules (including the secondary structure of proteins). The CD measurements were performed using JASCO-815 spectropolarimeter (JASCO International Co. Ltd, Tokyo, Japan) with a temperature controller attachment (Peltier) (Figure 3.3). The CD spectra were acquired using quartz cells of 0.1 and 1.0 cm path length. For proteins the typical concentration used for CD measurements were within 10 μM.

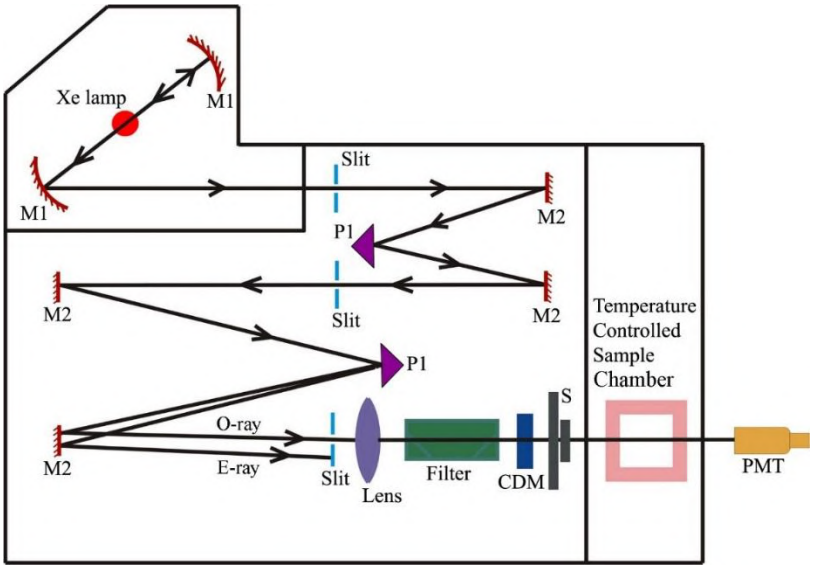

Figure 3.3. *Schematic ray diagram of a circular dichroism (CD) spectropolarimeter. M1, M2, P1, S, PMT, CDM, O-ray and E-ray represent concave mirror, plain mirror, reflecting prism, shutter, photomultiplier tube, CD-modulator, ordinary ray and extraordinary ray, respectively.*

3.1.3. Time-Correlated Single Photon Counting (TCSPC) Technique

All the picosecond-resolved fluorescence transients were recorded using TCSPC technique. The schematic block diagram of a TCSPC system is shown in

Figure 3.4. TCSPC setup from Edinburgh instruments, UK, was used during fluorescence decay acquisitions. The instrument response functions (IRFs) of the laser sources at different excitation wavelengths varied between 70 ps to 80 ps. The fluorescence from the sample was detected by a photomultiplier after dispersion through a grating monochromator [1]. For all transients, the polarizer in the emission side was adjusted to be at 54.7° (magic angle) with respect to the polarization axis of excitation beam.

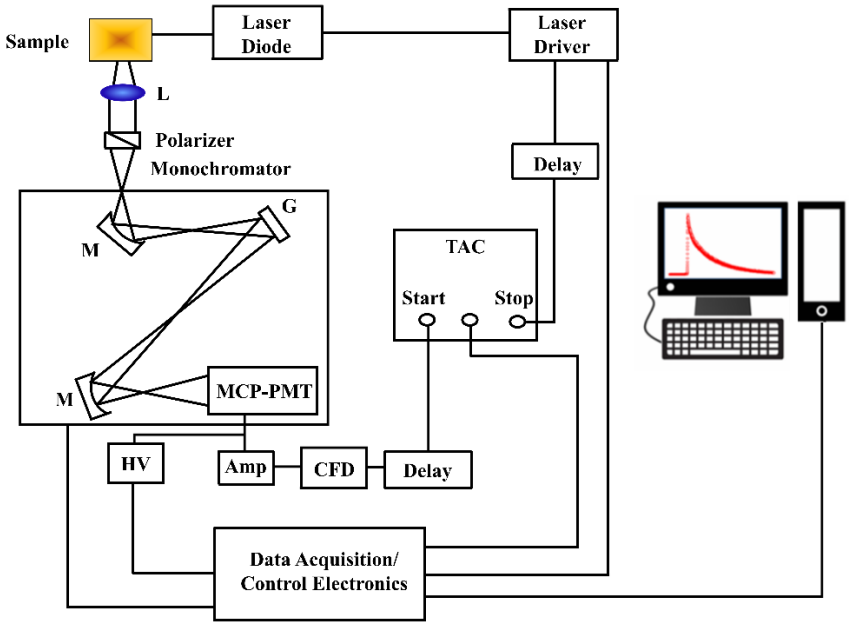

Figure 3.4. *Schematic ray diagram of a time correlated single photon counting (TCSPC) spectrophotometer. A signal from microchannel plate photomultiplier tube (MCP-PMT) is amplified (Amp) and connected to start channel of time to amplitude converter (TAC) via constant fraction discriminator (CFD) and delay. The stop channel of the TAC is connected to the laser driver via a delay line. L, M, G and HV represent lens, mirror, grating and high voltage source, respectively.*

3.1.4. Dynamic Light Scattering (DLS)

Dynamic light scattering (DLS), also known as Photon Correlation Spectroscopy (PCS) or Quasi-Elastic Light Scattering (QELS), is one of the most popular techniques used to determine the hydrodynamic size of the particle. DLS

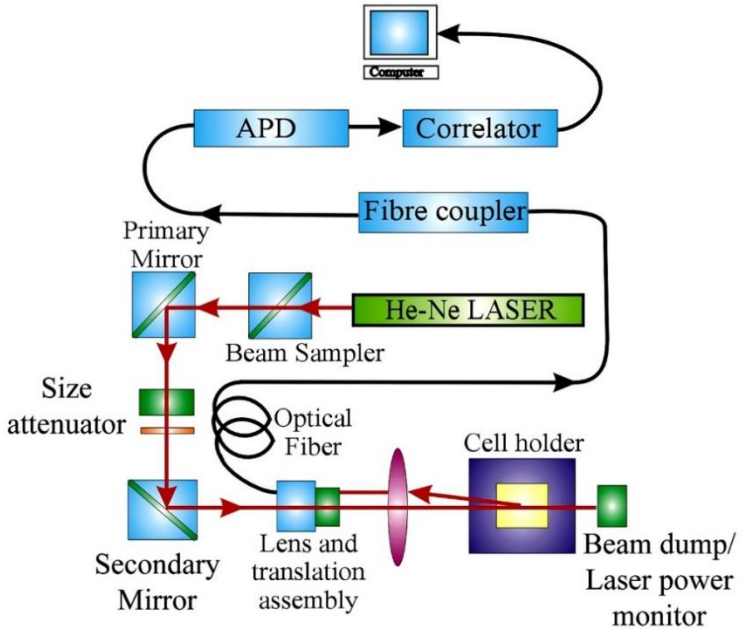

Figure 3.5. *Schematic ray diagram of dynamic light scattering (DLS) instrument. The avalanche photo diode (APD) is connected to preamplifier/amplifier assembly and finally to correlator. It has to be noted that lens and translational assembly, laser power monitor, size attenuator, laser are controlled by the computer.*

measurements were performed on a Nano S Malvern instruments, UK employing a 4 mW He-Ne laser (λ= 632.8 nm) and equipped with a thermostatic sample chamber. The instrument allows DLS measurements in which all the scattered photons are collected at 173˚ scattering angle (Figure 3.5). The instrument measures the time-dependent fluctuation in intensity of light scattered from the particles in solution at a fixed scattering angle. The ray diagram of the DLS setup is shown in Figure 3.5.

3.1.5. Fourier Transformed Infrared (FTIR) Measurement

FTIR spectroscopy is a technique that can provide very useful information about functional groups in a sample. An infrared spectrum represents the fingerprint of a sample with absorption peaks which corresponds to the frequencies of vibrations between the bonds of the atoms making up the material. As each different material is a unique combination of atoms, no two compounds produce the exact same infrared spectrum. Therefore, infrared spectroscopy can result in a positive identification

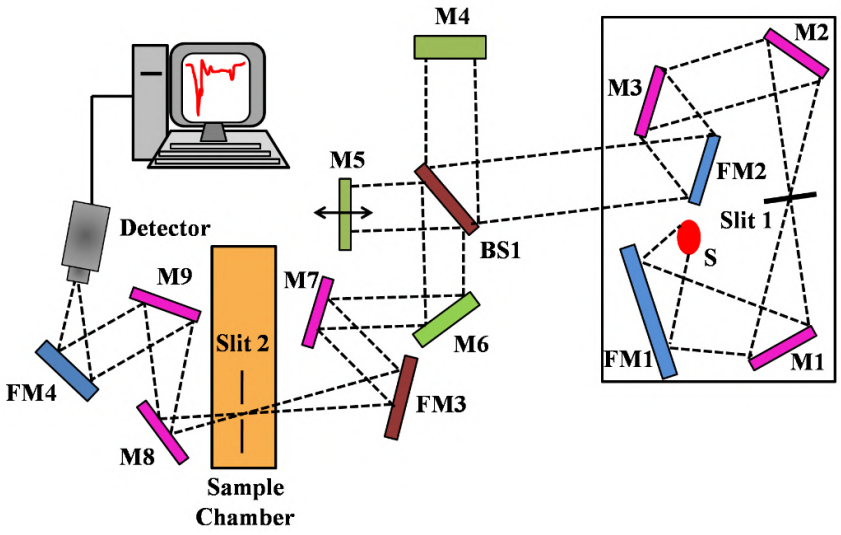

Figure 3.6. *Schematic of Fourier Transform Infrared (FTIR) spectrometer. It is basically a Michelson interferometer in which one of the two fully-reflecting mirrors is movable, allowing a variable delay (in the travel-time of the light) to be included in one of the beams. M, FM and BS1 represent the mirror, focussing mirror and beam splitter, respectively. M5 is a moving mirror.*

(qualitative analysis) of every different kind of material. In addition, the size of the peaks in the spectrum is a direct indication of the amount of material present.

The two-beam Michelson interferometer is the heart of FTIR spectrometer. It consists of a fixed mirror (M4), a moving mirror (M5) and a beam-splitter (BS1), as illustrated in Figure 3.6. The beam-splitter is a laminate material that reflects and transmits light equally. The collimated IR beam from the source is partially transmitted to the moving mirror and partially reflected to the fixed mirror by the beam-splitter. The two IR beams are then reflected back to the beam-splitter by the mirrors. The detector then sees the transmitted beam from the fixed mirror and reflected beam from the moving mirror, simultaneously. The two combined beams interfere constructively or destructively depending on the wavelength of the light (or frequency in wavenumbers) and the optical path difference introduced by the moving mirror. The resulting signal is called an interferogram which has the unique property that every data point (a function of the moving mirror position) which makes up the signal has information about every infrared frequency which comes from the source. Because the analyst requires a frequency spectrum (a plot of the intensity at each individual frequency) in order to make identification, the measured interferogram

signal cannot be interpreted directly. A means of "decoding" the individual frequencies is required. This can be accomplished *via* a well-known mathematical technique called the Fourier transformation. This transformation is performed by the computer which then presents the user with the desired spectral information for analysis. FTIR measurements were performed on a JASCO FTIR-6300 spectrometer (transmission mode). For the FTIR measurements, powdered samples were mixed with KBr powder and pelletized. The background correction was made using a reference blank of KBr pellet.

3.1.6. Transmission Electron Microscope (TEM)

A FEI TecnaiTF-20 field-emission high-resolution TEM (Figure 3.7) equipped with an energy dispersive X-ray (EDAX) spectrometer was used to characterize the

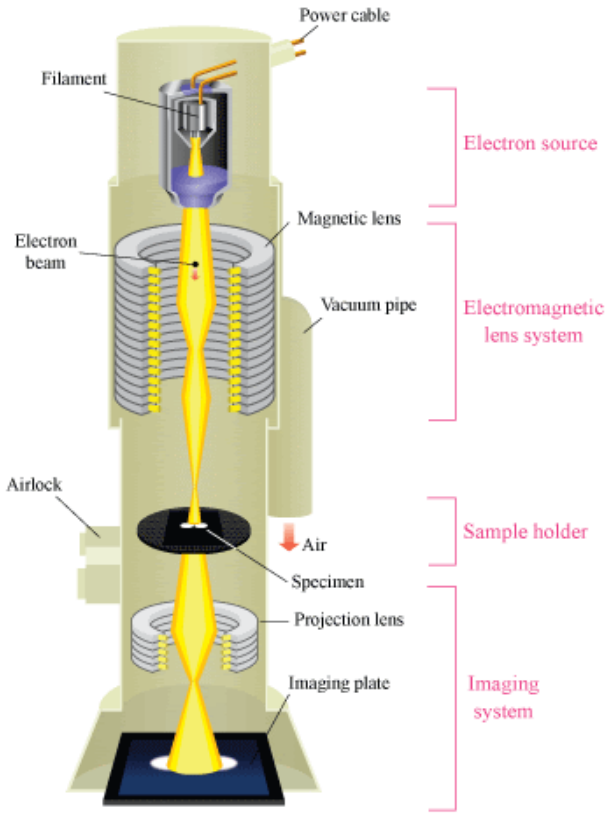

Figure 3.7. *Schematic diagram of a typical transmission electron microscope (TEM). After the transmission of electron beam through a specimen, the magnified image is formed either in the fluorescent screen or can be detected by a CCD camera.*

microscopic structures of samples and to analyze their elemental composition. The sizes of the nanoparticles were determined from the TEM images obtained at 200 kV acceleration voltage of the microscope. Samples for TEM were prepared by placing a drop of the nanoparticle solution on a 300-mesh carbon-coated copper grid and allowing the film to evaporate overnight at room-temperature.

3.1.7. Scanning Electron Microscope (SEM)

Characterization of mice red blood corpuscles (RBC) after treatment with nanoparticles were performed by field emission scanning electron microscopy

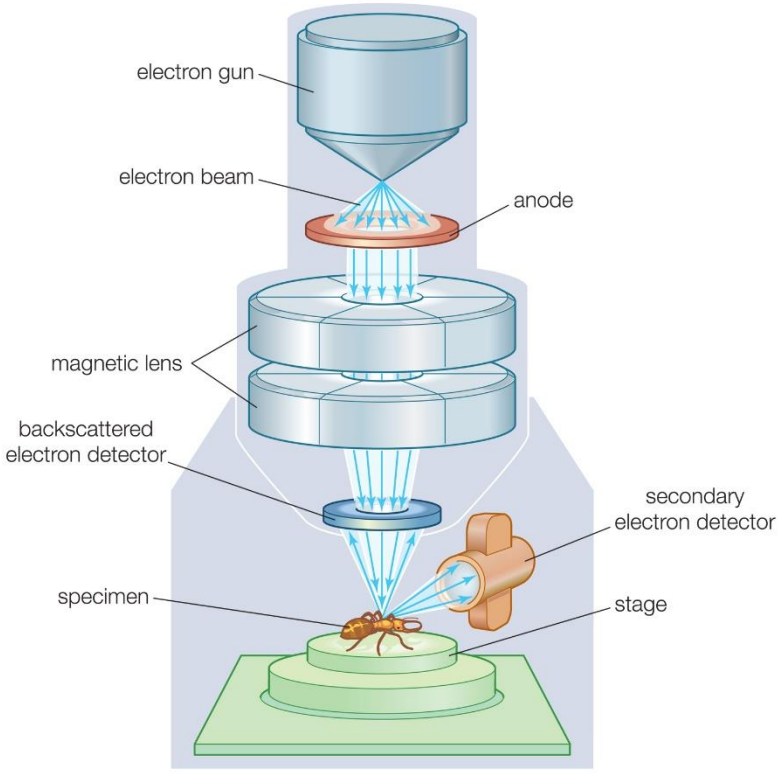

Figure 3.8. *Schematic diagram of typical scanning electron microscope (SEM).*

(FESEM, Quanta™ 250 FEG, FEI Company, Oregon, USA). An electron-gun is attached to SEM and the electrons from filament triggered by 0 KV to 30 KV voltages. These electrons go first through a condenser lens and then through an objective lens,

followed by an aperture to finally reach the specimen. The high energy electrons bombard the sample and back again giving secondary electrons. The signal from secondary electrons are detected by detector and amplified. The ray diagram of the SEM setup is shown in Figure 3.8.

3.1.8. Fluorescence Microscope

Commercially available fluorescence microscope (BX-51, Olympus America, Inc.) was used in our study. The light source is usually a mercury-vapor lamp. For bright field, Tungsten-halogen lamp was used. In particular, an inverted setup with a mercury-vapor lamp as light source is shown. The dichroic mirror, excitation and emission filter are joined together within the filter cube (Figure 3.9). Since mercury-vapor lamps emit light over the whole optical spectrum as well as in the ultraviolet range, an optical excitation filter is used to isolate one specific wavelength. Due to the Stokes shift, it is possible to separate excitation and emission light in the same light path optically via a dichroic mirror. This way, only the emission light is collected by the objective. An emission filter helps to suppress unwanted background light.

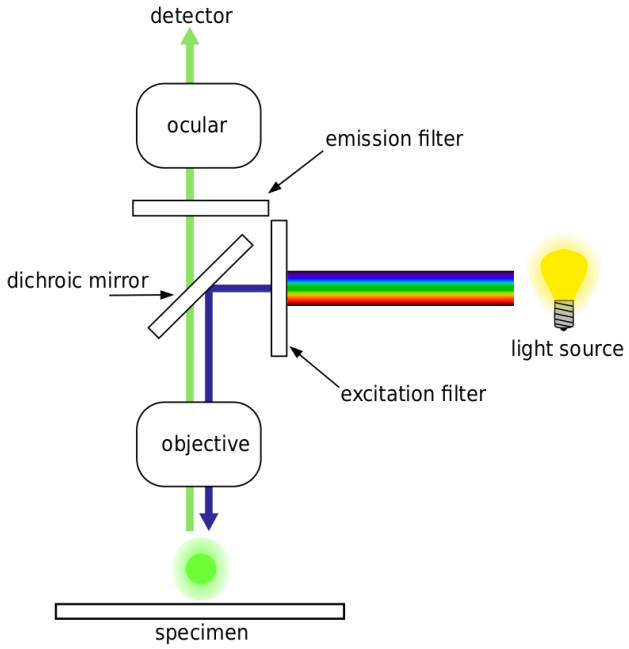

Figure 3.9. *Schematic presentation of the fluorescence microscope.*

3.1.9. X-ray Diffraction (XRD) Measurement

XRD is a popular and a powerful technique for determining crystal structure of crystalline materials. By examining the diffraction pattern, one can identify the crystalline phase of the material. Small angle scattering is useful for evaluating the average interparticle distance while wide-angle diffraction is useful for refining the atomic structure of nanoclusters. The widths of the diffraction lines are closely related to strain and defect size and distribution in nanocrystals. As the size of the nanocrystals decreases, the line width is broadened due to loss of long-range order relative to the bulk. This XRD line width can be used to estimate the size of the particle by using the Debye-Scherrer formula,

$$D = \frac{0.9\lambda}{\beta \cos\theta}$$

[Equation – 3.1]

Here, D is the nanocrystal diameter, λ is the wavelength of light, β is the full-width half-maximum (FWHM) of the peak in radians, and θ is the Bragg angle. XRD measurements were performed on a PANalytical XPERT-PRO diffractometer

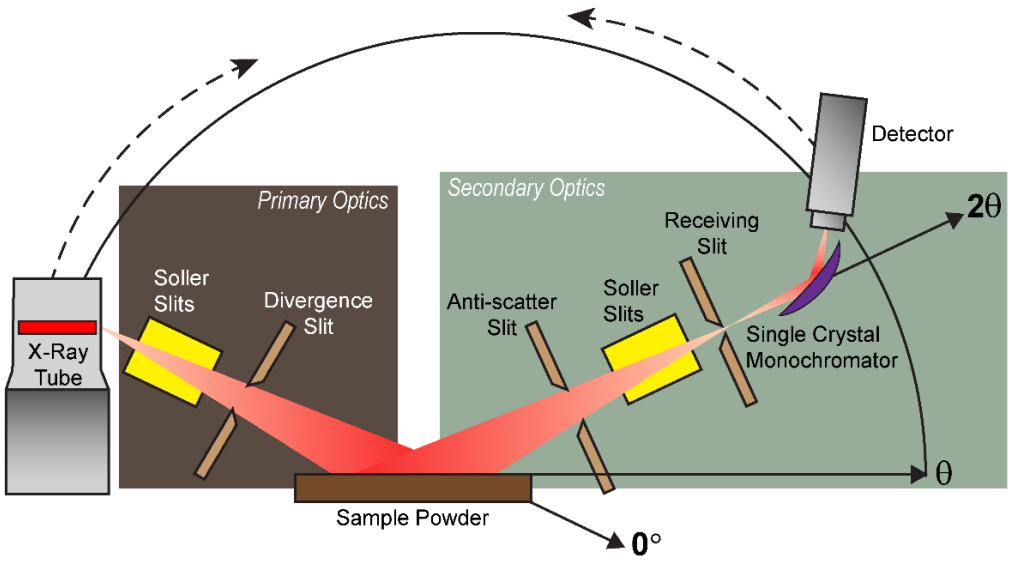

Figure 3.10. *Schematic diagram of X-ray diffraction (XRD) instrument. By varying the angle θ, the Bragg's law conditions, nλ = 2dsinθ are satisfied by different d-spacings in polycrystalline materials. Plotting the angular positions and intensities of the resultant diffracted peaks of radiation produces a pattern, which is characteristic of the sample.*

(Figure 3.10) equipped with CuKα radiation (λ = 1.5418 Å at 40 mA, 40 kV). XRD patterns were obtained by employing a scanning rate of 0.02° s^{-1} in the 2θ range from 15° to 75°.

3.1.10. Thermogravimetric-Differential Thermal Analyzer (TG-DTA) Setup

The thermogravimetric (TG) analysis was carried out using Diamond thermogravimetric (TG)-differential thermal analyzer (DTA) from Perkin Elmer, UK. The TG determines the weight change of a sample whereas the DTA measures the change in temperature between a sample and the reference as a function of temperature and/or time. The schematic of the TG-DTA setup is shown in Figure 3.11. When a weight change occurs on the sample side, the beam holding the platinum pans is displaced. This movement is detected optically and the driving coil current is changed to return the displacement to zero. The detected driving coil current change is proportional to the sample weight change and the output is the TG signal. The DTA detects the temperature difference between the sample holder and the reference holder using the electromotive force of thermocouples, which are attached to the holders. This difference is measured as the DTA signal.

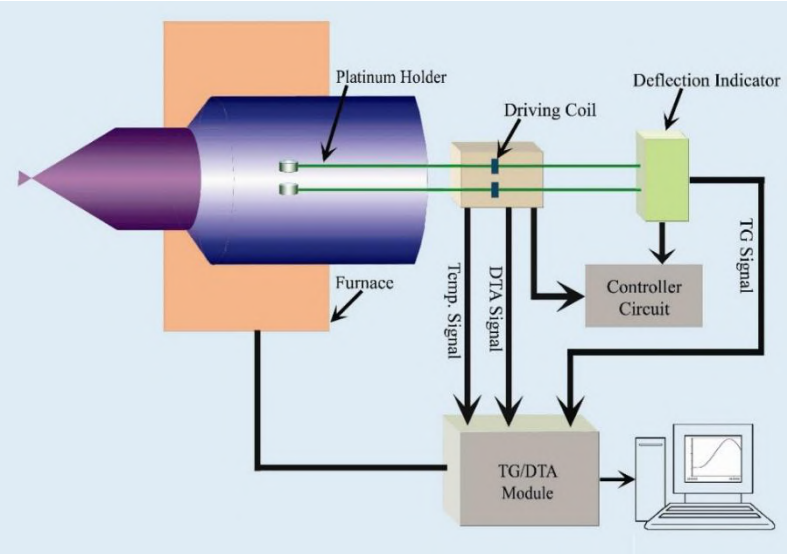

Figure 3.11. *The schematic representation of TG-DTA setup.*

3.2. SAMPLE PREPARATION

3.2.1. Chemicals Used

Morin, ellagic acid, naringin, quercetin, lead nitrate ($Pb(NO_3)_2$), sodium chloride (NaCl), sodium hydroxide (NaOH), JC-1, and 2,2-diphenyl-1-picrylhydrazyl (DPPH), and other chemicals were purchased from Sigma (St. Louis, MO, USA) unless otherwise stated. All solvents were obtained from Merck (NJ, USA) unless otherwise stated. All reagents were of analytical grade and used without further purification. Nanopure water (resistivity ≥18 MΩ cm) from Milli-Q system (Millipore GmbH, Germany) was used whenever required.

3.2.2. Synthesis of Citrate Functionalized Mn_3O_4 Nanoparticles (C-Mn_3O_4 NPs)

For synthesis of bulk Mn_3O_4 nanoparticles at standard temperature and pressure we followed a bottom up approach. In a typical procedure, 0.598 g of $MnCl_2$, $4H_2O$ (3 mmol) was added to 30 ml of ethanol amine (EA) in a beaker, and ultrasonicated at 56 kHz operating frequency for 15 mins. This dissolves $MnCl_2$ to form a clear brown solution. Then equal amount of Mili-Q (from Millipore) water (30 ml) was added and the resultant mixture was stirred at room temperature for 6 hrs. Then the suspension was centrifuged at 3000 rpm for 15 minutes, and the black precipitate was subsequently washed three times using ethanol in order to remove excess EA. After that it was dried in an incubator at 60°C to get a glossy black powder, the as prepared Mn_3O_4 NPs.

To functionalize the as-prepared Mn_3O_4 NPs with ligand citrate, at first, 0.5 M citrate solution (pH 7.0) was prepared in Milli-Q water. In the ligand solution, as-prepared Mn_3O_4 NPs (~150 mg of powder Mn_3O_4 NPs in 6 ml ligand solution) were added and extensively mixed for 10 hrs in a cyclomixer. Finally, we filtered out the nonfunctionalized large NPs using a syringe filter (0.22 μm diameter). The resulting filtrated solution (after proper dilution) was used in further experiments.

3.2.3. Preparation of Multi-herbal Formulation SKP17LIV01

All raw medicinal plants were collected from registered local herbal suppliers and authenticated by pharmacognosist. The plants and plant parts used in preparation of the extract (SKP17LIV01) are listed in Figure 3.12.

Plant parts were air dried after cleaning with double distilled water and kept in oven at 80°C for 10 min and 60°C for 30 min. Then they were ground by a blade mill to fine powder. Subsequently, the extraction of the polar fraction was performed according to the standard method of plant extract preparation with some modifications. In brief, 5 gm of dry plant parts were dissolved using 10 ml of methanol, sonicated at room temperature for 30 min using an ultrasonic bath, centrifuged at 3000 rpm for 15 min, and finally the supernatant was removed. This procedure was repeated

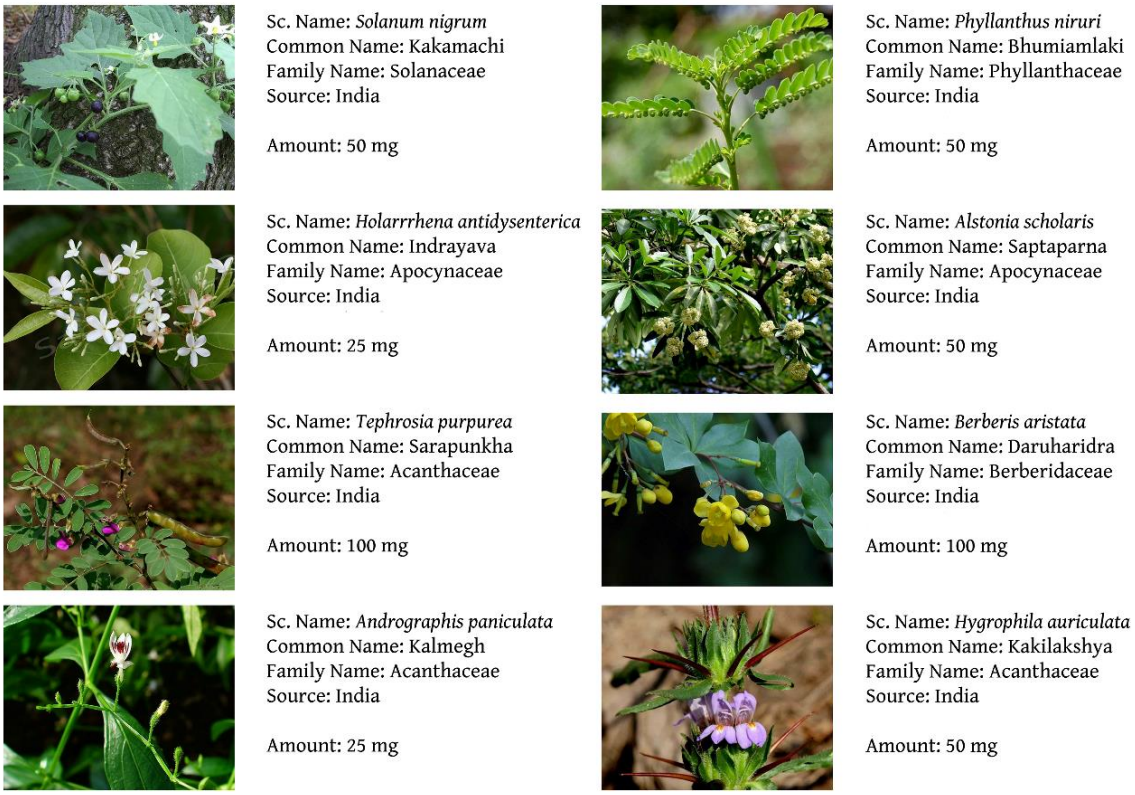

Figure 3.12. *Comprehensive description including common names and family names of the eight medicinal herbs used for preparation of the extract (SKP7LIV01). Amounts indicated were required for preparation of 5 ml extract.*

four times, collecting all the supernatants, which were finally evaporated in a rotary evaporator under reduced pressure at 35°C. Finally, the residue was re-constituted in 3 ml of methanol, filtered using Whatman filter papers (GE Healthcare, MA, USA) and kept at 4°C for further use.

3.2.4. Fingerprint Analysis of SKP17LIV01 using UHPLC-MS

For complete chemical characterization of SKP17LIV01, we used fingerprint analysis by ultra-high-resolution LC-MS. Mass spectra were recorded by electrospray ionization (ESI) in both negative and positive mode using an Agilent 1290 Infinity UHPLC System (MS Q-TOF, Model G6550A, Agilent Technologies, CA, USA) equipped with C-18 stainless steel column (30 cm × 0.46 cm). The capillary voltage was kept at 80V, and the air (nebulizing gas) pressure was 35 psi. Full scan data acquisition was performed by scanning from m/z 50 to 1000 with isolation width ≈4.0 amu. The oven temperature was set to 40°C and mobile phase A consisted of 100% water, while mobile phase B consisted of a mixture of 90% acetonitrile, 10% water and 0.1% formic acid. 0.02 ml sample was injected. A flow rate of 0.2 ml/minute was used. An elution gradient, ranging from 5% B to 95% B from 0 to 20 minutes was used. Identification of major compounds was accomplished by analyzing molecular ion peak and base peak using Agilent MassHunter Workstation (Agilent Technologies CA, USA).

3.2.5. Solutions and Experimental Method for Evaluating Heavy-Metal Binding

Stock solutions of morin, naringin and ellagic acid were prepared in 0.01 N NaOH. They were further diluted using water as solvent. NaCl was used to keep the ionic strength constant (0.1 M). Incremental volumes of $Pb(NO_3)_2$ stock solution (0.15 M) were added to the polyphenol reaction mixture in order to vary the molar ratio and the pH was maintained constant (pH=7.4) by small additions of NaOH. A syringe pump (Pump 11 Pico Plus Elite, Harvard Apparatus, MA, USA) was used to circulate

solution from the titration beaker to experiment cell. UV-vis absorbance and fluorescence spectra were recorded for each molar ratio and used for further calculations. All measurements were performed in 1 cm quartz cuvette, hermetically closed, and thermostatized at 298.0 ± 1.5 K.

3.2.6. Determination of Antioxidant Property

Free radical scavenging activity or the antioxidant capacity of the samples of interest were determined using DPPH method. 0.5 ml of sample (in varied concentration) was added to 3.0 ml of freshly prepared ethanolic DPPH solution (0.1 mM). The change in absorbance was monitored at 535 nm for 60 mins. EC_{50} values were measured from the percentage inhibition at different concentration.

$$\text{Percentage Inhibition} = \frac{Abs_{Control} - Abs_{Test}}{Abs_{Control}} \times 100\%$$

[Equation – 3.2]

EC_{50} is the concentration value which scavenged 50% of the DPPH radicals. Trolox and ascorbic acid were used as reference compounds.

3.2.7. Preparation of Dichlorofluorescein (DCFH) and ROS Measurements

DCFH was prepared from DCFH-DA (Calbiochem, USA) by mixing 0.5 mL of 1.0 mM DCFH-DA in methanol with 2.0 mL of 0.01 N NaOH. This deesterification of DCFH-DA proceeded at room temperature for 30 min and the mixture was then neutralized with 10 mL of 25 mM NaH_2PO_4, pH 7.4. This solution was kept on ice in the dark until use. All the measurements were performed in a total volume of 2.0 mL water that contained 10 μL of DCFH solution, and the nanoparticle of interest along with respective controls.

3.2.8. H_2O_2 Scavenging by C-Mn_3O_4 NPs

The ability of C-Mn_3O_4 NPs to prevent H_2O_2 mediated degradation of sodium containing dye Rose Bengal (RB) (Sigma, USA) was used as an indicator of its H_2O_2 scavenging activity. Addition of H_2O_2 (10 mM) in the aqueous solution of RB (3.5 μM) leads to decolourization of the dye reflected into a decrease in absorbance (λ_{max}=550 nm). Presence of C-Mn_3O_4 NPs (50 μg mL^{-1}) in the reaction mixture reduced degradation.

3.2.9. GPx-Mimicking Activity of C-Mn_3O_4 NPs

The GPx-like catalytic activity of C-Mn_3O_4 NPs was studied using the GR-coupled assay [2] by following the decrease in the concentration of NADPH spectrophotometrically at 340 nm on a Shimadzu Model UV-2600 spectrophotometer under kinetic mode. In a typical assay (1 ml), the reactants were added in the following order, C-Mn_3O_4 NPs (1.3 μM), GSH (2mM), NADPH (400 μM), GR (1.7 units), H_2O_2 (240 μM) in 100 mM, pH 7.4 phosphate buffer and reaction rate was followed for 30 s at 25°C. The control reactions were performed in the absence of at least one of the reactants. The steady-state kinetics of C-Mn_3O_4 NPs were studied by varying the concentration of C-Mn_3O_4 NPs, H_2O_2, and GSH at a time and at the fixed concentration of GR and NADPH in 100 mM phosphate buffer (pH 7.4). Michaelis–Menten curves and Lineweaver–Burk plots were obtained by using origin 9.0 software. To understand the effect of haloperoxidase substrates on the GPx-like activity of C-Mn_3O_4 NPs, the GPx-like activity of C-Mn_3O_4 NPs was followed in the presence of KI (2 mM) and tyrosine or dopamine (2 mM) with GR-coupled assay in 100 mM phosphate buffer (pH 7.4).

3.2.10. Cell Culture

Cells were maintained at 37°C in 5% CO_2 in RPMI 1640 growth medium (Himedia, India) that contained 10% foetal bovine serum (Invitrogen, USA), L-glutamine (2 mM), penicillin (100 units mL^{-1}), and streptomycin (100 ng mL^{-1}) (Sigma,

USA). Before experimentation, the cells were washed twice and incubated with RPMI 1640 medium (FBS, 0.5%) for 1 h and then treated as described in respective figure legends.

3.2.11. Measurement of Cell Viability

Cell viability was assessed by MTT and LDH assay. After achieving 75–80% confluence, cells were plated in 96-well plates at a density of 1×10^3 cells/well and cultured overnight at 37°C. The treatments were performed as described in the figure legends. Next, MTT (5 mg mL^{-1}; Himedia, India) was added to each well, with a final concentration of ~0.5 mg mL^{-1}, and the cells were cultured for 4 h at 37°C in a 5% CO_2 atmosphere. Resultant purple formazan was dissolved by the addition of 10% sodium dodecyl sulfate (Sigma, USA) and the absorbance was read at 570 nm and 630 nm using a microplate reader (BioTek Instruments, Inc., Vermont, USA). Cell viability was determined as follows:

$$\text{Cell viability (\%)} = \frac{Abs_{CONTROL} - Abs_{SAMPLE}}{Abs_{CONTROL}} \times 100$$

[Equation – 3.3]

here Abs_{SAMPLE} denotes the absorbance values of C-Mn_3O_4 NP-treated cell and $Abs_{CONTROL}$ denotes the same for untreated cells.

LDH release was analyzed using a colorimetric LDH cytotoxicity assay (Himedia, India) following the manufacturer's instructions. Three independent experiments were performed in each case.

3.2.12. Measurement of Intracellular ROS

The formation of intracellular ROS was measured with the DCFH-DA method using both FACS and confocal microscopy. For FACS, after treatment cells were trypsinized, washed with 1X PBS and stained with DCFDA-H2 (15 μM; Sigma, USA) for 10 mins at 30°C in dark. Ten thousand events were analyzed by flow cytometry (FACS Verse, Beckton Dickinson, SanJose, USA) and the respective mean

fluorescence intensity (in FL1 channel, set with a 530/30 nm bandpass filter) values were correlated with the ROS levels. For confocal microscopy, 5000 cells were seeded and treated with agents described earlier. Post-treatment cells were stained with DCFDA-H2 (5 μM) at 37°C in dark and images were acquired with a confocal microscope (Olympus IX84, Japan). All parameters (pinhole, contrast, gain, and offset) were held constant for all sections in the same experiment.

3.2.13. Mitochondrial Superoxide and $\Delta\Psi_M$ Detection in Cell

After treatment with the drug or vehicle, mitochondrial superoxide production was visualized using MitoSOX™ Red (Thermo Fisher Scientific, USA), a mitochondrial superoxide indicator. The $\Delta\Psi_M$ in intact cells was assessed by confocal microscopy using Rh 123. Cells were loaded with MitoSOX Red (0.5 μM) or Rh123 (1.5 μM) for 10 min at 37°C and imaged using a confocal microscope (Olympus IX84, Japan). All parameters (pinhole, contrast, gain, and offset) were held constant for all sections in the same experiment. ImageJ (http://imagej.nih.gov/ij/) was used to quantify area normalized florescence intensities from the confocal images.

3.2.14. Blood Collection and Serum Isolation

At the end of the experimental period, the animals were euthanized and decapitated after being fasted. Blood was collected from retro orbital plexus just before sacrifice, kept in sterile non-heparinized tubes in slanting position for 45 min and centrifuged at 3500×g for 20 min. The clear serum was obtained and used in subsequent biochemical analysis.

3.2.15. Biochemical Evaluations

Biochemical evaluations were performed using commercially available kits (Autospan Liquid Gold, Span Diagnostic Ltd., India) following the protocol described by respective manufacturers. δ-aminolevulinic acid dehydratase (δ-ALAD) activity

was measured using the European standardized method [30]. Complete blood count (CBC) was obtained using an automated cell counter (Medonic CA 620, Boule Diagnostics, Sweden). Urine samples were collected in metabolic cages during 24-h fasting conditions. Glomerular filtration rate (GFR) was estimated by the determination of urinary excretion of fluorescein-labeled inulin (FITC–inulin).

3.2.16. Bilirubin Estimation from Serum Samples

For bilirubin estimation, after collection of blood, serum was instantly separated by centrifugation (3500 rpm; 10 mins) at 4ºC, and in dark condition. Bilirubin measurements were completed within 30 mins of serum isolation. Care was taken to keep the samples at 4ºC and away from light exposure before beginning of measurements. Total serum bilirubin (TSB), and unconjugated bilirubin (UCB) were measured following di-azo method using commercially available test kits (Autospan Liquid Gold, Span Diagnostic Ltd., India), and double beam UV-Vis absorbance spectrometer (Model UV-Vis 2600, Shimadzu, Japan). Precision of the instrument was 0.001 OD. Each time instrument was calibrated using standard bilirubin solution (5.0 mg dL^{-1}). Variation of the measurements lied within 2 – 3%.

3.2.17. Histopathological Examination

For microscopic evaluation, a conventional technique of paraffin wax sectioning and differential staining was used [3]. Oragans were removed following incision, fixed in 10% neutral buffered formalin saline for 72 h, dehydrated in graduated ethanol (50–100%), cleared in xylene, and embedded in paraffin. Microtome was used to prepare ultrathin sections (4–5 μm), followed by staining with hematoxylin and eosin (H&E). Besides, liver sections were stained with Serius red and Masson's trichrome to evaluate extent of fibrosis. Brain sections were further stained with silver stain. Histopathological changes were examined under the microscope (Olympus BX51) equipped with a CCD based camera.

3.2.18. Immunohistochemistry (IHC)

Paraffin-fixed liver tissue slices were sectioned, deparaffinized, rehydrated, and immersed in 3% H_2O_2 for 10 min to block endogenous peroxidase activity. Antigen retrieval was performed in citrate buffer (pH 6.0) in a microwave oven for 15 min. Bovine serum albumin (BSA) (5%) was used to block non-specific protein binding. The sections were incubated with α-SMA primary antibody overnight at 4˚C. The sections were subsequently washed with PBS and incubated with horseradish peroxidase (HRP)-conjugated goat anti-mouse IgG secondary antibodies, followed by incubation for 5-10 min with 3, 3′-diaminobenzidine tetrachloride. Stained slides were analyzed using high-power field images captured under microscope (magnification × 400) (Olympus BX51). Computer-assisted semi-quantitative analysis was used to evaluate the α-SMA positive areas using ImageJ software following reported literature [4]. The data for α-SMA staining was expressed as the mean percentage of the positively stained area over the total tissue section area.

3.2.19. Tissue Homogenate Preparation

Tissue samples were collected, homogenized in cold phosphate buffer (0.1 M; pH 7.4), and centrifuged at 10,000 r.p.m. at 4°C for 15 min. The supernatants were collected and used to determine the activity of SOD, CAT, GPx and GSH as well as the content of malondialdehyde (MDA) as marker of lipid peroxidation.

3.2.20. Tissue Hydroxyproline Measurement

Hepatic and renal hydroxyproline content was measured using the method described elsewhere [5]. In brief, snap-frozen tissue samples (200 mg) were weighed, hydrolyzed in 6 M HCl overnight at 100°C (purified 4-hydroxy-L-proline standards for 20 minutes at 120°C). Free hydroxylproline content from each hydrolysate was oxidized with Chloramine-T. The addition of Ehrlich reagent resulted in the formation of a chromophore that was read at 550 nm. Data were normalized to liver wet weight.

3.2.21. Assessment of Lipid Peroxidation and Antioxidant Status

The supernatants obtained in the previous stage were used to measure the activity of SOD, CAT, GPx, and GSH as well as the content of lipid peroxidation (MDA). Lipid peroxidation was determined in TBARS formation using a reported procedure [6,7]. SOD (Sigma, MO, USA), CAT (Abcam, Germany), and GPx activities (Sigma, MO, USA) were estimated using commercially available test kits following protocols recommended by respective manufacturers. The tissue GSH level was determined by the method of Ellman with trivial modifications [8].

3.2.22. Mitochondria Isolation

Mitochondria isolation was done from mouse brain following the method of Graham [9] with some modifications. In brief, organs were excised and homogenized in homogenization medium that contains 250 mM D-mannitol, 125 mM sucrose, 0.05 mM EGTA, 0.01% BSA, 10 mM HEPES (pH 7.2), and 1X protease inhibitors. Then the homogenates were centrifuged for 15 minutes at 700 x g and the supernatants were again centrifuged as the previous step. Then supernatant was washed, collected and centrifuged at 10000 x g for 15 minutes. The resultant pellets were dissolved in ice cold buffer with added digitonin. The resuspended pellet was centrifuges at 10000 x g for 15 minutes and the supernatant was discarded, while the pellet was re-suspended in extraction buffer. For all procedure temperature was maintained at 4°C. Commercially available kit (Autospan Liquid Gold, Span Diagnostics Ltd., India) was used for determining protein concentration following the protocol described by the manufacturer.

3.2.23. Complex IV (of Respiratory Chain) Activity

Total complex IV activity was measured spectrophotometrically using isolated mitochondria [10]. Briefly, reduced cytochrome c was prepared by mixing cytochrome c and ascorbic acid in potassium phosphate buffer. Complex IV activity was taken as

the rate of ferrocytochrome c oxidation to ferricytochrome c, detected as the decrease in absorbance at 550 nm.

3.2.24. Measurement of Mitochondrial Membrane Permeability Transition (mPTP)

Opening of the pore causes mitochondrial swelling, which results in reduction of absorbance at 540 nm [11,12]. Mitochondrial permeability transition (swelling assay) was monitored as changes at 540 nm after addition of Ca^{2+} at 10 s intervals over 10 min time with 250 µg mitochondrial protein in the swelling buffer, which contained 120 mM KCl (pH 7.4) and 5 mM KH_2PO_4.

3.2.25. Measurement of Mitochondrial Membrane Potential

The mitochondrial membrane potential ($\Delta\psi_M$) was measured using the fluorescent probe rhodamine 123 (Sigma) [13,14]. Because rhodamine 123 is a cationic dye, it accumulates in the mitochondria driven by $\Delta\psi_M$. Under appropriate loading conditions, the concentration of rhodamine 123 within the mitochondria reaches sufficiently high levels that it quenches its own fluorescence (λ_{ex} = 503 nm, λ_{em} = 527 nm). In case of mitochondrial depolarization, rhodamine 123 leaks out into the cytoplasm and is associated with a reduction in the amount of quenching. Thus the changes in $\Delta\psi_M$ are revealed as changes in total fluorescence intensity following the method of Chen [15].

3.2.26. Mitochondrial Dehydrogenases Activity

The methyl tetrazolium (MTT) assay was used as a colorimetric method for the estimation of mitochondrial dehydrogenases activity in isolated mitochondria [16,17]. Briefly, mitochondrial suspension (1 mg protein/mL) in a buffer containing 320 mM sucrose, 10 mM Tris-HCl, 1 mM EDTA, and pH= 7.4, was incubated with 40 µL of theMTT solution (0.4% w: v) at 37°C (30 min, in the dark). The product of purple

formazan crystals was dissolved in DMSO (1 ml). Then, 100 µl of dissolved formazan product was added to a 96 well plate, and the optical density (OD) was measured at λ= 570 nm using an EPOCH plate reader (BioTek Instruments, USA).

3.2.27. Mitochondrial ATP Level

A luciferase-luciferin-based kit from Promega (ENLITEN, Madison, WI, USA) was used to assess brain mitochondrial ATP content [17]. Samples and buffer solutions were prepared based on the kit instructions. Briefly, mitochondria fractions (1 mg protein/ml) were treated with 100 µL of trichloroacetic acid (0.5% w: v). Samples were centrifuged (15,000 g, 15 min, 4°C). Then, 100 µL of the supernatant was added to 100 µL of the kit content, and the luminescence intensity was measured at λ= 560 nm.

3.2.28. Agarose Gel Electrophoresis for DNA Fragmentation

DNA was isolated from different organs following a standard procedure [18]. DNA fragmentation was assessed using agarose gel electrophoresis. In a typical procedure, DNA (5.0 µg) was loaded on 1.5% agarose gel stained with ethidium bromide. Electrophoresis was carried out for 2 h at 90 V, and the resultant gel was photographed under UV transillumination (InGenius 3 gel documentation system, Syngene, MD, USA).

3.2.29. Western Blotting Analysis

After the isolation, mitochondrial and cytosolic content of Bax, Bcl-2, and GAPDH were analyzed by Western blotting. In brief, tissue samples were homogenized in 25 mM HEPES buffer, pH 7.5, containing 5 mM EDTA, 2 mM dithiothreitol, 1% CHAPS, and 1 µg/ml pepstatin, leupeptin, and aprotinin. Homogenates were centrifuged at 14,000g for 20 min at 4°C and the supernatants were collected. Protein concentrations in the extracts were determined using the

bicinchoninic acid kit (Autospan Liquid Gold, Span Diagnostics Ltd., Surat). Aliquots of 10 µg of proteins were subjected to Western blotting analysis. After electrophoresis on 15% polyacrylamide gels containing 0.1% SDS, the proteins were transferred electrophoretically (Trans-Blot Turbo Transfer System, Biorad Laboratories Inc., CA, USA) onto poly screen polyvinylidene difluoride (PVDF) membranes (Biorad Laboratories Inc., CA, USA). The membranes were blocked with 5% non-fat dried milk in Tris-buffered saline containing 0.1% Tween 20 (TBST) for 1h at RT. After washing three times with the same, the membrane was incubated with TBST containing 5% dried milk and anti-Bcl-2, anti-Bax and anti-GAPDH monoclonal antibody (Cell Signaling Technology Inc., MA, USA) for 2h at RT. After repeated washing with TBST, the membrane was incubated with horseradish peroxidase (HRP) conjugated anti-rabbit IgG antibody (Santa Cruz Biotechnology, CA, USA) for 1h at RT. Protein bands were visualized by using an enhanced chemiluminescence kit and an image analyzer. Optical densities of the bands were measured using ImageJ software (http://rsb.info.nih.gov/ij/) and normalized against GAPDH.

3.2.30. Estimation of Metal Content in Organs

ICP-AES (ARCOS, SPECTRO Analytical Instruments GmbH, Germany) was carried out to determine the amount of Mn, and Pb in blood and other organs like liver, kidney, spleen and, brain. The open acid digestion method was used for sample preparation. In brief, tissues were dried using liquid nitrogen and weighted. The freeze-dried samples were dissolved in an acid mixture that contained HNO_3 (3 ml), H_2SO_4 (2 ml), and H_2O_2 (1 ml), heated at 120°C until only a residue remained, and then diluted with deionized water to 10 ml.

3.2.31. Hemolysis Assay

The hemolysis assay was performed on human RBCs. Ethylenediaminetetraacetate (EDTA) stabilized human whole blood was centrifuged five times and redispersed in 10 mL of phosphate-buffered saline (PBS) buffer. Then, 0.1 mL of RBC solution was mixed with variable concentrations of nanohybrids [19].

The samples were incubated at 37°C and 100 rpm for 30 min, and then the mixture was centrifuged at 5000 rpm for 5 min. The absorption of the supernatant solution was measured at 570 nm. RBCs incubated with PBS and 1% Triton X-100 were used as negative and positive controls, respectively. All sets were prepared in triplicate. The hemolysis percentage was calculated following the reported equation.

3.2.32. Behavioral Studies

3.2.32.1. Open field test (OFT)

This test measures thigmotaxis behavior of the subject which is the indicator of anxiety of the subject. For this test a box, animals were first acclimatized to the dimly lit experimental room (~15 lx) for 30 min and then individually placed in an illuminated open field apparatus (45 cm × 45 cm × 45 cm; ~1200 lx). They were permitted to explore freely for 5 min after an initial 1-min habituation phase. Movement pattern and associated parameters was analyzed from videos recorded during experiments. Time spent by the animal in the central zone and peripheral zone was measured to evaluate its anxiety level.

3.2.32.2. Gait analysis

For gait measurement, the forelimbs and hindlimbs of each mouse were coated with red and blue nontoxic paints, respectively. Then they were individually placed on the walkway (30 cm × 8 cm; closed sidewise), and allowed to move freely in both directions. Before final experiments, animals were allowed to habituate and cross the walkway 2 times. The gait parameters were calculated from the footprints imprinted on a sheet of white paper which was placed on the floor of the walkway.

3.2.32.4. Balance beam test

This test is a useful way to access fine motor coordination and balance of rodents. The ability of the animals to pass through a narrow wooden beam (1 cm × 80 cm; elevated 1 m above the floor) to reach a dark box was evaluated in balance beam test. A white light (~1200 lux) illuminated the origin to force the mice to cross the beam. The time required to reach the target box, and the number of forelimb and hind-

limb paw slips were recorded. A paw slip was defined as any paw coming off the top of the beam or any limb use on the side of the beam. Final data were recorded after 3 habituation trial.

3.2.32.5. Pole test

Individual animals were placed facing upward on the top of a vertically standing wooden pole (1 cm × 80 cm) whose base was positioned in the mouse home cage and titled at 45° to stand on a nearby wall. Mice were placed with their heads directed upwards on the upmost part and were forced to attempt descending the pole to enter the home cage. The time required for mice to descend and reach the floor with all four paws were recorded.

3.2.32.6. Forced swim test (FST)

Individual mouse was placed into a glass beaker of diameter 16 cm and height of 26 cm. The apparatus was filled up to 15 cm with water of temperature 25ºC. Time spent by the animal in the water was recorded and immobility (refers to the minimal movement of the animal to keep its head over the water surface) of the animal was measured. An increased in immobility reflects increase in depression. After test all animals were dried properly and put into new cages.

3.2.32.7. Tail flick test

Tail-flick test is a nociceptive essay based on the measurement of the latency of the avoidance response to thermal stimulus in rodents. Basically, a thermal stimulus is applied to the tail; when the animal feels discomfort, it reacts by a sudden tail movement. The tail flick reaction time is then measured and used as an index of animal pain sensitivity [20].

3.2.32.8. Elevated plus maze (EPM) test

Elevated plus maze is widely used for evaluating anxiety like behavior in the rodents. The test apparatus is made up of 4 arms two of which is closed and the other two is open. The apparatus is placed 50 cm above the ground level and the closed and open arms were perpendicularly crossed each other in a central area. All the arms were brightly lit. Closed arms were covered by wall of 15 cm and open arms had a barrier

of 3 cm that prevent slipping of animal. Animals were scored depending on the entry to the open arm and time spent in it. This score reflect the measurement of anxiety that is induced in the animal by the open space.

3.2.32.9. Sucrose preference test (SPT)

Consumption of a 2% sucrose solution between 08:00 am and 09:00 pm was recorded in all mice to measure sucrose anhedonia [21]. Before presentation of the sucrose solution, animals were administered water in modified water bottles for 3 consecutive days, to control for novelty of the bottles. The bottles were weighed before and after the 5-h sample time; the next day, animals were provided a choice between a 2% sucrose solution and water. Sucrose consumption was normalized to water consumption.

3.2.32.10. Novel object recognition

Two variations of the novel-object task were run. Both were conducted in an arena 36 cm long, 34 cm wide and 26 cm high. For both tests, the snouts of the mice were tracked and object interaction was measured as time spent with snout within 2 cm of the object. The objects (a plastic ball, a small rubber box and a small plastic cube) were secured to the arena with neodymium magnets to render them immovable. In the first variation, mice were habituated to the arena and objects 1 and 2 over the course of four 5-min trials separated by an inter-trial interval of 10 min. Mice were then tested for object recognition memory 1 h after the fourth trial during the 5-min-long fifth trial. Either object 1 or object 2 (counterbalanced) was swapped for object 3 during the fifth trial. In the second variation of this test, the mice were habituated to the empty arena for 10 min each day for three consecutive days. On day 4, the mice were exposed to a pair of either object 1 or object 2 for 5 min. Object recognition memory was tested 1 h after this trial by exposure to objects 1 and 2 for 5 min. In both protocols, object recognition memory was measured as the increased time spent investigating the novel object.

3.2.32.11. Morris water maze (MWM) test

After acclimatization, animals from each of the groups were taken for the Morris water maze study to evaluate their spatial learning ability. The complete study

consists of training period of 5 days and then test period. This training was done in a pool with a platform (target) whose top was lifted above the water surface. Distal cues were clearly visible for the animals at the time of training. The animals were placed in maze in a random fashions from 4 different start points. 10 days after training session animals were evaluate for their spatial learning ability. All the animals were placed from a fixed point and the platform were hidden beneath the water surface in this session. All the animals were given 90 sec for exploration. Time taken to reach the platform and no of time the animal entered in the target quadrant was analysis for accessing their spatial learning and memory that give insight to hippocampal damage.

3.2.32.12. Sociability test

This test was performed as described previously [22]. In brief, mice were placed in an arena divided into three equal-sized compartments by plastic mesh. On day 1 a 5-min sociability trial was conducted. A littermate was placed in the left or right compartment (systematically alternated) and the test subject was placed into the centre compartment. The time that the test subject spent investigating each compartment (snout within 2 cm of the mesh barrier) was measured, and a difference score was computed.

3.3. STATISTICAL ANALYSIS

Kaplan-Meier survival curves were used to illustrate mortality due to SNH after PHz intoxication, and NP co-treatment. Differences in survival between groups were assessed by the log-rank test with multiple pair-wise comparisons performed using the Mantel-Cox method. All quantitative data are expressed as Mean ± Standard Deviation (SD), unless otherwise stated. Unpaired *t* test with Welch's correction was used to compare between two groups. One-way analysis of variance (ANOVA) followed by Tukey's *post hoc* multiple comparison test was performed for comparison between multiple groups. Beforehand, the normality of each parameter was checked by normal quantile–quantile plots. Sample size in our animal studies were determined following the standard sample sizes previously been used in similar experiments as per relevant literature. For some experiments, sample size was adapted to the observed

effect size, and numbers were increased to 15–20 animals per group. Designated sample size (in figure legends) always refers to biological replicates (independent animals). GraphPad Prism v8.0 (GraphPad Software), and Sigmaplot v14.0 (Systat Software, Inc.) were used for statistical analysis. For all comparisons, a *P* value <0.05 was considered statistically significant.

3.4. COMPUTATIONAL STUDY

3.4.1. Density Functional Theory (DFT)

Computational study was performed on the Mn_4O_4 cluster using density functional theory (DFT) as implemented in Gaussian 16 software. Geometry optimizations were performed with unrestricted B3LYP functional and Pople's double zeta basis set 6-31g with added diffuse and polarization functions on the heavy atoms. High spin geometry of Mn(II) was considered. The spin multiplicity of the system was 21. Three oxygen atoms were passivated with three hydrogens, giving rise to +3 charge. GSH was mimicked with RSH, where the R is a methyl group. The first step of the reaction was modeled by O--O bond length perturbation of adsorbed H_2O_2. The proton transfer step was modeled by distance perturbation of donor hydrogen and acceptor oxygen. RSOH formation was modeled by sulfur-oxygen distance perturbation.

The e_g occupancy presented in the study is the average between integer occupations of Mn(II) and Mn(III) metal centers as suggested by Wang *et al.* [23]. There are no fractional electrons occupying these orbitals.

3.4.2. In silico Rationalization of SKP17LIV01

3.4.2.1. Compound library preparation

We first prepared a catalog of natural products with diverse chemical structures from the array of compounds isolated from a mixture (SKP17LIV01) of eight medicinal herbs. The compounds were identified using fingerprint analysis technique

in ultra-high resolution liquid chromatography mass spectrometry (UHPLC-MS). Their structures were drawn with ChemDraw Ultra 8.0 software and initially saved as .mol2 format, further converted into unified SDF or canonical SMILES format using OpenBabel toolkit (version 2.3.2). In the preparation process, duplicate entries were deleted, salt ions were removed, and dative bonds were standardized. Considering the deglycosylation process mediated by enteric bacteria in case of oral administration, we further deglycosylated the identified natural glycosides following the rule of glycosidase hydrolysis and incorporated the corresponding products into the dataset. Finally all the structures in SMILES format were included into a single text file for further calculations.

3.4.2.2. Molecular descriptors calculation

3.4.2.2.1. Drug likeness

We used FAF-Drug3 web server to compute physicochemical descriptors like number of rotatable bonds, rigid bonds, hydrogen bond acceptors (HBAs), hydrogen bond donors (HBDs), aromatic rings, heavy atoms, molecular weight (MW), lipophilicity (logP, logarithm of octanol-water partition coefficient), aqueous solubility (logS), logD (at pH 7.0), topological polar surface area (tPSA). Lipinski's rule of five (RO5) was employed for initial screening of drug likeness. Furthermore, Tanimato coefficient (Equation 01) was used to discriminate between drug-like and non-drug like molecules.

$$T(A,B) = \frac{A \cdot B}{[A]^2 + [B]^2 - A \cdot B}$$

[Equation – 3.4]

Here, A is the molecular descriptor properties of target small-molecule, and B is the molecular properties of compounds in DrugBank database (http://www.drugbank.ca/).

3.4.2.2.2. Computational pharmacokinetic profiling

In this step, we developed an *in silico* integrative model-ADMET (absorption, distribution, metabolism, excretion and toxicity) for selecting the molecules having favorable pharmacokinetic properties. Intestinal absorption (human), Caco-2

permeability, VDss (human), total clearance, CYP enzyme modulatory activity, maximum tolerated dose, oral rat acute toxicity (LD50) and hepatotoxicity were computed using pkCSM web server. For calculation of oral bioavailability, we used Veber's descriptors.

3.4.2.2.3. Drug-like properties

Several drugs, that are available in the market, have been found to have some common structural features that make them modulator of some target class of enzymes and cellular signaling pathways. Six of such major properties like GPCR ligand, ion channel modulation, kinase inhibition, nuclear receptor ligand, protease inhibition and enzyme inhibition were computed using Molinspiron toolkit (Molinspiron Cheminformatics, Bratislava, Slovak Republic, www.molinspiron.com).

3.4.2.3. Target fishing

Our proposed method includes three major steps in regards to network pharmacology: (1) finding known targets and candidate genes related to the disease of interest and making a disease target network (D-T); (2) constructing natural compound-target network (C-T); (3) constructing protein-protein network (PPIs) and elucidating target pathways (T-P) involved behind therapeutic action.

3.4.2.3.1. Disease-target genes

The proposed approach requires construction of a network, which includes all shortest paths between the drug targets and genes known to be associated with the disease. Drug-targets and disease related genes were retrieved from DrugBank and Comparative Toxicogenomics Database (CTD) with keyword search.

3.4.2.3.2. Compound-target proteins

In silico prediction of target profiles of small molecules is the most critical step in drug discovery. In this regard, we propose a systemic approach that effectively integrates data mining, chemogenomic, pharmacological and statistical methods. Firstly, text mining was carried out to find the target proteins in HIT (Herbal Ingredients' Targets Database, http://lifecenter.sgst.cn/hit/) and DrugBank. Secondly, the virtual chemical Fingerprint Similarity Ensemble Approach (SEA,

http://sea.bkslab.org/) and information integration method STITCH (http://stitch.embl.de/) were applied to predict the biological targets. Finally, the targets were mapped to the PharmGKB (http://www.pharmgkb.org/), CTD and Therapeutic Target Database (TTD, http://bidd.nus.edu.sg/group/ttd/) to eliminate the unrelated target proteins and obtain a greater accuracy view on the compound target interaction.

3.4.2.3.3. Network construction

To explore the multi-scale action mechanism of a single molecule or a mixture of molecules in prevention of heavy metal induced hepatotoxicity, we constructed C-T and D-T network. The intersecting nodes of the two networks were further amplified (up to two nearest neighbors) to construct T-P network using GeneMania prediction servers (http://genemania.org/) and STRING functional protein association network database (http://string-db.org/). All networks were generated and analysed by Cytoscape 3.5.1. In the graphic network, the nodes represent compounds/targets/pathways and edges represent the intermolecular-interactions. We applied ClueGO, a Cytoscape plugin, to explore molecular functions of the target proteins.

REFERENCES

[1] D. V. O'Conner, D. Philips, Time Correlated Single Photon Counting, Academic Press, London, (1984).

[2] N. Singh, M. A. Savanur, S. Srivastava, P. D'Silva, G. Mugesh, Angew. Chem. Int. Ed. Engl. 129 (2017) 14455.

[3] N. Polley, S. Saha, A. Adhikari, S. Banerjee, S. Darbar, S. Das, S. K. Pal, Nanomedicine 10 (2015) 2349.

[4] E. C. Jensen, Anat. Rec. 296 (2013) 378.

[5] A. Moles, N. Tarrats, A. Morales, M. Domínguez, R. Bataller, J. Caballería, C. García-Ruiz, J. C. Fernández-Checa, M. Marí, Am. J. Pathol. 177 (2010) 1214.

[6] K. Moore, L. J. Roberts, Free Radic. Res. 28 (1998) 659.

[7] Y. J. Garcia, A. J. Rodríguez-Malaver, N. Peñaloza, J. Neurosci. Methods 144 (2005) 127.

[8] G. L. Ellman, Arch. Biochem. Biophys. 82 (1959) 70.

[9] J. M. Graham, Biomembrane Protocols: I. Isolation and Analysis, (1993), 29.

[10] M. Spinazzi, A. Casarin, V. Pertegato, L. Salviati, C. Angelini, Nat. Protoc. 7 (2012) 1235.

[11] Y.-N. Liu, Z.-M. Zhou, P. Chen, Clin. Exp. Pharmacol. Physiol. 35 (2008) 211.

[12] K. N. Alavian, G. Beutner, E. Lazrove, S. Sacchetti, H.-A. Park, P. Licznerski, H. Li, P. Nabili, K. Hockensmith, M. Graham, G. A. Porter, E. A. Jonas, Proc. Natl. Acad. Sci. 111 (2014) 10580.

[13] R. C. Scaduto Jr, L. W. Grotyohann, Biophys. J. 76 (1999) 469.

[14] J. D. Ly, D. Grubb, A. Lawen, Apoptosis 8 (2003) 115.

[15] L. B. Chen, Annu. Rev. Cell Biol 4 (1988) 155.

[16] T. Mosmann, J. Immunol. Methods 65 (1983) 55.

[17] M. M. Ommati, R. Heidari, V. Ghanbarinejad, A. Aminian, N. Abdoli, H. Niknahad, Nutr. Neurosci. (2019) 1.

[18] J. Petrik, T. Žanić-Grubišić, K. Barišić, S. Pepeljnjak, B. Radić, Ž. Ferenčić, I. Čepelak, Arch. Toxicol. 77 (2003) 685.

[19] B. Duncan, X. Li, R. F. Landis, S. T. Kim, A. Gupta, L.-S. Wang, R. Ramanathan, R. Tang, J. A. Boerth, V. M. Rotello, ACS Nano 9 (2015) 7775.

[20] S.-L. Chen, H.-I. Ma, J.-M. Han, R.-B. Lu, P.-L. Tao, P.-Y. Law, H. H. Loh, J. Biomed. Sci. 17 (2010) 28.

[21] L. K. Fonken, E. Kitsmiller, L. Smale, R. J. Nelson, J. Biol. Rhythms 27 (2012) 319.

[22] L. M. DeVito, R. Konigsberg, C. Lykken, M. Sauvage, W. S. Young, H. Eichenbaum, J. Neurosci. 29 (2009) 2676.

[23] X. Wang, X. J. Gao, L. Qin, C. Wang, L. Song, Y.-N. Zhou, G. Zhu, W. Cao, S. Lin, L. Zhou, K. Wang, H. Zhang, Z. Jin, P. Wang, X. Gao, H. Wei, Nat. Commun. 10 (2019) 704.

CHAPTER 04

Nanotherapy of Neonatal Hyperbilirubinemia

4.1. INTRODUCTION

Unmonitored neonatal hyperbilirubinemia (resulting from an imbalance between production and clearance of bilirubin) and absence of chemopreventive approaches, other than hospital based phototherapy can lead to irreversible neurotoxicity, neurodevelopmental delay, or death [1-3]. Although benign at initial stages, incremental high concentrations of unconjugated bilirubin (UCB) in serum can lead to incipient bilirubin encephalopathy [4,5]. The population incidence of visually apparent neonatal jaundice affects almost 85% of term and late preterm neonates in the first seven days after birth and best defined by age in hours and percentiles and nearly 10% of breastfed babies remain jaundiced even at the age of one month [2,6]. In India 10-15% of babies are eligible for hospital-based phototherapy. It was estimated that each year, at least 0.5 million term or near-term newborns are affected with severe hyperbilirubinemia (>25 mg/dl), of whom 0.15 million die and more than 0.07 million survive with moderate or severe disability [7]. Currently, phototherapy is the most widely used and preferred treatment method even though hospitalization is required [8]. However, many infants are unnecessarily exposed to the risk of severe neonatal hyperbilirubinemia (SNH) because of our inability to have effective seamless continuity in health-care systems and to provide close individualized clinical

supervision during the first days of life [9]. In view of these national and global challenges, a drug that degrades bilirubin *in vivo* and can alter the subsequent trajectory of bilirubin rate of rise has the potential to protect infants from SNH [9]. Despite the tremendous advancement of medicinal chemistry, no chempreventive agents, including heme oxygenase inhibitors, have met FDA approval.

Manganese (Mn), an essential trace mineral nutrient, is a cofactor for many crucial metabolic enzymes including manganese superoxide dismutase, arginase, and pyruvate carboxylase. Mn plays vital role in metabolism of amino acid, cholesterol, glucose, and carbohydrate; scavenging of reactive oxygen species (ROS); bone formation; reproduction; and immune response [10-13]. Upon absorption, some of the Mn ions remain free, but remainder are mostly bound to transferrin, albumin, and plasma alpha-2-macroglobulin such that the circulating level ranges from 4-15 μg L^{-1} [14-17]. These levels vary largely and do not serve as useful indicator of body Mn status [14]. Overdose of Mn may lead to adverse neurological, reproductive, or respiratory effects, and has been reported among welders, miners, or persons with chronic inhalation exposure [18,19]. Despite the paradoxical behavior of this 'Janus-faced' metal in physiological systems, Mn oxides in nano-form (i.e., Mn_xO_y nanomaterials) possess exciting redox-modulatory and catalytic properties necessary for novel therapeutic applications [10,20-23].

Over the past decade, biomedical applications of nanometer-sized colloidal particles (i.e., nanoparticles) have been subject of intensive research due to their unique electronic, optical, and magnetic properties that are derived from the nanoscale dimensions and compositions [24]. Numerous therapeutic and diagnostic modalities have also been developed using diverse array of nanomaterials [25]. For example, Doxil® (doxorubicin liposomes), used for the treatment of AIDS-associated Kaposi's sarcoma, was the first nanosized drug delivery system to receive United States Food and Drug Administration (US-FDA) approval [26]. Similarly, Abraxane®, a 130 nm paclitaxel-decorated albumin was granted US-FDA approval as second-line treatment of breast cancer patients [27].Combidex® (ferumoxtran-10), an iron-oxide nanoparticle based imaging contrast agent is also being used in conjunction with magnetic resonance imaging (MRI) for differentiating cancer from normal lymph nodes [25]. Recently, among numerous engineered nanomaterials manganese oxide

nanomaterials showed promising results in treatment of chronic diseases like hepatic fibrosis [20], chronic kidney disease, neurodegenerative disorders [28] etc. in preclinical animal models. Our recent study demonstrated that manganese oxide nanoparticles do not display characteristic neurotoxicity (i.e., manganism), rather ameliorate Mn-induced neuralgic disorder (i.e., idiopathic Parkinson's disorder) through mitochondrial protection and intracellular redox modulation [28]. Interestingly in preliminary studies, the nanoparticle showed unprecedented catalytic activity towards bilirubin degradation without any photo- or chemo-activation in a controlled *in vitro* system [29].

The present study examines whether citrate functionalized trimanganese tetroxide nanoparticles (C-Mn_3O_4 NPs) can degrade bilirubin during *in vivo* administration and prevent bilirubin-induced neurotoxicity in a rodent model bred to exhibit severe neonatal hyperbilirubinemia (SNH).

4.2. RESULTS AND DISCUSSION

4.2.1. A Novel Nanoceutical Agent for Chemoprevention of Bilirubin Encephalopathy [30]

The C-Mn_3O_4 NPs are nearly spherical particles (Figure 4.1a) with an average diameter of 6.25±2.41 nm (Figure 4.1b). High-resolution TEM (HRTEM) analysis confirmed the crystalline nature of the particle with a clear atomic lattice fringe spacing of 0.312±0.02 nm (Figure 4.1c) corresponding to the separation between (112) lattice planes of tetragonal Mn_3O_4 nanocrystal. Dynamic light scattering (DLS) studies indicated two peaks at sub-1 nm and 24.3±4.2 nm (Figure 4.1d) with a polydispersity index (PDI) of 0.32±0.13. The sub-1 nm peak was probably an artifact while predominant 24.3±4.2 nm peak corresponds to the hydrodynamic diameter of C-Mn_3O_4 NPs. Zeta potential (ξ) measurements revealed the surface of C-Mn_3O_4 NPs to be anionic with ξ= -12.23±0.6 mV and electrophoretic mobility -0.96±0.05 $\mu cm V^{-1} s$ at pH 7.4.

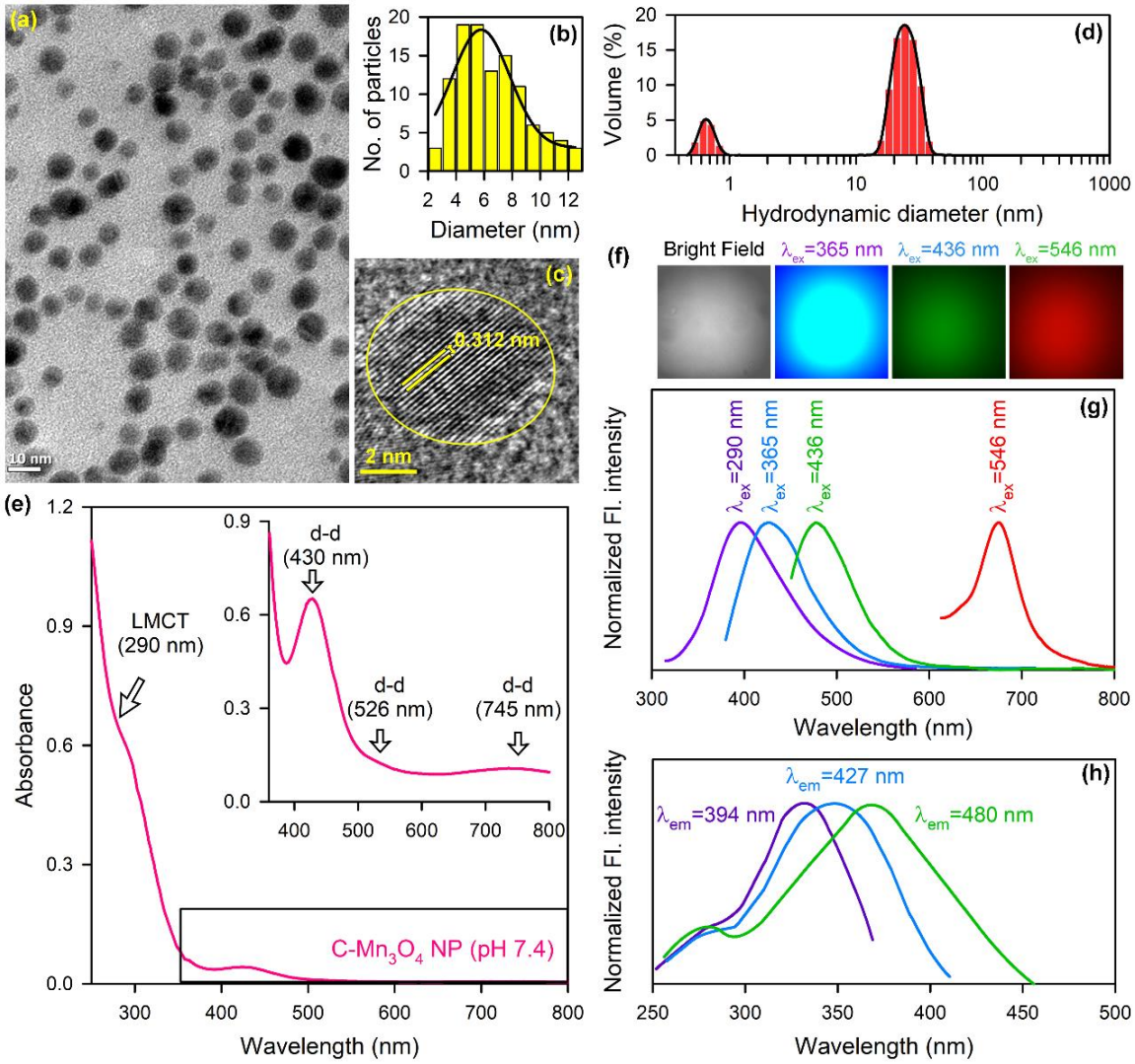

Figure 4.1. *Physicochemical properties of C-Mn_3O_4 NPs. (a) The particle distribution of the NPs as recorded using transmission electron microscope (TEM). (b) The particle size distribution of the NPs. (c) The high resolution transmission electron micrograph (HRTEM) of a single nanoparticle shows the interplannar distance of 0.312 nm corresponding to (112) facet of the nanocrystal. (d) Dynamic light scattering shows the hydrodynamic diameter of the NPs in aqueous solution. (e) The UV-visible absorbance spectra of the NPs. Inset shows a magnified version indicating the d-d transitions. (f) Fluorescence microscopic images of the liquid solution of the NPs. (g) Excitation dependent emission spectra of NPs. (h) Corresponding excitation spectra.*

X-ray diffraction (XRD) studies revealed the purity of the tetragonal hausmannite crystals of C-Mn_3O_4 NPs (Figure 4.2a). Fourier-transformed infrared spectroscopy (FTIR) studies clearly confirmed the functionalization through covalent binding of carboxylate's oxygen of citrate with the NP surface (Figure 4.2b). The

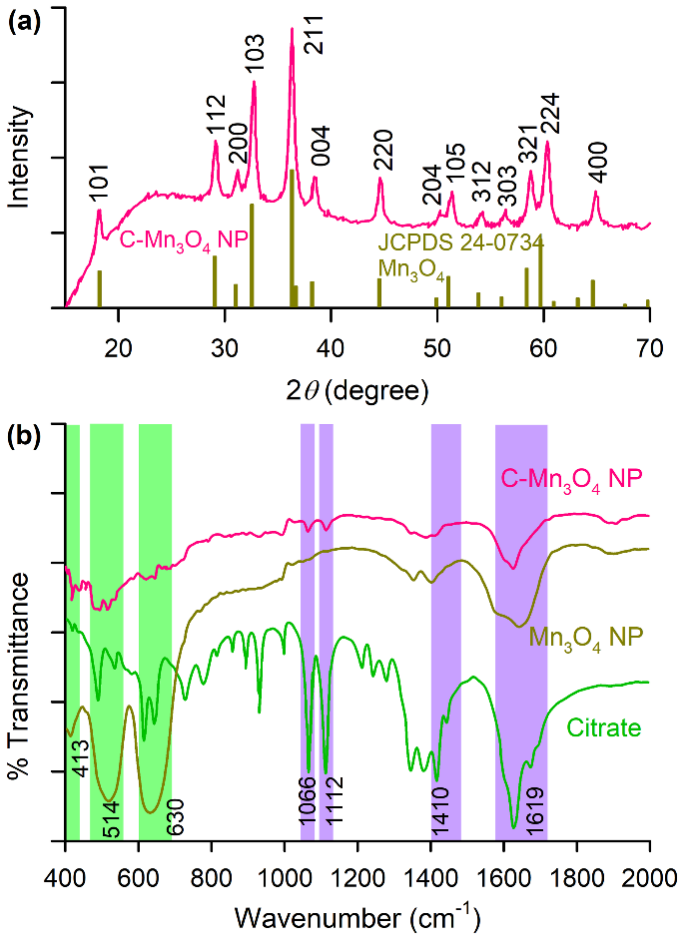

Figure 4.2. *Physicochemical properties of C-Mn_3O_4 NPs. (a) XRD spectra of C-Mn_3O_4 NPs indicates to its tetragonal structure. (b) FTIR spectra of C-Mn_3O_4 NPs confirms the functionalization by citrate. Bare as-prepared Mn_3O_4 NPs exhibit three characteristic bands (in the range of 400–1000 cm^{-1}) at 630, 514 and 413 cm^{-1}, which are associated with the stretching vibrations of Mn–O and Mn–O–Mn bonds which are not distinctly visible after functionalization, suggesting a potent surface modification of the NPs upon interaction with citrate ligands. The appearance of two sharp bands at 1066 and 1112 cm^{-1} could be assigned to the C–OH stretching modes of citrate. Substantial broadening of these two bands upon attachment to the NPs strongly indicates their significant interaction with the surface of the NPs. Considerable perturbation of the symmetric (1410 cm^{-1}) and asymmetric (1619 cm^{-1}) stretching modes of the carboxylate groups (COO^-) of citrate in C-Mn_3O_4 NPs clearly confirms the covalent binding of carboxylate's oxygen with the NP surface.*

optical spectroscopic studies revealed the previously reported [31] spectroscopic signatures of C-Mn_3O_4 NPs, which includes multiple photoluminescence due to high energy LMCT involving citrate-Mn^{4+} interaction, and Jahn–Teller (J-T) effect involving $5B_{1g} \rightarrow 5E_g$, $5B_{1g} \rightarrow 5B_{2g}$ and $5B_{1g} \rightarrow 5A_{1g}$ transitions (Figure 4.1e-4.1h).

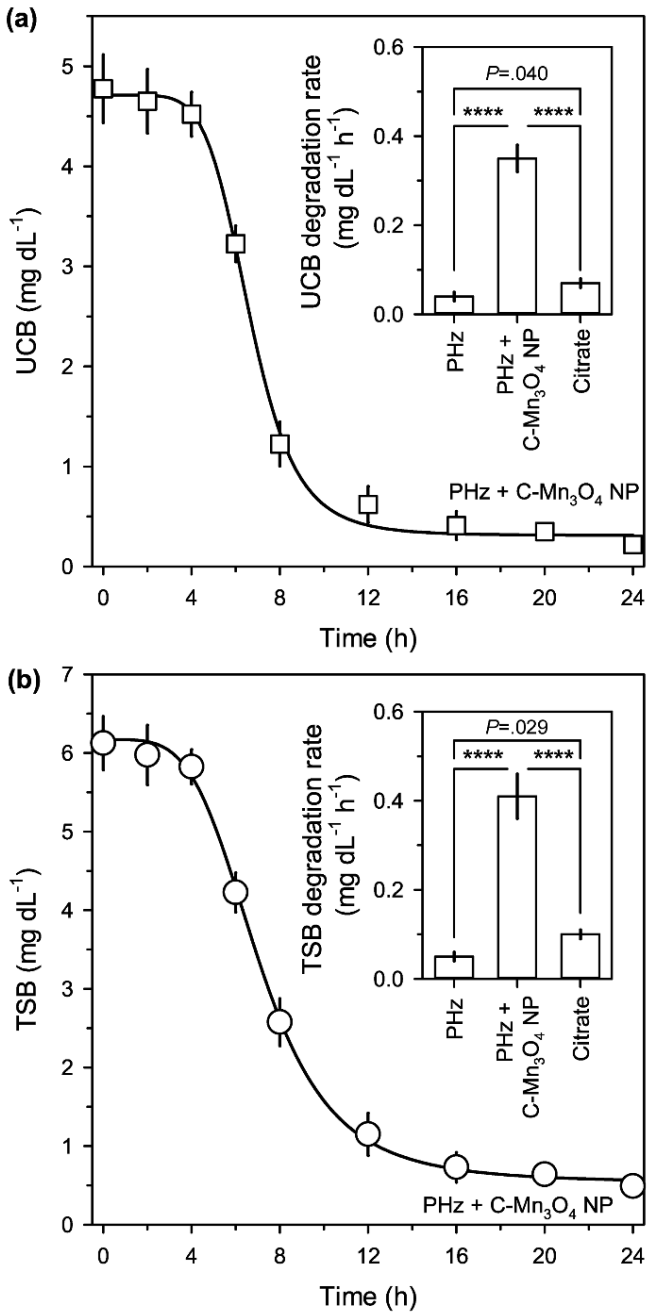

Figure 4.3. *In vivo bilirubin degradation kinetics after treatment with C-Mn_3O_4 NPs in PHz-induced hyperbilirubinemia mice. (a) Unconjugated bilirubin (UCB). (b) Total serum bilirubin (TSB). Insets show bilirubin degradation rates across different treatment groups. Error bars represent standard deviation from the mean (N = 6). **** signifies P<0.0001, one-way ANOVA, Tukey's Multiple Comparison Test (post-hoc).*

The C-Mn_3O_4 NPs used in subsequent preclinical animal studies were aqueous soluble (pH 7.0), endotoxin free, and stable upto one year in room temperature and pressure.

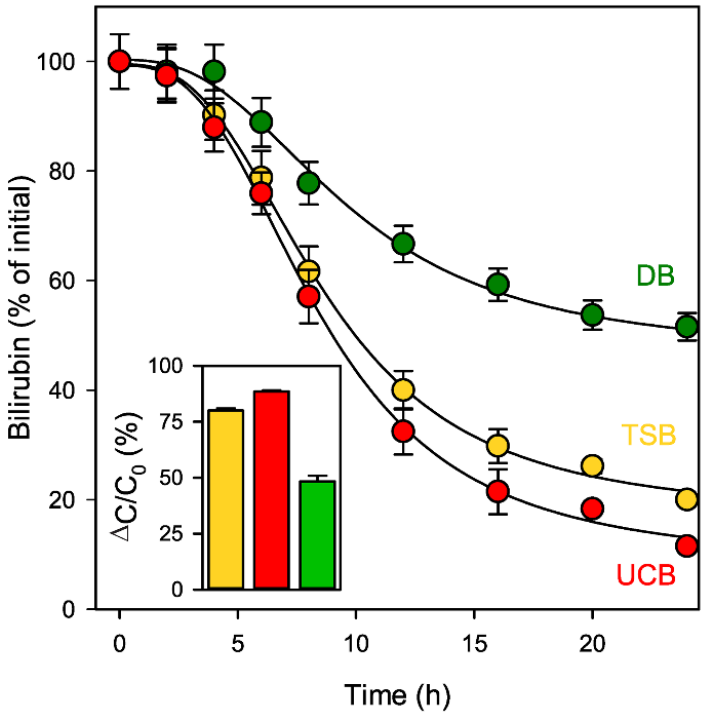

Figure 4.4. *Comparison of in vivo bilirubin degradation kinetics for different types of bilirubin in PHz+C-Mn_3O_4 NP co-treated group. Data represented as percentage (%) of initial concentration. Inset shows % degradation of different bilirubins (UCB, TSB, and DB) after 12 h of treatment. Error bars represents standard deviation (SD) from the mean (N = 6).*

Effect of C-Mn_3O_4 NPs on unconjugated bilirubin (UCB) level was monitored at 2 h interval upto 24 h, after treatment with single oral dose (0.25 mg kg^{-1} BW) of C-Mn_3O_4 NPs, once UCB level reached 4.78±0.34 mg dL^{-1} (compared to 0.22±0.05 mg dL^{-1} of control; P<.0001, two-tailed t-test), and TSB level reached 6.13±0.44 mg dL^{-1} (compared to 0.29±0.05 mg dL^{-1} of control; P<.0001, two-tailed t-test) due to PHz intoxication. As the results suggest, C-Mn_3O_4 NPs was able to irreversibly decrease both UCB (0.62±0.18 mg dL^{-1}; P<.0001, two-tailed t-test) (Figure 4.3a) and TSB levels (1.15±0.22 mg dL^{-1}; P<.0001, two-tailed t-test) (Figure 4.3b) to normal range within 12 h. Fitting the UCB degradation kinetic data in logistic regression model (adj. R^2 0.994), the time required for 50%, and 80% bilirubin degradation were found to be 6.6 h, and 8.3 h, respectively (Figure 4.4). Similarly, for TSB the time required for 50%, and 80% bilirubin degradation were 7.3 h, and 10.6 h, respectively (adj. R^2 0.996) (Figure 4.4). It is worth mentioning here that after oral exposure ~4 h is required for the NPs to reach sufficient plasma concentration (see PK-PD section for details). Thus,

effectively within 3 h of absorption, the C-Mn_3O_4 NPs were able to degrade 50% of the UCB, and ~45% of TSB *in vivo*. While comparing the time dependent changes in UCB, TSB, and direct bilirubin (DB) levels, we found lesser efficiency of the C-Mn_3O_4 NPs towards degradation of DB (~70%; P<.0001, one-way ANOVA) compared to UCB (~96%), and TSB (~92%) at 24 h (Figure 4.4). Treatment with citrate (0.15 mg kg^{-1} BW; oral) after PHz-intoxication did not affect the UCB (6.27±1.66 mg dL^{-1}; P=.9071 compared to PHz-treated, one-way ANOVA, F (4, 45) = 12.57), and TSB levels (7.19±1.53 mg dL^{-1}; P=.9944 compared to PHz-treated, one-way ANOVA, F (4, 45) = 10.53) (Figure 4.5a & 4.5b). Cumulatively, these results indicate that C-Mn_3O_4 NPs can efficiently degrade bilirubin *in vivo* and, the bilirubin degradation observed after C-Mn_3O_4 NP treatment is due to the catalytic nature of the nanoceutical complex itself, not because of the outer citrate coating.

Duration of the chemoprevention effect was evident from our phase-2 study. PHz drastically increased both UCB (6.69±1.56 mg dL^{-1}; P<.0001, F (2,15) = 45.96, one-way ANOVA), and TSB (7.39±1.65 mg dL^{-1}; P<.0001, F (2,15)=58.00, one-way ANOVA) compared to control (UCB: 0.22±0.05 mg dL^{-1}; TSB: 0.29±0.05 mg dL^{-1}) (Figure 4.5a & 4.5b) simulating a condition of SNH. Reduction in hematocrit (Hct) value further confirmed induction of PHz-induced hemolytic condition (Figure 4.6a). Co-treatment with C-Mn_3O_4 NPs (0.25 mg kg^{-1} BW; oral) significantly reduced both UCB (0.31±0.11 mg dL^{-1}), and TSB (0.42±0.14 mg dL^{-1}) compared to PHz-induced untreated littermates (P<.0001; one-way ANOVA) (Figure 4.5a & 4.5b). We further monitored the UCB and TSB levels for additional one week once the treatment ended (Figure 4.6b & 4.6c). There was no recurrent increase in UCB or TSB during the one week period, indicating sustainability of the chemoprevention by C-Mn_3O_4 NP. Animals co-treated with citrate (0.15 mg kg^{-1} BW; oral) + PHz showed UCB (6.27±1.66 mg dL^{-1}) and TSB (7.19±1.53 mg dL^{-1}) levels similar to that of PHz-intoxicated group (UCB: 6.69±1.55 mg dL^{-1}, P=.8457; TSB: 7.39±1.65 mg dL^{-1}, P=.9653, one-way ANOVA) (Figure 4.5a & 4.5b). The successful reduction of UCB and TSB by oral administration further suggest that C-Mn_3O_4 NPs with high stability and gastric passage will be of potential easy use in human neonates too.

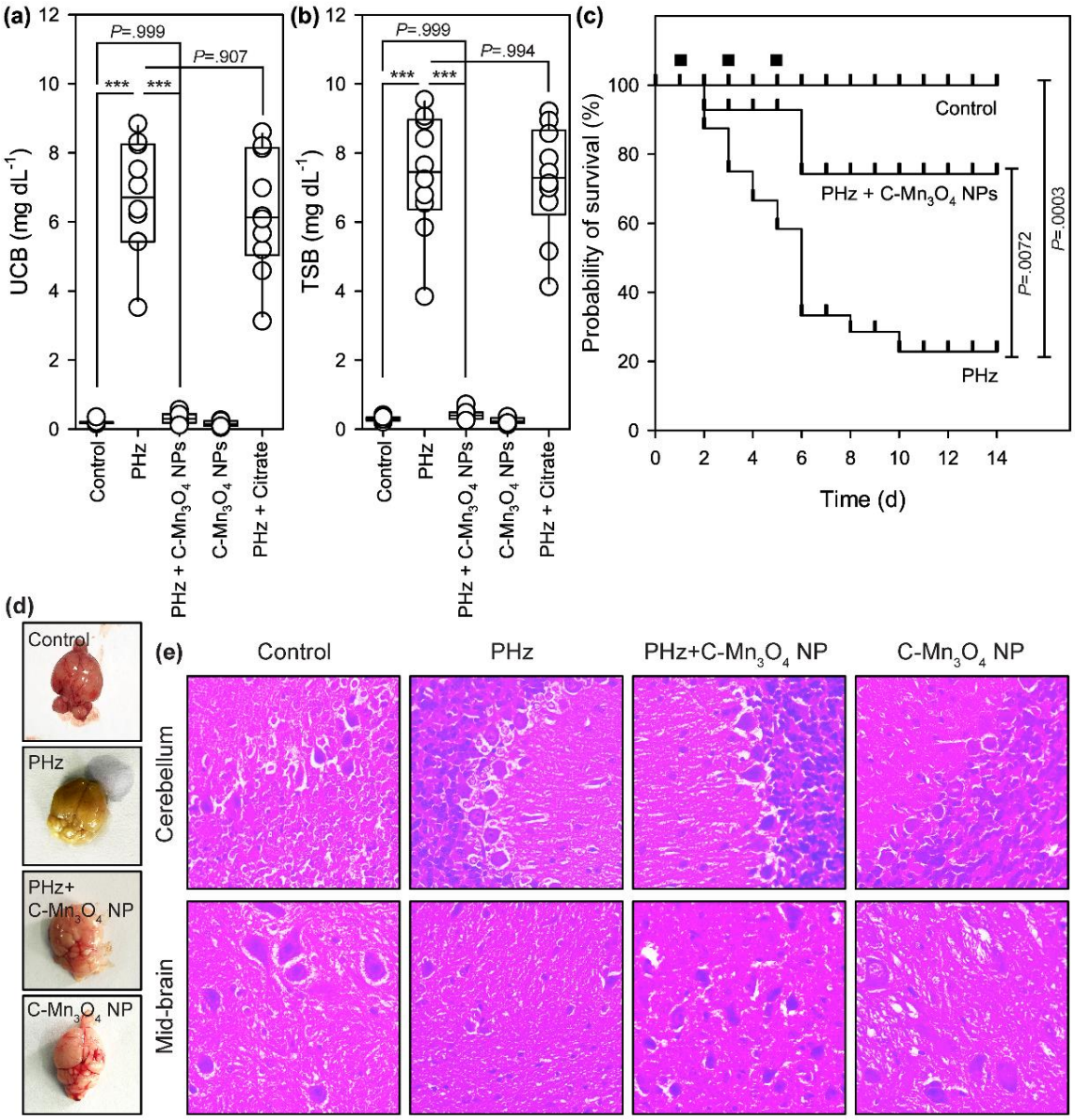

Figure 4.5. *Effect of C-Mn_3O_4 NPs on severe neonatal hyperbilirubinemia (SNH) and associated neurotoxicity. (a) Unconjugated bilirubin (UCB) level. (b) Total serum bilirubin (TSB) level. (c) Probability of survival of differently treated mice as a function of time (Kaplan–Meier analysis). The black squares represents days of treatment. (d) Photograph of isolated brains at the end of the experimental period. (e) Micrographs (100X) of hematoxylin and eosin (H & E) stained brain sections. *** signifies P<0.001, one-way ANOVA, Tukey's Multiple Comparison Test (post-hoc). n=6.*

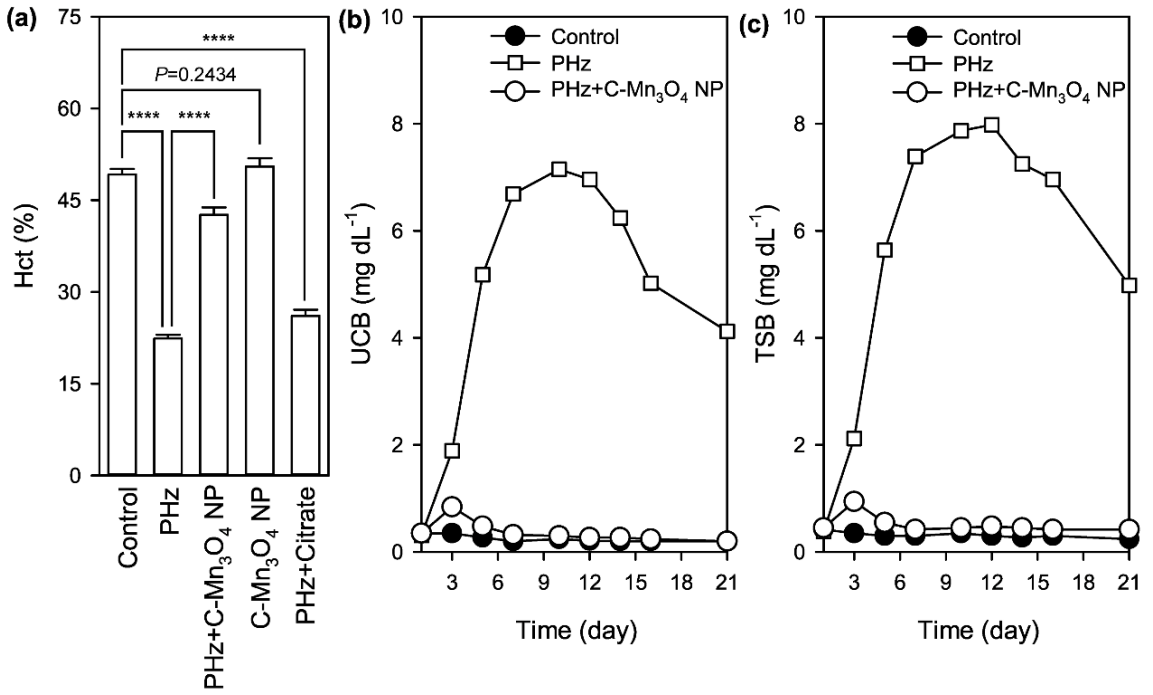

Figure 4.6. *Effect of C-Mn_3O_4 NPs on severe neonatal hyperbilirubinemia. (a) Hct values across treatment groups. (b) & (c) Sustained action of C-Mn_3O_4 NPs for amelioration of severe neonatal hyperbilirubinemia. Data represented as Mean±SD (N = 6). *, **, ***, **** signifies P<0.05, P<0.01, P<0.001, and P<0.0001 respectively, one-way ANOVA, Tukey's Multiple Comparison Test (post-hoc).*

Repeated dose PHz administration induced significant lethality in the study mice (Hazards Ratio, HR (Mantel-Haenszel): 0.158; 95% CI of HR: 0.058-0.32; log rank χ^2 (Mantel-Cox): 12.94; df: 1; *P*=.0003) (Figure 4.5c). Nearly 50% of the animals died during the first week due to PHz-induced SNH (median survival: 6 days). Strikingly, C-Mn_3O_4 NP treatment was not only well tolerated by the study mice (Group 5; No mortality) but also significantly reduced lethality in PHz-intoxicated C-Mn_3O_4 NP co-treated mice (Group 3; 10% mortality) as compared to the untreated PHz-intoxicated group (Group 2; 60% mortality) (HR (Mantel-Haenszel): 3.650; 95% CI of HR: 1.419-9.391; log rank χ^2 (Mantel-Cox): 7.210; df: 1; *P*=0.0072). The difference in the survival rates of PHz + C-Mn_3O_4 NP co-treated mice and PHz-intoxicated untreated mice was most notable during the first week of the treatment (Figure 4.5c). Necropsy revealed, consistent with the blood biochemical analysis, bilirubin induced acute neurotoxicity and extreme hemolysis as the cause of death.

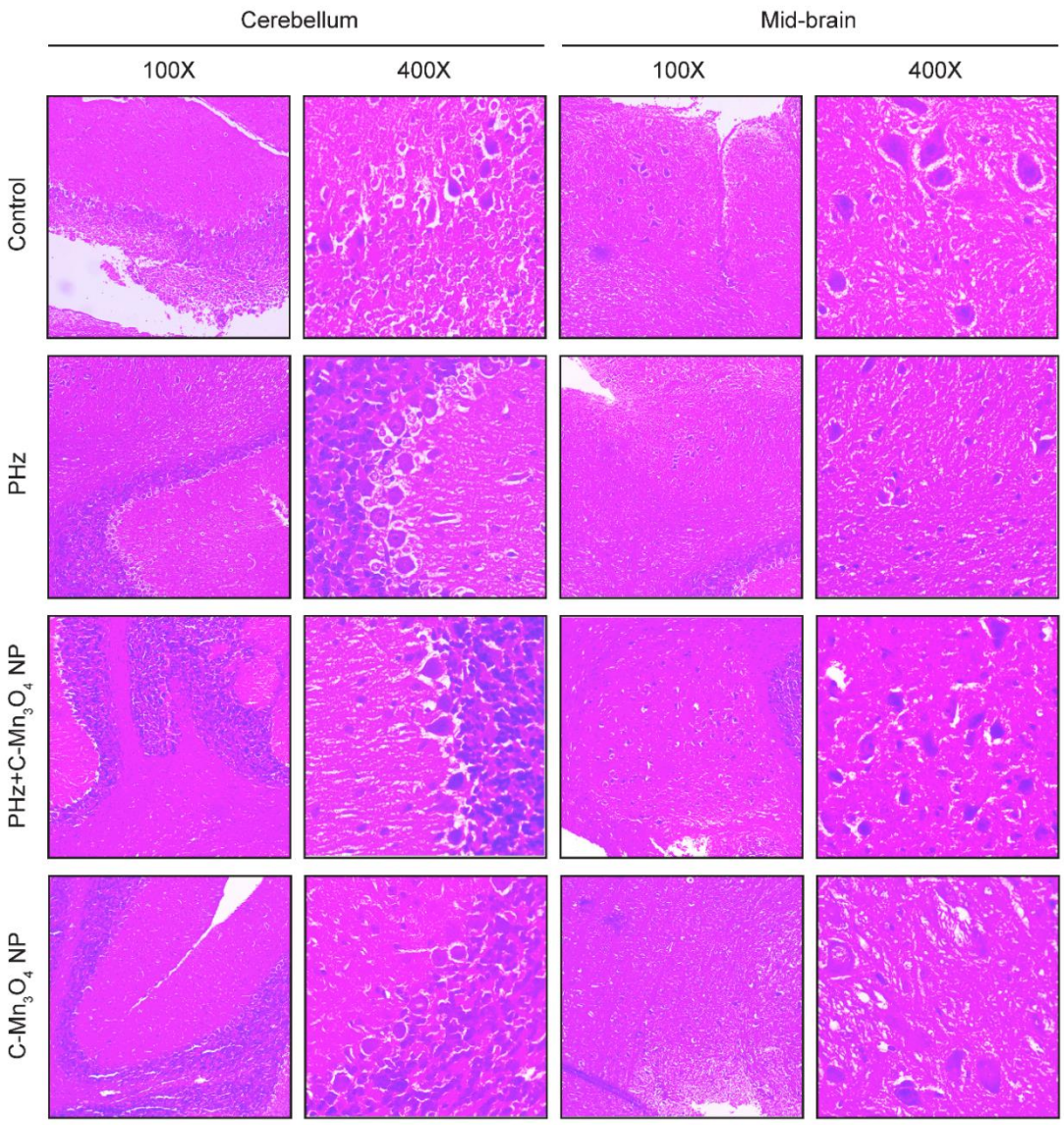

Figure 4.7. *Micrographs of hematoxylin and eosin stained brain sections. Cerebellum and mid-brain sections are shown at different magnification for various treatment groups.*

Therefore, our study evidently suggest that C-Mn_3O_4 NPs can reduce the severity and mortality of SNH through reduction of bilirubin level in experimental rodent model.

To induce kernicterus-like syndrome, prolonged repeated PHz administration was used, and *in vivo* bilirubin-induced neurotoxicity in the PHz-treated animals are evident from the digital photograph of isolated brains (Figure 4.5d). The intense yellow discoloration, attributed to bilirubin, in gross brain photograph of PHz-induced rodents indicated accumulation of bilirubin in the brain. This yellow discoloration was

not observed in C-Mn_3O_4 NP + PHz co-treated group, indicating low accumulation of neurotoxic bilirubin in brain. In accordance with the biochemical results, histopathological investigations of the isolated brain sections revealed severe bilirubin-induced damage to the PHz-intoxicated animals (Figure 4.5e and Figure 4.7). In cerebellum, marked reduction (~35%) in number of cells per field, a hallmark of bilirubin induced severe neurotoxicity was noticed in PHz-intoxicated animals. Number of Purkinje neurons (~30%) and cells of substantia nigra (~40%) were also decreased significantly compared to control. Other pathological features include extensive fibrosis, spongiosis (vacuolation) in brain parenchyma (linked to depletion of neurons), shrinkage in cell size, eosinophilic neurons (characteristic of degenerating cells) and gliosis. In contrast, the PHz+C-Mn_3O_4 NP co-treated animals showed normal cellular architecture with mild gliosis, remnant of PHz-induced brain damage. Number of cells per field in both cerebellum and mid-brain region were comparable to control animals. No shrinkage of cells were observed. C-Mn_3O_4 NP treated animal showed brain architecture similar to those of untreated control. In summary, the histopathological examinations illustrate the protective action of C-Mn_3O_4 NPs at cellular level to ameliorate bilirubin-induced neurotoxicity.

In view of chronic sequelae, i.e., motor dysfunction and ataxia, we tested the performance of the animals in OFT (Figure 4.8a). The measured total distance moved (Figure 4.8b) by affected rodents, and the time spent at the center of the field (Figure 4.8c) was less in PHz-treated group compared to control (Total distance moved: 41.7±5.1 m vs. 47.8±3.4 m, P=.0112, F (2, 15)=13.24, one-way ANOVA; Time spent at the center: 16.2±4.1% vs. 29.1±4.7%; P=.0007, F (2, 15)=6.99, one-way ANOVA) and PHz+C-Mn_3O_4 NP co-treated group (Total distance moved: 41.7±5.1 m vs. 48.2±4.4 m, P=.0068; Time spent at the center: 16.2±4.1% vs. 27.2±5.2%; P=.0028, one-way ANOVA), and illustrate serious movement disorders. In addition, the time to cross a beam (Figure 4.8d: P=.0018, F (2, 15) = 9.29, one-way ANOVA), and time to descend a pole (Figure 4.8e: Time to descend: P<.0001, F (2, 15) = 34.93, one-way ANOVA) were also higher in PHz-induced group to indicate severe motor dysfunction, one of the characteristic features of bilirubin-induced severe neurotoxicity. Treatment with C-Mn_3O_4 NP was protective against motor dysfunction injury (Time to cross: P=.0532; Time to descend: P<.0001, one-way ANOVA).

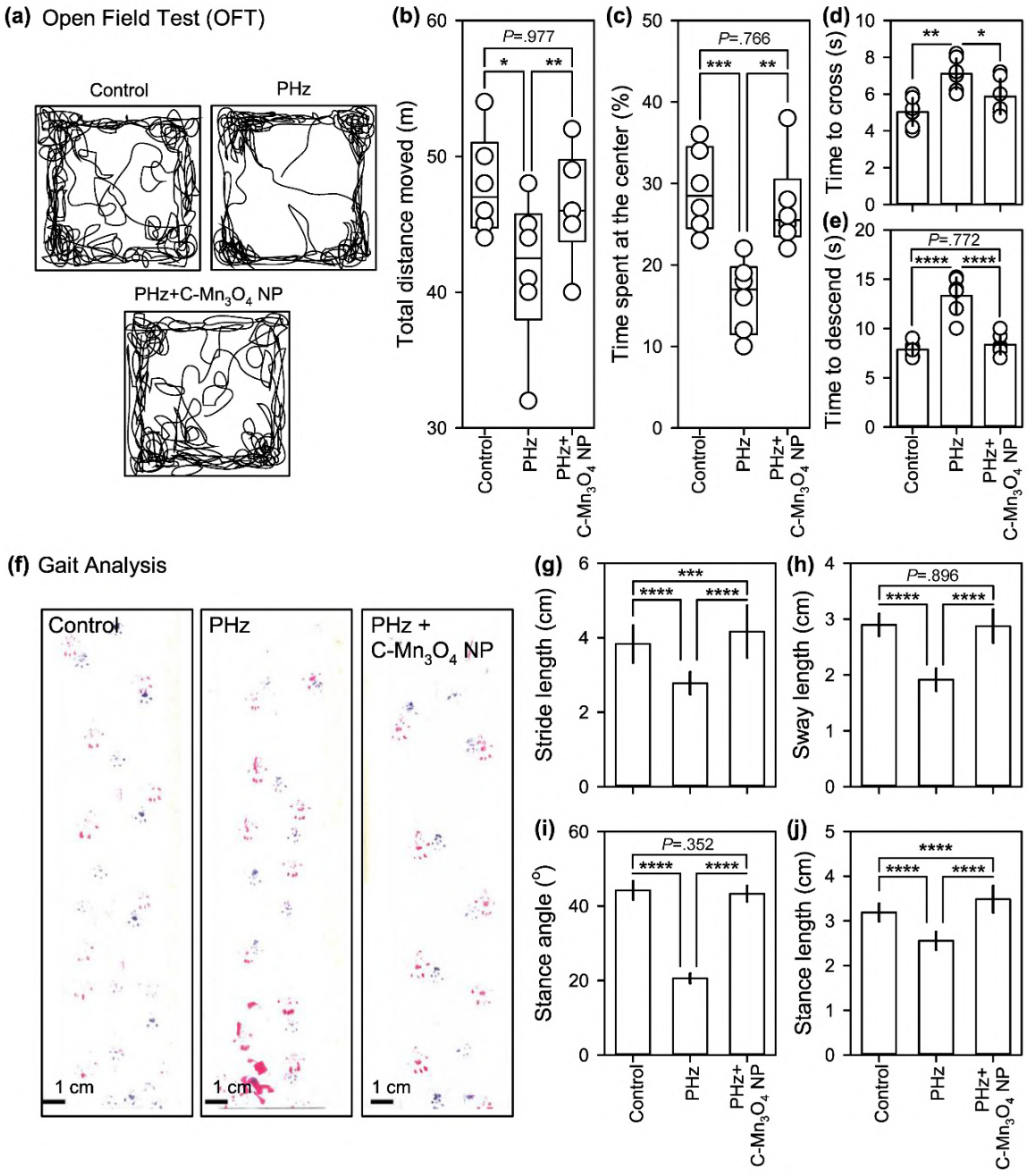

Figure 4.8. *Effect of C-Mn_3O_4 NPs on severe neonatal hyperbilirubinemia induced neurobehavioral changes. (a) Trace of open field activity. (b) Total distance moved in open field apparatus. (c) Time spent at the center of the open field. (d) Time to cross a beam. (e) Time to descend a pole. (f) Trace of movement. (g) Stride length. (h) Sway length. (i) Stance angle. (j) Stance length. Error bars (except box and whisker plots) represent standard deviation from the mean (N = 6). *, **, ***, **** signifies P<0.05, P<0.01, P<0.001, and P<0.0001 respectively, one-way ANOVA, Tukey's Multiple Comparison Test (post-hoc).*

In order to get further insight, we monitored movement patterns of the animals (Figure 4.8f). The results show a significant decrease in stride length (Figure 4.8g: 3.83±0.15 cm vs. 2.78±0.14 cm; $P<.0001$, two-tailed *t*-test) and stride width (Figure 4.8h: 2.89±0.11 cm vs. 1.92±0.13 cm; $P<.0001$, two-tailed *t*-test) in PHz-induced group. Stance length (Figure 4.8j: 3.19±0.12 cm vs. 2.55±0.14 cm; $P<.0001$, two-tailed *t*-test), and stance angle (Figure 4.8i: 44.2±2.1° vs. 20.6±1.2°; $P<.0001$, two-tailed *t*-test) were also significantly decreased in the PHz-treated group. Use of C-Mn_3O_4 NPs allowed the rodents to retain their regular movement pattern (Figure 4.8f-4.8j; $P<.0001$ compared to PHz-intoxicated group for all parameters, two-tailed *t*-test), similar to the control animals.

Pharmacokinetics and pharmacodynamics dictated by translocation and biodistribution of C-Mn_3O_4 NPs are the two major factors that mediate *in vivo* therapeutic activity. Time dependent plasma concentration profile of C-Mn_3O_4 NPs indicating its absorption and elimination is reported after oral delivery of a 0.25 mg kg^{-1} BW dose of C-Mn_3O_4 NP in plasma Mn concentration versus time plot (Figure 4.9a). The PK parameters, calculated by a non-compartmental approach, yield a maximum plasma concentration (C_{MAX}) of 1.71±0.25 μg mL^{-1} of Mn for the C-Mn_3O_4 NPs at (t_{MAX}) 12.1±0.2 h (Table 4.1). The plasma area under the curve (AUC) was 18.01±1.47 μg mL^{-1} h with a clearance of 12.3±0.8 L h^{-1} kg^{-1}. A steady low concentration of NPs (Mn ~0.1 μg mL^{-1}) was maintained in plasma throughout 48 h window of experiment. The mean plasma concentration curve presented three-peak absorption phases (at ~1.0 h, ~6.0 h, and 12.0 h) indicated as I, II, and III in Figure 4.9a. The deconvoluted spectra shows a significant overlap between intestinal absorption and hepato-biliary reabsorption, which resulted in the higher third peak (~12 h). The first peak

Table 4.1. Pharmacokinetic parameters of C-Mn_3O_4 NPs.

Parameters	Oral Gavage	Delivery to Stomach
C_{MAX} (mg mL^{-1})	1.71±0.25	1.84±0.21
t_{MAX} (h)	12.1±0.2	10.4±0.2
AUC (μg h mL^{-1})	18.01±1.47	16.08±2.17
Clearance (L h^{-1} kg^{-1})	12.3	11.3
Bioavailability (%)	12.2	11.9

All data represented as Mean ± Standard Deviation (SD). N=6 for each measurement.

may be due to the absorption in the upper gastro-intestinal tract, as direct delivery of C-Mn_3O_4 NPs to the stomach by oral gavage resulted in disappearance of the first peak (Figure 4.9c). Urinary Mn-levels were below detectable range upto 48 h. Mn content of feces are illustrated in Figure 4.9b with maximum concentration (C_{MAX} = 0.68±0.07 μg g^{-1}) at ~18.0 h.

The effect of C-Mn_3O_4 NPs on bilirubin degradation are correlated with plasma C-Mn_3O_4 NP concentration profile (Figure 4.9d). The results show an inverse relationship between UCB and plasma C-Mn_3O_4 NP concentration. UCB levels plotted against plasma C-Mn_3O_4 NP concentration (Figure 4.9e) describes a dose dependent correlation (adj. R^2 0.860; non-linear logistic regression model) suggestive of *in vivo* catalytic degradation of bilirubin by C-Mn_3O_4 NPs.

Our study demonstrates that the nanoceutical compound C-Mn_3O_4 NPs can degrade bilirubin during *in vivo* administration and prevent bilirubin induced neurotoxicity in a rodent model of SNH. A single oral dose reduces total as well as unconjugated bilirubin level and importantly, the nanoceutical agent has the capacity to significantly decrease or reverse early bilirubin neurotoxicity. These signs are described by impaired motor functions as observed in OFT, motor movements and gait analysis in PHz intoxicated group. The movement was less in OFT, and significant decrease was observed in step length, and step width in gait analysis. The motor function as measured using beam traversal, and pole test were also less. In addition, stance length, and stance angle were significantly decreased in the study group. We report that administration of C-Mn_3O_4 NPs facilitated the rodents to retain their normal movement pattern and sensory motor function. The histopathological examination reveals that C-Mn_3O_4 NPs can protect the neural cells (particularly of mid-brain and cerebellum region of the brain) from bilirubin-induced severe damages. The pharmacokinetics and pharmacodynamics studies further indicates the sustainable therapeutic action of this novel agent. The intestinal reabsorption after hepatobiliary recirculation was found to be important in maintaining longer blood circulation time of C-Mn_3O_4 NPs. Within 24 hours the materials is completely excreted from blood, the major route of excretion was found to be through feces.

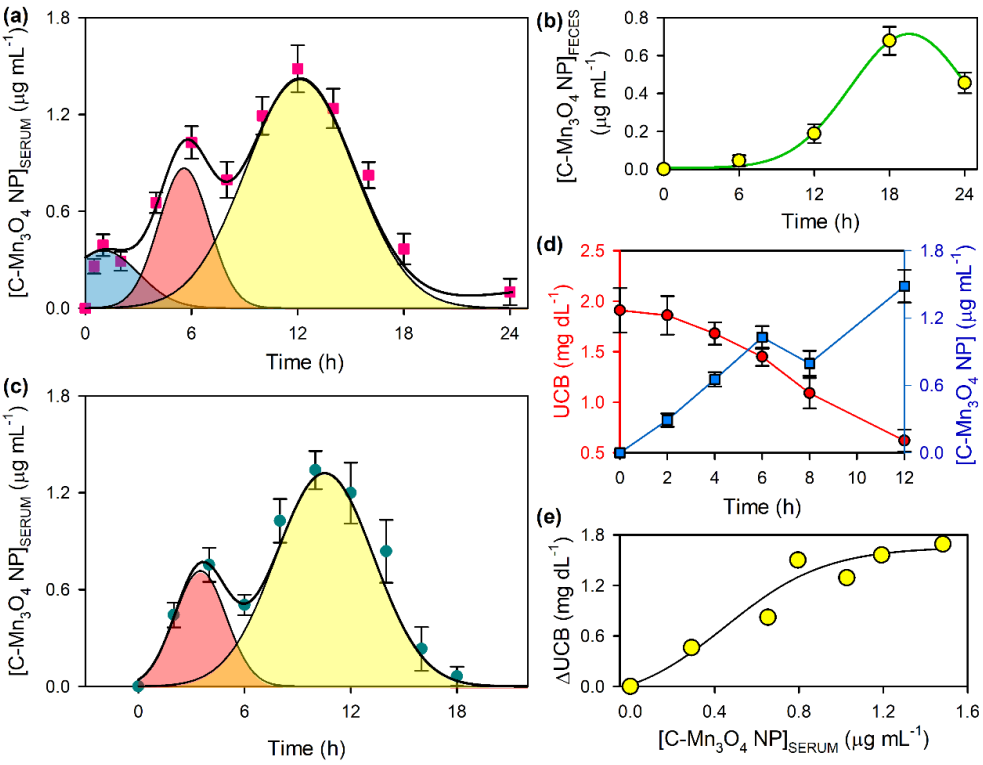

Figure 4.9. *Pharmacokinetics and pharmacodynamics of C-Mn_3O_4 NPs. (a) Plasma concentration-time profile following oral administration of NPs as measured using inductively coupled plasma-atomic emission spectroscopy (ICP-AES). The three peaks can be assigned to upper gastro intestinal (GI) tract absorption (peak 1), intestinal absorption (peak 2) and intestinal reabsorption (peak 3). (b) The elimination profile of C-Mn_3O_4 NPs through faeces (the main excretion route). (c) The first peak disappears in plasma concentration-time profile when administered directly to stomach. This confirms the upper GI tract absorption of NPs as the source of first peak. (d & e) Pharmacodynamics of bilirubin degradation.*

Mn_3O_4 nanoparticles are mixed-valence transition metal oxides with a spinel structure, and are an important class of nanomaterials that have been investigated extensively [20-22,28,29]. They primarily serve as catalysts due to their efficient activity, low cost, simple preparation, and high stability [32]. They have become one of the key topics in contemporary research because of their excellent bifunctional oxygen electrode activity, photocatalytic efficiency and potential applications in several redox reactions [29]. Manganese oxide-based NPs have emerged as potent MRI contrast agents owing to their impressive contrast ability, low toxicity, and longer circulation time in the bloodstream compared to the conventional gadolinium (Gd) or iron oxide based probes [33,34]. Successful *in vivo* use of manganese oxide

nanomaterials as diagnostic agents paved the way to their therapeutic use. In 2016, our group for the first time has demonstrated that citrate functionalized trimanganese tetroxide nanoparticles (C-Mn_3O_4 NPs) can be administered orally to treat hepatic fibrosis in a rodent model [20]. It is worth mentioning that chronic liver diseases (including fibrosis) represent a major global health problem both for their high prevalence worldwide and, in the more advanced stages, for the limited available curative treatment options [35,36]. In fact, when lesions of different etiologies chronically affect the liver, triggering the fibrogenesis mechanisms, damage has already occurred, and the progression of fibrosis will have a major clinical impact entailing severe complications, expensive treatments and death in end-stage liver disease [37]. Recently, we have showed that the C-Mn_3O_4 NPs do not possess the characteristic manganese mediated neurotoxicity, rather it ameliorates Mn-induced Parkinson's like syndrome [28]. Therefore, it is safe for *in vivo* administration. Moreover, we have studied the systemic toxicity of C-Mn_3O_4 NPs upon 90 days of repeated dose chronic exposure in C57BL/6j mice [38]. The preliminary results revealed no signs of toxicity at therapeutic dose, further supporting the biocompatibility of the nanomedicine.

Previously in controlled *in vitro* laboratory settings, we have demonstrated that C-Mn_3O_4 NPs has unprecedented catalytic activity towards degradation of bilirubin without any photo-activation [29]. The *in vivo* bilirubin degradation ability of C-Mn_3O_4 NPs in SNH rodent model can be attributed to its inherent redox behavior. Briefly, in binary spinel Mn_3O_4 NPs all the tetrahedral A sites hold a divalent cation, Mn^{2+} ($3d^5$) whereas all the octahedral B sites are occupied by trivalent cations, Mn^{3+} ($3d^4$) [39]. Our preliminary *in vitro* studies showed that the spontaneous comproportionation and disproportionation of surface Mn-ions lead to exceptional redox activity of the NPs [29,40]. The redox activity together with the ligand to metal charge transfer (LMCT) from the coordinating ligand citrate to NP surface results into the unprecedented bilirubin degradation ability [21,22]. The degraded product was identified as methyl-venyl-maleimide (MVM), one of the well-known oxidative breakdown products of bilirubin [41]. These initial findings alluded us to explore the potential clinical use of C-Mn_3O_4 NPs for human subjects at risk for bilirubin neurotoxicity, which have led us to consider a novel *in vivo* approach in a rodent model of neonatal hyperbilirubinemia.

This is particularly important from pediatric point of view to find a drug that degrades bilirubin *in vivo* and can alter the subsequent trajectory of bilirubin rate of rise has the potential to protect infants from severe neonatal hyperbilirubinemia because each year, at least 0.5 million term or near-term newborn infants are affected with severe hyperbilirubinemia (TSB>25 mg/dl), of whom 0.15 million die and over 0.07 million sustain moderate or severe disability [7].

These preliminary studies have to be taken in context with other metallic chemopreventive agents, notably metalloporphyrins (such as, tin and zinc mesoporhyrin) reduces bilirubin production and bilirubin levels in human newborns through competitive inhibition of heme oxygenase (HO), the rate-limiting enzyme in the catabolism of heme to bilirubin, and therefore inhibits formation of bilirubin [9,42,43]. This approach compares to facilitated bilirubin elimination by phototherapy or an exchange transfusion. After 3 decades of extensive and comprehensive scholarly and industry sponsored studies, the FDA studied the submission of clinical translation data and has declined the industry's request for license.

One limitation of the study is the use of chemically induced rodent model of SNH. Although, PHz-induced mice model is one of the standard and most widely used animal model for testing efficacy of drugs against SNH [44,45], evaluating the efficacy of C-Mn_3O_4 NPs in genetically modified animals like Gunn rat can provide more insight into the therapeutic mechanism. Administration of C-Mn_3O_4 NPs in combination with phototherapy could be more effective, and needs to be studied further. However, to the best of our knowledge our robust preclinical study provides strong support to the hypothesis that C-Mn_3O_4 NPs could effectively reduce SNH when administered orally and possibly reverse acute bilirubin neurotoxicity.

4.3. CONCLUSION

We report the first, to our knowledge, chemoprevention nanoceutical agent that selectively degrades bilirubin *in vivo* and likely to ameliorate acute bilirubin neurotoxicity. Our data primarily provides direct evidence that single oral administration of citrate functionalized Mn_3O_4 nanoparticles (C-Mn_3O_4NPs) can

reduce severe neonatal hyperbilirubinemia (SNH) in a rodent model. We documented an alternate catalytic-therapeutic mechanism that governs targeted disruption of bilirubin metabolism. Robust properties of nanoparticles were studied to demonstrate stability in acidic conditions, thus protected from low pH of stomach that would enable lysosomal degradation and oral administration. This novel nano-particle, C-Mn_3O_4 NPs may have the potential to become an affordable therapeutic option for the newborn infant who may be at the risk for acute bilirubin neurotoxicity. Risk-benefit studies are warranted prior to any clinical application or inquiry.

REFERENCES

[1] G. S. Drummond, A. Kappas, Science 217 (1982) 1250.

[2] P. A. Dennery, D. S. Seidman, D. K. Stevenson, N. Engl. J. Med. 344 (2001) 581.

[3] K. E. Muchowski, Am. Fam. Physician 89 (2014) 873.

[4] A. Lavin, C. Sung, A. M. Klibanov, R. Langer, Science 230 (1985) 543.

[5] J. F. Watchko, N. Engl. J. Med. 354 (2006) 1947.

[6] J. Rennie, S. Burman-Roy, M. S. Murphy, BMJ 340 (2010) c2409.

[7] V. K. Bhutani, A. Zipursky, H. Blencowe, R. Khanna, M. Sgro, F. Ebbesen, J. Bell, R. Mori, T. M. Slusher, N. Fahmy, V. K. Paul, L. Du, A. A. Okolo, M. F. de Almeida, B. O. Olusanya, P. Kumar, S. Cousens, J. E. Lawn, Pediatr. Res. 74 (2013) 86.

[8] M. J. Maisels, A. F. McDonagh, N. Engl. J. Med. 358 (2008) 920.

[9] V. K. Bhutani, R. Poland, L. D. Meloy, T. Hegyi, A. A. Fanaroff, M. J. Maisels, J. Perinatol. 36 (2016) 533.

[10] D. S. Avila, R. L. Puntel, M. Aschner, in: A. Sigel, H. Sigel, R. K. O. Sigel (Eds.), Interrelations between Essential Metal Ions and Human Diseases, Springer Netherlands, Dordrecht, (2013), 199.

[11] D. R. Mattison, B. Milton, D. Krewski, L. Levy, D. C. Dorman, P. J. Aggett, H. A. Roels, M. E. Andersen, N. A. Karyakina, N. Shilnikova, S. Ramoju, D. McGough, Neurotoxicology 58 (2017) 203.

[12] J. Emsley, Nat. Chem. 5 (2013) 978.

[13] L. Li, X. Yang, Oxid. Med. Cell. Longev. 2018 (2018) 7580707.

[14] IOM - Panel on Micronutrients, Dietary Reference Intakes for Vitamin a, Vitamin K, Arsenic, Boron, Chromium, Copper, Iodine, Iron, Manganese, Molybdenum, Nickel, Silicon, Vanadium, and Zinc, National Academies Press, Washington DC, USA, (2001), 394.

[15] A. L. Buchman, in: C. B. Ross, R. J. Cousins, K. L. Tucker, T. R. Ziegler (Eds.), Modern Nutrition in Health and Disease Wolters Kluwer Health, Lippincott Williams & Wilkins, Philadelphia, USA, (2014), 238.

[16] L. Davidsson, B. Lönnerdal, B. Sandström, C. Kunz, C. L. Keen, J. Nutr. 119 (1989) 1461.

[17] D. S. Harischandra, S. Ghaisas, G. Zenitsky, H. Jin, A. Kanthasamy, V. Anantharam, A. G. Kanthasamy, Front. Neurosci. 13 (2019) 654.

[18] C.-C. Huang, N. S. Chu, C.-S. Lu, J.-D. Wang, J. L. Tsai, J. L. Tzeng, E. C. Wolters, D. B. Calne, Arch Neurol. 46 (1989) 1104.

[19] J. Crossgrove, W. Zheng, NMR Biomed. 17 (2004) 544.

[20] A. Adhikari, N. Polley, S. Darbar, D. Bagchi, S. K. Pal, Fut. Sci. OA 2 (2016) FSO146.

[21] A. Adhikari, P. Biswas, S. Mondal, M. Das, S. Darbar, A. M. Hameed, A. Alharbi, S. A. Ahmed, S. S. Bhattacharya, D. Pal, S. K. Pal, ChemMedChem 15 (2020) 420.

[22] A. Adhikari, S. Mondal, S. Darbar, S. K. Pal, Biomol. Concepts 10 (2019) 160.

[23] N. Singh, M. A. Savanur, S. Srivastava, P. D'Silva, G. Mugesh, Nanoscale 11 (2019) 3855.

[24] H. B. Na, J. H. Lee, K. An, Y. I. Park, M. Park, I. S. Lee, D. H. Nam, S. T. Kim, S. H. Kim, S. W. Kim, K. H. Lim, K. S. Kim, S. O. Kim, T. Hyeon, Angew Chem. Int. Ed. Engl. 46 (2007) 5397.

[25] N. Doshi, S. Mitragotri, Adv. Funct. Mater. 19 (2009) 3843.

[26] A. Udhrain, K. M. Skubitz, D. W. Northfelt, Int. J. Nanomed. 2 (2007) 345.

[27] M. R. Green, G. M. Manikhas, S. Orlov, B. Afanasyev, A. M. Makhson, P. Bhar, M. J. Hawkins, Ann. Oncol. 17 (2006) 1263.

[28] A. Adhikari, M. Das, S. Mondal, S. Darbar, A. K. Das, S. S. Bhattacharya, D. Pal, S. K. Pal, Biomater. Sci. 7 (2019) 4491.

[29] A. Giri, N. Goswami, C. Sasmal, N. Polley, D. Majumdar, S. Sarkar, S. N. Bandyopadhyay, A. Singha, S. K. Pal, RSC Adv. 4 (2014) 5075.

[30] A. Adhikari, V. K. Bhutani, S. Mondal, M. Das, S. Darbar, R. Ghosh, N. Polley, A. K. Das, S. S. Bhattacharya, D. Pal, A. K. Mallick, S. K. Pal, bioRxiv (2021) https://doi.org/10.1101/2020.12.31.425023.

[31] A. Giri, N. Goswami, M. Pal, M. T. Z. Myint, S. Al-Harthi, A. Singha, B. Ghosh, J. Dutta, S. K. Pal, J. Mater. Chem. C 1 (2013) 1885.

[32] S. Dey, V. V. Praveen Kumar, Curr. Opin. Green Sustain. Chem. 3 (2020) 100012.

[33] X. Cai, Q. Zhu, Y. Zeng, Q. Zeng, X. Chen, Y. Zhan, Int. J. Nanomed. 14 (2019) 8321.

[34] B. H. McDonagh, G. Singh, S. Hak, S. Bandyopadhyay, I. L. Augestad, D. Peddis, I. Sandvig, A. Sandvig, W. R. Glomm, Small 12 (2016) 301.

[35] T. Zhou, S. S. Glaser, EBioMedicine 44 (2019) 22.

[36] G. D'Haens, M. Pinzani, Lancet Gastroenterol. Hepatol. 4 (2019) 820.

[37] L. Giannitrapani, M. Soresi, M. L. Bondì, G. Montalto, M. Cervello, World J. Gastroenterol. 20 (2014) 7242.

[38] A. Adhikari, S. Mondal, M. Das, R. Ghosh, P. Biswas, S. Darbar, S. Singh, A. K. Das, S. S. Bhattacharya, D. Pal, A. K. Mallick, S. K. Pal, bioRxiv (2021) https://doi.org/10.1101/2021.03.14.435286.

[39] F. Guillou, S. Thota, W. Prellier, J. Kumar, V. Hardy, Phys. Rev. B 83 (2011) 094423.

[40] T. Takashima, K. Hashimoto, R. Nakamura, J. Am. Chem. Soc. 134 (2012) 18153.

[41] W. E. Kurtin, Photochem. Photobiol. 27 (1978) 503.

[42] R. A. Galbraith, G. S. Drummond, A. Kappas, Pediatrics 89 (1992) 175.

[43] R. J. Wong, H. J. Vreman, S. Schulz, F. S. Kalish, N. W. Pierce, D. K. Stevenson, J. Perinatol. 31 (2011) S35.

[44] G. Bortolussi, A. F. Muro, Pediatr. Res. 87 (2020) 17.

[45] A. C. Rice, S. M. Shapiro, Pediatr. Res. 64 (2008) 265.

CHAPTER 05

Oral Nanotherapy of Chronic Liver Diseases

5.1. INTRODUCTION

Manganese oxide nanoparticles (NPs) are now receiving enormous attention due to their unique catalytic activity and associated optical, magnetic, thermal and electrical properties [1]. The many oxidation states of manganese (II, III, IV and VII) provide manganese oxide with significant advantages as a redox medium for scavenging of reactive oxygen species (ROS) [2], which is solely responsible for generating oxidative stress in living system. In case of vertebrates, liver is the primary target organ for oxidative stress and related damage due to its unique metabolic function and relationship to the gastrointestinal (GI) tract [3]. Despite significant scientific advancement in the field of hepatology in recent years, liver problems are on the rise and account for a high death rate [4-7]. According to the Office for National statistics in the United Kingdom, liver disease is the fifth most common cause of death after heart disease, stroke, chest disease and cancer [8]. Hepatitis is one of the most common liver diseases and the potential causes are autoimmunity, infections from hepatitis viruses, bacteria, or parasites, liver injury from alcohol, poisons, or hepatotoxic drugs [9]. Chronic hepatitis leads to the recruitment of inflammatory cells, cytokines production and ROS generation which appear to have a central role in development of steatosis and fibrosis [10-12]. Development of

fibrosis, particularly cirrhosis, is associated with significant morbidity and mortality [13,14]. Although, numerous pharmaceutical agents have been tried, they all lead to unacceptable side effects and limited efficacy during long term therapy [9,15-17]. Therefore, it is necessary and of considerable interest to develop new medicines for treatment of chronic liver diseases. In this context, use of an effective antioxidant without side-effects may necessarily be advantageous to reduce the oxidative stress, which can subsequently lead to the healing of liver insults.

Currently, there is a great deal of interest in the health benefits of inorganic nanoparticles. In past two decades, several NP based therapeutics have been successfully introduced for the treatment of cancer, pain and infectious diseases. But use of inorganic NPs in treatment of chronic diseases is sparse in literature. One of the major problems in application of nanomedicine against chronic diseases is the route of administration [18]. Oral administration of drugs are mostly preferred for these types of diseases due to their convenience and compliance. But unfortunately, the NPs are not sufficiently effective because of their nonspecific distribution to the entire body, metabolism in the GI tract, low retention in the lesion area and undesired adverse effects [19]. Citrate functionalized Mn_3O_4 NP (C-Mn_3O_4 NP) is an inorganic nanoparticle that has previously shown therapeutic promise in safe and symptomatic treatment of hyperbilirubinemia in preclinical models [20].

In the present study, we have demonstrated the potential of orally administered C-Mn_3O_4 NPs in effective treatment of severe liver damage in CCl_4-induced mice model of hepatic fibrosis. To the best of our knowledge, this is the first study that demonstrates direct oral treatment of an inorganic NP (i.e. C-Mn_3O_4 NP) without any delivery system can efficiently reduce chronic hepatotoxicity and liver fibrosis through its pH dependent antioxidant activity.

5.2. RESULTS AND DISCUSSION

5.2.1. Citrate Functionalized Mn_3O_4 in Nanotherapy of Hepatic Fibrosis by Oral Administration [21]

The present study was conducted to explore the potential of C-Mn_3O_4 NPs as orally administered drug against chronic liver diseases. Liver being the major detoxifying organ receives 75% of the blood directly from gastro intestinal viscera and spleen [3]. So, all orally applied drugs need to pass through highly acidic

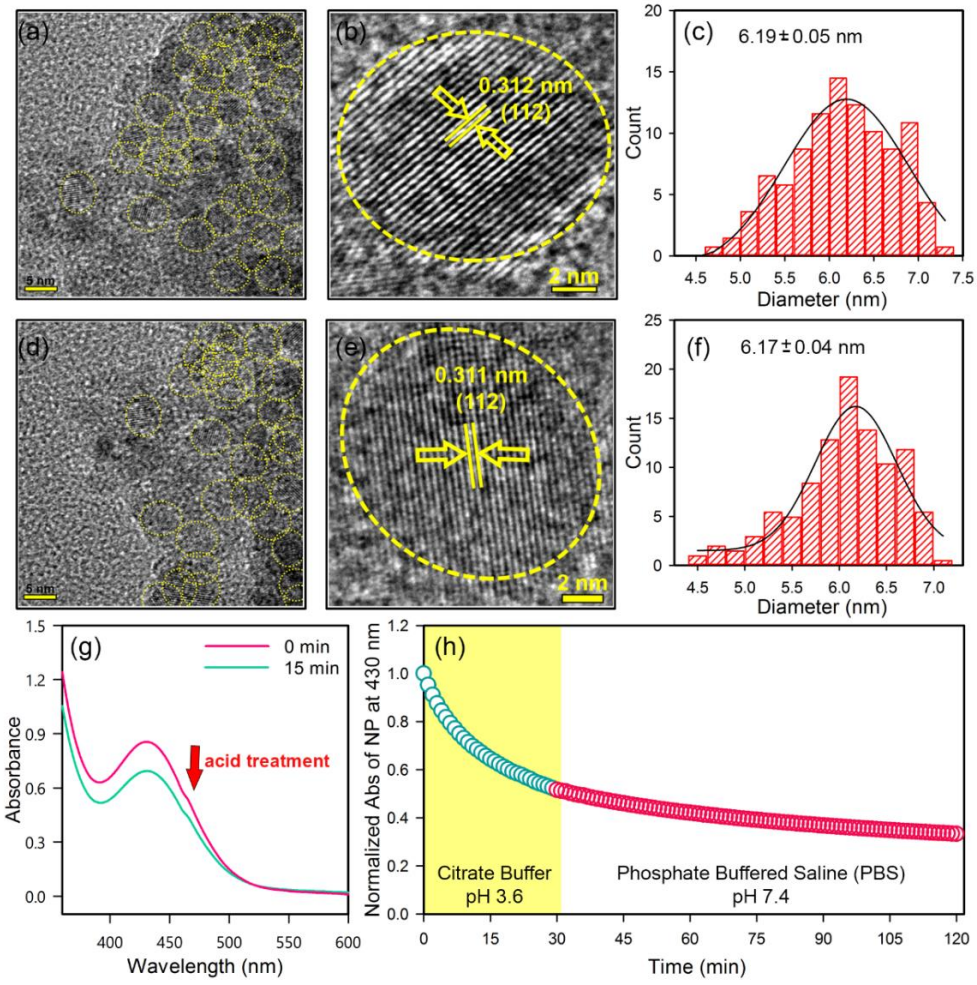

Figure 5.1. *Effect of acid treatment on physicochemical characteristics of C-Mn_3O_4 NPs. (a) TEM image of NP at pH 7.4 (b) HRTEM image of NP at pH 7.0 (c) Size distribution of NPs at pH 7.4 (d) TEM image of acid treated (pH 3.8) NP (e) HRTEM image of acid treated (pH 3.8) NP (f) Size distribution of acid treated (pH 3.8) NP (g) Change in absorbance of NPs due to acid treatment. (h) Change in absorbance at 430 nm of NPs during acid treatment and stability after acid treatment.*

stomach before entering hepatic circulation and it is well known that pH and ionic conditions greatly affect stability and functionalization of NPs [22,23]. Therefore, the effect of pH (mimicking the stomach condition) on physicochemical characteristics and activity of NPs was evaluated. The C-Mn_3O_4 NPs applied in this study shaped nearly spherical (Figure 5.1a & 5.1b), with size distribution of about 6-10 nm (mean particle size: 6.19±0.05 nm) (Figure 5.1c). HRTEM image of single NP (Figure 5.1b) confirmed the crystalline nature of it with interfringe distance of 0.312 nm (corresponding to the (112) planes of the Mn_3O_4 tetragonal crystal lattice). Upon acid treatment there was no significant change in shape, size (mean particle size: 6.17±0.04 nm) or crystallinity (interfringe distance of 0.311 nm) of the NPs as evident from Figure 5.1d-5.1f. However, the effective concentration of NPs in the solution decreased during acid treatment which is clear from the observed time dependent decline in the absorption peak of NPs at 430 nm (resembles d-d transition of Mn) (Figure 5.1g). Subsequent transfer of acid treated NPs to neutral pH showed little or no change in concentration over time, indicating its stability after acid digestion in stomach (Figure 5.1h).

The catalytic efficacy of C-Mn_3O_4 NPs to degrade bilirubin in dark condition [24] was monitored to compare the activities of neutral and acid treated NPs. The bilirubin degradation kinetics (Figure 5.2a) clearly showed an increase in bilirubin degradation activity of NPs upon acid treatment. The increased catalytic activity due to acid treatment is consistent with the fact that, at high pH, Mn^{3+} in the NPs surface is stable due to comproportionation of Mn^{2+} and Mn^{4+} and dose not tend to react with bilirubin [24]. In acidic pH, Mn^{3+} ions are unstable and tend to disproportionate into Mn^{2+} and Mn^{4+} which are highly reactive towards bilirubin [25]. The recyclability of catalyst was also tested. Figure 5.2b and 5.2c describes that both neutral and acid treated NPs could be recycled upto ten cycles.

In various studies, it has been observed that inorganic NPs has a tendency to produce ROS in solution, and C-Mn_3O_4 NPs are no exception to this. Nonfluorescent DCFH-DA is a useful indicator of ROS, which is oxidized to fluorescent DCF in presence of ROS. The emission intensity at 520 nm

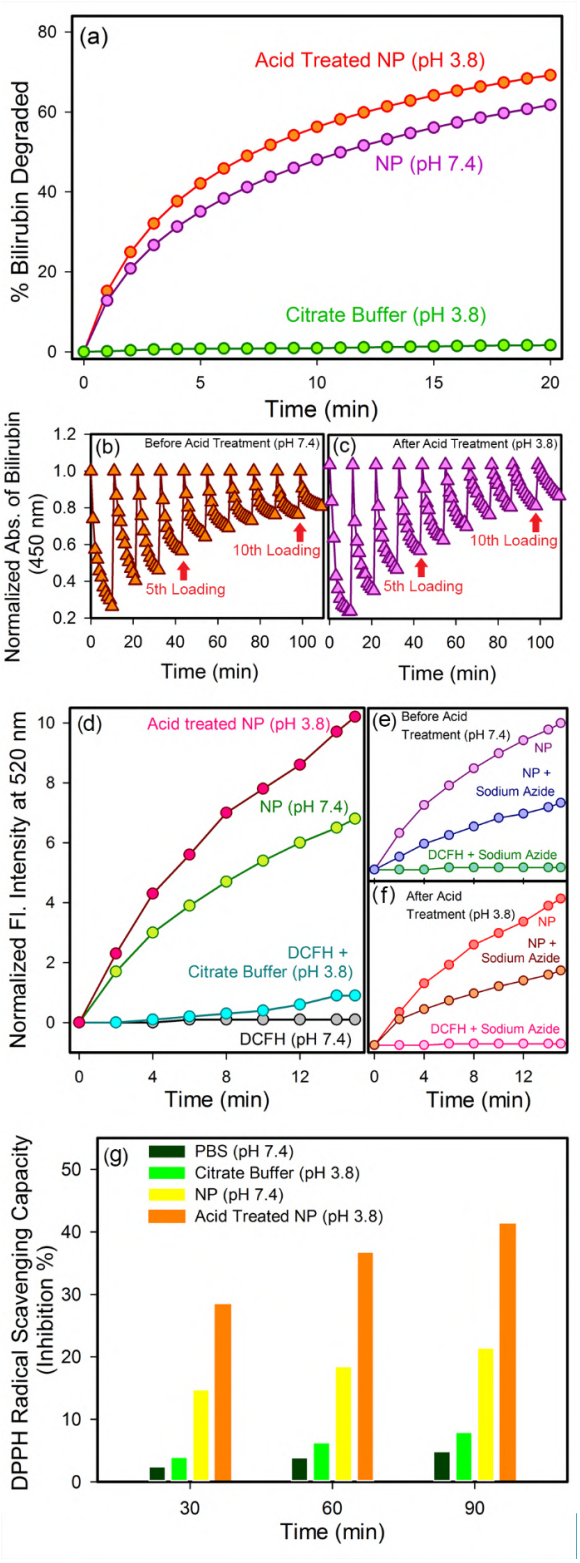

Figure 5.2. *Physico-chemical characteristics of C-Mn_3O_4 NP. (a) Change in percentage bilirubin degradation by NPs due to acid treatment. (b & c) recyclability of the catalyst before and after acid treatment, respectively. (d) Comparative representation of ROS generation capability of NPs due to acid treatment. (e & f) Change in ROS generation ability due to acid treatment in presence of sodium azide. (g) Percentage antioxidant activity as measured by DPPH assay.*

was monitored with time to evaluate the extent of ROS generation. We observed an increase in ROS generation upon acid treatment (Figure 5.2d). The nature of ROS was found to be singlet oxygen, because emission of DCF reduced significantly in presence of sodium azide, a well-known singlet oxygen quencher (Figure 5.2e and 5.2f).

It is also well known that the hepatoprotective effects of a compound largely depends on its antioxidant capacity. So, we evaluated the antioxidant capacity of C-Mn_3O_4 NPs (both neutral and acid treated) using DPPH• method, a non-enzymatic test widely used to provide basic information on the free radical scavenging ability of compounds. Figure 5.2g clearly indicates that C-Mn_3O_4 NPs provide substantial radical scavenging activity and can act as an antioxidant. Moreover, acid treatment significantly increased its free radical scavenging capability (Figure 5.2g). This antioxidant activity of C-Mn_3O_4 NPs is likely to involve redox reaction between the Mn(II) and Mn(III) states due to ligand to metal charge transfer (LMCT, originated from the interaction of $Mn^{3+/4+}$ centers in the NPs with the surface bound citrate ligands). The formation of complex between Mn and an anion causes a decrease in the redox potential of the Mn (II) ⟷ Mn(III) couple, enhancing the disproportionation of Mn(III) to Mn(II) [26]. Previous studies have revealed that Mn(II) can act as a free radical scavenger [27]:

Mn(II) scavenging of superoxide

$$Mn(II)+O_2^{\cdot-}+ 2H^+ \rightarrow Mn(III)+ H_2O_2 \rightarrow Mn(II)+ O_2+ 2H^+$$

[Equation – 5.1]

Mn(II) scavenging of hydrogen peroxide

$$Mn(II)+ H_2O_2 \rightarrow\rightarrow\rightarrow Mn(III)+ O_2+ 2H^+$$

[Equation – 5.2]

In previous section we have discussed that acid treatment increased effective concentration of Mn(II) state in NP surface, in turn facilitating the free radical scavenging reactions indicated in Equation – 5.1 and Equation – 5.2.

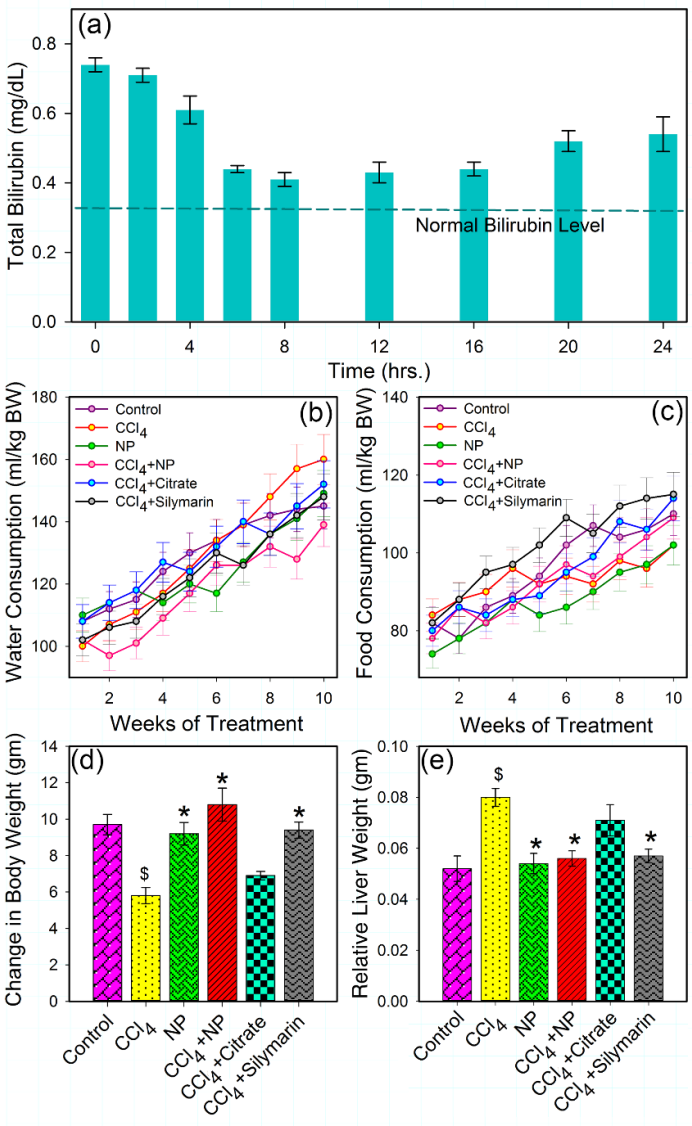

Figure 5.3. *Effect of nanoparticles on various physiological parameters. (a) Effect on total bilirubin level. Single dose of nanoparticles was able to restore serum bilirubin to almost normal level upto 12 hrs from hyperbilirubinemia condition. Then it again starts to increase indicating need for twice a day administration of NPs. (b) & (c) Daily intake of water and food respectively. (d) Change in body weight throughout the experimental period. (e) Relative liver weight (liver weight/body weight) after sacrifice. Data are expressed as mean ± SD (N=6/group). $ P<0.05 compared to control; * p<0.01 compared to* CCl_4.

For assessing the maximal-tolerated dose of C-Mn_3O_4 NPs, we executed single-dose acute toxicity study following OECD guideline. Oral administration of C-Mn_3O_4 NPs (1000 mg kg^{-1} body weight) did not cause any mortality throughout the experimental period for all three dose groups. During the study period no behavioral and physical symptoms of acute toxicity such as decreased activity or decreased uptake of food and water were observed.

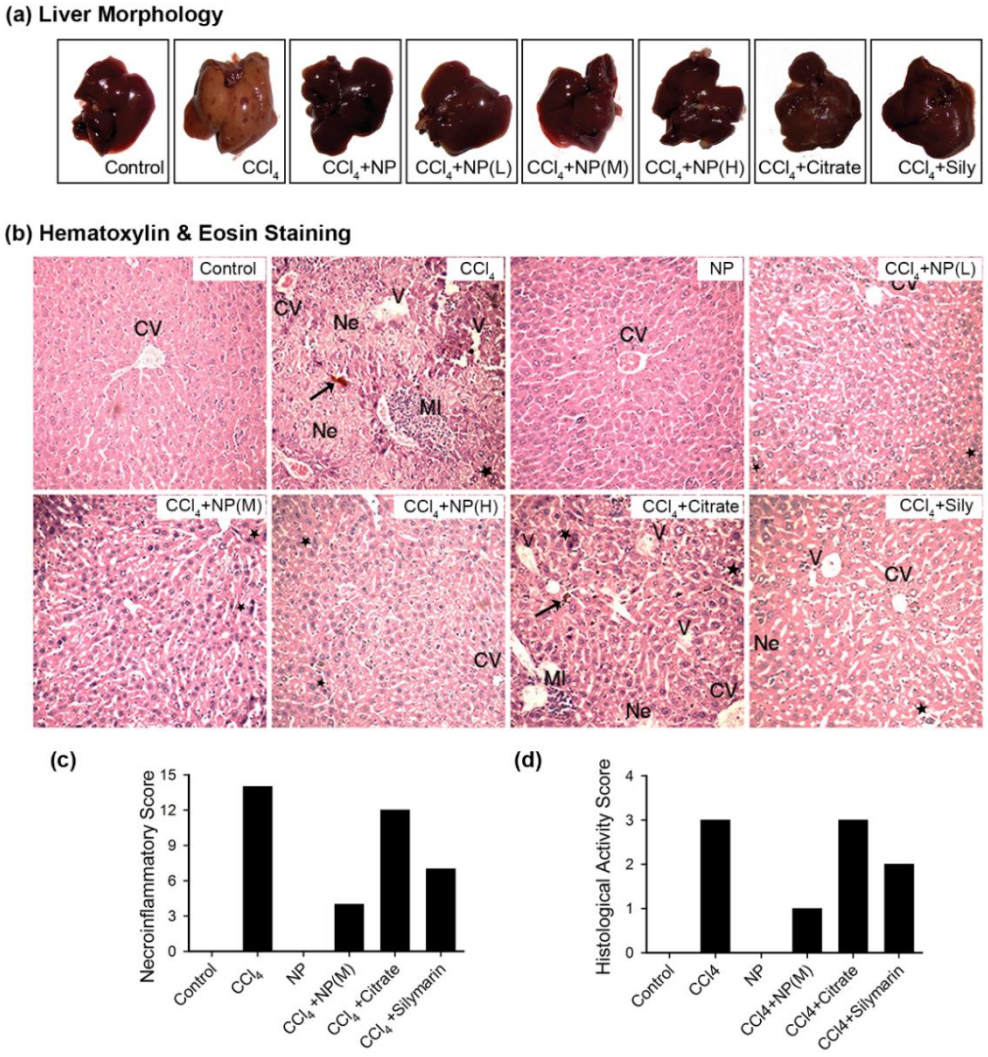

Figure 5.4. *Effect of nanoparticles on hepatic morphological analysis in CCl_4-intoxicated mice. (a) Representative photographs of liver after the experimental period. (b) Hematoxylin and eosin stained liver sections under microscope of Group I-VIII. (c & d) Ishak modified hepatic activity index and METAVIR scoring for necro-inflammatory staging, respectively. Maximal score possible for Ishak HAI is 16, and for METAVIR is 3. CV-central vein; Ne-necrosis, MI-mononuclear infiltration; *-increased mitotic activity; →-hemorrhage; V-vacuolation.*

In order to investigate the catalytic effectiveness of the NPs *in vivo*, serum bilirubin concentration was monitored in a time dependent manner after single oral administration of the NPs in hyperbilirubinemia mice model. The results (as described in Figure 5.3a) indicated that the catalytic efficiency of the NPs was retained for almost 12 hours in circulatory system, after that it started to diminish resulting in consequent rise in the bilirubin concentration. The decreased activity may be attributed to excretion of the NPs from the body.

The internalization of NPs from GI tract is a delicate subject that should be addressed carefully. We estimated Mn content in liver and circulation by ICP-AES, in order to pursue an idea about internalization and biodistribution of NPs. The results show increased deposition of Mn in liver 12 hrs after treatment with C-Mn_3O_4 NPs (4.04±0.2 μg gm^{-1} tissue compared to 2.54±0.1 μg gm^{-1} tissue of Control; $p<0.05$). The Mn content of blood also increased from 0.81±0.1 to 1.54±0.3 μg gm^{-1} ($p<0.05$) after 2 hrs of treatment.

Figure 5.3b shows the change in body weight of mice during the experimental period of 10 weeks. Growth of mice was significantly retarded upon CCl_4 injection (Group II). Three weeks administration of C-Mn_3O_4 NPs and Silymarin improved the growth of CCl_4 intoxicated mice almost comparable to the normal ones (Group I), however, C-Mn_3O_4 NPs exhibited slightly better result than Silymarin. Figure 5.3b & 5.3c shows consumption of water and food respectively. Significant decrease in food uptake and an increase in water uptake for the CCl_4 intoxicated group signifies the toxicity induced by the xenobiotics. Figure 5.3d shows the change in body weight of the mice during experimental period. Increase in relative liver weight was observed in CCl_4 treated mice (Figure 5.3e) which may be due to the enlargement of liver as well as accumulation of lipids i.e. triglycerides. C-Mn_3O_4 NPs and Silymarin both seemed to decrease the fat deposition effectively.

CCl_4 is a well-known hepatotoxic agent widely used to study hepatoprotective activity of new drugs in *in vivo* experimental models of liver cirrhosis and fibrosis [28-30]. Chronic CCl_4 administration induces critical liver damage in mice which in turn simulates a condition of acute hepatitis showing similar symptoms as humans [29,31,32]. The liver fibrosis induced by CCl_4 is the result of reductive dehalogenation. The highly reactive metabolite trichloromethyl radical ($\bullet CCl_3$) is formed from the metabolic conversion of CCl_4 by cytochrome P-450. These radicals readily interact with O_2 to form a more reactive trichloromethylperoxy radical ($CCl_3OO\bullet$), [33] which is capable of binding to protein or lipid, or of abstracting hydrogen atoms to form chloroform, that leads to lipid peroxidation and liver damage as well as plays significant role in liver pathogenesis [34-36].

In order to assess the protective effect of C-Mn_3O_4 NPs against CCl_4 induced chronic hepatitis, structural changes of hematoxylin and eosin (H/E) stained liver sections were analyzed under microscope. Figure 5.4a shows the morphometric condition of the liver of different groups. Effect of CCl_4 toxicity was evident in case of Group II and VII. Liver sections of the vehicle control animals showed a typical hepatic architecture with hepatic plates directed from the portal triads towards the central vein (CV) where they freely anastomose. Irregularly dilated normal sinusoids and spaces of Disse along with healthy hepatic cells having well-preserved cytoplasm and prominent nucleus have been seen in this group (Figure 5.4b). In the CCl_4-intoxicated mice (Group II, Figure 5.4b), moderate to severe hepatocellular vacuolation with massive centrilobular necrosis and hydropic degeneration were detected. Increased cellular mitosis and dilation of Disse spaces with focal disruption of the sinusoidal endotheliam, inflammatory infiltrations into the portal triads and distortion of CVs have also been observed. Occurrence of mononuclear cell infiltrations, hemorrhage, and fatty degeneration further confirmed acute liver injury caused by CCl_4. The animals treated with NPs (Group IV-VI) and Silymarin (Group VIII) revealed mild hepatocellular vacuolation and improved liver architecture (Figure 5.4b). They also displayed occasional periportal inflammatory infiltrate, smaller dialation of Disse space and renovation of compact liver structure. Although treatment with both NPs and Silymarin protected the hepatic architecture, NPs showed better activity compared to Silymarin as observed in histological analysis. The nontoxic effect of NPs on hepatocytes were evident as the animals treated with only C-Mn_3O_4 NPs (Group III, Figure 5.4b) showed normal liver architecture comparable to Group I. Citrate alone has shown no or very little restorative effect on hepatic morphology (Group VII, Figure 5.4b). Based on the microscopic observations, we quantified the necroinflammatory changes of tissue sections using Ishak modified hepatic activity index (HAI) (Figure 5.4c) and METAVIER system (Figure 5.4d) [37,38]. In the Ishak's grading highest score possible is 18 and for METAVIER it is 3. Tissue sections from CCl_4 induced mice scored 14 (HAI) and 3 (severe, METAVIR) respectively. However treatment with C-Mn_3O_4 NPs decreased it to the level of control (0 for both scoring). Thus, according to the microscopic

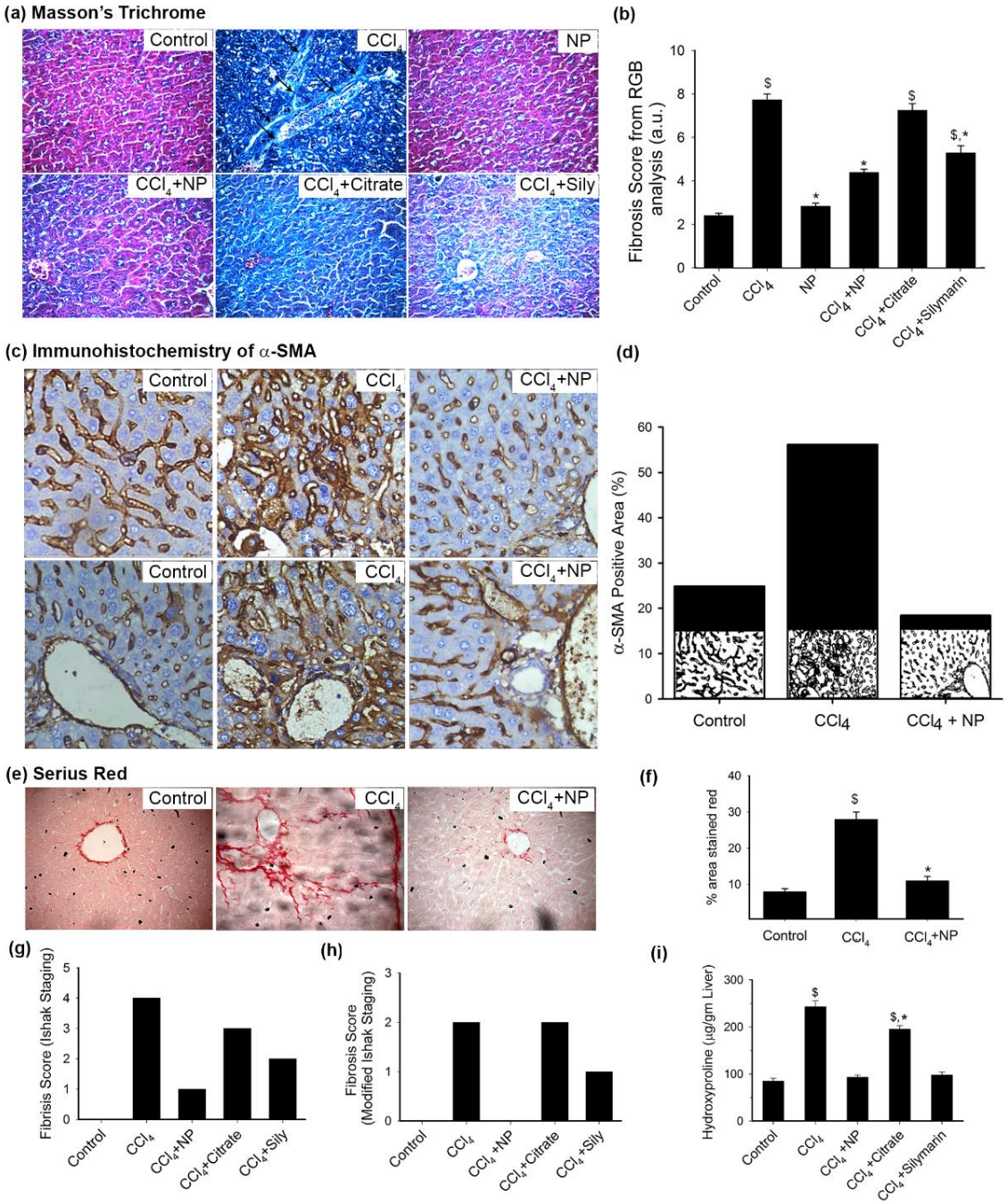

Figure 5.5. *Effect of nanoparticles on CCl_4 induced hepatic fibrosis. (a) Masson's trichrome stained liver sections under microscope. CCl_4 treated group shows marked fibrous septa (portal to potal bridging) however other groups except Citrate shows no signs of fibrosis. (b) Fibrosis score of different groups as calculated by RGB analysis from MT staining. (c) α-SMA immunohistochemistry. Portal arears showed high immunoreactivity in case of CCl_4 treated mice. (d) α-SMA positive area as quantified with ImageJ. (e) Sirius red stained liver sections. CCl_4 treated group shows fibrous expansion of portal areas with portal to portal and occasional portal to central bridging. (f) Red stained collagen content as calculated by ImageJ. (g & h) Ishak and modified Ishak fibrosis scoring. Highest possible scores are 6 and 4 respectively. (i) Hepatic hydroxyproline content. $ values differ significantly from sham control group (Group I) ($p^{\$}<0.001$); * values differ significantly from CCl_4 treated group (Group II) ($p^{*}<0.05$).*

examinations, severe cellular liver damage induced by CCl_4 intoxication was remarkably reduced by oral administration of the NPs.

For evaluation of fibrosis and its recovery, we used three staining methods; Masson's trichrome, Sirius red and immunohistochemical staining of α-SMA. Masson's trichrome staining is a well-established technique to demonstrate the accumulation of collagen fibers in the liver tissue during fibrosis and cirrhosis [39]. The results of the Masson's trichrome staining demonstrating accumulation of matured collagen fibers (stained blue) during CCl_4-induced hepatic fibrosis and decreased collagen deposition in the liver after C-Mn_3O_4 NP treatment is depicted through Figure 5.5a. Trichrome staining of normal liver did not show any alteration or collagen deposition (Figure 5.5a, Control), whereas CCl_4 intoxicated livers showed bile duct proliferation with dense fibrous septa and portal to portal bridging (Figure 5.5a, CCl_4) and increased deposition of collagen fibers around the congested central vein, indicating fibrosis. The liver sections from CCl_4 induced fibrotic mice administered with NPs had fewer fibers (Figure 5.5a, CCl_4+NP), while those treated with Citrate and Silymarin had more fibers compared to the NP treated ones (Figure 5.5a, Sily). There was no fibrosis and deposition of blue collagen fibers in case of NP control group (Figure 5.5a, NP). The numbers of blue pixels relative to the total pixels in Masson-stained liver sections were measured to quantify degree of fibrosis. CCl_4 significantly ($p<0.001$) increased the number of blue pixels in liver sections (Figure 5.5b). Administration with the NPs resulted in significantly lower number of blue pixels, but Silymarin treated ones had a significant (<0.05) higher number of blue pixels compared to both control and NP treated ones. Thus, direct evaluation of extracellular matrix (ECM) deposition in hepatic tissue by Masson's trichrome staining clearly depicts the therapeutic efficiency of NPs against chronic hepatic fibrosis.

Hepatic stellate cell (HSC) activation plays a key role in liver fibrosis at the early phase and activated HSC is accompanied with high expressions α-SMA proteins. So, hepatic α-SMA immunoreactivity, which detects activated HSC, a definitive marker of fibrotic liver, has been shown in Figure 5.5c. With regard to the distribution of α-SMA-positive fibrogenic cells, in the livers of control animals, the α-SMA immunopositivity was restricted to the smooth musculature belonging to the

arterial tunica media, as well as to the wall of majority of portals and central veins, while other liver cells remain negative (Figure 5.5c, Control). CCl_4 strongly induced perisinusoidal α-SMA expression, which was recognized as activated HSCs, through affected lobule, connected between themselves with thin, "bridging" immunopositivity (Figure 5.5c, CCl_4). The livers of mice receiving C-Mn_3O_4 NPs showed staining pattern similar to control animal (Figure 5.5c, CCl_4+NP) with sporadic α-SMA positivity. The α-SMA positive area were calculated and shown in Figure 5.5d. It clearly showed that CCl_4 treatment caused more than two fold increase in α-SMA level, which upon treatment with NPs decreased to a level comparable to control animals, indicating an attenuation of the fibrogenic properties of HSCs after administration of C-Mn_3O_4 NPs.

Sirius red selectively stains collagen, the most abundant ECM protein produced during fibrogenesis. Figure 5.5e shows Sirius red stained liver sections of different groups. CCl_4 treatment caused fibrous expansion of portal areas with portal to portal bridging, occasional portal to central bridging and characteristic perisinusoidal chicken wire fence pattern, indicative of progression of fibrosis. Treatment with C-Mn_3O_4 NPs caused marked decrease in fibrous extensions which has also been reflected in Figure 5.5f, which describes the quantification of the Sirius red stained collagen area.

On the basis of histological findings, we applied scoring to the livers of different groups. Both Ishak and Ishak modified fibrosis staging was performed (Figure 5.5g and 5.5h respectively). After 6 weeks of CCl_4 administration, most mice had fibrous portal expansion with short fibrous septa (Ishak 3), and occasionally progressed to complete bridging fibrosis with appearance of a few of regenerative nodules (Ishak 4). However, treatment with C-Mn_3O_4 NPs decreased the extent of fibrosis, reducing the score to normal.

The degree of fibrosis was also assessed by measuring hydroxyproline content, a product of collagen metabolism. The results, as depicted in Figure 5.5g, indicates CCl_4 induced hepatic fibrosis with almost three fold increase ($p<0.05$) in hydroxyproline content. Treatment with NPs decreased that level almost to control,

which was also apparent in histological and immunohistochemical findings, further confirming protective effect of C-Mn_3O_4 NPs against fibrosis.

Results of histopathological studies were further supported by changes in biochemical parameters in serum. In order to assess the protective effect of C-Mn_3O_4 NPs against CCl_4 induced chronic hepatitis, serum activities of various hepatic lysosomal enzymes were used as diagnostic indicators (Table-5.1). The dramatically elevated serum levels of transaminases, AST and ALT (~400% and ~200% respectively), after CCl_4 treatment have been attributed to damaged structural integrity of the liver [35,40]. Leakage of large quantities of these enzymes from liver pool into the blood stream is associated with massive centrilobular necrosis, ballooning degeneration and cellular infiltration of the liver. Other liver specific preclinical and clinical biomarkers showed same trend. Elevated levels of ALP (~265%), GGT (~100%), TB (~330%), DB (~200%) and decrease in total protein concentration further confirmed chronic hepatitis induced by CCl_4 [40]. Treatment with C-Mn_3O_4 NPs at a dose of 1.5 ml (OD_{430} 0.5) kg^{-1} BW for 14 days considerably reduced the elevated serum levels of aforementioned enzymes to almost normal (AST ~80%, ALT ~55%, ALP ~ 70%, GGT ~30%, TB ~84%, DB ~80% compared to CCl_4 treated group; $p<0.05$) with subsequent improvement in serum protein concentration (45% compared to CCl_4 treated group; $p<0.05$), implying that C-Mn_3O_4 NPs tended to prevent damage and suppressed the leakage of enzymes. Treatment with a well-known hepatoprotective drug Silymarin also improved the liver parameters, however with lesser efficacy (AST ~67%, ALT ~50%, ALP ~ 65%, GGT ~22%, TB ~73%, DB ~72% compared to CCl_4 treated group; $p<0.05$). Moreover, it could not restore the above mentioned enzymes particularly AST and ALT (1.8 and 1.4 times higher respectively compared to control; $p<0.05$) to normal level within the treatment period compared to NPs. This clearly implies that, NPs could heal hepatic damage faster than the conventional drug Silymarin. The liver function parameters for the NP control group (group III) remained almost similar to the vehicle treated group (group I) demonstrating nontoxicity of NPs on liver at the administered dose. No significant improvement in the citrate control group confirmed ineffectiveness of the ligand citrate alone in prevention of hepatotoxicity.

Table 5.1. Effect of C-Mn_3O_4 NP on liver function parameters of CCl_4 intoxicated mice.

Group	Design of Treatment	AST (IU/L)	ALT (IU/L)	ALP (IU/L)	GGT (IU/L)	Total Bilirubin (mg dL^{-1})	Direct Bilirubin (mg dL^{-1})	Total Protein (gm dL^{-1})
I	Sham Control	87.3 ± 15.4^{a}	80.4 ± 12.1^{a}	44.5 ± 5.8^{a}	3.1 ± 0.26^{a}	0.32 ± 0.04^{a}	0.18 ± 0.01^{a}	$8.84 \pm 0.09^{a,c}$
II	CCl_4 Control	$427.5 \pm 62.1^{b,c}$	$230.1 \pm 35.6^{b,c}$	$161.2 \pm 14.3^{b,c}$	$6.3 \pm 0.41^{b,c}$	$1.28 \pm 0.04^{b,c}$	$0.54 \pm 0.02^{b,c}$	$5.11 \pm 0.07^{b,c}$
III	NP Control	95.6 ± 12.5^{a}	88.2 ± 7.3^{a}	59.8 ± 4.9^{a}	3.8 ± 0.21^{a}	0.18 ± 0.05^{a}	0.09 ± 0.01^{a}	$8.12 \pm 0.64^{a,c}$
IV	CCl_4 + NP (L)	$142 \pm 12.8^{a,b}$	$126.8 \pm 14.3^{a,b}$	$95.4 \pm 11.1^{a,b}$	$5.7 \pm 0.67^{a,b}$	$0.24 \pm 0.05^{a,b}$	$0.13 \pm 0.01^{a,b}$	$6.24 \pm 0.09^{a,b,c}$
V	CCl_4 + NP (M)	$82.7 \pm 11.2^{a,c}$	$102.57 \pm 5.8^{a,c}$	$50.1 \pm 4.5^{a,c}$	$4.4 \pm 0.23^{a,c}$	$0.21 \pm 0.07^{a,c}$	$0.11 \pm 0.01^{a,c}$	$7.44 \pm 0.11^{a,b,c}$
VI	CCl_4 + NP (H)	115.4 ± 13.6^{a}	108.5 ± 10.2^{a}	64.5 ± 6.8^{a}	5.2 ± 0.62^{a}	0.22 ± 0.04^{a}	0.11 ± 0.01^{a}	$6.84 \pm 0.14^{a,b}$
VII	CCl_4 + Citrate	$324.6 \pm 45.4^{a,b}$	$194.6 \pm 22.7^{a,b}$	$145.7 \pm 12.3^{a,b}$	$5.9 \pm 0.52^{a,b}$	$0.99 \pm 0.06^{a,b}$	$0.32 \pm 0.03^{a,b}$	$5.70 \pm 0.03^{b,c}$
VIII	CCl_4 + Silymarin	$137.9 \pm 17.8^{a,b}$	$116.6 \pm 14.3^{a,b}$	$55.6 \pm 3.2^{a,b}$	$4.9 \pm 0.51^{a,b}$	$0.34 \pm 0.02^{a,b}$	$0.15 \pm 0.02^{a,b}$	$6.68 \pm 0.06^{a,b}$

NPs: nanoparticle. Data are expressed as mean ± SD (N=6)

One-way ANOVA Tukey post hoc: $^{a}p< 0.05$ compared with CCl_4. $^{b}p< 0.05$ compared with vehicle control. $^{c}p< 0.05$ compared with silymarin. Dosage:- Olive Oil: 2.4 ml/kg BW.CCl_4 + Olive Oil (1:4) Sol.: 3ml/kg BW. NPs: 1 ml (OD_{430} 0.5)/kg BW (L) 1.5 ml (OD_{430} 0.5)/kg BW (M) 2 ml (OD_{430} 0.5)/kg BW (H). Silymarin: 1.5 ml/kg BW. Citrate: 750 µl/kg BW.

The ratio of serum activities of AST and ALT (De Ritis Ratio) is useful in differential diagnosis and classification of hepatic disorders. For normal individuals, this ratio varies from 0.7 to 1.4 (as in case of Group I; 1.08) [17]. The value of De Ritis Ratio in case of CCl_4 administered group (Group II) has increased to 1.85. This increased value of >1.5 along with ALT:ALP ratio of 1.42 (<2.0) are indicative of intrahepatic lesion formation and chronic liver disorders such as fibrosis, post necrotic cirrhosis, drug induced cholestasis etc [16,17,41]. Treatment with C-Mn_3O_4 NPs restored the De Ritis ratio to normal level (Group V; 0.80), whereas conventional drug silymarin (Group VIII) decreased it to 1.18. However, other two C-Mn_3O_4 NP dose control groups (group IV and VI) also showed similar activities with reduced efficiency.

Rapid lipid peroxidation of the membrane structural lipids has been proposed as the basis of CCl_4 liver toxicity and a marker of fibrosis. So, we monitored the levels of malondialdehyde (MDA), an index of oxidative damage and one of the decomposition products of peroxidised polyunsaturated fatty acids, to evaluate the effect of C-Mn_3O_4 NPs against CCl_4-induced liver peroxidation. As shown in Figure 5.6a & 5.6b, significant increase of MDA level (~172% and ~205% respectively for hepatic and serum MDA content; $p<0.05$) in the CCl_4-treated group confirmed that oxidative damage had been induced. Consistent with liver function tests, treatment with C-Mn_3O_4 NPs and Silymarin significantly reduced both hepatic (~59% and ~44% respectively; $p<0.05$) and serum (~57% and ~49% respectively; $p<0.05$) MDA content.

Superoxide dismutase (SOD), catalase (CAT) and glutathione peroxidase (GPx) comprise the major antioxidant system in mammalian cells, which constitutes a mutually supportive team for defense against ROS [42]. SOD converts superoxide anions to H_2O_2, which is further converted to H_2O by GPx and CAT [9]. Maintaining the balance between ROS and antioxidant enzymes is crucial for prevention of oxidative stress [43] which can damage all single aspects of a cell, including its protein, lipids and DNA [9,44]. As shown in Figure 5.6c-5.6f, CCl_4 induced substantial modifications to the hepatic antioxidant enzymes and significantly decreased hepatic SOD (~60%), CAT (~68%) and GPx (~62%) activities. Treatment with orally administered NPs and Silymarin considerably

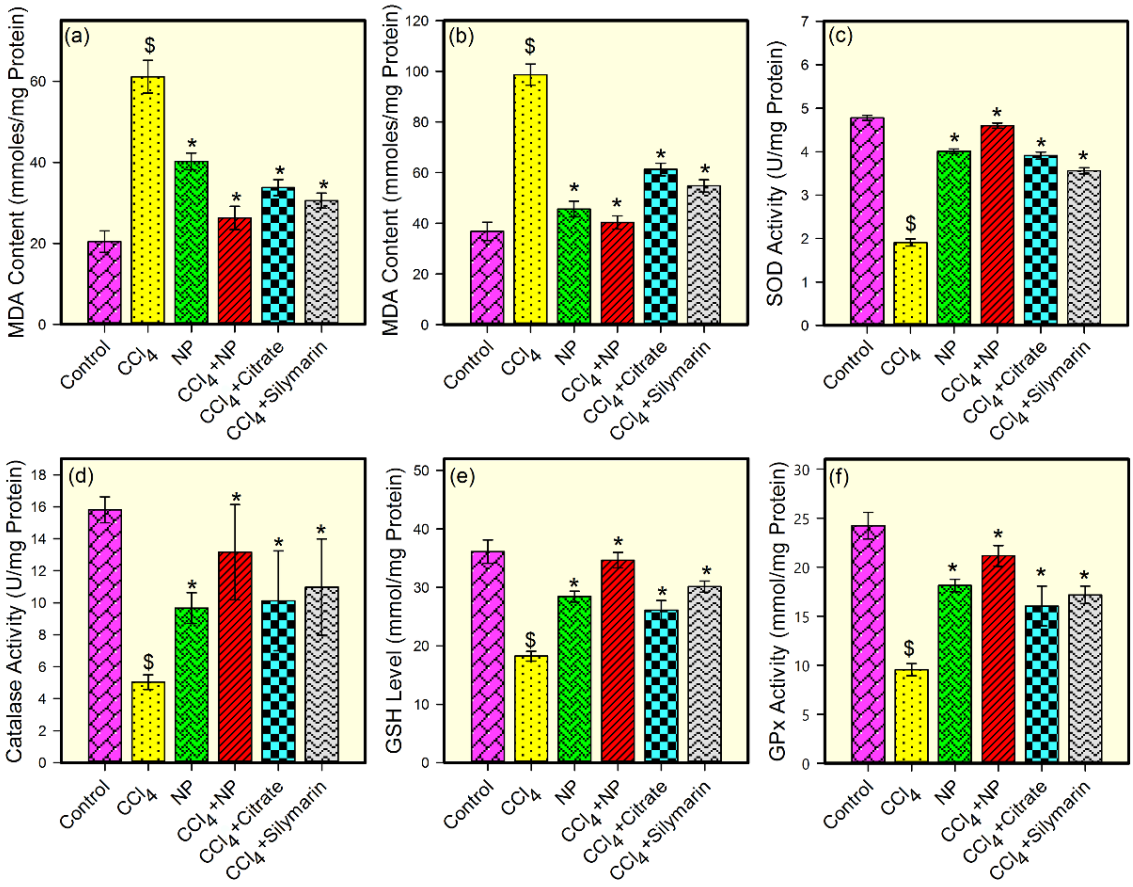

Figure 5.6. *Effects of orally treated C-Mn_3O_4 NPs on liver SOD, catalase, GPx, GSH and MDA content in CCl_4 intoxicated mice. (a) Serum MDA content (b) MDA content from liver homogenate (c) SOD activity (d) Catalase activity (e) GSH level (f) GPx activity. $ values differ significantly from sham control group (Group I) ($p^{\$}<0.001$); * values differ significantly from CCl_4 treated group (Group II) ($p^{*}<0.05$)*

elevated the antioxidant enzyme levels. Citrate also showed some amount of efficacy in reversal of antioxidant defense mechanism. In case of NP control group (Group III), some pro-oxidant effects were observed. This may be due to the inherent property of the NPs to produce ROS in solution as described in our *in vitro* studies. However, this has no detrimental effect on liver or on liver marker enzymes. Reduced glutathione (GSH), a non-enzymatic antioxidant, plays excellent role in protection of cells from CCl_4-induced hepatotoxicity [9]. GSH combines with trichloromethyl radical, in presence of glutathione-S-transferase (GST), which in turn contributes to detoxification of CCl_4. Usually, GSH stores are markedly depleted

when liver necrosis initiates. In this study, we observed decrease in hepatic GSH (~50%) level upon CCl_4 administration. Treatment with C-Mn_3O_4 NPs restored normal GSH level. The effect could be due either to the *de novo* synthesis of GSH, its regeneration, or both. The observed *in vivo* ability of C-Mn_3O_4 NPs in protection against lipid peroxidation and oxidative damage may involve various mechanisms. Firstly, redox reaction between the Mn(II) and Mn(III) states in C-Mn_3O_4 NPs due to LMCT may help it to act as a scavenger of hydroxyl and superoxide radicals (details are discussed in previous section of the text). Secondly, it may act as a chain-breaker in inhibiting iron-induced lipid peroxidation chain reactions [45,46], and as proposed in other studies, Mn(II) may scavenge peroxyl lipid radicals via the following reaction [47,48]:

$$LOO\bullet + Mn(II) + H^+ \rightarrow LOOH + Mn(III)$$

[Equation – 5.3]

Third, during comproportionation/disproportionation reactions small amounts of Mn^{2+} is dissoluted in solution [25], which being a cofactor can enhance Mn-SOD activity (an essential isozyme of SOD in antioxidant defense system) [49]. Fourth, it can promote the synthesis of metallothionein, which then scavenges oxidant radicals and fifth, being a trivalent cation, Mn(III) can interfere with the effects of Fe^{3+}, which is known to be involved in reactive oxidant radical generation.

To elucidate the possible link between antifibrotic and axtioxidative properties of NPs, we further studied its effect on mitochondria. Increasing evidence supports the dependence of mitochondrial defense mechanisms on the cytosolic pool of reducing equivalents such as GSH. Depletion of these equivalents (also evident in our study) in the cytosol has direct consequences on the mitochondrial redox state. Previous studies have shown that Complex IV in the respiratory chain plays a critical role in oxidative stress and associated apoptosis [50]. So, at first, we measured the activity of Complex-IV and found them to be significantly decreased in CCl_4 treated mice (Figure 5.7a) which is in accordance with previous studies [51,52]. Although, treatment with C-Mn_3O_4 NPs has significantly ($p<0.05$) increased its activity, normal level was not restored. Ca^{2+}-induced liver mitochondria permeability transition

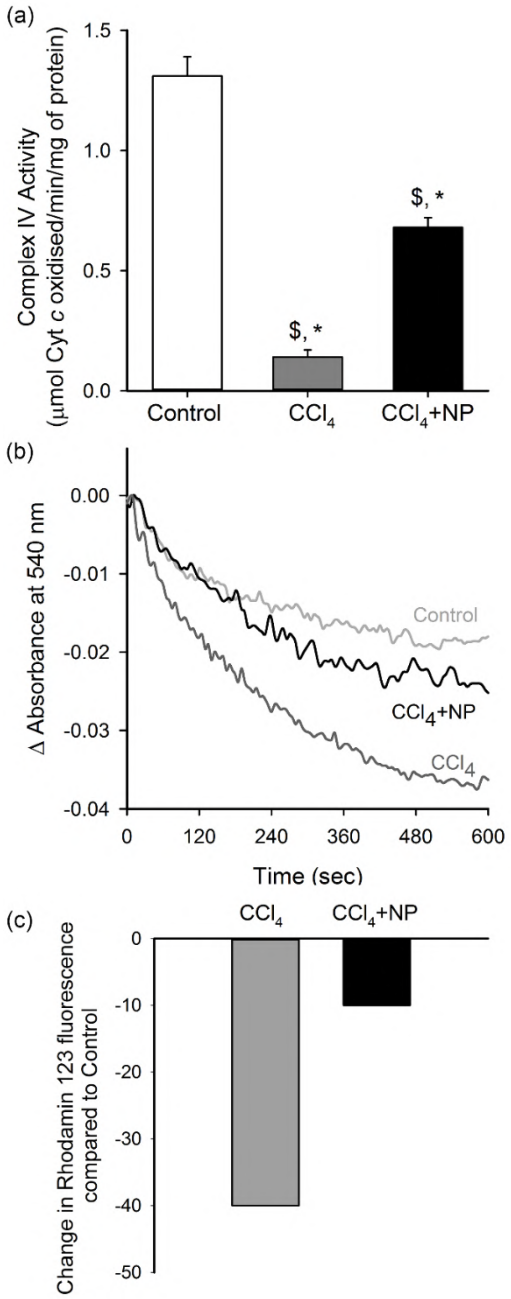

Figure 5.7. *Effect of C-Mn_3O_4 NPs on mitochondria. (a) Complex IV activity. (b) Effect on mitochondria permeability transition (MPT), measured as decrease in absorbance at 50 nm. (c) Change in mitochondrial membrane potential ($\Delta\psi_M$). In CCl_4 treated mice fluorescence of rhodamine 123 was recovered by 40% compared to control, indicative of decrease in MMP ($\Delta\Psi_m$). Treatment with C-Mn_3O_4 NPs partially restored the potential.*

(MPT) is a useful model for evaluating the effects of drugs or other substances on mitochondrial function [53]. The data clearly showed that the absorbance at 540 nm (A_{540}) was decreased after the addition of Ca^{2+}. The mitochondria isolated from the

CCl_4 intoxicated-group were more sensitive towards Ca^{2+} as shown by a quick decline of 540 nm absorbance. C-Mn_3O_4 NPs attenuated Ca^{2+}-induced MPT, as shown by slow decline of A_{540} that mimicked the control group (Figure 5.7b). This indicates a protective role of C-Mn_3O_4 NPs in maintenance of normal MTP of mitochondria. In addition, we investigated the effect of C-Mn_3O_4 NPs on mitochondrial membrane potential ($\Delta\psi_M$). CCl_4 intoxication caused dissipation of $\Delta\psi_M$, reflected in lower quenching of initial rhodamine 123 fluorescence which was in agreement with previous reports [54]. However, treatment with NPs, prevented the collapse in $\Delta\psi_M$ (Figure 5.7c). In order to evaluate any potential toxicity of the NPs, we examined necessary hematological parameters. All of them were similar to sham control except the CCl_4 induced group. The number of WBCs in CCl_4 induced mice were significantly higher than Group I, since the liver tissues were infiltrated by huge amount of inflammatory cells due to liver fibrosis (also evident from histological studies). Treatment with NPs significantly decreased the inflammatory infiltration. Data are presented in Table 5.2.

5.3. CONCLUSION

In conclusion, the present study showed, C-Mn_3O_4 NPs when administered orally can protect liver from CCl_4-induced cirrhosis, fibrosis and oxidative stress owing to its increased antioxidant properties upon acid treatment in stomach. Its possible promising therapeutic role against oxidative stress and related chronic liver diseases deserves consideration. However, cautions must be taken as there is prevalent debate about nanotoxicity. Detailed toxicity study and more preclinical trials are required before it reaches the clinics for use in prevention of chronic liver diseases.

Table 5.2. Summary of hematology parameters studied across the groups.

Parameters	Groups					
	I	II	III	V	VII	VIII
	Control	CCl_4	NP	CCl_4+NP	CCl_4+Citrate	CCl_4+Silymarin
Hb (g/dL)	11.9 ± 1.2	8.8 ± 0.6[a]	12.3 ± 1.1[b]	12.6 ± 0.7[b]	11.8 ± 1.3[b]	11.4 ± 1.1[b]
RBC ($x10^6$/µL)	10.8 ± 0.7	9.0 ± 0.4[a]	10.2 ± 0.8[b]	11.1 ± 0.2[b]	10.6 ± 0.4[b]	10.5 ± 0.2[b]
RT (%)	2.8 ± 0.2	4.9 ± 0.5[a]	3.0 ± 0.1[b]	3.4 ± 0.4[b]	3.2 ± 0.3[b]	3.3 ± 0.3[b]
HCT (%)	34.8 ± 2.5	30.0 ± 2.2	35.2 ± 2.4	35.2 ± 3.6	31.2 ± 2.5	33.9 ± 2.1
MCV (fl)	37.0 ± 2.9	32.4 ± 3.1	34.6 ± 3.2	36.8 ± 3.8	37.1 ± 3.2	36.8 ± 2.9
MCH (pg)	21.1 ± 2.1	20.2 ± 1.7	21.8 ± 1.5	21.5 ± 1.4	22.0 ± 1.8	21.7 ± 1.7
MCHC (g/dL)	41.4 ± 3.2	31.6 ± 2.1[a]	40.6 ± 3.8[b]	40.2 ± 3.8[b]	39.6 ± 4.3[b]	34.9 ± 3.2
Platelets ($x10^3$/µL)	6.6 ± 0.7	6.1 ± 0.6	6.6 ± 0.4	5.9 ± 0.6	5.8 ± 0.3	5.7 ± 0.5[a]
WBC ($x10^5$/µL)	8.8 ± 0.4	13.0 ± 0.8[a]	8.6 ± 0.3[b]	7.1 ± 0.5[b]	6.4 ± 0.4[b]	8.2 ± 0.3[b]
L	76 ± 5.1	78 ± 6.3	74 ± 5.8	72 ± 6.2	76 ± 5.8	75 ± 5.1
N	25 ± 2.3	20 ± 1.8[a]	24 ± 1.6[b]	21 ± 1.5	19 ± 2.1	24 ± 1.8[b]

Data are expressed as mean ± SD (N=6).

One-way ANOVA Tukey post hoc: [a] $p< 0.05$ compared with vehicle control. [b] $p< 0.05$ compared with CCl_4. [c] $p< 0.05$ compared with silymarin. Dosage:- Olive Oil: 2.4 ml/kg BW.CCl_4 + Olive Oil (1:4) Sol.: 3ml/kg BW. NPs: 1.5 ml (OD_{430} 0.5)/kg BW. Silymarin: 1.5 ml/kg BW. Citrate: 750 µl/kg BW.

Hb: Hemoglobin, RBC: Total Red Blood Corpuscles, Rt: Reticulocyte, HCT: Hematocrit, MCV: Mean Corpuscular Volume, MCH: Mean Corpuscular Hemoglobin, MCHC: Mean Corpuscular Hemoglobin Concentration, WBC: Total White Blood Corpuscles, N: Neutrophils, L: Lymphocytes.

REFERENCES

[1] A. Giri, N. Goswami, M. Pal, M. T. Z. Myint, S. Al-Harthi, A. Singha, B. Ghosh, J. Dutta, S. K. Pal, J. Mater. Chem. C 1 (2013) 1885.

[2] J. Tu, Z. Yang, C. Hu, J. Chem. Technol. Biotechnol. 90 (2015) 80.

[3] H. Jaeschke, G. J. Gores, A. I. Cederbaum, J. A. Hinson, D. Pessayre, J. J. Lemasters, Toxicol. Sci. 65 (2002) 166.

[4] S. Chen, L. Zou, L. Li, T. Wu, PLoS ONE 8 (2013) e53662.

[5] H. K. Kim, L. Li, H. S. Lee, M.-O. Park, D. Bilehal, W. Li, Y. H. Kim, Food Sci. Biotechnol. 18 (2009) 1186.

[6] G. Hsiao, M. Y. Shen, K. H. Lin, M. H. Lan, L. Y. Wu, D. S. Chou, C.-H. Lin, C. H. Su, J. R. Sheu, J. Agric. Food Chem. 51 (2003) 3302.

[7] N. Polley, S. Saha, S. Singh, A. Adhikari, S. Das, B. R. Choudhury, S. K. Pal, J. Biomed. Opt. 20 (2015) 067001.

[8] U. N. Statistics, Http://Www.Statistics.Gov.Uk/.

[9] H. Zhang, C. H. Yu, Y.-P. Jiang, C. Peng, K. He, J. Y. Tang, H. L. Xin, PLoS ONE 7 (2012) e46574.

[10] C. S. Lieber, Adv. Pharmacol. 38 (1996) 601.

[11] C. Matte, F. M. Stefanello, V. Mackedanz, C. D. Pederzolli, M. L. Lamers, C. S. Dutra-Filho, M. F. dos Santos, A. T. Wyse, Int. J. Dev. Neurosci. 27 (2009) 337.

[12] S. K. Mantena, A. L. King, K. K. Andringa, H. B. Eccleston, S. M. Bailey, Free Radic. Biol. Med. 44 (2008) 1259.

[13] M. Srinivasan, R. Rukkumani, A. R. Sudheer, V. P. Menon, Fundam. Clin. Pharmacol. 19 (2005) 491.

[14] R. Benyon, J. Iredale, Gut 46 (2000) 443.

[15] P. Hall, J. Cash, Ulster Med. J. 81 (2012) 30.

[16] M. Botros, K. A. Sikaris, The Clinical biochemist. Rev. Austral. Assoc. Clinic. Biochem. 34 (2013) 117.

[17] K. S. Parmar, G. K. Singh, G. P. Gupta, T. Pathak, e. Nayak, Int. J. Med. Sci. Public Health 5 (2016).

[18] A. Eguchi, T. Yoshitomi, M. Lazic, C. D. Johnson, L. B. Vong, A. Wree, D. Povero, B. G. Papouchado, Y. Nagasaki, A. E. Feldstein, Nanomedicine 10 (2015) 2697.

[19] S. Sha, L. B. Vong, P. Chonpathompikunlert, T. Yoshitomi, H. Matsui, Y. Nagasaki, Biomaterials 34 (2013) 8393.

[20] N. Polley, S. Saha, A. Adhikari, S. Banerjee, S. Darbar, S. Das, S. K. Pal, Nanomedicine 10 (2015) 2349.

[21] A. Adhikari, N. Polley, S. Darbar, D. Bagchi, S. K. Pal, Fut. Sci. OA 2 (2016) FSO146.

[22] S. W. Bian, I. A. Mudunkotuwa, T. Rupasinghe, V. H. Grassian, Langmuir 27 (2011) 6059.

[23] A. M. E. Badawy, T. P. Luxton, R. G. Silva, K. G. Scheckel, M. T. Suidan, T. M. Tolaymat, Environ. Sci. Technol. 44 (2010) 1260.

[24] A. Giri, N. Goswami, C. Sasmal, N. Polley, D. Majumdar, S. Sarkar, S. N. Bandyopadhyay, A. Singha, S. K. Pal, RSC Adv. 4 (2014) 5075.

[25] T. Takashima, K. Hashimoto, R. Nakamura, J. Am. Chem. Soc. 134 (2012) 1519.

[26] Y. Kozlov, A. Kazakova, V. Klimov, Membr. Cell Biol. 11 (1996) 115.

[27] M. J. Horsburgh, S. J. Wharton, M. Karavolos, S. J. Foster, Trends Microbiol. 10 (2002) 496.

[28] G. Tan, S. Pan, J. Li, X. Dong, K. Kang, M. Zhao, X. Jiang, J. R. Kanwar, H. Qiao, H. Jiang, PLoS ONE 6 (2011) e25943.

[29] L. W. Weber, M. Boll, A. Stampfl, Crit. Rev. Toxicol. 33 (2003) 105.

[30] L. Yuan, N. Kaplowitz, J. Mam. 30 (2009) 29.

[31] S. Basu, Toxicology 189 (2003) 113.

[32] N. Kabir, H. Ali, M. Ateeq, M. F. Bertino, M. R. Shah, L. Franzel, RSC Adv. 4 (2014) 9012.

[33] J. Weerachayaphorn, A. Chuncharunee, S. Jariyawat, B. Lewchalermwong, S. Amonpatumrat, A. Suksamrarn, P. Piyachaturawat, J. Ethnopharmacol. 129 (2010) 254.

[34] W. J. Brattin, E. A. Glende, R. O. Recknagel, J. Free Radic. Biol. Med. 1 (1985) 27.

[35] R. O. Recknagel, E. A. Glende, J. A. Dolak, R. L. Waller, Pharmacol. Ther. 43 (1989) 139.

[36] N. Jia, J. Wen, L. Qian, X. Qian, Y. Wu, G. Fan, Toxicology 237 (2007) 1.

[37] E. M. Brunt, Hepatology 31 (2000) 241.

[38] N. D. Theise, Mod. Pathol. 20 (2007) S3.

[39] J. George, M. Tsutsumi, Gene Ther. 14 (2007) 790.

[40] G. J. Huang, J. S. Deng, S. S. Huang, Y. Y. Shao, C. C. Chen, Y. H. Kuo, Food Chem. 132 (2012) 709.

[41] P. Hall, J. Cash, Ulster Med J. 81 (2012) 30.

[42] M. Venukumar, M. Latha, Indian J. Clin. Biochem. 17 (2002) 80.

[43] M. Taniguchi, T. Takeuchi, R. Nakatsuka, T. Watanabe, K. Sato, Life Sci. 75 (2004) 1539.

[44] B. Halliwell, J. Gutteridge, Method Enzymol. 186 (1990) 1.

[45] I. Sziraki, K. Mohanakumar, P. Rauhala, H. Kim, K. Yeh, C. Chiueh, Neuroscience 85 (1998) 1101.

[46] I. Sziraki, P. Rauhala, K. K. Koh, P. Van-Bergen, C. Chiueh, Neurotoxicology 20 (1998) 455.

[47] K. Valachová, G. Kogan, P. Gemeiner, L. Šoltés, Interdiscip. Toxicol. 3 (2010) 26.

[48] M. Coassin, F. Ursini, A. Bindoli, Arch. Biochem. Biophys. 299 (1992) 330.

[49] S. Vertuani, A. Angusti, S. Manfredini, Curr. Pharm. Des. 10 (2004) 1677.

[50] S. Orrenius, V. Gogvadze, B. Zhivotovsky, Annu. Rev. Pharmacol. Toxicol. 47 (2007) 143.

[51] L. Knockaert, A. Berson, C. Ribault, P. E. Prost, A. Fautrel, J. Pajaud, S. Lepage, C. Lucas-Clerc, J. M. Bégué, B. Fromenty, Lab. Invest. 92 (2012) 396.

[52] C. Mitchell, M. A. Robin, A. Mayeuf, M. Mahrouf-Yorgov, A. Mansouri, M. Hamard, D. Couton, B. Fromenty, H. Gilgenkrantz, Am. J. Pathol. 175 (2009) 1929.

[53] J. Gao, X. Tang, H. Dou, Y. Fan, X. Zhao, Q. Xu, J. Pharm. Pharmacol. 56 (2004) 1449.

[54] L. Xu, J. Gao, Y. Wang, W. Yu, X. Zhao, X. Yang, Z. Zhong, Z.-M. Qian, Evid. Based Complement. Alternat. Med. 2011 (2011) 518302.

CHAPTER 06

Nanomedicine for Chronic Kidney Disease

6.1. INTRODUCTION

Reactive oxygen species (ROS) have long been considered as an unwanted but inevitable byproduct of aerobic oxygen metabolism [1]. Excessive generation of ROS may lead to tissue damage and numerous undesired physiological consequences. Increased ROS level is linked to inflammation, aging, and pathogenesis of diseases like diabetes, cancer, atherosclerosis, chronic kidney disease (CKD), and neurodegeneration [2-5]. Recent understanding about the pivotal role of ROS as secondary messengers in cellular signaling to control processes like metabolism, energetics, cell survival, and death lead to a paradigm shift to the traditional "oxidants are bad – antioxidants are good" based simplistic view of redox biology [6-10]. Apathy towards the paradox between lethality of excessive intracellular ROS (oxidative distress) and beneficial role of low level of ROS (oxidative eustress) is the major reason underlying the failure of conventional antioxidant therapies using natural or synthetic antioxidants (e.g., α-tocopherol, ascorbic acid, β-carotene, curcumin, and numerous polyphenols present in the diet), which not only scavenges the intracellular free radicals in a stoichiometric way, but also insulates redox signaling [10-12]. Moreover, meta-analyses of clinical trials show that the conventional antioxidants are not only ineffective, but harmful, and even increase mortality [12,13]. The understanding that

proper cell functioning critically requires a dynamic balance between oxidative eustress and distress (i.e., cellular redox homeostasis) forms the conceptual framework of redox medicine, a novel therapeutics that passivates the oxidative distress while maintaining the normal redox circuitry [10,12,14-16]. The cellular redox dynamics and its regulations, however, are still largely elusive because of the lack of effective pharmacological interventions [17]. In this regard, biocompatible transition metal oxide nanoparticles with potential electron-donating as well as accepting capability could be a viable option provided they are stable in the biological system, able to assimilate in the targeted tissue, and functional in the physiological *milieu*.

Recently, we have shown that spinel structured citrate functionalized Mn_3O_4 nanoparticles (C-Mn_3O_4 NPs) have the unique ability to generate ROS in dark, and when injected into jaundiced animals can selectively degrade bilirubin (a toxic byproduct of heme metabolism) without showing adverse effects to other blood parameters [18]. In the *in vitro* reaction system, we found that the nanoparticles can catalytically scavenge free radicals particularly H_2O_2. The microenvironment-controlled (i.e., presence of ROS, subsequent changes in pH and dissolved O_2) dynamic equilibrium between disproportionation and comproportionation involving Mn^{3+}, Mn^{4+} and Mn^{2+} charge states present in the hausmannite structure of C-Mn_3O_4 NPs is responsible for such dual activity [19,20]. Hence, depending upon the intracellular redox condition, the nanoparticle has the potential to balance the oxidative distress and eustress, the most important feature of a redox medicine.

In this study, our major aim was to evaluate the potential of C-Mn_3O_4 NPs as a redox medicine against CKD. CKD, the progressive decline in kidney function, is one of the most serious global public health problem (with 8-16% worldwide prevalence) that originates from the redox imbalance due to mitochondrial dysfunction and lacks effective medication [21-24]. To evaluate the therapeutic potential of C-Mn_3O_4 NPs we used a cisplatin-induced C57BL/6j mice model of CKD. The mechanistic details of their pharmacological action in the maintenance of redox homeostasis and mitoprotection were further explored using cellular (human embryonic kidney cell, HEK 293) as well as the animal model.

6.2. RESULTS AND DISCUSSION

6.2.1. Redox Nanomedicine Cures Chronic Kidney Disease (CKD) by Mitochondrial Reconditioning [25]

Previously, we showed that C-Mn_3O_4 NPs can selectively degrade bilirubin without affecting other blood parameters [20,26]. Here, initially, we evaluated their potential to scavenge H_2O_2 in an *in vitro* system using Rose Bengal (RB) degradation assay. RB has a distinct absorption peak at 540 nm. In the presence of H_2O_2, RB degenerates with a subsequent decrease in the 540 nm absorbance. When added to the reaction mixture, C-Mn_3O_4 NPs efficiently prevented the RB from H_2O_2 mediated degradation (Figure 6.1) indicating its strong radical scavenging potential towards H_2O_2.

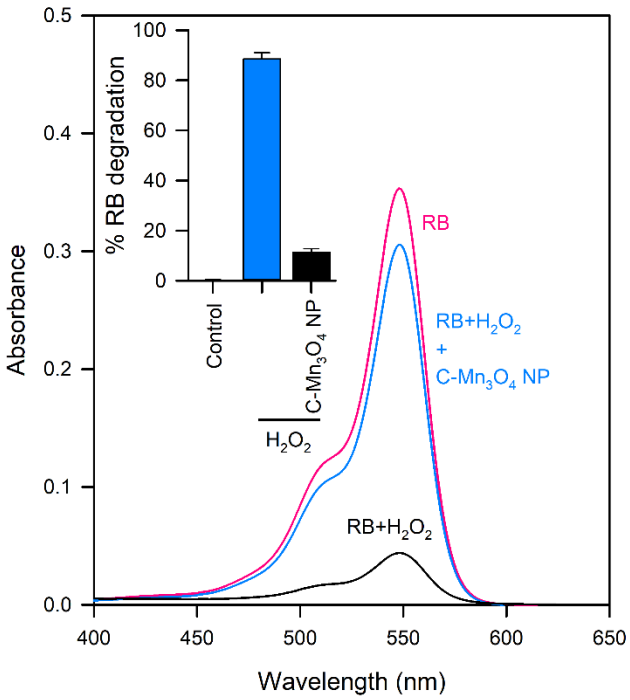

Figure 6.1. *H_2O_2 scavenging activity of C-Mn_3O_4 NPs using Rose Bengal (RB) assay. The RB undergoes oxidative degradation upon interaction with H_2O_2 as indicated in significantly decreased absorbance spectra. In presence of C-Mn_3O_4 NPs, H_2O_2 cannot degrade RB due to radical scavenging activity of the NPs. The inset shows the percentage of RB degradation by H_2O_2 in absence and presence of C-Mn_3O_4 NPs.*

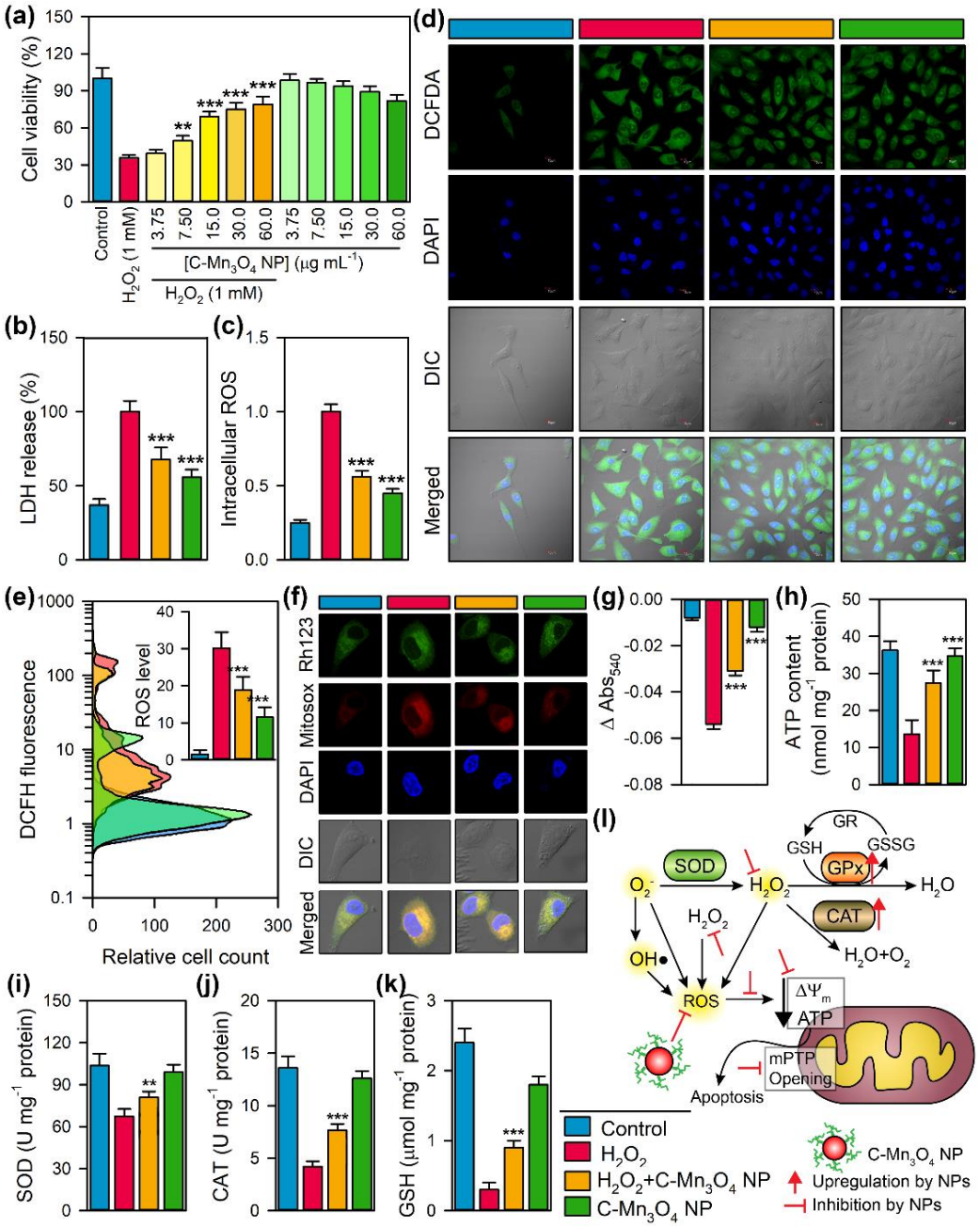

Figure 6.2. *Ability of C-Mn_3O_4 NPs in regulation of cellular redox and protection of mitochondria from oxidative damage. (a) Cell viability as measured using MTT. (b) LDH release. (c) Quantification of intracellular ROS estimated from fluorescence microscopy. (d) Fluorescence micrographs of differently stained HEK 293T cells. (e) Intracellular ROS content as measured using flow cytometry using DCFDA. (f) Changes in mitochondrial membrane potential (stained with rhodamie 123) and mitochondrial ROS (stained with Mitosox^{TM}) measured using fluorescence imaging. (g) Change in Ca^{2+}-induced mPTP opening. (h) ATP content. (i) Superoxide dismutase (SOD) activity. (j) Catalase activity. (k) Reduced glutathione (GSH) content. (l) Schematic representation of the redox homeostasis by C-Mn_3O_4 NPs against H_2O_2 distress through mitochondrial protection. For all experiments, [H_2O_2] =1 mM; [C-Mn_3O_4 NPs] =30 μg mL^{-1}. *, **, *** Values differ significantly from H_2O_2 treated cells (without treatment) (***$p < 0.001$; **$p < 0.01$; *$p < 0.05$).*

To test the ability of C-Mn_3O_4 NPs to combat oxidative stress in the cellular environment, we used a cell-based approach. The HEK 293 cells pretreated with different concentrations of nanoparticles (3.75 to 60 μg mL^{-1}) were exogenously exposed to H_2O_2 (1 mM) and cell viability was estimated using well known 2-(4,5-dimethylthiazol-2-yl)-2,5-diphenyltetrazolium bromide (MTT) assay (Figure 6.2a). The survival rate for H_2O_2 treated cells was ~35% ($p<0.001$ compared to control). The C-Mn_3O_4 NPs protected the cells from H_2O_2 induced cell death in a dose-dependent manner. Cell viability reached a maximum of ~85% and ~88% ($p<0.001$ compared to H_2O_2 treated cells) in H_2O_2 exposed cells when pretreated with 30 and 60 μg mL^{-1} NPs respectively. Pretreatment of the cells with similar concentrations of the NPs alone did not cause significant cellular mortality. Therefore, we selected the 30 μg mL^{-1} concentration of C-Mn_3O_4 NPs for further experiments. Identical results were observed in the lactate dehydrogenase (LDH) assay (Figure 6.2b). The presence of a high concentration of H_2O_2 inside the cell caused oxidative damage to the plasma membrane resulting in an increased release of LDH, a cytosolic enzyme, into the surrounding cell culture medium. Pretreatment with C-Mn_3O_4 NPs protected the cells from H_2O_2 induced oxidative damage resulting in a ~40% reduction in the LDH release ($p<0.001$ compared to H_2O_2 treated cells). To evaluate the scavenging of H_2O_2 by C-Mn_3O_4 NPs under stress condition, we monitored the intracellular oxidative stress using a ROS-sensitive fluorescence probe, dihydrodichloro-fluoresceindiacetate (DCFDA-H2). DCFDA-H2 is transported across the cell membrane and hydrolyzed by intracellular esterases to form nonfluorescent 2′,7′-dichlorofluorescein (DCFH), which is rapidly converted to highly fluorescent 2′,7′-dichlorofluorescein (DCF) in presence of ROS. H_2O_2 exposure caused a substantial increase in the cellular ROS levels indicated by the enhancement of the relative green fluorescence ($\lambda_{em/DCFDA\text{-}H2}$=520 nm) intensity of DCFDA-H2 when measured with fluorescence microscopy (Figure 6.2c & 2d) or flow cytometry (Figure 6.2e). However, pretreatment with 30 μg mL^{-1} C-Mn_3O_4 NPs significantly lowered intracellular ROS level which was reflected in reduced fluorescence (~ 50% reduction; $p<0.001$ compared to H_2O_2 treated cells) of the probe. The morphological observations in differential interference contrast (DIC) microscopy (Figure 6.2d) support the results of cell viability and oxidative damage

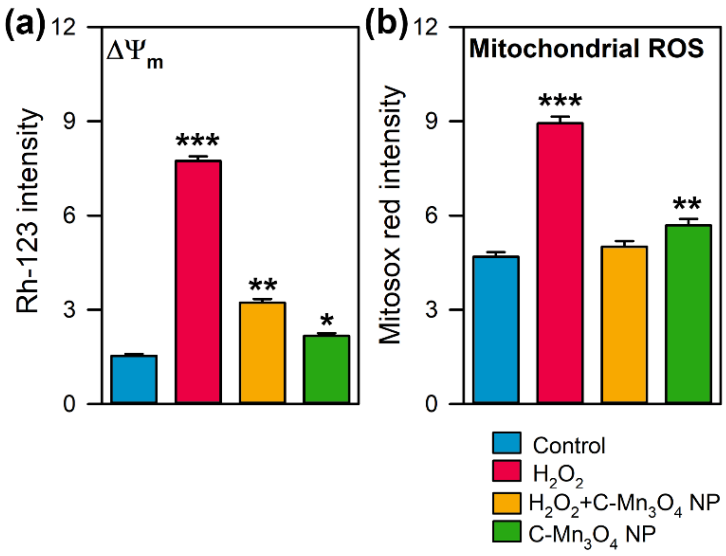

Figure 6.3. *Quantification of fluorescence intensity (Figure 6.2f) using ImageJ. (a) Intensity of Rh-123 as a marker of mitochondrial membrane potential ($\Delta\Psi_m$). More intensity indicates increased depolarization. (b) Intensity of Mitosox red™ as a marker of mitochondrial ROS. All measurements are in arbitrary unit and expressed as Mean ± SD (N=5). *, **, *** Values differ significantly from cells without treatment (***p < 0.001; **p < 0.01; *p < 0.05).*

evaluation. The cells pretreated with C-Mn_3O_4 NPs prevented the shrinkage and congregation of the cell body due to H_2O_2 overexposure and maintained normal cellular architecture.

Mitochondria despite being the primary source of intracellular ROS and its control are the most susceptible organelle to oxidative damage leading to redox imbalance and cell death [27,28]. So, to get further insight into the free radical scavenging activity of C-Mn_3O_4 NPs we evaluated their protective effect towards mitochondria. Treatment with H_2O_2 drastically decreased the mitochondrial membrane potential ($\Delta\Psi_m$), as measured by enhanced rhodamine 123 (Rh123) fluorescence (Figure 6.2f; Figure 6.3a) along with a burst in mitochondrial ROS production, as indicated by the increased fluorescence of Mito-sox red (Figure 6.2f; Figure 6.3b). Pretreatment with 30 μg mL^{-1} C-Mn_3O_4 NPs significantly restored the $\Delta\Psi_m$ and reduced the mitochondrial ROS. $\Delta\Psi_m$ has a causal relationship with mitochondrial permeability transition pore (mPTP). The results of Ca^{2+} induced mitochondrial swelling assay indicated that the NPs were effective in preventing the H_2O_2 induced mPTP opening (Figure 6.2g) and maintaining mitochondrial integrity.

The mitochondrial membrane depolarization and subsequent opening of mPTP led to a significant fall in the cellular ATP content (Figure 6.2h). In C-Mn_3O_4 NPs pretreated cells, such loss in ATP content was not observed. The opening of mPTP, fall in $\Delta\Psi_m$ and ATP content cumulatively functions as a proapoptotic signal to initiate the cell death pathways. Superoxide dismutase (SOD), catalase (CAT), and glutathione peroxidase (GPx) constitute the intracellular antioxidant defense system that works in consort with mitochondria [29-31]. The accumulation of highly reactive oxygen radicals cause damage to biomolecules in cells and alters enzyme activities [32-34]. Hence, we extended our study towards evaluating the effect of H_2O_2 and C-Mn_3O_4 NPs in the ROS regulatory network. H_2O_2 exposure significantly reduced the activity of SOD, CAT, and GPx resulting in a decrease of the reducing pool of cellular thiol constituents (e.g., GSH) (Figure 6.2i-6.2k). Pretreatment with C-Mn_3O_4 NPs significantly attenuated the damage. In cells treated with C-Mn_3O_4 NPs alone, none of the detrimental effects were observed.

Thus, our cellular studies indicate that C-Mn_3O_4 NPs possess the distinctive property of scavenging intracellular ROS, inhibiting apoptotic trigger, preventing loss of antioxidant enzymes and maintaining high cell viability by acting as a protector of mitochondria, the master regulator of cellular redox equilibrium (Figure 6.2l schematically summarizes the whole sequence).

There is always a gap in the efficacies of a pharmacological agent tested between cellular and animal models. The limited bioavailability, nonspecific distribution, or unwarranted metabolism often restricts the use of a cytoprotective agent *in vivo* [35-37]. Therefore, we evaluated the potential of C-Mn_3O_4 NPs in the treatment of cisplatin-induced C57BL/6j mice, a well-known animal model for testing therapeutic interventions against CKD [38-40]. Chronic administration of cisplatin resulted in significant mortality (~40% compared to control) (Figure 6.4a).

The fourfold higher blood urea nitrogen (BUN) content (Figure 6.4b), threefold higher GFR (Table 6.1), fourfold higher urinary albumin excretion (albuminuria) (Figure 6.4c) and high urine albumin to creatinine ratio (ACR) (Table 6.1) along with significantly increased serum urea (Figure 6.4d) and creatinine (Figure 6.4e) illustrated

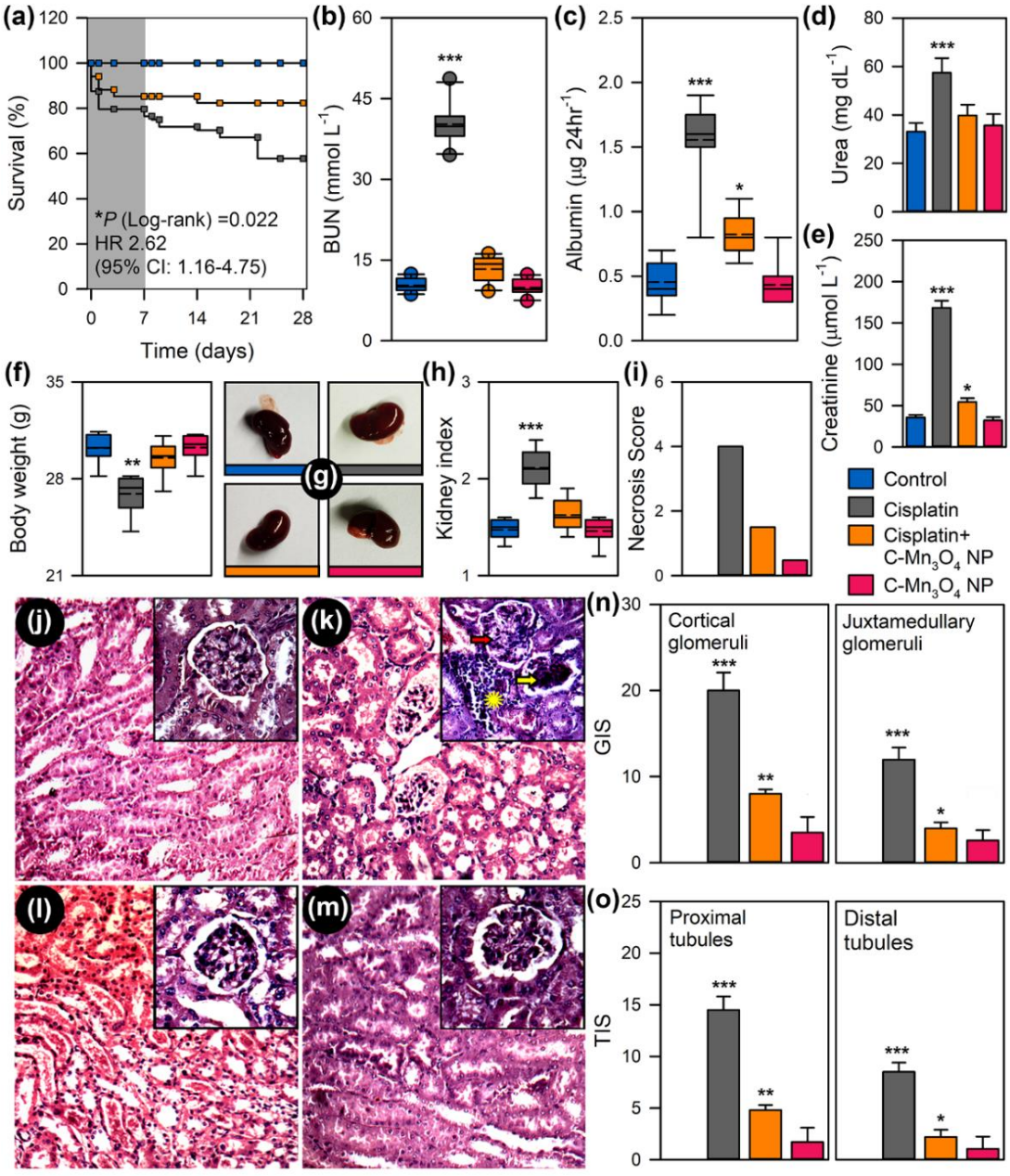

Figure 6.4. *Efficacy of C-Mn_3O_4 NPs in reversal of CKD in animal model. (a) Kaplan-Meir survival analysis curve. The darker shaded area represents co-treatment period. (b) Blood urea nitrogen (BUN) content. (c) Urinary albumin excretion as an indicator of albuminuria, hallmark of CKD. (d) Serum urea concentration. (e) Serum creatinine level. (f) Body weight at the end of experimental period. (g) Photographs of kidneys incised after experimental period. (h) Kidney index, defined as kidney to body weight ratio (mg g^{-1}). (i) Necrosis score as per the observation of expert clinical pathologist. (j-m) Hematoxylin and eosin stained liver sections. j: Control; k: Cisplatin; l: Cisplatin+C-Mn_3O_4 NPs; m: C-Mn_3O_4 NPs. Inset shows magnified image of single glomerulus. Red arrow: segmental glomerulosclerosis; Yellow arrow: global glomerulosclerosis; Yellow star: mononuclear infiltration (n) Glomerular injury score (GIS). (o) Tubular injury score (TIS). Data are expressed as Mean ± SD. N=6. *, **, *** Values differ significantly from control group (without treatment) (***p < 0.001; **p < 0.01; *p < 0.05).*

induction of proteinuria and notable damage to the renal function of mice, the two hallmarks of CKD [41-43]. Treatment with C-Mn_3O_4 NPs (0.25 mg kg^{-1} body weight (BW)) considerably reduced BUN, GFR, urinary albumin, ACR, serum urea, and creatinine (Figure 6.4b-6.4e; Table 6.1). The treatment also improved survivability (Log-rank p=0.022; hazards ratio 2.62) (Figure 6.4a). Treatment with citrate (the functionalization group) was unable to reduce any of the aforementioned parameters, confirming the observed effects solely due to the conjugated nanomaterial. Cisplatin intoxication caused weight loss in mice (Figure 6.4f), suggestive of the systemic toxicity that frequently arises in individuals receiving this anticancer drug. Animals treated with C-Mn_3O_4 NPs were capable of mitigating the weight loss. Next, we examined the external morphology of isolated kidneys from each group. The kidneys from the cisplatin exposed group were deviated from the usual darkish brown to a pale brown color with a rough and uneven surface (Figure 6.4g). The kidney to body weight ratio (i.e, kidney index) was also significantly higher (i.e., edema) in cisplatin-treated animals (2.1±0.2 compared to 1.5±0.1 mg g^{-1} of control, $p<0.001$; Figure 6.4h). Subsequent treatment with C-Mn_3O_4 NPs overturned the observed changes in morphology and kidney index.

Table 6.1. Effect of C-Mn_3O_4 NPs on nephrotoxic biomarkers.

Groups	GFR (μL min^{-1} g^{-1} BW)	Urine ACR	Creatinine clearance (μmol min^{-1})	Uric acid (mg dL^{-1})	Hydroxyproline (mg g^{-1} tissue)
Control	10.2±1.5	0.34±0.06	1.41±0.08	1.2±0.1	0.51±0.03
Cisplatin	30.4±4.1[b]	5.62±0.08[b]	0.35±0.04[b]	2.6±0.2[b]	1.43±0.07[b]
Cisplatin + C-Mn_3O_4 NPs	14.1±2.3[a]	1.87±0.09[a,b]	0.92±0.05[a,b]	1.6±0.1[a]	0.79±0.06[a,b]
C-Mn_3O_4 NPs	9.8±1.2[a]	0.41±0.05[a]	1.38±0.07[a]	1.3±0.1[a]	0.42±0.04[a]

Data expressed as Mean ± SD (N=6/group). GFR: glomerular filtration rate; ACR: albumin to creatinine ratio. One way ANOVA Tukey *post hoc*. [a]$p<0.05$ compared to Cisplatin treated animals; [b]$p<0.05$ compared Control animals.

Hematoxylin and eosin-stained kidney sections of the control and C-Mn_3O_4 NP treated groups showed normal histologic features (Figure 6.4j & 6.4m) with negligible necrosis score (Figure 6.4i). The kidney sections from cisplatin intoxicated mice displayed several pathological features of CKD like focal segmental as well as global

glomerulosclerosis along with interstitial fibrosis, diffused thickening of the capillary walls, glomerular hyalinosis, dilated or collapsed Bowman's space and glomerular retraction (Figure 6.4k). Tubular atrophy, dilation of cortical tubules, increased mesangial matrix, obliteration of capillaries, necrosis, vacuolization, and interstitial mononuclear infiltrations were the other features observed in this group. Treatment with C-Mn_3O_4 NPs notably reduced focal glomerular necrosis (Figure 6.4l). However, sparse tubular changes like vacuolization, dilation, mild mononuclear infiltration, and detachment of epithelial cells were observed in this group. Overall, C-Mn_3O_4 NPs were able to efficiently revert the marked detrimental changes in the renal architecture of CKD animals. The histological observations are quantitatively reflected in the necrosis score (Figure 6.4i), glomerular injury score (GIS; Figure 6.4n), and tubular injury score (TIS; Figure 6.4o).

Previous studies and our histological observations suggested an association between renal fibrosis and CKD [44-46]. So, we measured the renal hydroxyproline content, a byproduct of collagen metabolism and biochemical marker of fibrosis. The results indicate almost a threefold increase in the hydroxyproline content (1.43±0.07 compared to 0.51±0.03 mg gm^{-1} tissue of control; $p<0.001$) in the cisplatin intoxicated group (Table 6.1). In accordance with the histological findings, treatment with C-Mn_3O_4 NPs markedly reduced the hydroxyproline content (0.79±0.06 mg gm^{-1} tissue; $p<0.001$ compared to cisplatin treated ones), suggesting a decrease in fibrotic damage (Table 6.1).

Oxidative stress proved to be one of the major causes of cisplatin-induced nephrotoxicity [47-49]. Therefore, we tried to ascertain whether C-Mn_3O_4 NPs contributed to nephroprotection by ameliorating oxidative stress. Signs of ROS mediated damage including lipid peroxidation (in terms of thiobarbituric acid reactive substances, TBARS), reduction in cellular GSH pool, and inhibition of antioxidant enzyme activity were estimated. Exposure to cisplatin markedly increased the level of TBARS (Figure 6.5a) and oxidative glutathione along with a reduction in GSH concentration. Furthermore, it inhibited the antioxidant actions of enzymes like SOD, CAT, and GPx (Figure 6.5b-6.5d). In consensus with our cellular studies, C-Mn_3O_4 NPs rescued the detrimental pleiotropic effects of increased ROS while maintaining the normal signaling circuitry.

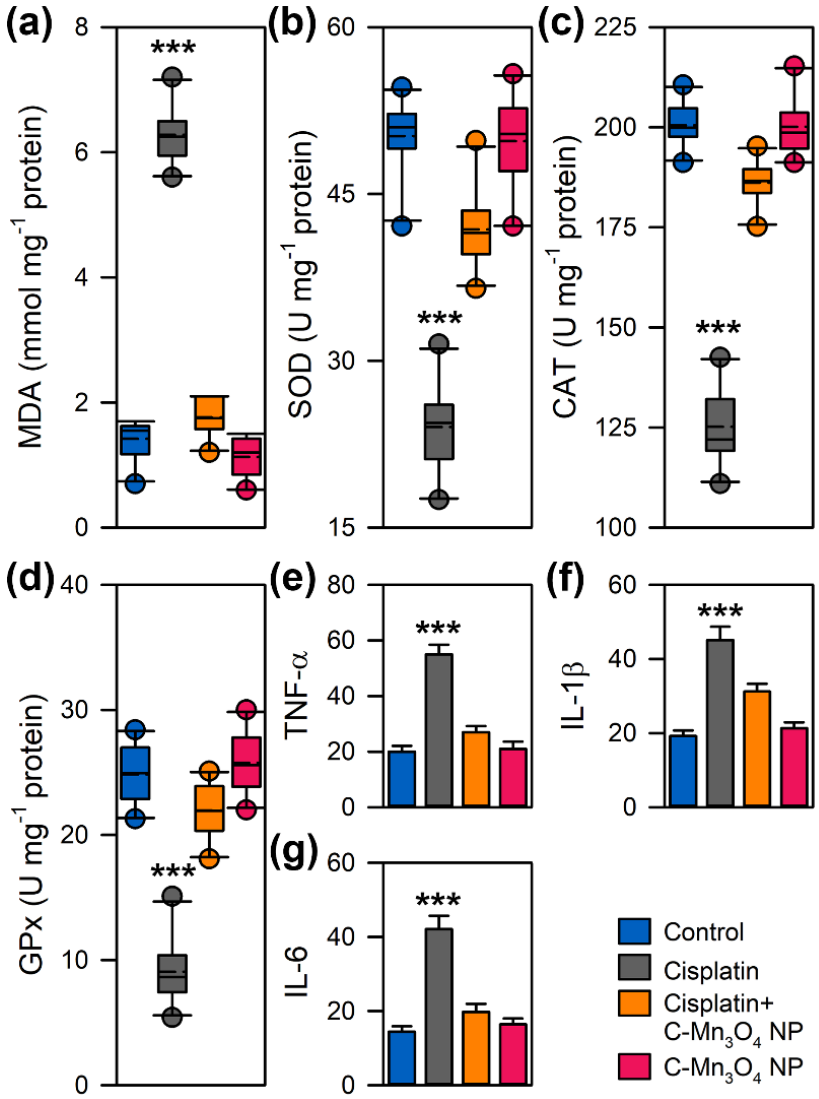

Figure 6.5. *Effect of C-Mn_3O_4 NPs in protection of intracellular redox regulatory network and inhibition of anti-inflammatory response. (a) Extent of lipid peroxidation (MDA, malonaldehyde content) measured in terms of thiobarbituric acid reactive substances (TBARS). (b) Superoxide dismutase (SOD) activity. (c) Catalase activity. (d) Gluthione peroxidase (GPx) activity. (e) Tumor necrosis factor-α level. (f) Interleukin-1β level. (g) Interleukin-6 level. MDA, SOD, CAT and GPx were estimated from kidney homogenate. TNF-β, IL-1β and IL-6 were measured from serum.Data are expressed as Mean ± SD. N=6. *, **, *** Values differ significantly from control group (without treatment) (***p < 0.001; **p < 0.01; *p < 0.05).*

Macrophage infiltration in the kidney and subsequent rise in the plasma concentrations of pro-inflammatory cytokines like TNF-α are well-known features of CKD [50-52]. We found significant increases in plasma concentrations of TNF-α, IL-1β, and IL-6 in cisplatin-induced animals (Figure 6.5e-6.5g). Treatment with C-Mn_3O_4

NPs resulted in a notable decrease in the cytokine levels. No difference was observed between the C-Mn_3O_4 NP treated and the control groups.

Considering the inevitable role of mitochondria in the pathogenesis of CKD [24,53-56] and results of our *in cellulo* observations that C-Mn_3O_4 NPs protect mitochondria from H_2O_2 induced oxidative damage, we assessed the role of mitoprotection in the therapeutic efficacy of C-Mn_3O_4 NPs in animals. Ca^{2+}-induced renal mPTP opening is one of the salient features of CKD [24,57]. Our data clearly show that the mitochondria isolated from the cisplatin intoxicated group were more sensitive towards Ca^{2+} manifested into a sharp decrease in 540 nm absorbance (Figure 6.6a). Treatment with C-Mn_3O_4 NPs inhibited mPTP opening and maintained membrane integrity. $\Delta\Psi_m$ and ATP content declined significantly as a result of cisplatin administration (Figure 6.6b & 6.6c). These were accompanied by an increase in cytochrome c oxidase activity (Figure 6.6d) and a reduction in dehydrogenase activity (Figure 6.6e). The alterations were upended by C-Mn_3O_4 NP treatment. Thus cisplatin-induced renal damage triggered the opening of mPTP, the decline in $\Delta\Psi_m$, and induction of mitochondrial swelling that resulted in the release of cytochrome c in the cytosol leading to apoptosis. The ladder-like DNA fragmentation, a hallmark of apoptosis, was evident in the case of cisplatin-treated diseased groups (Figure 6.6f). Whereas, treatment with C-Mn_3O_4 NPs notably protected the mitochondria, inhibited cell death and decreased the extent of DNA fragmentation. Figure 6.6g schematically represents the entire phenomena of redox-mediated nephroprotection by C-Mn_3O_4 NPs.

In this study, we determined whether C-Mn_3O_4 NPs could be used as a redox medicine to treat CKD, an important clinical question considering the high prevalence of the disease and the non-availability of effective medication. CKD is defined as the progressive and irreversible loss of renal function characterized by reduced glomerular filtration rate (GFR), increased urinary albumin excretion (albuminuria), or both [41,43,58]. Our results present evidence that treatment with the C-Mn_3O_4 NPs significantly improved renal function, glomerular and tubulointerstitial injury, cellular antioxidant defense network along with inhibition of pro-inflammatory immune

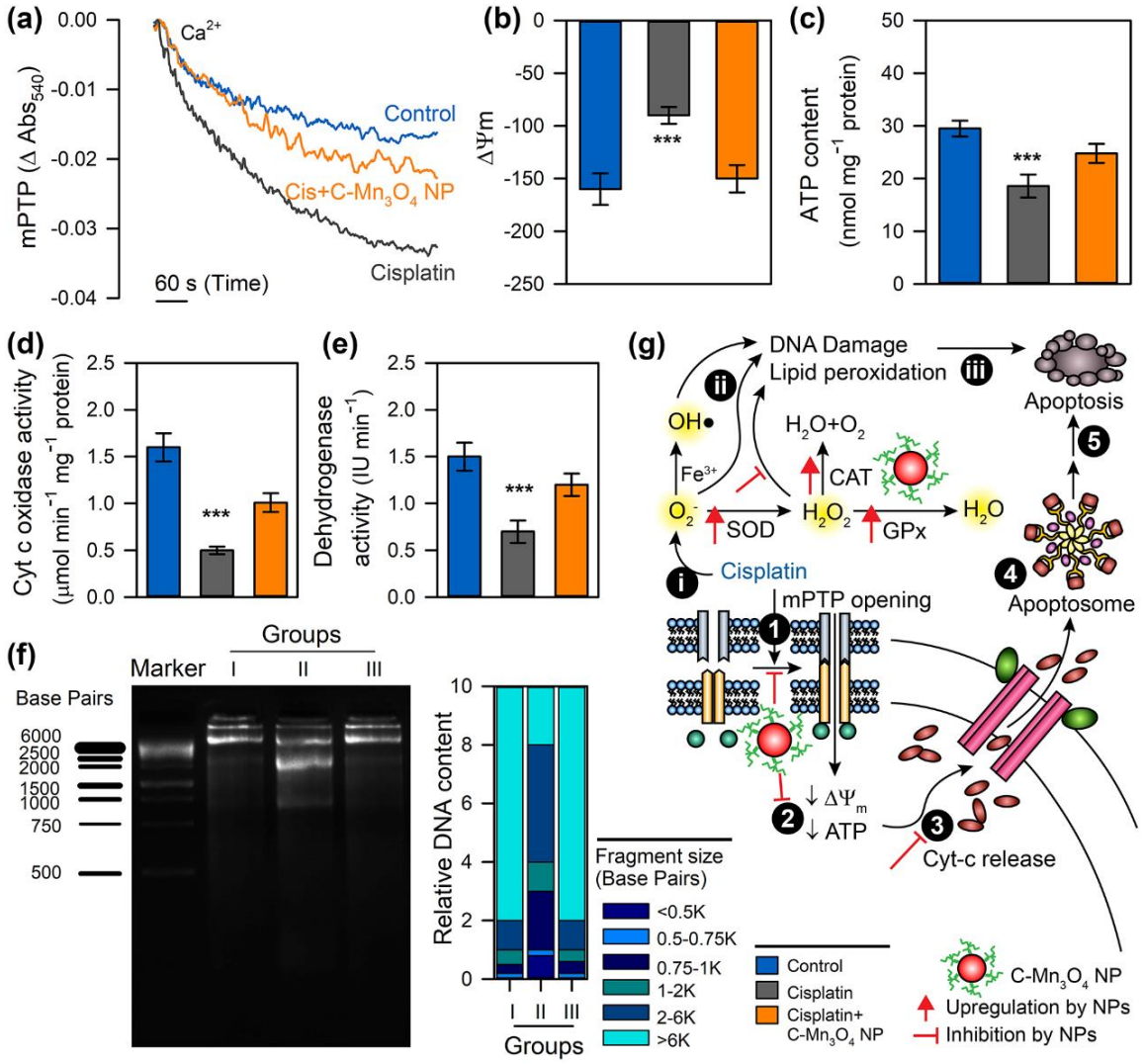

Figure 6.6. *Efficacy of C-Mn_3O_4 NPs in protection of mitochondria, the master redox regulator in mice. (a) Ca^{2+} induced mPTP opening. (b) Mitochondrial membrane potential measured using JC-1. (c) ATP content. (d) Cytochrome c oxidase (complex IV) activity in isolated mitochondria. (e) Succinate dehydrogenase (SDH, complex II) activity in isolated mitochondria. (f) DNA fragmentation level as a result of oxidative damage measured using agarose gel electrophoresis. Group I: Control; Group II: Cisplatin; Group II: Cisplatin+C-Mn_3O_4 NPs. (g) Schematic overview of the comprehensive mechanism of action of C-Mn_3O_4 NPs as a redox medicine against cisplatin induced CKD. The numbers in the black circles indicate the sequence of events. Data are expressed as Mean ± SD. N=6. *, **, *** Values differ significantly from control group (without treatment) (***p < 0.001; **p < 0.01; *p < 0.05).*

response and attenuation of mitochondrial dysfunction in response to the cisplatin toxicity. Our cellular and animal studies further enlightened the role of unique mitoprotective as well as redox modulatory activity of C-Mn_3O_4 NPs in the therapeutic mechanism.

Mitochondria have long been recognized for their canonical roles in cellular respiration and energy production [24]. Recently, they have emerged as the master regulator of a spectrum of molecular pathways including biosynthesis of macromolecules, maintenance of cellular redox equilibrium, calcium homeostasis, inflammation, and cell death [59-62]. Thus, mitochondria play a pivotal role in the functioning of the kidney, an organ with high energy demand, and rich in mitochondria, second to the heart [54]. Our findings that C-Mn_3O_4 NPs maintain cellular redox homeostasis through the prevention of mPTP opening and ATP depletion discloses a key redox-mediated nephroprotective mechanism. Virtually, the renal proximal tubules are exclusively dependent on ATP generated by mitochondrial oxidative phosphorylation and are therefore vulnerable to the oxidative distress due to mitochondrial damage [47,63]. Cisplatin accumulates in mitochondria and reduces the activity of all four respiratory complexes (I–V) involved in the electron transport chain, thereby a surge in mitochondrial ROS formation takes place along with mPTP opening, membrane depolarization and impairment in ATP production, leading to cell death [64,65]. The mitotoxic mechanism of cisplatin essentially mimics the pathogenesis of CKD, thus an efficient reversal of damage in this rodent model is supposed to reflect the possible effects of a compound in higher animals. Data from our cellular as well as animal studies provide sufficient evidence that C-Mn_3O_4 NPs prevent mitochondrial ROS surge, prevent loss of membrane potential, inhibit mPTP opening, and stops ATP depletion, thereby prevents mitochondrial dysfunction, cellular redox imbalance, and tubular or glomerular cell death. As a result, the markers of CKD like increased BUN, plasma creatinine, serum urea, and glomerular filtration rate (GFR) returns to homeostatic condition.

This study provides direct evidence that C-Mn_3O_4 NPs can scavenge ROS, particularly H_2O_2 the longest living one in the cellular *milieu*. It also proves the ability of the NPs in the prevention of mPTP from opening and subsequently maintenance of mitochondrial structure and function. However, it is not clear whether ROS scavenging protects mitochondria or mitochondrial integrity which results in ROS depletion. Several studies showed that a compound with the sole property of free radical scavenging cannot be effective in the reversal of oxidative stress-related diseases in higher animals because the antioxidant property is not sustainable and the

compound becomes inactive after one reaction [66-68]. So, to mitigate the burst of ROS, the intracellular concentration required for a conventional antioxidant molecule is enormous and practically hard to achieve [66-68]. Thus, to become an effective medicine a compound should have some additional mechanisms that will ensure the sustainable effect in the therapeutic regime. Therefore, considering the causal relationship between mitochondria and cellular redox homeostasis and the efficacy of C-Mn_3O_4 NPs in the treatment of multifaceted diseases like CKD, we propose that both the mechanisms (i.e., ROS scavenging and mitochondrial protection) take place simultaneously.

The findings that C-Mn_3O_4 NPs can accelerate the revival of proximal tubule epithelium embodies a crucial nephroprotective function mediated by the nanoparticles. Kidneys show higher regenerative property following tubulointerstitial damage [47]. The proliferation of a subset of sublethally damaged, yet surviving, proximal tubule cells contribute to the regenerative property of the kidney [69]. The acceleration of this process is sufficient to confer nephroprotection [70]. As revealed in our histological findings, the recovery rate of these cells in C-Mn_3O_4 NP treated cisplatin exposed animals is significantly faster and efficient than the auto-recovery. Several mechanisms can be proposed for the enhanced proliferation by C-Mn_3O_4 NPs. The restoration of structural and functional integrity of mitochondria and recovery of respiratory complexes may contribute towards the increased proliferation. It is well known that the mitochondrial electron transport chain (ETC) has a crucial role in cell proliferation through regulation of ATP generation, and supply of energy to proliferative pathways [71,72]. Previous studies have demonstrated that mutations in ETC genes, or presence of ETC complex inhibitors causes a reduction in ATP synthesis obstructing progression through cell cycle leading to a blockage in proliferation [73-75]. Thus, the mitoprotective activity of C-Mn_3O_4 NPs may have played a significant role in the revival of tubulointerstitial epithelial cells, in turn protecting the renal architecture. Additionally, ROS scavenging by C-Mn_3O_4 NPs may boost the proliferation because oxidative distress in proximal tubules causes cell cycle arrest and impedes cell-cycle progression [76].

The role of intracellular redox regulation through mitoprotection in the therapeutic action of C-Mn_3O_4 NPs opens up further avenues for the treatment of

several unmet diseases like diabetic nephropathy, neurodegeneration (e.g., Parkinson's, Huntington's, Alzheimer's, multiple sclerosis), cardiovascular disorders, obesity, etc. where pathogenesis is very much dependent upon mitochondrial damage and associated redox imbalance [77-81].

6.3. CONCLUSION

There are very few published articles that utilize the promising redox regulatory approach for treatment of chronic diseases like CKD. On the other hand, several chronic kidney diseases are reported to be due to redox imbalance in mitochondria. Our study suggests that C-Mn_3O_4 NPs could be an efficient redox medicine to attenuate renal injury and tubule-intestinal fibrosis as evidenced by the improved renal functions, reduction in biochemical markers of nephrotoxicity, reduced fibrotic content, and downregulated pro-inflammatory cytokines. The molecular mechanism involves regulation of the redox balance through synchronization of the causal relationship between mitoprotection and ROS scavenging by C-Mn_3O_4 NPs. The findings highly suggested the translational potential of C-Mn_3O_4 NPs as a redox nanomedicine for treating CKD in the clinic.

REFERENCES

[1] H. L. Wong, K. Shimamoto, Sci. Signal. 2 (2009) PE60.

[2] P. Storz, Science's STKE 2006 (2006) RE3.

[3] B. Carroll, E. G. Otten, D. Manni, R. Stefanatos, F. M. Menzies, G. R. Smith, D. Jurk, N. Kenneth, S. Wilkinson, J. F. Passos, J. Attems, E. A. Veal, E. Teyssou, D. Seilhean, S. Millecamps, E. L. Eskelinen, A. K. Bronowska, D. C. Rubinsztein, A. Sanz, V. I. Korolchuk, Nat. Commun. 9 (2018) 256.

[4] T. Finkel, N. J. Holbrook, Nature 408 (2000) 239.

[5] A. Podkowińska, D. Formanowicz, Antioxidants 9 (2020).

[6] D. P. Jones, Antioxid. Redox. Signal. 8 (2006) 1865.

[7] H. Sies, Redox Biol. 4 (2015) 180.

[8] B. Saleme, V. Gurtu, Y. Zhang, A. Kinnaird, A. E. Boukouris, K. Gopal, J. R. Ussher, G. Sutendra, Sci. Transl. Med. 11 (2019) eaau8866.

[9] H. Sies, J. Biol. Chem. 289 (2014) 8735.

[10] A. I. Casas, V. T. V. Dao, A. Daiber, G. J. Maghzal, F. Di Lisa, N. Kaludercic, S. Leach, A. Cuadrado, V. Jaquet, T. Seredenina, K. H. Krause, M. G. López, R. Stocker, P. Ghezzi, H. H. H. W. Schmidt, Antioxid. Redox. Signal. 23 (2015) 1171.

[11] E. Niki, Arch. Biochem. Biophys. 595 (2016) 19.

[12] M. H. Elbatreek, M. P. Pachado, A. Cuadrado, K. Jandeleit-Dahm, H. H. H. W. Schmidt, Trends Endocrinol. Metab. 30 (2019) 312.

[13] H. H. H. W. Schmidt, R. Stocker, C. Vollbracht, G. Paulsen, D. Riley, A. Daiber, A. Cuadrado, Antioxid. Redox Signal. 23 (2015) 1130.

[14] H. Sies, D. P. Jones, Nat. Rev. Mol. Cell Biol. 21 (2020) 363.

[15] B. D'Autréaux, M. B. Toledano, Nat. Rev. Mol. Cell Biol. 8 (2007) 813.

[16] F. Ursini, M. Maiorino, H. J. Forman, Redox Biol. 8 (2016) 205.

[17] N. Li, A. Than, C. Sun, J. Tian, J. Chen, K. Pu, X. Dong, P. Chen, ACS Nano 10 (2016) 11475.

[18] N. Polley, S. Saha, A. Adhikari, S. Banerjee, S. Darbar, S. Das, S. K. Pal, Nanomedicine 10 (2015) 2349.

[19] T. Takashima, K. Hashimoto, R. Nakamura, J. Am. Chem. Soc. 134 (2012) 18153.

[20] A. Giri, N. Goswami, C. Sasmal, N. Polley, D. Majumdar, S. Sarkar, S. N. Bandyopadhyay, A. Singha, S. K. Pal, RSC Adv. 4 (2014) 5075.

[21] D. M. Small, J. S. Coombes, N. Bennett, D. W. Johnson, G. C. Gobe, Nephrology 17 (2012) 311.

[22] E. Dounousi, E. Papavasiliou, A. Makedou, K. Ioannou, K. P. Katopodis, A. Tselepis, K. C. Siamopoulos, D. Tsakiris, Am. J. Kidney Dis. 48 (2006) 752.

[23] S. Ruiz, P. E. Pergola, R. A. Zager, N. D. Vaziri, Kidney Int. 83 (2013) 1029.

[24] D. L. Galvan, N. H. Green, F. R. Danesh, Kidney Int. 92 (2017) 1051.

[25] A. Adhikari, S. Mondal, T. Chatterjee, M. Das, P. Biswas, S. Darbar, H. Alessa, J. T. Al-Thakafy, S. A. Ahmed, A. K. Das, M. Bhattacharyya, S. K. Pal, bioRxiv (2021) https://doi.org/10.1101/2021.03.14.435287.

[26] A. Adhikari, V. K. Bhutani, S. Mondal, M. Das, S. Darbar, R. Ghosh, N. Polley, A. K. Das, S. S. Bhattacharya, D. Pal, A. K. Mallick, S. K. Pal, bioRxiv (2021) https://doi.org/10.1101/2020.12.31.425023.

[27] N. Nissanka, C. T. Moraes, FEBS Lett. 592 (2018) 728.

[28] A. Musatov, N. C. Robinson, Free Radic. Res. 46 (2012) 1313.

[29] A. Adhikari, S. Darbar, T. Chatterjee, M. Das, N. Polley, M. Bhattacharyya, S. Bhattacharya, D. Pal, S. K. Pal, ACS Omega 3 (2018) 15975.

[30] A. Adhikari, N. Polley, S. Darbar, D. Bagchi, S. K. Pal, Future Sci. OA 2 (2016) FSO146.

[31] A. Adhikari, S. Mondal, S. Darbar, S. K. Pal, Biomol. Concepts 10 (2019) 160.

[32] M. Schieber, N. S. Chandel, Curr. Biol. 24 (2014) R453.

[33] L. M. Guachalla, K. L. Rudolph, Cell Cycle 9 (2010) 4058.

[34] M. D. Temple, G. G. Perrone, I. W. Dawes, Trends Cell Biol. 15 (2005) 319.

[35] E. A. G. Blomme, Y. Yang, J. F. Waring, Toxicol. Lett. 186 (2009) 22.

[36] A. P. Li, Drug Discov. Today 6 (2001) 357.

[37] I. Kola, J. Landis, Nat. Rev. Drug Discov. 3 (2004) 711.

[38] M. Shi, K. L. McMillan, J. Wu, N. Gillings, B. Flores, O. W. Moe, M. C. Hu, Lab. Invest. 98 (2018) 1105.

[39] S. V. Shah, M. M. Rajapurkar, Hemoglobin 33 (2009) 378.

[40] S. I. Landau, X. Guo, H. Velazquez, R. Torres, E. Olson, R. Garcia-Milian, G. W. Moeckel, G. V. Desir, R. Safirstein, Kidney Int. 95 (2019) 797.

[41] C. K. D. P. Consortium, Lancet 375 (2010) 2073.

[42] A. M. El Nahas, A. K. Bello, Lancet 365 (2005) 331.

[43] V. Jha, G. Garcia-Garcia, K. Iseki, Z. Li, S. Naicker, B. Plattner, R. Saran, A. Y. M. Wang, C. W. Yang, Lancet 382 (2013) 260.

[44] J. He, Y. Xu, D. Koya, K. Kanasaki, Clin. Exp. Nephrol. 17 (2013) 488.

[45] N. Liu, E. Tolbert, M. Pang, M. Ponnusamy, H. Yan, S. Zhuang, J. Am. Soc. Nephrol. 22 (2011) 1064.

[46] V. Ninichuk, O. Gross, S. Segerer, R. Hoffmann, E. Radomska, A. Buchstaller, R. Huss, N. Akis, D. Schlöndorff, H. J. Anders, Kidney Int. 70 (2006) 121.

[47] X. Yu, X. Meng, M. Xu, X. Zhang, Y. Zhang, G. Ding, S. Huang, A. Zhang, Z. Jia, EBioMedicine 36 (2018) 266.

[48] Y. I. Chirino, J. Pedraza-Chaverri, Exp. Toxicol. Pathol. 61 (2009) 223.

[49] N. Pabla, Z. Dong, Kidney Int. 73 (2008) 994.

[50] B. T. Lee, F. A. Ahmed, L. L. Hamm, F. J. Teran, C. S. Chen, Y. Liu, K. Shah, N. Rifai, V. Batuman, E. E. Simon, J. He, J. Chen, BMC Nephrol. 16 (2015) 77.

[51] H. W. Kim, C. K. Lee, H.-S. Cha, J. Y. Choe, E. J. Park, J. Kim, Rheumatol. Int. 35 (2015) 727.

[52] R. L. Amdur, H. I. Feldman, J. Gupta, W. Yang, P. Kanetsky, M. Shlipak, M. Rahman, J. P. Lash, R. R. Townsend, A. Ojo, A. Roy-Chaudhury, A. S. Go, M. Joffe, J. He, V. S. Balakrishnan, P. L. Kimmel, J. W. Kusek, D. S. Raj, Clin. J. Am. Soc. Nephrol. 11 (2016) 1546.

[53] J. M. Forbes, D. R. Thorburn, Nat. Rev. Nephrol. 14 (2018) 291.

[54] J. M. Forbes, Trends Endocrinol. Metab. 27 (2016) 441.

[55] P. Bhargava, R. G. Schnellmann, Nat. Rev. Nephrol. 13 (2017) 629.

[56] H. H. Szeto, J. Am. Soc. Nephrol. 28 (2017) 2856.

[57] D. Singh, V. Chander, K. Chopra, Toxicology 207 (2005) 339.

[58] Y. F. Lin, Y. H. Lee, Y. H. Hsu, Y. J. Chen, Y. F. Lin, F. Y. Cheng, H. W. Chiu, Nanomedicine 12 (2017) 2741.

[59] E. Gulbins, S. Dreschers, J. Bock, Exp. Physiol. 88 (2003) 85.

[60] S. W. G. Tait, D. R. Green, J. Cell Sci. 125 (2012) 807.

[61] R. Zhou, A. S. Yazdi, P. Menu, J. Tschopp, Nature 469 (2011) 221.

[62] P. D. Ray, B. W. Huang, Y. Tsuji, Cell. Sig. 24 (2012) 981.

[63] K. L. Klein, M. S. Wang, S. Torikai, W. D. Davidson, K. Kurokawa, Kidney Int. 20 (1981) 29.

[64] G. Y. Nowak, J. Biol. Chem. 277 (2002) 43377.

[65] R. Marullo, E. Werner, N. Degtyareva, B. Moore, G. Altavilla, S. S. Ramalingam, P. W. Doetsch, PLoS ONE 8 (2013) e81162.

[66] A. Warnholtz, T. Münzel, Trials 1 (2000) 38.

[67] S. R. Steinhubl, Am. J. Cardiol. 101 (2008) S14.

[68] T. Persson, B. O. Popescu, A. Cedazo-Minguez, Oxid. Med. Cell. Longev. 2014 (2014) 427318.

[69] K. Berger, M. J. Moeller, Semin. Nephrol. 34 (2014) 394.

[70] C. Bagnis, H. Beaufils, C. Jacquiaud, Y. Adabra, C. Jouanneau, G. Le Nahour, M. C. Jaudon, R. Bourbouze, C. Jacobs, G. Deray, Nephrol. Dial. Transplant. 16 (2001) 932.

[71] K. Kawaida, K. Matsumoto, H. Shimazu, T. Nakamura, Proc. Nat. Acad. Sci. 91 (1994) 4357.

[72] H. O. Byun, H. Y. Kim, J. J. Lim, Y. H. Seo, G. Yoon, J. Cell. Biochem. 104 (2008) 1747.

[73] Y. S. Yoon, H. O. Byun, H. Cho, B. K. Kim, G. Yoon, J. Biol. Chem. 278 (2003) 51577.

[74] S. Mandal, P. Guptan, E. Owusu-Ansah, U. Banerjee, Dev. Cell 9 (2005) 843.

[75] C. U. Vohwinkel, E. Lecuona, H. Sun, N. Sommer, I. Vadász, N. S. Chandel, J. I. Sznajder, J. Biol. Chem. 286 (2011) 37067.

[76] A. E. Nel, L. Mädler, D. Velegol, T. Xia, E. M. V. Hoek, P. Somasundaran, F. Klaessig, V. Castranova, M. Thompson, Nat. Mater. 8 (2009) 543.

[77] M. R. Duchen, Diabetes 53 (2004) S96.

[78] M. T. Lin, M. F. Beal, Nature 443 (2006) 787.

[79] A. Johri, M. F. Beal, J. Pharmacol. Exp. Ther. 342 (2012) 619.

[80] V. B. Ritov, E. V. Menshikova, J. He, R. E. Ferrell, B. H. Goodpaster, D. E. Kelley, Diabetes 54 (2005) 8.

[81] S. W. Ballinger, Free Radic. Biol. Med. 38 (2005) 1278.

CHAPTER 07

Nanoformulation for Amelioration of Manganese Neurotoxicity

7.1. INTRODUCTION

Manganese (Mn) is an essential trace element ubiquitously present in earth's crust [1], required as an activator or cofactor of various enzymes (e.g., galactosyltransferase [2], agmatinase [3], arginase [4], glutamine synthetase [5], pyruvate carboxylase [6,7] and Mn-superoxide dismutase [8,9], as well as several kinases, hydrolases, transferases, and decarboxylases [10]) that govern several important physiological processes including bone development, connective tissue growth, metabolism, mitochondrial antioxidant systems, and cell death [11]. But, in *in vivo* cellular environment Mn behaves like a double-edged sword. At physiological concentration this redox active transition metal acts as an interface between the genome of the organism and exposome (i.e., the environment) [11,12] to facilitate proper functioning of the aforementioned processes. On the other hand, excessive occupational, iatrogenic, medical, and environmental exposure causes its accumulation in the liver, kidney and brain, resulting in various symptoms, including hepatic cirrhosis, dystonia, polycythemia, and hypermanganesemia [13-15]. Excessive Mn in its ionic form (both +2 and +3) accumulates in the brain, particularly in basal ganglia, cerebellum, hippocampus and cause clinical signs and morphological lesions analogous to idiopathic Parkinson's disease (PD) [16-18]. The etiology of Mn-induced

neurotoxicity is multifactorial and numerous studies illustrated the complex mechanism that starts from mitochondrial inactivation and subsequent enhancement of reactive oxygen species (ROS) in the affected brain areas, resulting into dysregulation of nigrostriatal dopaminergic pathway [19-21]. Further induction of classical activation (M1 activation) of microglial cells and astrocytes in the central nervous system (CNS) leads to the production of proinflammatory cytokines that causes neuronal damage [20,22]. This 'Dr. Jekyll and Mr. Hyde' nature of Mn in physiological *milieu* is well documented [1,21,23,24]. But little is known about its *in vivo* behavior and toxicity in the nano form. Over the past decade, the use of Mn-containing nanomaterials in wide range of applications starting from catalysis [25-27], gas sensing [28-30], energy storage [31-33], molecular adsorption [34,35], magnetic data storage [31,36] to biomedical imaging [37-40] and therapeutics (e.g., in treatment of neonatal hyperbilirubinemia [41], hepatic fibrosis [42,43] etc.) have grown in leaps and bounds, so is the potential risk of human exposure.

Recently, we explored organ specific toxic effects of surface coated Mn_3O_4 nanoparticles (NPs) in BALB/c mice upon repeated dose (90 days) oral exposure. The NPs, at a dose of 0.5 mg kg^{-1} body weight (BW), showed impaired liver function and mild reversible lung inflammation, owing to their inherent ability to generate ROS and modulate cellular redox equilibrium. However, due to limited scope of the study, we were unable to explore the neurologic consequences of chronic Mn_3O_4 NP exposure and as a result of which, significant ignorance still exists about its interference in neurobehavioral function. The work presented here extends these observations and focuses on the effect of chronic repeated dose exposure of manganese oxide nanoparticles at the similar dose that displayed hepatic and reproductive toxicity in earlier studies (0.5 mg kg^{-1} BW) on some selected behavioral, neurochemical and molecular parameters in rodent model (C57BL/6j). The results illustrate that citrate functionalized Mn_3O_4 NPs (C- Mn_3O_4 NPs) are not only non-toxic to CNS but also have the potential to ameliorate the otherwise irreversible PD like neurologic sequelae induced by overexposure to $MnCl_2$. Sequestration of Mn-ions on NP surface, and subsequent modulation of cellular redox system through mitochondrial protection plays the major role in this therapeutic aspect.

7.2. RESULTS AND DISCUSSION

7.2.1. Manganese Neurotoxicity: Nano-oxide Compensates the Ion-damage in Mammals [44]

Excess Mn initially accumulates in globus pallidus, one of the four nuclei (i.e., globus pallidus, substantia nigra, subthalamic nucleus and the striatum) present in basal ganglia with inhibitory gamma aminobutyric acid (GABA) projection, and induces TNF-α and inducible nitrogen synthase (iNOS) [45,46], which leads to mitochondrial dysfunction and cellular damage [20,47]. An initial insult to globus pallidus results in decreased inhibitory GABA input to the subthalamic nucleus, and subsequent disinhibition of the down-stream Glu output to the substantia nigra (Figure 7.1a), leading to chronic over-stimulation. The glutamatergic system of the basal ganglia is also disrupted in Mn overexposure, due to the involvement of the subthalamic nucleus. Glu deregulation can lead to significant cellular consequences, as excess extracellular Glu and its ensuing excitotoxicity are well documented. The nuclei comprising the basal ganglia are responsible for integrating and coordinating information from various brain regions associated with motor movements [48-50]. So, we evaluated the motor functions of C57BL/6j mice administered with either normal saline, $MnCl_2$, C-Mn_3O_4 NPs or a combination of $MnCl_2$ and C-Mn_3O_4 NPs via four tests: beam traversal, pole descent, nasal adhesive removal, and hind limb clasping reflexes. $MnCl_2$-administered mice (4 weeks) required significantly more time to cross a challenging beam (Figure 7.1b), and to descend a pole (Figure 7.1c), two measures of gross motor function compared to control- or C-Mn_3O_4 NP-treated littermates. Interestingly, treatment with C-Mn_3O_4 NP (0.5 mg kg^{-1} BW for 21 days) on $MnCl_2$-intoxicated mice resulted in recovery of above mentioned two gross motor functions (Figure 7.1b-7.1c). Removal of an adhesive from nasal bridge, a test for fine motor control, was impaired in $MnCl_2$ mice compared to other three (Figure 7.1d). Finally, the hindlimb clasping reflex, a measure of striatal dysfunction, was defective in $MnCl_2$-treated mice, which was recovered upon treatment with C-Mn_3O_4 NP (Figure 7.1e).

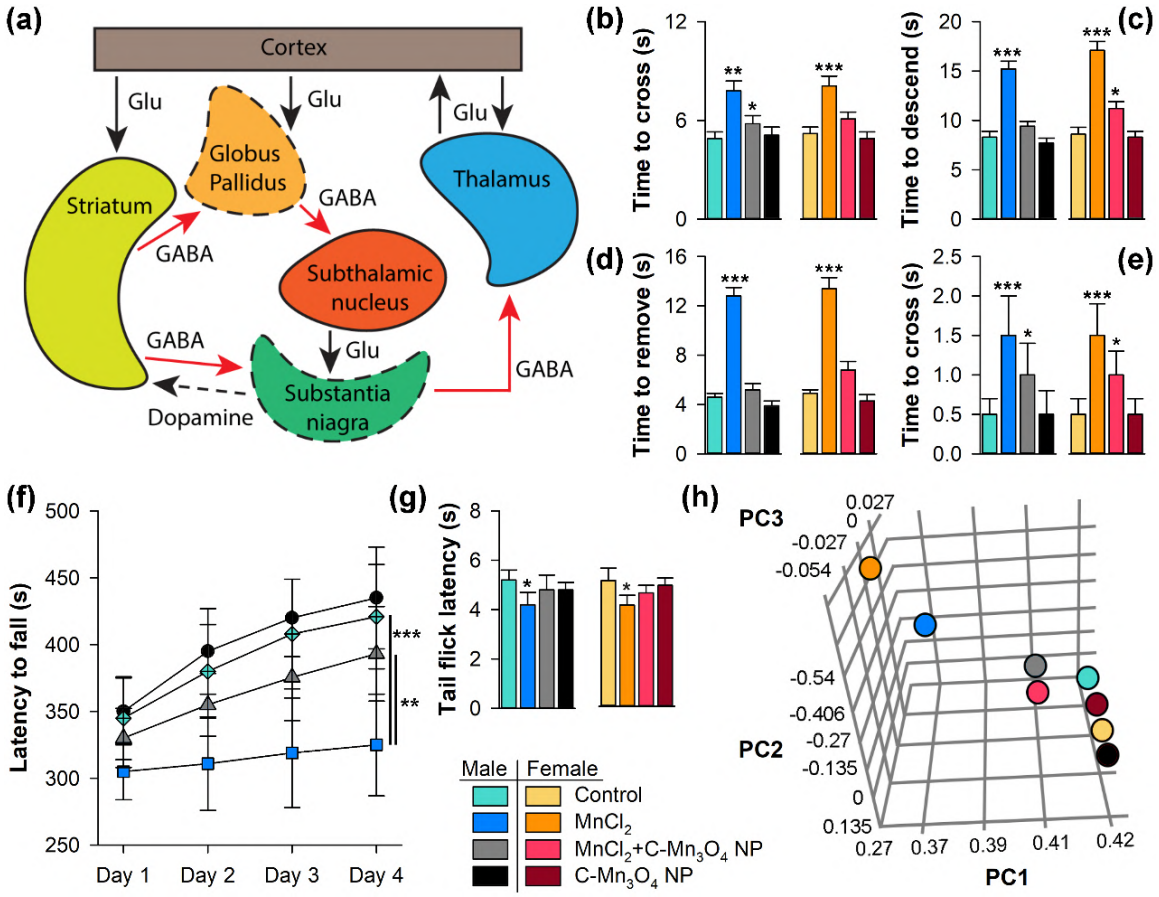

Figure 7.1. *Effect of C-Mn_3O_4 NPs on motor function, anxiety like behaviour and brain antioxidant enzyme status. (a) Schematic of the basal ganglia circuitry and relevant neurotransmitters during high Mn exposure. Nuclei with dotted outlines are those putatively affected during the pathogenic condition, resulting in degeneration and down-regulation of their respective neurotransmitters. (b) Time to traverse beam apparatus. (c) Time to descend poles. (d) Time to remove adhesive from nasal bridge. (e) Hind-limb clasping reflex score. (f) Latency to fall in rotarod test. (g) Tail flick latency. (h) Principal component analysis shows, both control and C-Mn_3O_4 NPs treated mice showed similar motor function while the $MnCl_2$ treated mice were significantly different. Data are expressed as Mean ± SD. N=10. *, **, *** Values differ significantly from control group (without treatment) (***p < 0.001; **p < 0.01; *p < 0.05).*

Administration of C-Mn_3O_4 NPs alone did not affect any of the functions (Figure 7.1e). To evaluate the sensory motor functions, tail-flick assay and rotarod tests were performed. In rotarod test, motor learning was characterized by improvement of the performances (latency to fall) over three trials. Only in $MnCl_2$-treated mice, latencies to fall were lower in all three trials (Figure 7.1f) which is a signature of sensory motor function deficit. Although, the C-Mn_3O_4 NP treated animals apparently performed better than control mice (Figure 7.1f), the change is

statistically insignificant. Similar results were found in tail-flick test (Figure 7.1g), where the mice administered with $MnCl_2$ showed longer tail-flick latency, thus lower pain sensitivity in the first trial, although this difference was not apparent in subsequent trials (data not shown). Indeed, compilation of all motor phenotypes into a principal-component analysis (PCoA) displays a striking segregation by the $MnCl_2$ treated group, while animals treated with C-Mn_3O_4 NPs cluster more similarly to control animals (Figure 7.1h). Together, these data demonstrate that Mn in the ionic form promotes the hallmark motor dysfunction that resembles Parkinson's like syndrome, while Mn in nano-oxide form reverses them.

Next, we evaluated the anxiolytic behavior of C-Mn_3O_4 NPs. It is well documented that Mn^{2+} causes toxic effects on hippocampal neurons via mitochondrial dysfunction. As hippocampus is affected, the limib system gets distorted and as a result emotional events like anxiety, fear, and memory are also altered [51,52]. Open field test (OFT) was used to evaluate thigmotaxis of the animals as an index of anxiety. $MnCl_2$-treatment increased the thigmotactic behavior, as indicated by reduced time spent in the center zone (Figure 7.2a-7.2b). C-Mn_3O_4 NP- treated mice spent the highest time at the center, while $MnCl_2$+C-Mn_3O_4 NP treated mice were somewhat in the middle. The total distance covered by the animals and respective velocity were comparable for all, except the $MnCl_2$ intoxicated mice (Figure 7.2c-7.2d). Probably the decreased locomotor function played a role in this observation. However, it was quite clear that C-Mn_3O_4 NPs possess anxiolytic property, which effectively reversed the anxiety like behavior induced due to Mn-toxicity. To further confirm this hypothesis, mice were tested for anxiety-like behavior in elevated plus maze (EPM) apparatus. In line with previous works, $MnCl_2$-treated mice spent significantly less time in the open arms of the EPM compared to other three groups (Figure 7.2e-7.2f). The distance moved in the open arms showed similar trends (Figure 7.2g). Like OFT, here also, total distance moved was less for the $MnCl_2$-treated mice (Figure 7.2h). In accordance with this behavior, the $MnCl_2$-treated mice spent more time in the center of the apparatus. All these behavioral features indicated the anxiety induced due to severe Mn-neurotoxicity, which was ameliorated upon treatment with C-Mn_3O_4 NPs. We used another behavioral method, light preference test [53], to validate the observations about anxiolytic effects of Mn_3O_4 NPs. Here, decreased mobility in the light area is

considered as a symbol of anxiety [53,54]. $MnCl_2$-treated mice showed both lower activity (Figure 7.2i) and transitions in the light zone (Figure 7.2j), whereas C-Mn_3O_4 NPs treatment recovers their normal activity.

Another aspect of Mn-induced neurotoxicity is its ability to introduce depression-like behavior in rodents [1,55]. We used forced swim test (FST) to evaluate depression-like behavior. Here, high immobility time is considered as a signature of depression [56]. In accordance with previous studies, $MnCl_2$ treatment resulted in increased immobility time (Figure 7.2k) [1,55]. Treatment with C-Mn_3O_4 NPs decreased the sign of depression reflected in lower immobility time (Figure 7.2k). The other two groups remain similar. The antidepressant like action of C-Mn_3O_4 NPs were further analyzed by measuring climbing, swimming time and latency to first immobility event. We found that climbing activity was reduced in $MnCl_2$ treated groups, even after C-Mn_3O_4 NP treatment (Figure 7.2l). Total swimming time (Figure 7.2m) or latency to first immobility (Figure 7.2n) were similar across the groups. The depression-like behavior in $MnCl_2$-treated mice were followed by anhedonia, as measured in sucrose preference test (SPT) (Figure 7.2o). All of the other three groups showed similar preference for sucrose, indicating therapeutic effect of C-Mn_3O_4 NPs (Figure 7.2o).

Previous works suggested that chronic exposure of manganese may display memory deficit and affective disturbances reminiscent of early stage of PD [57]. To characterize whether C-Mn_3O_4 NP can reverse the degeneration of mesolimbic dopamine pathway by manganism, we used novel object recognition, Morris water maze (MWM) and sociability test. To elucidate the behavioral complications of $MnCl_2$-treated mice, we examined the recall memory using a novel object recognition task. After three days of 15-min habituation trials in the testing field, mice were allowed to explore two identical objects for 5 min and were then returned to their home cages. After a delay period of 60 min, one familiar object was replaced with a similar but novel object and the mice were allowed another 2 min of exploration time during which their interaction time with each object was measured (Figure 7.3a). As expected in animals with a fully intact recall memory, the control mice spent more time with the novel object than the familiar one (Figure 7.3b & 7.3c). In contrast, $MnCl_2$-treated

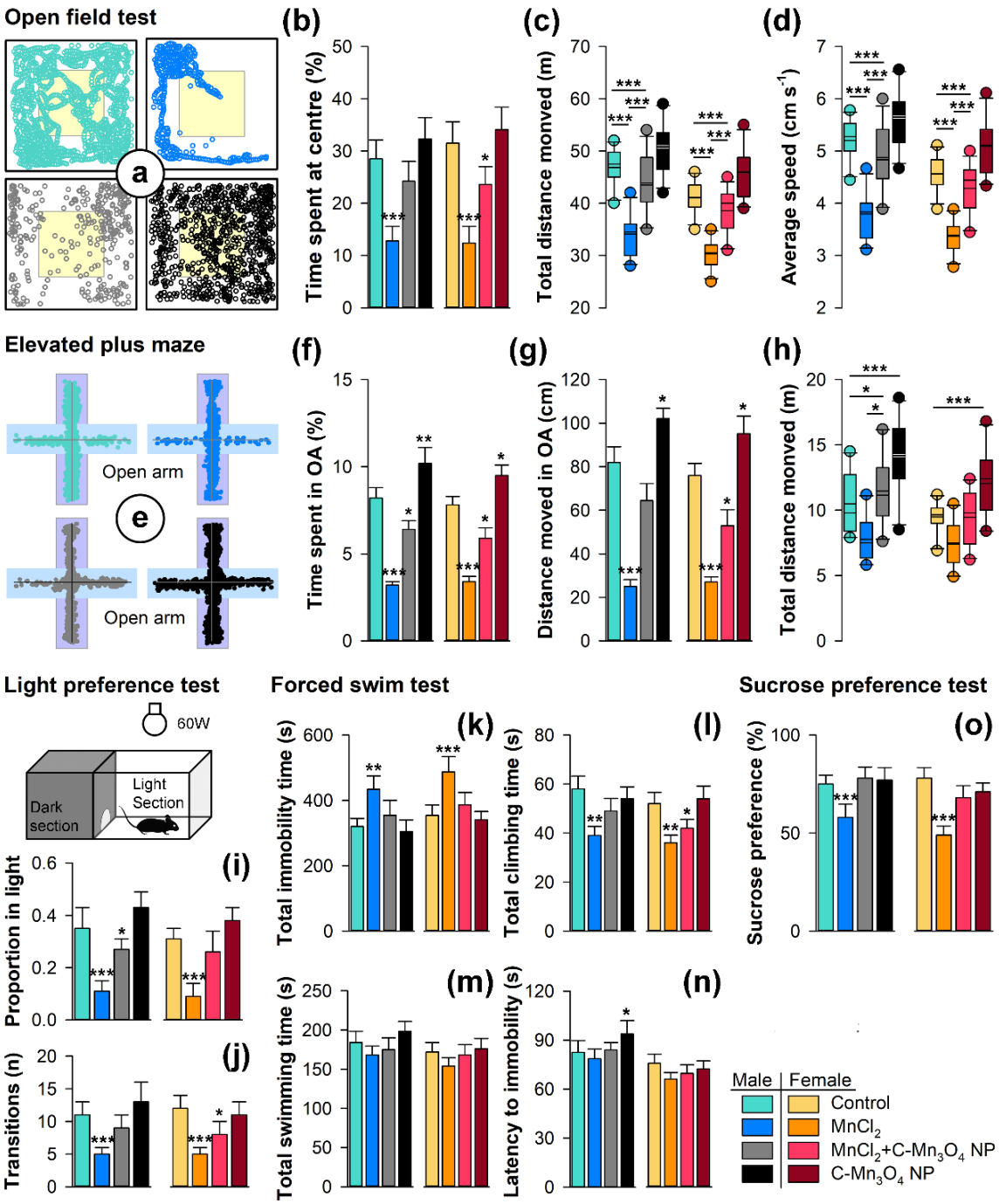

Figure 7.2. *Effect of C-Mn_3O_4 NPs on anxiety and depression like behaviour. Open field test. (a) Trace of open field activity. (b) Time spent at the centre. (c) Total distance moved. (d) Average speed. Elevated plus maze test. (e) Trace of movement in EPM. (f) Time spent in open arm. (g) Distance moved in open arm. (h) Total distance moved. Light preference test. (i) Time spent in light zone. (j) Transitions into light zone. Forced swim test. (k) Total immobility time (l) Total climbing time (m) Total swimming time and (n) Latency to first immobility event in forced swim test (FST). (o) Sucrose preference test. Data are expressed as Mean ± SD. N=10. *, **, *** Values differ significantly from control group (without treatment) (***p < 0.001; **p < 0.01; *p < 0.05).*

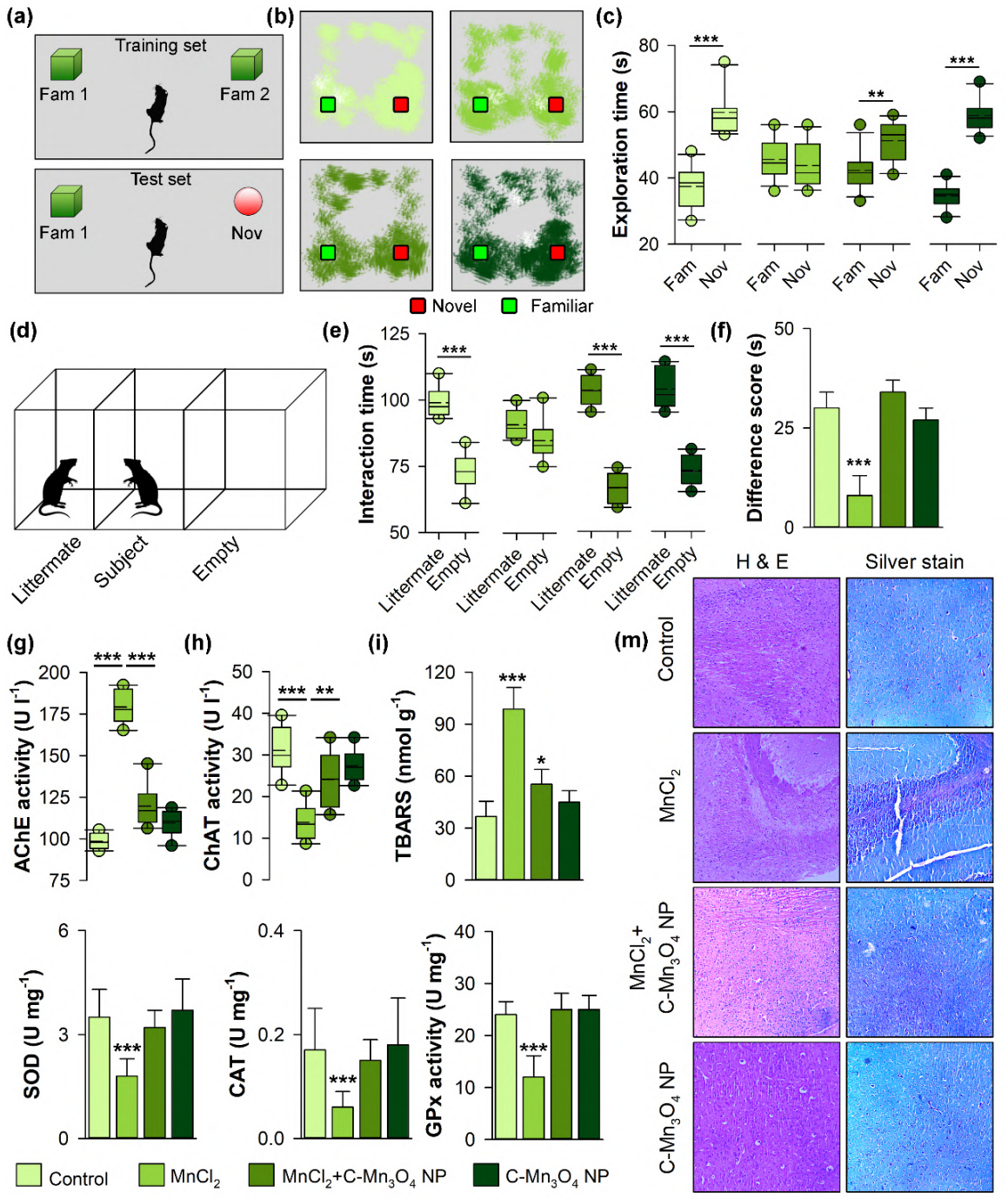

Figure 7.3. *Effect of C-Mn_3O_4 NPs on memory and oxidative parameters of brain. (a) Representation novel object recognition test. (b) Trace of movement in novel object recognition test. (c) Exploration time. (d) Representative diagram for Sociability Test. (e) Interaction time with littermate and time spent at empty space over 5 minutes of test (f) Difference scores. (g & h) Acetylcholine esterase and choline acetyltransferase activity in brain. (i-l) Effect of C-Mn_3O_4 NPs on brain antioxidant defence system. (m) Histological sections of brain. Data are expressed as Mean ± SD. N=10. *, **, *** Values differ significantly from control group (without treatment) (***p < 0.001; **p < 0.01; *p < 0.05).*

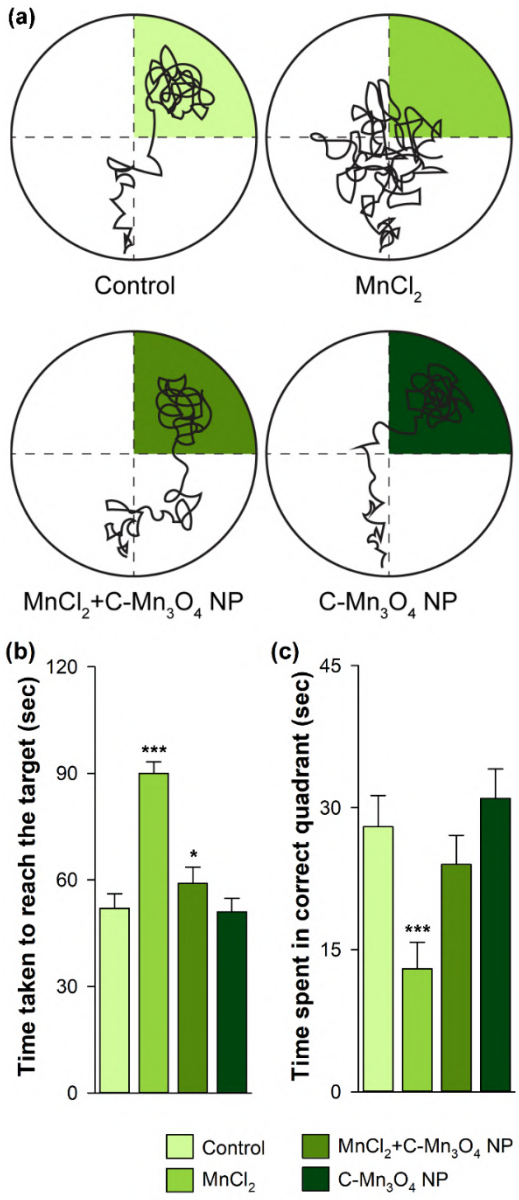

Figure 7.4. *Effect of C-Mn_3O_4 NPs on hippocampus dependent spatial learning as measured by Morris water maze test. (a) Representative swimming paths in the Morris water maze. The colored part depicts the target quadrant. (b) Time taken to reach the target. (c) Time spent in the target quadrant.Data are expressed as Mean ± SD. N=6. *, **, *** Values differ significantly from control group (without treatment) (***p < 0.001; **p < 0.01; *p < 0.05).*

mice showed no discrimination between the novel and familiar objects (Figure 7.3b & 7.3c). However, treatment with C-Mn_3O_4 NPs recovered the $MnCl_2$-treated mice from profound cognitive deficit resulting from dysregulation of hippocampus dependent learning and memory (Figure 7.3b & 7.3c). To further test the effect of C-Mn_3O_4 NPs on $MnCl_2$ induced dysregulation of hippocampus dependent learning and memory we

used MWM test. For the $MnCl_2$ treated group we found severe decline in spatial learning reflected into its failure to find the platform within the given time (Figure 7.4a). Number of time these animals entered the target quadrant is very minimal and insignificant (Figure 7.4b & 7.4c). On the other hand, the animals that received both $MnCl_2$ and C-Mn_3O_4 NPs successfully found the hidden platform within the given time, although the time taken to reach the platform was longer than the control group (Figure 7.4b & 7.4c). Other group i.e. the C-Mn_3O_4 NP treated group performed as good as the control group (Figure 7.4b & 7.4c). The above outcomes indicates severe hippocampal damage due to the $MnCl_2$ treatment. Co-treatment with C-Mn_3O_4 NPs successfully retrieved the animals from hippocampal damage.

To assess directly the impact of $MnCl_2$ and subsequent administration of C-Mn_3O_4 NPs on hippocampus mediated social behavior, we first compared the performance of $MnCl_2$-treated mice with that of control ones in a three-chamber test of sociability [58], which examines the normal preference of a subject mouse for a chamber containing a littermate versus an empty chamber (Figure 7.3d). Control mice spent more time investigating the compartment containing the littermate versus the empty compartment, resulting in a difference score of 30.15 ± 4.04 s. In contrast, $MnCl_2$-treated mice had a difference score of 8.23 ± 5.12, which is significantly lower than that of control mice ($p<0.001$) (Figure 7.3e & 7.3f). C-Mn_3O_4 NP treatment of $MnCl_2$-intoxicated mice recovered the difference score similar to the control (34.05 ± 3.57). The mouse treated with C-Mn_3O_4 NPs showed no difference (difference score 27.43 ± 3.21) with that of control. The average investigation time for the control mice was 99.01 ± 5.51 s for the littermate and 73.14 ± 6.83 s for the empty compartment. The average investigation time for the $MnCl_2$-treated mice was 90.83 ± 5.21 s for the littermate and 84.83 ± 7.90 s for the empty compartment. Therefore, $MnCl_2$-treated mice are less attracted to social stimuli than their wild-type littermates. However, treatment with C-Mn_3O_4 NPs can recover the social deficit (average investigation time was 103.16 ± 5.21 s for the littermate and 69.33 ± 5.39 s for the empty compartment) as observed in sociability test (Figure 7.3e & 7.3f). In summary, the C-Mn_3O_4 NPs do not show the hallmark neurotoxicity displayed by manganism, rather, protect the CNS from it.

Motor deficits and other changes in emotional behaviors in Mn-induced Parkinson's like syndromes coincide with increase in acetylcholinesterase (AChE) activity in different brain regions of $MnCl_2$ treated mice (Figure 7.3g), which is well in agreement with previous studies [59-61]. C-Mn_3O_4 NP treatment in $MnCl_2$-intoxicated mice, reduced the AChE activities in brain (Figure 7.3g) while sub-chronic administration of C-Mn_3O_4 NPs showed no significant effect (Figure 7.3g). AChE is a vital enzyme required in cholinergic neurotransmission and its regulatory role in many neurobehavioral processes is well established [62-64]. The increased AChE activity in $MnCl_2$-treated mice could result in decreased acetylcholine levels in the synaptic cleft, consequently reduced cholinergic neurotransmission efficiency and impaired locomotor and exploratory activities described in previous section of this study. The hypothesis was further supported by the decreased level of choline acetyltransferase (ChAT), an enzyme responsible for the synthesis of the neurotransmitter acetylcholine [65], in $MnCl_2$-treated mice (Figure 7.3h). Treatment with C-Mn_3O_4 NPs regenerated the normal level of ChAT (Figure 7.3h). The damage in cholinergic system was accompanied by notable decrease in antioxidant enzymes, i.e., superoxide dismutase (SOD), catalase (CAT), and glutathione peroxidase (GPx) and subsequent increase in biomarkers of oxidative stress, i.e., malonaldehyde (MDA) level (Figure 7.3i-7.3l). C-Mn_3O_4 NPs were able to recover their activities within the treatment regime.

Behavioral outcomes and biochemical assessments were complemented with histological findings (Figure 7.3m and Figure 7.5). The control and C-Mn_3O_4 NP treated groups showed normal cellular architecture with defined cell structure and prominent nuclei in all of the brain regions (Figure 7.5a-e). $MnCl_2$-intoxication caused marked neuronal degeneration in the basal ganglia region showing pathological features like apoptotic bodies, necrotic cells, degenerated and pyknotik nuclei, moderate to high cytoplasmic swelling and vacuolated cells (Figure 7.5a). As illustrated in Figure 7.5b, the substantia nigra region of $MnCl_2$-intoxicated group suffered from loss of pigmented, catecholaminergic neurons. Some of the remaining neurons contained Lewy bodies (a cytoplasmic, eosinophilic, round to elongated inclusions having dense core surrounded by pale halo), a characteristic feature of PD (Figure 7.5b). Sections from the cerebellum region shows cortical atrophy,

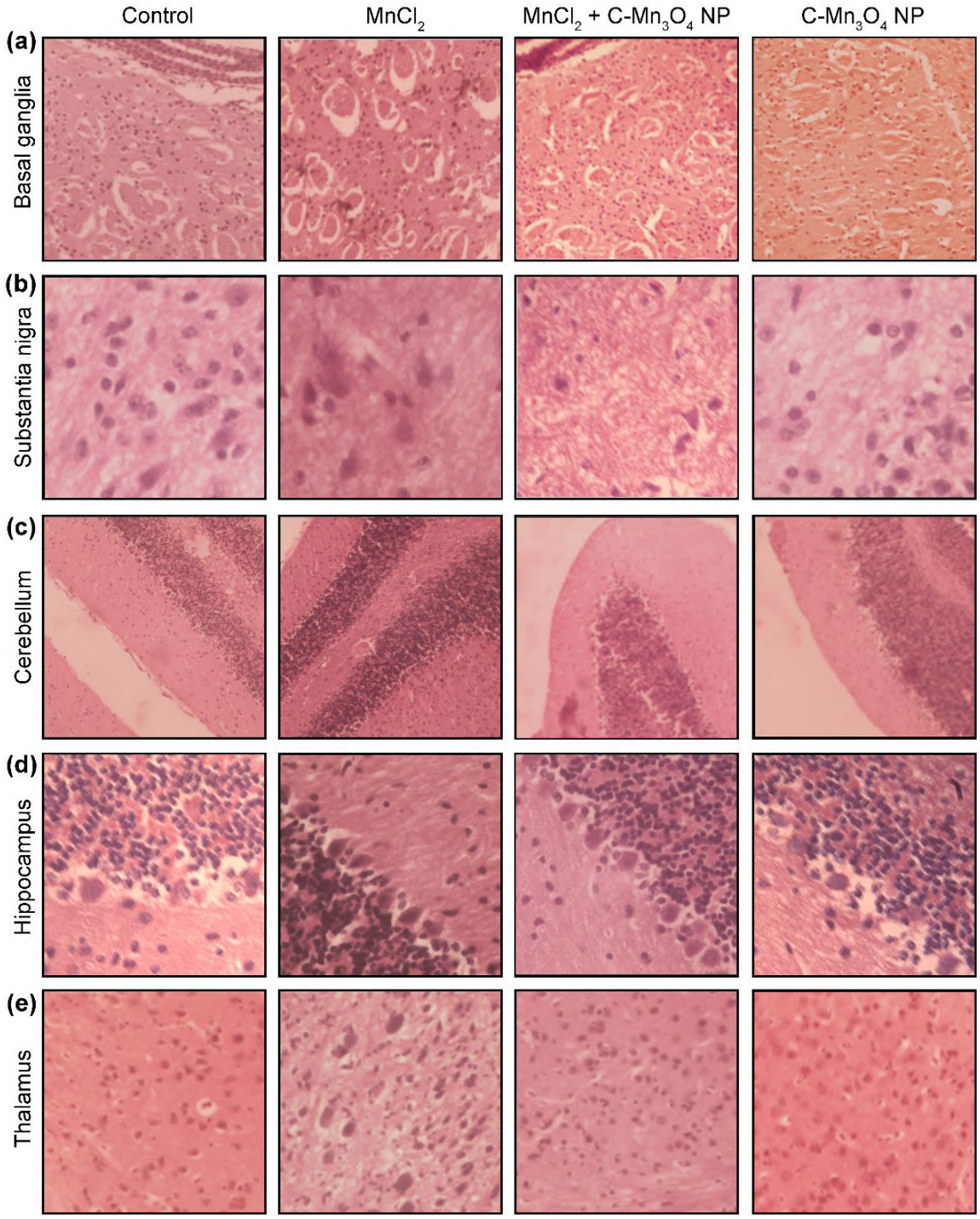

Figure 7.5. *Effect of C-Mn_3O_4 NPs on histological changes at different brain regions caused by $MnCl_2$. Control and C-Mn_3O_4 NP treated groups showed normal cellular architecture. $MnCl_2$ treated sections (particularly the basal ganglia region) showed marked apoptosis with degenerated and pyknotic nuclei. Sections from the cerebellum region shows cortical atrophy, degeneration of Purkinje neurones and small shrunken cells. Co-treatment with C-Mn_3O_4 NPs ameliorated the changes.All sections are stained with haematoxylin and eosin.*

degeneration of Purkinje neurones, deeply stained dark nuclei, and small shrunken cells (Figure 7.5c). In the hippocampal section of $MnCl_2$-treated group (Figure 7.5d), degenerative features of neuronal cells like cellular atrophy, dark neucleus and necrotic cells were observed. The thalamus region showed hyper chromatic cells and necrotic changes (Figure 7.5e). On the other hand, the aforementioned pathological features were less prominent in the C-Mn_3O_4 NP and $MnCl_2$ co-treated group (Figure 7.5) indicating the ameliorative action of C-Mn_3O_4 NPs against Mn-induced structural damage. Thus, it is clear from the above studies that C-Mn_3O_4 NPs protect the brain and neuronal cells from oxidative damage which subsequently helps in recovery of the behavioral changes that took place due to Mn-intoxication.

The therapeutic action displayed by C-Mn_3O_4 NPs could be due to two reasons, firstly through protection of Globus pallidus from oxidative stress and subsequent decrease in the excitatory damage and secondly, through chelation and subsequent removal of the Mn-ions from the brain regions. To check the second hypothesis, we performed *in vitro* spectroscopic studies. UV-vis absorption spectrum of C-Mn_3O_4 NPs at pH 7.4 (Figure 7.6) shows a prominent peak at around 290 nm which could be assigned to the possible high energy ligand-to-metal charge transfer transition (LMCT) involving citrate-Mn^{4+} interaction. The other bands at 430, 520 and 752 nm are attributed to the Jahn-Teller (J-T) distorted d-d transitions centered over Mn^{3+} ions in C-Mn_3O_4 NPs [66]. The interaction of C-Mn_3O_4 NPs with Mn^{2+} increased the intensity of the absorbance peak at 520 nm with subsequent decrease in 430 nm (Figure 7.6a). It indicates that C-Mn_3O_4 NPs can make a chelator complex with Mn^{2+} that resulted into an increase in one of the distorted d-d transitions in lower energy level. An isosbestic point at 470 nm indicates the two processes are in equilibrium. Due to interaction with protonated Mn^{2+}, the forbidden d-d transition band was further lifted with a decrease in higher energy band at 430. This was further confirmed when we compared the absorbance spectra of Mn^{2+}-C-Mn_3O_4 NPs with that of $MnCl_2$ in ethanolamine (Figure 7.7a). Here, the presence of protonated N^+ gave rise to similar lower energy d-d transition band. The LMCT band at 290 nm was simultaneously decreased due to delocalization of charge as a result of Mn^{2+} interaction with COO^- group of citrate. The stoichiometry of complexation was investigated by using

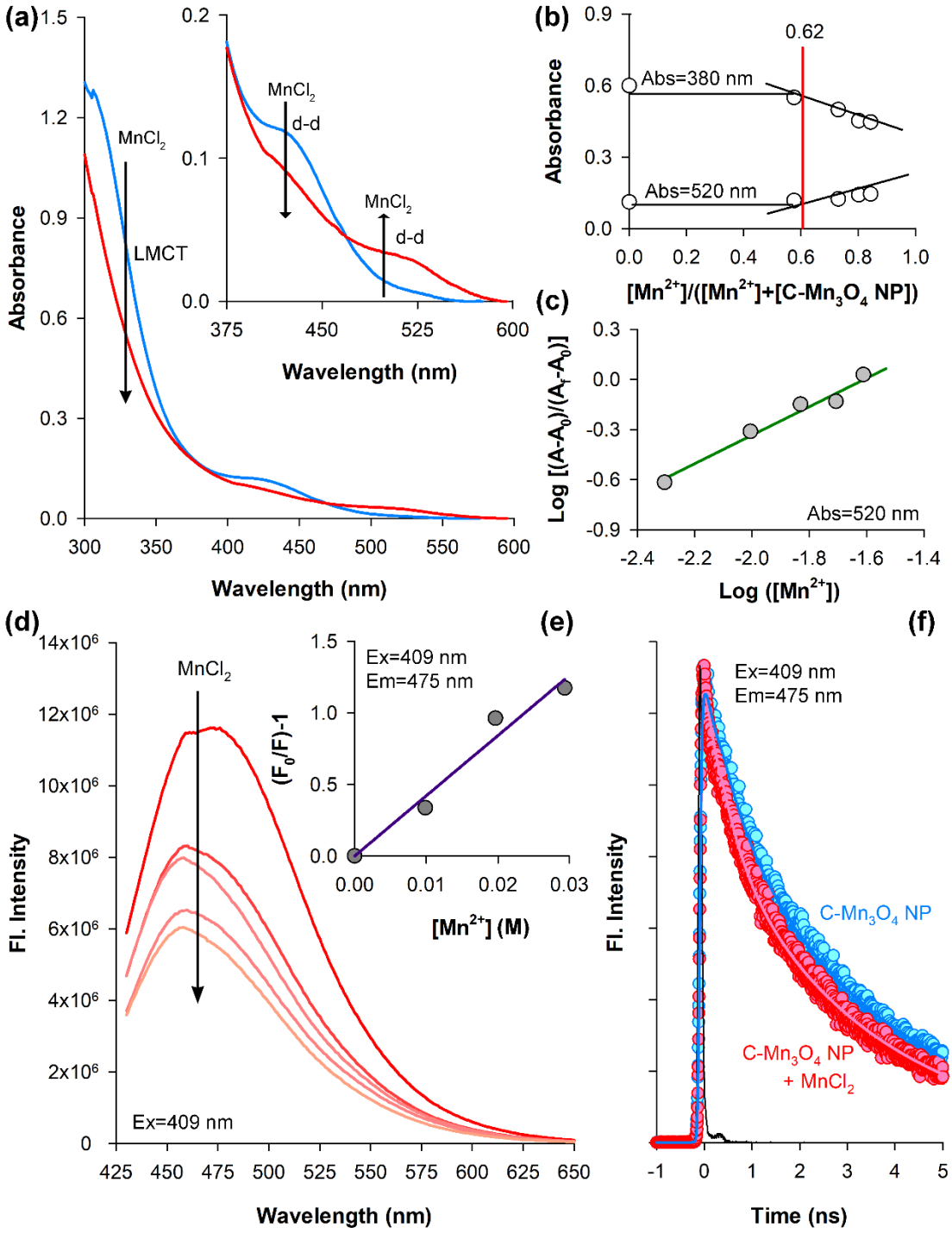

***Figure 7.6**. Interaction of Mn^{2+} with C-Mn_3O_4 NPs. (a) Absorption spectra of 3.64 × 10^{-3} M C-Mn_3O_4 NPs in the presence of varying concentrations (2.9 × 10^{-2} M) of $MnCl_2$. Arrows indicate the increase in the concentration of Mn^{2+}. (b & c) Job plot for binding of Mn^{2+} to C-Mn_3O_4 NPs. (d) Fluorescence spectra of C-Mn_3O_4 NPs (3.64 × 10^{-3} M) in the presence of different concentrations (9.8 × 10^{-3} to 94.6 × 10^{-3} M) of $MnCl_2$ (λ_{ex} = 409 nm). (e) Stern–Volmer plots for the interaction (λ_{em} = 475 nm). (f) Time-resolved fluorescence transients of C-Mn_3O_4 NPs (3.64 × 10^{-3} M) in the absence and presence of Pb^{2+} (94.6 × 10^{-3} M).*

Job's method (the method of continuous variation). Considering a global equilibrium of Mn^{2+} and n chelators (NP) on the form

$$Mn+nNP=MnNP_n$$

[Equation – 7.1]

where n is determined from the plot of the absorbance as a function of the mole fraction, f, of the added ligand.

In the absorbance maximum

$$n=\frac{f_{max}}{1-f_{max}}$$

[Equation – 7.2]

Inset of Figure 7.6b represents a typical Job plot for the Mn^{2+}–NP system, in which the transition point for absorbance appeared at the molar fraction of 0.62, suggesting that C-Mn_3O_4 NPs bound to Mn^{2+} with a 1:2 ratio in the complex. The binding constant of the C-Mn_3O_4 NPs–Mn^{2+} complex was found to be 45.70 M^{-1} (R^2 = 0.972) using the Benesi–Hildebrand equation.

$$\log\left[\frac{A-A_0}{A_f-A_0}\right]=\log\left[Mn^{2+}\right]+\log K_b$$

[Equation – 7.3]

where, A_0, A, and A_f are the absorption values, in the absence of, at the intermediate, and at the saturation of the interaction of Mn^{2+} ion, respectively, and [Mn^{2+}] represents the concentration of aqueous Mn^{2+} ion added. The binding constant (K_b) was determined by linear fitting of absorption titration curve (Figure 7.6c).

In the photoluminescence study, C-Mn_3O_4 NP shows strong emissions at ~420 nm and ~470 nm when excited at ~310 nm and ~409 nm respectively (Figure 7.6d). In the presence of Mn^{2+}, both the fluorescence quenched (Figure 7.6d). The phenomenon of fluorescence quenching can be attributed to several molecular mechanisms including excited-state reactions, molecular rearrangements, energy transfer, ground-state complex formation, and collisional quenching. In the case of C-Mn_3O_4 NP, no discernible shift in emission maxima (~420 nm and ~470 nm) or shape

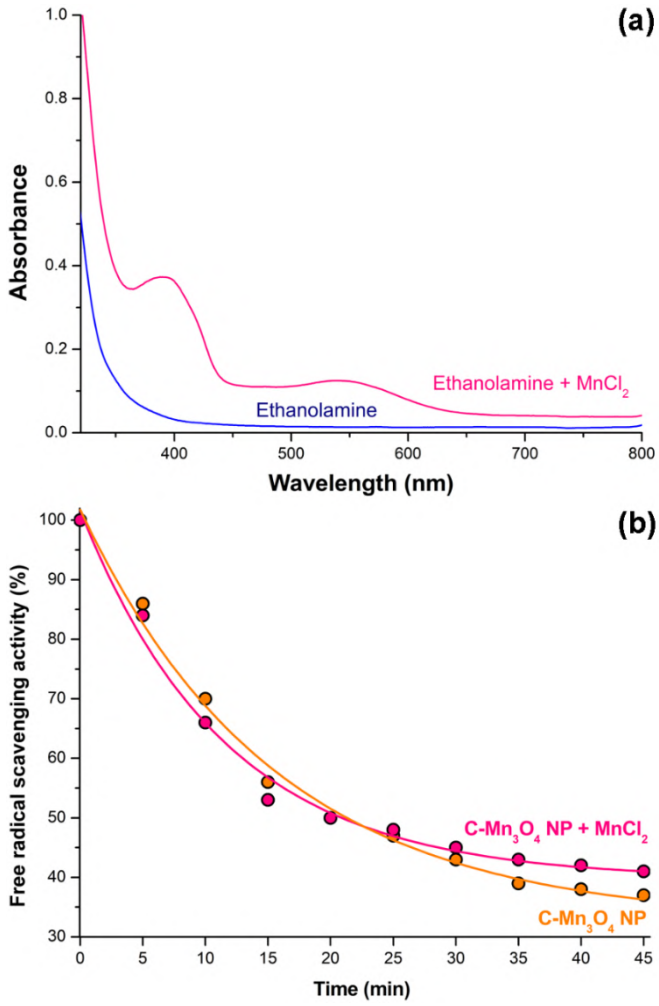

Figure 7.7. *Effect of Mn-chelation on antioxidant activity of the nanoparticle. (a) Absorbance spectra of $MnCl_2$ in ethanolamine displays prominent d-d transition bands. (b) No change in free radical scavenging activity was observed after formation of C-Mn_3O_4 NP-Mn^{2+} chelator complex, as evident from DPPH radical scavenging experiments.*

of the fluorescence spectrum accompanied quenching and the quenching behavior generally adhered to the Stern–Volmer equation (Equation – 7.4).

$$\frac{F_0}{F}-1=K_{sv}[Q]=k_q\tau_0[Q]=\frac{\tau_0}{\tau}$$

[Equation – 7.4]

where F_0 and F are the fluorescence intensities in the absence and presence of a quencher, [Q], K_{sv} is the Stern–Volmer quenching constant, k_q is the bimolecular quenching rate constant, and τ_0 and τ are the fluorescence lifetimes of the fluorophore in the absence and presence of the quencher, respectively. The linearity in the Stern–

Volmer plot (Figure 7.6e, inset) indicates the existence of a single type of quenching, either static or dynamic. To get further insight into the phenomena, we measured the excited-state fluorescence lifetime of the fluorophore (C-Mn_3O_4 NP) with increasing concentrations of the quencher, Mn^{2+} (Figure 7.6d). It is well-known that in the case of dynamic quenching, the fluorescence lifetime decreases with increasing concentrations. However, in this case, no significant change in fluorescence lifetime was observed, which clearly specifies the quenching mechanism to be static. This was further supported by the calculation of the bimolecular quenching constant, k_q (K_{sv}/τ_0), which was found to be ~1.95×10^{11} M^{-1} s^{-1} higher than that of diffusion-controlled limit (~10^{10} M^{-1} s^{-1}). This along with no change in fluorescence lifetime indicates ground-state complex formation between Mn^{2+} and C-Mn_3O_4 NPs (association constant, $K_a = K_{sv} = 42.09$ M^{-1}, similar to that found in the absorbance experiment). Probably, binding of Mn^{2+} to the NP surface inhibits the intramolecular proton transfer, resulting in the formation of a nonemissive or low-emission complex at room temperature. Thus, it can be inferred from optical spectroscopic studies that C-Mn_3O_4 NPs acted as a chelator and formed a mononuclear complex with Mn^{2+}.

One of the major concerns after chelation of Mn-ions by the NPs is their release. So, we have studied the dissolution of chelates in different pH using absorbance spectroscopic techniques. As depicted in Figure 7.8a, the dissolution was nominal both in physiological pH (~pH 7.4) and lysosomal pH (~pH 5.4). However, at very low pH (~3.0) the dissolution takes place at greater rate i.e., 50% in 4 hrs. Another concern is, the Mn ions could undergo intracellular Fenton like reaction by utilizing intracellular H_2O_2 and producing cytotoxic hydroxyl radical (OH•), which have been declared in some articles recently [67-69]. So, we tested whether the NPs can produce OH• radicals in presence of H_2O_2 using chemiluminescence of luminol. In presence of OH• radicals, luminol emits at 430 nm [70]. The results show that, the NPs were unable to produce OH• radicals in presence of H_2O_2 at pH 7.4 and pH 5.4. However, at pH 3.0 there was a significant amount of OH• radicals production (Figure 7.8b). Thus, it can be concluded that at physiological milieu the chelate is very stable, and non-cytotoxic.

To explore the possibility of C-Mn_3O_4 NPs' ability to protect cells from oxidative damage, we evaluated the antioxidant activity of C-Mn_3O_4 NPs before and

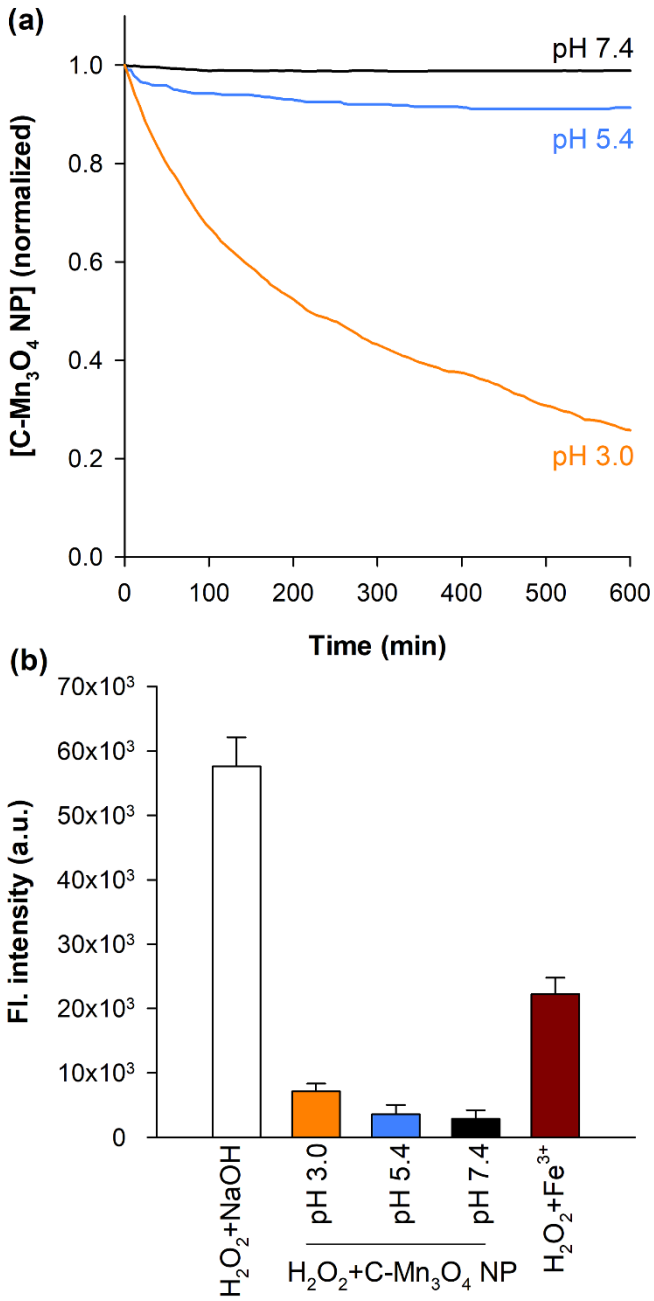

Figure 7.8. *Effect of pH on dissolution of Mn ions from C-Mn_3O_4 NPs and their effect on in vitro Fenton like reaction. (a) Dissolution profile of Mn_3O_4 NPs at different pH. (b) Chemiluminiscence of luminol as a marker of OH• free radical.*

after Mn^{2+} chelation using the DPPH assay. Figure 7.7b shows that C-Mn_3O_4 NPs were able to retain its free-radical scavenging activity even after Mn^{2+} chelation. This antioxidant activity could be linked to the transfer of electron density from oxygen atom to odd electron located at nitrogen atom in DPPH which results in decreasing $n \rightarrow \pi^*$ transition intensity at 535 nm [71,72]. Another possibility could be the transfer

of free electrons to DPPH• radical due to disproportionation and comproportionation phenomena involving the Mn^{2+}, Mn^{3+} and Mn^{4+} ions of the Mn_3O_4 spinnel structure [43,73]. As depicted in the spectroscopic studies, even after binding of Mn-ions, the structure remains same and redox active, resulting into unaltered antioxidant capacity. This *in vitro* antioxidant activity was exactly reflected in brain antioxidant enzyme system. As a result, $MnCl_2$ induced declined activity of SOD, CAT and GPx activities were recovered upon C-Mn_3O_4 NP treatment.

To understand the molecular mechanism of action, we examined effect of C-Mn_3O_4 NPs on mitochondria as the critical role of mitochondrial injury in the pathogenesis of Mn toxicity is well documented [74]. It has been found that Mn is accumulated in the mitochondrial matrix via calcium transporters [75,76]. After its accumulation, Mn ions can cause mitochondrial damage by disrupting the respiratory electron transport chain (ETC) resulting into ATP depletion that may cause apoptosis [74,75]. Mn ions can further induce cell death via opening of a non-specific pore in the inner mitochondrial membrane, i.e, mitochondrial permeability transition (mPT) that alters the mitochondrial membrane potential leading to necrosis [43,74]. In addition, manganese ions also facilitate fenton like reaction (the conversion of O_2•- radicals to OH radicals) that in turn induces apoptosis via DNA damage and lipid peroxidation. In the current *in vivo* model of manganism, we found that brain mitochondrial function was impaired in Mn-treated animals (Figure 7.9). Increased mitochondrial permeabilization (mitochondrial swelling or mPTP formation) (Figure 7.9a), decreased mitochondrial dehydrogenases activity (Figure 7.9b), dysregulated mitochondrial membrane potential (Figure 7.9c), decreased ATP level (Figure 7.9d), decreased complex IV activity (Figure 7.9e) and increased mitochondrial lipid peroxidation (Figure 7.9f) was evident in the brain tissue of Mn-exposed animals. These deteriorating changes in mitochondrial parameters resulted into neuronal degenerations observed in the histological findings. C-Mn_3O_4 NPs were able to protect mitochondria from aforementioned damages (Figure 7.9). The ability of the NPs in chelation of Mn-ions and subsequent antioxidant activity, both are responsible for the observed ameliorative activity. Chelation of Mn-ions protects the mitochondrial membrane from pore formation, whereas the antioxidant activity helps in scavenging

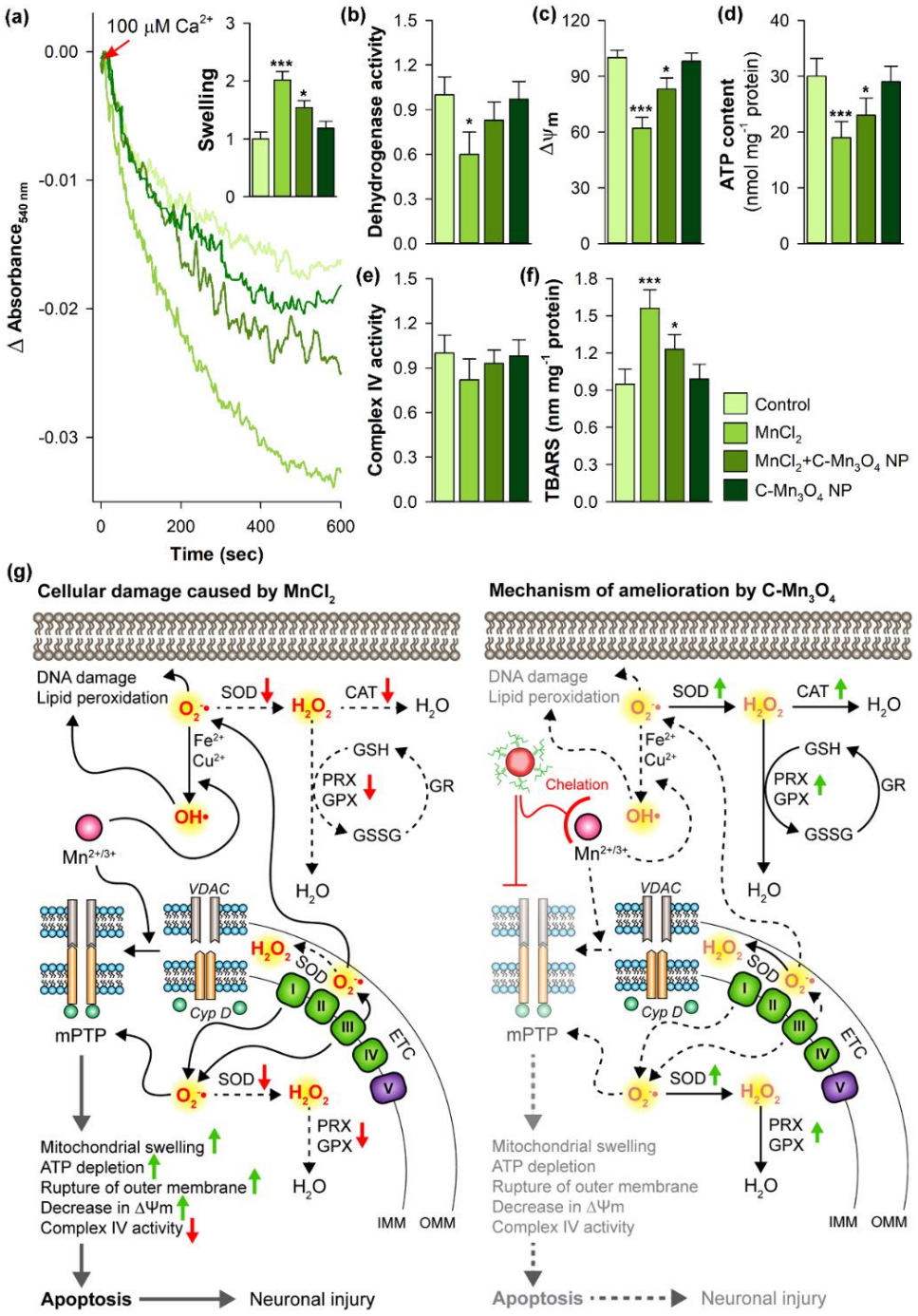

Figure 7.9. *Effect of C-Mn_3O_4 NPs on mitochondria. (a) Effect on mitochondria permeability transition, measured as decrease in absorbance at 540 nm. Inset shows extent of mitochondrial swelling in comparison to Control. (b) Mitochondrial dehydrogenase activity. (c) Relative change in mitochondrial membrane potential. (d) ATP content. (e) Complex IV activity. (f) Mitochondrial lipid peroxidation. (g) Schematic representation of the mechanism of action of C-Mn_3O_4 NPs on intracellular antioxidant system (SOD, CAT, GSH, and GPx) and mitochondria. Red and green arrows represent up- and down-regulation respectively. The dotted arrows represent deregulated pathways. The faded processes in the right panel describes inhibition by C-Mn_3O_4 NPs. Data are expressed as Mean ± SD. N=6. *, **, *** Values differ significantly from control group (without treatment) (***$p < 0.001$; **$p < 0.01$; *$p < 0.05$).*

of the free radicals and reduction of associated oxidative damage. The aforementioned possible molecular biology mechanism of the Mn-induced brain injury at convalescence is schematically represented in Figure 7.9g.

7.3. CONCLUSION

In summary, from neurobehavioral point of view, C-Mn_3O_4 NPs are completely biocompatible and do not exhibit the characteristic PD like symptoms of manganese toxicity. Furthermore, it is capable of ameliorating Mn-induced neurotoxicity owing to its unique property of chelating harmful excess Mn^{2+}-ions *in vivo* and subsequent antioxidant activity to heal the oxidative damage caused by mitochondrial dysfunction. To, the best of our understanding, engineering of such biocompatible nanoparticles capable of chelating harmful metal ions along with substantial antioxidant activity may pave a new way in designing therapeutic strategy against other neurobehavioral disorders like Parkinson's, Alzheimer's, Huntington's which are pathophysiologically modulated by mitochondrial oxidative damage.

REFERENCES

[1] S. Bouabid, C. Delaville, P. De Deurwaerdère, N. Lakhdar-Ghazal, A. Benazzouz, PLoS ONE 9 (2014) e98952.

[2] R. Leach Jr, A. M. Muenster, E. M. Wien, Arch. Biochem. Biophys. 133 (1969) 22.

[3] H.-G. Bernstein, C. Derst, C. Stich, H. Prüss, D. Peters, M. Krauss, B. Bogerts, R. Veh, G. Laube, Amino Acids 40 (2011) 453.

[4] Z. F. Kanyo, L. R. Scolnick, D. E. Ash, D. W. Christianson, Nature 383 (1996) 554.

[5] F. C. Wedler, R. B. Denman, W. G. Roby, Biochemistry 21 (1982) 6389.

[6] A. S. Mildvan, M. C. Scrutton, M. F. Utter, J. Biol. Chem. 241 (1966) 3488.

[7] M. C. Scrutton, M. F. Utter, A. S. Mildvan, J. Biol. Chem. 241 (1966) 3480.

[8] J. M. McCord, I. Fridovich, J. Biol. Chem. 244 (1969) 6049.

[9] J. M. McCord, I. Fridovich, J. Biol. Chem. 244 (1969) 6056.

[10] B. Groppel, M. Anke, Arch. Exp. Veterinarmed. 25 (1971) 779.

[11] M. R. Smith, J. Fernandes, Y. M. Go, D. P. Jones, Biochem. Biophys. Res. Commun. 482 (2017) 388.

[12] Y. M. Go, D. P. Jones, Redox Biol. 2 (2014) 358.

[13] M. Quadri, A. Federico, T. Zhao, G. J. Breedveld, C. Battisti, C. Delnooz, L. A. Severijnen, L. D. T. Mammarella, A. Mignarri, L. Monti, Am. J. Hum. Genet. 90 (2012) 467.

[14] K. Tuschl, P. T. Clayton, S. M. Gospe Jr, S. Gulab, S. Ibrahim, P. Singhi, R. Aulakh, R. T. Ribeiro, O. G. Barsottini, M. S. Zaki, Am. J. Hum. Genet. 90 (2012) 457.

[15] K. Mukhtiar, S. Ibrahim, K. Tuschl, P. Mills, Brain Dev. 38 (2016) 862.

[16] T. R. Guilarte, N. C. Burton, J. L. McGlothan, T. Verina, Y. Zhou, M. Alexander, L. Pham, M. Griswold, D. F. Wong, T. Syversen, J. Neurochem. 107 (2008) 1236.

[17] R. G. Lucchini, C. J. Martin, B. C. Doney, NeuroMolecular Med. 11 (2009) 311.

[18] M. G. Cersosimo, W. C. Koller, Neurotoxicology 27 (2006) 340.

[19] S. Sarkar, E. Malovic, D. S. Harischandra, H. A. Ngwa, A. Ghosh, C. Hogan, D. Rokad, G. Zenitsky, H. Jin, V. Anantharam, Neurotoxicology 64 (2018) 204.

[20] S. Sarkar, D. Rokad, E. Malovic, J. Luo, D. S. Harischandra, H. Jin, V. Anantharam, X. Huang, M. Lewis, A. Kanthasamy, Sci. Signal. 12 (2019) eaat9900.

[21] E. A. Malecki, Brain Res. Bull. 55 (2001) 225.

[22] J. Y. Chang, L. Z. Liu, Mol. Brain Res. 68 (1999) 22.

[23] J. Crossgrove, W. Zheng, NMR in Biomed. 17 (2004) 544.

[24] S. L. O'Neal, W. Zheng, Curr. Environ. Health Rep. 2 (2015) 315.

[25] Y. F. Han, F. Chen, Z. Zhong, K. Ramesh, L. Chen, E. Widjaja, J. Phys. Chem. B. 110 (2006) 24450.

[26] T. Rhadfi, J. Y. Piquemal, L. Sicard, F. Herbst, E. Briot, M. Benedetti, A. Atlamsani, Appl. Catal. A 386 (2010) 132.

[27] E. Saputra, S. Muhammad, H. Sun, H. M. Ang, M. O. Tadé, S. Wang, J. Colloid Interface Sci. 407 (2013) 467.

[28] L. Zhang, Q. Zhou, Z. Liu, X. Hou, Y. Li, Y. Lv, Chem. Mater. 21 (2009) 5066.

[29] J. J. Kellogg, T. N. Graf, M. F. Paine, J. S. McCune, O. M. Kvalheim, N. H. Oberlies, N. B. Cech, J. Nat. Prod. 80 (2017) 1457.

[30] T. Zhou, X. Liu, R. Zhang, L. Wang, T. Zhang, Adv. Mater. Interfaces 5 (2018) 1800115.

[31] W. S. Seo, H. H. Jo, K. Lee, B. Kim, S. J. Oh, J. T. Park, Angew Chem. Int. Ed. Engl. 43 (2004) 1115.

[32] D. K. Kim, P. Muralidharan, H. W. Lee, R. Ruffo, Y. Yang, C. K. Chan, H. Peng, R. A. Huggins, Y. Cui, Nano Lett. 8 (2008) 3948.

[33] E. Hosono, T. Kudo, I. Honma, H. Matsuda, H. Zhou, Nano Lett. 9 (2009) 1045.

[34] Y. F. Shen, R. P. Zerger, R. N. DeGuzman, S. L. Suib, L. McCurdy, D. I. Potter, C. L. O'Young, Science 260 (1993) 511.

[35] P. Li, C. Nan, Z. Wei, J. Lu, Q. Peng, Y. Li, Chem. Mater. 22 (2010) 4232.

[36] V. Pan'kov, Ceram. Int. 14 (1988) 87.

[37] J. Shin, R. M. Anisur, M. K. Ko, G. H. Im, J. H. Lee, I. S. Lee, Angew Chem. Int. Ed. Engl. 48 (2009) 321.

[38] B. H. McDonagh, G. Singh, S. Hak, S. Bandyopadhyay, I. L. Augestad, D. Peddis, I. Sandvig, A. Sandvig, W. R. Glomm, Small 12 (2016) 301.

[39] T. Kim, E. J. Cho, Y. Chae, M. Kim, A. Oh, J. Jin, E. S. Lee, H. Baik, S. Haam, J. S. Suh, Angew Chem. Int. Ed. Engl. 50 (2011) 10589.

[40] X. Ding, J. Liu, J. Li, F. Wang, Y. Wang, S. Song, H. Zhang, Chem. Sci. 7 (2016) 6695.

[41] N. Polley, S. Saha, A. Adhikari, S. Banerjee, S. Darbar, S. Das, S. K. Pal, Nanomedicine 10 (2015) 2349.

[42] A. Adhikari, N. Polley, S. Darbar, D. Bagchi, S. K. Pal, Fut. Sci. OA 2 (2016) FSO146.

[43] A. Adhikari, N. Polley, S. Darbar, S. K. Pal, Mater. Focus 6 (2017) 280.

[44] A. Adhikari, M. Das, S. Mondal, S. Darbar, A. K. Das, S. S. Bhattacharya, D. Pal, S. K. Pal, Biomater. Sci. 7 (2019) 4491.

[45] J. A. Moreno, K. A. Sullivan, D. L. Carbone, W. H. Hanneman, R. B. Tjalkens, J. Neurosci. Res. 86 (2008) 2028.

[46] J. A. Moreno, K. M. Streifel, K. A. Sullivan, M. E. Legare, R. B. Tjalkens, Toxicol. Sci. 112 (2009) 405.

[47] Z. Yin, J. L. Aschner, A. P. dos Santos, M. Aschner, Brain Res. 1203 (2008) 1.

[48] A. M. Graybiel, T. Aosaki, A. W. Flaherty, M. Kimura, Science 265 (1994) 1826.

[49] A. M. Graybiel, Curr. Biol. 10 (2000) R509.

[50] A. V. Kravitz, B. S. Freeze, P. R. Parker, K. Kay, M. T. Thwin, K. Deisseroth, A. C. Kreitzer, Nature 466 (2010) 622.

[51] A. Daoust, Y. Saoudi, J. Brocard, N. Collomb, C. Batandier, M. Bisbal, M. Salomé, A. Andrieux, S. Bohic, E. L. Barbier, Hippocampus 24 (2014) 598.

[52] G. Liang, H. Qin, L. e. Zhang, S. Ma, X. Huang, Y. Lv, L. Qing, Q. Li, Y. xiong, Y. Huang, K. Chen, Y. Huang, Y. Shen, J. Nong, X. Yang, Y. Zou, Food Chem. Toxicol. 83 (2015) 261.

[53] N. Sestakova, A. Puzserova, M. Kluknavsky, I. Bernatova, Interdiscip. Toxicol. 6 (2013) 126.

[54] M. M. V. Gaalen, T. Steckler, Behav. Brain Res. 115 (2000) 95.

[55] P. Chen, S. Chakraborty, T. V. Peres, A. B. Bowman, M. Aschner, Toxicol. Res. 4 (2015) 191.

[56] D. A. Slattery, J. F. Cryan, Nat. Protoc. 7 (2012) 1009.

[57] H. Roels, R. Bowler, Y. Kim, B. C. Henn, D. Mergler, P. Hoet, V. Gocheva, D. C. Bellinger, R. Wright, M. Harris, Neurotoxicology 33 (2012) 872.

[58] L. M. DeVito, R. Konigsberg, C. Lykken, M. Sauvage, W. S. Young, H. Eichenbaum, J. Neurosci. 29 (2009) 2676.

[59] K. Fernsebner, J. Zorn, B. Kanawati, A. Walker, B. Michalke, Metallomics 6 (2014) 921.

[60] C. Liapi, A. Zarros, P. Galanopoulou, S. Theocharis, N. Skandali, H. Al-Humadi, F. Anifantaki, E. Gkrouzman, Z. Mellios, S. Tsakiris, Basic Clin. Pharmacol. Toxicol. 103 (2008) 171.

[61] M. A. Lebda, M. S. El-Neweshy, Y. S. El-Sayed, Neurotoxicology 33 (2012) 98.

[62] T. L. Rosenberry, Advances in Enzymology and Related Areas of Molecular Biology, Wiley, (2006).

[63] A. Blokland, Brain Res. Rev. 21 (1995) 285.

[64] H. Soreq, S. Seidman, Nat. Rev. Neurosci. 2 (2001) 294.

[65] Y. Oda, Pathol. Int. 49 (1999) 921.

[66] A. Giri, N. Goswami, C. Sasmal, N. Polley, D. Majumdar, S. Sarkar, S. N. Bandyopadhyay, A. Singha, S. K. Pal, RSC Adv. 4 (2014) 5075.

[67] C. Zhang, W. Bu, D. Ni, S. Zhang, Q. Li, Z. Yao, J. Zhang, H. Yao, Z. Wang, J. Shi, Angew Chem. Int. Ed. Engl. 55 (2016) 2101.

[68] Y. Zang, H. Shen, D. Huang, C.-A. Di, D. Zhu, Adv. Mater. 29 (2017) 1606088.

[69] Z. Tang, Y. Liu, M. He, W. Bu, Angew Chem. Int. Ed. Engl. 58 (2019) 946.

[70] G. Yıldız, A. T. Demiryürek, J. Pharmacol. Toxicol. Methods 39 (1998) 179.

[71] S. Kanagesan, M. Hashim, S. AB Aziz, I. Ismail, S. Tamilselvan, N. Alitheen, M. Swamy, B. Purna Chandra Rao, Appl. Sci. 6 (2016) 184.

[72] H. R. Madan, S. C. Sharma, Udayabhanu, D. Suresh, Y. S. Vidya, H. Nagabhushana, H. Rajanaik, K. S. Anantharaju, S. C. Prashantha, P. Sadananda Maiya, Spectrochim. Acta A: Mol. Biomol. Spectrosc. 152 (2016) 404.

[73] A. Giri, N. Goswami, M. Pal, M. T. Zar Myint, S. Al-Harthi, A. Singha, B. Ghosh, J. Dutta, S. K. Pal, J. Mater. Chem. C 1 (2013) 1885.

[74] M. M. Ommati, R. Heidari, V. Ghanbarinejad, A. Aminian, N. Abdoli, H. Niknahad, Nutr. Neurosci. (2019) 1.

[75] M. A. Verity, Neurotoxicology 20 (1999) 489.

[76] C. E. Gavin, K. K. Gunter, T. E. Gunter, Neurotoxicology 20 (1999) 445.

CHAPTER 08

Dual Function Nanochelator for the Treatment of Heavy Metal Toxicity

8.1. INTRODUCTION

Chelation therapy, introduced by Alfred Werner and Paul Ehrlich in early 1900s [1], is still the most effective and widely used method for treatment of heavy metal overload and associated spectrum of disorders that includes heavy metal toxicity [2-5], anaemia [6], Alzheimer's [7,8], Parkinson's [9,10], Friedreich's ataxia [11], and Wilson's disease [12,13]. All of the aforementioned conditions involve the accumulation of metal ions in certain tissues or cellular compartments of the body and the inability of the physiological systems to mobilize them [13]. Being non-redox in nature, most of the heavy metals lack pro-oxidant catalytic activity, rather they covert to some indirect mechanisms (through destruction of sulfhydryl (–SH) containing enzymes essential for *in vivo* antioxidant defence) to exert pathogenesis through free radical mediated damage [14,15]. Thus, regulating the free radical-induced intracellular damage is equally essential in combating heavy metal overload diseases besides the elimination of the same from various organ systems [15]. The conventionally used chelating agents for treatment of heavy metal overload disorders were introduced more than four decades ago (i.e., $CaNa_2EDTA$ – 1985 [16]; BAL – 1949 [16]; DMSA – 1978 [17]; DMPS – 1958 [18]), and they suffer from inherent toxic effects owing to non-specificity and unwanted distribution throughout the body

including several essential organs [19-21]. Most dangerously, some of the chelators redistribute the heavy metals to the brain instead of excretory organs resulting in severe cognitive disorders, particularly in children [4]. The aforementioned causal relationship between heavy metal and oxidative stress and inherent toxicity of the conventional chelators makes co-administration of antioxidants necessary during chelation therapy for comprehensive treatment. Unfortunately, to date, there is no commercially available therapeutic agent that can serve both the aforementioned purposes.

In this regard knowledge of nanoscience and technology can open new avenues for treatment of heavy metal associated disorders. Numerous *in vitro* studies have described the ability of metallic nanoparticles to bind heavy metals. For example, nanosized silver and gold particles can efficiently bind bivalent metal ions like mercury (Hg^{2+}), copper (Cu^{2+}), lead (Pb^{2+}) etc. [22-25]. However, low biocompatibility and other complicacies limit their administration *in vivo.* Previously, we have shown that surface functionalized Mn_3O_4 NPs are not only biocompatible with substantial antioxidant capacity but also can interact with positively charged materials like methylene blue, bilirubin, etc. [26-30]. Therefore, we hypothesize that these NPs could be a possible alternative treatment of cationic heavy metal toxicity and associated disorders.

Among cationic heavy metals, Lead (Pb) is a ubiquitous environmental as well as industrial pollutant that affects almost every organ system of the human body. In this work, through *in vitro* spectroscopic and *in vivo* animal studies we explored the possible Pb(II)-chelating activity of C-Mn_3O_4 NPs. UV-vis and fluorescence spectroscopic techniques were used to confirm the Pb-chelating efficacy of the NPs. We also investigated whether the NPs were able to retain their antioxidant activity after chelation of the heavy metal. Using Pb(II)-intoxicated C57BL/6j mice, we confirmed that C-Mn_3O_4 NPs were able to mobilize the heavy metal *in vivo* through chelation. Detailed analysis of biochemical, histological and molecular parameters revealed the enhanced antioxidant activity of the NPs after chelation of Pb(II) and subsequent reduction in free radical induced cellular damage. Thus, use of the C-Mn_3O_4 NPs as a dual action nanomedicine for both heavy metal chelation and

remediation associated with oxidative stress may uncover a new paradigm in nanoparticle mediated therapy.

8.2. RESULTS AND DISCUSSION

8.2.1. A Smart Nanotherapeutic Agent for *in vitro* and *in vivo* Reversal of Heavy Metal Induced Causality: Key Information from Optical Spectroscopy [31]

We have synthesized the bulk Mn_3O_4 NPs following a previously described ultrasonic-assisted approach [32] and functionalized them with a carboxylate-rich biocompatible ligand, citrate. The electronic absorption spectra of C-Mn_3O_4 NPs at pH ~7.0 (Figure 8.1a) illustrates three well-defined regions i.e., from 250-330 nm (region 1), from 330 to 500 nm (region 2) and from 500 to 700 nm (region 3). The first region having high energy absorption bands at 250 nm and 290 nm can be attributed to the possible high energy ligand to metal charge transfer (LMCT) transitions involving the interaction between ligand functional groups and Mn^{2+}/Mn^{3+} on the NP surface [33]. The other two low energy regions can reasonably be assigned to the Jahn–Teller (J–T) distorted d–d crystal field transitions (i.e., $^3E_g(G)\leftarrow{}^3T_{1g}$, $^3A_{2g}(F)\leftarrow{}^3T_{1g}$, $^3A_{2g}(G)\leftarrow{}^3T_{1g}$, $^3T_{2g}(H)\leftarrow{}^3T_{1g}$, $^3T_{1g}(H)\leftarrow{}^3T_{1g}$, and $^3E_g(H)\leftarrow{}^3T_{1g}$) centered over octahedral Mn^{3+} species of the NPs [26,34,35]. Upon interaction with heavy metal Pb(II), the charge transfer band (~290 nm) vanishes (Figure 8.2a) along with a decrease in 435 nm band and increase in other two d-d bands (~360 nm and ~520 nm) (Figure 8.2b). The disappearance of charge transfer band is, probably, due to the chemical bonding or electron transfer to the Pb^{2+} ions, as a result of strong metal support interaction [36,37]. The apparent changes in d-d transitions bands could be interpreted as an effect of the interaction of many small Pb^{2+} ions at nanoscale interparticle distances within a single Mn_3O_4 nanocluster [37]. Isosbestic points at ~270 nm, ~330 nm, ~380 nm, and ~460 nm describe the processes to be in equilibrium (Figure 8.2a & 8.2b). The binding constant ($K_b = 5.89 \times 10^4\ M^{-1}$) of the NP–$Pb^{2+}$ complex was calculated using the Benesi–Hildebrand equation (Equation – 8.1) ($R^2 = 0.98$) [38].

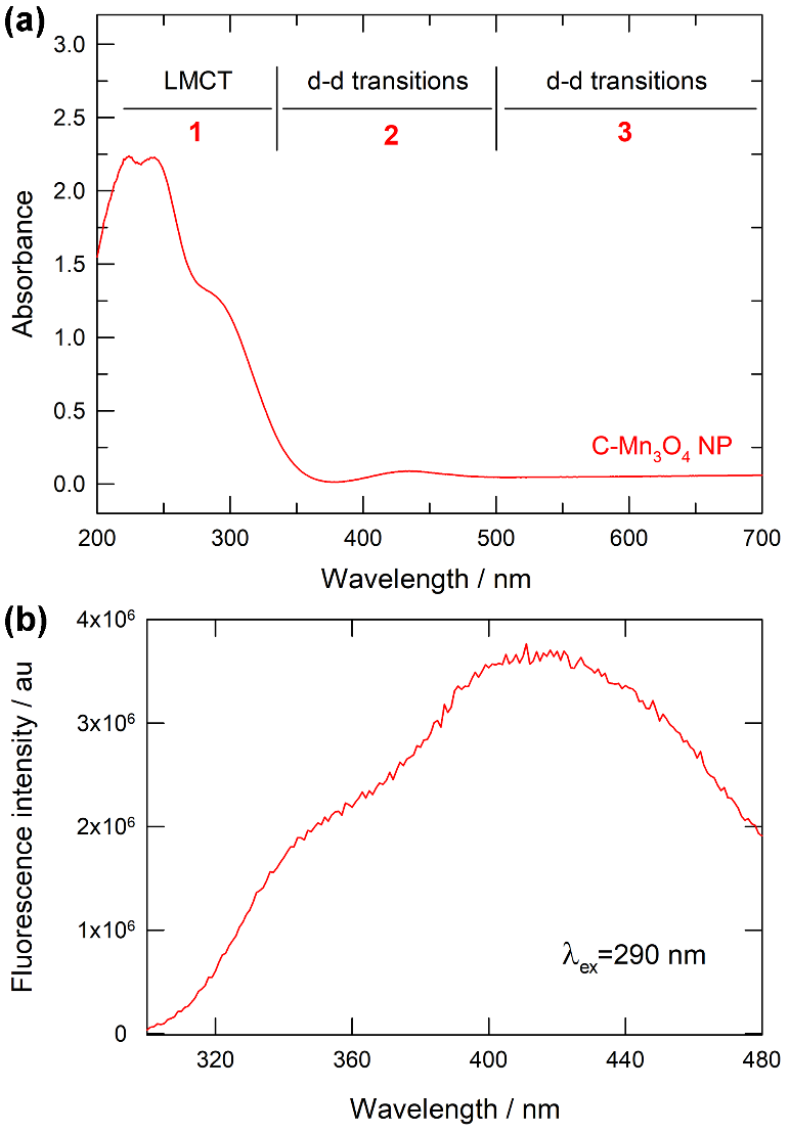

Figure 8.1. *(a) Electronic absorbance spectra of C-Mn_3O_4 NPs (after correction of Raleigh scattering). (c) Fluorescence emission spectra of C-Mn_3O_4 NPs when excited at 290 nm.*

$$\log\left(\frac{A\text{-}A_0}{A_f\text{-}A_0}\right) = \log[Pb^{2+}] + \log K_b$$

[Equation – 8.1]

where, A_0, A, and A_f are the initial (without Pb^{2+}), intermediate (with Pb^{2+}) and final absorbance (with saturated amount of Pb^{2+}) at 290 nm respectively. The binding constant (K_b) was calculated by linear fitting of absorption titration curve (Figure 8.2b-inset).

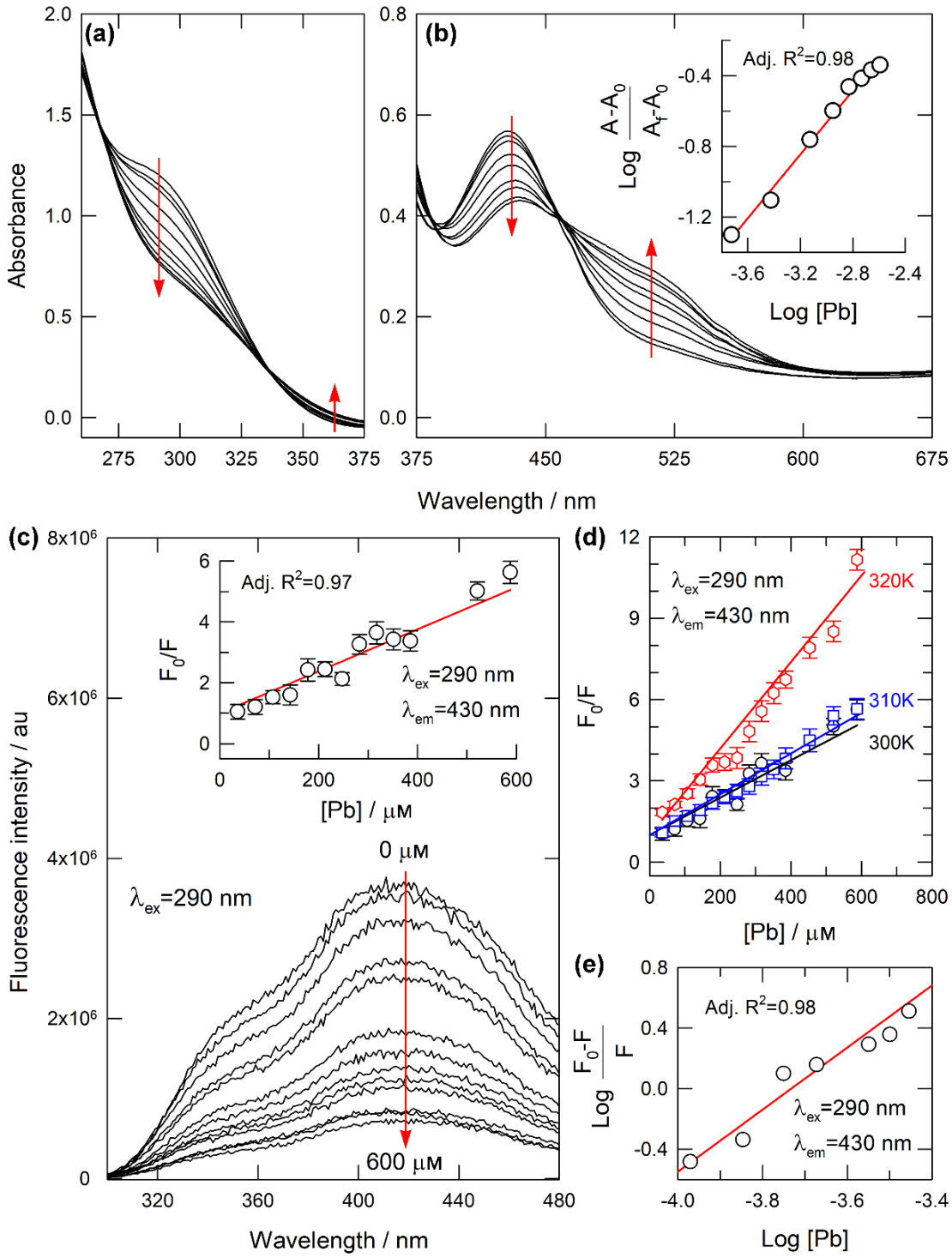

Figure 8.2. *Interaction of Pb(II) with C-Mn_3O_4 NPs. (a & b) Absorption spectra of C-Mn_3O_4 NPs (after correction of Raleigh scattering) in presence of varying concentrations (0 to 4.14 × 10^{-4} M) of $Pb(NO_3)_2$. Arrows indicate the increase in the concentration of Pb^{2+}. Inset shows the Benesi–Hildebrand plot for the determination of binding constant. (c) Fluorescence spectra of C-Mn_3O_4 NPs in the presence of different concentrations (0 to 6 × 10^{-4} M) of $Pb(NO_3)_2$ (λ_{ex} = 290 nm). Inset shows Stern–Volmer plot for the interaction (λ_{em} = 430 nm). (d) Stern–Volmer plots at different temperatures. (e) Modified Stern–Volmer plot.*

In the fluorescence study, NPs show a strong emission at ~420 nm and a shoulder at ~350 nm when excited at ~290 nm (Figure 8.1b). In the presence of Pb^{2+}, both fluorescence were quenched (Figure 8.2c). The phenomenon of fluorescence quenching can be accredited to numerous molecular events e.g., molecular rearrangements, ground-state complex formation, energy transfer, excited-state reactions, collisional quenching, etc. [39]. In the case of C-Mn_3O_4 NPs, there was no visible shift in the emission maxima (~420 nm) or shape of the fluorescence spectrum. Instead, the quenching behavior followed the classical Stern-Volmer (SV) equation,

$$\frac{F_0}{F} = 1 + K_D[Q] = k_q \tau_0 [Q]$$

[Equation – 8.2]

Where F_0 denotes the fluorescence intensity in absence of quencher, and F is the same in the presence of quencher. [Q] is the quencher concentration, K_D denotes the SV quenching constant, k_q the bimolecular quenching rate constant, τ_0 is the fluorescence lifetime of the fluorophore [39]. The linearity in the SV plot (Figure 8.2c-inset) indicates a single type of quenching, either static or dynamic [15]. To identify the nature of quenching, we repeated the experiments at three different temperatures (300K, 310K, and 320K). The quenching efficiency (K_D) increased with an increase in temperature (6896.19 M^{-1}, 7520.29 M^{-1}, and 14179.52 M^{-1} respectively), which clearly indicates the quenching mechanism to be collisional in nature (Figure 8.2d). The value of bimolecular quenching constant, k_q (K_D/τ_0), was calculated to be ~1.71×10^{12} M^{-1} s^{-1} (at ~300K, τ_0=4.04 ns), larger than that of the diffusion controlled limit (~10^{10} M^{-1} s^{-1}) indicating some type of binding interaction to be present [39]. The double logarithmic plot (Figure 8.2e) reveals the association constant, ($K_a = 6.4 \times 10^4$ M^{-1}, similar to that found in the absorbance experiment) and number of binding sites (n=1.29) using the following equation,

$$\log\frac{F_0 - F}{F} = \log K_a + n\log[Q]$$

[Equation – 8.3]

K_a denotes association constant and n denotes the number of probable binding sites. Thus, spectroscopic studies indicate a strong binding between the NPs and the Pb^{2+} ions probably through the surface carboxyl groups of the capping ligand citrate.

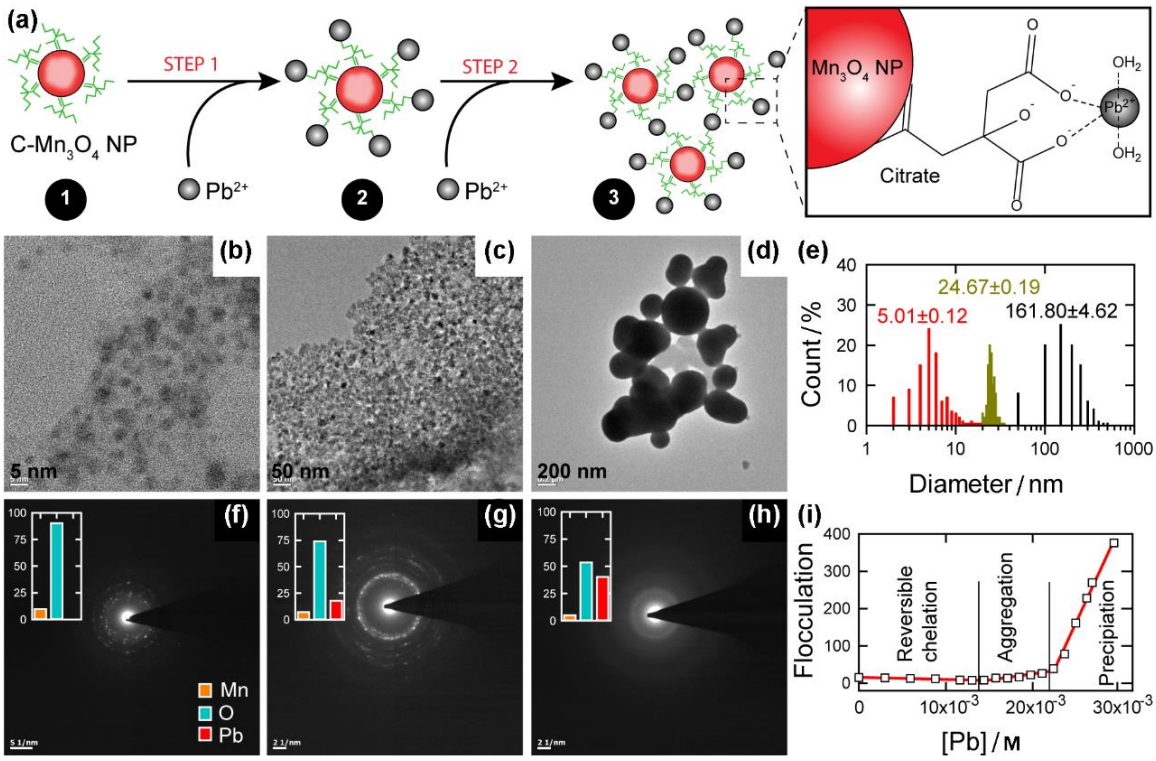

Figure 8.3. *Interaction of Pb(II) with C-Mn_3O_4 NPs. (a) Schematics of the cluster formation (see text for details). Box shows probable structure of the Pb- C-Mn_3O_4 NP chelate. (b-d) TEM images of C-Mn_3O_4 NPs in absence and presence of different concentrations of Pb(II). (e) Change in size distribution pattern of C-Mn_3O_4 NPs due to interaction with Pb(II). Size of the NPs were manually calculated from TEM images. (f-h) SAED pattern of C-Mn_3O_4 NPs in absence and presence of different concentrations of Pb(II). Inset shows the relative abundance of Mn, O, and Pb as investigated by Edax analysis. (i) Flocculation parameters define the stages of agglomerate formation (see text for details).*

There are two possible ways Pb^{2+} can interact with the NPs, either through replacement of the Mn^{2+} ions in the spinel hausmannite structure (so that the overall size remains almost same) or through binding to the surface of the NPs (overall size of the cluster will increase and form agglomerate). To find out the right way, we carried TEM studies. In Figure 8.3b, we show typical TEM micrographs of the ~5-nm C-Mn_3O_4 NPs before the addition of Pb^{2+} ions. The Selective area electron diffraction (SAED) pattern (Figure 8.3f) indicates the crystalline structure of the NPs. After the addition of Pb^{2+} (<5 mM) in the system, the size of NPs increased to ~25 nm (Figure 8.3c), probably due to the binding of the ions to the surface modulating ligand citrate (Figure 8.3a,-STEP 1). It should be noted that even after interaction the complexes remain isolated with little or no aggregation, and the NPs were able to retain their

crystallinity (Figure 8.3g). Further increase in Pb^{2+} concentration in the system, resulted in a drastic increase in NP size (Figure 8.3e), accompanied by agglomeration (Figure 8.3d) and the degree of aggregation (the fraction of particles that is making an aggregate) increases with the increasing concentration of Pb^{2+} in the system. Subsequent addition of Pb^{2+} ions beyond the dilute regime (>15 mM) brings about drastic changes to the microscopic structure of the complex, as well as visible precipitates, were formed in the solution (Figure 8.3a, STEP-2). The SAED pattern confirms the loss of crystallinity in the precipitates (Figure 8.3h). Another interesting aspect is, along with the increase in size and decreasing crystallinity, there was an enhancement in the contrast of the electron micrographs. The enhanced TEM contrast may be attributed to the enhanced coverage of NP-surface with Pb(II), which is a well-known staining agent used in electron microscopic studies [40].

The above observations were further supported by changes in the electronic absorbance spectra of the NPs at the red end. The NP-Pb^{2+} complex generally scatters at longer wavelengths, which is basically constant at a higher dilution of Pb^{2+}. With increasing concentration of Pb^{2+}, the scattering increases gradually. In order to detect the changes, we employed a slightly modified version of the flocculation parameter described previously [41]. In this study, the flocculation parameter is defined as the integrated area in the 650-800 nm region of the absorbance spectra. As depicted in Figure 8.3i, the value of the flocculation parameter increased with the increasing Pb^{2+} concentration that coincides with the aggregation phenomena described in the earlier section of the manuscript. The addition of EDTA could not reverse the change in the flocculation parameter after a certain concentration regime (Figure 8.3i), hence, the chelation is irreversible [42]. The addition of polyvinyl alcohol (PVA) into the system stabilizes the sol and permits further addition of Pb^{2+} ions. We thus have three states of chelation i.e., a reversible regime (<15 mM Pb^{2+}), an irreversible regime (<22 mM Pb^{2+}), followed by a regime where precipitation occurs (Figure 8.3i). To test the chelating ability of C-Mn_3O_4 NP towards other metals, we studied its interaction with Cu^{2+} and Fe^{3+} by means of UV-vis spectroscopy. Interestingly, neither Cu^{2+} nor Fe^{3+} was chelated by the NPs. Although, detailed study using other heavy metals (e.g., cadmium, chromium, and thallium) could provide more extensive information about

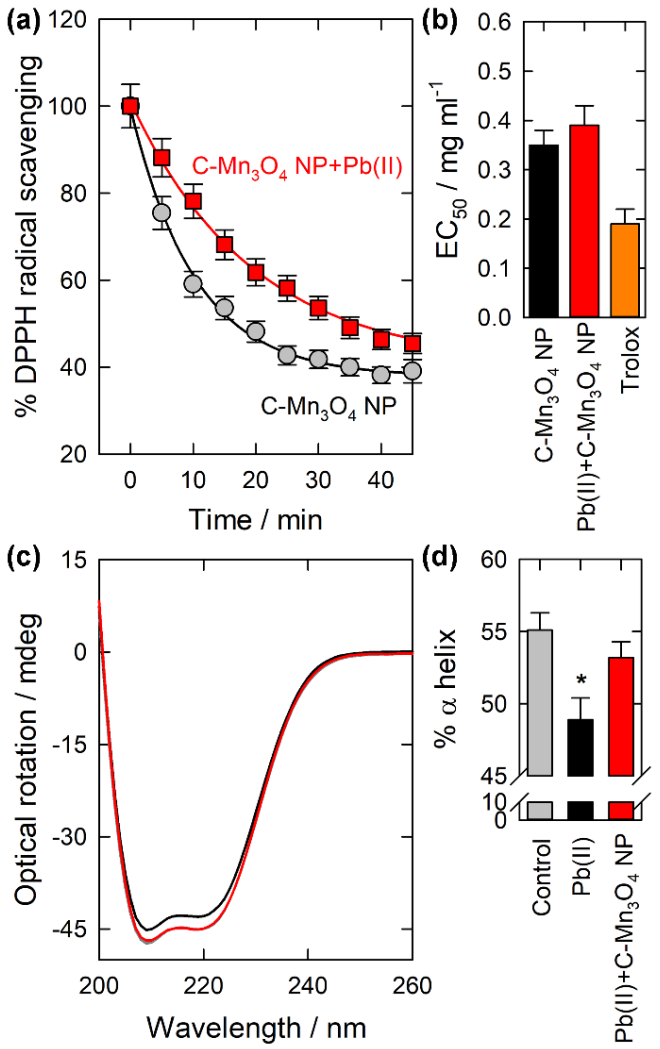

Figure 8.4. *(a & b) Effect of Pb(II) chelation on antioxidant activity of C-Mn_3O_4 NPs as studied using UV-vis assisted DPPH radical scavenging assay. (c & d) Interaction of Pb(II) with HSA in presence and absence of C-Mn_3O_4 NPs. * P<0.05; ** p<0.01; *** p<0.001*

the specificity and applicability of the NP as a sensing agent, it is beyond the scope of this work.

One of the major ways the heavy metals exert their toxicity is through induction of oxidative stress. So, treatment with antioxidants has proved to be successful in the treatment of metal overload diseases [3,14]. C-Mn_3O_4 NPs have previously shown antioxidant activity both *in vitro* and *in vivo*. So, we tried to investigate whether the NPs were able to retain their antioxidant activity even after chelating the heavy metal. UV-vis assisted DPPH assay (Figure 8.4a) revealed that the Pb^{2+}-chelated NPs (EC_{50}=0.39±0.3 mg ml^{-1}) retained their antioxidant activity and were almost

comparable to their native counterpart (EC_{50}=0.35±0.3 mg ml^{-1}) (Figure 8.4b). Previous studies have shown that bivalent heavy metals can decrease the helix content in proteins [43]. Our results show that (Figure 8.4b), upon interaction with Pb^{2+}, α-helix content of HSA decreased significantly compared to control (from 55.9% to 49.7%; p<0.05) (Figure 8.4c & 8.4d). The decrease in α-helix was accompanied by an increase in the β-sheet, turn and random coil structures (data not shown) which indicated partial protein destabilization [43]. However, treatment with C-Mn_3O_4 NPs recovers the helix content to normal (55.1%). The reversal may be caused due to the NPs' ability to chelate the metal out of the protein pocket. The results of CD-spectroscopy indicates that the NPs can function as effective chelator even in the presence of biological macromolecules.

Various chemical assays have been developed to date that exactly mimic the pathophysiological conditions in the human body. However, the success of the chemical models for realistic assumptions are vastly dependent on the existence of an effective correlation between chemical and biological models [15]. Therefore, we developed an animal (Pb^{2+}-induced C57BL/6j mice) model which exactly mimics the pathogenicity of heavy metal overload disorders. As described in Figure 8.5a, 28 days of $Pb(NO_3)_2$ exposure significantly increased Pb concentration in the blood (35.64 ± 3.12 μg ml^{-1}) compared to day 1 (0.23 ± 0.07 μg ml^{-1} ; p < 0.001) of the study. Thereafter, treatment with C-Mn_3O_4 NPs for 3 weeks lead to a significant decrease in the blood Pb-level (4.23 ± 0.91 μg ml^{-1}; p < 0.001). As evident from Figure 8.5A, further extension of treatment regime (another 4 weeks) could completely bring down the blood Pb levels of the Mn_3O_4 NP treated animals. However, the current 3 weeks of treatment was sufficient enough to reverse the damages caused by Pb(II)-intoxication (Table 8.1 and 8.2). The complete biodistribution study (Figure 8.5b) revealed that, the NPs were successful enough to mobilize the Pb from various important organs (Liver: 2.67±0.99 μg ml^{-1} compared to 15.50±1.96 μg ml^{-1}, p<0.001; Kidney: 4.15±1.40 μg ml^{-1} compared to 14.75±2.11 μg ml^{-1}, p<0.001; Spleen: 3.78±1.01 μg ml^{-1} compared to 12.38±2.99 μg ml^{-1}, p<0.001; Brain: 0.23±0.07 μg ml^{-1} compared to 4.65±1.41 μg ml^{-1}, p<0.001). The results show that C-Mn_3O_4 NPs were able to chelate and successfully mobilize Pb^{2+} through excretion.

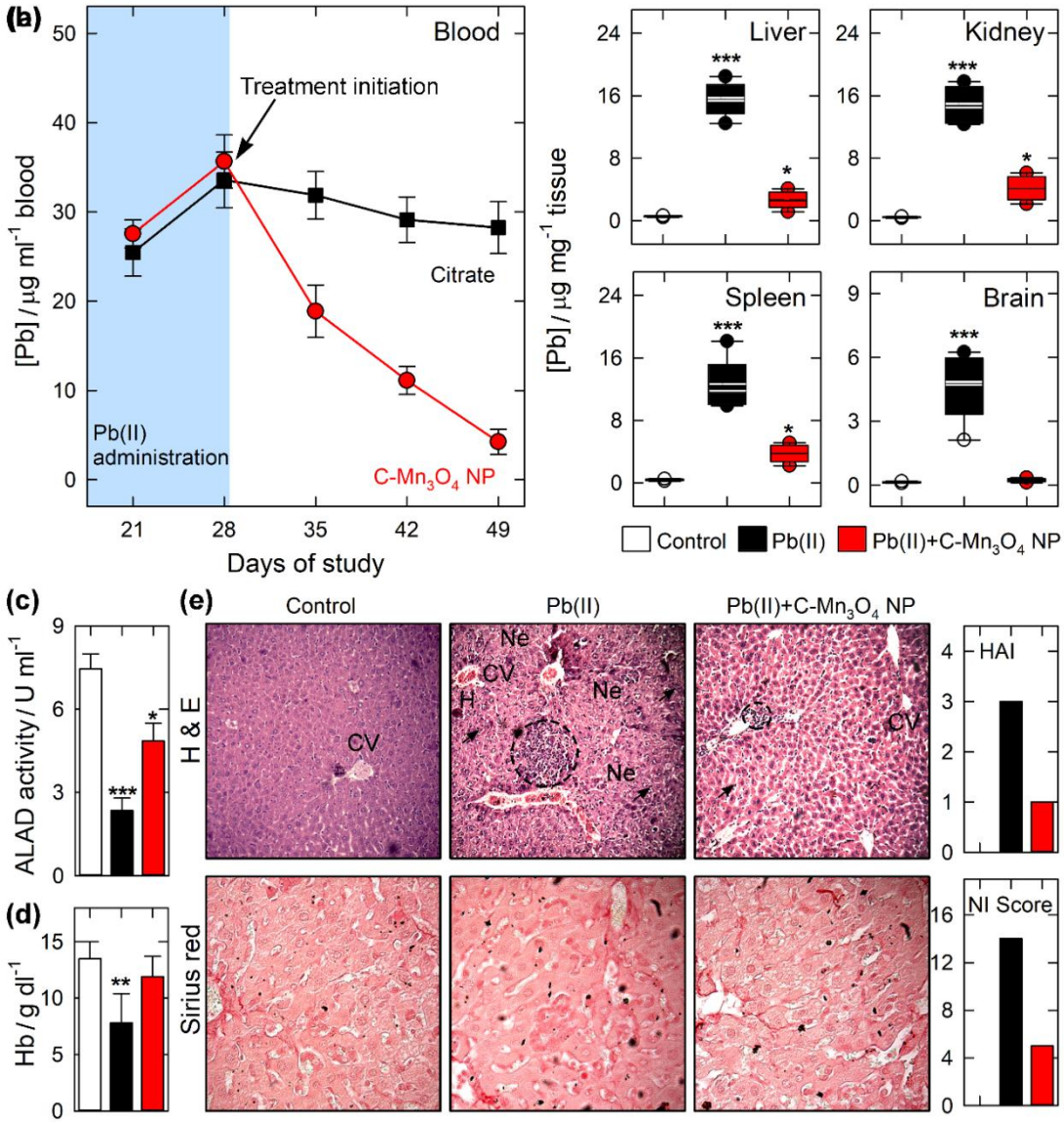

Figure 8.5. *Effect of C-Mn_3O_4 NPs on Pb(II) intoxicated C57BL/6j mice. (a) Effect of 21 day treatment with C-Mn_3O_4 NPs on plasma Pb concentration. (b) Effect of 21 day treatment with C-Mn_3O_4 NPs on biodistribution of Pb in various vital organs. (c & d) Effect of 21 day treatment with C-Mn_3O_4 NPs on ALAD activity and haemoglobin count. (e) Effect of C-Mn_3O_4 NPs on liver histology stained with haematoxylin and eosin (H & E) and serius red. * P<0.05; ** p<0.01; *** p<0.001*

Abbreviations. HAI: hepatic activity index; NI score: necro inflammatory score; Ne: necrosis; CV: central vein; H: haemorrhage; circle means mononuclear infiltrations.

In most of the studies on the utilization of chelating agents for the treatment of metal intoxication, the emphasis has been on mobilization (mainly through renal excretion) of the toxic metals. However, growing evidence suggests that the reduction

Table 8.1. Summary of hematology parameters studied across the groups.

Parameters	Groups		
	Control	Pb(II)	Pb(II) + C-Mn_3O_4 NP
Hb (g dl^{-1})	13.5±1.5	7.8±2.6[a]	11.9±1.8[b]
RBC (x10^6 μl^{-1})	10.9±4.1	9.1±5.3	11.4±4.2[b]
RT (%)	2.7±1.1	4.9±1.6[a]	3.1±2.4[b]
HCT (%)	34.6±1.3	39.4±2.1[a]	33.4±2.1[b]
MCV (μm^3)	37.4±2.6	31.0±2.3[a]	35.9±1.4[b]
MCH (pg)	21.2±2.4	22.2±2.8	21.1±1.7
MCHC (%)	41.2±7.6	35.4±2.4[a]	38.4±1.4
Platelets (x10^3 μl^{-1})	6.4±2.0	5.9±1.2[a]	6.2±1.2[b]
WBC (x10^3 μl^{-1})	9.2±1.1	12.4±1.2[a]	10.4±1.1[b]
PT(sec)	7.3±0.7	8.2±1.1	7.4±0.6
APTT (sec)	16.9±4.3	18.7±2.6	16.1±2.5

Data are expressed as mean ± standard deviation (SD) (*N*=6/group).
One-way ANOVA Tukey post hoc: [a] $p < 0.001$ compared with control. [b] $p < 0.001$ compared with lead intoxicated group. Abbreviations: Hb: Hemoglobin; RBC: read blood corpuscle; RT: reticulocyte; HCT: hematocrit; MCV: mean corpuscular volume; MCH: mean corpuscular hemoglobin; MCHC: mean corpuscular hemoglobin concentration; WBC: white blood corpuscle; PT: prothrombin time; APTT: activated partial thromboplastin time.

of oxidative damage in affected organs is equally important for recuperation. So, along with Pb-chelation, we investigated the therapeutic effect of C-Mn_3O_4 NPs in various organ systems that are prone to heavy metal-induced damage. It is well known that the hematopoietic system is the most vulnerable one, as Pb inhibits δ-ALAD, one of the key enzymes in heme biosynthesis. The activity of blood δ-ALAD reduced significantly (2.35 ± 0.45 compared to 7.45 ± 0.54 nmol min^{-1} ml^{-1} erythrocytes of control; $p < 0.001$) in Pb(II)-intoxicated animals (Figure 8.5c). The inhibition of δ-ALAD was significantly low in animals administered with C-Mn_3O_4 NPs (4.85 ± 0.65 nmol min^{-1} ml^{-1} erythrocytes). The effect of δ-ALAD inhibition was exactly reflected on haemoglobin (Hb) level. As depicted in Figure 8.5d, Pb(II) intoxication resulted in anaemia (Hb-level 7.8±2.6 g dl^{-1} compared to 13.5±1.5 g dl^{-1}; $p<0.001$). Treatment with C-Mn_3O_4 NPs helped in regaining the normal Hb-level in the blood (11.9±1.8 g dl^{-1}). The results concerning other hematological parameters are described in Table 8.1.

The next system that is hugely affected by heavy metal toxicity is the liver. Several studies have shown that serum aminotransferase activity as sensitive indicators

Table 8.2. Summary of liver function parameters studied across the groups.

Parameters	Groups		
	Control	Pb(II)	Pb(II) + C-Mn_3O_4 NP
AST (IU l^{-1})	88.21±9.54	505.65±26.35[a]	100.25±12.11[b]
ALT (IU l^{-1})	55.67±4.98	289.51±12.55[a]	79.66±9.97[a,b]
ALP (IU l^{-1})	27.11±2.56	148.26±13.24[a]	45.58±9.69[a,b]
GGT (IU l^{-1})	2.84±0.21	5.98±0.32[a]	3.02±0.35[b]
TP (g dl^{-1})	6.58±0.32	4.24±0.45[a]	6.06±0.66[b]
Total Bilirubin (mg dl^{-1})	0.32±0.01	1.30±0.03[a]	0.51±0.02[a,b]
Direct Bilirubin (mg dl^{-1})	0.15±0.01	0.52±0.01[a]	0.21±0.01[a,b]

Data are expressed as mean ± standard deviation (SD) (*N*=6/group).
One-way ANOVA Tukey post hoc: [a] $p<0.001$ compared with Control. [b] $p<0.001$ compared with Pb(II) intoxicated group. Abbreviations. AST: aspartate aminotransferase; ALT: alanine aminotransferase; ALP: alkaline phosphatase; GGT: γ-glutamyltranferase; TP: total protein.

of liver injury. Damage to the hepatic cells alters their membrane permeability, which leads to the leakage of enzymes from the cells [15]. As described in Table 8.2, three weeks of Pb(II) exposure significantly enhanced the AST and ALT levels by 5.7-fold and 5.2-fold, respectively, compared to control ($p < 0.001$). The significantly increased levels of AST and ALT into the circulation pointed towards severe damage to hepatocyte membranes. C-Mn_3O_4 NPs were competent enough in the reduction of the AST and ALT levels by 80.1 and 72.4%, respectively, compared to the Pb(II)-exposed group ($p<0.001$). It is well known that reversal of aminotransferase levels are associated with the healing of liver parenchyma and the regeneration of hepatic cells. The other liver function parameters showed similar trends, e.g., increase in ALP (~446%), GGT (~110%), total bilirubin (~225%), direct bilirubin (~150%), and a noticeable decrease in TP (~35%) in Pb-intoxicated group ($p < 0.001$ compared to control). Treatment with C-Mn_3O_4 NPs improved all the liver function parameters back to normal levels (Table 8.2).

Figure 8.5e shows the microscopic images of H&E and serius red-stained liver sections. The control group showed clear nuclei and hexagonal, distinctly visible normal hepatocytes separated by interlobular septa, and traversed by portal veins. There were notable degenerative histopathological changes (e.g., damaged hepatocyte structure, cytoplasmic vacuolation, disorganization of hepatic chords, massive necrosis, mononuclear infiltration, and haemorrhage) in Pb(II)-exposed animals. Treatment with C-Mn_3O_4 NP leads to the regeneration of normal hepatocytes with a

mild degree of mononuclear infiltration and necrosis. The substantial cellular damage induced by Pb(II) exposure might be due to its ability to generate ROS that induces oxidative damage in tissues through increased lipid peroxidation (detailed study in the next section of the manuscript). Modified Ishak and METAVIR histological activity index (HAI) were applied (Figure 8.5e) to get an overview of the necroinflammatory damage instigated by Pb(II). The Pb-exposed animals scored 14 and 3 (the maximum possible score is 16 and 3). Treatment with C-Mn_3O_4 NPs decreased it to 5 and 0, respectively. The serius red staining of the liver sections showed no signs of fibrotic changes in any of the animals (Figure 8.5e).

As described in previous sections, damage induced by reactive oxygen species (ROS) plays an important role in the progression of heavy metal-induced toxicity. However, the currently used chelating agents lack the ability to scavenge ROS. On the other hand, our in vitro studies depicted that, C-Mn_3O_4 NPs possess antioxidant activity, even after chelation of Pb^{2+}. So, to test whether the NPs are able to protect hepatic cells from metal-induced oxidative stress, we investigated the activities of SOD, CAT, and GSH-Px, the trio that makes up the intracellular antioxidant defense system. The balance between oxidant and the antioxidant system seemed to be disturbed in our study due to Pb(II)-intoxication. The chronic administration of Pb(II) caused an increase in hepatic lipid peroxidation (~280%) and impairment of antioxidant enzymes, i.e., SOD (~62%), CAT (~57%) and GSH-Px (~45%), in the present study (Table 3). Treatment with C-Mn_3O_4 NPs however, ameliorated the damage by increasing the activities of all three enzymes along with a significant decrease in lipid peroxidation.

Thus, in the light of biochemical and microscopic results, it can be assumed that C-Mn_3O_4 NPs not only chelate the metal ions but also play an important role in the reduction of heavy metal-induced damage by the way of its antioxidant and radical scavenging effects.

8.3. CONCLUSION

In summary, we confirm the removal of ubiquitous pollutant, lead (Pb), through an efficient chelating activity of C-Mn_3O_4 NPs. The high resolution TEM images along with selected area X-ray diffraction (SAED) studies confirmed the complete inclusion of the toxic bivalent metal (Pb^{2+}) inside C-Mn_3O_4 NPs significantly affecting the overall size and crystallinity of the chelating nanoparticles. The spectroscopic studies on the NPs before and after Pb(II) chelation revealed significant alterations in both d-d transition and ligand to metal charge transfer (LMCT) bands, although, the antioxidant capacity of Pb-included NPs remained unaltered as depicted from DPPH assay. We have confirmed the integrity of our in vitro studies in the Pb-intoxicated C57BL/6j mice model where biochemical parameters including δ-ALAD, AST, ALT, ALP, total haemoglobin clearly indicate a reversal of Pb-toxicity upon administration of C-Mn_3O_4 NPs. Histopathological studies of Pb(II)-intoxicated mice liver also showed recovery from hepatic damage in the presence of the administered nanoparticles. Mobilization and excretion of Pb from different organ systems are clearly evident from ICP-AES studies. The reduction of associated metal-induced oxidative stress is also evident from the recovery of intracellular antioxidant defence system as studied using biochemical methods. To the best of our understanding, the findings may find relevance in the development of new nanotherapeutic strategies for effective treatment of heavy metal toxicity and associated disorders.

REFERENCES

[1] O. Andersen, Chem. Rev. 99 (1999) 2683.

[2] H. M. Benhangi, S. Ahmadi, M. Hakimi, A. Molafilabi, H. Faraji, B. Mashkani, Toxicol. In Vitro 54 (2019) 232.

[3] P. C. Hsu, Y. L. Guo, Toxicology 180 (2002) 33.

[4] C. D. Klaassen, J. Liu, S. Choudhuri, Annu. Rev. Pharmacol. Toxicol. 39 (1999) 267.

[5] F. Zahir, S. J. Rizwi, S. K. Haq, R. H. Khan, Environ. Toxicol. Pharmacol. 20 (2005) 351.

[6] H. Horiguchi, M. Sato, N. Konno, M. Fukushima, Arch. Toxicol. 71 (1996) 11.

[7] A. Budimir, Acta Pharm. 61 (2011) 1.

[8] M. A. Santos, K. Chand, S. Chaves, Coord. Chem. Rev. 327 (2016) 287.

[9] V. N. Uversky, J. Li, A. L. Fink, J. Biol. Chem. 276 (2001) 44284.

[10] D. Dexter, F. Wells, A. Lee, F. Agid, Y. Agid, P. Jenner, C. Marsden, J. Neurochem. 52 (1989) 1830.

[11] E. Becker, D. R. Richardson, Int. J. Biochem. Cell Biol. 33 (2001) 1.

[12] P. C. Bull, D. W. Cox, Trends Genet. 10 (1994) 246.

[13] L. E. Scott, C. Orvig, Chem. Rev. 109 (2009) 4885.

[14] H. Gurer, N. Ercal, Free Radic. Biol. Med. 29 (2000) 927.

[15] A. Adhikari, S. Darbar, T. Chatterjee, M. Das, N. Polley, M. Bhattacharyya, S. Bhattacharya, D. Pal, S. K. Pal, ACS Omega 3 (2018) 15975.

[16] C. D. Klaassen, in: J.G. Hardman, L.E. Limbird, G.A. G. (Eds.), The Pharmacological Basis of Therapeutics, McGraw-Hill, NY, USA, (1985), 1851.

[17] E. Friedheim, J. H. Graziano, D. Popovac, D. Dragovic, B. Kaul, Lancet 312 (1978) 1234.

[18] H. V. Aposhian, D. C. Bruce, W. Alter, R. C. Dart, K. M. Hurlbut, M. M. Aposhian, FASEB J. 6 (1992) 2472.

[19] H. V. Aposhian, R. M. Maiorino, D. Gonzalez-Ramirez, M. Zuniga-Charles, Z. Xu, K. M. Hurlbut, P. Junco-Munoz, R. C. Dart, M. M. Aposhian, Toxicology 97 (1995) 23.

[20] G. Liu, M. R. Garrett, P. Men, X. Zhu, G. Perry, M. A. Smith, Biochim. Biophys. Acta - Mol. Basis Dis. 1741 (2005) 246.

[21] S. Flora, P. Kumar, Drug Investig. 5 (1993) 269.

[22] Y. Wang, F. Yang, X. Yang, ACS Appl. Mater. Interfaces 2 (2010) 339.

[23] F. Li, J. Wang, Y. Lai, C. Wu, S. Sun, Y. He, H. Ma, Biosens. Bioelectron. 39 (2013) 82.

[24] X. Xue, F. Wang, X. Liu, J. Am. Chem. Soc. 130 (2008) 3244.

[25] C. Y. Lin, C. J. Yu, Y. H. Lin, W. L. Tseng, Anal. Chem. 82 (2010) 6830.

[26] A. Giri, N. Goswami, M. Pal, M. T. Zar Myint, S. Al-Harthi, A. Singha, B. Ghosh, J. Dutta, S. K. Pal, J. Mater. Chem. C 1 (2013) 1885.

[27] A. Adhikari, N. Polley, S. Darbar, D. Bagchi, S. K. Pal, Fut. Sci. OA 2 (2016) FSO146.

[28] A. Adhikari, M. Das, S. Mondal, S. Darbar, A. K. Das, S. S. Bhattacharya, D. Pal, S. K. Pal, Biomater. Sci. 7 (2019) 4491.

[29] A. Adhikari, S. Mondal, S. Darbar, S. K. Pal, Biomol. Concepts 10 (2019) 160.

[30] A. Adhikari, N. Polley, S. Darbar, S. K. Pal, Mater. Focus 6 (2017) 280.

[31] A. Adhikari, P. Biswas, S. Mondal, M. Das, S. Darbar, A. M. Hameed, A. Alharbi, S. A. Ahmed, S. S. Bhattacharya, D. Pal, S. K. Pal, ChemMedChem 15 (2020) 420.

[32] S. Lei, K. Tang, Z. Fang, H. Zheng, Cryst. Growth Des. 6 (2006) 1757.

[33] A. Giri, N. Goswami, C. Sasmal, N. Polley, D. Majumdar, S. Sarkar, S. N. Bandyopadhyay, A. Singha, S. K. Pal, RSC Adv. 4 (2014) 5075.

[34] W. S. Kijlstra, E. K. Poels, A. Bliek, B. M. Weckhuysen, R. A. Schoonheydt, J. Phys. Chem. B. 101 (1997) 309.

[35] M. E. Bodini, L. A. Willis, T. L. Riechel, D. T. Sawyer, Inorg. Chem. 15 (1976) 1538.

[36] K. Kim, N. Winograd, Chem. Phys. Lett. 30 (1975) 91.

[37] S. K. Ghosh, J. Kang, M. Inokuchi, N. Toshima, Appl. Catal. A Gen. 464 (2013) 225.

[38] D. Roy, A. Chakraborty, R. Ghosh, RSC Adv. 7 (2017) 40563.

[39] J. R. Lakowicz, Principles of Fluorescence Spectroscopy, Springer, Boston, MA, (2006).

[40] W. Barker, J. Banfield, Chem. Geol. 132 (1996) 55.

[41] C. S. Weisbecker, M. V. Merritt, G. M. Whitesides, Langmuir 12 (1996) 3763.

[42] S. Berchmans, P. J. Thomas, C. Rao, J. Phys. Chem. B. 106 (2002) 4647.

[43] A. Belatik, S. Hotchandani, R. Carpentier, H. A. Tajmir-Riahi, PLoS ONE 7 (2012) e36723.

CHAPTER 09

Biomimetic Nanozyme for the Treatment of Neurodegenerative Disorder

9.1. INTRODUCTION

Over the past decade, nanozymes, nanomaterials with intrinsic enzyme-like properties have attracted significant interest for application in multiple fields owing to their advantages (i.e., high and tunable catalytic activity, low cost, easy large scale production, and high stability) over the drawbacks of natural enzymes (i.e., low stability, high cost, laborious preparation, and low recyclability) [1-3]. Since the discovery of first iron-containing nanozyme in last decade [4], numerous nanomaterials have been elucidated to have oxidase [5], catalase [6], SOD [7,8], peroxidase [9], monooxygenase [10], hydrolase [11], laccase [12] mimicking activities and therefore been used in diverse applications like the destruction of biofilm, removal of algal bloom, immunoassay, tissue staining, cancer treatment, and glucose biosensing. However, despite being the most promising candidate as catalytic biomedicine, the clinical translation of nanozymes for therapeutic usage is still lacking [13-15]. Inherent toxicity of the materials used in the preparation of contemporary nanozymes, low aqueous solubility, inability to properly function in the physiological *milieu*, lack of selectivity (towards biological substrate), and incompatibility with other

enzymes in catalyzing intracellular cascade reactions are considered to be the confounding factors [15-18].

Highly connected networks of natural enzymes regulate the majority of the biological functions that occur in living systems. Dysregulation in any of these enzyme controlled networks often necessitates disease onset and progression. For example, redox imbalance due to downregulation of cellular antioxidant enzymes i.e., superoxide dismutase (SOD), catalase, or glutathione peroxidase (GPx) may lead to pathogenesis of cancer, diabetes, atherosclerosis, neurodegeneration, and aging [19-22]. Recently, GSH dependent GPx with pan cellular distribution has emerged as the key antioxidant enzyme (presence of isoforms in both cytosol and mitochondria highlights its significance) for maintenance of cellular redox homeostasis [23-25]. The deregulation in GPx activity and associated redox imbalance are associated with the pathogenesis of Huntington's disease (HD), one of the most prevalent neurodegenerative disorders with early-onset and progressive fatality [26-28]. Despite lack of effective therapeutics till date, one promising approach to treat the disease was found to be by replenishing the maladaptive enzyme (GPx) with an artificial one [28]. However, to successfully introduce any artificial enzyme as a direct surrogate of traditional enzyme for therapeutic use, the cooperative functionality needs to be mimicked to allow cascade reactions to take place in a parallel and efficient manner [29-31]. Recently, some of the nanozymes have been found to function in intracellular cascade reactions, however, concern over toxicity and metabolism have restricted their use in living organisms [9,32-34]. Thus, a biocompatible nanozyme that retains functionality in the physiological *milieu* and can easily be incorporated in the cellular enzymatic cascade is urgently needed for therapeutic usage.

Thus, considering the limitations and opportunities in clinical translation of nanozymes, particularly in neurodegenerative disorders, our objective for this study was to develop a non-toxic, aqueous soluble, biomimetic nanozyme capable of catalyzing intracellular cascade reactions and assess its therapeutic efficacy as redox medicine in an animal model of neurodegenerative disease where redox imbalance, associated oxidative distress and damage to the intracellular GPx system play a major role in the pathogenesis.

Here, we have shown that citrate functionalized Mn_3O_4 nanoparticles can efficiently mimic the enzymatic activity of glutathione peroxidase using GSH as co-factor. The nanozyme is highly specific towards H_2O_2 and can be incorporated into the glutathione reductase coupled reaction to scavenge H_2O_2, and oxidize NADPH simultaneously. Detailed experimental and computational studies reveal the mechanism of nanozyme action involving the generation of an intermediate peroxido species that accounts for the remarkable specific activity. Using, 3-nitro propionic acid (3-NPA) intoxicated C57BL/6j mice we confirmed that C-Mn_3O_4 NPs can cross the blood-brain barrier, retain its enzymatic activity in brain cells, and treat Huntington's like neurodegenerative disorder in animals. Scavenging of intra and extramitochondrial ROS by GPx action, maintenance of cellular redox equilibrium, and subsequent reduction of oxidative damages lead to the therapeutic effect. Thus, the use of the C-Mn_3O_4 nanozyme as a nanomedicine against neurodegenerative disorders may uncover a new paradigm in nanozyme based therapeutic strategy.

9.2. RESULTS AND DISCUSSION

9.2.1. Incorporation of a Biocompatible Nanozyme in Cellular Antioxidant Enzyme Cascade Reverses Huntington's Like Disorder in Preclinical Mouse Model [35]

Encouraged by the apparent non-toxicity (permissible limit ~12 mg day^{-1}), abundance of manganese (Mn) as the catalytic metal center or cofactor in several enzymes, and preferable e_g occupancy of 1.33 (*vide infra*) we selected nano-sized Mn_3O_4 as our compound of interest. A template or surfactant-free sol-gel based three-step approach was used to synthesize Mn_3O_4 nanoparticle at room temperature and pressure using $MnCl_2$ as a precursor. Citrate functionalization was performed to make the nanoparticle aqueous soluble, biocompatible, and competent to cross the blood-brain barrier (BBB) [36,37]. Transmission electron micrograph (TEM) shows the citrate functionalized Mn_3O_4 nanoparticles (C-Mn_3O_4 NPs) to be well-dispersed uniform spheres with an average diameter of ~6.12±2.24 nm (Figure 9.1a & 9.1b). High resolution (HR) TEM image of a single nanoparticle confirms the crystalline

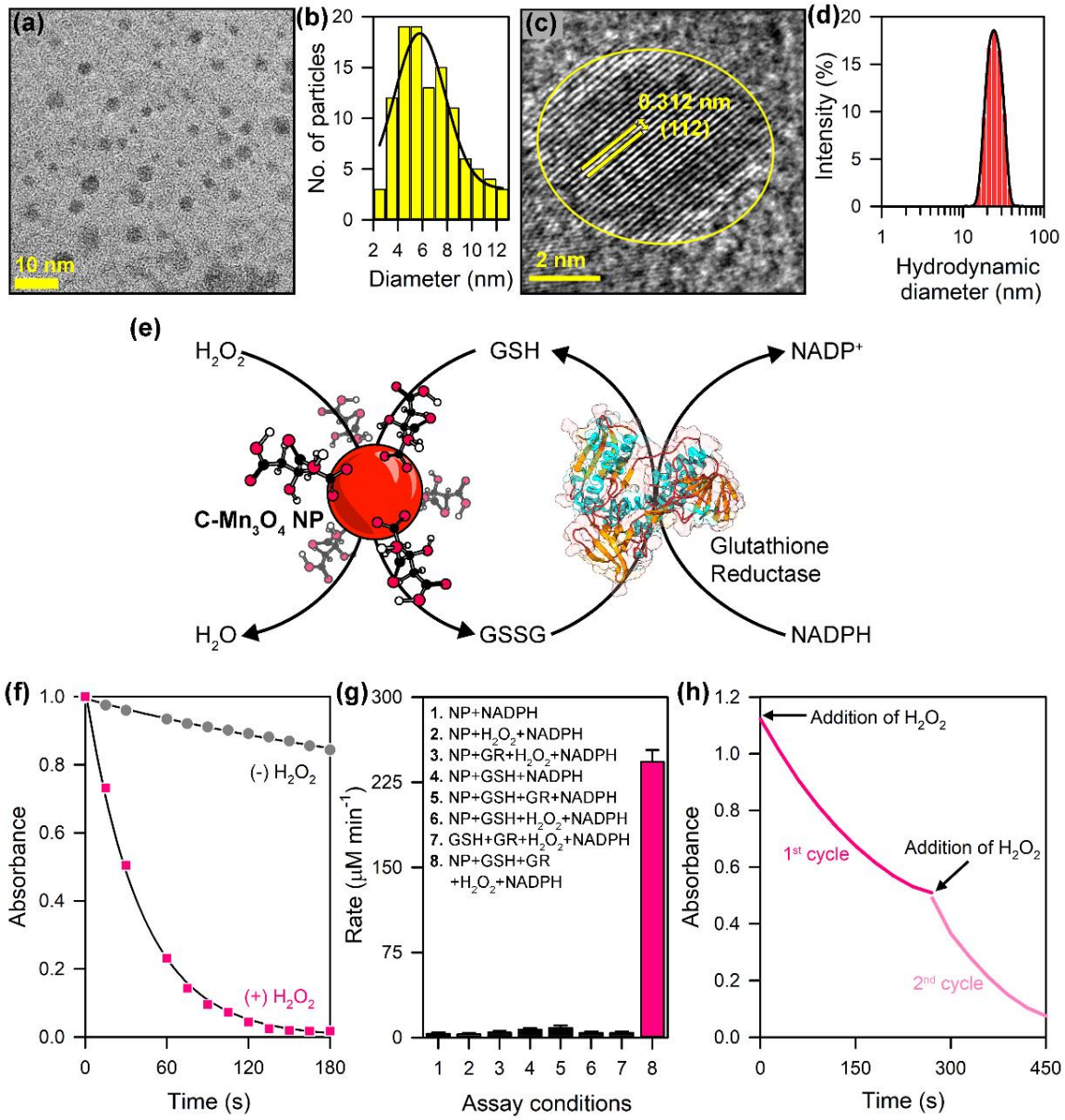

Figure 9.1. *Characterization and GPx-mimetic activity of C-Mn_3O_4 NPs. (a) TEM image of C-Mn_3O_4 NPs. (b) Size distribution of the nanoparticles as measured from TEM. (c) HRTEM image of single nanoparticle. (d) Hydrodynamic diameter from DLS study. (e) Schematic diagram depicting the GPx-like activity of C-Mn_3O_4 NPs in presence of GSH, and recycling by GR in coupled reaction. (f) The change in absorbance of NADPH (340 nm) during the reaction. In absence of H_2O_2, no reactivity was observed. (g) Comparison of initial reaction rate at different assay conditions. (h) The reaction kinetics shows the mechanism to be cyclic/ catalytic. The activity was studied for two cycles in UV-visible spectroscopy by addition of H_2O_2 (240 μM) and following the decrease of NADPH concentration at 340 nm.*

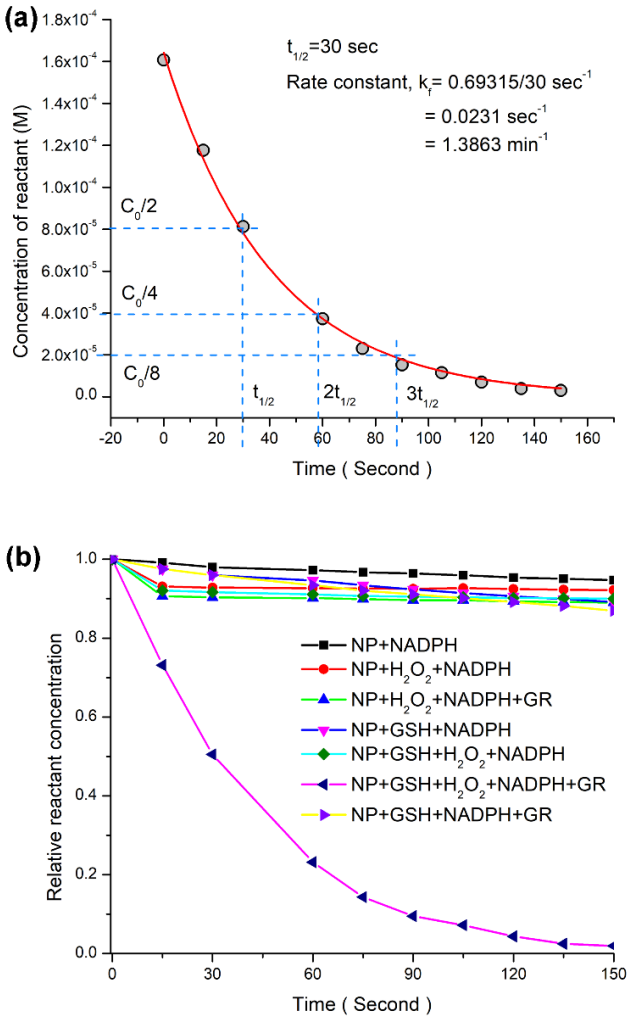

Figure 9.2. *(a) The enzymatic reaction of H_2O_2 catalysis follows first order kinetics. (b) The reaction kinetics at different reaction conditions listed in the legend.*

nature with clear atomic lattice fringe spacing of 0.312±0.021 nm (Figure 9.1c) corresponding to the separation between (112) lattice planes.

The GPx mimetic activity of aqueous soluble C-Mn_3O_4 NP was evaluated at physiological pH (pH ~7.4) using the glutathione reductase (GR)-coupled assay where the decrease in NADPH concentration was monitored spectrophotometrically at 340 nm. Figure 9.1e schematically illustrates the GPx like activity of C-Mn_3O_4 NPs in GR coupled cascade. Although nanozymes are known to have an incompatibility with other enzymes in a cascade [2,9], we found that the C-Mn_3O_4 NPs to be perfectly compatible with GR (Figure 9.1f). The reaction followed first-order reaction kinetics with a rate constant, k = 1.38±0.01 min^{-1} (Figure 9.2a). The initial reaction rates

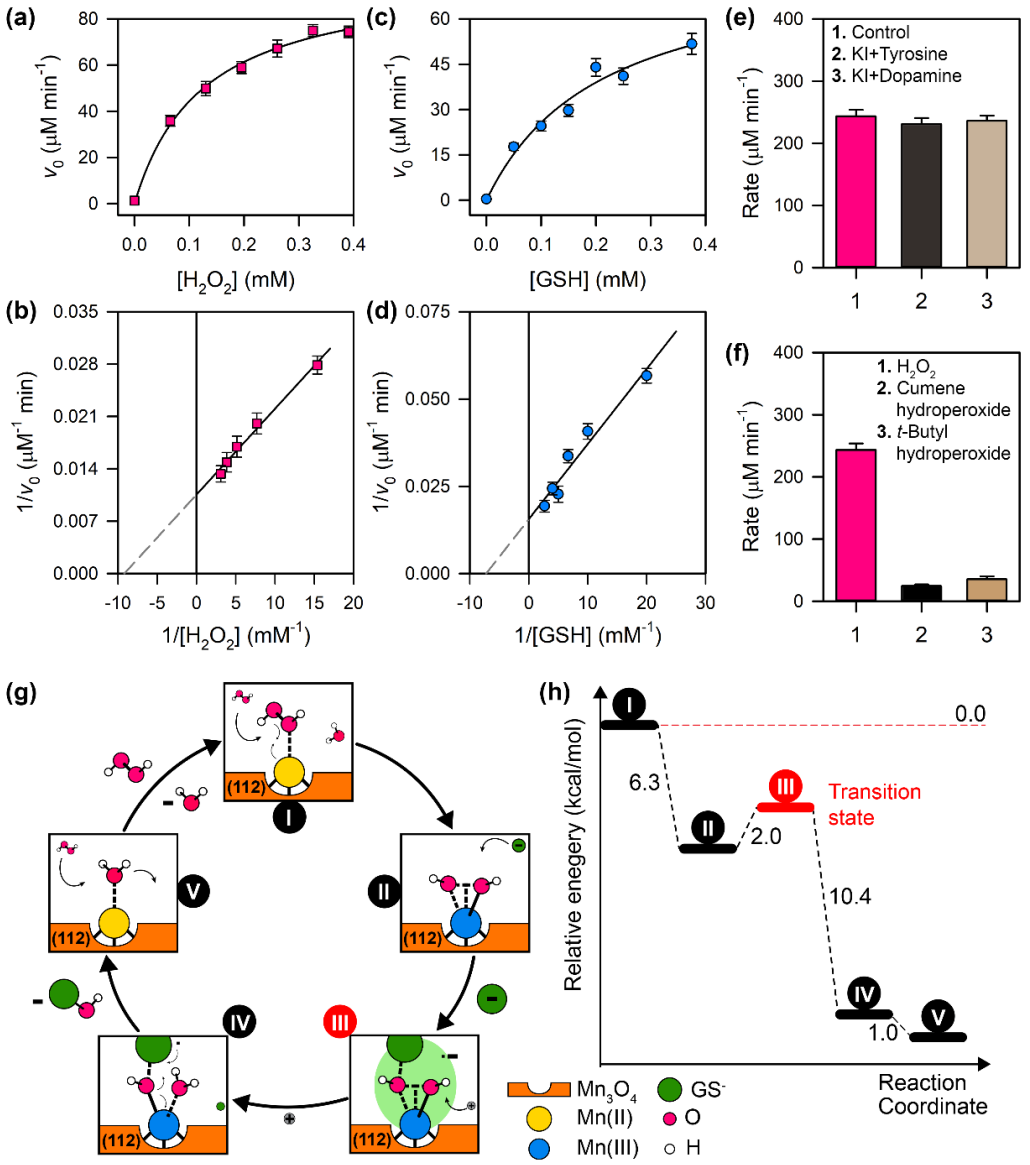

Figure 9.3. *Kinetic parameters and mechanism of action. (a & b) Michaelis-Menten and Lineweaver-Burk plot for variable concentration of H_2O_2. (c & d) Michaelis-Menten and Lineweaver-Burk plot for variable concentration of GSH. (e) Effect of haloperoxidase substrate on GPx-like activity of C-Mn_3O_4 NP. (f) Selectivity of C-Mn_3O_4 NP towards H_2O_2. (g) Possible mechanism of GPx-like action of C-Mn_3O_4 NPs. (h) Energy profile for the reaction scheme.*

determined at various assay conditions indicate that the GPx-like activity of C-Mn_3O_4 NPs was hindered by the absence of any one of the components in the reaction mixture (Figure 9.1g; Figure 9.2b). The repeated H_2O_2 scavenging activity for several cycles indicates the reaction to be catalytic or recyclable (Figure 9.1h). A gradual increase in the initial reaction rate with an increasing concentration of C-Mn_3O_4 NPs was observed for the reduction of H_2O_2 (data not shown). The apparent steady-state kinetic

parameters were determined by independently varying the concentrations of H_2O_2 (0-480 μM), and GSH (0-6.0 mM) in presence of GR (1.7 units), C-Mn_3O_4 NPs (1.3 μM), and NADPH (400 μM). Both reactions followed typical Michaelis-Menten kinetics (Figure 9.3a & 9.3c). The Michaelis-Menten constant (K_M) and the maximum initial velocity (V_{max}) were determined based on Lineweaver-Burk linearization (Figure 9.3b & 9.3d). K_M for H_2O_2 and GSH are ~1.09±0.06 and ~1.36±0.09 mM, respectively. V_{max} for H_2O_2 and GSH are ~0.095±0.011 and ~0.064±0.008 mM min^{-1}, respectively. The K_M for H_2O_2 is higher compared to the natural GPx1 enzyme (~0.01 mM) [38,39] indicating a lower affinity towards substrate which is a very common phenomenon in artificial enzymes. Still, the observed K_M is lower compared to Ebselen (~2.34 mM), the most studied GPx mimic; and equivalent to V_2O_5 nanowires (~0.11 mM), one of the rare nanozymes that has the ability to be incorporated into enzymatic cascade but concern over toxicity limited their *in vivo* application. Interestingly, the affinity of C-Mn_3O_4 NPs for co-factor GSH is significantly higher compared to the native GPx1 (K_M ~10 mM), indicating the explicit role of GSH in the catalytic activity of the nanozyme. The C-Mn_3O_4 nanozyme catalyzed the reduction of H_2O_2 with a turnover number (k_{cat}) of ~69.12±0.52 min^{-1} and an apparent second-order rate constant, k_{cat}/K_M ~10530.17±975.25 M s^{-1}. For oxidation of GSH, the values were found to be k_{cat} ~46.73±0.31 min^{-1} and k_{cat}/K_M ~5717.85±345.72 M s^{-1}. Although, both turnover number and enzyme efficiency (for H_2O_2 reduction) were several orders of magnitude lower compared to the natural GPx1 enzyme isoform (k_{cat} ~5780 min^{-1}; k_{cat}/K_M ~9.63×10^6 M s^{-1}), C-Mn_3O_4 NPs outperformed several other artificial GPx mimics (Table 9.1). For example, C-Mn_3O_4 NPs have shown ~17 times higher turnover and ~390 times higher enzyme efficiency compared to Ebselen (k_{cat} ~3.85 min^{-1}; k_{cat}/K_M ~27.33 M s^{-1}); ~18 times higher turnover and ~17 times higher enzyme efficiency compared to V_2O_5 nanowires (k_{cat} ~3.9 min^{-1}; k_{cat}/K_M ~590 M s^{-1}) (a detailed comparison with other GPx mimics is provided in Table 9.1). As the kinetic data suggest, the remarkable enhancement in catalytic efficiency (k_{cat}/K_M) of C-Mn_3O_4 nanozyme was achieved not by reducing the K_M but through enhancement of the k_{cat}, which is considered as one of the most challenging demands in the evolution of artificial enzymes [40,41]. It has to be noted that, C-Mn_3O_4 nanozyme showed excellent catalytic activity at physiological pH (pH ~7.4). While sufficient catalytic

Table 9.1. Comparison of kinetic parameters of different GPx mimic.

Name of the Enzyme	K_M (mM)	k_{cat} (min^{-1})	V_{max} ($M\ s^{-1}$)	k_{cat}/K_M ($M^{-1}\ s^{-1}$)
C-Mn_3O_4 NP	0.11	69.12 min^{-1}	1.58×10^{-6}	10530.17
Ebselen	0.83	2.36 min^{-1}	3.13×10^{-6}	47.5
Ebselen (for GSH)	2.34	3.85 min^{-1}	5.13×10^{-6}	27.33
$CoFe_2O_4$ NP	8.89	NA	1.93×10^{-8}	NA
HRP	3.7	58 min^{-1}	8.71×10^{-8}	15675.68
6-SeCD	0.35	5.5 min^{-1}	NA	255
6-diSeCD	0.243	10.81 min^{-1}	NA	740
2-SeCD	0.321	16.0 min^{-1}	NA	830
GPx (Rabbit liver)	0.01	5780 min^{-1}	NA	9.63×10^{6}
2-TeCD	0.33	26.65 min^{-1}	5.33×10^{-7}	1331.67
V_2O_5 Nanowire	0.11	3.9 min^{-1}	7.16×10^{-6}	590
Fe_3O_4 NP	154	1430 min^{-1}	9.78×10^{-8}	154
Fe_3O_4 NP	54.6	NA	1.8×10^{-8}	NA
Selenoglutaredoxin	0.01	0.042 min^{-1}	NA	70
GPx (Bovine)	5.3	9000 min^{-1}	NA	28301
MoO_3 Nanowire	5.61	NA	4.6×10^{-6}	NA

NA: Data not available.

activity at physiological, or neutral pH is obligatory for potential therapeutic application, most of the previously reported nanozymes require acidic condition for peroxidase-mimicking activity [2] limitting their cellular or *in vivo* applications [42,43].

Most of the peroxidase mimics exert their catalytic activity through the generation of •OH radical which in the presence of metal ions mediates the oxidation of organic substrates [44,45]. In order to investigate the role of •OH in the catalytic mechanism of C-Mn_3O_4 nanozyme, we introduced luminol, an •OH indictor into the reaction mixture. Non-appearance of any chemiluminescence signal indicated the absence of •OH during catalysis (Figure 9.4). Therefore, the mechanism of C-Mn_3O_4 nanozyme was different from other peroxidase mimics. The exceptional selectivity of the nanozyme towards H_2O_2 is probably due to the formation of a polar peroxido species rather than •OH radicals [9]. The peroxido species reacts further with the nucleophile (GSH cofactor) to form glutathione disulfide (GSSG) (detailed in computational studies). GPx mimics often tend to show haloperoxidase activity [44]. So, we monitored the reaction of C-Mn_3O_4 NPs with H_2O_2 in the presence of haloperoxidase substrates i.e., dopamine/iodide or tyrosine/iodide. The reaction rate

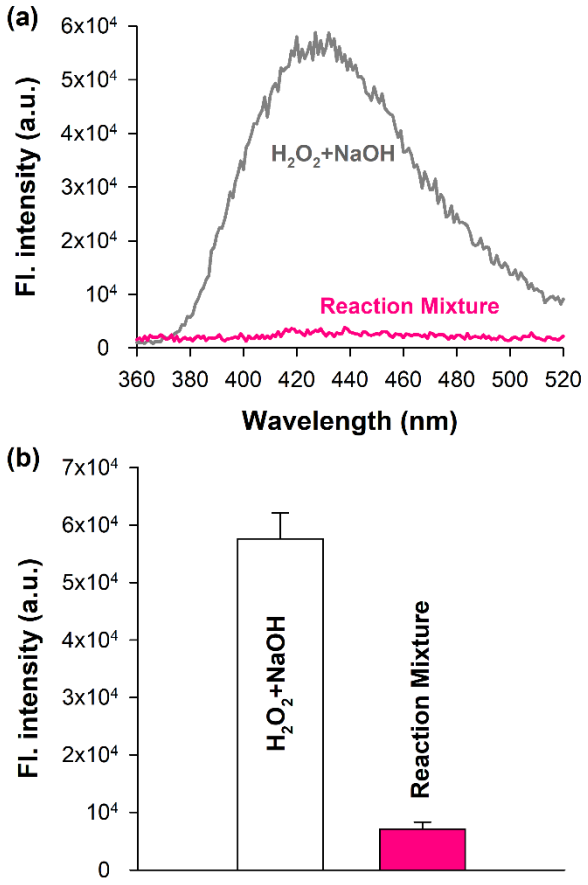

Figure 9.4. *Luminol assay. (a) The chemiluminescence spectra of luminol in presence of H_2O_2 + NaOH (positive control). While in reaction mixture no chemiluminescence peak of luminol was observed. (b) Quantitative estimation of the chemiluminescence intensity at 430 nm.*

remained unaffected (Figure 9.3e). The unaltered reaction rate could be attributed to the facile attack of GS^- at the polarized oxygen atom of the peroxido species formed on the surface of C-Mn_3O_4 NPs upon reaction with H_2O_2 as a result of greater nucleophilic character of GS^- compared to halides. Further comparison between the reactivity of C-Mn_3O_4 NP (in terms of reaction rate) with various peroxide substrates e.g., H_2O_2, *t*-butyl hydroperoxide, and cumene hydroperoxide indicates that the catalytic action is specific to H_2O_2 (Figure 9.3f). In addition, we studied the possible interference of other metabolites (e.g., glucose, cysteine) present in the cellular *milieu*. As the results suggest (Figure 9.5), neither glucose (15 mM) nor low concentration of cysteine (1 mM) have any effect on the enzyme action of the C-Mn_3O_4 NPs. However, high concentration of cysteine (10 mM) inhibited the enzyme like activity of the NPs. Previous studies have also repoted similar inhibitory effects of high concentration of

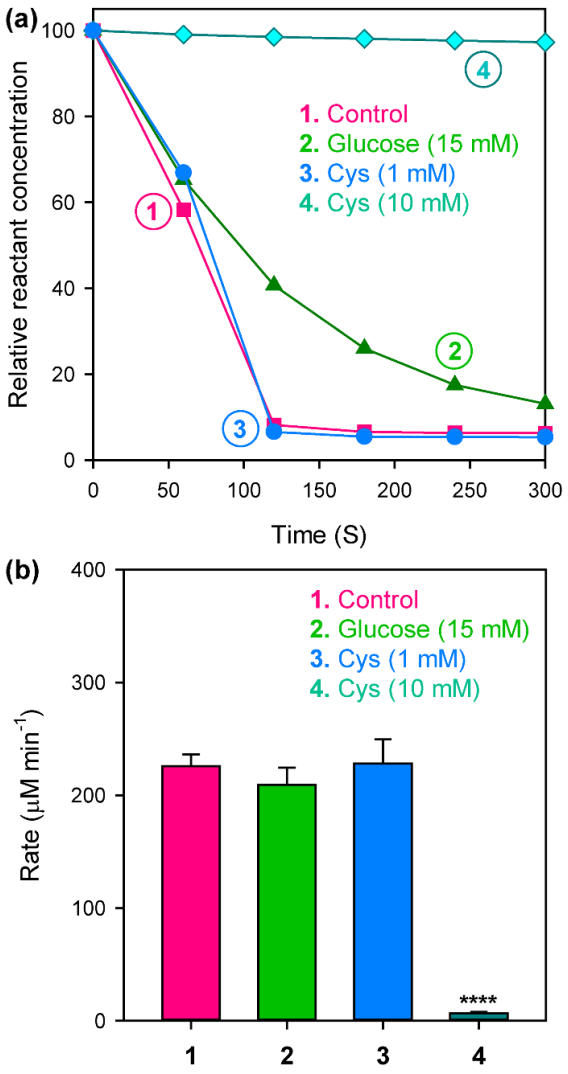

Figure 9.5. *Effect of Glucose and Cysteine (Cys) in GPx mimicking activity of the nanozyme. (a) The reaction kinetics. (b) The reaction rates.*

cysteine against natural GPx isoform [46]. Such inhibition could arise from the possible reaction of thiol metabolites (e.g., cysteine) with GSH in the last step of the GPx reaction so that the enzyme cannot be regenerated and activity is decreased [46].

In order to validate the catalytic reaction mechanism of the nanozyme, as postulated above, a quantum chemical computational study using density functional theory (DFT) was performed (*vide* Chapter 3, Section 3.4.1). The schematic of the reaction mechanism starting from the adsorption of H_2O_2 on the Mn(II) catalytic center to the formation of a water molecule and hydroxy-glutathione (GSOH) is illustrated in Figure 9.3g and Figure 9.6a & 9.6b. The computed Gibbs free energy

profile of the reaction path (Figure 9.3h) suggests that the adsorbed H_2O_2 spontaneously undergoes splitting (ΔG = -6.3 kcal/mol) on the Mn(II) center forming a peroxido species. In the next step, one proton is transferred from GSH to one of the OH groups attached to the catalytic center resulting in formation of water. This proton transfer process has a very low activation energy of 2 kcal/mol and a large Gibbs free energy of -10.4 kcal/mol suggesting a highly favourable reaction. After the proton donation, GS^- readily attacks the other OH group attached to the metal center and forms the GSOH intermediate, which then dissociates by regenerating the Mn(II) catalytic center. Water is then replaced by H_2O_2 and the next cycle begins. Thus, a •OH radical is never released. Water on the Mn(II) catalytic center is then replaced by H_2O_2 and the next cycle begins. GSOH undergoes a condensation reaction with a molecule of GSH to form the GSSG [47]. Regarding the efficiency of such as catalysis, Wang et al. recently showed that e_g orbital (d_{x2-y2} and d_{z2}) occupancy could be an excellent measure of peroxidase like activity of transition metal oxide nanozymes [48]. Their study established a volcano relationship of activity with the average e_g occupancy on a scale of 0--2. i.e., the maximum activity was observed for a nanozyme with e_g occupancy of 1; the activity decreased as the e_g occupancy approaches 0 or 2. This explains why our Mn_3O_4 nanozyme (calculated e_g occupancy of ~1.33) shows very high peroxidase like activity. In OH dissociation reaction during water oxidation as well, Saha-Dasgupta et al. previously showed that population of e_g state in the high spin Mn catalytic center of Mn_4O_4 cubane is associated with their higher catalytic efficiency over other transition metal catalysts such as Co_4O_4 [49]. The mechanism is illustrated in Figure 9.3g and Figure 9.6. The energy diagram for different steps is indicated in Figure 9.3h.

Preclinical animal studies are essential for the translation of potential therapies from bench to bedside [50]. Considering the *in vitro* adaptability of C-Mn_3O_4 nanozyme in redox regulatory mechanisms we tested their efficacy in an animal model as a prelude to clinical translation. Huntington's disease (HD), one of the most prevalent neurodegenerative disorders, is an autosomal-dominant disorder caused by an expansion of CAG repeats in the gene huntingtin, *htt*, and characterized by lesions in the striatum of the brain that cause progressive behavioral and cognitive impairments

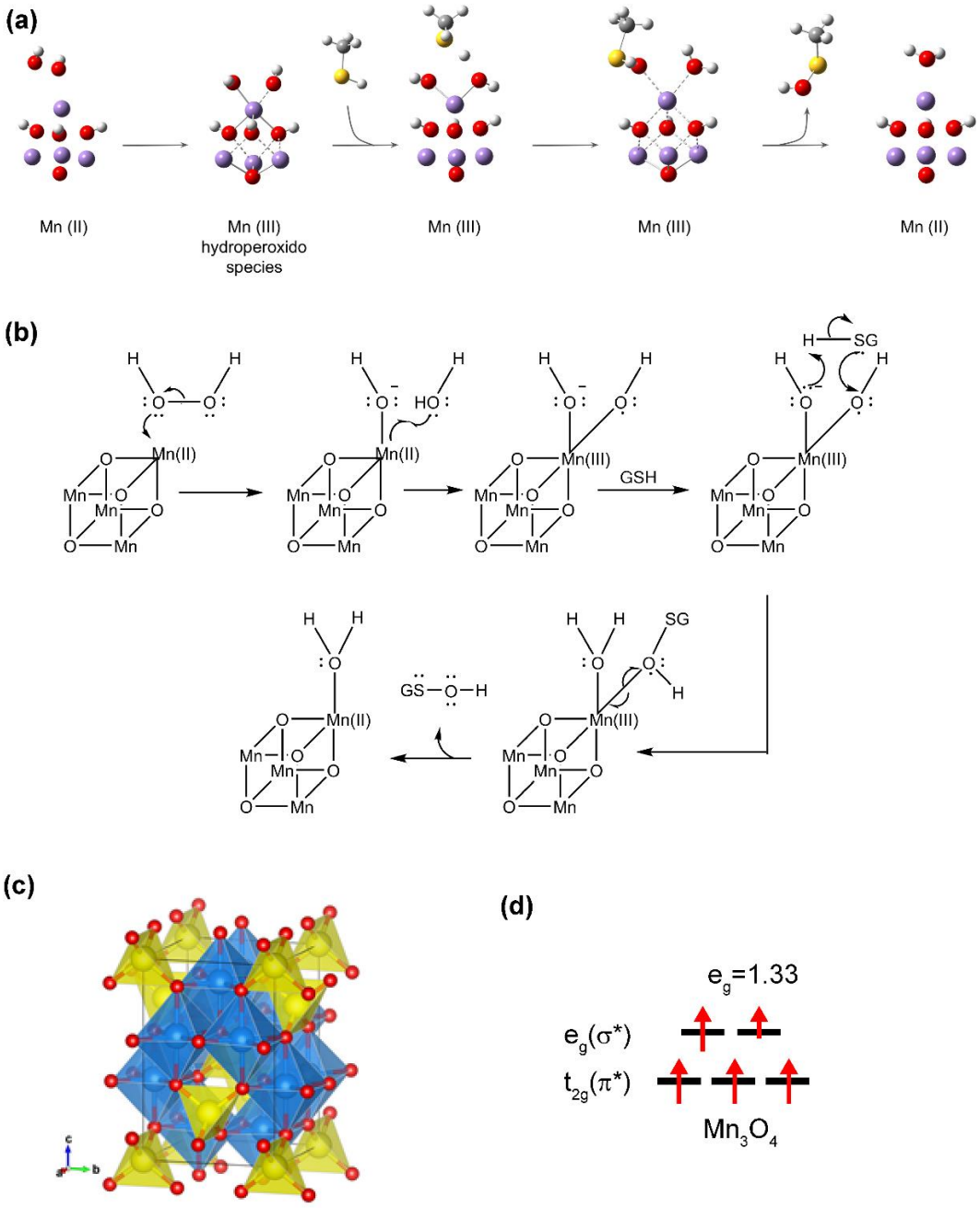

Figure 9.6. *Computational analysis of reaction mechanism. (a) DFT optimized atomistic model of H_2O_2 splitting on the Mn_4O_4 cubane complex. Color keys: Mn, purple; O, red; C, gray; S, yellow; H, white. (b) Mechanism of nano-enzymatic action. (b) Peroxidase reaction mechanism. H_2O_2 adsorbs on the Mn(II) catalytic center by donating a lone pair from one oxygen atom to a vacant 4sp3 orbital of Mn(II). This leads to the splitting of H_2O_2 into two OH groups. In this process one e_g electron of Mn(II) is shared with one of the OH groups, oxidizing the Mn(II) center. Then a proton is transferred from GSH to the OH- attached to the Mn(III) center forming a water and GS- attacks the OH group forming GSOH which gets dissociated from the Mn(III) center reducing it to Mn(II). (c) Geometry of Mn_3O_4 spinel unit cell with 4 Mn(II), 8 Mn(III) and 16 O atoms. Tetrahedral Mn(II) centers are shown in yellow, Octahedral Mn(III) centers are shown in blue and oxygen atoms are shown in red. (d) Average 3d electron occupancy of t_{2g} (π^*) and e_g (σ^*) antibonding orbitals associated with the transition metal Mn.*

and involuntary choreiform movements [26,27]. Unfortunately, to date, there is no satisfactory medicine to prevent or slow the pathogenesis of HD [27,51]. Strong evidence suggests a causal relationship between oxidative stress and HD [27]. Elevated markers of oxidative damage such as protein oxidation, lipid peroxidation, and DNA damage have been linked to the pathogenesis. Other than oxidative stress, transcriptional impairment, excitotoxicity, inflammation, apoptosis, and mitochondrial dysfunction leads to disease onset and striatal degeneration [52]. Interestingly in one recent study, Mason et. al., has shown that overexpression of GPx (neither SOD nor catalase) in cellular, yeast, or drosophila models of HD could mitigate the mHtt (mutant huntingtin) toxicity and associated oxidative damage [28]. Therefore, we hypothesized that pharmacological interventions with GPx mimic like C-Mn_3O_4 nanozyme could be a viable treatment option to prevent HD pathogenesis considering the mimic would be able to cross the BBB, enter the brain cells and efficiently supplement the intracellular GPx activity. We selected a well-studied 3-NPA induced C57BL/6j mice model of HD to test the *in vivo* therapeutic efficacy of C-Mn_3O_4 nanozyme [53-56]. 3-NPA is known to inhibit mitochondrial respiratory complex-II (succinate dehydrogenase, SDH) in neuronal cells instigating mitochondrial impairment, ATP depletion, increase in reactive oxygen species (ROS), excitotoxicity and thereby, simulates a neurobehavioral condition exactly similar to mHtt toxicity and HD [57].

Several studies have indicated that 3-NPA damages striatal medium spiny neurons, which lead to a progressive deficit in fine and gross motor function [55]. Motor function was evaluated through four tests: beam traversal, pole descent, nasal adhesive removal, and hindlimb clasping reflexes. 3-NPA treatment caused a progressive decline in the hind limb clasping reflex score, a hallmark of HD pathogenesis, and definitive measure of striatal dysfunction throughout the experimental regime (Figure 9.7a). Treatment with C-Mn_3O_4 nanozymes protected the animals from derogatory motor impairment. From the 10^{th} day of the experimental period the hind limb clasping reflex started to improve significantly compared to the 3-NPA intoxicated group (Figure 9.7a). The other two groups (control and C-Mn_3O_4 nanozyme treated) retained baseline performance. Treatment solely with the constituent ligand citrate did not affect clasping behavior (Figure 9.8a).

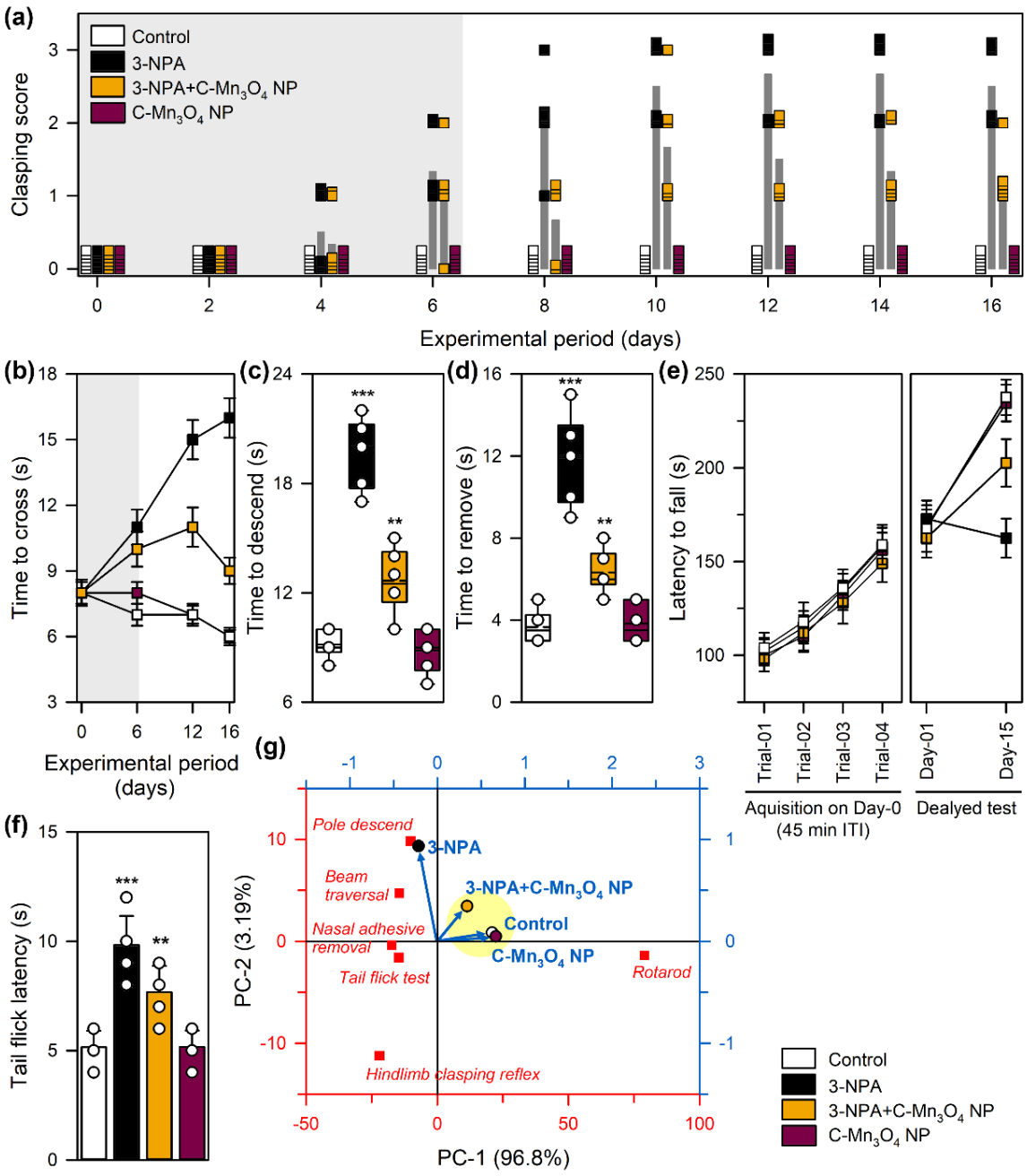

Figure 9.7. *Effect of C-Mn_3O_4 NPs on 3-NPA induced motor impairment, hallmark of Huntington's disorder. (a) Hind limb clasping reflex shows progressive improvement due to C-Mn_3O_4 NP treatment during the experimental regime. Darker shaded region represents co-treatment period. (b) Time to cross a beam in beam traversal test. (c) Time to descend a pole. (d) Nasal adhesive removal time. (e) Rotarod test. (f) Tail flick latency. (g) PCoA analysis considering all motor phenotypes. Data are expressed as Mean ± SD. N= 6. *, **, *** Values differ significantly from control group (without treatment) (***p< 0.001; **p< 0.01; *p< 0.05).*

3-NPA-administered mice required significantly extra time to cross a challenging beam (Figure 9.7b), and to descend a pole (Figure 9.7c), the two methods of accessing gross motor function, compared to untreated control or C-Mn_3O_4 nanozyme-treated littermates. Treatment with C-Mn_3O_4 nanozyme resulted in significant improvement in both of them (Figure 9.7b & 9.7c). In contrast, treatment with citrate showed no signs of improvement in the tests (Figure 9.8). Removal of an adhesive from the nasal bridge, which provides information about fine motor control, was impaired in 3-NPA intoxicated mice compared to the other three groups (Figure 9.7d). While, citrate treated animals displayed similar results to 3-NPA treated ones (Figure 9.8d). The observed recovery in both gross motor function, and fine motor control due to treatement with C-Mn_3O_4 nanozyme were found to be dose-dependent (Figure 9.8). Considering the therapeutic inefficacy of citrate, we excluded the citrate treated group from further experiments. The striatum and related basal ganglia circuits are known to contribute towards the acquisition of repetitive and stereotyped behaviors [58,59]. To assess fine motor movements, we performed rotarod test. In the rotarod study, motor learning was evaluated considering the improvement in performance (i.e., latency to fall) over three trials. In 3-NPA-treated mice, latencies to fall were lesser in delayed tests at day-1 and day-15 (Figure 9.7e), which is a marker of fine-motor function deficit. For the group that received both 3-NPA and C-Mn_3O_4 NPs, latency to fall was significantly increased compared to the 3-NPA treated group. So, the C-Mn_3O_4 nanozyme was successful in improving the fine motor movements casued by 3-NPA administration. To evaluate the sensory motor functions, we used tail-flick assay (Figure 9.7f), where the 3-NPA intoxicated mice in the first trial exhibited lengthier tail-flick latency, thus poorer pain sensitivity. However, this variance was not observed in successive trials. The tail-flick latencies of 3-NPA+C-Mn_3O_4 NP treated, and C-Mn_3O_4 NP treated groups were similar to untreated control (Figure 9.7f). Furthermore, we compiled all motor phenotypes into a principal component analysis (PCoA). The result displays the prominent segregation of the 3-NPA intoxicated group with the others (Figure 9.7g). The animals co-treated with 3-NPA+C-Mn_3O_4 NPs, or C-Mn_3O_4 NPs alone clusped together with the control animals (Figure 9.7g). Collectively, these results indicate that C-Mn_3O_4 nanozyme significantly protected 3-NPA intoxicated mice from the hallmark motor dysfunctions that resemble HD-like syndrome.

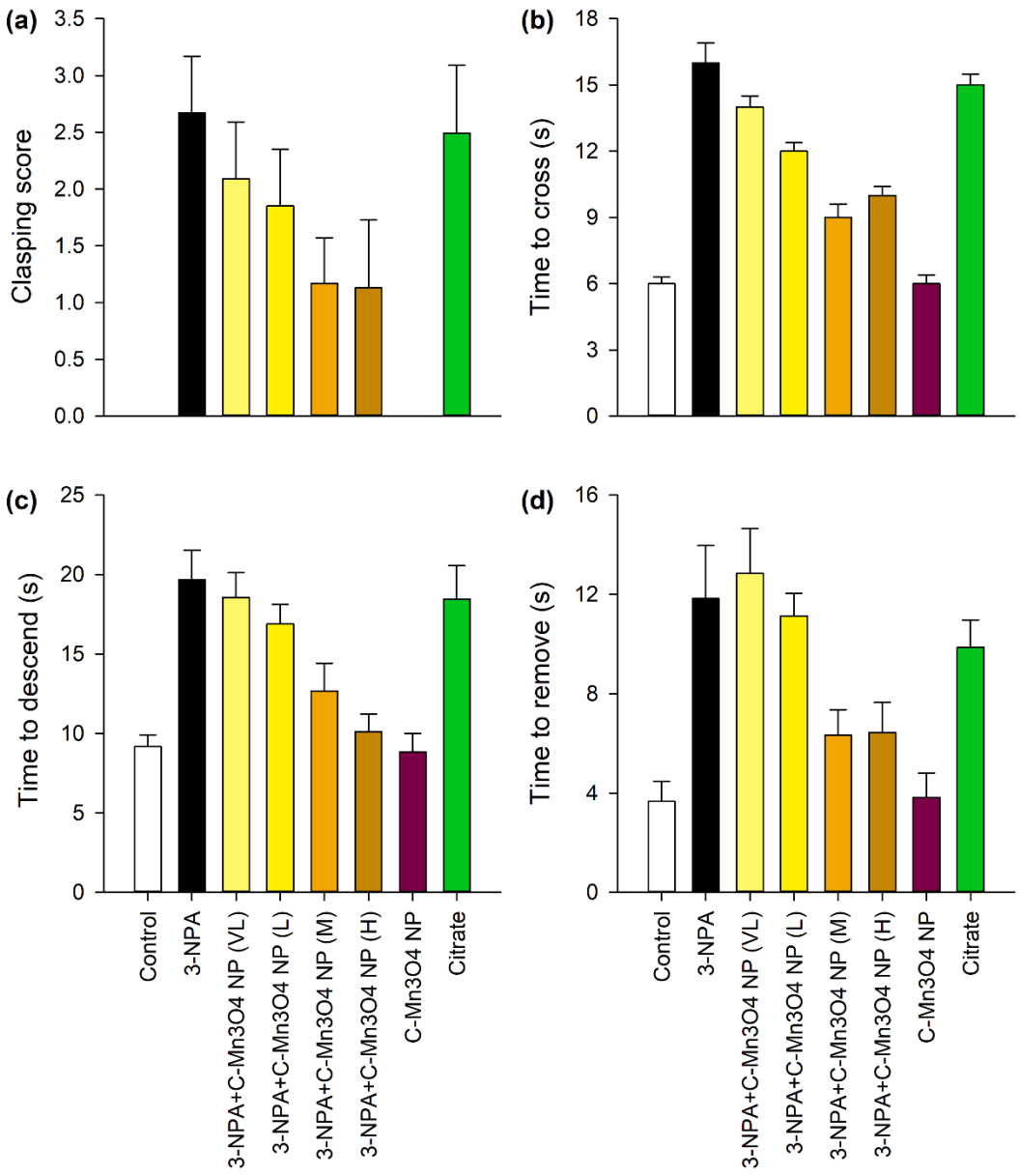

Figure 9.8. *Effect of different doses of C-Mn_3O_4 NPs and citrate on 3-NPA induced Huntington's like motor dysfunction. (a) Hindlimb clasping reflex. (b) Time to cross a beam. (c) Time to descend a pole. (d) Time to remove nasal adhesive. Data expressed as Mean ± SD (N=6).*

Previous studies indicate that 3-NPA causes striatal damage and produces anxiety-like behavior, similar to human HD [56,60]. Therefore, we evaluated the effect of C-Mn_3O_4 NPs on the anxiogenic behavior of 3-NPA induction. The thigmotactic behavior as an index of anxiety of the animals was evaluated using open field test (OFT). 3-NPA intoxication significantly enhanced the thigmotactic behavior (an indicator of increased anxiety), as showed by the lesser affinity of the animals to spent

time in the central zone of the apparatus (Figure 9.9a & 9.9b). Animals solely treated with C-Mn_3O_4 nanozyme spent the highest time at the central zone, while 3-NPA+C-Mn_3O_4 nanozyme-treated animals spent sufficiently enough time compared to control animals. The total distance moved by the animals and velocity were similar for all the groups, with the exception of the 3-NPA intoxicated mice (Figure 9.9c & 9.9d). The deteriorated locomotor function was probably one of the major reasons behind this observation. Nevertheless, it can reasonably indicate that the C-Mn_3O_4 nanozymes possess anxiolytic property that commendably overturned the 3-NPA induced anxiety-like behavior. To further check this hypothesis, elevated plus maze (EPM) test for anxiety-like behavior was employed. Consistent with previous studies, the 3-NPA-intoxicated mice spent significantly lesser amount of time in the open arms of the EPM compared to the other three groups (Figure 9.9e and 9.9f). Similar observations were found in terms of the distance they moved in the open arms (Figure 9.9g). Similar to OFT, in case of EPM too, the total distance moved was lesser for the 3-NPA-treated mice (Figure 9.9h). In agreement with this behavior, the 3-NPA-treated mice spent more time in the closed arms of the apparatus. Both OFT and EPM studies were performed in a regular time interval, throughout the experimental period. The results showed similar trends like other motor functions discussed in previous section (data not shown). Combination of the observed behavioral features indicated that the anxiety was induced due to severe 3-NPA neurotoxicity, which was ameliorated upon treatment with C-Mn_3O_4 nanozymes. Light preference test was further used to validate our observations about the anxiolytic effects of C-Mn_3O_4 nanozymes. In light preference test, reduced movement in the light area is considered as an indicator of anxiety. 3-NPA-treated mice exhibited both lesser activity and transitions in the light zone of the apparatus, while treatment with C-Mn_3O_4 nanozyme efficiently recovered their normal activity (Figure 9.9i).

Another prominent feature of 3-NPA-induced neurotoxicity is the introduction of depression-like behavior in rodents, a symptom similar to the HD affected human counterpart. Therefore, we employed the forced swim test (FST) to assess depression-like behavior. In FST, high immobility time reflects increased depression. Consistent with previous studies, 3-NPA treatment resulted in increased immobility time (Figure 9.9j). Treatment with C-Mn_3O_4 nanozyme reduced the indications of depression as

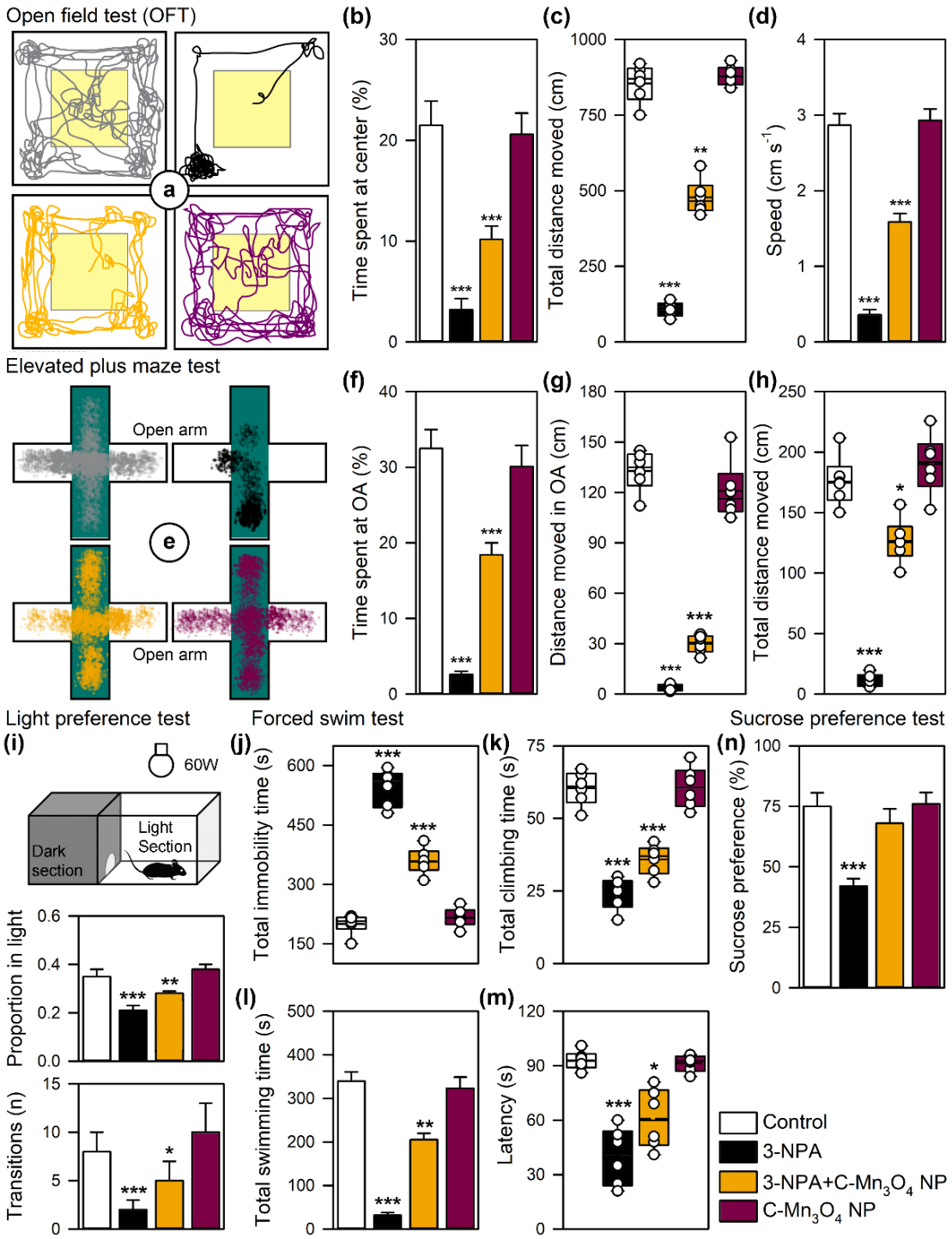

Figure 9.9. *Effect of C-Mn_3O_4 NPs on anxiety and depression-like behavior. Open field test. (a) Trace of open field activity. (b) Time spent at the center. (c) Total distance moved. (d) Average speed. Elevated plus maze test. (e) Trace of movement in EPM. (f) Time spent in open arm. (g) Distance moved in open arm. (h) Total distance moved. (i) Light preference test. Time spent in light zone and transitions into light zone. Forced swim test. (j) Total immobility time, (k) Total climbing time, (l) Total swimming time and (m) Latency to first immobility event. (n) Sucrose preference test. Data are expressed as Mean ± SD. N= 6. *, **, *** Values differ significantly from control group (without treatment) (***p< 0.001; **p< 0.01; *p< 0.05).*

imitated in the lower immobility time (Figure 9.9j). The untreated control group and C-Mn_3O_4 nanozyme treated group showed comparable results. Measurements of the climbing time, swimming time, and latency to the first immobility event further highlighted the antidepressant-like action of the nanozyme. The climbing activity was significantly lower in 3-NPA-treated animals (Figure 9.9k). There was no observable improvement even after treatment with the nanozyme. Total swimming time (Figure 9.9l), or latency to first immobility (Figure 9.9m) were comparable throughout all four groups. Observed depression-like behavior of the 3-NPA-treated mice was accompanied by anhedonia (i.e., inability to experience pleasure from activities usually found enjoyable, in this case tasting the sweetness of sucrose), as indicated by the sucrose preference test (SPT) (Figure 9.9n). The preference for sucrose was almost identical for all the other three groups, demonstrating the healing effect of the C-Mn_3O_4 nanozyme (Figure 9.9n).

According to previous studies, 3-NPA exposure may increase oxidative stress in the hippocampus leading to memory deficit and affective disturbances reminiscent of the HD [61,62]. To characterize whether C-Mn_3O_4 nanozyme can reverse the 3-NPA persuaded hippocampal damage, we employed novel object recognition, and Morris water maze (MWM) test. Novel obeject recognition was used to illuminate the behavioral complications (disturbances in recall memory) due to 3-NPA-intoxication, and the effect of the nanozyme over it. Next to three days of 15 min habituation trials in the testing apparatus, animals were permitted to explore two identical objects for 5 min and were then returned to their home cages. After an interval of 60 mins, one familiar object was replaced with a novel object, and the animals were permitted another 2 mins of exploration time. Their time of interaction with each of the two objects were measured during the experimental period (Figure 9.10a). As anticipated, the untreated control animals with entirely intact recall memory, spent more time with the novel object than the familiar one (Figure 9.10b and 9.10c). In contrast, 3-NPA-intoxicated animals were unable to discriminate between the novel and familiar objects, and spent almost similar time with both of them (Figure 9.10b and 9.10c). Conversely, treatment with C-Mn_3O_4 nanozymes recovered the 3-NPA-treated animals from the profound cognitive deficit resulted from disturbances in hippocampus dependent learning and memory (Figure 9.10b and 9.10c). To further

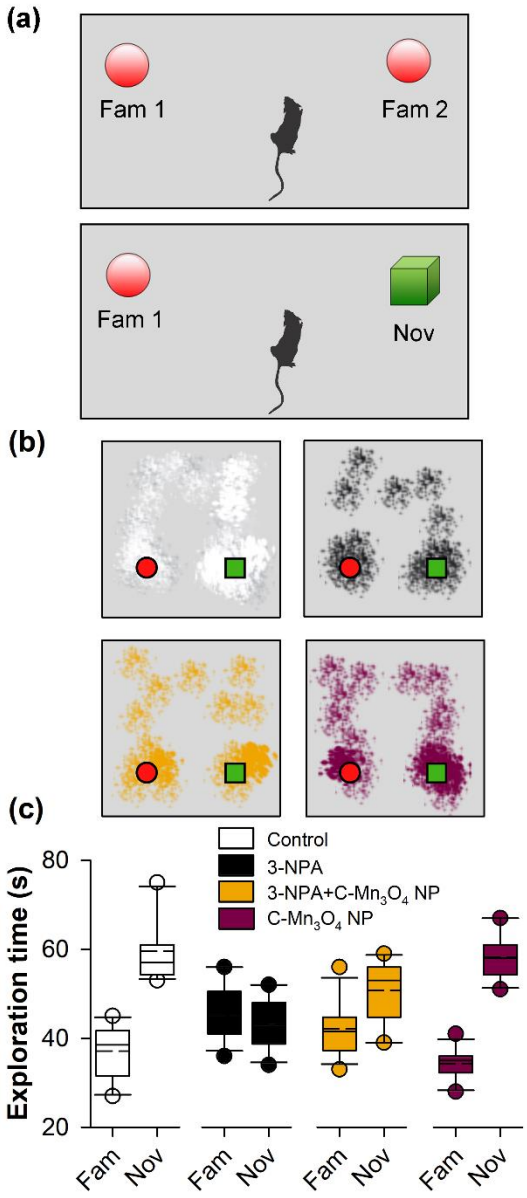

Figure 9.10. *Novel object recognition test. (a) The experimental setup. (b) The movement pattern of the mice during experiment. (c) Novel object exploration time compared to the familiar one. Data expressed as Mean ± SD (N=6).*

verify the results of novel object recognition, MWM test was used. In case of 3-NPA-intoxicated animals, severe decline in spatial learning was found as the animals were failed to find the platform within the provided timeframe (Figure 9.11a). The amount of time the 3-NPA treated animals spent in the target quadrant was nominal and insignificant (Figure 9.11b and 9.11c). In contrst, the animals co-treated with 3-NPA

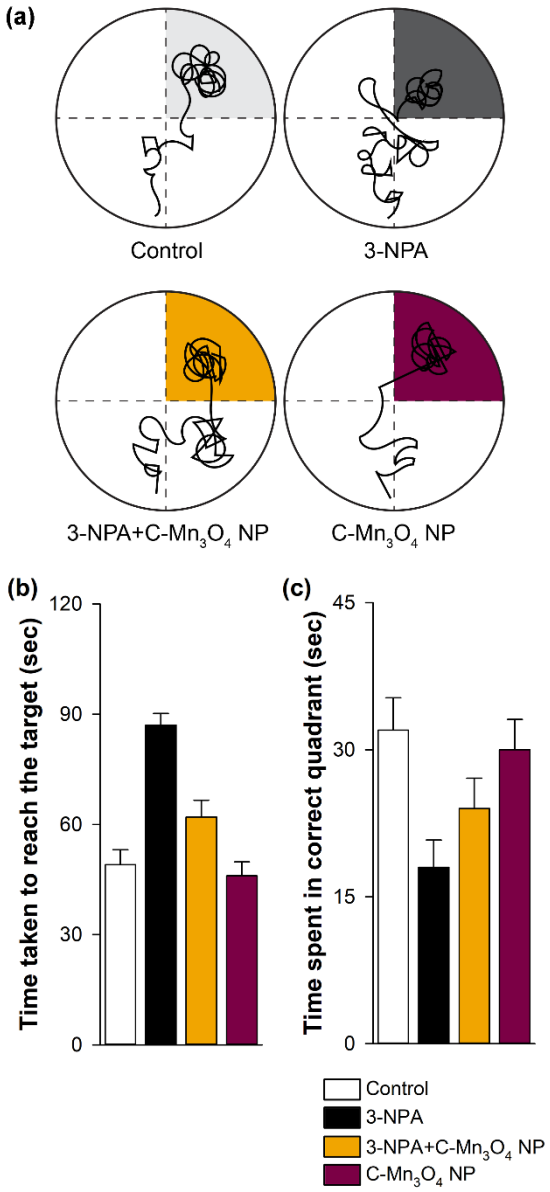

Figure 9.11. *Morris Water Maze Test. (a) The movement of mice during experiment. The shaded region indicates the target quadrant. (b) Time taken to reach the target. (c) Time spent in the correct quadrant. Data expressed as Mean ± SD (N=6).*

and C-Mn_3O_4 nanozyme were successful in finding the hidden platform, although the time taken to reach the platform was longer compared to the control animals (Figure 9.11b and 9.11c). The other group, i.e.the C-Mn_3O_4 nanozyme-treated group, performed similar to the untreated control group (Figure 9.11b and 9.11c). Results of the aforementioned two tests indicate towards severe hippocampal damage caused due to the 3-NPA treatment, and its prevention by C-Mn_3O_4 nanozyme treatment.

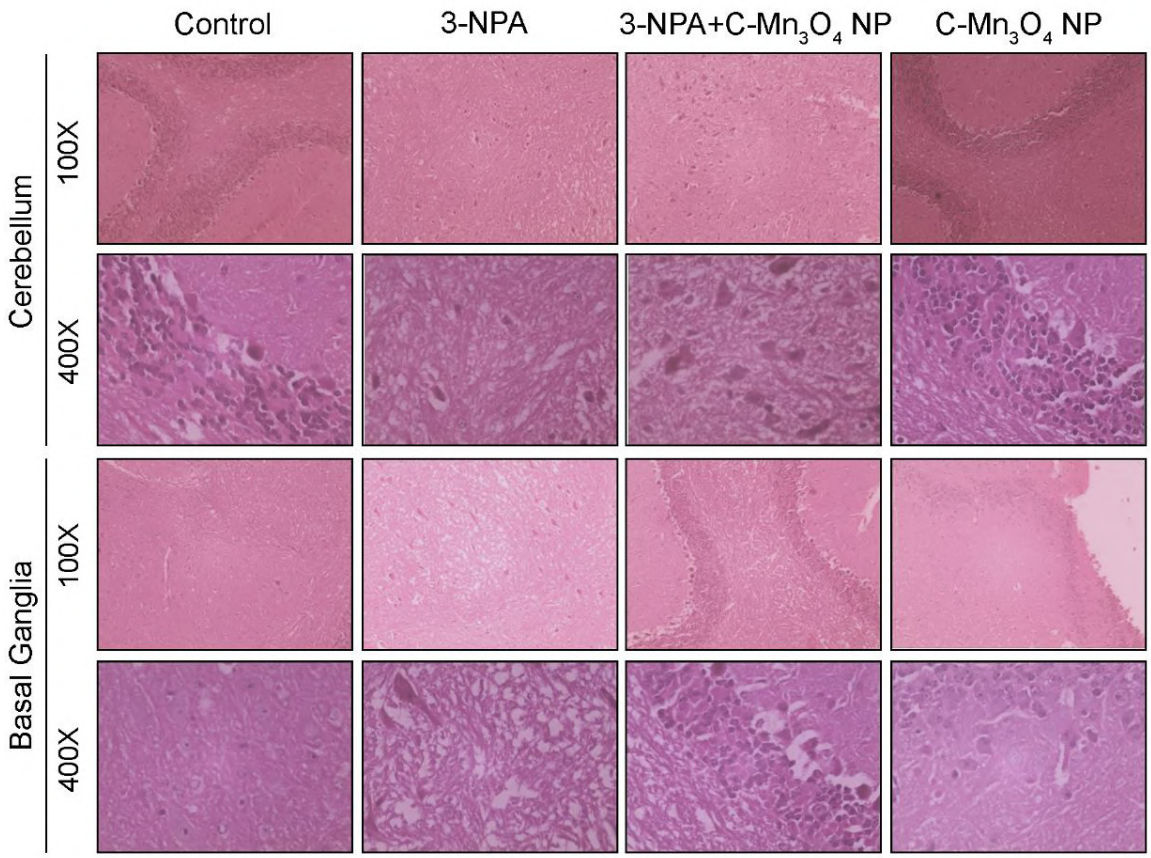

Figure 9.12. *Effect of C-Mn_3O_4 NPs on 3-NPA induced histopathological damages. Microscopic images of haematoxylin and eosin stained sections of cerebellum and basal ganglia are shown at 100X and 400X magnifications.*

The results of behavioural studies were further supported by our histopathological findings (Figure 9.12). The hematoxylin and eosine stained brain sections of control mice showed normal brain tissue architecture. In 3-NPA treated mice, several signs of damage, particularly increase in apoptotic cells were evident in cerebellum and basal ganglia region of the brain. In basal ganglia focal degeneration of cells were also observed. In cerebellum region, the number of Purkinje cells were found to be reduced. Fibrillary gliosis was also evident in some regions. In co-treated (3-NPA+ C-Mn_3O_4 NP) and C-Mn_3O_4 NP-treated mice no significant damage in brain cell architechture was observed. This clearly indicated that treatment with the nanozyme decreased the Huntington like damage in the brain. It further implies that, the NPs are extremey safe to administer for treatment of neuronal damages.

The changes in the behavioral phenotype and morphometric histological findings indicate toards the retention of GPx mimic activity *in vivo*. To further confirm its effects, we measured the lipid peroxidation in the brain tissue. Upon 3-NPA administration the lipid peroxidation increased significantly, while the NPs were able to protect the neuronal cells from its. The SOD, catalase and GPx activities were almost identical from the two groups, while less lipid peroxidation indicated towards the GPx mimic activity of C-Mn_3O_4 NPs. As the oxidative damage decreased, it was expected that the mitochondrial damage will decline upon nanozyme treatment. In rodents, high doses of 3-NPA cause degeneration of striatal neurons and motor dysfunction similar to Huntington's disease [63]. The primary mechanism of 3-NPA-induced neurotoxicity involves the suicide inhibition of the mitochondrial electron transport chain (ETC) linked enzyme succinate dehydrogenase (SDH or complex-II) [53]. Inhibition of SDH interferes with ETC and oxidative phosphorylation leading to cellular energy deficit (a decrease in ATP production) [54], oxidative stress, depletion of reduced glutathione (GSH), and alteration in the activities of cellular antioxidant enzymes [57]. In agreement with previous observations, 3-NPA alone increased the lipid peroxidation (Figure 9.13a), a marker of oxidative damage, and significantly reduced the activities of cellular antioxidant enzymes, SOD, Catalase, and GPx (Figure 9.13b-9.13d). Treatment with C-Mn_3O_4 NPs significantly increased the activity of GPx (Figure 9.13d) and to some extent rescued the activities of SOD and catalase (Figure 9.13b & 9.13c). The observed change in GPx activity can be attributed to the GPx-mimic activity of the nanozyme to support the H_2O_2 scavenging by natural GPx. Whereas, the regain of SOD and catalase activities may be due to the indirect beneficial effect of an overall decrease in oxidative distress reflected in the reduction in lipid peroxidation (Figure 9.13a). Consistent with previous observations, in the current *in vivo* model of HD, we found that brain mitochondrial function was impaired in 3-NPA-treated animals (Figure 9.13e-9.13j). Increased mitochondrial permeabilization (mitochondrial swelling or mPTP formation) (Figure 9.13e), deregulated mitochondrial membrane potential (Figure 9.13f), decreased ATP level (Figure 9.13g), decreased mitochondrial dehydrogenase activity (Complex-II; Figure 9.13h), decreased complex IV activity (Figure 9.13i), increased mitochondrial ROS (Figure 9.13j) were evident in the brain tissue of HD animals. These deteriorating

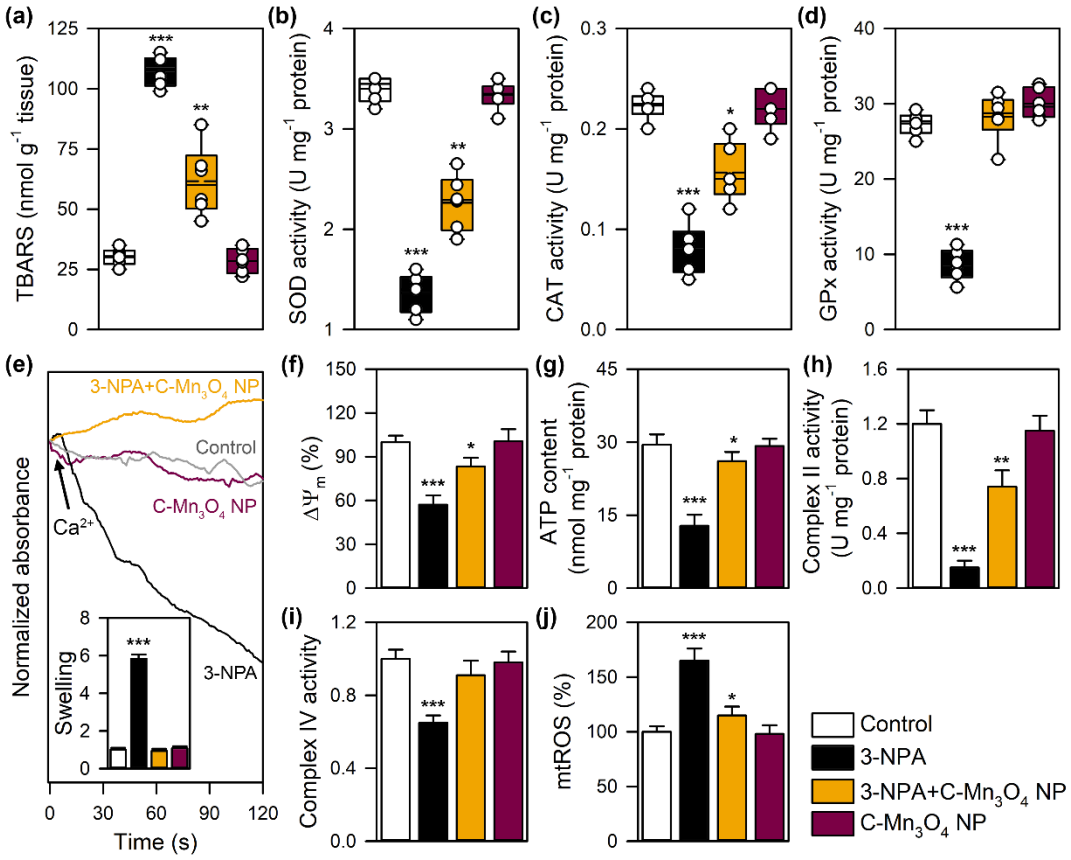

Figure 9.13. *Effect of C-Mn_3O_4 NPs on antioxidant enzymes and mitochondrial parameters of brain. (a) Lipid peroxidation. (b) SOD activity. (c) Catalase activity. (d) GPx activity. (e) Effect on mitochondria permeability transition, measured as a decrease in absorbance at 540 nm. Inset shows extent of swelling in comparison to the control. (f) Change in mitochondrial membrane potential ($\Delta\Psi_m$). (g) ATP content. (h) Complex-II activity of the electron transport chain. (i) Complex-IV activity of the electron transport chain. (j) Mitochondrial ROS (mtROS) as measured using DCFH assay. Data are expressed as Mean ± SD. N= 6. *, **, *** Values differ significantly from control group (without treatment) (***p< 0.001; **p< 0.01; *p< 0.05).*

changes in mitochondrial parameters resulted in neuronal degeneration observed in the histological findings and motor behaviours. C-Mn_3O_4 NPs were able to efficiently protect mitochondria from the aforementioned damages (Figure 9.13e-9.13j). Our results strongly suggest that the GPx mimic activity of C-Mn_3O_4 nanozyme helped in scavenging the free radicals and reducing the associated oxidative damage, thereby prevented the mitochondrial dysfunctions and concomitant redox imbalance, the major underlying causes of neurodegenerative diseases like HD. The interesting cellular redox modulatory and mitochondria protective action of the nanozyme further open up the future possibility to study intracellular distribution and transport of the

C-Mn_3O_4 nanozyme in cellular *milieu*. However, considering the nature of the nanozyme we assume that it will be located mostly in the cytosol and mitochondria because earlier studies depicted that both the constituting metal Mn and ligand citrate has an affinity towards mitochondria as well as cytosol [64,65].

As described in earlier section, one of the major limiting step in therapeutic translation of nanozymes in living organisms is their inherent toxicity. Therefore, we examined the cytocompatibility of C-Mn_3O_4 nanozyme in human embryonic kidney (HEK 293) cell line, which is one of the most widely used non-cancerous cell lines used for cytotoxicity assessment. The results of dose dependant MTT assay (after 24 h of exposure) shows upto 50 μg mL^{-1} of the nanozyme, cell viability was similar to untreated control, upto ~200 μg mL^{-1}, mortality was minimal (~20 %) (Figure 9.14). Further increase in dose resulted into exponential decrease in cell viability. The LD_{50} value (concentration of nanoparticles to induce 50% cell mortality) obtained after 24 h exposure was ~795 μg mL^{-1}, which is significantly higher (i.e., lower toxicity) than other contemporary nanoparticles like SiO_2 (~140 μg mL^{-1}) [66], CeO_2 (~90 μg mL^{-1}) [67], multi wall carbon nanotubes (MWCNT) (~40 μg mL^{-1}) [68], ZnO (~50 μg mL^{-1}) [69], TiO_2 (~200 μg mL^{-1}) [70] in HEK 293 cell lines. The results of cytotoxicity studies

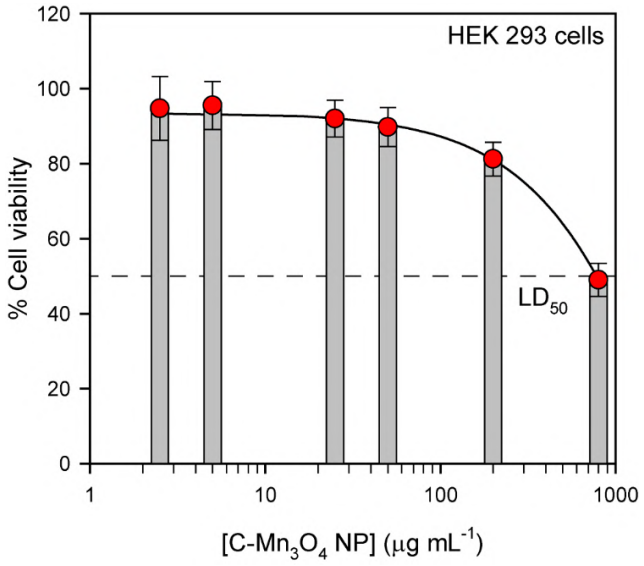

Figure 9.14. *Dose dependent cytotoxicity (MTT assay) of C-Mn_3O_4 nanozyme in HEK 293 cell line. Data expressed as Mean ± SD (N=6).*

Table 9.2. Hematological parameters.

Parameters	Control	C-Mn_3O_4 Nanozyme
Hb (g/dl)	11.6±1.2	12.1±1.1
RBC (x10^6 μL^{-1})	10.13±1.1	9.93±0.7
RT (%)	2.4±1.3	2.9±1.7
HCT (%)	35.4±1.5	34.9±1.8
MCV (μm^3)	36.7±2.0	37.1±2.3
MCH (pg)	21.5±2.2	21.8±1.9
MCHC (%)	41.9±1.9	41.8±2.6
Platelets (x10^3 μL^{-1})	6.1±1.7	6.8±1.1
WBC (x10^5 μL^{-1})	8.0±1.5	8.2±2.4
Lymphocyte (%)	72±5.5	68±6.0
Neutrophil (%)	30±6.4	27±5.9
Monocyte (%)	2.9±0.02	2.5±0.02
Eosinophil (%)	8.9±2.1	9.4±3.6
Basophil (%)	1.4±0.03	1.2±0.02
PT (sec)	7.7±1.9	7.5±2.3
APTT (sec)	15.9±3.8	16.2±3.2

Data are expressed as mean ± SD (N=6).

Abbreviations: Hb: Hemoglobin; RBC: Red Blood Corpuscle; RT: Reticulocyte; HCT: Hematocrit; MCV: Mean Corpuscular Volume; MCH: Mean Corpuscular Hemoglobin; MCHC: Mean Corpuscular Hemoglobin Concentration; WBC: White Blood Corpuscle; PT: Prothrombin Time; APTT: Activated Partial Thromboplastin Time.

are in line with previously reported results from our group, which showed that C-Mn_3O_4 nanoparticles do not exhibit deleterious effects on biological macromolecules rather protects them from other hazardous elements like bilirubin, or heavy metals [71,72]. In order to assess *in vivo* biocompatibility, we measured various hematologic parameters of study mice after 16 days of treatment with therapeutic dose of C-Mn_3O_4 nanozyme. Insignificant changes in blood parameters (i.e., hemoglobin level, hematocrit value, mean corpuscular haemoglobin, mean corpuscular hemoglobin concentration, mean corpuscular volume, red blood corpuscle count, reticulocyte count, white blood corpuscle count, platelet count) (Table 9.2) clearly demonstrate that C-Mn_3O_4 nanozyme is extremely hemocompatible when administered *in vivo*.

9.3. CONCLUSION

In conclusion, our study suggests that in neutral pH and temperature (or, in physiological milieu) C-Mn_3O_4 NPs possess distinctive GSH dependent GPx mimic activity with excellent catalytic efficiency and substrate selectivity, the two most important parameters of evaluating artificial enzymes for therapeutic use essentially in a non-toxic manner. The unique ability of the nanozyme to be incorporated in a cellular redox modulatory enzyme network without causing adverse side effects makes C-Mn_3O_4 NPs suitable for biomedical application. A detailed computational study reveals mechanistic pathway behind the enzymatic action and is consistent with the *in vitro* studies. Results of animal studies further demonstrate its ability to pass the blood-brain barrier and treat progressive neurodegenerative disorders like Huntington's disease. Enzymatic scavenging of neuronal reactive oxygen species and subsequent protection of mitochondria from oxidative damage resulted in the observed therapeutic effect. Successful clinical translation may open a new avenue in the nanozyme bases therapeutics of several other diseases (e.g., cancer, diabetes, Parkinson's, Alzheimer's, cardiovascular and chronic kidney diseases) where redox imbalance plays a key role in the pathogenesis.

REFERENCES

[1] M. Liang, X. Yan, Acc. Chem. Res. 52 (2019) 2190.

[2] H. Wei, E. Wang, Chem. Soc. Rev. 42 (2013) 6060.

[3] B. Jiang, D. Duan, L. Gao, M. Zhou, K. Fan, Y. Tang, J. Xi, Y. Bi, Z. Tong, G. F. Gao, N. Xie, A. Tang, G. Nie, M. Liang, X. Yan, Nat. Protoc. 13 (2018) 1506.

[4] L. Gao, J. Zhuang, L. Nie, J. Zhang, Y. Zhang, N. Gu, T. Wang, J. Feng, D. Yang, S. Perrett, X. Yan, Nat. Nanotechnol. 2 (2007) 577.

[5] L. Jiang, S. Fernandez-Garcia, M. Tinoco, Z. Yan, Q. Xue, G. Blanco, J. J. Calvino, A. B. Hungria, X. Chen, ACS Appl. Mater. Interfaces 9 (2017) 18595.

[6] W. Zhang, S. Hu, J. J. Yin, W. He, W. Lu, M. Ma, N. Gu, Y. Zhang, J. Am. Chem. Soc. 138 (2016) 5860.

[7] R. Ragg, A. M. Schilmann, K. Korschelt, C. Wieseotte, M. Kluenker, M. Viel, L. Völker, S. Preib, J. Herzberger, H. Frey, K. Heinze, P. Blümler, M. N. Tahir, F. Natalio, W. Tremel, J. Mater. Chem. B 4 (2016) 7423.

[8] G. Wu, V. Berka, P. J. Derry, K. Mendoza, E. Kakadiaris, T. Roy, T. A. Kent, J. M. Tour, A. L. Tsai, ACS Nano 13 (2019) 11203.

[9] A. A. Vernekar, D. Sinha, S. Srivastava, P. U. Paramasivam, P. D'Silva, G. Mugesh, Nat. Commun. 5 (2014) 5301.

[10] B. E. R. Snyder, P. Vanelderen, M. L. Bols, S. D. Hallaert, L. H. Böttger, L. Ungur, K. Pierloot, R. A. Schoonheydt, B. F. Sels, E. I. Solomon, Nature 536 (2016) 317.

[11] M. Sun, L. Xu, A. Qu, P. Zhao, T. Hao, W. Ma, C. Hao, X. Wen, F. M. Colombari, A. F. de Moura, N. A. Kotov, C. Xu, H. Kuang, Nat. Chem. 10 (2018) 821.

[12] H. Liang, F. Lin, Z. Zhang, B. Liu, S. Jiang, Q. Yuan, J. Liu, ACS Appl. Mater. Interfaces 9 (2017) 1352.

[13] P. Wang, S. Liu, M. Hu, H. Zhang, D. Duan, J. He, J. Hong, R. Lv, H. S. Choi, X. Yan, M. Liang, Adv. Funct. Mater. 30 (2020) 2000647.

[14] S. Hong, Q. L. Zhang, D. W. Zheng, C. Zhang, Y. Zhang, J.-J. Ye, H. Cheng, X. Z. Zhang, iScience 23 (2020) 100778.

[15] D. P. Cormode, L. Gao, H. Koo, Trends Biotechnol. 36 (2018) 15.

[16] Y. Lv, M. Ma, Y. Huang, Y. Xia, Chem. Eur. J. 25 (2019) 954.

[17] K. Fan, H. Wang, J. Xi, Q. Liu, X. Meng, D. Duan, L. Gao, X. Yan, Chem. Commun. 53 (2017) 424.

[18] Y. Yoshihisa, Q. L. Zhao, M. A. Hassan, Z. L. Wei, M. Furuichi, Y. Miyamoto, T. Kondo, T. Shimizu, Free Radic. Res. 45 (2011) 326.

[19] P. Storz, Science's STKE 2006 (2006) re3.

[20] T. Finkel, Nat. Rev. Mol. Cell Biol. 6 (2005) 971.

[21] T. Finkel, N. J. Holbrook, Nature 408 (2000) 239.

[22] M. Patel, Trends Pharmacol. Sci. 37 (2016) 768.

[23] J. R. Arthur, Cell. Mol. Life Sci. 57 (2001) 1825.

[24] R. Brigelius-Flohé, Free Radic. Biol. Med. 27 (1999) 951.

[25] R. Brigelius-Flohé, M. Maiorino, Biochim. Biophys. Acta. - General Subjects 1830 (2013) 3289.

[26] J. K. McGill, M. F. Beal, Cell 127 (2006) 465.

[27] B. D. Paul, S. H. Snyder, Front. Mol. Neurosci. 12 (2019).

[28] R. P. Mason, M. Casu, N. Butler, C. Breda, S. Campesan, J. Clapp, E. W. Green, D. Dhulkhed, C. P. Kyriacou, F. Giorgini, Nat. Genet. 45 (2013) 1249.

[29] J. E. Dueber, G. C. Wu, G. R. Malmirchegini, T. S. Moon, C. J. Petzold, A. V. Ullal, K. L. J. Prather, J. D. Keasling, Nat. Biotechnol. 27 (2009) 753.

[30] B. Wörsdörfer, K. J. Woycechowsky, D. Hilvert, Science 331 (2011) 589.

[31] J. D. Keasling, ACS Chem. Biol. 3 (2008) 64.

[32] J. M. Wörle-Knirsch, K. Kern, C. Schleh, C. Adelhelm, C. Feldmann, H. F. Krug, Environ. Sci. Technol. 41 (2007) 331.

[33] E. J. Park, G. H. Lee, C. Yoon, D. W. Kim, Environ. Res. 150 (2016) 154.

[34] W. Lin, Y. W. Huang, X. D. Zhou, Y. Ma, Int. J. Toxicol. 25 (2006) 451.

[35] A. Adhikari, S. Mondal, M. Das, P. Biswas, U. Pal, S. Darbar, S. S. Bhattacharya, D. Pal, T. Saha-Dasgupta, A. K. Das, A. K. Mallick, S. K. Pal, Adv. Healthcare Mater. 10 (2021) 2001736.

[36] R. A. Yokel, NeuroMolecular Med. 11 (2009) 297.

[37] R. A. Yokel, M. Wilson, W. R. Harris, A. P. Halestrap, Brain Res. 930 (2002) 101.

[38] L. Flohé, I. Brand, Biochim. Biophys. Acta - Enzymology 191 (1969) 541.

[39] D. E. Paglia, W. N. Valentine, J. Lab. Clin. Med. 70 (1967) 158.

[40] R. Obexer, A. Godina, X. Garrabou, P. R. E. Mittl, D. Baker, A. D. Griffiths, D. Hilvert, Nat. Chem. 9 (2017) 50.

[41] W. J. Albery, J. R. Knowles, Biochemistry 15 (1976) 5631.

[42] S. Singh, Front. Chem. 7 (2019).

[43] N. V. S. Vallabani, A. S. Karakoti, S. Singh, Colloids Surf. B.: Biointerfaces 153 (2017) 52.

[44] F. Natalio, R. André, A. F. Hartog, B. Stoll, K. P. Jochum, R. Wever, W. Tremel, Nat. Nanotechnol. 7 (2012) 530.

[45] R. André, F. Natálio, M. Humanes, J. Leppin, K. Heinze, R. Wever, H.-C. Schröder, W. E. G. Müller, W. Tremel, Adv. Funct. Mater. 21 (2011) 501.

[46] A. Durmaz, N. Dikmen, J. Enzyme Inhib. Med. Chem. 22 (2007) 733.

[47] J. R. Prohaska, Biochim. Biophys. Acta - Enzymology 611 (1980) 87.

[48] X. Wang, X. J. Gao, L. Qin, C. Wang, L. Song, Y. N. Zhou, G. Zhu, W. Cao, S. Lin, L. Zhou, K. Wang, H. Zhang, Z. Jin, P. Wang, X. Gao, H. Wei, Nat. Commun. 10 (2019) 704.

[49] S. Sarkar, M. Kabir, M. Greenblatt, T. Saha-Dasgupta, J. Mater. Chem. A 1 (2013) 10422.

[50] T. Denayer, T. Stöhr, M. Van Roy, New Horiz. Transl. Med. 2 (2014) 5.

[51] N. Wang, M. Gray, X. H. Lu, J. P. Cantle, S. M. Holley, E. Greiner, X. Gu, D. Shirasaki, C. Cepeda, Y. Li, H. Dong, M. S. Levine, X. W. Yang, Nat. Med. 20 (2014) 536.

[52] A. Johri, M. F. Beal, Biochim. Biophys. Acta - Mol. Basis Dis. 1822 (2012) 664.

[53] P. Kumar, S. S. V. Padi, P. S. Naidu, A. Kumar, Fundam. Clin. Pharmacol. 21 (2007) 297.

[54] A. C. Ludolph, F. He, P. S. Spencer, J. Hammerstad, M. Sabri, Can. J. Neurol. Sci. 18 (2015) 492.

[55] R. G. Mealer, S. Subramaniam, S. H. Snyder, J. Neurosci. 33 (2013) 4206.

[56] C. E. Teunissen, H. W. M. Steinbusch, M. Angevaren, M. Appels, C. de Bruijn, J. Prickaerts, J. de Vente, Neuroscience 105 (2001) 153.

[57] M. N. Herrera-Mundo, D. Silva-Adaya, P. D. Maldonado, S. Galván-Arzate, L. Andrés-Martínez, V. Pérez-De La Cruz, J. Pedraza-Chaverrí, A. Santamaría, Neurosci. Res. 56 (2006) 39.

[58] H. H. Yin, B. J. Knowlton, Nat. Rev. Neurosci. 7 (2006) 464.

[59] P. E. Rothwell, M. V. Fuccillo, S. Maxeiner, S. J. Hayton, O. Gokce, B. K. Lim, S. C. Fowler, R. C. Malenka, T. C. Südhof, Cell 158 (2014) 198.

[60] P. Pla, S. Orvoen, F. Saudou, D. J. David, S. Humbert, Front. Behav. Neurosci. 8 (2014).

[61] G. K. Shinomol, Muralidhara, Neurotoxicology 29 (2008) 948.

[62] R. H. Silva, V. C. Abílio, S. R. Kameda, A. L. Takatsu-Coleman, R. C. Carvalho, R. D. A. Ribeiro, S. Tufik, R. Frussa-Filho, Prog. Neuropsychopharmacol. Biol. Psychiatry 31 (2007) 65.

[63] M. P. Mattson, A. Cheng, Trends Neurosci. 29 (2006) 632.

[64] R. A. Colvin, Q. Jin, B. Lai, L. Kiedrowski, PLoS ONE 11 (2016) e0159582.

[65] M. R. Smith, J. Fernandes, Y. M. Go, D. P. Jones, Biochemical and Biophysical Research Communications 482 (2017) 388.

[66] F. Wang, F. Gao, M. Lan, H. Yuan, Y. Huang, J. Liu, Toxicol. in Vitro 23 (2009) 808.

[67] A. Datta, S. Mishra, K. Manna, K. D. Saha, S. Mukherjee, S. Roy, ACS Omega 5 (2020) 9714.

[68] A. R. N. Reddy, Y. N. Reddy, D. R. Krishna, V. Himabindu, Toxicology 272 (2010) 11.

[69] R. Guan, T. Kang, F. Lu, Z. Zhang, H. Shen, M. Liu, Nanoscale Res. Lett. 7 (2012) 602.

[70] R. Meena, M. Rani, R. Pal, P. Rajamani, Appl. Biochem. Biotechnol. 167 (2012) 791.

[71] N. Polley, S. Saha, A. Adhikari, S. Banerjee, S. Darbar, S. Das, S. K. Pal, Nanomedicine 10 (2015) 2349.

[72] A. Adhikari, P. Biswas, S. Mondal, M. Das, S. Darbar, A. M. Hameed, A. Alharbi, S. A. Ahmed, S. S. Bhattacharya, D. Pal, S. K. Pal, ChemMedChem 15 (2020) 420.

CHAPTER 10

Redox Buffering Capacity of Nanomaterials as an Index of ROS-Based Therapeutics and Toxicity

10.1. INTRODUCTION

Reactive oxygen species (ROS) and associated oxidative stress (so-called) remain the most fascinating paradigm for elucidating the adverse effects of engineered nanomaterials at cellular and molecular levels [1]. ROS generating nanomaterials are generally considered cytotoxic for biomedical use, and their therapeutic applications are restricted to anticancer or anti-microbial activities [2-5]. Indeed, elevated ROS levels have the capacity to oxidize unsaturated fatty acids in lipids, and amino acids in proteins, inducing irreversible damage to vital organelles, and DNA, ultimately leading to cellular apoptosis, and necrosis resulting in various chronic disorders including neurodegenerative, diabetes, and cardiovascular diseases [6-8]. However, recent understandings in free radical biology illustrates the pivotal role of ROS (at low concentration) as second messengers to modulate essential cellular functions like signaling, adhesion, migration, proliferation and homeostasis [9]. This inherent duality of ROS, the purposeful beneficial functions at physiological level (i.e., oxidative eustress), as well as, deleterious effects at supraphysiological concentration (i.e., oxidative distress) highlights the importance of maintaining

proper redox balance for healthy organismal functions, and leads to the concept of redox medicine [9,10]. Redox medicine epitomize a promising tool for restoration of cell and tissue homeostasis via direct detoxification of reactive intermediates and/or by triggering cytoprotective and antioxidant signaling pathways [10]. In this sense, an interesting (perhaps the most important) avenue in redox medicine is the maintenance of oxidative eustress to regulate redox signaling and associated cell functions in addition to modulation of oxidative distress (i.e., inhibition to counteract pathological cell loss and induction to promote death of pathological cells). The disappointing history of efforts to prevent, or treat diseases with exogenous antioxidants (e.g., vitamin c, ascorbic acid, polyphenols etc.) further reflect the importance of redox-based therapeutics for clinical translation [11].

In this new front of redox medicine, ROS-based nanomedicines that involve nanomaterials with ROS-regulating properties, holds promise for optimized therapeutic efficacies [9]. Recent advancements in controlled synthesis process resulted into a wave of multifunctional nanomaterials with unique ROS generation, transition, or depletion functions. However, for *in vivo* application, it is a double-edged sword. After exerting expected therapeutic functions, the elevated ROS level may also impair adjacent normal tissues [5]. Moreover, if the nanomaterials are not degraded or excreted, their ROS-generating functions may still exist that may result in sustained oxidative damage. Therefore, balancing the therapeutic outcome and side effect of ROS generating nanomaterials is important for the optimization of therapeutic effects, which needs more careful characterization of the *in vivo* behavior of ROS and more exhaustive safety assessment of the nanomaterials [9]. In other words, information about ROS-mediated changes in cellular redox state, or ability of a nanomaterial to maintain eustress condition could be instrumental in dictating the therapeutic potential of a nanomaterial.

Unfortunately, the quantitative basis of changes in the intracellular redox state of the cells is not well-defined, thus leading to the dilemma that redox changes induced by oxidants in distinct cells types cannot be predicted [12]. The current state of the art measurement methods for estimating changes in cellular redox state is by measuring the concentration variation of intracellular redox couple GSSG/2GSH, and calculating the reduction potentials using Nernst equation, which is grossly

misleading as spatial-temporal control exists between redox couples, and information about single couple cannot reflect the actual redox status [12-14]. Moreover, the method is cumbersome and prone to errors.

In this study, we introduce the concept of redox buffering capacity as a therapeutic index of engineered nanomaterials. As a steady redox state is maintained for the normal functioning of the cells, we hypothesize that the ability of a nanomaterial to preserve this homeostatic condition will dictate its therapeutic efficacy. Additionally, the redox buffering capacity is expected to provide information about the nanoparticle toxicity. Here, using citrate functionalized trimanganese tetroxide nanoparticles (C-Mn_3O_4 NPs) as a model nanosystem we explored its redox buffering capacity in erythrocytes. In this regard it is worth mentioning that, C-Mn_3O_4 NPs has previously been well studied from our group and showed therapeutic efficacy using both ROS generation and ROS scavenging abilities in *in vitro* as well as *in vivo* models. It treats hyperbilirubinemia by oxidative breakdown of bilirubin inside the body. On the other hand, it can mimic glutathione peroxidase to scavenge ROS and treat several diseases including hepatic fibrosis, heavy metal toxicity and Huntington's disorder. Thus, it is of considerable interest to assess the redox modulatory properties of this multifunctional nanoparticle. Furthermore, we went on to study the chronic toxic effects (if any) of this nanomaterial in animal model in order to co-relate with the experimentally estimated redox buffering capacity. This study could function as a framework for assessing the capability of a nanomaterial as redox medicine (whether maintains eustress or damages by creating distress), thus orienting its application and safety for clinical use.

10.2. RESULTS AND DISCUSSION

10.2.1. Redox Buffering Capacity of Nanomaterials as an Index of ROS-based Therapeutics and Toxicity: A Preclinical Animal Study [15]

In order to explore the redox buffering effect of C-Mn_3O_4 NPs, we used the DCFH assay and measured the DCF intensity as a quantitative marker of ROS present in the reaction medium. First, we evaluated the *in vitro* redox buffering capacity of the synthesized NPs using H_2O_2 as an oxidant molecule. Figure 10.1a reflects the rate of DCFH oxidation with increasing concentrations of H_2O_2 added to aqueous medium. The results clearly shows that the DCFH oxidation increased significantly with increasing concentration of H_2O_2. On the other hand, introduction of C-Mn_3O_4 NPs into the medium resulted into insignificant alteration in DCF intensity even after the addition of the highest concentration of H_2O_2. As shown in Figure 10.1a, the DCFH oxidation rate remained almost constant up to the addition of 2.5 mM of H_2O_2. It signifies the efficient quenching of ROS generated from H_2O_2 by C-Mn_3O_4 NPs. It should be noted that C-Mn_3O_4 NPs have always maintained a constant ROS concentration in the reaction medium instead of eliminating all the ROS. Figure 10.1a depicts the relation between the DCFH oxidation rate (V_f) and oxidant (H_2O_2) concentration. Here, it is evident that DCFH oxidation by H_2O_2 follows an exponential kinetics and the oxidation rate is clearly reduced in presence of C-Mn_3O_4 NPs.

Next we quantified the *in vitro* redox buffering capacity of the synthesized NPs. As per definition, the redox buffering capacity of a system is numerically equal to the magnitude of change in concentration of an oxidant (or a reductant) added to a solution, which is reduced or oxidized, to change the effective reduction potential by 1 unit (1 V) [12]. Thus, the redox buffering capacity (β) can be represented as:

$$\beta = \frac{\delta c_{ox}}{\delta E^{eff}}$$

[Equation 10.1]

Where c_{ox} represents the concentration of the oxidant added to the system.

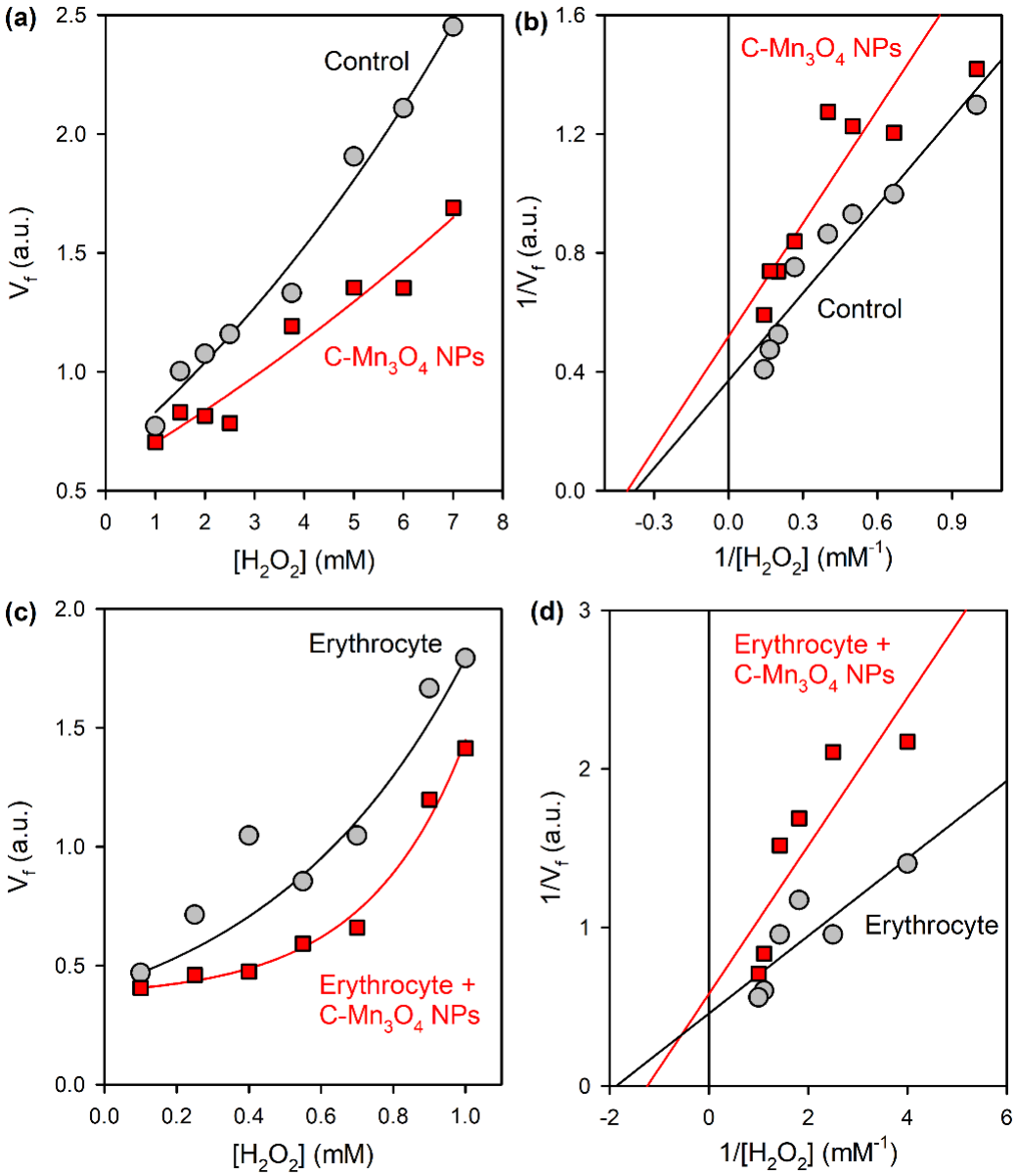

Figure 10.1. *Redox buffering capacity of C-Mn_3O_4 NPs. (a) Rate of DCFH oxidation in presence of H_2O_2. (b) Double reciprocal plot of the same. (c) Rate of DCFH oxidation in presence of H_2O_2 in erythrocytes. (d) Double reciprocal plot of the same.*

Experimentally, the redox buffering capacity and the effective reduction potential can be determined from the dependence of $1/V_f$ on $1/c_{ox}$ (Figure 10.1b). The correlation can be described by the following equation:

$$\frac{1}{\Delta V_f} = \frac{1}{\Delta V_f^{max}} + \frac{k_{cap}}{\Delta V_f^{max}} \cdot \frac{1}{c_{ox}}$$

[Equation 10.2]

Where, ΔV_f^{max} is the highest rate of DCFH oxidation and k_{cap} is a constant having dimension of concentration. According to Eq. 2, the redox buffering capacity ($\frac{k_{cap}}{\Delta V_f^{max}}$) can be calculated from the tangent of slope angle of the plot of $1/V_f$ (Y-axis) vs. $1/c_{ox}$ (X-axis).

Figure 10.1b shows the significantly higher (~1.3 times) redox buffering capacity of C-Mn_3O_4 NPs (1.29 unit) compared to Mili-Q water (0.97 unit).

To test the aforementioned redox buffering ability of C-Mn_3O_4 NPs in the cellular *milieu* we used human erythrocytes, or red blood corpuscle (RBC). The choice of erythrocytes was based on the fact that (i) their continuous exposure to high oxygen tensions, (ii) inability to replace damaged components, and (iii) the composition of membrane lipids partly of polyunsaturated fatty acid side chains that are vulnerable to peroxidation. Exogenously introduced H_2O_2 served as the inducer of oxidative stress. It is well-known that H_2O_2 generates massive oxidative stress and perturbs the intracellular redox state. For living cells, the electron donating and electron accepting capabilities of the intracellular medium can be specified by the value of effective redox potential, and any change in effective redox potential can be measured using specific redox sensor like DCFH in our study. Figure 10.1c and 2d represent the *in-cellulo* redox buffering capacity of C-Mn_3O_4 NPs. It is evident from the results that the DCF intensity of the RBCs treated with C-Mn_3O_4 NPs is significantly lower than the control RBCs treated with normal saline (Figure 10.1c). Following the method described above we found that the redox buffering capacity of C-Mn_3O_4 NPs (0.46 units) when integrated in erythrocytes is significantly higher (~1.9 times) compared to the intrinsic cellular components (0.24 units) (Figure 10.1d). It has to be noted that the redox buffering capacity of the C-Mn_3O_4 NPs in cellular system is considerably higher compared to *in vitro* aqueous system. This may be due to the additional (i.e., other than direct antioxidant activity) GPx mimicking activity of the C-Mn_3O_4 NPs [16] which can only happen in presence of GSH, and intracellular metabolite.

Redox buffering requires sensing and rapid adjustment in the redox environment to maintain the oxidative eustress in cells. Cumulative data obtained from the experiments (both *in vitro* and *in cellulo*) suggests that C-Mn_3O_4 NPs can

sense and swiftly shift the redox state in the favour of oxidative eustress. This behaviour of C-Mn_3O_4 NPs as a redox modulator is consistent with that of pH buffers. pH buffers adjust the pH of the solution by sensing the concentration of H^+ ions present. Similarly, C-Mn_3O_4 NPs perceive the amount of ROS in the medium and change its redox state accordingly. Also, it has been shown that a significant change in the concentration of C-Mn_3O_4 NPs in the solution can cause a change in the redox state just like a pH buffer.

Previous studies suggest that for maintaining the oxidative eustress, C-Mn_3O_4 NPs generate ROS from dissolved O_2 and H_2O through continuous disproportionation and comproportionation of the surface $Mn^{2+}/Mn^{3+}/Mn^{4+}$ ions present at the spinel structure [17]. Electrons, produced from this process of conversion of $Mn^{2+} \rightarrow Mn^{3+} \rightarrow Mn^{4+}$, react with the dissolved O_2 and H_2O of the medium and produce ROS. The ROS produced in this process is simultaneously neutralized by the conversion of $Mn^{4+} \rightarrow Mn^{3+} \rightarrow Mn^{2+}$, i.e. the opposite pathway [18-20]. Therefore, when the cells stay at oxidative eustress condition, a dynamic equilibrium is maintained between the generation and elimination of ROS by C-Mn_3O_4 NPs. However, in many instances, the ROS level in the cells decreases resulting into immune suppression. During this condition the ROS generated by C-Mn_3O_4 NPs can take part in the cellular signalling process and maintain the normal cell functions. On the other hand, in oxidative distress conditions, the scenario becomes more complicated. The C-Mn_3O_4 NPs can follow numerous buffering strategies to mitigate the oxidative distress. Besides quenching of ROS through the conversion of $Mn^{2+}/Mn^{3+}/Mn^{4+}$, another likely strategy is that, in a medium with excess ROS, NPs act as a cofactor to some antioxidant enzymes and directly help intracellular anti-oxidant defence system [18,20,21]. Furthermore, the NPs can function as a GSH-dependent GPx mimic and scavenge excess ROS being incorporated into the cellular antioxidant enzyme network, as described in our previous study.

The combined results suggest that the C-Mn_3O_4 NPs can efficiently function as a redox buffer in intracellular condition. The described 'redox titration' method could be beneficial for comparing buffering capacity, as a marker of cyto-compatibility of different nanomaterials using minimum resources.

Next, we evaluated chronic toxicity of C-Mn_3O_4 NPs in animal model. With all newly developed nanoparticles, the potential for toxicity remains a factor in determining their specific applications in experimental small-animal, and ultimately clinical application. When NPs are administered *in vivo*, the most important physiological system they interact with is the blood and blood components. Only after the clearance by immune cells, they leave away from the bloodstream and reach the target organ [22]. Thus, it is important to measure the hemocompatibility of the NPs targeted for therapeutic use. We performed the hemolysis assay for evaluation of the hemolytic behaviors of C-Mn_3O_4 NPs on isolated mouse erythrocytes. The erythrocytes were first isolated by centrifugation and purified by sequential washes with sterile isotonic phosphate-buffered saline (PBS) pH 7.4, then diluted to 5% hematocrit and incubated with different concentrations of NP suspensions (0.01, 0.05- or 0.1-ml ml^{-1} PBS). The same amount of PBS was used as the negative control. An aqueous solution of RBCs was used as a positive control that is likely to show hemolysis. After 6 hrs incubation at room temperature, the samples were spun down to check the extent of hemolysis. Considering the hemolytic ability of positive control (water) as 100%, all the NP treated samples showed negligible (<5%) hemolysis (Figure 10.2a and 10.1b). Corresponding absorbance spectra (with the supernatant after final centrifugation) showed the optical features of C-Mn_3O_4 NPs (Figure 10.2c) with ligand to metal charge transfer band at 300 nm and d-d transition bands at 429, 526 nm. Only the positive control sample showed a distinct absorbance signature of hemoglobin with the Sorret band at 420 nm and Q-bands at 546 and 576 nm (Figure 10.2c). The scanning electron micrographs (SEM) of erythrocytes and Leishman stained whole blood smears supported the same (Figure 10.2e and 10.1f). The cell membrane remained unaltered after particle interaction, and the erythrocytes maintained normal biconcave shape just like control ones (Figure 10.2e). To study the *in vivo* effect of C-Mn_3O_4 NPs on blood, different hematology and serum biochemical indicators were measured after 90-days administration of the particles. The values of hematological parameters were within normal ranges and did not indicate a trend of toxicity associated with NPs (Table 10.1). We further went on to assay ALAD activity, an important enzyme in the hematopoietic pathway

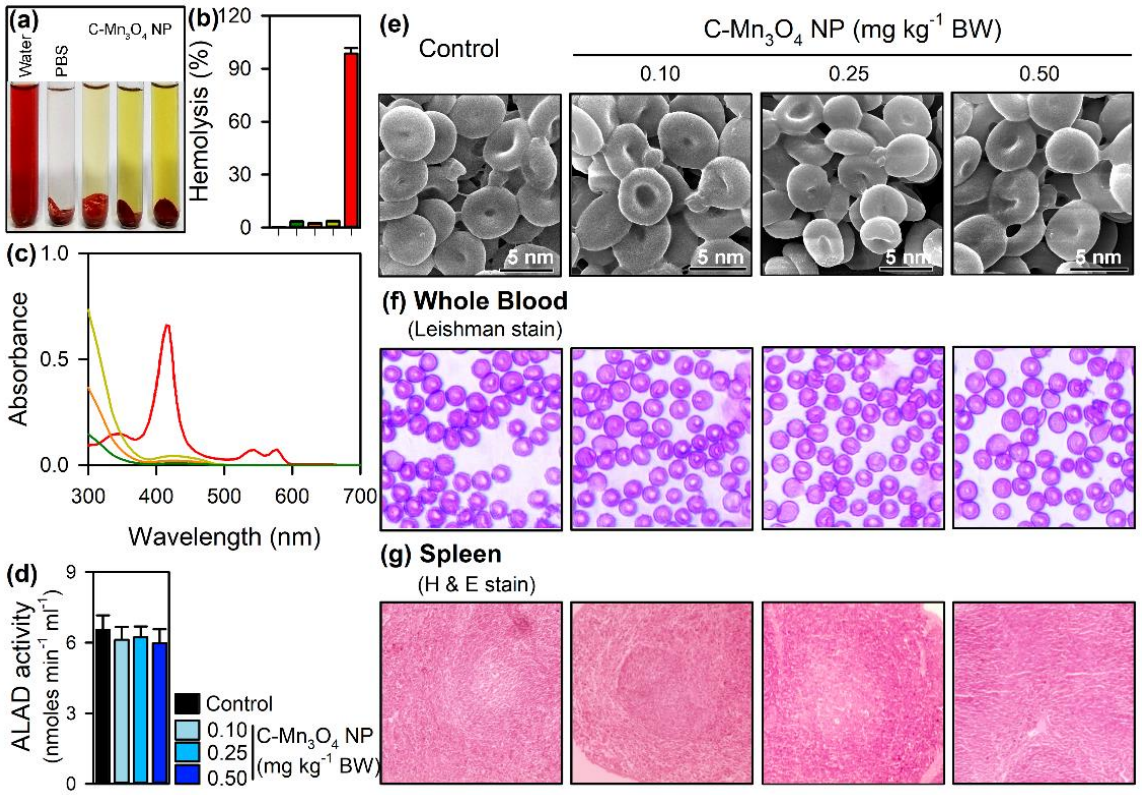

Figure 10.2. *Effect of C-Mn_3O_4 NPs on haematological system. (a) Visual inspection of the tubes containing RBC after exposure to NPs. No visible haemolytic behaviour was observed for NPs, water was used as positive control and PBs as negative control. (b)The bar plot shows percentage of haemolysis induced by C-Mn_3O_4 NPs. (c) UV-vis absorbance spectra of the supernatant. (d) ALAD activity. (e) Scanning electron micrographs of the RBCs incubated with C-Mn_3O_4 NPs shows no visible damage to the membrane or morphology. (f) Leishman stained whole blood from the BALB/c mice treated with different doses of NPs for 90 days. (g) H&E stained spleen sections after 90 days' oral administration of NPs.*

All data represented as Mean ± Standard Deviation (SD). N=6 for each measurement.

which usually gets downregulated in cases of metal toxicity, particularly due to exposure of heavy metals like lead, mercury, etc. [23]. We found no change in the activity of ALAD (Figure 10.2d). The hematoxylin and eosin stained spleen showed no abnormality (Figure 10.2g). These results indicate C-Mn_3O_4 NPs have excellent hemocompatibility.

In the biodistribution profile (*vide infra*), we found the affinity of C-Mn_3O_4 NPs towards the liver. So, we extensively examined its effect on the liver. The gross morphology (Figure 10.3a) and relative liver weights did not reveal any toxic effect on the organ. However, compared to control animals, 0.5 mg kg^{-1} BW NP-treated

mice (not the other two groups of NP treated ones) displayed significantly higher serum alanine aminotransferase (ALT) and aspartate aminotransferase (AST) activity (Figure 10.3b and 10.2c, $p<0.001$ in one way ANOVA). A similar trend was observed in the case of alkaline phosphatase (ALP) and γ-glutamyl transferase (γGT) activity, however, both total and direct bilirubin levels showed no significant differences among groups (Figure 10.3d-10.2f). The increased serum activity of transferases, normally confined within hepatic cells (not in serum), can be attributed to the damaged structural integrity of hepatocytes and subsequent release into the circulation. To know the actual reason behind such elevated liver function parameters in the case of 0.5 mg kg^{-1} BW NP-treated mice we went of histological analysis. In vehicle control animals, liver sections showed normal hepatic cells with well-preserved cytoplasm, prominent nucleus and nucleolus, and central vein (Figure 10.3a). They along with 0.1 and 0.25 mg kg^{-1} BW NP-treated livers displayed characteristic hepatic architecture with hepatic plates directed from the portal triads toward the central vein where they freely anastomose. Inflammatory cells were seen intervening the hepatic strands and surrounding degenerative hepatocytes (Figure 10.2a). In addition, pericentral vein inflammation was also seen. Further histological damages including necrosis, ballooning degeneration, vacuolation, increased mitosis, and calcification were observed in the same group of mice (Figure 10.3a). So, it is evident from the results of histopathological observations and liver function tests that C-Mn_3O_4 NPs at the highest administered dose (0.5 mg kg^{-1} BW) can cause hepatic toxicity. In the previous section, we have described the NPs' ability to generate reactive oxygen species (ROS) in aqueous solution. So, to understand the pathophysiological mechanism of observed toxicity, we measured plasma thiobarbituric acid reactive substances (TBARS) or malondialdehyde (MDA) content, a byproduct of lipid peroxidation and also an index of oxidative damage, which was found to be high in 0.5 mg kg^{-1} BW NP-treated group (Figure 10.2i). We further extended our investigation to the changes in activities of superoxide dismutase (SOD), catalase (CAT) and glutathione peroxidase (GPX) which creates a mutually supportive team to fight against increased ROS [24,25]. SOD converts superoxide anions to H_2O_2, which is further converted to H_2O with the help of GPx

Table 10.1 Hematological parameters across the groups.

Parameters	Male				Female			
	Control	Low Dose	Middle Dose	High Dose	Control	Low Dose	Middle Dose	High Dose
Hb (g/dl)	11.9±1.8	11.8±1.6	10.8±0.5	9.8±1.1	11.8±1.2	11.6±1.5	11.2±4.4	10.8±0.9
RBC ($x10^6$ μL^{-1})	10.8±0.9	9.81±0.7	10.1±0.5	9.2±0.3	10.6±1.1	10.4±0.9	10.2±1.4	10.2±0.8
RT (%)	2.8±1.1	2.5±2.3	2.8±2.4	2.4±1.6	2.9±1.6	2.2±2.1	2.2±1.6	2.5±1.1
HCT (%)	34.8±1.3	34.8±2.2	32.8±2.1	31.8±2.1	35.1±3.1	34.9±1.6	33.8±2.1	34.1±1.4
MCV (μm^3)	37.0±2.6	37.4±2.4	36.0±1.4	36.1±2.3	37.2±1.1	37.4±1.9	37.1±1.4	36.0±2.4
MCH (pg)	21.1±2.4	21.7±1.7	20.1±1.7	21.8±2.8	21.4±2.6	21.1±1.6	21.4±1.6	20.1±2.4
MCHC (%)	41.4±2.6	41.2±2.1	40.4±1.4	41.7±2.4	41.4±1.4	40.6±2.1	41.2±1.8	41.4±1.6
Platelets ($x10^3$ μL^{-1})	6.6±2.0	6.5±1.8	6.3±1.2	6.9±1.2	6.5±2.6	6.6±2.8	6.6±2.7	5.6±1.1
WBC ($x10^5$ μL^{-1})	8.8±1.1	8.4±1.9	8.1±1.5	7.8±1.2	8.5±1.1	8.1±1.2	7.8±1.4	8.2±1.3
Lymphocyte (%)	76±6.3	71±5.3	73±5.4	72±3.3	73±3.4	76±3.6	74±1.3	78±2.2
Neutrophil (%)	25±6.2	25±5.1	21±5.1	22±4.3	25±6.9	22±6.8	24±5.7	26±5.5
Monocyte (%)	2.3±0.01	2.1±0.01	1.1±0.02	1.6±0.01	2.4±0.01	2.1±0.01	1.8±0.02	1.4±0.03
Eosinophil (%)	9.6±2.6	9.1±3.2	9.4±2.5	8.3±4.1	9.2±3.6	9.1±1.4	9.4±2.9	9.2±1.2
Basophil (%)	1.2±0.05	1.1±0.04	1.2±0.02	1.5±0.02	1.2±0.04	1.1±0.02	1.1±0.01	1.3±0.04
PT (sec)	7.3±2.2	7.2±2.1	8.5±3..9	9.1±3.8	7.1±4.1	7.4±2.6	8.2±3.1	9.3±3.1
APTT (sec)	16.9±4.3	16.5±2.8	17.1±4.1	18.7±2.6	16.1±2.5	15.2±2.6	16.4±3.2	19.6±4.2

Data are expressed as mean ± standard deviation (N=6).

Abbreviations: Hb: Hemoglobin; RBC: Red Blood corpuscle; RT: Reticulocyte; HCT: Hematocrit; MCV: Mean Corpuscular Volume; MCH: Mean Corpuscular Hemoglobin; MCHC: Mean Corpuscular Hemoglobin Concentration; WBC: White Blood Corpuscle; PT: Prothrombin Time; APTT: Activated Partial Thromboplastin Time.

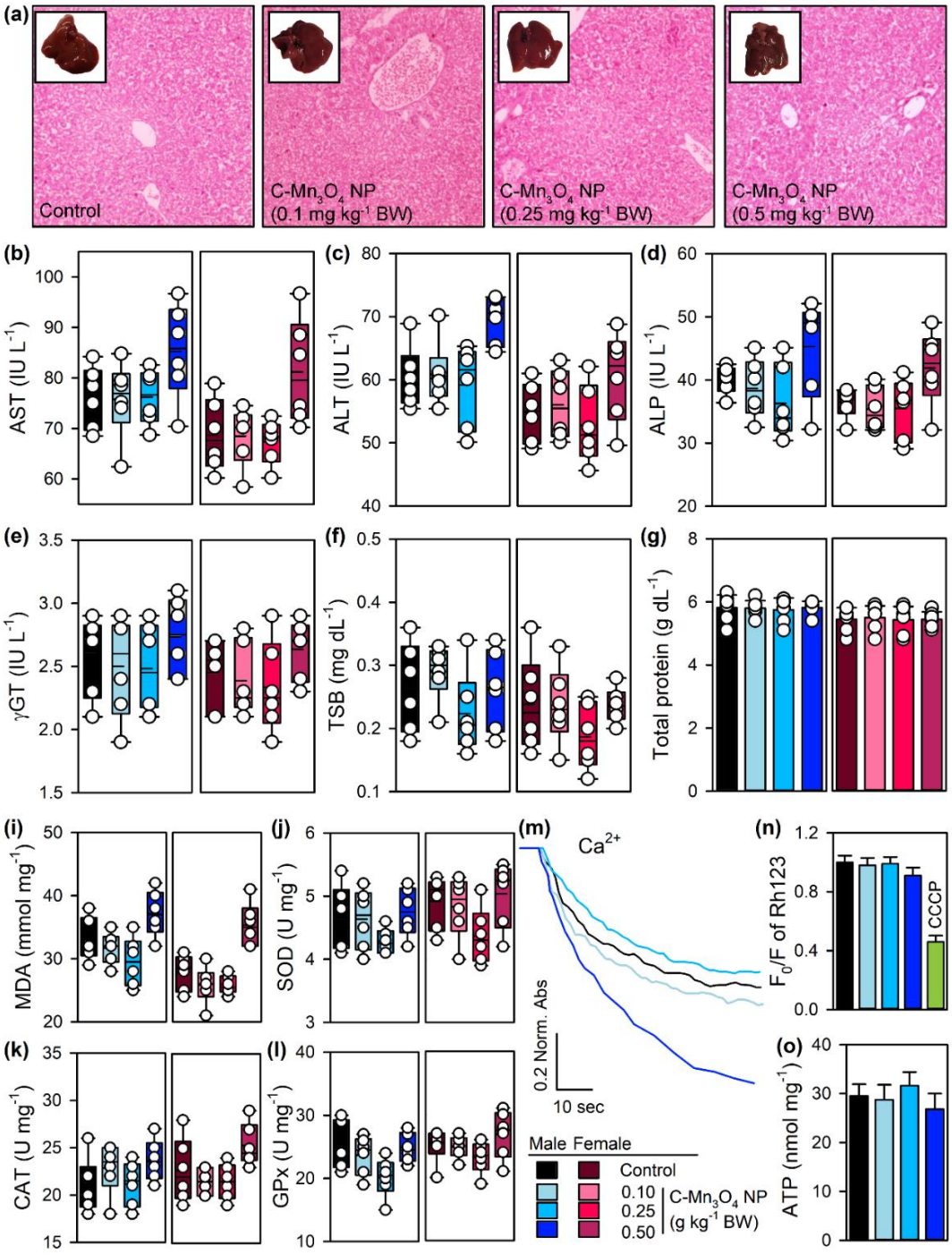

Figure 10.3. *Effect of C-Mn_3O_4 NPs on hepatic function after chronic administration. (a) Morphology of the liver and H&E stained liver sections. (b-g) Effect on liver function parameters show chronic administration of high dose of NPs can cause damage hepatic cells. However, the therapeutic dose has no detrimental effect. (i-l) Assessment of cellular antioxidant enzymes revealed the damage to be ROS mediated. (m-o) Effect of the NPs on mitochondria reveals membrane depolarization along with increased MPTP which in turn increase cellular apoptosis through release of cytochrome c.*

All data represented as Mean ± Standard Deviation (SD). N=6 for each measurement.

and CAT. SOD also inhibits OH• radical production. Upholding the equilibrium between free radicals and antioxidant enzymes is vital for the prevention of oxidative damages which can destroy all aspects of a cell, including its proteins, lipids, and DNA. We found the downregulation of all the antioxidant enzyme activities in 0.5 mg kg^{-1} BW NP-treated mice compared to control (Figure 10.3j-10.3l). Though previous studies have shown that, C-Mn_3O_4 NPs can display antioxidant enzyme mimetic (particularly SOD and CAT) activity in the cellular environment, the humongous amount of ROS instantaneously generated due to high local concentration of NPs cannot be quenched through that mechanism. It should be noted that at the therapeutic dose (0.25 mg kg^{-1} BW NPs) there is no evidence of oxidative damage.

Sections of lung tissue from control and low dose C-Mn_3O_4 NP treated animals have the normal appearance of fine lace because most of the lung is composed of thin-walled alveoli (Figure 10.4a). The alveoli are composed of a single layer of flattened epithelial cells and pneumocytes. Between the alveoli a thin layer of connective tissue and numerous capillaries are also lined with endothelium. However, the sections from moderate and high dose groups showed signs of nonspecific interstitial pneumonia in patchy manner other than normal lung architecture. The cellular pattern consists primarily of mild to moderate chronic interstitial inflammation, containing lymphocytes and a few plasma cells, in a uniform and patchy distribution. Signs of fibrosis, honeycombing, hyaline membranes and granulomas are absent. This kind of histological features may arise from the localization of particulate matters (as evident from our biodistribution study) in lungs [26]. These features are generally reversible and do not cause long term harm to the subjects [26].

Affinity of nanoparticles towards testes is contradictory. Several nanoparticles such as gold and magnetic nanoparticles have been reported to enter testes in small quantities, whereas carbon nanotubes behave oppositely [27]. Our biodistribution results indicate that C-Mn_3O_4 NPs could enter or accumulate in the testis.The average testis weight, morphology (Figure 10.5a and 10.3c) and epididymis index (data not shown) of NP-treated mice did not show any significant difference compared to the control mice. The tight junctions of Sertoli cells form the blood–

testis barrier (BTB), a structure that functions as a blockade between the interstitial blood compartment and the adluminal compartment of testes and seminiferous tubules respectively. Besides their role in BTB formation, Sertoli cells also foster the premature sperm cells through the phases of spermatogenesis. The observed accumulation of C-Mn_3O_4 NPs in the testes upon chronic repeated dose administration have not shown any adverse effect on Sertoli cells and seminiferous tubules. Figure 10.4c presents hematoxylin and eosin stained cross-section structure of the testes of control and C-Mn_3O_4 NP treated mice. It is well known that within the seminiferous tubules, sperm cells are generated through differentiation of spermatozoa by meiosis. Microscopic images show normal testes structure for control mice (Figure 10.4c). Histologic examination of the cross sections of testes from all three dose groups showed no alteration even after 90 days of administration (Figure 10.4c). Leydig cells or spermatids were similar in all groups. The sperm counts and sperm motility showed similar trends (Figure 10.5e-10.5g). We further microscopically observed eosin-Y stained sperms, and found slight deformity in 0.5 mg kg^{-1} BW NP treated group (Figure 10.4c). Next we studied the changes in MDA levels in homogenates prepared from testes as oxidative stress-mediated damage of the male reproductive system contributes to 30–80% of cases of male infertility. However, the MDA levels were similar to the control groups. Appropriate levels of male sex hormones are crucial for spermatogenesis. Follicle stimulating hormone (FSH) stimulates both the production of androgen binding protein (ABP) by Sertoli cells and the construction of the BTB. ABP is essential for elevating testosterone to levels required for starting and upholding spermatogenesis. FSH may initiate the sequestering of testosterone in the testes, but once developed, only testosterone is required to maintain spermatogenesis. However, higher FSH level enhances spermatozoa production through prevention of apoptosis of type-A spermatogonia. Other hormones such as luteinizing hormone (LH) also play significant roles in spermatogenesis. However, these functions can be affected by xenobiotics or foreign substances. Some endocrine toxicants, such as polychlorinated biphenyls and inorganic heavy metals, can alter the levels of these hormones, causing injury to testes, fault in spermatogenesis and male infertility. Notably nanoparticle-rich diesel

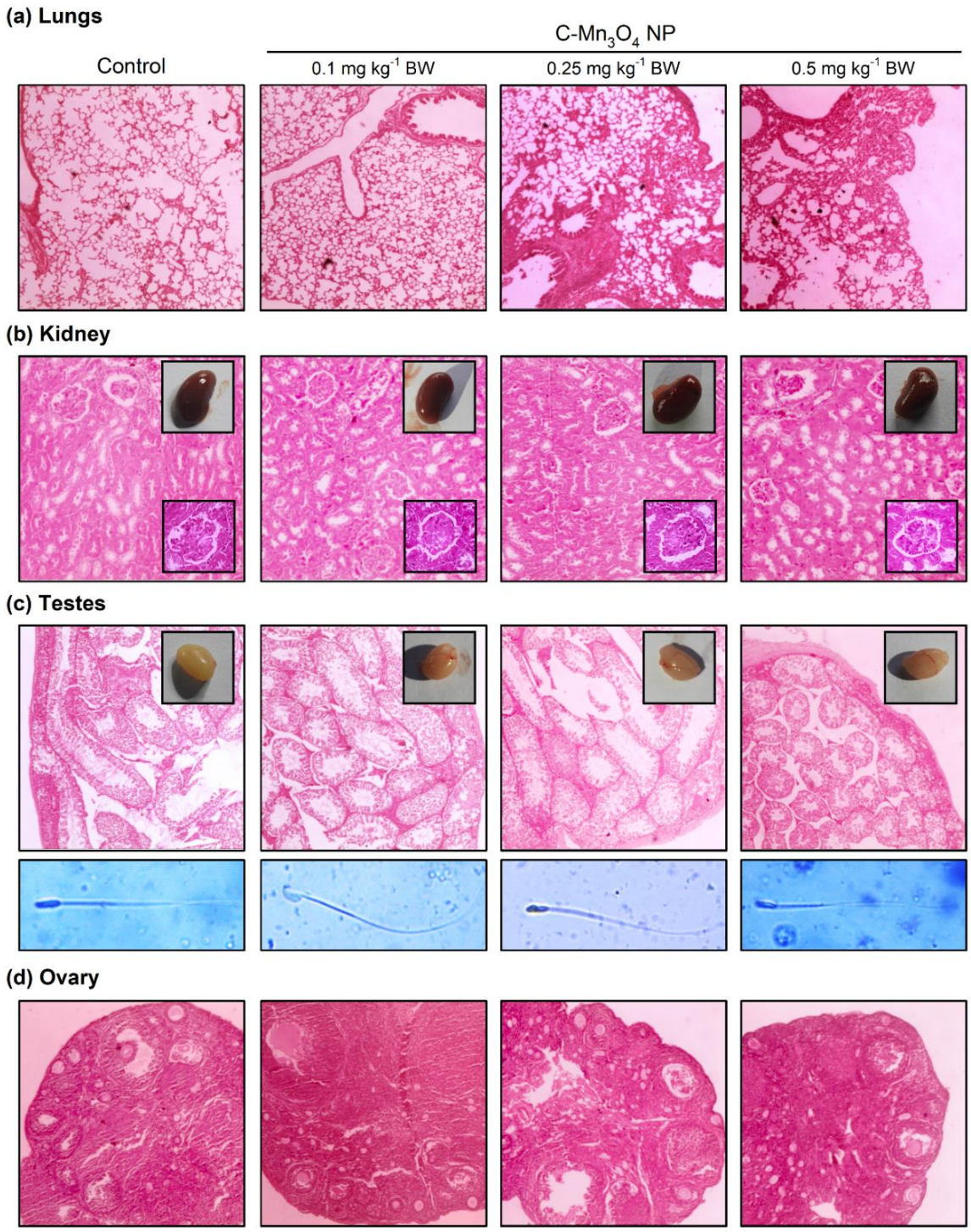

Figure 10.4. *Hematoxylin and eosin stained tissue sections from different groups. (a) Lungs. (b) Kidney. Inset shows morphology of kidney and Bowman's capsule. (c) Testes. Inset shows morphology of testes. Lower pannel shows morphology of sperm from respective groups. (d) Ovary.*

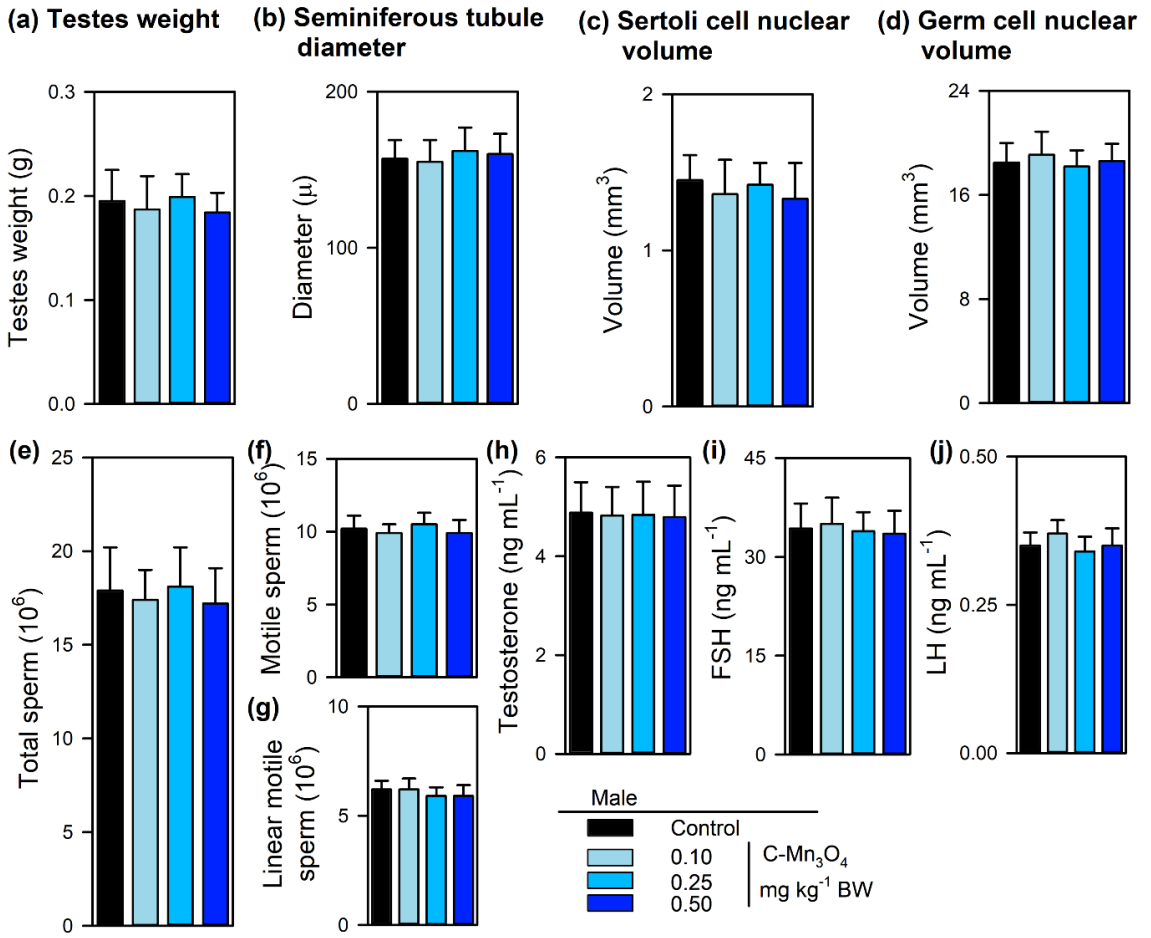

Figure 10.5. *Effect of C-Mn_3O_4 NPs on male reproductive system. (a) Weight of testes. (b-d) The quantity of different types of spermatogonia as observed in histology. (e-g) Sperm counts and sperm viability has no difference in between groups. Micrographs of single sperm (stained with Eosin Y) in Figure 10.4c depicts the same. (h-j) Male reproductive hormones remained unchanged across the groups.*

All data represented as Mean ± Standard Deviation (SD). N=6 for each measurement.

exhaust inhalation disturbs the endocrine action of the male reproductive system by increasing the plasma testosterone levels in male rats. In this study, we determined the plasma concentrations of testosterone, LH and FSH on day 90 by enzyme-linked immunosorbent assay (ELISA). The results (Figure 10.5h-10.5j) indicate that the NPs did not alter plasma sex hormone levels in any of the groups.

Similar to male reproductive system, no observable sign of toxicity was found in case of female reproductive system. The haematoxylin and eosin stained sections

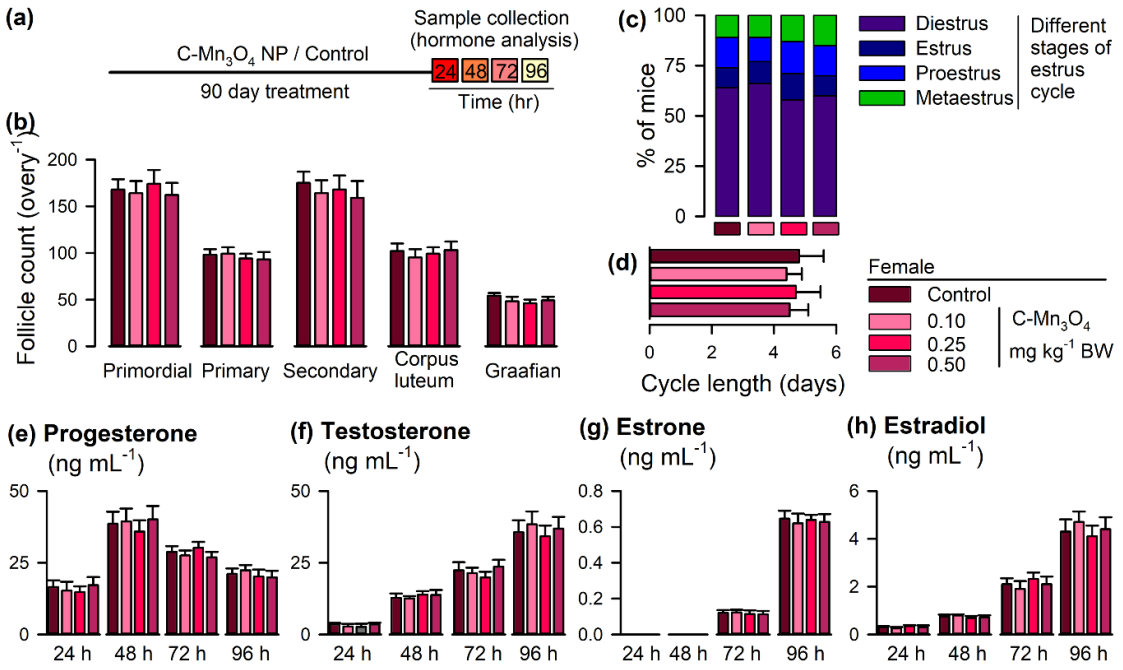

Figure 10.6. *Effect of C-Mn_3O_4 NPs on female reproductive system. (a) Collection protocol. (b) Differential counts of the follicles as observed in histological sections. (c) Distribution of estrus cycle across the groups. (d) Cycle length. (e-h) Changes in female reproductive hormones due to chronic C-Mn_3O_4 NPs exposure.*

All data represented as Mean ± Standard Deviation (SD). N=6 for each measurement.

of ovary from control animals displayed normal morphology. Developing follicles (primordial, primary, pre-antral and antral follicles), corpora luteum, Graafian follicles and atretic follicles were found in the cortex of the ovary which was covered by a surface epithelium (Figure 10.4d). The ovary of Mn_3O_4 NPs treated mice (at any dose) did not show any noticeable changes in histology such as formation of fibrosis or cyst (Figure 10.4d). The total number of healthy follicles (all categories) remains same after chronic exposure of Mn_3O_4 NPs across three dose groups (Figure 10.6b). The mean number of corpora lutea in mice remained same in all groups (data not shown). The estrus cycle was normal with typical distribution of diestrus, estrus, proestrus and metestrus stages (Figure 10.6c-10.6d). The hormone levels also showed no discrepancy (Figure 10.6e-10.6h).

Most of the drugs and xenobiotics pass through the kidney for excretion. But earlier studies have described that Mn cannot be excreted through it. Our

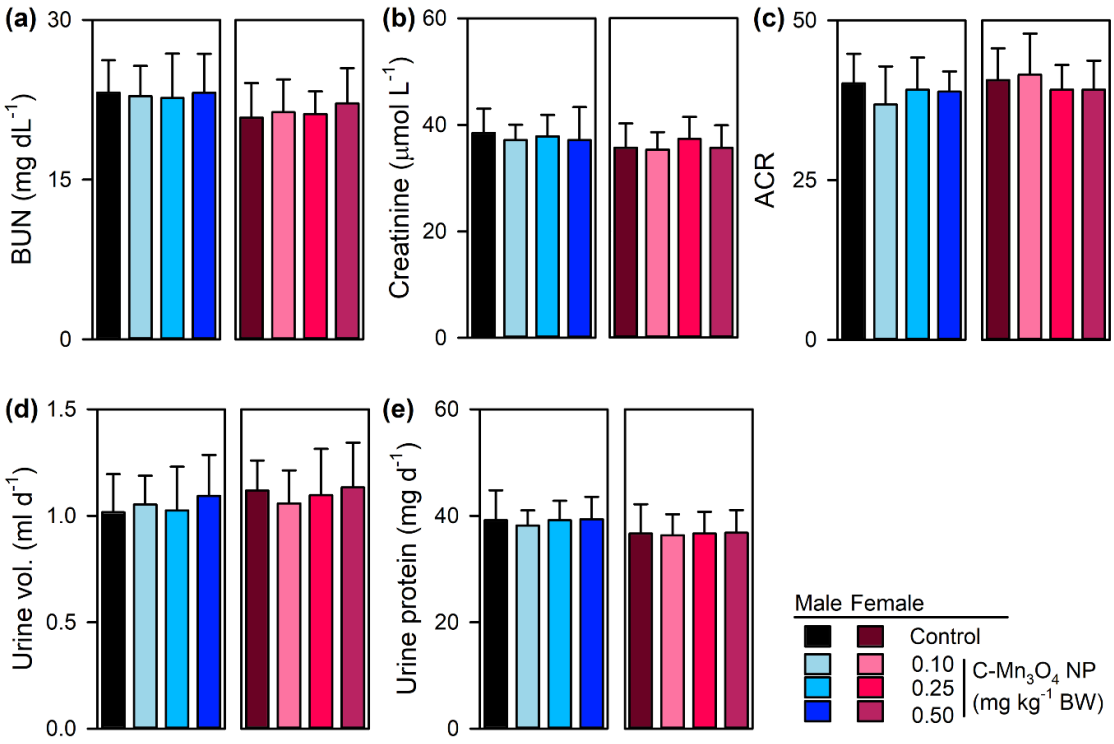

Figure 10.7. *Effect of C-Mn_3O_4 NPs on renal system. (a-e) Effect of C-Mn_3O_4 NPs on kidney antioxidant enzyme functions.*

All data represented as Mean ± Standard Deviation (SD). N=6 for each measurement.

biodistribution results also revealed minimal deposition of Mn in the Kidney (Figure 10.9). Histological analysis showed no damage and the normal structure of medulla and cortex was maintained in all four groups in spite of sexuality (Figure 10.4b). There was hardly any change in relative kidney weight. As discussed earlier that C-Mn_3O_4 NPs can produce ROS, we evaluated thiobarbituric acid reactive substance (TBARS), superoxide dismutase (SOD) activity and Total thiols in kidney cells. The results showed no change in these parameters across the groups. Consistent with these findings' other parameters like BUN, Creatinine, Urine Volume, Urine Protein and albumin to creatinine ratio remained similar to that of the control group (Figure 10.7a-10.7e).

We further investigated the effect of C-Mn_3O_4 NPs on plasma glucose levels and its metabolism. Microscopic investigation of the pancreas, the major organ responsible for glucose homeostasis, showed normal pancreatic tissue forming characteristic pancreatic acini with basal nuclei and amphiphilic cytoplasm in both

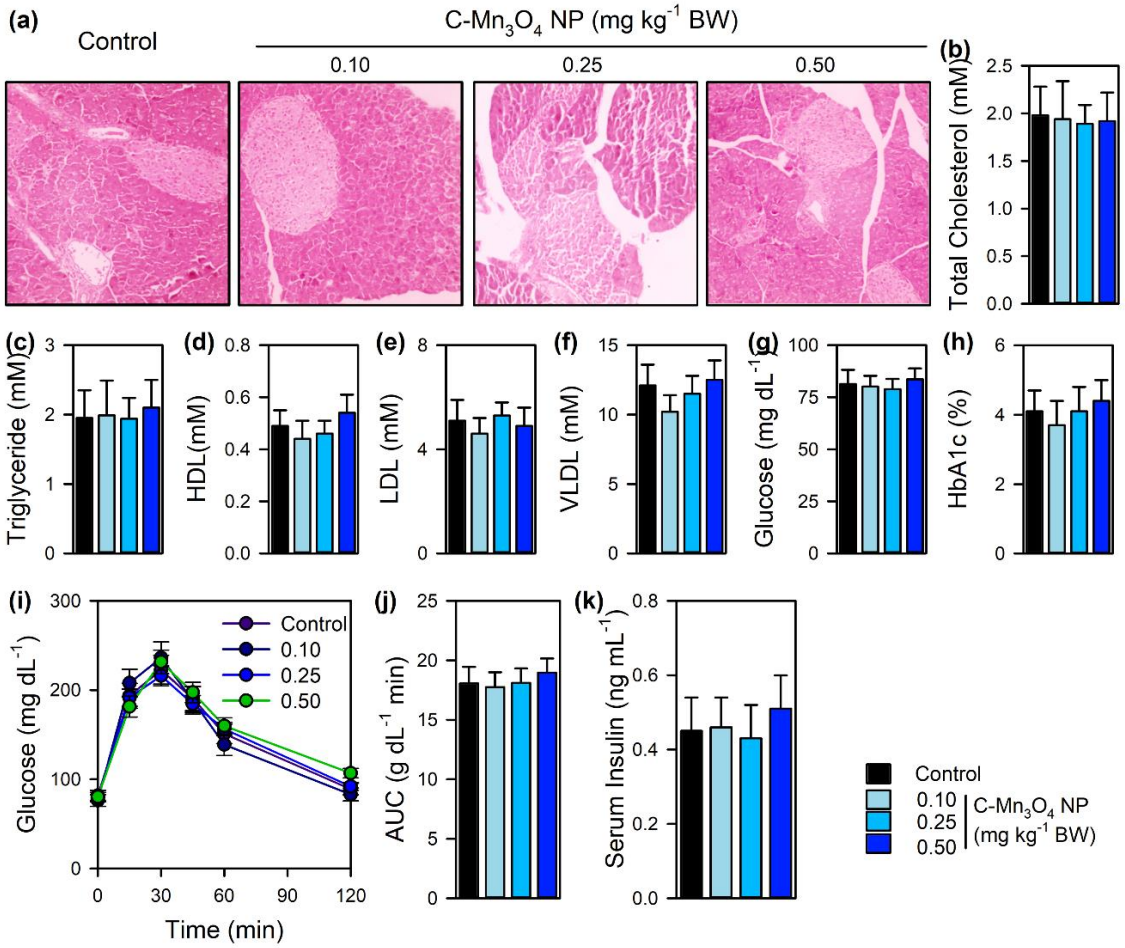

Figure 10.8. *Effect of the C-Mn_3O_4 NPs on glucose metabolism. (a) H&E stained sections of pancreas. (b-f) Lipid profile of the BALB/c mice treated with C-Mn_3O_4 NPs for 90 days. (g) Glucose uptake test. (h) HbA1c (i-k) AUC and other glucose metabolism parameters.*

All data represented as Mean ± Standard Deviation (SD). N=6 for each measurement.

control, and NP-treated mice (Figure 10.8a). The islet of Langerhans's displayed islet cells arranged in trabecular and acinar pattern with abundant eosinophilic cytoplasm and central small nucleus, separated by thin loose connective tissue with thin vessels. Islets have their typical spherical shape with a large number of β-cells with normal round shape distinct round nuclei. 2h glucose tolerance test showed indistinctive results among the groups with identical AUC (Figure 10.8i and 10.8j). Plasma glucose levels (12h fasting), HbA_{1c} and serum insulin concentration remained similar to control animals (Figure 10.8g, 10.8h and 10.8k). We extended the study with the evaluation of the lipid profile of the experimental groups. No significant changes were observed among the groups for total cholesterol, triglyceride, LDL, HDL or

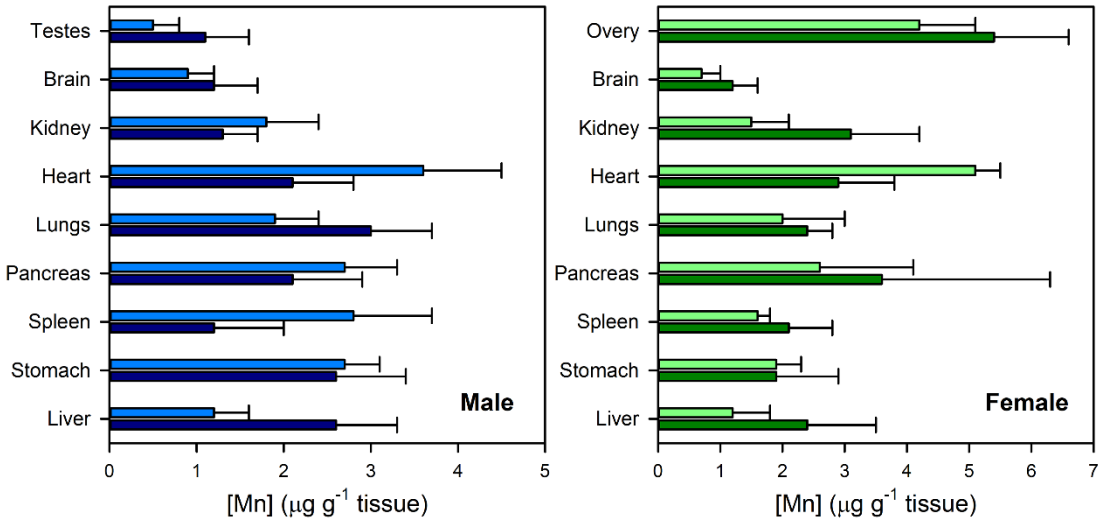

Figure 10.9. *Organ specific distribution of C-Mn_3O_4 NPs upon 90 days of repeated oral exposure.*

All data represented as Mean ± Standard Deviation (SD). N=6 for each measurement.

VLDL (Figure 10.8b-10.8f). Thus, the NPs neither affects glucose metabolism nor changes the lipid profile in the experimental regime.

Finally, we examined the distribution of C-Mn_3O_4 NPs into various organs after it leaves the bloodstream. The results after 90-days of chronic administration at therapeutic dose (0.25 g kg^{-1} BW daily) revealed that the C-Mn_3O_4 NPs were predominantly distributed in the liver, lungs, brain and reproductive organs (testes and ovary) irrespective of gender (Figure 10.9). Interestingly, in females (not in males) small increases in the Mn-content was observed in the pancreas and kidneys. The reason for such gender-specific differences is not clear to us. As the results suggest, liver contained the highest amount of NPs (Figure 10.9). The reason may be the lower surface charge (ζ= -12.23±0.6 mV) and elimination profile (hepatobiliary) described in Chapter 04. Earlier studies on mesoporous silica nanoparticles (MSNs) suggested that less charged moieties (e.g., -17.6 mV MSNs, which is comparable to the -12.23±0.6 mV of C-Mn_3O_4 NPs) remain sequestered within the liver while highly charged moieties (e.g., +34.4 mV) are excreted quickly [22]. Moreover, the functionalizing ligand, citrate, has an affinity towards hepatic cells [28]. The accumulation in lungs could be due to the very small (~6 nm) size of the particles. Several studies have reported that ultra-small sized nanoparticles have an affinity

towards lungs [29-31]. Many previous reports have indicated that NPs can reach specific sites for diagnosis and therapy of disease, such as the lymph nodes and brain parenchyma across the blood-brain barriers (BBB) [32]. Besides, Mn has an affinity towards brain tissue [33,34]. However, no significant change in Mn levels in brain or lymph nodes were observed in our study.

10.3. CONCLUSION

In conclusion, our study suggests that C-Mn_3O_4 NPs are extremely safe for long term oral administration at therapeutic regimen. However, at higher dose it may cause moderate organ specific toxicity (i.e., liver and lungs) which is reversible once the treatment stops. The exerted toxic effects at higher dose is due to the shifting of cellular redox homeostasis to a eustress condition. However, at therapeutic dose the nanoparticles show no toxic effects and opens up a new avenue for safe and efficacious use as a nanomedicine against a plethora of diseases.

REFERENCES

[1] V. Stone, K. Donaldson, Nat. Nanotechnol. 1 (2006) 23.

[2] S. Wang, F. Li, X. Hu, M. Lv, C. Fan, D. Ling, Adv. Ther. 1 (2018) 1800059.

[3] T. Xia, M. Kovochich, J. Brant, M. Hotze, J. Sempf, T. Oberley, C. Sioutas, J. I. Yeh, M. R. Wiesner, A. E. Nel, Nano Lett. 6 (2006) 1794.

[4] A. Nel, T. Xia, L. Mädler, N. Li, Science 311 (2006) 622.

[5] B. Yang, Y. Chen, J. Shi, Chem. Rev. 119 (2019) 4881.

[6] C. C. Winterbourn, Nat. Chem. Biol. 4 (2008) 278.

[7] Z. Wang, Y. Zhang, E. Ju, Z. Liu, F. Cao, Z. Chen, J. Ren, X. Qu, Nat. Commun. 9 (2018) 3334.

[8] D. Trachootham, J. Alexandre, P. Huang, Nat. Rev. Drug Discov. 8 (2009) 579.

[9] H. Sies, D. P. Jones, Nat. Rev. Mol. Cell Biol. 21 (2020) 363.

[10] C. M. Sims, S. K. Hanna, D. A. Heller, C. P. Horoszko, M. E. Johnson, A. R. Montoro Bustos, V. Reipa, K. R. Riley, B. C. Nelson, Nanoscale 9 (2017) 15226.

[11] C. Nathan, A. Cunningham-Bussel, Nat. Rev. Immunol. 13 (2013) 349.

[12] G. G. Martinovich, I. V. Martinovich, S. N. Cherenkevich, H. Sauer, Cell Biochem. Biophys. 58 (2010) 75.

[13] B. Morgan, D. Ezeriņa, T. N. E. Amoako, J. Riemer, M. Seedorf, T. P. Dick, Nat. Chem. Biol. 9 (2013) 119.

[14] G. G. Martinovich, S. N. Cherenkevich, H. Sauer, Eur. Biophys. J. 34 (2005) 937.

[15] A. Adhikari, S. Mondal, M. Das, R. Ghosh, P. Biswas, S. Darbar, S. Singh, A. K. Das, S. S. Bhattacharya, D. Pal, A. K. Mallick, S. K. Pal, bioRxiv (2021) https://doi.org/10.1101/2021.03.14.435286.

[16] A. Adhikari, S. Mondal, M. Das, P. Biswas, U. Pal, S. Darbar, S. S. Bhattacharya, D. Pal, T. Saha-Dasgupta, A. K. Das, A. K. Mallick, S. K. Pal, Adv. Healthcare Mater. 10 (2021) 2001736.

[17] A. Giri, N. Goswami, C. Sasmal, N. Polley, D. Majumdar, S. Sarkar, S. N. Bandyopadhyay, A. Singha, S. K. Pal, RSC Adv. 4 (2014) 5075.

[18] A. Adhikari, N. Polley, S. Darbar, D. Bagchi, S. K. Pal, Fut. Sci. OA 2 (2016) FSO146.

[19] M. J. Horsburgh, S. J. Wharton, M. Karavolos, S. J. Foster, Trends Microbiol. 10 (2002) 496.

[20] T. Takashima, K. Hashimoto, R. Nakamura, J. Am. Chem. Soc. 134 (2012) 18153.

[21] A. Adhikari, M. Das, S. Mondal, S. Darbar, A. K. Das, S. S. Bhattacharya, D. Pal, S. K. Pal, Biomater. Sci. 7 (2019) 4491.

[22] X. Huang, L. Li, T. Liu, N. Hao, H. Liu, D. Chen, F. Tang, ACS Nano 5 (2011) 5390.

[23] A. Adhikari, S. Darbar, T. Chatterjee, M. Das, N. Polley, M. Bhattacharyya, S. Bhattacharya, D. Pal, S. K. Pal, ACS Omega 3 (2018) 15975.

[24] A. Adhikari, P. Biswas, S. Mondal, M. Das, S. Darbar, A. M. Hameed, A. Alharbi, S. A. Ahmed, S. S. Bhattacharya, D. Pal, S. K. Pal, ChemMedChem 15 (2020) 420.

[25] A. Adhikari, N. Polley, S. Darbar, S. K. Pal, Mater. Focus 6 (2017) 280.

[26] V. Kumar, A. K. Abbas, N. Fausto, J. C. Aster, Robbins and Cotran Pathologic Basis of Disease, Elsevier/Saunders, Philadelphia, PA, (2014).

[27] Y. Bai, Y. Zhang, J. Zhang, Q. Mu, W. Zhang, E. R. Butch, S. E. Snyder, B. Yan, Nat. Nanotechnol. 5 (2010) 683.

[28] J. Sun, S. Aluvila, R. Kotaria, J. A. Mayor, D. E. Walters, R. S. Kaplan, Mol. Cell Pharmacol. 2 (2010) 101.

[29] W. G. Kreyling, S. Hirn, C. Schleh, Nat. Biotechnol. 28 (2010) 1275.

[30] N. Li, T. Xia, A. E. Nel, Free Radic. Biol. Med. 44 (2008) 1689.

[31] M. Ahamed, M. J. Akhtar, H. A. Alhadlaq, S. A. Alrokayan, Nanomedicine 10 (2015) 2365.

[32] R. Wen, X. Yang, L. Hu, C. Sun, Q. Zhou, G. Jiang, J. Appl. Toxicol. 36 (2016) 445.

[33] P. K. Pal, A. Samii, D. B. Calne, Neurotoxicology 20 (1999) 227.

[34] K. S. Kirkley, K. A. Popichak, M. F. Afzali, M. E. Legare, R. B. Tjalkens, J. Neuroinflammation 14 (2017) 99.

CHAPTER 11

Rationalization of a Polyherbal Medicine by Combined Computational and Experimental Approach

11.1. INTRODUCTION

Lead (Pb), one of the most widely used metals in industry and simultaneously a versatile, subtle and persistent poison present in Earth's crust, can induce a wide array of physiological, biochemical and behavioral dysfunction affecting almost every organ system (central and peripheral nervous, hematopoietic, respiratory, cardiovascular, renal, hepatic and reproductive system) cumulating in death [1-4]. Although, the lead toxicity has been documented as early as 2000 BC and found to be preventable, victims of such toxicity in human civilization are evident in recent times [5]. Even in 2015, 494550 deaths occurred due to lead exposure, which is 0.6% of the global burden of diseases and 9.3 million disability-adjusted life years (DALYs) [4,6,7]. Of particular concern is the role of lead exposure in the development of intellectual disability in children [6]. Even though there is wide recognition of this problem and many countries have acted, exposure to lead (Pb), particularly in childhood, remains a key concern for the healthcare providers and public health officials worldwide. Although, lead (Pb) itself is a non-redox metal and does not possess any pro-oxidant catalytic activity, rather coverts to some indirect mechanisms

(e.g., auto-oxidation of hemoglobin (Hb), accumulation and subsequent auto-oxidation of δ-aminolevulinic acid (δ-ALA) induced by Pb) for imparting pathogenesis via oxidative disturbances [4,8-10]. Thus, controlling the free radical-induced intracellular damage is equally important in combating lead poisoning alongside removal of the same from organs. On the other hand, the currently approved treatment for Pb-toxicity (use of chelating agents like DMSA, $CaNa_2EDTA$ etc.) can neither be used at therapeutically adequate dose for a prolonged period of time owing to number of shortcomings and inherent toxicity (e.g., nephrotoxicity, cardiotoxicity, zinc-diarrheasis, nausea, fever, breathing trouble etc.) nor reduce the significant oxidative stress generated due to cellular Pb-exposure [3,11]. Therefore, considering the indispensable necessity of an alternative therapeutic approach, an exogenously supplied chelator with sustainable antioxidant activity even after complexation with Pb can be an ideal therapeutic detoxification strategy.

Flavonoids, a class of natural polyphenols with a benzo-γ-pyrone structure ubiquitously present in plants, are widely known for their antioxidant activity [12-14]. Since the discovery in 1936, several studies have determined the flavonoid antioxidant activity, many of which have used pure compounds, calculated individual antioxidation power and performed structure-activity relationship studies [14-16]. In other studies, the antioxidation power of a given food or plant sample has been characterized in depth and, in some cases, the correlation between flavonoid composition and antioxidation power has been examined [17-19]. The other most studied property of flavonoids is the metal ion-chelation ability. Several studies have reported interactions between flavonoids and metal ions leading to chelate formation that are only slightly active in the promotion of free-radical reactions [13,20-22]. Although, several studies have shown that plants use this chelation property for detoxification of heavy metals [23-25], in-depth study on interaction of heavy metals with flavonoids is sparse in contemporary literature. Some of the recent studies focus on the antioxidation properties of flavonoid-transition metal complex (e.g., Fe^{3+}, Cr^{3+}, Cu^{2+}, Al^{3+} etc.) [26-31]. But, to the best of our knowledge, no study has addressed the sustainable antioxidation activity imparted due to heavy metal chelation to flavonoid alone or in mixture with other polyphenols and is one of the motives of the present study.

Here, we have studied a model heavy metal (lead, Pb) chelating efficacy of a model flavonoid (morin) using steady state and picosecond resolved optical spectroscopy. The efficacy of morin in presence of other flavonoid (naringin) and polyphenol (ellagic acid) leading to synergistic combination has also been confirmed from the spectroscopic studies. This is particularly important, because it has previously been observed that polyphenolic mixtures show fewer side effects than the pure compounds due to interactions amongst themselves [32,33]. Our studies reveal that antioxidant activity (DPPH assay) of the lead-morin complex is sustainable compared to that of lead-free morin. We have also found that the solubility of the Pb-morin complex increases significantly compared to that of morin in aqueous environment. Heavy metal chelation and sustainable antioxidant activity of the chelate complex were found to accelerate the Pb-detoxification in the chemical bench (*in vitro*). Considering the synergistic effect of flavonoids in Pb-detoxification and their omnipresence in medicinal plants, we have prepared a mixture (SKP17LIV01) of flavonoids containing 34 flavonoids and 76 other polyphenols, and investigated the lead detoxification in mouse model. The biochemical and histopathological studies confirm the dual action in preclinical studies. Our studies on biodistribution of Pb in various target organs of the intoxicated mice using inductively coupled plasma assisted atomic emission spectroscopy (ICP-AES) confirm that SKP17LIV01 efficiently facilitates excretion of Pb from mice body after heavy metal chelation and sustainable ROS scavenging *in vivo*.

Over the past decade, there has been a severe decline in the rate at which new drug candidates are being translated into effective therapies in the clinics [34]. In particular, the lack of efficacy and clinical safety of the synthetic drugs resulted into a worrying rise in late-stage attrition in phase-2 and phase-3 clinical trials [35]. These late-stage attrition rates are at the heart of the relative decrease in productivity of the pharmaceutical industry creating a major financial shock [36]. In this regard, natural products with diverse chemical scaffolds can be an invaluable alternative source of compounds in drug discovery and development [37]. Several of these natural products have been in use as ancient traditional remedies (e.g., Traditional Chinese Medicine, Ayurveda, etc.) since time immemorial [38]. They are considered to be less toxic as they have undergone the mill of coevolution with human protein [39]. However,

limited knowledge about the active ingredients and molecular mechanism of action restrict their use in modern medicine [40,41]. The current paradigm of systematic identification of drug targets of the natural products at the human proteome level via various experimental assays is highly expensive and time-consuming [37]. So, an alternative approach is required, which will preferably include *in silico, in vitro,* and *in vivo* methods in a synchronous manner to reduce the cost and time of drug discovery. Network pharmacology encompassing systems biology, network analysis, connectivity, redundancy, and pleiotropy can be an alternative strategy for the invention of new drugs [36]. Although several studies have used computational approaches to identify target molecules [42-46], a systematic modus operandi for rationalization of the medicinal activities of natural products and their mechanism of action is lacking. In recent years, Wu et. al. [47], and Gao et. al. [48] have successfully used a combined computational and experimental approach to predict hepatotoxicity and cytotoxicity of natural compounds identified from traditional Chinese medicine.

In this study, heavy metal-induced liver disease was chosen as the model considering the rise in liver problems throughout the last decade [49]. Despite a plethora of drugs being introduced, liver diseases are the fifth most common cause of death (National Statistics, UK). Since, liver disease is caused by disorganization of a complex cellular network comprising of numerous proteins [50,51], the traditional concept of 'one drug, one protein, one disease' becomes highly redundant. Such complex diseases may best be attempted using polypharmacological approaches [36]. In this paper, we propose a systems biology approach that efficiently predicts the drug-like properties of the constituent compounds (identified by UHPLC-MS) of an indigenously developed formulation (SKP17LIV01) from medicinal plants to find out the active ingredients (leads), their targets (hits) inside the body and the signaling pathways that are most likely to be modulated during the therapeutic process. By performing a combined system-level analysis on disease-protein expression signatures and compound-target protein expression signatures, our approach could estimate the amount of perturbation caused by the active ingredients on the proteins that are associated with a disease of interest. Pathway enrichment analysis provides a holistic view of the molecular mechanism of action through identification of the therapeutic target pathways. The systems biology predictions were verified in the Pb-intoxicated

animal model. A detailed biochemical, histopathological and molecular study confirmed the robustness of computational predictions as well as proved the efficacy of SKP17LIV01 in treatment of heavy metal-induced liver damage. Thus, this study is expected to provide a more accurate prediction approach in rationalization (or repurposing) of traditional medicines (or natural medicines including nutraceuticals) in a low cost and timely manner.

11.2. RESULTS AND DISCUSSION

11.2.1. Spectroscopic Studies on Dual Role of Natural Flavonoids in Detoxification of Lead Poisoning: Bench to Bedside-Preclinical Trial [52]

Primarily we chose morin (3,5,7,2',4'-pentahydroxyflavone) (Figure 11.1a) as a representative of flavonoid class for understanding their heavy metal chelating activity. Morin is very special among flavonols as it is one of those few natural flavonols that bears a OH group in position 2' that can be involved in a hydrogen bond with 3-OH leading to far reaching consequences [13].Despite being the most abundant polyphenol in our diet or in nature, this unique structural feature along with previously reported antiradical activity [53] made morin our molecule of interest. The absorbance spectra of morin (Figure 11.1b) shows two absorption maxima centered at ~255 nm (Band II) and ~354 nm (Band I) corresponding to the $\Pi \rightarrow \Pi^*$ electronic transition originating at benzoyl (flavonoid ring A) and cinamoyl (flavonoid ring B) systems respectively. The interaction of morin with Pb^{2+} produced large bathochromatic shift (~45 nm) in band I maxima (Figure 11.1b). In contrast, band II remained unaffected. The exclusive change in band I indicates the involvement of cinamoyl system in complexation process. Among the three probable binding sites (3-OH and 4-oxo, 3-OH and 2'-OH or 5-OH and 4-oxo) present in morin, 3-OH and 4-oxo is the most preferable site of co-ordination due to the presence of highly acidic proton, stronger chelation ability and greater delocalization of the oxygen at 3-OH [54,55]. The stoichiometry of the complexation was investigated by using the Job's method

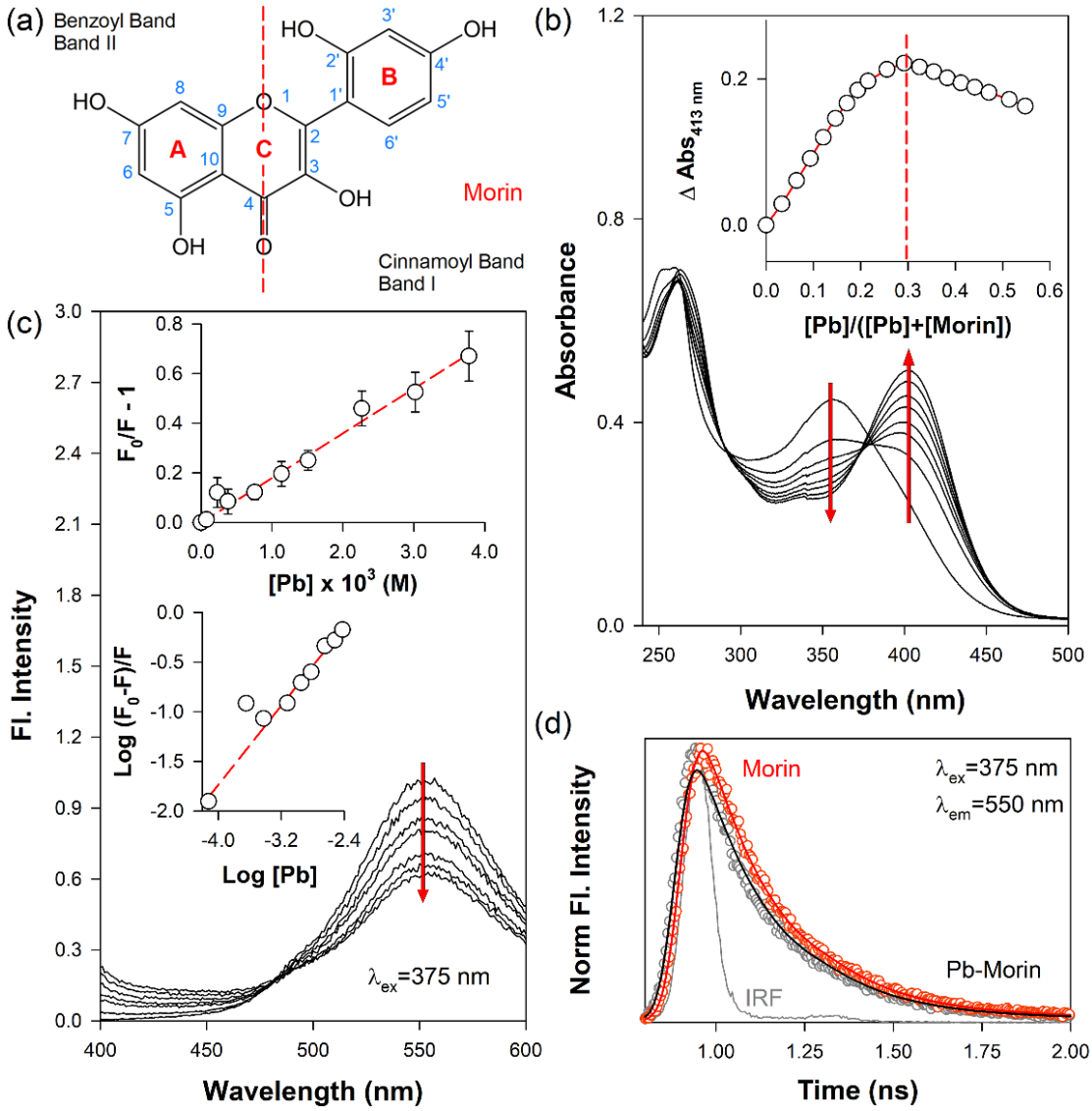

Figure 11.1. *Interaction of Pb(II) with morin, a flavonol. (a) Chemical structure, numbering system and UV-vis absorption bands of morin. (b) Absorption spectra of 4.09×10^{-5} M morin in presence of varying concentrations (0.15×10^{-5} M - 4.14×10^{-4} M) of $Pb(NO_3)_2$. Arrows indicate increase in concentration of Pb^{2+}. Inset shows the Job plot for binding of Pb^{2+} to morin. (c) Fluorescence spectra of morin (2.66×10^{-4} M) in presence of different concentrations (0.75×10^{-4} M – 37.74×10^{-4} M) of $Pb(NO_3)_2$ (λ_{ex}=375 nm). Inset shows Stern-Volmer and modified Stern-Volmer plots for the interaction (λ_{em}=550 nm). (d) Time-resolved fluorescence transients of morin (2.66×10^{-4} M) in absence and presence of Pb^{2+} (37.7×10^{-4} M).*

(method of continuous variation) [56]. Considering a global equilibrium of Pb(II) and *n* ligands (L) on the form,

$$Pb+nL=PbL_n$$

[Equation – 11.1]

where, *n* is determined from the plot of the absorbance as a function of the mole fraction, of the added ligand. In the absorbance maximum,

$$n = \frac{f_{max}}{1-f_{max}}$$

[Equation – 11.2]

Figure 11.1b-inset represents a typical Job plot for the Pb(II)/morin system, in which the transition point for absorbance appeared at the molar fraction of 0.33, suggesting that morin (L) bound to Pb^{2+} with a 2:1 ratio in the complex (PbL_2).The observed new band at ~413 nm (Figure 11.1b) due to complexation corresponds to the formation of Pb-3-OH, forming a big extended Π-bonding system with inclusion of C ring leading to further stabilization [57]. The electronic transition within morin shifts from n–Π* to lower energy Π–Π* favoring the development of a new band at higher wavelength [58,59]. The binding constant of the Morin-Pb^{2+} complex was found to be 1.803×10^4 M^{-1} ($R^2 = 0.987$) using the Benesi–Hildebrand equation [60]:

$$\log\left(\frac{A-A_0}{A_f-A_0}\right) = \log[Pb^{2+}] + \log K_b$$

[Equation – 11.3]

where, A_0, A and A_f are the absorption values, in the absence of, at the intermediate and at the saturation of the interaction of Pb^{2+} ion respectively, and [Pb^{2+}] represents the concentration of aqueous Pb^{2+} ion added. The binding constant (K_b) was determined by linear fitting of absorption titration curve.

In the photoluminescence study, morin shows a strong emission at ~550 nm when excited at ~375 nm (Figure 11.1c). The observed fluorescence is probably originating from the anion form of the 7-OH group of the pyrone ring, as it gets deprotonated first owing to its low pK_a of deprotonation (pK_a 3.80) and as a result, morin stays as mono deprotonated species in a solution of physiological pH [61,62]. In presence of Pb^{2+}, the fluorescence quenched (Figure 11.1c). The phenomenon of fluorescence quenching can be attributed to several molecular mechanisms including excited-state reactions, molecular rearrangements, energy transfer, ground-state complex formation, and collisional quenching. In case of morin, no discernible shift in emission maxima (~550 nm) or shape of the fluorescence spectrum accompanied

quenching and the quenching behavior generally adhered to the Stern-Volmer equation (Equation – 11.4).

$$\frac{F_0}{F}-1=K_{sv}[Q]=k_q\tau_0[Q]=\frac{\tau_0}{\tau}-1$$

[Equation – 11.4]

where, F_0 and F are the fluorescence intensities in the absence and presence of the quencher, [Q], K_{sv} Stern-Volmer quenching constant, k_q the bimolecular quenching rate constant, τ_0 and τ are the fluorescence lifetime of the fluorophore in absence and presence of quencher respectively [63]. The linearity in the Stern-Volmer plot (Figure 11.1c-inset) indicates existence of a single type of quenching, either static or dynamic [63]. To get further insight of the phenomena, we measured excited state fluorescence lifetime of the fluorophore (morin) with increasing concentrations of the quencher, Pb^{2+} (Figure 11.1d). It is well known that in case of dynamic quenching, the fluorescence lifetime decreases with increase in quencher concentrations [63]. But in this case, no change in fluorescence lifetime (Table 11.1) was observed, which clearly specifies the quenching mechanism to be static. This was further supported by the calculation of the bimolecular quenching constant, k_q (K_{sv}/τ_0) which was found to be

Table 11.1. Fluorescence lifetime components of polyphenols and Pb(II)-polyphenol complexes.

	α_1 (%)	τ_1 (ps)	α_2 (%)	τ_2 (ps)	α_3 (%)	τ_3 (ps)	$<\tau>$ (ps)
Morin	97.3	189.90	2.7	1858.50	-	-	234.95
Morin-Pb(II)	97.3	189.90	2.7	1858.00	-	-	234.95
Naringin	-	-	90.1	127.09	9.8	378.04	151.47
Naringin-Pb(II)	93.9	27.56	5.5	127.00	0.5	378.00	34.94
EA	-	-	100	3072.45	-	-	3072.45
EA-Pb(II)	75.6	88.59	24.4	3072.00	-	-	816.54
MNEA	-	-	96.2	141.38	3.8	2088.00	213.29
MNEA-Pb(II)	82.6	30.83	16.1	141.00	1.2	2088.84	73.22
SKP17LIV01	65.7	38.03	15.7	475.00	18.5	3156.55	683.52
SKP17LIV01-Pb(II)	77.4	32.77	9.7	475.46	12.7	3156.00	472.32

τ represents the time constant, and α represents relative contribution of the component. λ_{ex}=375 nm for all systems; λ_{em} (Morin)=550 nm; λ_{em} (Naringin)=500 nm; λ_{em} (EA)=440 nm; λ_{em} (MNEA)=550 nm; λ_{em} (SKP17LIV01)=550 nm.

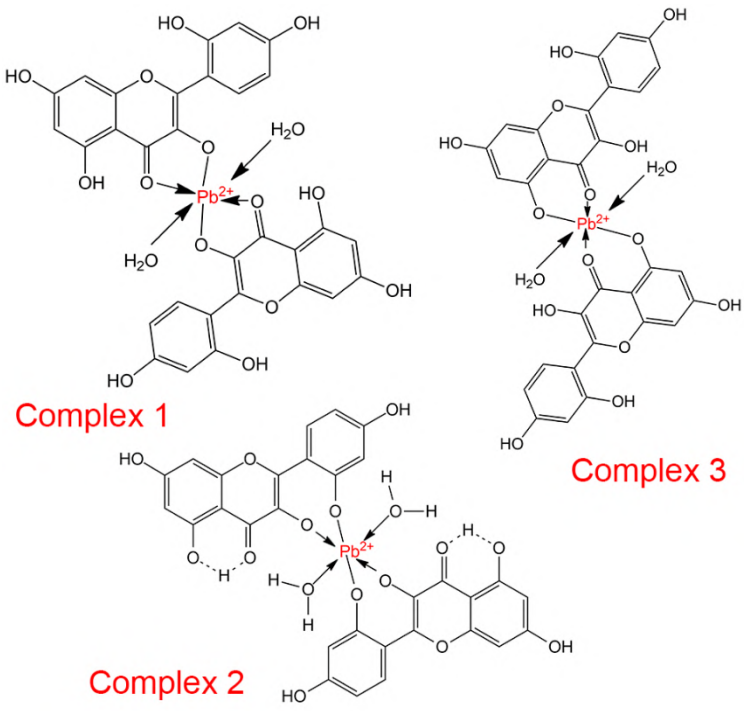

Figure 11.2. *The three possible structures of morin-Pb^{2+} complex. Complex 1 is the most probable one.*

~7.69×10^{12} M^{-1} sec^{-1}, higher than that of diffusion-controlled limit (~10^{10} M^{-1} s^{-1}) [63]. This along with no change in fluorescence lifetime indicates ground state complex formation between Pb^{2+} and morin (association constant, $K_a=K_{sv}=1.819\times10^4$ M^{-1}, similar to that found in absorbance experiment). Probably, the binding of Pb^{2+} to the carbonyl and 3-OH groups of the pyrone ring inhibits the intramolecular proton transfer, resulting in formation of a non-emissive or low emission photo-tautomer at room temperature [62]. Thus, it can be inferred from optical spectroscopic studies that morin acted as a bidentate ligand and formed a mononuclear complex with Pb^{2+}, where one ion is bound to two ligands (Figure 11.2).

Generally in natural products, flavonoids never stay as a single entity, rather, as a mixture of flavonoids and other polyphenols. So, we prepared an equimolar mixture of morin, naringin (a flavonoid glycoside) and ellagic acid (an ellagotannin) to see whether the blending exerts any effect on heavy metal binding property. naringin and ellagic acid were selected as representatives of two different classes of polyphenols commonly found in natural products. Figure 11.3a shows the absorbance spectra of

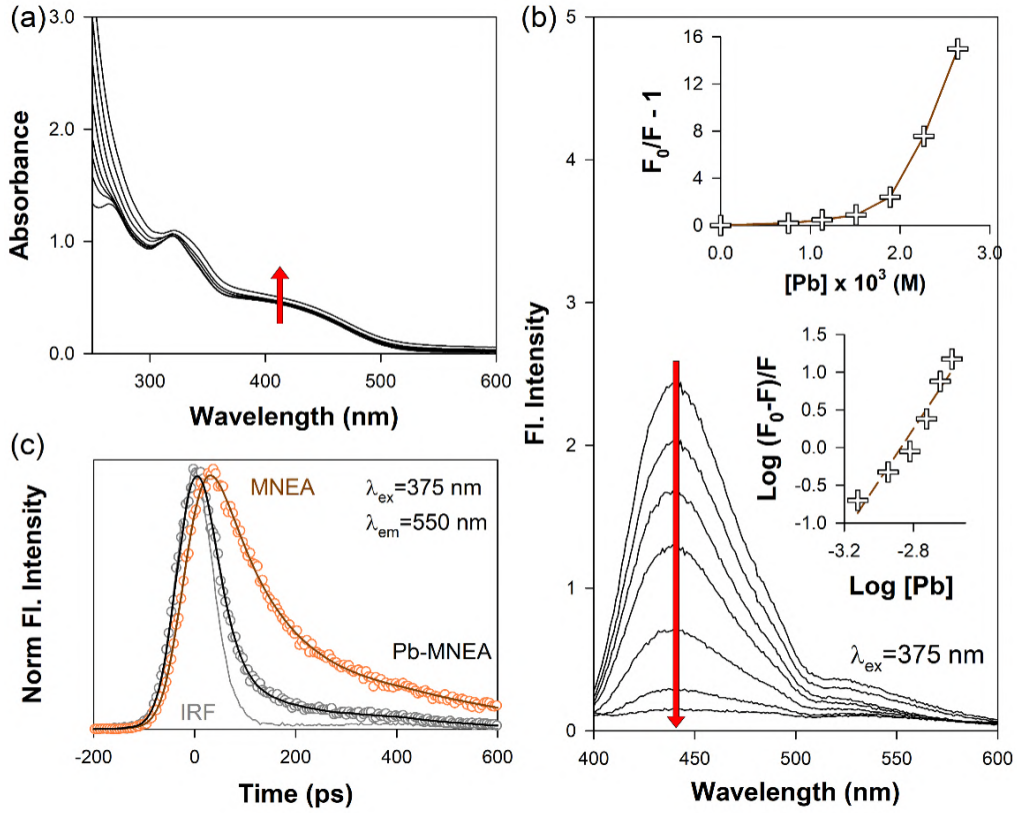

Figure 11.3. *Interaction of Pb(II) with MNEA, an equimolar mixture of three polyphenols morin (a flavanol), naringin (a flavonol glycoside) and ellagic acid (an ellagitannin). (a) Absorption spectra of MNEA (0.62×10^{-4} M) in presence of varying concentrations (0.91×10^{-4} M - 1.46×10^{-4} M) of $Pb(NO_3)_2$. Arrows indicate increase in concentration of Pb^{2+}. (b) Fluorescence spectra of MNEA (0.62×10^{-4} M) in presence of different concentrations (0.75×10^{-4} M – 30.19×10^{-4} M) of $Pb(NO_3)_2$ (λ_{ex}=375 nm). Inset shows Stern-Volmer and modified Stern-Volmer plots for the interaction (λ_{em}=550 nm). (c) Time-resolved fluorescence transients of MNEA (0.62×10^{-4} M) in absence and presence of Pb^{2+} (30.19×10^{-4} M).*

the mixture (we call it MNEA). Addition of Pb^{2+} to MNEA caused minimal or no change in absorbance. However in fluorescence studies (Figure 11.3b), quenching phenomena was clearly evident at both λ_{em}=450 (probably originating from ellagic acid) and λ_{em}=550 nm (a tail probably originating from morin). Positive deviation of F_0/F from linearity indicates the possible involvement of combined static and dynamic quenching. The Stern-Volmer constant for both types of quenching can be determined from the equation (Equation – 11.5).

$$\frac{F_0}{F}=(1+K_D[Q])(1+K_S[Q])$$

[Equation – 11.5]

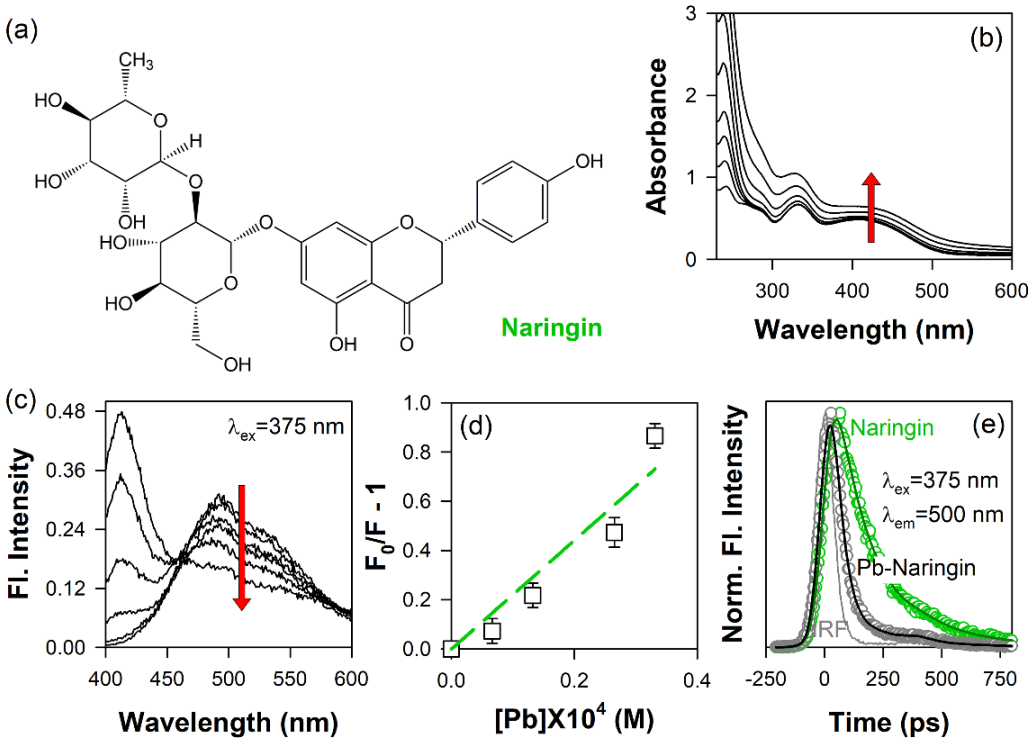

Figure 11.4. *Interaction of Pb(II) with naringin, a flavonol glycoside. (a) Structure of naringin. (b) Absorption spectra of naringin in presence of varying concentrations (0.91×10^{-4} M - 1.46×10^{-4} M) of $Pb(NO_3)_2$. Arrows indicate increase in concentration of Pb^{2+}. Inset shows the Job plot for binding of Pb^{2+} to naringin. (c) Fluorescence spectra of naringin in presence of different concentrations (0.91×10^{-4} M - 1.46×10^{-4} M) of $Pb(NO_3)_2$ (λ_{ex}=375 nm). (d) Stern-Volmer and modified Stern-Volmer plots for the interaction (λ_{em}=500 nm). (e) Time-resolved fluorescence transients of naringin in absence and presence of Pb^{2+} (1.46×10^{-4} M).*

where, K_D is the dynamic quenching constant and K_S is the static quenching constant. The double logarithmic plot (Figure 11.3b-inset) reveals the association constant (K_a = 3.16×10^4 M^{-1}) and number of binding sites (n=1.25) using the following equation (Equation 11.6).

$$\log\frac{F_0-F}{F}=\log K_a+n\log[Q]$$

[Equation – 11.6]

Where K_a is the association constant and n is the number of possible binding sites. The decrease in lifetime, as observed in TCSPC (Table 11.1) also supports our conjecture. The ground state complex formation between morin and Pb^{2+}, observed in the earlier section of this study, is primarily responsible for the static part of the observed

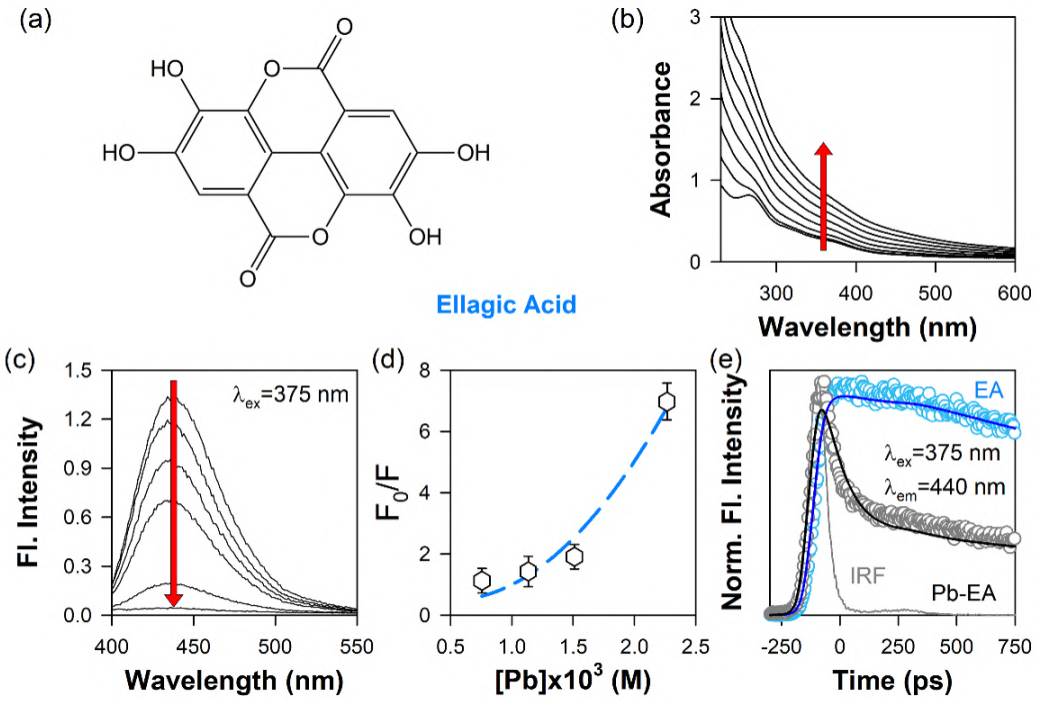

Figure 11.5. *Interaction of Pb(II) with ellagic acid, an ellagitannin. (a) Structure of ellagic acid (EA) and different chemical properties of it. (b) Absorption spectra of ellagic acid in presence of varying concentrations (0.91×10^{-4} M - 1.46×10^{-4} M) of $Pb(NO_3)_2$. Arrows indicate increase in concentration of Pb^{2+}. Inset shows the Job plot for binding of Pb^{2+} to EA. (c) Fluorescence spectra of EA in presence of different concentrations (0.91×10^{-4} M - 1.46×10^{-4} M) of $Pb(NO_3)_2$ (λ_{ex}=375 nm). (d) Stern-Volmer and modified Stern-Volmer plots for the interaction (λ_{em}=440 nm). (e) Time-resolved fluorescence transients of EA in absence and presence of Pb^{2+} (1.46×10^{-4} M).*

quenching phenomena. To find out the origin of the dynamic quenching component, we further investigated the interaction of Pb^{2+} with the other two compounds in the mixture.

In case of naringin (Figure 11.4a), as there was observable changes in the absorbance at λ_{ex} (375 nm) or λ_{em} (500 nm) (Figure 11.4b), we employed inner filter-effect correction using the following equation (Equation – 11.7):

$$F_{obs}=F_{corr}\times10^{-\frac{A_{ex}\times d_{ex}}{2}\frac{A_{em}\times d_{em}}{2}}$$

[Equation 11.7]

where, F_{obs} is the observed fluorescence intensity, F_{corr} is the corrected fluorescence intensity after correction of inner filter effect, d_{ex} and d_{em} are the path lengths in the excitation and emission detection (in cm), respectively, and A_{ex} and A_{em} are the

detected change in absorbance value at the excitation and emission wavelengths, respectively, caused by ligand addition [63,64]. The Stern-Volmer plot (Figure 11.4d) constructed using the corrected fluorescence intensities showed linearity. The significant change in the lifetime (Table 11.1) describes the quenching process to be dynamic in nature. For ellagic acid (Figure 11.5a) also, the inner filter correction was employed due to presence of significant change in absorbance (Figure 11.5b). Addition of Pb^{2+} in the solution caused quenching of the fluorescence (Figure 11.5c) and the Stern-Volmer plot showed an upward curvature without any dependence onto [Pb^{2+}] (Figure 11.5d). Thus, neither simple dynamic (linear F_0/F, vs [Pb^{2+}]) nor combined static and dynamic (second-degree polynomial) quenching model was accurately able to describe the data. Rather, a combined "sphere of action"-dynamic quenching model was helpful. This includes by means of a Poisson distribution the probability that a Pb^{2+} ion is close enough to instantaneously quench the fluorescent species [63]. This deviation from linear Stern-Volmer behavior is plausible for species such as Pb(II), where strong Coulombic interactions are likely to occur between the excited state and the quenching ion [65]. This could further be supported from the time resolved studies (Figure 11.5e) which showed a decrease in lifetime of the fluorophore (Table 11.1). The functional form of the quenching model is:

$$\frac{F_0}{F} = (1+K_D[Q])e^{(K_e[Q])}$$

[Equation – 11.8]

The constants K_D and K_e, were found by nonlinear least squares regression of the data. The dashed line on Figure 11.5d represents this model equation with the above empirical constants. So, it can be concluded that, excited state interaction between naringin-Pb(II) and ellagic acid-Pb(II) are responsible for the observed dynamic quenching component of MNEA-Pb(II) interaction. In order to investigate the mutual interaction among the flavonoids and polyphenols, we have performed spectroscopic studies on the mixture. While, morin-naringin or naringin-ellagic acid showed insignificant changes in the steady state emission and absorption spectroscopic data, mixing of morin with ellagic acid resulted in spectroscopic changes as shown in the Figure 11.6a. The steady state fluorescence spectra reveal the quenching at 550 nm with subsequent increase at 450 nm with an iso-emissive point at 500 nm

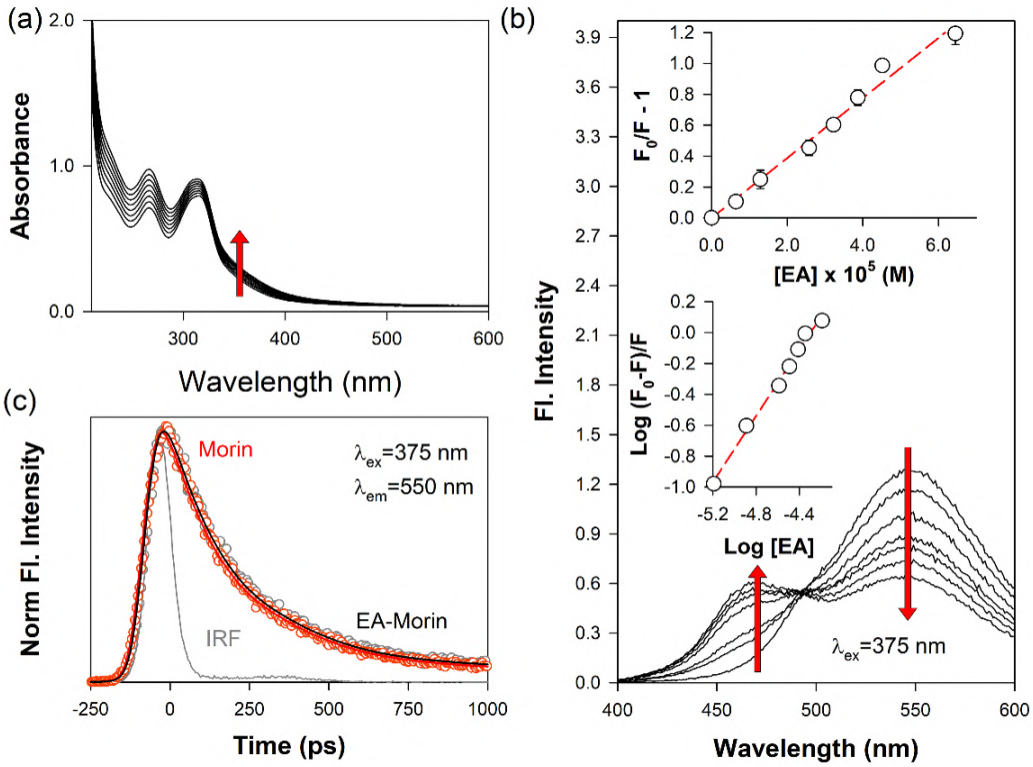

Figure 11.6. *Interaction of EA with morin. (a) Absorption spectra of morin in presence of varying concentrations of EA. Arrows indicate increase in concentration of EA. (b) Fluorescence spectra of morin in presence of different concentrations of EA (λ_{ex}=375 nm). Inset shows Stern-Volmer and modified Stern-Volmer plots for the interaction (λ_{em}=550 nm). (c) Time-resolved fluorescence transients of morin in absence and presence of EA.*

(Figure 11.6b). The Stern-Volmer plot (Figure 11.6b – inset) indicated presence of a single type of quenching which is found to be static in nature as fluorescence lifetime remained unchanged (Figure 11.6c). Thus, the flavonoids even in presence of other polyphenols can effectively bind heavy metals and increase the detoxification possibility inside the body. The other polyphenols do not hamper the detoxification procedure, rather shows a synergistic effect by chelating the heavy metal. In this process, as many of the polyphenols are potential lead chelators, competition for metal complexation might occur between these natural chelators, resulting in synergistic effect.

Next, we proceed to a more complex mixture of flavonoids and polyphenols, SKP17LIV01 (total phenolic content = 4.71×10^{-3} M; total flavonoid content = 3.97×10^{-3} M; morin-2.9%, naringin-1.2%, ellagic acid-1.8%). The mixture was

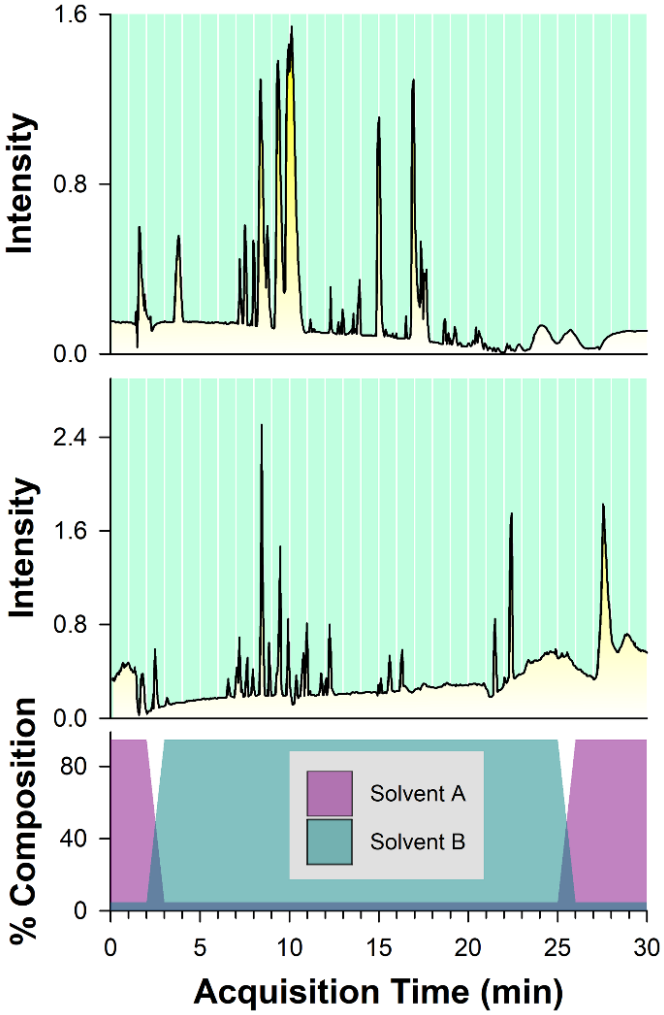

Figure 11.7. *Determination of phytoconstituents in SKP17LIV01. HR-LCMS analysis of the extract. Upper and Middle panel shows the chromatogram in positive and negative mode respectively. Lower panel shows the composition of solvent during the experiment.*

completely characterized by ultra-high performance liquid chromatography mass spectrometry (UHPLC-MS) (Figure 11.7; Dataset 11.1 and 11.2). Although, it is hard to draw any conclusion from a mixture of ~100 polyphenols either by absorption or by emission, still we tried to find observable change (if any). In brief, the absorbance spectra of SKP17LIV01 show no or minimal changes upon gradual addition of Pb^{2+} (Figure 11.8a). However, in steady state fluorescence spectra, quenching was observed (Figure 11.8b).The Stern-Volmer plot (Figure 11.8b-inset) suggests the presence of a single type of quenching, which is static in nature, as also is found from time resolved studies (Figure 11.8c and Table 11.1). This is further supported by the calculation of

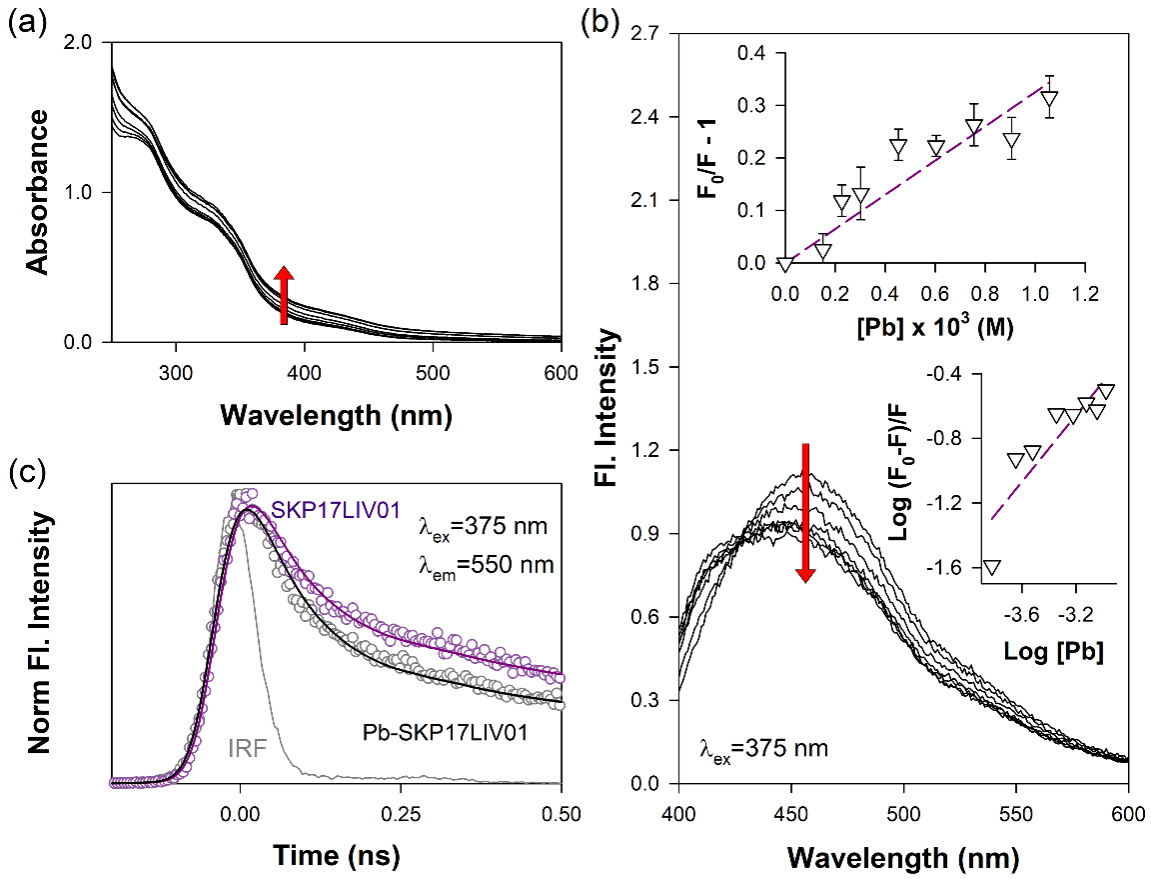

Figure 11.8. *Interaction of Pb(II) with SKP17LIV01, an ethanolic plant extract containing numerous polyphenols (listed in Dataset 11.1 and 11.2). (a) Absorption spectra of SKP17LIV01 in presence of varying concentrations (0.91×10^{-4} M - 1.46×10^{-4} M) of $Pb(NO_3)_2$. Arrows indicate increase in concentration of Pb^{2+}. (b) Fluorescence spectra of SKP17LIV01 in presence of different concentrations (0.75×10^{-5} M – 1.509×10^{-4} M) of $Pb(NO_3)_2$ (λ_{ex}=375 nm). Inset shows Stern-Volmer and modified Stern-Volmer plots for the interaction (λ_{em}=550 nm). (c)Time-resolved fluorescence transients of SKP17LIV01 in absence and presence of Pb^{2+}.*

the bimolecular quenching constant, k_q (K_{sv}/τ_0), which is found to be ~4.81×10^{12} M^{-1} sec^{-1} and higher than that of diffusion-controlled limit (~10^{10} M^{-1} s^{-1}) [63]. The association constant (K_a) of SKP17LIV01 with Pb is found to be, $K_a = 4.26\times10^4$ M^{-1}. It has to be noted that the mixture (SKP17LIV01) of flavonoids and lots of other polyphenols is able to retain the heavy metal binding activity of constituent molecules. For the ease of extraction from medicinal plants, low cost and efficient metal binding, the mixture is more attractive as a therapeutic agent than the individual compounds like morin or naringin.

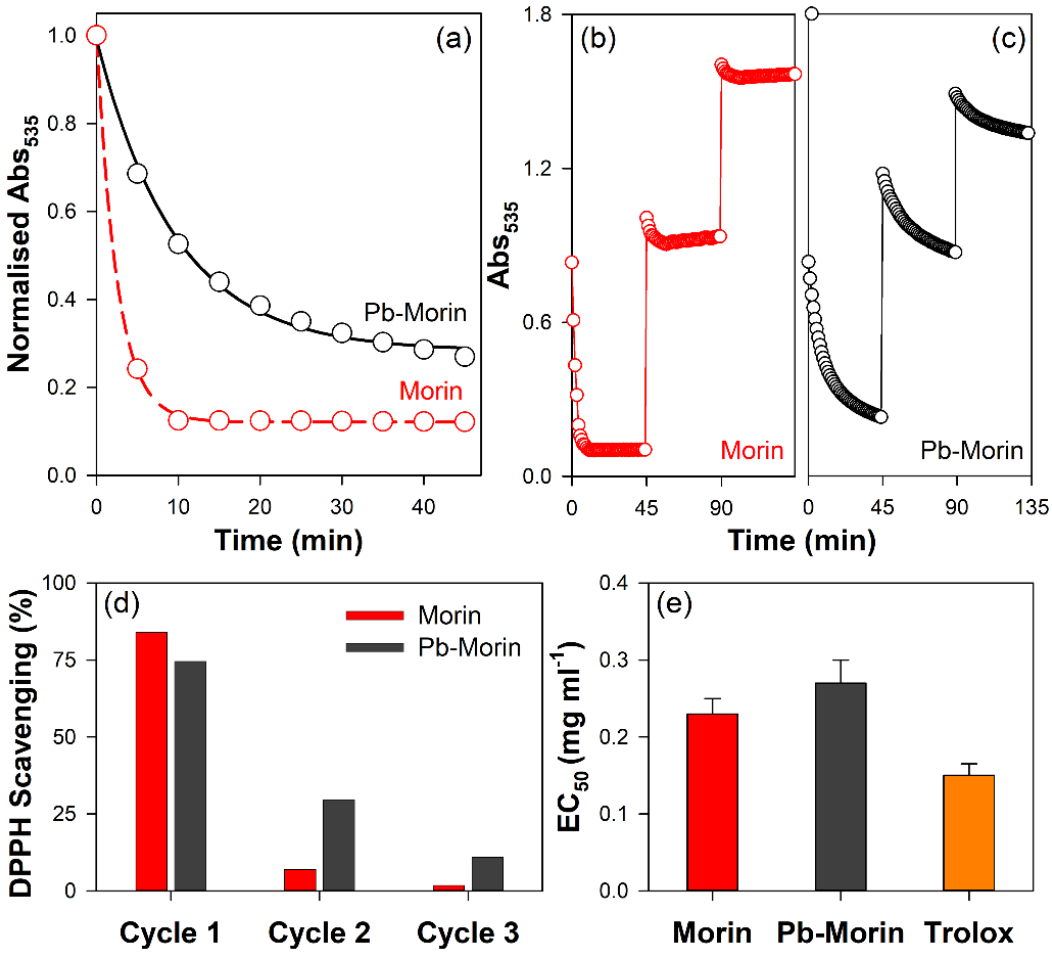

Figure 11.9. *Antioxidant activity of the polyphenols and mixtures. (a) Free radical scavenging activity of morin before and after chelate formation as measured by DPPH method. (b) & (c) Recyclability of morin and the chelate in DPPH scavenging. DPPH was added to the mixture in each 45 minutes, and the degradation was monitored at 535 nm. (d) DPPH radical scavenging activity of the compounds in each cycles. (e) EC_{50} values (mg ml^{-1}) of morin, Pb(II)-morin complex and trolox (standard) for DPPH scavenging.*

Several studies suggested that polyphenols have a number of potential health benefits due, in part, to their antioxidant activity [8,16,55,66,67]. Even in case of heavy metal toxicity, this property is vital along with chelation, as this would help to make the healing faster. Whether the flavonoid will retain the antioxidant property even after heavy metal chelation was the major question. So, we evaluated the antioxidant activity of model flavonoid, morin before and after Pb(II)-chelation using DPPH assay. Figure 11.9a shows, morin was able to retain its free radical scavenging activity even after Pb(II)-chelation. The reaction between morin and DPPH occurs in two steps: (i) DPPH absorbance (λ_{max} = 535 nm in methanol) decays quickly (typical time,

60–120 s); and (ii) DPPH absorbance decays slowly in ~1 h to reach a constant value. The fast step essentially refers to the abstractions of the most labile H-atom from the antioxidant (3-OH in the case of morin) [55,68], whereas, the slow step reflects the remaining activity in the oxidation-degradation products. Binding of Pb^{2+} to morin slows down the process. The possible cause for this compromised free radical scavenging activity may be the binding of Pb^{2+} to the 3-OH of morin that results in abrogation in coplanarity and conjugation of the molecule. Previous studies have shown that planarity permits conjugation, electron dislocation, and a corresponding increase in flavonoid phenoxyl radical stability [69,70]. We further studied the recyclability of the compounds in DPPH radical scavenging (Figure 11.9b-11.9d). Interestingly, although morin scavenged free radical very fast in the first cycle, it failed in successive cycles. In contrast, Pb^{2+}-morin complex was able to sustainably scavenge free radicals upto 3 cycles. The EC_{50} value of Pb^{2+}-morin complex remained almost same as morin (Figure 11.9e), which further signifies the retention of antiradical activity even after heavy metal chelation. This comes with increase in solubility of the chelate in aqueous media than that of free morin. It may be one of the causes of sustainable antioxidant activity of the chelate. The increased solubility is also important in quick removal of the heavy metal from the body. Similar results of sustainable antioxidant activity after Pb-chelation were also obtained in case of MNEA and SKP17LIV01 (data not shown). Thus, the metal chelation imparted sustainability to the flavonoid as well as flavonoid-polyphenol mixtures in their antioxidant activity, leading to higher therapeutic efficacy.

Diverse chemical assays have been developed with an aim to mimic the actual situation in human body. But, chemical models can be realistic assumptions only if a positive correlation between chemical and biological models is established. So, we used an animal (Pb-intoxicated Swiss albino mouse) model that perfectly mimics the pathogenicity of heavy metal associated disorders, involving a complexity of physiological, immunological, environmental, and genetic phenomena. Pb-intoxication causes severe damage to multiple organs leading to morbidity and mortality. According to many preceding studies, liver is one of the major target organs of Pb(II)-toxicity [66,71,72]. Figure 11.10a shows the morphometric conditions of the isolated livers of different groups. Even from outside, there are visible damages to the

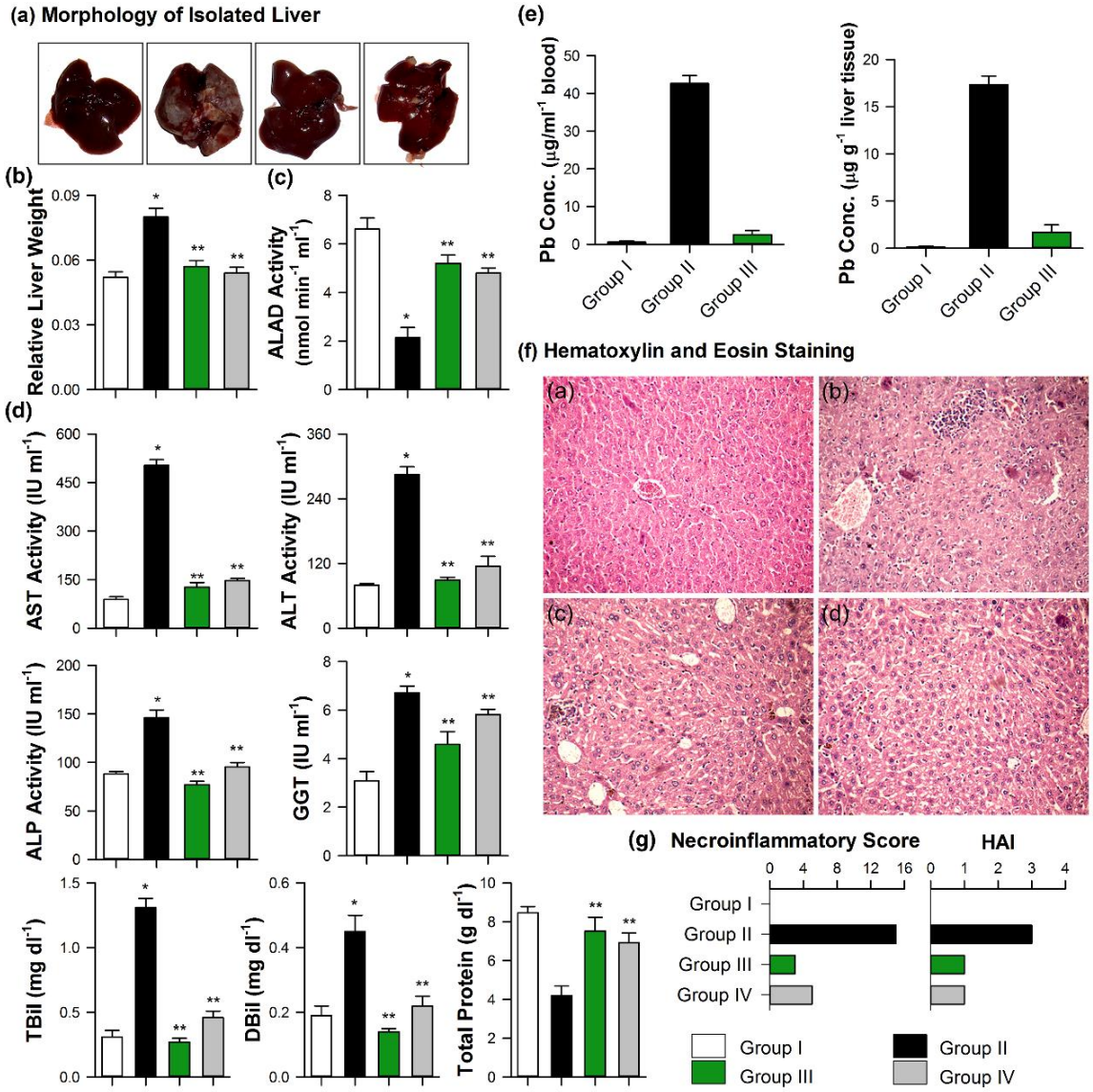

Figure 11.10. *Effect of SKP17LIV01 on Pb(II) intoxicated liver. (a) Photographs to show morphology of the isolated livers. From left, Group I, Group II, Group III, and Group IV. Group II (Pb-intoxicated) liver shows visible detrimental changes from outside, which is absent in other animals. (b) Relative liver weight (liver weight to body weight ratio) in the four groups of mice. (c) Change in ALAD activity, a marker of lead toxicity. (d) Results of liver function test. Serum AST, ALT, ALP, GGT, total bilirubin, direct bilirubin and total protein (e) Distribution of Pb in blood and liver respectively as investigated by ICP-AES method after acid digestion. (f) Histopathological changes in hepatic architecture of livers isolated from representative mouse from each treatment group as observed after hematoxylin and eosin (H & E) staining (original magnification 200X). Liver of mice treated with SKP17LIV01 did not show the inflammatory or necrotic features distinct in Pb(II) treated group. (g) Necroimflammatory score and histological activity index (HAI). All data are presented as mean±SD (*P<0.05 compared to control, ** P<0.05 compared to Pb(II)-intoxicated group).*

liver isolated from $Pb(NO_3)_2$ treated mice. Absence of such signs in other groups indicates the healing effect of SKP17LIV01 as well as silymarin, the conventional drug. The observed enlargement of liver (~54% increase in liver weight to body weight ratio compared to control; $p<0.05$) in pathophysiological situation (Figure 11.10b) is well in agreement with previous studies [72]. Increased proliferation of hepatocytes along with surge in cholesterol synthesis have found to be associated with such hyperplastic effect of Pb on liver [72]. Treatment with SKP17LIV01 reduced the relative liver weight (~30% compared to group II; $p<0.05$) to normal. One of major ways Pb exerts its toxicity is through affecting the hematopoetic system by inhibition of ALAD. The activity of blood ALAD reduced significantly (2.1±0.4 compared to 6.2±0.8 nmol min^{-1} ml^{-1} erythrocytes of control; $p<0.001$) in animals exposed to Pb (Figure 11.10c). The inhibition of ALAD was significantly less marked in animals administered with SKP17LIV01 (group III; 5.2±0.8 nmol min^{-1} ml^{-1} erythrocytes) and silymarin (group IV; 4.8±0.8 nmol min^{-1} ml^{-1} erythrocytes). Treatment after lead exposure with SKP17LIV01 was most effective in reversing blood ALAD inhibition ($p<0.05$ compared to silymarin).

Serum aminotransferase activities have long been considered as sensitive indicators of hepatic injury [49,73]. Injury to the hepatocytes alters their transport function and membrane permeability, leading to leakage of enzymes from the cells [74]. As shown in Figure 11.10d , four weeks of Pb treatment increased the AST and ALT levels by 4.7 fold and 2.6 fold respectively compared to control ($p<0.001$). This marked release of AST and ALT into the circulation indicates severe damage to hepatic tissue membranes due to chronic Pb exposure. Treatment with SKP17LIV01 produced dose-dependent reduction in AST and ALT levels. In the final standardized dose, SKP17LIV01 was able to reduce the AST and ALT levels by 75% and 70% respectively, compared to Pb intoxicated group ($p<0.001$). Previous studies suggest, returning of aminotransferase levels to normalcy is associated with the healing of liver parenchyma and regeneration of hepatocytes [75]. There was also surges in other liver function parameters such as ALP (~66%), GGT (~120%), total bilirubin (~320%), direct bilirubin (~135%) and marked decrease in total protein concentration (~50%) in Pb treated group ($p<0.001$ compared to the normal ones). Treatment with SKP17LIV01 recovers all the parameters to normal levels (Figure 11.10d).

Table 11.2. Summary of the haematological parameters studied across the groups.

	Group I	Group II	Group III	Group IV
Hb (g%)	12.1± 1.05	9.03± 0.89	12.51±0.95	12.06±0.97
RBC (x10^6 cm^2)	10.8±0.82	9.1±0.71	9.77±0.81	9.62±0.84
RT (%)	2.7±0.12	4.9±0.26	3.2±0.16	2.8±0.15
HCT (%)	34.6±0.48	39.4±0.55	36.8±0.61	34.9±0.56
MCV (μm^3)	37.8±0.32	31.0±0.68	36.5±0.44	36.9±0.71
MCH (pg)	21.2±0.15	22.2±0.14	21.8±0.14	21.1±0.13
MCHC (%)	41.2±1.06	32.4±0.95	37.6±0.96	39.6±0.87
Platelets	6.5±0.02	5.5±0.03	5.9±0.07	6.1±0.07
WBC (x10^5 $cm^{2)}$)	9.2±0.09	12.4±0.11	10.6±0.14	9.2±0.11
Lymphocyte	74±2.98	79±3.04	73±3.05	71±2.58
Neutrophil	26±1.12	15±0.49	23±0.57	25±0.69

Data are expressed as mean ± standard deviation (N=6). Hb: Haemoglobin; RBC: Read Blood corpuscle; RT: Reticulocyte; HCT: Haematocrit; MCV: Mean corpuscular volume; MCH: Mean corpuscular haemoglobin; MCHC: Mean corpuscular haemoglobin concentration; WBC: White Blood corpuscle

As described in Figure 11.10e, $Pb(NO_3)_2$ exposure increased Pb levels both in blood and liver of mice (17.34±0.91 µg ml^{-1} and 42.63±2.1 µg gm^{-1} respectively) compared to control (0.13±0.09 µg ml^{-1} and 0.58±0.11 µg gm^{-1} respectively; $p<0.001$). We hereby found that SKP17LIV01 markedly decreased Pb in blood and liver (1.69±0.05 µg ml^{-1} and 2.58±0.2 µg gm^{-1} respectively; $p<0.001$). This is consistent with our *in vitro* spectroscopic studies, where the ability of SKP17LIV01 to chelate the Pb^{2+} is found. The microscopic images of H & E stained liver sections are depicted in Figure 11.10f. The control group (Group I) showed normal hepatocytes and nuclei where the hepatic lobules were hexagonal, clearly distinguishable, separated by interlobular septa and traversed by portal veins. In Pb-treated animals, the remarkable degenerative histological changes of liver, such as structural damage, disorganization of hepatic chords, cytoplasmic vacuolation, hepatocellular necrosis, leukocyte infiltration and massive hemorrhage had been observed [75]. The SKP17LIV01 treated Pb intoxicated mice (Group III) showed almost normal hepatocytes with a mild degree of mononuclear infiltration and necrosis, almost comparable to the control. The significant tissue damage induced by $Pb(NO_3)_2$ intoxication might be attributed to its ability to generate ROS that induce oxidative damage in several tissues by enhancing lipid peroxidation [71]. Also the degradative effect of Pb on cellular enzymes particularly those associated with energy production leads to hydropic degeneration

of mitochondria and causes cytoplasmic vacuolization [76]. We applied modified Ishak and METAVIR histological activity index (Figure 11.10g) to assess the necro-inflammatory damage caused by Pb(II). The lead intoxicated animals scored 15 and 3 (maximum possible score 16 and 3), where SKP17LIV01 treatment decreased it to 3 and 0. Thus, as evident from the microscopic images, the SKP17LIV01 is able to protect and preserve the normal liver structure even better than conventional drug silymarin.

The circulatory system is one of the target organs of Pb toxicity [77]. The results concerning hematologic parameters (Table 11.2) showed a significant ($p<0.001$) decline in total erythrocyte count, total leukocyte count, hemoglobin concentration, lymphocyte and monocyte content in the $Pb(NO_3)_2$ treated animals (Group II), in comparison to control animals ($p<0.05$), while neutrophil content insignificantly increased in lead nitrate treated group, when compared with control animals ($p<0.05$). Recovery of above mentioned parameters were evident in the SKP17LIV01 treated group.

A number of *in vitro* and *in vivo* studies indicated that lead causes oxidative stress by inducing the generation of reactive oxygen species (ROS), including hydroperoxides, singlet oxygen, hydrogen peroxide and superoxide. It has also been observed that Pb can decrease antioxidant enzymatic activity in liver [66]. In the present study, the increase in hepatic ROS production manifested in depletion of superoxide dismutase (SOD), Catalase (CAT) and glutathione peroxidase (GPx) levels, the major enzyme triad responsible for scavenging of free radicals inside the body. To be particular, SOD converts superoxide anions to H_2O_2, which is further converted to H_2O with the help of GPx and CAT [78]. In this study, four weeks of chronic lead exposure decreased these enzyme levels by 63%, 57% and 45% respectively compared to control group ($p<0.05$) and caused severe oxidative damage to the liver cells. However, treatment with SKP17LIV01 helped the Pb-intoxicated mice to replenish their antioxidant enzyme system to normal (increase in SOD ~132%, CAT ~115% and GPx ~50%; $p<0.05$ in all cases) (Figure 11.11a).

Thiol based antioxidant system plays second line of cellular protection against reactive free radicals mediated oxidative damage in pathophysiological situation [66].

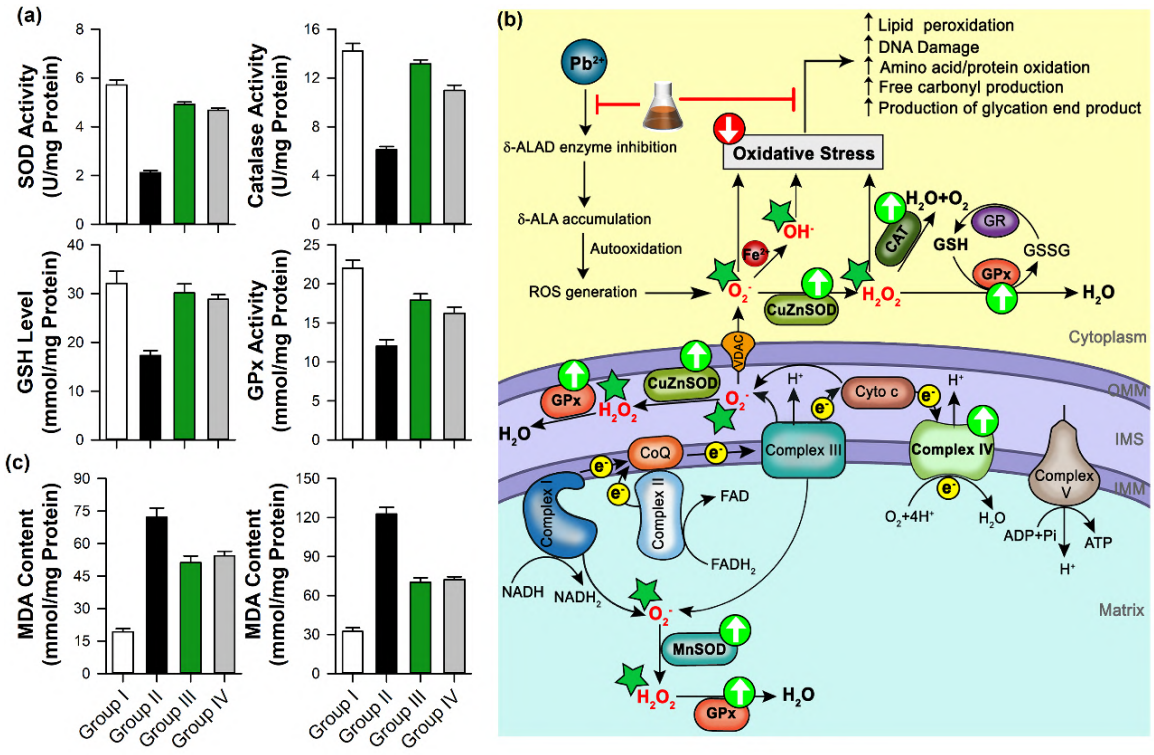

Figure 11.11. *Molecular mechanism of action of SKP17LIV01 through redox modulatory activity. (a) Effect on cellular antioxidant system. (b) Schematic representation of the mechanism of action of SKP17LIV01 on antioxidant system (SOD, Catalase, GSH and GPx). (c) Effect on lipid peroxidation. All data are presented as mean±SD (*P<0.05 compared to control, ** P<0.05 compared to Pb(II)-intoxicated group).*

Cellular metabolite like GSH has been presented in Figure 11.11a. The level of GSH has been considerably decreased due to intoxication along with the increased level of GSSG. Post treatment with SKP17LIV01 after the Pb(II) exposure restored the levels of cellular metabolites close to normal, demonstrating its protective nature. Figure 11.11b provides a schematic overview of the proposed mechanism of action of SKP17LIV01 in protection of oxidative stress induced by Pb. The model clearly indicates that SKP17LIV01, despites direct sustainable free radical scavenging activity, boosts the *in vivo* enzymatic antioxidant defense system resulting in protection from increased levels of ROS. The model is further supported by the observations of lipid peroxidation and protein carbonylation, the two important markers of oxidative stress. The increase in the MDA level (Figure 11.11c) in the serum and liver (~3.8 fold compared to control in both cases, $p<0.01$) upon $Pb(NO_3)_2$ treatment suggests enhanced peroxidation leading to tissue damage and failure of antioxidant mechanism

to prevent the formation of excessive free radicals. Post treatment with SKP17LIV01 ($Pb(NO_3)_2$ + SKP17LIV01) significantly attenuated these changes (decrease in MDA level by ~1.8 folds (liver) and ~1.5 folds (serum) compared to $PbNO_3$ treated group, $p<0.05$ in all cases). The flavonoids and polyphenols exert their antioxidant effects in the body by preventing generation of ROS, direct scavenging of it or through enhancement of cellular antioxidant system. Thus, the observed recovery of antioxidant enzyme pool in the animal model of Pb-intoxication after administration of SKP17LIV01 is the consequence of synergistic activity between its various phytoconstituents as evident from our spectroscopic studies. The flavonoids may have played a crucial role in reduction of the treatment period by controlling the accumulation and bioavailability of Pb(II) in the tissue through complexation, subsequent sustainable antioxidant activity and removal.

The disaster due to the lead poisoning is evident from the ancient human civilization till date, although it is concluded to be preventable. Understanding the mechanism of Pb detoxification by low cost medicinally important molecules and cost-effective herbal mixture is very important for the promotion of lots of folk medicines in developing countries. Here, we have explored the detailed mechanism of Pb detoxification by morin, a model flavonoid, which is omnipresent in medicinal herbs using steady state and picosecond resolved optical spectroscopy. We have shown that Pb-morin chelate becomes sustainable antioxidant revealing dual role of the flavonoid in the heavy metal detoxification process. Our spectroscopic studies also reveal that the dual nature in the detoxification remain intact in the controlled mixture of few flavonoid and polyphenol molecules (MNEA) and even in a mixture of many such molecules extracted from medicinal plants (SKP17LIV01). We have studied the efficacy of the complex mixture in mouse model for the detoxification of Pb-poisoning in detail. Subsequent, biochemical, histopathological and biodistribution studies confirm that the molecular mixture (SKP17LIV01) facilitates excretion of Pb from the mammal (mice) body after heavy metal chelation and ROS scavenging. The study is expected to have impact in the discovery of new drugs of ethnobotanical origin.

11.2.2. Rationalization of a Traditional Liver Medicine Using Systems Biology Approach and Its Evaluation in Preclinical Trial [79]

The natural products isolated from different organisms (largely plants and bacteria) or their derivatives have been the staple tool of healers from the dawn of history until the birth of modern synthetic chemistry [39,80]. However, the use of these traditional remedies in the modern age is retarded due to limited knowledge of their active ingredients as well as their molecular mechanism of actions [40]. The naturally occurring small molecules, or the active ingredients, are perhaps less likely to cause damage to living systems as they have moved through the co-evolutionary mill [39]. Thus, the major aim of this study is to develop a computational strategy for preliminary identification of active ingredients of a natural medicine, their target inside the body, the molecular mechanism of action and probable side effects. Figure 11.12 summarizes the approach taken up in this study for rationalization of a traditional natural medicine. For identification of the chemical compounds extracted from the plant materials, UHPLC-Q-TOF-MS/MS in both positive and negative ion modes were employed. Figure 11.7 and Dataset 11.1 and 11.2 show the total ion chromatograms both in positive and negative mode. Altogether 272 compounds were characterized; 162 (50 unidentified and 23 amino acids) in positive and 110 (20 unidentified and 20 amino acids) in negative ion mode. The identified compounds were used to set up the library.

To find out the active ingredients from the library of 272 compounds the well-established concept of drug-likeness was used. The concept aims to identify virtual or real molecules that fall into what is considered to be drug-like chemical space, based on one or more physicochemical properties [81]. The compounds were primarily screened according to the Lipinski's RO5 (Figure 11.13a) [82-84]. The rule states that a compound is more likely to be membrane-permeable and easily absorbed via passive diffusion in the human intestine if logP $\leq$5; MW $\leq$500; HBAs $\leq$10 and HBDs $\leq$5. Molecules violating two or more of this criterion, are less likely to reach the bloodstream from the gut. Study of these parameters is very important in the drug

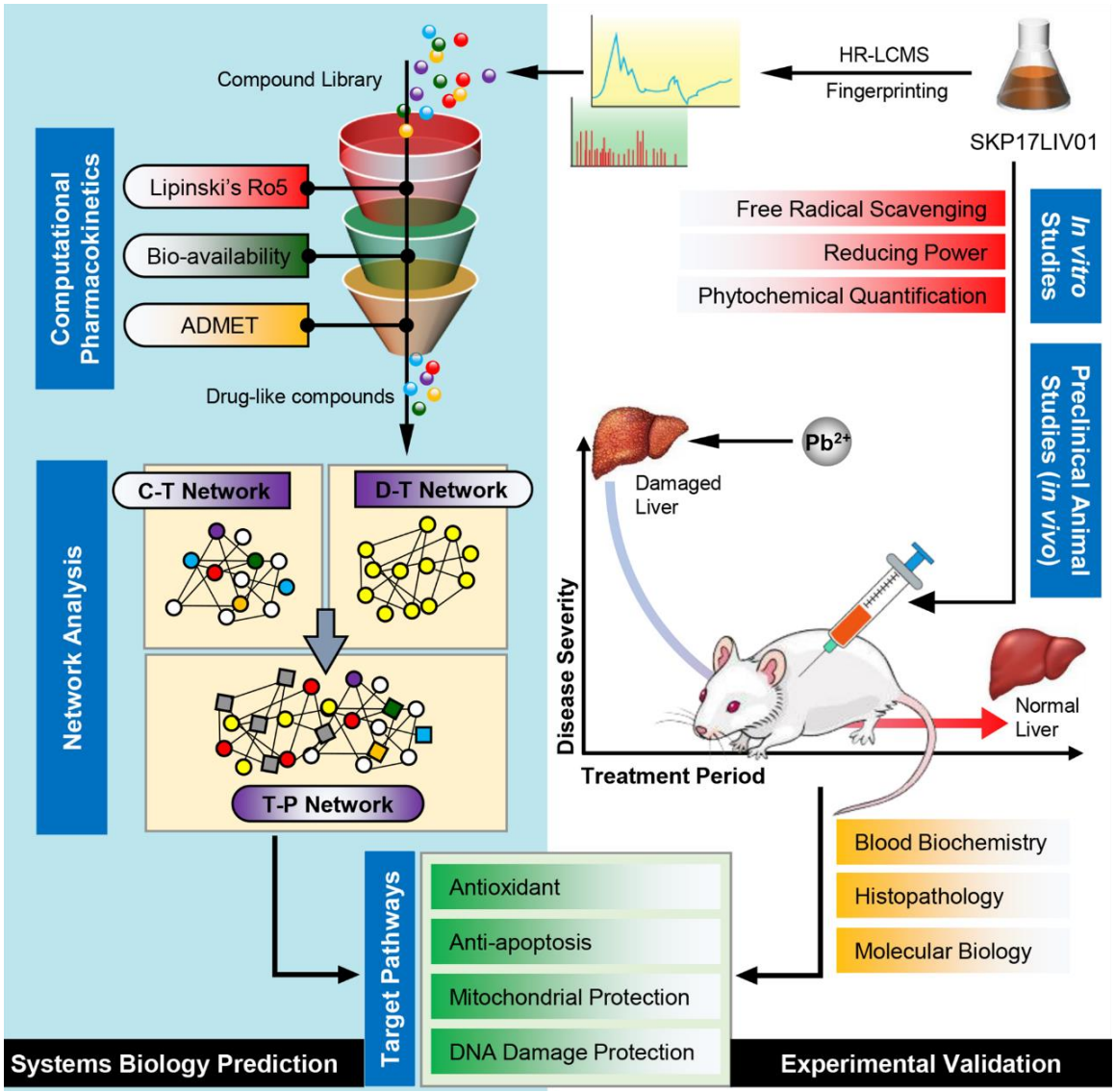

Figure 11.12. *Schematic overview of the approach taken up in the study for the rationalization of a traditional medicine. The left panel describes the systems biology techniques used to predict the active ingredients (leads) from a library of natural small molecules (generated experimentally using UHPLC-MS) and respective hits to identify their mechanism of action. The right panel shows the in vivo experimental approach taken up to validate the systems biology (in silico) predictions.*

discovery process as they dictate a molecule's fate inside the body. For instance, MW can impact several molecular events like absorption, bile elimination rate, blood-brain-barrier penetration, interaction with targets (on- and off-targets), etc [81]. Whereas, lipophilicity, characterized by logP and logD values, plays a crucial role in various ADMET parameters like solubility and metabolism. Solubility and metabolism are

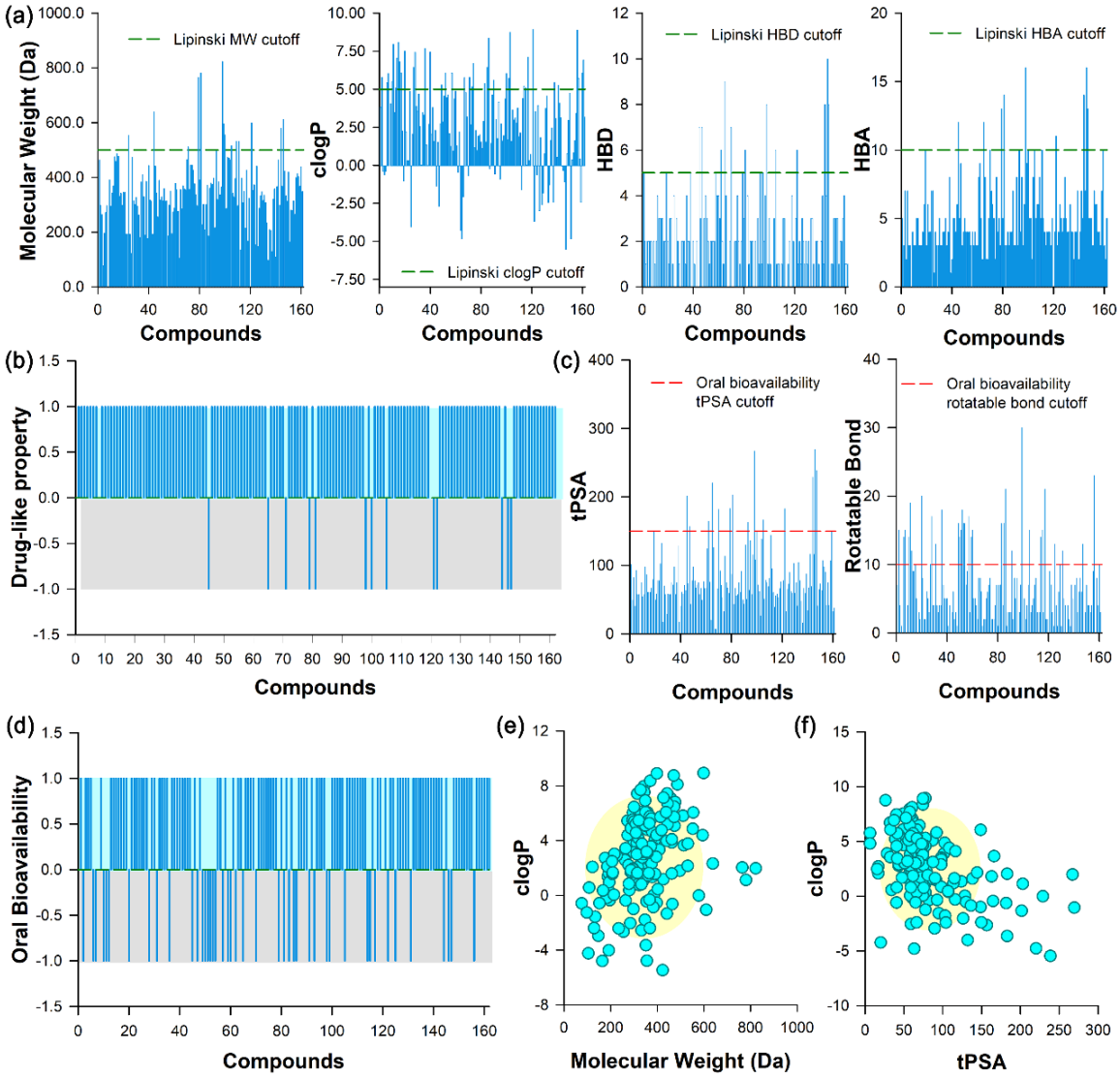

Figure 11.13. *Drug likeness of the phytoconstituents identified in UHPLC-MS. (a) The physicochemical descriptors described in Lipinski's rule of five (RO5) for each of the identified compounds. (b) Drug likeness score for the identified compounds. Compounds falling in the grey region violate two or more criteria of Lipinski's RO5 and are not drug-like. (c) Two major properties of the phytoconstituents (tPSA and number of the rotatable bond) that dictate oral bioavailability. (d) Calculated oral bioavailability (see text for more details). (e) Golden triangle study. The compounds falling into the yellow areas have more probability to function as drugs.*

compromised at high lipophilicity, while low lipophilicity can reduce the permeability of a molecule [85]. Our analysis based on Lipinski's RO5 showed, only 5% of the identified compounds in SKP17LIV01 fell outside the drug-like chemical space (Figure 11.13b). Oral bioavailability (OB) of a molecule dictates drug-likeness in oral administration, which is regarded as the most convenient and predominant way to

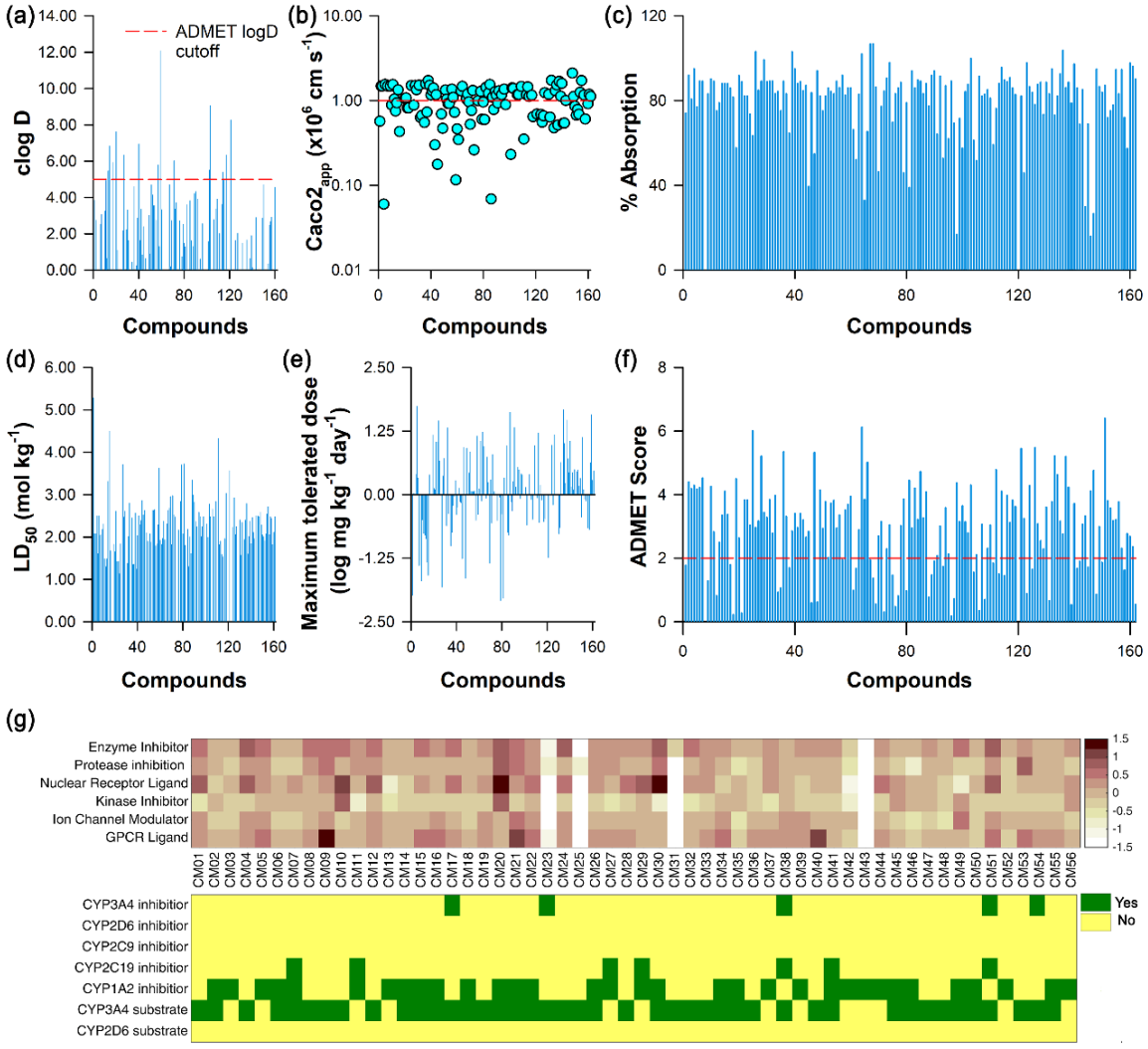

Figure 11.14. *Systems pharmacology analysis of the identified phytoconstituents. (a) clogD of the compounds. (b) Caco-2 permeability of the compounds as computed by PkCSM software. (c) Predicted % absorption. (d) The LD_{50} value of individual compounds. (e) The maximum tolerated dose of the same. (f) ADMET score (see text for details). (g) The ability of the active ingredients as found after ADMET screening on certain common therapeutic targets and their effect on CYP enzymes.*

administer drugs [86]. OB, in turn, is dictated by tPSA in combination with rotatable bond count, which reflects molecular flexibility. Owing to high tPSA (>140 Å) and rotatable bond counts (>10) (Figure 11.13c), 30% of the compounds scored negative in OB calculation, hence were deleted from the library. Figure 11.13e and 11.13f depict the robustness of the calculations as most of the compounds screened through the aforementioned processes fell into the golden triangle of drug-likeness.

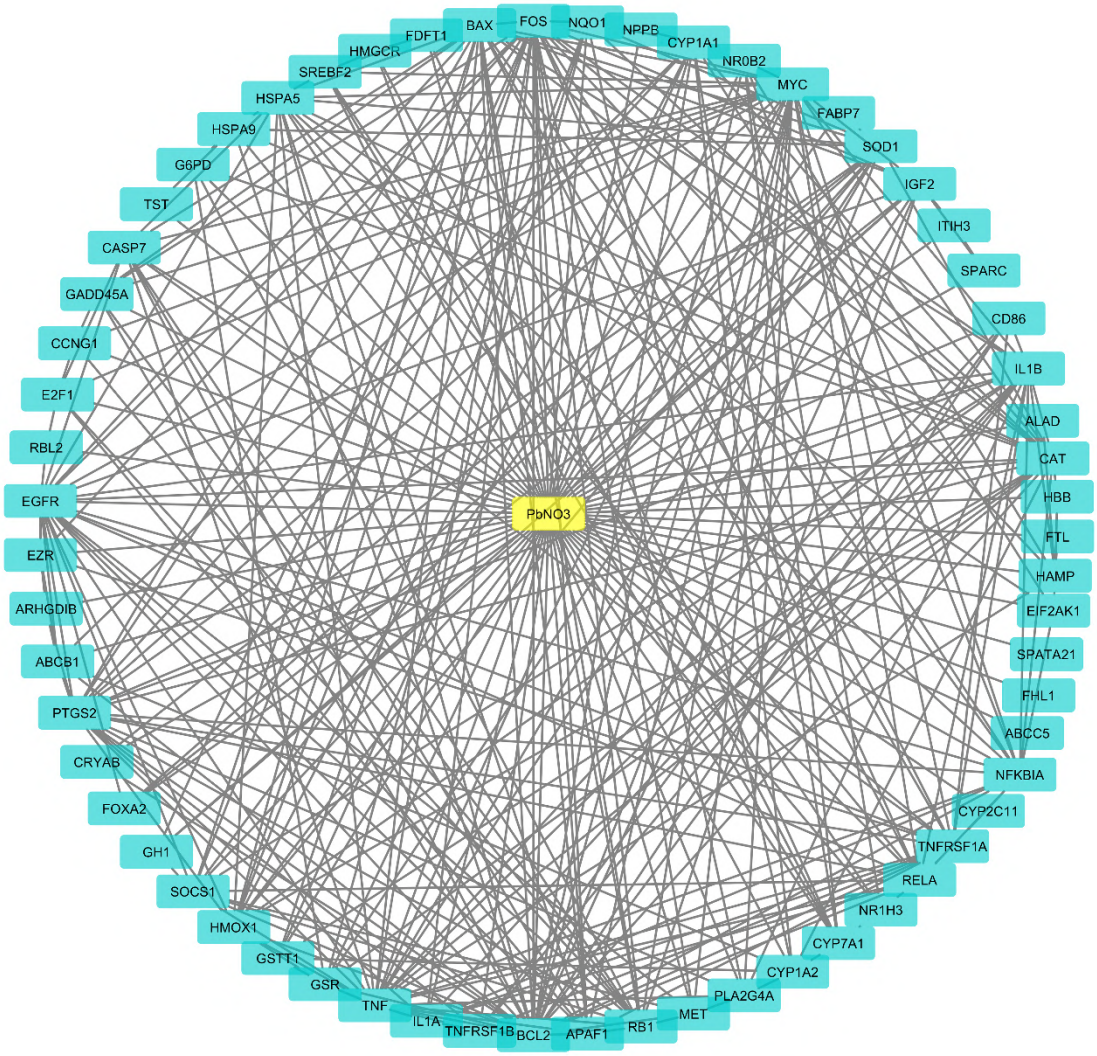

Figure 11.15. *Disease-target (D-T) network. Yellow node represent the intoxicant $Pb(NO_3)_2$ and the blue nodes denote its targets inside the body. Black edges represent interactions between the nodes.*

Although the revised library contained a considerable number of bioactive components, only those with desirable pharmacodynamics and pharmacokinetic profiles could be responsible for the therapeutic effects. Thus, we studied four crucial ADMET parameters including % absorption (>30%), Caco-2 cell permeability (>-0.4), LD_{50} and maximum tolerated dose (Figure 11.14a-11.14f), which lead to the identification of 56 molecules (ADMET score >2) with excellent pharmacological properties (Dataset 11.3). It has to be noted that, despite lower % absorption, phenolic

constituents and phthalides were accounted for as they exhibit remarkable pharmacological effects.

Targets of FDA-approved drugs generally belong to one of the ten gene-families namely: Rhodopsin-like GPCRs (26.8%), nuclear receptor (13%), ligand-gated ion channels (7.9%), voltage-gated ion channels (5.5%), penicillin-binding protein (4.1%), myeloperoxidase like (3%), neurotransmitter symporter family (2.7%), cytochrome P450 (1.9%) etc [87]. So, before attempting the polypharmacology based approach through networking, we evaluated target gene family distribution of the 56 compounds (Figure 11.14g) which revealed their probability of targeting one or more gene families listed above. Since the cytochrome P450 monooxygenase (CYP) enzyme superfamily plays a pivotal role in drug metabolism [81] the modulatory effects of the compounds were investigated on them (Figure 11.14g). These results have to be considered with caution as pertinent prediction models are difficult to develop due to complex molecular mechanisms involved in CYP inhibition, however, it allows for an overall comparison among different classes of molecules.

Searching for the targets of candidate drugs solely by experimental approaches is overspending, labor-intensive, and time-consuming [86]. In the present work, we propose an integrated *in silico* approach to identify target proteins of the active ingredients. The predictive models include SEA [88] and STITCH [89]. At first, we constructed the D-T network (Figure 11.15), which consisted of 63 druggable proteins affected by Pb(II)-intoxication and 650 edges (average degree of nodes = 20.3) representing interaction among them. While searching for *in vivo* targets, 28 out of the 56 compounds filtered in the previous phase were found to have no target proteins, hence not considered in the network analysis. Figure 11.16 shows the C-T network, mapping the compounds of interest and their potential targets. The network highlights a number of proteins that are modulated by the synergistic action of more than one phytoconstituent. Caspase, CYP, NOS and some other proteins bridged together potential targets constructing a large network. The network embodies 210 nodes (28 candidate compounds and 182 potential targets) and 914 edges. The 28 candidate compounds constituted 215 compound-target interactions. The mean degree value of candidate compounds was 15.4, and 17 compounds possess a degree larger than 10, which indicates that most of the compounds exert therapeutic effect via multi-target

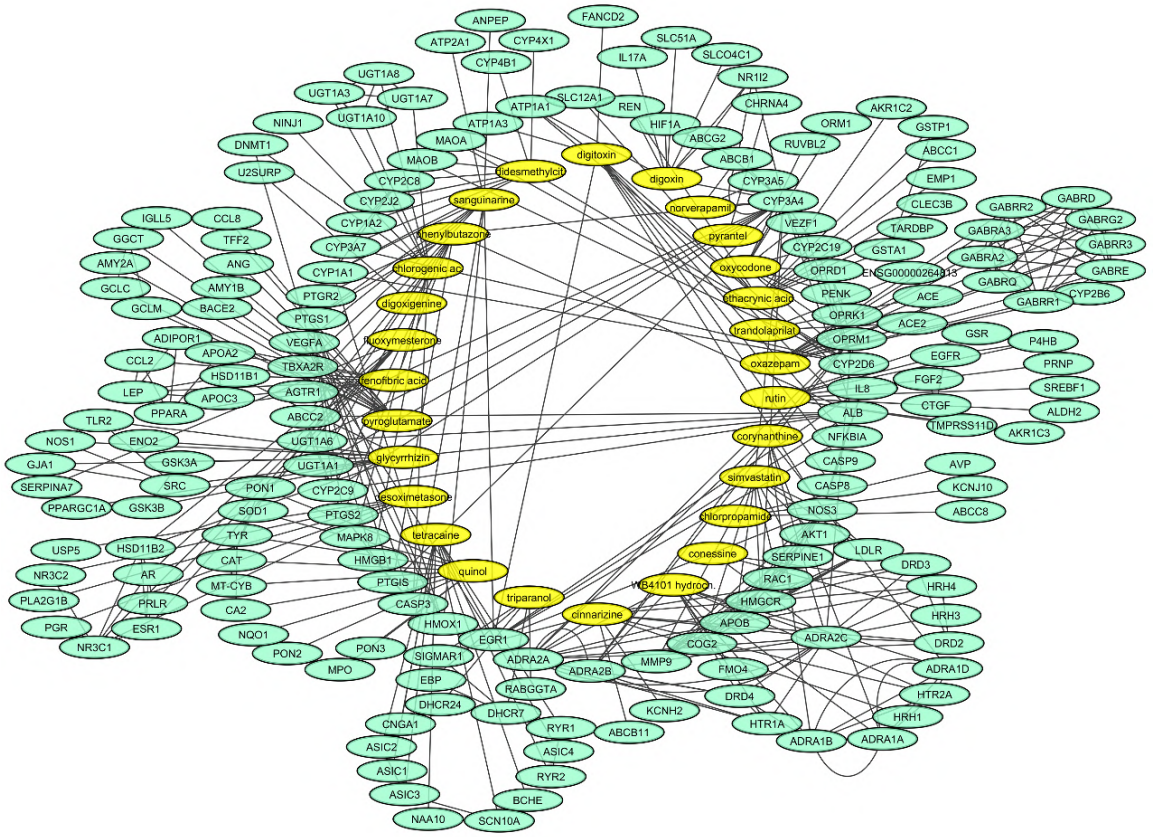

Figure 11.16. *Compound-target (C-T) network. Yellow nodes represent the bioavailable drug like phytoconstituents (active ingredients) present in SKP17LIV01 and the green nodes denote their targets inside the body. Black edges represent interactions between the nodes.*

regulation. In network analysis, the compounds that show a higher degree are considered to be pharmacologically more important. To further clarify the relationship between active ingredients and their targets related to heavy metal-induced hepatotoxicity, the C-T network was mapped against the D-T network. The common targets for both disease and therapeutic compounds (acting in antagonistic way) were identified and a network was constructed among them after expanding to two nearest neighbor proteins with the help of GeneMania prediction servers [90] and STRING functional protein association network [91]. This resulted in a highly complex T-P network as shown in Figure 11.17. The PPI network (T-P) comprises of 85 nodes and 1584 edges with mean degree value 37.3, indicating high correlation amongst themselves. The major proteins with the most number of edges are Bcl-2 (118), BAK (16), Bax (28), SOD (55), CAT (25), GSR (14), EGFR (21), etc. It can be easily observed that these proteins are primarily associated with two vital biochemical

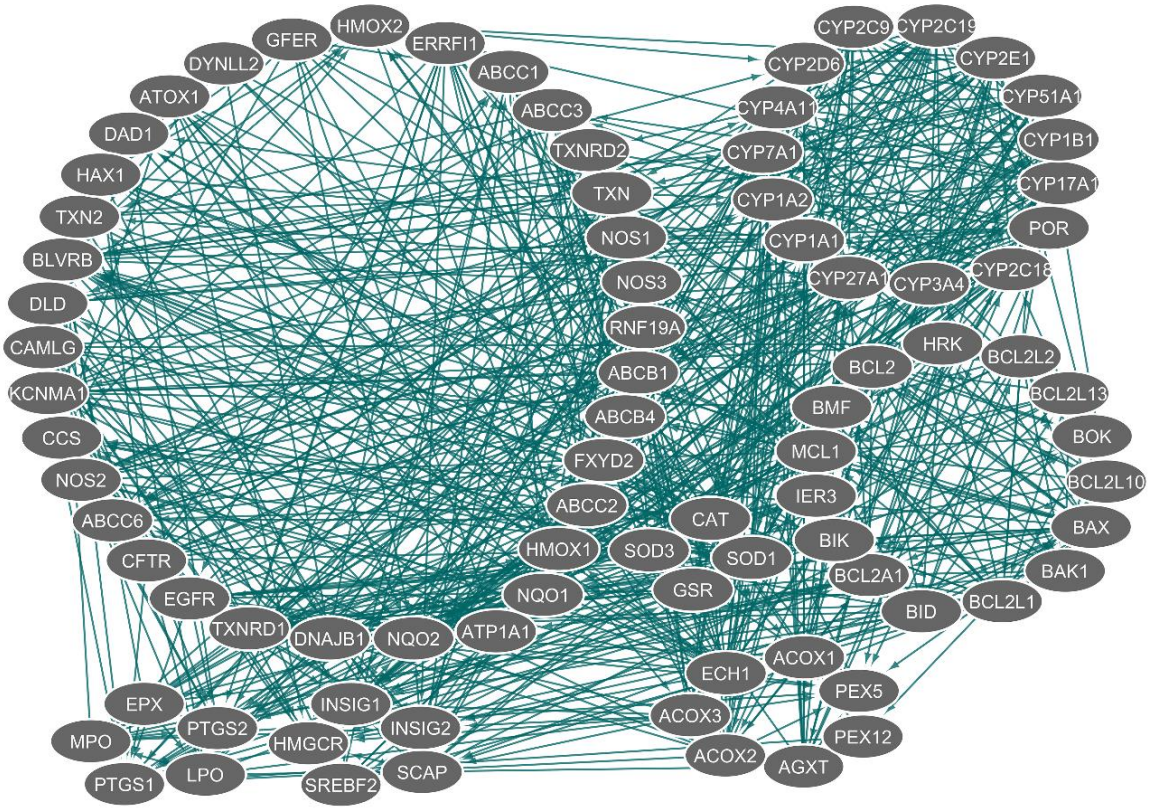

Figure 11.17. *Protein-protein interaction network (T-P network) among the identified target proteins that are responsible for the therapeutic effect. The network was built by expanding the intersecting proteins of C-T and D-T networks upto two nearest neighbor proteins. Circular nodes represent proteins and the edges are their interactions.*

pathways i.e., antioxidant defense and apoptosis. Recent studies have reported the role of oxidative stress and apoptosis in pathogenesis of Pb-poisoning [52,92-95]. SOD, CAT, and GPx make the cellular antioxidant enzyme triad that scavenges free radicals inside the body [52,96,97]. To be particular, SOD converts superoxide anions to H_2O_2, which is further converted to H_2O with the help of GPx and CAT [95,97]. Pb-exposure alters the activity of this antioxidant enzyme triad, thereby becomes proficient therapeutic targets in the treatment of Pb toxicity [52,95]. On the other hand, Bcl-2 and Bax are proteins belonging to the Bcl-2 family that regulates cells' fate [98,99]. Bax upregulates the permeability of the mitochondrial membrane accompanied by the release of cytochrome c from the mitochondria into the cytosol, while Bcl-2 has the opposite role [99,100]. Cytochrome c in the cytosol activates the caspase family of proteins and forms the cytochrome c/Apaf1/caspase-9 apoptosome complex, which

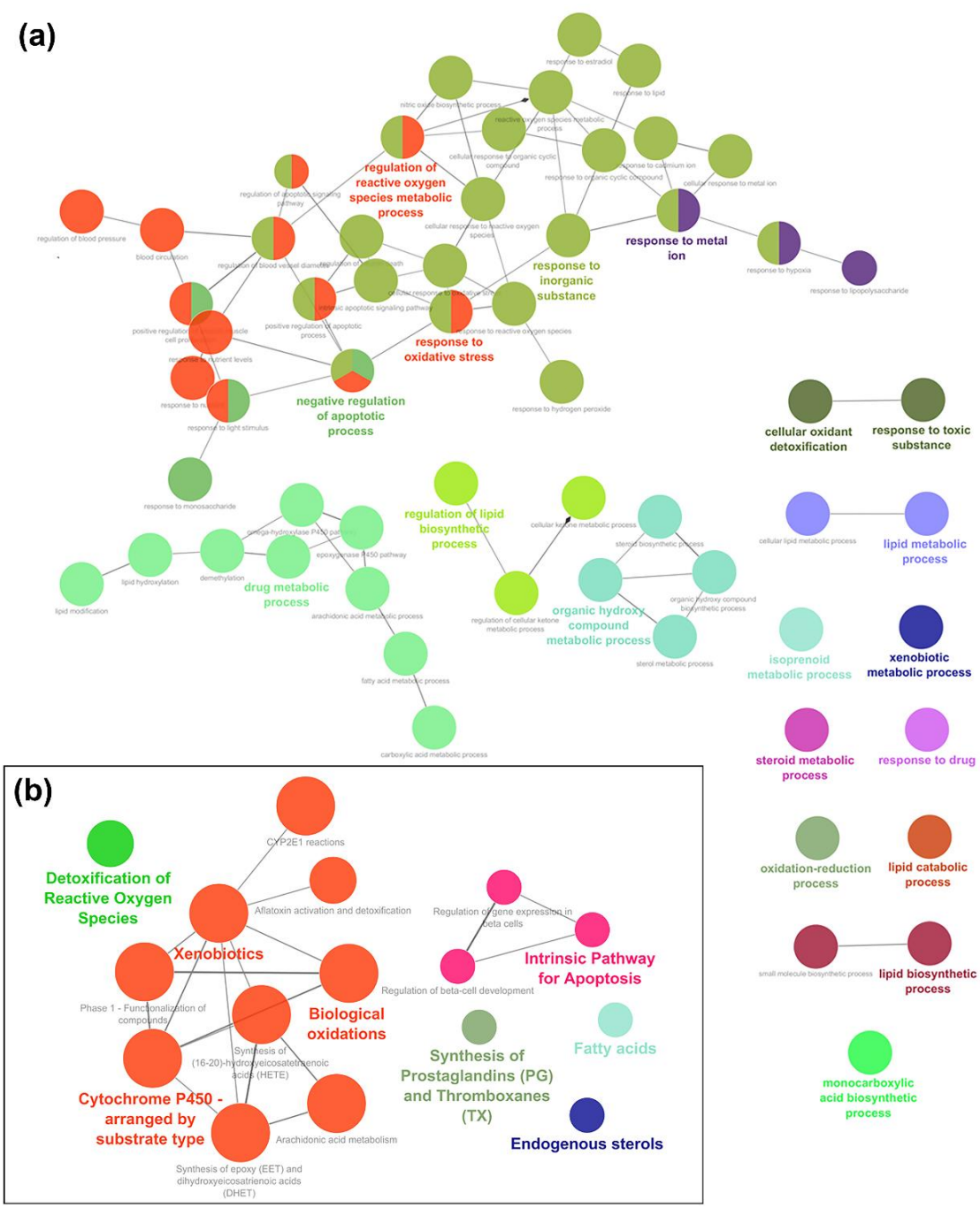

Figure 11.18. *Target pathway network for identification of the molecular mechanism of action. (a) Clue-GO analysis applied to the T-P network to identify the biological functions associated with the protein networks. (b) Clue-Go analysis applied to the same to find the target pathways of SKP17LIV01.*

then leads to apoptosis [101]. Thus, a higher degree of these proteins in the T-P network provides us with the primary impression that SKP17LIV01 works through

modulation of these pathways. In the next sections of the study, we investigated their mechanism of action in greater detail.

The signaling pathways, as a crucial component of system pharmacology, link compound-target interactions to pharmacodynamics output. Thus, to get a better understanding of the mechanism of action of the active ingredients of SKP17LIV01 on heavy metal-induced hepatotoxicity, the canonical pathways and biological functions associated with treatment and prophylaxis were extracted from T-P network depicted in Figure 11.17 using ClueGo [102]. As shown in Figure 11.18a and 11.18b, the results of ClueGo analysis are divided into two strata: biological functions and the reactome analysis. The biological functions showed a number of activities: response to the oxidative stress, response to inorganic substances, drug metabolic process and sterol metabolic process being the major ones. The reactome of the targets was mainly related to detoxification of ROS, xenobiotic metabolism, CYP modulation, biological oxidation, intrinsic pathways of apoptosis, etc. Previous studies have linked these biological functions as target pathways to treat various liver diseases including heavy metal-induced ones [66,100]. Thus, it is reasonable to believe that the active ingredients of SKP17LIV01 are linked to the treatment of heavy metal-induced liver toxicity. The results also confirm the reliability of our prediction models and the T-P network in the identification of leads and hits from a library of compounds. However, it is worth noting that the computational models can only provide hints that need to be verified by experimental data. Therefore, in the next phase, we studied the therapeutic efficacy of SKP17LIV01 against Pb-induced hepatotoxicity in mice model and verified its molecular mechanism of action.

A series of events take place in the liver following exposure to Pb(II), i.e., its accumulation in the liver, changes in liver function parameters, induction of Kupffer cell-mediated oxidative stress and alterations in xenobiotic metabolism. These alterations lead to striking morphological changes in the liver (Figure 11.19a-11.19c). Histopathological studies reveal degenerative changes like structural damage, disorganization of hepatic chords, cytoplasmic vacuolation, hepatocellular necrosis, leukocyte infiltration, and massive haemorrhage, while, SKP17LIV01 protects the liver resisting the onset of Pb(II) induced damages (Figure 11.19c). These observations

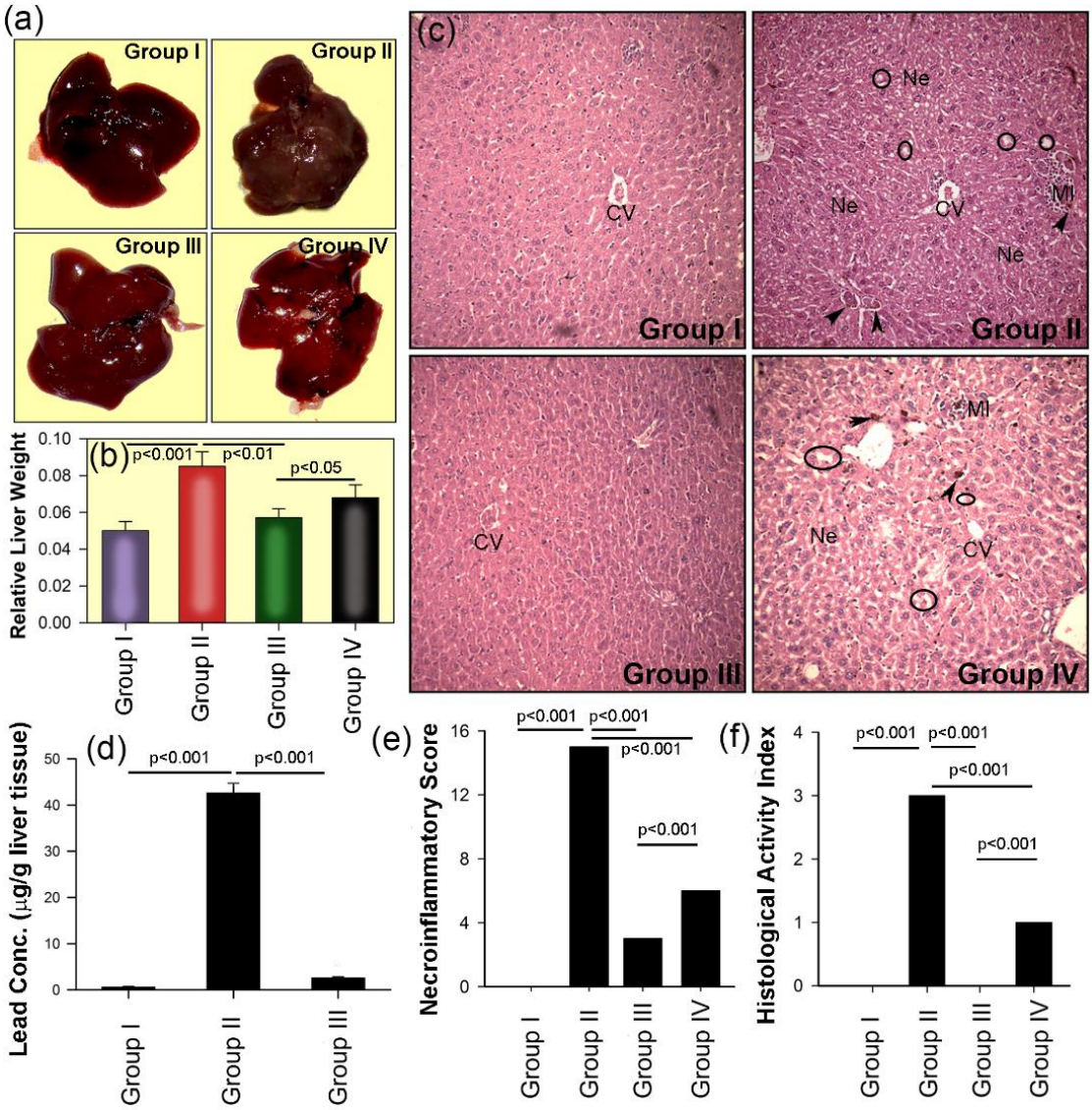

Figure 11.19. *Protective effect of SKP17LIV01 on $Pb(NO_3)_2$-intoxicated liver. (a) Outer morphology of the isolated livers. (b) Relative liver weight. (c) Histopathological changes as observed after hematoxylin and eosin staining. (d) Biodistribution of Pb(II) in the liver as determined by ICP-AES. (e & f) Necroinflammatory score and histological activity index (HAI).Group I: Control; Group II: $Pb(NO_3)_2$; Group III: $Pb(NO_3)_2$+SKP17LIV01; Group IV: $Pb(NO_3)_2$+Silymarin.*

All data represented as Mean ± Standard Deviation (SD). N=6 for each measurement.

were further supported by biochemical tests of liver function enzymes (Table 11.3). The deposition of Pb(II) in the liver was significantly reduced after treatment with SKP17LIV01 (Figure 11.19d). Necro-inflammatory score as well as histological activity index followed a similar trend. The intra-nucleosomal DNA fragmentation in

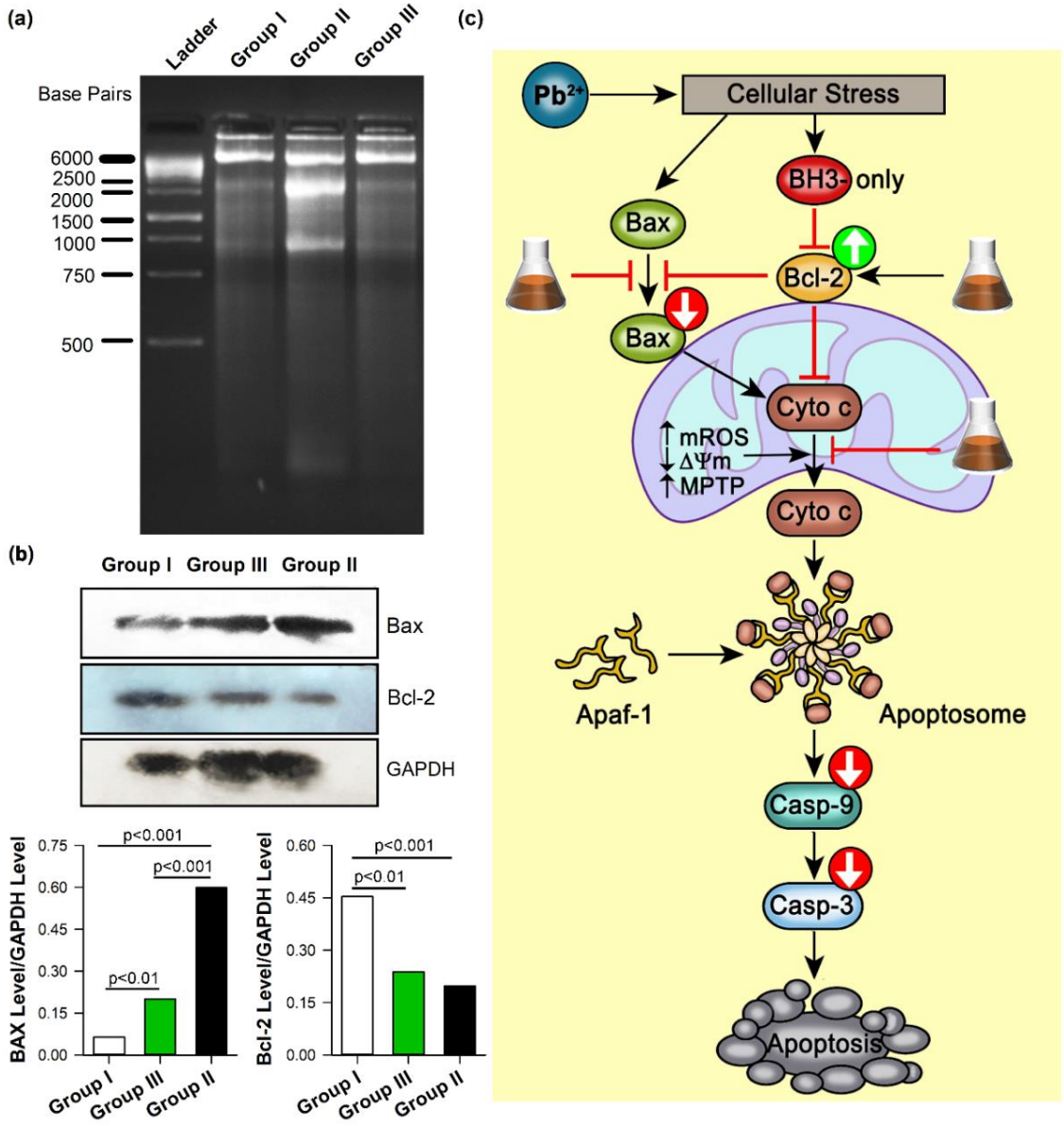

Figure 11.20. *The molecular mechanism behind the therapeutic action of SKP17LIV01. (a) DNA fragmentation assay as a marker of apoptosis. (b) Effect of SKP17LIV01 in expression profiles (Western blots) of Bcl-2 and Bax, two important proteins in the regulation of the intrinsic apoptotic pathway. GAPDH was used as a loading control. The graphs illustrate relative expression levels of the proteins as quantified using ImageJ. (c) Schematic representation of the anti-apoptotic mechanism of SKP17LIV01 against $Pb(NO_3)_2$ intoxication. Group I: Control; Group II: $Pb(NO_3)_2$; Group III: $Pb(NO_3)_2$+SKP17LIV01.*

the case of Pb-intoxicated mice, as visualized by gel electrophoresis (Figure 11.20a), is considered to be a biochemical hallmark of apoptosis [66,103]. Various studies suggest that the balance between proapoptotic (Bax/Bad) and antiapoptotic (Bcl-2/Bcl-xL)

Table 11.3. Effect of SKP17LIV01 on liver function parameters.

	Group I	**Group II**	**Group III**	**Group IV**
	Control	$PbNO_3$	$PbNO_3$+SKP17LIV01	$PbNO_3$+Silymarin
AST	88.71±8.16	503.13±17.56 [a]	126.32±4.73[a,b]	147.23±6.27[a,b]
ALT	79.65±3.03	284.79±14.66 [a]	88.96±2.33 [b]	114.87±18.59[a,b]
ALP	88.14±2.36	146.05±7.85 [a]	76.92±1.57[a,b]	95.22±4.64 [b]
GGT	3.08±0.38	6.72±0.27 [a]	4.58±0.53[a,b]	5.82±0.21[a,b]
Tbil	0.31±0.05	1.31±0.07 [a]	0.27±0.03 [b]	0.46±0.05[a,b]
Dbil	0.19±0.03	0.45±0.05 [a]	0.14±0.01 [b]	0.22±0.03[a,b]
TP	8.46±0.32	4.20±0.49 [a]	7.52±0.71 [b]	6.92±0.49[a,b]

All data represented as Mean ± Standard Deviation (SD). N=6 for each measurement.

Tbil: Total bilirubin; Dbil: Direct bilirubin; TP: Total protein. Data are expressed as mean ± SD (n=6). One-way ANOVA Tukey post hoc: [a] $p< 0.001$ compared with control (Group I). [b] $p< 0.001$ compared with vehicle lead intoxicated group (Group II).

members of the Bcl-2 protein family determine the fate of a cell in organ pathophysiology [98,104,105]. Here, SKP17LIV01 upregulates Bax and downregulates Bcl-2 (Figure 11.20b), resulting in cellular protection. It further preserves MMP ($\Delta\psi_M$), which in turn protects MPT pore formation in the mitochondrial membrane (Figure 11.21) and inhibits the release of cytochrome c into the cytosol. Thus, SKP17LIV01 protects Pb(II)-induced cellular damage through subsequent inhibition of downstream pathways (Figure 11.20c). The experimentally observed molecular mechanism of prevention of the intrinsic pathway of apoptosis is well in agreement with the computed results, as described in the earlier section of this work (Figure 11.18). Further studies were performed to observe its effect on mitochondria and associated enzymes triad that regulated cellular redox equilibrium. The protective effect of SKP17LIV01 extended onto the intracellular antioxidant enzymes (SOD, CAT, GSH, and GPx) opened another important pathway responsible for its therapeutic action. The systems pharmacology approach also leads to a similar conclusion through the prediction of 'detoxification of ROS' pathway as a therapeutic mechanism (Figure 11.18). Thus, the *in silico* analysis shows a strong agreement with the experimental results, which in turn signifies the possibility of other computed findings of this study (that have not been extensively studied experimentally) to exactly mimic the *in vivo* system.

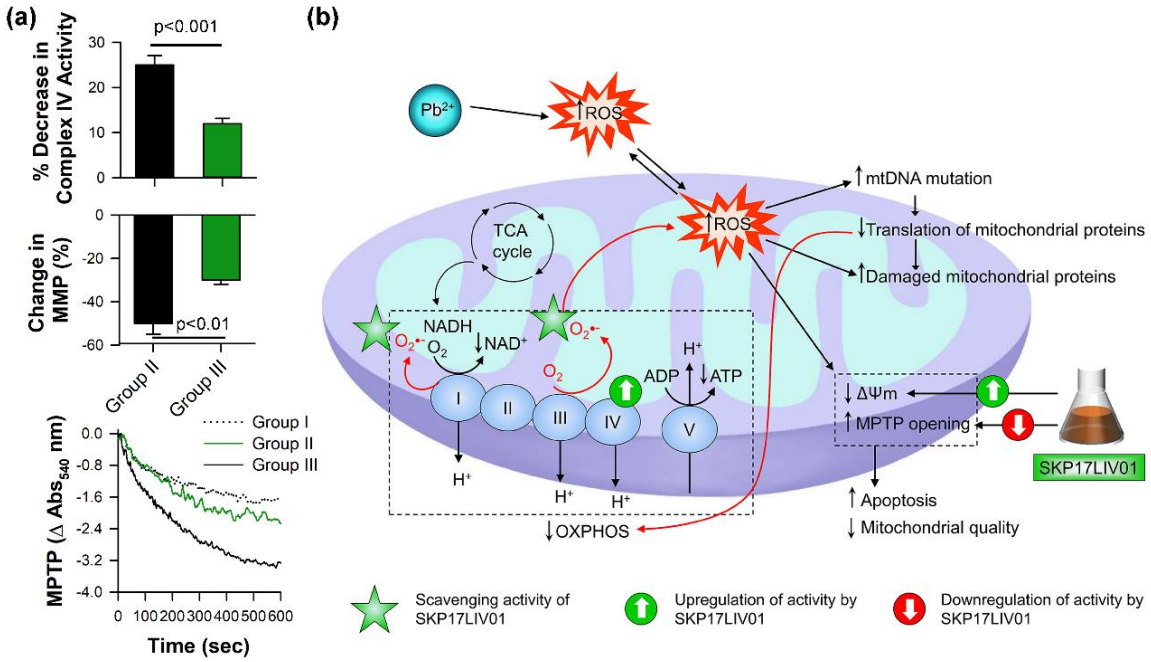

Figure 11.21. *The molecular mechanism behind the therapeutic action of SKP17LIV01. (a) Effect on mitochondria. Change in complex-IV activity, change in mitochondrial membrane potential (MMP or $\Delta\Psi_M$) and effect in Ca^{2+} induced opening of mitochondrial permeability transition pore (MPTP). (b) Schematic representation of the protective action of the extract (SKP17LIV01) on mitochondria.*

Group I: Control; Group II: $Pb(NO_3)_2$; Group III: $Pb(NO_3)_2$+SKP17LIV01. All data represented as Mean ± Standard Deviation (SD). N=6 for each measurement.

11.3. CONCLUSION

We have prepared an herbal extract (SKP7LIV01) from medicinal plants, traditionally known for liver remedies. HR-LCMS studies identified 272 ingredients, including numerous polyphenols and amino acids. Using the computational sieving method, 52 compounds were identified as drug-like molecules with excellent pharmacological properties. A detailed network analysis of the drug-like molecules showed that they were having anti-apoptotic, antioxidant and mitochondria protective in nature. We evaluated the efficacy of the preparation, SKP17LIV01 in a hepatitis mouse model. The preparation was found to cure the disease in a hepatoprotective way as evidenced by hematological and histopathological parameters. Molecular biology techniques (DNA fragmentation assay, western blot, etc.) to validate the

systems biology predictions in the pathways of mice hepatitis remedy. To our understanding, the current study not only finds an impact in the rationalization of the traditional drugs but also opens a new paradigm in drug repurposing and rediscovery bypassing the rigorousness of the animal studies in the pipeline of new drug discovery.

Dataset 11.1. Compounds and Metabolites identified in non-polar extract of SKP17LIV01 in positive mode Q-TOF LCMS.

RT	Name	Measured Mass	Formula	Error	Max M/Z
1.214	1,2-propanediol	76.053	C3H8O2	-7.63	59.0497
1.626	Choline	104.1094	C5H14NO	-17.83	104.1088
1.73	Tetracaine	264.1829	C15H24N2O2	3.27	247.1798
1.799	Propoxur	209.1078	C11H15NO3	-12.26	192.1045
1.934	Quinone	108.023	C6H4O2	-17.06	113.0016
2.379	O-acetylserine	147.0552	C5H9NO4	-14.08	130.0519
2.52	Methyldopamine	167.0969	C9H13N02	-13.49	150.0936
2.571	4,10-undecadiynal	162.1054	C11H140	-5.98	167.0841
3.801	Ecgonine	185.1075	C9H15NO3	-12.64	168.1042
3.804	Triparanol	143.0966	C7H13NO2	-13.64	126.0933
6.032	Cimetidine sulfoxide	284.1036	C10H16N6O2S	6.69	307.0929
6.288	N-Methyl-2-pyridone-5-carboxamide (Nudifloramide)	152.0609	C7H8N2O2	-15.24	135.0575
6.581	3-Methylsuberic acid	188.1073	C9H16O4	-12.86	171.104
6.593	S-methylmethionine	164.0735	C6H14NO2S	6.39	146.0623
6.593	Conessine	356.323	C24H40N2	-10.92	357.3304
6.975	Oxitropium	332.1892	C19H26NO4	-9.09	314.1782
7.003	(+/-)11,12-EPETre-d8	328.2913	C20H24D8O3	-18.01	329.2987
7.125	2-hydroxy-nonadecanoic acid	314.2759	C19H3803	19.77	315.2832
7.155	3-(4-Hydroxyphenyl)pyruvic acid	180.0444	C9H8O4	-11.65	163.0411
7.182	Isocorydine (+)	341.1662	C20H23NO4	-10.17	342.1735
7.316	14-hydroxy-heneicosanoic acid	342.3067	C21H42O3	19.53	343.314
7.337	AGC	299.1552	C15H25NO3S	1.11	300.1625
7.378	2- (2,6-dimethoxyphenoxyethyl)aminomethyl-1,4-benzodioxane (WB 4101)	345.1617	C19H23NO5	-11.79	328.1583
7.41	1-o-octadecylglycerol	344.3221	C21H4403	20.22	345.3294
7.436	Melengestrol acetate	396.2316	C25H32O4	-3.95	401.2107
7.445	6beta-Naltrexol	343.1812	C20H25NO4	-8.35	344.1888
7.785	Oxycodone	315.1502	C18H21NO4	-9.91	298.147
8.063	Oxitropium Nizatidine sulfoxide	347.1072	C12H21N5O3S2	4.1	370.0959
8.158	3,12-Dioxochola-1,4,9(11)-trien-24-oic Acid	382.2155	C24H3004	-2.87	387.1952
8.203	Methyl bixin/ (Bixin dimethyl ester)	408.2322	C26H3204	-5.26	413.2111
8.256	TTNPB	348.2104	C24H28O2	-4.15	371.1997
8.369	Glycyrrhizic acid	822.4004	C42H62O16	4.07	805.3995
8.425	Trandolaprilat	402.2188	C22H30N2O5	-8.29	385.2155
8.458	Sulfameter	280.064	C11H12N4O3S	-3.55	303.053

8.478	Corynanthine	354.1974	C21H26N2O3	-8.74	355.205
8.594	Fluoxymesterone	336.2105	C20H29FO3	-1.18	341.1891
8.671	Retinol phosphate	366.1979	C20H31O4P	-5.09	367.205
8.726	Morphinan-3-ol, hydrogen sulfate	323.1192	C16H21NO4S	-0.34	324.1262
8.812	Estrone benzoate	374.1874	C25H26O3	2.16	357.1841
8.843	7alpha-(Thiomethyl)spironolactone	388.2059	C23H32O3S	3.27	411.195
8.883	Ketanserin	395.1643	C22H22FN3O3	0.49	400.1429
8.958	1H-Indole-3-carboxylic acid, octahydro-3-hydroxy-2,6- methano-2H-quinolizin-8-yl ester, N-oxide	326.1659	C19H22N2O3	-8.89	309.1626
9.278	Tomatidinol	413.3329	C27H43NO2	-8.43	414.3401
9.286	Desoximetasone	376.2054	C22H29FO4	-1.07	381.184
9.392	2-hydroxypromazine	300.1277	C17H20N2OS	6.28	323.117
9.402	Dextrorphan sulfate	337.1347	C17H23NO4S	0.16	338.1417
9.432	Gpcho(11:0/11:0[U])	594.4048	C30H61NO8	14.58	576.3936
9.633	Vincamine	354.1972	C21H26N2O3	-8.17	337.1939
9.707	Anandamide (20:3, n-3)	349.3012	C22H39NO2	-8.89	332.298
9.853	Desmethylastemizole	444.2298	C27H29FN4O	6.07	427.2265
10.143	1-methylguanosine	297.1066	C11H15N5O5	2.32	320.0949
10.155	7,8-dihydroneopterin	255.095	C9H13N5O4	7.06	278.0841
10.506	Estriol benzyl ether	378.2213	C25H3003	-4.82	383.2
10.567	Phosphoric acid	97.9784	H3O4P	-14.96	98.9856
11.309	Methyl bisnorbiotinyl ketone	214.0807	C9H14N2O2S	-14.595	215.0877
11.426	2,10-dihydroxy-4,6,8-decatriynoic acid	192.0444	C10H8O4	-11.19	175.041
11.495	Quercetin tetramethyl (5,7,3',4') ether	358.1085	C19H18O7	-9.09	359.1159
12.009	Fenoterol sulfate	383.1042	C17H21NO7S	-0.94	384.1112
12.322	Ritodrine sulfate	367.1091	C17H21NO6S	-0.29	368.1162
12.332	C16 sphinganine	273.2694	C16H35NO2	-9.56	274.2766
12.398	Morin	305.738	C15H10O7	+3.50	302.238
12.512	Elephantopin	360.124	C19H20O7	-8.64	343.1208
12.516	C17 sphinganine	287.2851	C17H37O2	-9.45	288.2925
13.277	Ethacrynic acid M2	397.1193	C18H23NO7S	0.45	398.1264

13.406	Sulfamethazine	278.0844	C12H14N4O2S	-2.34	283.0628
13.449	9-hydroxy-2E-decenoic acid	186.1207	C10H18O3	26.54	187.1284
13.538	Desmethylmianserin glucuronide	426.1713	C23H26N2O6	18.29	427.1787
13.548	(Z)-N-(2-hydroxyethyl)hexadec-7-enamide	297.2691	C18H35NO2	-7.76	280.2659
13.594	Chondrosin	355.1083	C12H21NO11	8.82	338.105
13.609	Gummiferol	286.0865	C16H14O5	-8.44	269.0833
13.617	Dihydrosphingosine	301.3004	C18H39NO2	-7.86	302.3077
13.72	Sappanone a dimethyl ether	312.1022	C18H16O5	-7.72	313.1095
13.903	3-Piperidinemethanol, 4-(4-fluorophenyl)-, (3S,4R)-glucuronide	385.1553	C18H24FNO7	-4.22	368.152
14.196	Dimethylcaffeic acid	208.0754	C11H12O4	-9.04	191.0722
15.025	N-Acetyl-7-Oacetylneuraminic acid	351.1183	C13H21NO10	7.81	352.121
15.135	Sanguinarine	333.1004	C20H15NO4	-0.91	315.0893
15.447	Dihydrojasmonic acid methyl ester	226.159	C13H22O3	-9.1	209.1557
15.786	Euparin	216.0809	C13H12O3	-10.22	217.0881
15.856	Naringin	575.394	C27H32O14	-5.145	580.539
15.97	15-methyl-15R-PGF2alpha	368.259	C21H36O5	-7.42	351.2558
16.028	Deoxysappanone b 7,3'-dimethyl ether acetate	356.1291	C20H20O6	-8.78	339.1259
16.042	Hydrocortisone succinate	462.2191	C25H34O8	13.56	445.2159
16.463	2,10-dihydroxy-4,6,8-decatriynoic acid	192.0442	C10H8O4	-10.06	175.0409
16.545	2-Thiopheneacetic acid, 5-(hydroxyphenylmethyl)-alphamethyl-	262.0654	C14H14O3S	3.66	263.0725
16.85	Di-demethylcitalopram	296.131	C18H17FN2O	5.11	301.1095
16.925	5,7-dihydroxy-4-methylcoumarin	192.0439	C10H8O4	-8.7	175.0406
16.948	2-methyl-5,7,8-trimethoxyisoflavone	326.1179	C19H18O5	-7.7	309.1146
17.173	1-hexadecanoyl-sn-glycerol	330.2823	C19H38O4	-15.94	353.2716
17.417	Retusin 7-methyl ether	298.0866	C17H14O5	-8.46	299.0939

17.514	13-oxoode	294.2219	C18H30O3	-8.23	277.2186
17.56	Digoxigenin	390.2415	C23H34O5	-2.21	391.2487
17.591	Isotectorigenin, 7-methyl ether	328.0975	C18H16O6	-8.46	329.1047
18.708	12-hydroxy-10-octadecynoic acid	296.2373	C18H3203	-7.3	279.234
19.032	2,4,6-octatrienal	122.0743	C8H10O	-8.95	105.071
19.295	PGA2	334.2143	C20H30O4	0.18	317.211
19.325	9-hydroxy-12-oxo-10-octadecenoic acid	312.2324	C18H32O4	-7.55	295.229
19.567	2R-hydroxy-9Z,12Z,15Zoctadecatrienoic acid	294.2216	C18H30O3	-7.12	277.2184
20.314	Lactone of PGF-MUM	296.1646	C16H24O5	-7.54	301.1434
20.461	5,7,4'-trimethoxyflavone	312.1018	C18H16O5	-6.5	295.0985
20.673	Methyl 9,10-epoxy-12,15-octadecadienoate	308.2372	C19H32O3	-6.56	291.2339
20.997	9,13-dihydroxy-12-ethoxy-10-octadecenoic acid	358.2744	C20H38O5	-6.81	263.2531
22.269	Methyl 9-hydroperoxy-5,7,11,14,17-eicosapentaenoate	348.2298	C21H32O4	0.61	331.2267
22.883	3beta,6alpha,7alpha-Trihydroxy-5beta-cholan-24-oic Acid	408.2903	C24H40O5	-6.68	413.2691

RT: Retention time.

Dataset 11.2. Compounds and Metabolites identified in non-polar extract of SKP17LIV01 in negative mode Q-TOF LCMS.

RT	Name	Measured Mass	Formula	Error (ppm)	Max M/Z
1.757	1,3-Dimethyluric Acid	196.0632	C7H8N4O3	-18.41	195.056
1.882	Fenofibric acid	318.0652	C17H15CLO4	2.29	317.0579
2.293	Chlorpropamide	276.0329	C10H13CLN2O3S	2.25	275.0256
2.294	Malic acid	134.0249	C4H6O5	-24.94	133.0176
2.382	Pyroglutamic acid	129.0457	C5H7NO3	-23.84	128.0384
2.478	2,3-Dioxogulonic acid	192.0318	C6H8O7	-24.99	191.0245
3.154	1-(3-Carboxypropyl)-3,7-dimethylxanthine	266.1046	C11H14N4O4	-11.45	265.0972
6.249	Phenylglycol 3-O-sulfate	234.0248	C8H10O6S	-21.51	233.0176
6.41	Chlorogenic acid	354.0984	C16H18O9	-9.46	353.0912
7.286	Pyrantel	206.0845	C11H14N2S	16.1	205.0772
8.154	Rhoifolin	578.1652	C27H30O14	-2.87	577.1582
8.409	N-Dealkylzuclopenthixol sulfoxide	372.109	C20H21CLN2OS	-7.18	371.1017
8.446	Rutin	610.1555	C27H30O16	-3.5	609.1481
8.45	Trans-3-Hydroxycotinine glucuronide	368.1143	C16H20N2O8	20.81	367.107
8.793	Demeclocycline	464.0979	C21H21CLN2O8	1.68	463.0906
9.419	Morphinan-3-ol, hydrogen sulfate	323.1201	C16H21NO4S	-3.12	322.1129
9.545	Cinnarizine	368.2237	C26H28N2	4.27	367.2164
9.987	Ellagic Acid	306.231	C14H6O8	4.037	302.194
10.041	S-(1,2-dicarboxyethyl)glutathione	423.1027	C14H21N3O10S	-18.76	422.0962
10.386	Ketoconazole	530.1583	C26H28CL2N4O4	-17.93	529.1511
10.752	Benzaldehyde, p-amino-, thiosemicarbazone	194.064	C8H10N4S	-7.29	193.0567
10.968	QH2	320.2033	C19H28O4	-14.13	319.196
10.97	Gibberellin A44 diacid	364.1931	C20H28O6	-12.41	363.1856
11.148	Fenirofibrate glucuronide	496.1163	C23H25CLO10	-5.46	495.1091
11.251	Oxazepam	286.0527	C15H11CLN2O2	-6.44	285.0455
11.269	4-hydroxyclobazam	316.063	C16H13CLN2O3	-4.86	315.0557
11.436	Norverapamil	440.2554	C26H36N2O4	27.59	439.2496
12.032	Idebenone Metabolite	516.25	C25H40O11	13.67	515.2446

11.767	9,12,13-trihydroxy-10,15-octadecadienoic acid	328.2296	C18H32O5	-14.19	327.2224
13.123	Digoxin	780.4325	C41H64O14	-3.66	779.4252
13.131	Retinyl glucuronide	462.2643	C26H38O7	-5.51	461.257
13.277	Deoxygedunol acetate	510.2491	C30H38O7	24.88	509.2418
15.055	Sulfaphenazole	314.0843	C15H14N4O2S	-1.76	313.0769
15.112	9-hydroxy-12-oxo-10-octadecenoic acid	312.2355	C18H32O5	-17.47	311.2283
15.609	Digitoxin	764.4399	C41H64O13	-6.87	763.4328
16.107	9,13-dihydroxy-11-octadecenoic acid	314.2508	C18H34O4	-16.32	313.2436
16.607	5'-demethoxydeoxypodophyllotoxin	368.1302	C21H20O6	-11.5	367.1229
17.457	8,9-dihydroxy stearic acid	316.2666	C18H36O4	-16.42	315.2593
17.679	Phenylbutazone	308.1464	C19H20N2O2	19.84	307.1391
18.571	Gpser(18:1(9Z)/18:2(9Z,12Z))[U]	785.5357	C42H76NO10P	-19.13	784.5299
18.577	2,3-diacetoxy-7,8-epoxy-24,29-dinor-1,3,5- friedelatriene-20-carboxylic acid	552.3077	C33H44O7	1.76	551.3027
18.589	12-hydroxy-10-octadecynoic acid	296.2408	C18H32O3	-18.92	295.2335
19.238	L-Oleandrosyl-oleandolide	530.3124	C27H46O10	-6.24	529.3052
20.404	Gpgro(10:0/10:0)[U]	554.3239	C26H51O10P	-3.44	553.3183
21.3	Simvastatin	418.2763	C25H38O5	-10.57	417.2691
21.507	1alpha,25-dihydroxy-26,27-dimethyl-24a-homovitamin D3 / 1alpha,25- dihydroxy-26,27-dimethyl-24a-homoc	458.365	C30H50O3	23.92	457.3579
21.578	(24R)-1alpha,24,25,26-tetrahydroxyvitamin D2 /(24R)-1alpha,24,25,26-tetrahydroxyergocalciferol	460.3228	C28H44O5	-8.46	459.3154
21.953	Hecogenin acetate	472.3228	C29H44O5	-8.22	471.3156
22.056	1alpha-hydroxy-23-[3-(1-hydroxy-1-methylethyl)phenyl]-22,22,23,23-tetradehydro24,25,26,27-tetrano	474.3024	C32H42O3	23.2	473.2949
22.318	18-acetoxy-1alpha,25-dihydroxyvitamin D3	474.3387	C29H46O5	-8.83	473.3316

	/ 18- acetoxy-1alpha,25-dihydroxycholecalciferol				
22.397	11-hydroxy palmitic acid	272.2415	C16H32O3	-23.31	271.2342
22.501	Hopane-29-acetate	470.401	C32H54O2	24.28	469.394
22.814	9R-hydroxy-10Eoctadecenoic acid	298.2569	C18H34O3	-20.48	297.2496
22.856	3-hydroxy-eicosanoic acid	328.3033	C20H40O3	-16.85	327.296
23.258	Docosanedioic acid	370.3135	C22H42O4	-14.15	369.3064
23.392	5'-Hydroxysulfapyridine glucuronide	441.0843	C17H19N3O9S	-0.3	440.0787
23.885	1alpha,25-dihydroxy-2betapentylvitamin D3 / 1alpha,25-dihydroxy2betapentyl cholecalcife	486.396	C32H54O3	23.15	485.3889
24.033	12-Ketodeoxycholic acid	400.3597	C24H48O4	-11.08	399.3525
24.1	1-heptadecanoyl-rac-glycerol	344.2976	C20H40O4	-14.21	343.2903
24.935	4,4-Dimethyl-14ahydroxymethyl-5a-cholesta-8,24-dien3b-ol	442.3702	C30H50O2	24.71	241.363
25.138	DL-10-hydroxy stearic acid	300.2724	C18H36O3	-19.77	299.2652
25.601	Desmethylhalofantrine	443.1011	C22H22CL2F3 N O	4.31	442.0942
26.148	Mytiloxanthin	598.4015	C40H54O4	1.19	597.3964
26.148	Tetracosanedioic acid	398.3438	C24H46O4	-10.49	397.3365
27.109	26,27-diethyl-1alpha,25-dihydroxy-20,21-didehydro-23-oxavitamin D3 / 26,27-diethyl-1alpha,25-dihydro	472.359	C30H48O4	-7.95	471.3519
27.438	Carbenicillin	378.0969	C17H18N2O6S	-22.13	377.0901

RT: Retention time.

Dataset 11.3. The identified active ingredients of SKP17LIV01 with drug like properties.

Compound ID	Name	logP	RB	tPSA	MW	HBA	HBD	MR	No. of Atoms	Volume	RO5 Violation
CM01	12-Ketodeoxycholic acid	4.06	4	74.6	390.56	4	2	105.55	67	391.77	0
CM02	2- (2,6-Dimethoxyphenoxyethyl)aminomethyl-1,4-benzodioxane (wb 4101)	2.2	8	58.2	345.39	6	1	103.59	48	319.09	0
CM03	2-Thiopheneacetic acid, 5-(hydroxyphenylmethyl)-alphamethyl-	2.57	4	57.53	262.33	3	2	79.36	32	231.1	0
CM04	3beta,6alpha,7alpha-Trihydroxy-5beta-cholan-24-oic Acid	3.33	4	97.98	408.58	5	4	105.66	69	405.68	0
CM05	3-Piperidinemethanol, 4-(4-fluorophenyl)-, (3S,4R)-glucuronide	0.02	2	128.48	385.39	8	5	64.45	34	333.72	0
CM06	4-Hydroxyclobazam	2.07	1	60.85	316.74	5	1	91.35	35	263.06	0
CM07	5,7,4'-Trimethoxyflavone	3.81	4	57.91	312.32	5	0	95.27	39	276.63	0
CM08	5'-Hydroxy Sulfapyridine glucuronide	-1.34	6	201.53	441.42	12	7	108.53	51	348.74	2
CM09	6beta-Naltrexol	1.53	2	73.16	343.42	5	3	92.02	50	310.39	0
CM10	7alpha-(Thiomethyl)spironolactone	2.77	1	43.28	388.57	3	0	112.71	64	368.64	0
CM11	Agc	1.28	9	66.4	299.44	4	2	84.65	45	294.26	0
CM12	Chlorogenic acid	-0.45	4	164.74	354.31	9	6	85.8	43	296.27	1
CM13	Chlorpropamide	2.21	4	75.27	276.75	5	2	67.11	30	222.96	0
CM14	Cinnarizine	5.76	6	6.48	368.52	2	0	132.28	56	369.84	1
CM15	Conessine	4.79	1	6.48	356.6	2	0	108.61	66	379.4	0
CM16	Corynanthine	3.22	1	65.56	354.45	5	2	99.95	52	330.78	0
CM17	Deoxygedunol acetate	5.8	3	92.06	510.63	7	0	138.1	75	477.47	2
CM18	Deoxysappanone b 7,3'-dimethyl ether acetate	2.68	5	71.08	356.37	6	0	103.18	46	318.53	0

CM19	Desmethylmianserin glucuronide	1.17	2	113.69	426.47	8	4	118.74	57	376.71	0
CM20	Desoximetasone	2.32	2	74.6	376.47	4	2	100.05	56	350.38	0
CM21	Dextrorphan sulfate	0.99	2	66.84	337.44	5	1	86.7	46	297.07	0
CM22	Di-demethylcitalopram	1.95	4	59.05	296.35	3	2	88.29	39	270.38	0
CM23	Digitoxin	2.03	7	182.85	764.95	13	5	183.37	118	712.09	2
CM24	Digoxigenin	1.56	1	86.99	390.52	5	3	100.51	62	372.66	0
CM25	Digoxin	1.12	7	203.08	780.95	14	6	184.46	119	720.14	3
CM26	Estriol benzyl ether	4.64	3	49.69	378.51	3	2	116.99	58	365.96	0
CM27	Ethacrynic acid M2	-0.54	6	130	397.45	8	3	76.52	31	349.51	0
CM28	Fenirofibrate glucuronide	1.79	7	162.98	496.9	10	5	124.38	59	413.75	0
CM29	Fenofibric acid	4.18	5	63.6	318.76	4	1	91.47	37	273.58	0
CM30	Fluoxymesterone	2.76	0	57.53	336.45	3	2	89.23	53	320.43	0
CM31	Glycyrrhizic acid	1.97	7	267.04	822.94	16	8	198.84	120	741.93	2
CM32	Hecogenin acetate	5.72	1	61.84	472.67	5	0	121.25	78	464.29	1
CM33	Idebenone metabolite	3.65	15	166.14	514.61	10	6	121.87	78	485.89	2
CM34	Isocorydine (+)	3	3	51.17	341.41	5	1	103.37	48	315	0
CM35	Isotectorigenin, 7-methyl ether	3.13	4	78.14	328.32	6	1	95.64	40	284.65	0
CM36	Ketanserin	2.81	5	75.18	395.43	6	1	351.26			0
CM37	Lactone of PGF-MUM	1.91	8	80.67	296.36	5	1	68.15	45	283.4	0
CM38	Norverapamil	3.96	13	72.75	440.58	6	1	134.09	68	437.36	0
CM39	Oxazepam	1.84	1	61.69	286.72	4	2	83.32	31	237.64	0
CM40	Oxycodone	0.79	1	59.01	315.37	5	1	87.29	44	282.23	0
CM41	Phenylbutazone	4.56	5	40.62	308.38	4	0	95.25	43	291.94	0
CM42	Pyrantel	2.47	2	15.6	206.31	2	0	63.79	28	194.34	0
CM43	Pyroglutamic acid	-2.4	1	66.4	129.12	4	2	25.44	16	110.61	0
CM44	QH2	5.47	0	58.92	320.43	4	2	34.17	14	322.65	1
CM45	Quercetin tetramethyl (5,7,3',4') ether	3.11	5	87.38	358.35	7	1	103.59	44	310.2	0
CM46	Retusin 7-methyl ether	3.14	3	68.91	298.29	5	1	89	36	259.11	0

CM47	Rhoifolin	-0.02	6	228.97	578.52	14	8	143.89	71	480.03	3
CM48	Rutin	-1.06	6	269.43	610.52	16	10	147.17	73	496.07	3
CM49	Sanguinarine	0.8	0	40.82	332.33	5	0	97.3	39	279.51	0
CM50	Sappanone A dimethyl ether	2.99	3	65	312.32	5	1	94.47	39	275.91	0
CM51	Simvastatin	4.76	6	72.84	418.57	5	1	111.46	68	416.81	0
CM52	Tetracaine	3.43	8	41.57	264.37	4	1	78.8	43	270.89	0
CM53	Trandolaprilat	0.45	8	106.93	402.49	7	3	102.4	59	378.84	0
CM54	Triparanol	6.07	10	32.7	438.01	3	1	141.08	63	420.38	1
CM55	Vincamine	3.18	2	54.7	354.45	5	1	103.03	52	330.22	0
CM56	Quercetin	1.54	1	131.03	302.24	7	5	-	-	-	0

RB: number of rotatable bond; MR: molar refractivity; tPSA: total polar surface area; MW: molecular weight; HBD: hydrogen bond donor; HBA: hydrogen bond acceptor; RO5: Lipinski's Rule of Five

All *in silico* parameters (except logD; computed from ACD-I-lab property prediction tool) were computed using Molinspiron Cheminformatics software.

REFERENCES

[1] S. Tong, Y. E. V. Schirnding, T. Prapamontol, Bull. World Health Organ. 78 (2000) 1068.

[2] N. C. Papanikolaou, E. G. Hatzidaki, S. Belivanis, G. N. Tzanakakis, A. M. Tsatsakis, Med. Sci. Monit. 11 (2005) RA329.

[3] T. K. Dua, S. Dewanjee, R. Khanra, S. Joardar, S. Barma, S. Das, M. Zia-Ul-Haq, V. D. Feo, PLoS ONE 11 (2016) e0148757.

[4] P. C. Hsu, Y. L. Guo, Toxicology 180 (2002) 33.

[5] H. Dapul, D. Laraque, Adv. Pediatr. 61 (2014) 313.

[6] WHO, Childhood Lead Poisoning, World Health Organization, Geneva, Switzerland, (2010).

[7] WHO, International Lead Poisoning Prevention Week of Action: Http://Www.Who.Int/Ipcs/Lead_Campaign/En/. World Health Organization, 2017.

[8] K. Chander, K. Vaibhav, M. E. Ahmed, H. Javed, R. Tabassum, A. Khan, M. Kumar, A. Katyal, F. Islam, M. S. Siddiqui, Food Chem. Toxicol. 68 (2014) 297.

[9] H. Gurer, N. Ercal, Free Radic. Biol. Med. 29 (2000) 927.

[10] S. Dewanjee, R. Sahu, S. Karmakar, M. Gangopadhyay, Food Chem. Toxicol. 55 (2013) 78.

[11] D. Xia, X. Yu, S. Liao, Q. Shao, H. Mou, W. Ma, J. Ethnopharmacol. 130 (2010) 414.

[12] S. Kumar, A. K. Pandey, Sci. World J. 2013 (2013) 16.

[13] A. Moncomble, D. J. Thaviligadu, A. R. Djendja, J. P. Cornard, New J. Chem. 42 (2018) 7691.

[14] M. Hidalgo, C. Sánchez-Moreno, S. de Pascual-Teresa, Food Chem. 121 (2010) 691.

[15] G. W. Plumb, S. De Pascual-Teresa, C. Santos-Buelga, V. Cheynier, G. Williamson, Free Radic. Res. 29 (1998) 351.

[16] C. A. Rice-Evans, N. J. Miller, G. Paganga, Free Radic. Biol. Med. 20 (1996) 933.

[17] G. W. Plumb, S. J. Chambers, N. Lambert, B. Bartolomé, R. K. Heaney, S. Wanigatunga, O. I. Aruoma, B. Halliwell, G. Williamson, J. Food Lipids 3 (1996) 171.

[18] R. Mateos, M. M. Domínguez, J. L. Espartero, A. Cert, J. Agric. Food Chem. 51 (2003) 7170.

[19] M. Garcia-Alonso, G. Rimbach, J. C. Rivas-Gonzalo, S. De Pascual-Teresa, J. Agric. Food Chem. 52 (2004) 3378.

[20] D. Bagchi, S. Chaudhuri, S. Sardar, S. Choudhury, N. Polley, P. Lemmens, S. K. Pal, RSC Adv. 5 (2015) 102516.

[21] M. Samsonowicz, E. Regulska, Spectrochim. Acta A: Mol. Biomol. Spectrosc. 173 (2017) 757.

[22] J. P. Cornard, J. C. Merlin, J. Mol. Struct. 651-653 (2003) 381.

[23] A. Michalak, Pol. J. Environ. Stud. 15 (2006).

[24] J. Barcelo, C. Poschenrieder, Environ. Exp. Bot. 48 (2002) 75.

[25] K. Keilig, J. Ludwig-Müller, Bot. Stud. 50 (2009) 311.

[26] L. Mira, M. Tereza Fernandez, M. Santos, R. Rocha, M. Helena Florêncio, K. R. Jennings, Free Radic. Res. 36 (2002) 1199.

[27] Y. A. Dávila, M. I. Sancho, M. C. Almandoz, E. Gasull, J. Chem. Eng. Data 63 (2018) 1488.

[28] V. Kuntic, I. Filipovic, Z. Vujic, Molecules 16 (2011) 1378.

[29] X. Chen, L.-J. Tang, Y.-N. Sun, P.-H. Qiu, G. Liang, J. Inorg. Biochem. 104 (2010) 379.

[30] M. M. Kasprzak, A. Erxleben, J. Ochocki, RSC Adv. 5 (2015) 45853.

[31] W. Chen, S. Sun, W. cao, Y. Liang, J. Song, J. Mol. Struct. 918 (2009) 194.

[32] S. Mao, K. Wang, Y. Lei, S. Yao, B. Lu, W. Huang, Sci. Rep. 7 (2017) 46501.

[33] F. Dai, W.-F. Chen, B. Zhou, Biochimie 90 (2008) 1499.

[34] I. Kola, J. Landis, Nat. Rev. Drug Discov. 3 (2004) 711.

[35] F. Sams-Dodd, Drug Discov. Today 10 (2005) 139.

[36] A. L. Hopkins, Nat. Chem. Biol. 4 (2008) 682.

[37] J. Fang, Z. Wu, C. Cai, Q. Wang, Y. Tang, F. Cheng, J. Chem. Inf. Model. 57 (2017) 2657.

[38] W.-Y. Jiang, Trends Pharmacol. Sci. 26 (2005) 558.

[39] C. M. Dobson, Nature 432 (2004) 824.

[40] A. G. Atanasov, B. Waltenberger, E.-M. Pferschy-Wenzig, T. Linder, C. Wawrosch, P. Uhrin, V. Temml, L. Wang, S. Schwaiger, E. H. Heiss, J. M. Rollinger, D. Schuster, J. M. Breuss, V. Bochkov, M. D. Mihovilovic, B. Kopp, R. Bauer, V. M. Dirsch, H. Stuppner, Biotechnol. Adv. 33 (2015) 1582.

[41] S.-Y. Pan, S.-F. Zhou, S.-H. Gao, Z.-L. Yu, S.-F. Zhang, M.-K. Tang, J.-N. Sun, D.-L. Ma, Y.-F. Han, W.-F. Fong, Evid. Based Complement. Alternat. Med. 2013 (2013).

[42] S. Das, M. A. Laskar, S. D. Sarker, M. D. Choudhury, P. R. Choudhury, A. Mitra, S. Jamil, S. M. A. Lathiff, S. A. Abdullah, N. Basar, Phytochem. Anal. 28 (2017) 324.

[43] J. Li, P. Zhao, Y. Li, Y. Tian, Y. Wang, Sci. Rep. 5 (2015) 15290.

[44] J. Sun, L. Zhang, Y. He, K. Zhang, L. Wu, Y. Fan, Z. Xie, Sci. Rep. 6 (2016) 34328.

[45] R.-S. Wang, J. Loscalzo, Mol. Biosyst. 12 (2016) 1653.

[46] C. S. Zheng, X. J. Xu, H. Z. Ye, G. W. Wu, X. H. Li, S. P. Huang, X. X. Liu, Mol. Med. Rep. 7 (2013) 1812.

[47] Q. Wu, C. Cai, P. Guo, M. Chen, X. Wu, J. Zhou, Y. Luo, Y. Zou, A.-l. Liu, Q. Wang, Z. Kuang, J. Fang, Front. Pharmacol. 10 (2019).

[48] L. Gao, K. X. Wang, Y. Z. Zhou, J. S. Fang, X. M. Qin, G. H. Du, Sci. Rep. 8 (2018) 624.

[49] A. Adhikari, N. Polley, S. Darbar, D. Bagchi, S. K. Pal, Fut. Sci. OA 2 (2016) FSO146.

[50] A.-L. Barabási, N. Gulbahce, J. Loscalzo, Nat. Rev. Genet. 12 (2011) 56.

[51] S. Lee, C. Zhang, Z. Liu, M. Klevstig, B. Mukhopadhyay, M. Bergentall, R. Cinar, M. Ståhlman, N. Sikanic, J. K. Park, Mol. Syst. Biol. 13 (2017) 938.

[52] A. Adhikari, S. Darbar, T. Chatterjee, M. Das, N. Polley, M. Bhattacharyya, S. Bhattacharya, D. Pal, S. K. Pal, ACS Omega 3 (2018) 15975.

[53] Z. Marković, D. Milenković, J. Đorović, J. M. D. Marković, V. Stepanić, B. Lučić, D. Amić, Food Chem. 134 (2012) 1754.

[54] Q. K. Panhwar, S. Memon, J. Coord. Chem. 64 (2011) 2117.

[55] S. V. Jovanovic, S. Steenken, M. Tosic, B. Marjanovic, M. G. Simic, J. Am. Chem. Soc. 116 (1994) 4846.

[56] J. S. Renny, L. L. Tomasevich, E. H. Tallmadge, D. B. Collum, Angew. Chem. Int. Ed. Engl. 52 (2013) 11998.

[57] A. A. Ensafi, R. Hajian, S. Ebrahimi, J. Braz. Chem. Soc. 20 (2009) 266.

[58] M. M. Silva, M. R. Santos, G. Caroço, R. Rocha, G. Justino, L. Mira, Free Radic. Res. 36 (2002) 1219.

[59] Q. K. Panhwar, S. Memon, J. Coord. Chem. 65 (2012) 1130.

[60] D. Roy, A. Chakraborty, R. Ghosh, RSC Adv. 7 (2017) 40563.

[61] N. Binbuga, J. K. Hasty, S. R. Gwaltney, W. P. Henry, T. P. Schultz, Inorganica Chim. Acta 360 (2007) 2339.

[62] A. C. Gutierrez, M. H. Gehlen, Spectrochim. Acta A: Mol. Biomol. Spectrosc. 58 (2002) 83.

[63] J. R. Lakowicz, Principles of Fluorescence Spectroscopy, Springer, Boston, MA, (2006).

[64] M. V. de-Weert, L. Stella, J. Mol. Struct. 998 (2011) 144.

[65] R. L. Auger, A. M. Jacobson, M. M. Domach, Environ. Sci. Technol. 29 (1995) 1273.

[66] P. B. Pal, K. Sinha, P. C. Sil, PLoS ONE 8 (2013) e56894.

[67] P. Manna, S. Bhattacharyya, J. Das, J. Ghosh, P. C. Sil, Evid. Based Complement. Alternat. Med. 2011 (2011) 17.

[68] Q. K. Panhwar, S. Memon, M. I. Bhanger, J. Mol. Struct. 967 (2010) 47.

[69] K. E. Heim, A. R. Tagliaferro, D. J. Bobilya, J. Nutr. Biochem. 13 (2002) 572.

[70] S. A. B. E. V. Acker, M. J. D. Groot, D. J. V. D. Berg, M. N. J. L. Tromp, G. D. O. P. D. Kelder, W. J. F. V. D. Vijgh, A. Bast, Chem. Res. Toxicol. 9 (1996) 1305.

[71] M. S. El-Neweshy, Y. S. El-Sayed, Exp. Toxicol. Pathol. 63 (2011) 221.

[72] G. M. Ledda-Columbano, A. Columbano, P. Pani, Am. J. Pathol. 113 (1983) 315.

[73] A. Adhikari, N. Polley, S. Darbar, S. K. Pal, Mater. Focus 6 (2017) 280.

[74] N. Polley, S. Saha, A. Adhikari, S. Banerjee, S. Darbar, S. Das, S. K. Pal, Nanomedicine 10 (2015) 2349.

[75] Y. S. El-Sayed, M. S. El-Neweshy, Toxicol. Environ. Chem. 92 (2010) 765.

[76] K. Buchheim, G. Stoltenburg-Didinger, H. Lilienthal, G. Winneke, Neurotoxicology 19 (1998) 539.

[77] R. Fonte, A. Agosti, F. Scafa, S. M. Candura, Haematologica 92 (2007) e13.

[78] P. K. Sarkar, A. Halder, A. Adhikari, N. Polley, S. Darbar, P. Lemmens, S. K. Pal, Sens. Actuators B Chem. 255 (2018) 2194.

[79] A. Adhikari, S. Darbar, M. Das, S. Mondal, S. S. Bhattacharya, D. Pal, S. K. Pal, Comp. Biol. Chem. 84 (2020) 107196.

[80] G. M. Cragg, D. J. Newman, Biochim. Biophys. Acta. - General Subjects 1830 (2013) 3670.

[81] D. Lagorce, D. Douguet, M. A. Miteva, B. O. Villoutreix, Sci. Rep. 7 (2017) 46277.

[82] C. A. Lipinski, J. Pharmacol. Toxicol. Methods 44 (2000) 235.

[83] C. A. Lipinski, Drug Discov. Today: Technol. 1 (2004) 337.

[84] C. A. Lipinski, Adv. Drug Deliv. Rev. 101 (2016) 34.

[85] S. K. Bhal, K. Kassam, I. G. Peirson, G. M. Pearl, Mol. Pharm. 4 (2007) 556.

[86] S.-J. Yue, L.-T. Xin, Y.-C. Fan, S.-J. Li, Y.-P. Tang, J.-A. Duan, H.-S. Guan, C.-Y. Wang, Sci. Rep. 7 (2017) 40318.

[87] J. P. Overington, B. Al-Lazikani, A. L. Hopkins, Nat. Rev. Drug Discov. 5 (2006) 993.

[88] Z. Wang, L. Liang, Z. Yin, J. Lin, J. Cheminformatics 8 (2016) 20.

[89] M. Kuhn, C. von-Mering, M. Campillos, L. J. Jensen, P. Bork, Nucleic Acids Res. 36 (2007) D684.

[90] D. Warde-Farley, S. L. Donaldson, O. Comes, K. Zuberi, R. Badrawi, P. Chao, M. Franz, C. Grouios, F. Kazi, C. T. Lopes, Nucleic Acids Res. 38 (2010) W214.

[91] C. v. Mering, M. Huynen, D. Jaeggi, S. Schmidt, P. Bork, B. Snel, Nucleic Acids Res. 31 (2003) 258.

[92] N. Aykin-Burns, E. A. Franklin, N. Ercal, Arch. Environ. Contam. Toxicol. 49 (2005) 119.

[93] L. Chen, X. Yang, H. Jiao, B. Zhao, Chem. Res. Toxicol. 16 (2003) 1155.

[94] J. Xu, L.-J. Lian, C. Wu, X.-F. Wang, W.-Y. Fu, L.-H. Xu, Food Chem. Toxicol. 46 (2008) 1488.

[95] F. Farmand, A. Ehdaie, C. K. Roberts, R. K. Sindhu, Environ. Res. 98 (2005) 33.

[96] A. Adhikari, M. Das, S. Mondal, S. Darbar, A. K. Das, S. S. Bhattacharya, D. Pal, S. K. Pal, Biomater. Sci. 7 (2019) 4491.

[97] A. Adhikari, S. Mondal, S. Darbar, S. K. Pal, Biomol. Concepts 10 (2019) 160.

[98] C. M. Knudson, S. J. Korsmeyer, Nat. Genet. 16 (1997) 358.

[99] S. Cory, J. M. Adams, Nat. Rev. Cancer 2 (2002) 647.

[100] Y. Wang, H. Su, X. Song, S. S. Fiati Kenston, J. Zhao, Y. Gu, Int. J. Mol. Med. 41 (2018) 233.

[101] V. S. Marsden, L. O'Connor, L. A. O'Reilly, J. Silke, D. Metcalf, P. G. Ekert, D. C. S. Huang, F. Cecconi, K. Kuida, K. J. Tomaselli, S. Roy, D. W. Nicholson, D. L. Vaux, P. Bouillet, J. M. Adams, A. Strasser, Nature 419 (2002) 634.

[102] G. Bindea, B. Mlecnik, H. Hackl, P. Charoentong, M. Tosolini, A. Kirilovsky, W.-H. Fridman, F. Pagès, Z. Trajanoski, J. Galon, Bioinformatics 25 (2009) 1091.

[103] S. Mondal, A. Adhikari, M. Das, S. Darbar, A. Alharbi, S. A. Ahmed, S. S. Bhattacharya, D. Pal, S. K. Pal, RSC Adv. 9 (2019) 30216.

[104] G. Kroemer, Nat. Med. 3 (1997) 614.

[105] E. Z. Bagci, Y. Vodovotz, T. R. Billiar, G. B. Ermentrout, I. Bahar, Biophys. J. 90 (2006) 1546.

LIST OF PUBLICATIONS

International Peer-Reviewed Journals

[1] **Adhikari, A.**, Mondal, S., Das, M., Biswas, P., Pal, U., Darbar, S., Bhattacharya, S. S., Pal, D., Saha-Dasgupta, T., Das, A. K., Mallick, A. K., Pal, S. K. (2021). Incorporation of a Biocompatible Nanozyme in Cellular Antioxidant Enzyme Cascade Reverses Huntington's Like Disorder in Preclinical Model. *Advanced Healthcare Materials*, 10(7), 2001736. https://doi.org/10.1002/adhm.202001736

[2] **Adhikari, A.**, Das, M., Mondal, S., Darbar, S., Das, A. K., Bhattacharya, S. S., Pal, D., Pal, S. K. (2019). Manganese Neurotoxicity: Nano-oxide Compensates the Ion-damage in Mammals. *Biomaterials Science*, 7(11), 4491-4502. https://doi.org/10.1039/c9bm01039d

[3] **Adhikari, A.**, Biswas, P., Mondal, S., Das, M., Darbar, S., Hameed, A. M., Alharbi, A., Ahmed, S. A., Bhattacharya, S. S., Pal, D., Pal, S. K. (2020). A Smart Nanotherapeutic Agent for in vitro and in vivo Reversal of Heavy Metal Induced Causality: Key Information from Optical Spectroscopy. *ChemMedChem*, 15(5), 420-429. [Front Cover Highlighted] https://doi.org/10.1002/cmdc.201900543

[4] **Adhikari, A.**, Darbar, S., Das, M., Mondal, S., Bhattacharya, S. S., Pal, D., Pal, S. K. (2020). Rationalization of a Traditional Liver Medicine Using Systems Biology Approach and Its Evaluation in Preclinical Trial. *Computational Biology and Chemistry*, 84, 107196. https://doi.org/10.1016/j.compbiolchem.2019.107196

[5] **Adhikari, A.**, Mondal, S., Darbar, S., Pal, S. K. (2019). Role of Nanomedicine in Redox Mediated Healing at Molecular Level. *Biomolecular Concepts*, 10(1), 160-174. https://doi.org/10.1515/bmc-2019-0019

[6] **Adhikari, A.**,* Darbar, S.,* Chatterjee, T., Das, M., Polley, N., Bhattacharyya, M., Bhattacharya, S., Pal, D., Pal, S. K. (2018). Spectroscopic Studies on Dual Role of Natural Flavonoids in Detoxification of Lead Poisoning: Bench to Bedside-Preclinical Trial. *ACS Omega*, 3(11), 15975-15987.
[* These authors contributed equally]
https://doi.org/10.1021/acsomega.8b02046

[7] **Adhikari, A.**, Polley, N., Darbar, S., Bagchi, D., Pal, S. K. (2016). Citrate Functionalized Mn_3O_4 in Nanotherapy of Hepatic Fibrosis by Oral Administration. *Future Science (OA)*, 2(4), FSO146.
https://doi.org/10.4155/fsoa-2016-0029

[8] **Adhikari, A.**, Polley, N., Darbar, S., Pal, S. K. (2017). Therapeutic Potential of Surface Functionalized Mn_3O_4 Nanoparticles against Chronic Liver Diseases in Murine Model. *Materials Focus*, 6(3), 280-289.
https://doi.org/10.1166/mat.2017.1403

[9] **Adhikari, A.**, Bhutani, V. K., Mondal, S., Das, M., Darbar, S., Ghosh, R., Polley, N., Das, A. K., Bhattacharya, S. S., Pal, D., Mallick, A. K., Pal, S. K. (2021) A Nanoceutical Agent for Chemoprevention of Bilirubin Encephalopathy. *bioRxiv*.
https://doi.org/10.1101/2020.12.31.425023

[10] **Adhikari, A.**, Mondal, S., Chatterjee, T., Das, M., Biswas, P., Darbar, S., Alessa, H., Al-Thakafy, J. T., Ahmed, S. A., Das, A. K., Bhattacharyya, M., Pal, S. K. (2021) Redox Nanomedicine Cures Chronic Kidney Disease (CKD) by Mitochondrial Reconditioning. *bioRxiv*.
https://doi.org/10.1101/2021.03.14.435287

[11] **Adhikari, A.**, Mondal, S., Das, M., Ghosh, R., Biswas, P., Darbar, S., Singh, S., Das, A. K., Bhattacharya, S. S., Pal, D., Mallick, A. K., Pal, S. K. (2021) Redox Buffering Capacity of Nanomaterials as an Index of ROS-based Therapeutics and Toxicity: A Preclinical Animal Study**.** *bioRxiv*.
https://doi.org/10.1101/2021.03.14.435286

[12] Polley, N., Saha, S., **Adhikari, A.**, Banerjee, S., Darbar, S., Das, S., Pal, S. K. (2015). Safe and Symptomatic Medicinal Use of Surface Functionalized Mn_3O_4 Nanoparticles for Hyperbilirubinemia Treatment in Mice. *Nanomedicine (Lond.)*, 10(15), 2349-2363.
https://doi.org/10.2217/nnm.15.83

[13] Mondal, S., **Adhikari, A.**, Das, M., Darbar, S., Alharbi, A., Ahmed, S. A., Bhattacharya, S. S., Pal, D., Pal, S. K. (2019). Novel One Pot Synthesis and Spectroscopic Characterization of Folate-Mn_3O_4 Nanohybrid for Potential Photodynamic Therapeutic Application. *RSC Advances*, 9(52), 30216- 30225. https://doi.org/10.1039/C9RA06835J

[14] Biswas, P., **Adhikari, A.**, Pal, U., Singh, P., Das, M., Saha-Dasgupta, T., Choudhury, S. S., Das, R., Pal, S. K. (2020). Flexibility Modulates Catalytic Activity of a Themostable Enzyme: Key Information from Optical Spectroscopy and Molecular Dynamics Simulation. *Soft Matter*, 16(12), 3050-302. https://doi.org/10.1039/C9SM02479D

[15] Halder, A., Shikha, D., **Adhikari, A.**, Ghosh, R., Singh, S., Adhikari T., Pal, S. K. (2020). Development of a Nano-sensor (FeNSOR) Based Device for Estimation of Iron ions in Biological and Environmental Samples. *IEEE Sensors Journal*, 20(3), 1268-1274. https://doi.org/10.1109/JSEN.2019.2947607

[16] **Adhikari, A.**,* Halder, A.,* Ghosh, R., Singh, S., Banerjee, A., Ghosh, N., Bhattacharya, A. M., Mandal, S., Chakrabarti, P., Bhattacharyya, D., Altass, H. M., Morad, M., Ahmed, S. A., Mallick A. K., Pal, S. K. (2020). Large scale Validation of a new Non-Invasive and Non-Contact Bilirubinometer in Neonates with risk factors. *Scientific Reports*, 10, 11149. [* These authors contributed equally] https://doi.org/10.1038/s41598-020-67981-9

[17] Singh, S., Halder, A., Sinha, O., Chakrabarty, N., Chatterjee, T., **Adhikari, A.**, Singh, P., Shikha, D., Ghosh, R., Banerjee, A., Mahapatra, P. D., Mandhar, A., Bhattacharyya, M., Bose, S., Ahmed, S. A., Alharbi, A., Hameed A. M., Pal, S. K. (2020). Spectroscopic Studies on the Biomolecular Recognition of Toluidine Blue: Key Information towards Development of a Non-Contact, Non-Invasive Device for Oral Cancer Detection. *Frontiers in Oncology*, 10, 2293. https://doi.org/10.3389/fonc.2020.529132

[18] Halder, A., Singh, S., **Adhikari, A.**, Singh, P., Sarkar, P., Pal, U., Ghosh, R., Shikha, D., Solanki, Y., Agarwal, M., Gupta, A. B., Chakraborty, R., Saha-Dasgupta, T., Das R., Pal, S. K. (2019). Selective and Fast Responsive Sensitized Micelle for Detection of Fluoride Level in Drinking Water. *ACS Sustainable Chemistry & Engineering*, 7(19), 16355-16363. https://doi.org/10.1021/acssuschemeng.9b03447

[19] **Adhikari, A.**,* Halder, A.,* Singh, S.,* Ghosh, S., Shikha, D., Saha, D., Chakraborty, R., Kundu, A., Tripathi, S. K., Pal, S. K. (2019). NaLiK, a Self-developed Device for Rapid, Reliable and Simultaneous Assessment of Sodium, Lithium and Potassium for Management of Fluid Balance and Bipolar Disorder in Human Subjects. *Journal of Analytical Atomic Spectrometry*, 34(9), 1875-1881.
[* These authors contributed equally]
https://doi.org/10.1039/C9JA00183B

[20] Halder, A., Banerjee, M., Singh, S., **Adhikari, A.**, Sarkar, P. K., Bhattacharya, A. M., Chakrabarti, P., Bhattacharyya, D., Mallick, A. K., Pal, S. K. (2019). A Novel Whole Spectrum-based Non-invasive Screening Device for Neonatal Hyperbilirubinemia. *IEEE Journal of Biomedical and Health Informatics*, 23(6), 2347-2353.
https://doi.org/10.1109/JBHI.2019.2892946

[21] Sarkar, P. K., Halder, A., **Adhikari, A.**, Polley, N., Darbar, S., Lemmens, P., Pal, S. K. (2018). DNA-based Fiber Optic Sensor for Direct In-vivo Measurement of Oxidative Stress. *Sensors and Actuators B: Chemical*, 255(2), 2194-2202.
https://doi.org/10.1016/j.snb.2017.09.029

[22] Singh, P., Choudhury, S., Dutta, S., **Adhikari, A.**, Bhattacharya, S., Pal, D., Pal, S. K. (2017). Ultrafast Spectroscopy on DNA-Cleavage by Endonuclease in Molecular Crowding. *International Journal of Biological Macromolecules*, 103, 395-402.
https://doi.org/10.1016/j.ijbiomac.2017.05.058

[23] Sarkar, P. K., Pal, S., Polley, N., Aich, R., **Adhikari, A.**, Halder, A., Chakrabarti, S., Chakrabarti, P., Pal, S. K. (2017). Development and Validation of a Noncontact Spectroscopic Device for Hemoglobin Estimation at Point-of-Care. *Journal of Biomedical Optics*, 22(5), 055006.
https://doi.org/10.1117/1.JBO.22.5.055006

[24] Polley, N., Saha, S., Singh, S., **Adhikari, A.**, Das, S., Choudhury, B. R., Pal, S. K. (2015). Development and Optimization of a Non-contact Optical Device for Online Monitoring of Jaundice in Human Subjects. *Journal of Biomedical Optics*, 20(6), 067001.
https://doi.org/10.1117/1.JBO.20.6.067001

[25] Bhattacharyya, N., Singh, S., Halder, A., **Adhikari, A.**, Ghosh, R., Shikha, D., Tripathi, S. K., Mallick, A. K., Mondal, P., Pal, S. K. (2021) An Energy-Resolved Optical Non-Invasive Device Detects Essential Electrolyte Balance in Humans at Point-of-Care. *Transactions of the Indian National Academy of Engineering*.
https://doi.org/10.1007/s41403-021-00204-3

Book Chapters

[1] Halder, A., Singh, S., **Adhikari, A.**, Sarkar, P. K., Pal, S. K. (2019). Development of Spectroscopy-based Medical Devices for Disease Diagnosis in Low Resource Point of Care Setting. In K. Pal, H-B. Kraatz, A. Khasnobish, S. Bag, I. Banerjee, U. Kuruganti (Eds.), *Bioelectronics and Medical Devices* (pp. 483-492). Cambridge, UK: Woodhead Publishing (ELSEVIER).

Peer-reviewed Conference Publication

[1] Mondal, S., **Adhikari, A.**, Singh, M., Ghosh, R., Goswami, M., Biswas, P., Pal, S. K. (2020). Spectroscopic Study on the Interaction of Co^{2+} with Citrate-Mn_3O_4: Towards the Development of Nanotherapy against Cobalt Toxicity. *Materials Today: Proc.*, (In Press).
https://doi.org/10.1016/j.matpr.2020.10.981

[2] Biswas, P., **Adhikari, A.**, Mondal, S., Das, M., Bhattacharya, S. S., Pal, D., Choudhury, S. S., S. K. Pal, (2020). Synthesis and Spectroscopic Characterization of a Zinc Oxide-Polyphenol Nanohybrid from Natural Resources for Enhanced Antioxidant Activity with Less Cytotoxicity. Materials Today: Proc., (In Press)
https://doi.org/10.1016/j.matpr.2020.09.567

[3] **Adhikari, A.**, Mondal, S., Pal, S. K. (2019). Nano Sized Mn_3O_4 Can Treat Hepatic Fibrosis: Alteration in Route of Administration Gives a New Twist to the Tale. *Journal of Gastroenterology and Hepatology (Suppl. 3)*, 34, 68
https://doi.org/10.1111/jgh.14859

[4] S. S. Bhattacharya, **A. Adhikari**, D. Pal. (Eds.) (2017). *Proceedings of Workshop on Advanced Nano Therpeutics (WANT)*. Kolkata, India: Uluberia College Publication Dept.

Patents Filed

[1] Bayan, S., **Adhikari, A.**, Pal, U., Saha-Dasgupta, T., Ray, S. K., Pal, S. K. (2020). Development of Tribo-electroceutical Fabric for Potential Application in Self Sanitizing Personal Protective Equipment (PPE). Patent Ref. No.- 202031038150; Patent Application No.- TEMP/E-1/42583/2020-KOL.

[2] **Adhikari, A.**, Bayan, S., Pal, U., Saha-Dasgupta, T., Ray, S. K., Pal, S. K. (2020). A Nanoceutical Fabric for Source Control to Prevent COVID-19 Spread Including through Expelled Respiratory Droplets, Patent Ref. No.- 202031038152; Patent Application No.- TEMP/E-1/42574/2020-KOL.

The first 11 publications (Sl. No. [1] – [11]) are included in the thesis.

List of International and National Conferences Attended

[1] Discussion Leader at '*Gordon Research Seminar-Oxygen Radicals 2020*', Ventura, USA on 2nd February, 2020.

[2] Poster presentation at '*Gordon Research Conference-Oxygen Radicals 2020*', Ventura, USA on 2nd–7th February, 2020.

[3] Discussion Leader at '*Gordon Research Seminar-Clusters and Nanostructures 2019*', Switzerland on 15th June, 2019.

[4] Oral presentation at '*APDW-2019*' organized by Asian Pacific Digestive Week Federation held at Kolkata, India on 10-12 December, 2019. (Poster of Distinction Award)

[5] Poster presentation at '*Gordon Research Conference-Clusters and Nanostructures 2019*', Switzerland on 16-21st June, 2019.

[6] Poster presentation delivered in Conference '*Paris Redox-2019*' held at University Pierre and Marie Curie, Paris, France on 20th June- 21st June, 2019.

[7] Poster presentation delivered in Conference on '*Ultrafast Science- 2015*' held at SN Bose National Centre for Basic Sciences, India on 9th November- 21st November, 2015. (Best Poster Award)

[8] Poster presentation delivered in Conference on '*International Conference on Nanoscience and Technology (ICONSAT 2016)*' held at Indian Institute of Science Education and Research, Pune, India on 29th February-2nd March, 2016.

[9] Oral presentation delivered at '*Bose Fest-2019*', SN Bose National Centre for Basic Sciences, India on 20th February, 2019. (Best oral presentation award)

[10] Poster presentation delivered at '*Bose Fest-2016*', SN Bose National Centre for Basic Sciences, India on 31st March, 2017.

[11] Poster presentation delivered at '*Bose Fest-2017*', SN Bose National Centre for Basic Sciences, India on 8th March, 2018.

[12] Workshop Instructor at '*Workshop on Advanced Nanotherapeutics 2017 (WANT 2017)*' organized by BOOST Biotechnology Lab, Uluberia College, India on 10-11th March, 2017.

[13] Poster presentation delivered in Conference on '*International Conference on Nanoscience and Technology (ICONSAT 2018)*' held at Indian Institute of Science, Bangalore, India on 21st March- 23rd March, 2018.

[14] Oral Presentation at '*National Conference on Nanotechnology in Medicine-2017*' organized by Chettinad Academy of Research and Education, India (2017). (Best Oral Presentation Award)

[15] Oral Presentation at '*7th Masterclass in Liver Diseases (MCLD) 2017*' organized by Institute of liver Disease and Transplantation (ILDT), Gleneagles Global Hospitals, Chennai, India (2017). (Best Abstract Award)

[16] Oral Presentation at '*NanoBioCon 2016*' organized by Institute of Electrical and Electronics Engineers (IEEE) and Maulana Abul Kalam Azad University of Technology (MAKAUT; formerly WBUT), India (2016).(Best Oral Presentation Award)

[17] Oral Presentation at '*Nanochallenge 2017*' organized by Suny Polytechnic Institute, New York, USA and PSG Institute of Advanced Studies, Coimbatore, India (2018). (Winner)

[18] Invited talk at '*International Conference on Biomedical Science and Instrumentation 2016 (ICBSI -2016)*' organized by University of Calcutta, India (2016).